SERIES EDITOR: AKHLESH LAKHTAKIA

ALL-DIELECTRIC NANOPHOTONICS

EDITED BY
ALEXANDER S. SHALIN, ADRIÀ CANÓS VALERO,
ANDREY MIROSHNICHENKO

ELSEVIER

NANOPHOTONICS SERIES

ALL-DIELECTRIC NANOPHOTONICS

This page intentionally left blank

Nanophotonics Series

ALL-DIELECTRIC NANOPHOTONICS

Edited by

ALEXANDER S. SHALIN

ADRIÀ CANÓS VALERO

ANDREY MIROSHNICHENKO

Series Editor

AKHLESH LAKHTAKIA

ELSEVIER

Elsevier
Radarweg 29, PO Box 211, 1000 AE Amsterdam, Netherlands
The Boulevard, Langford Lane, Kidlington, Oxford OX5 1GB, United Kingdom
50 Hampshire Street, 5th Floor, Cambridge, MA 02139, United States

Copyright © 2024 Elsevier Ltd. All rights reserved.

No part of this publication may be reproduced or transmitted in any form or by any means, electronic or mechanical, including photocopying, recording, or any information storage and retrieval system, without permission in writing from the publisher. Details on how to seek permission, further information about the Publisher's permissions policies and our arrangements with organizations such as the Copyright Clearance Center and the Copyright Licensing Agency, can be found at our website: www.elsevier.com/permissions.

This book and the individual contributions contained in it are protected under copyright by the Publisher (other than as may be noted herein).

Notices

Knowledge and best practice in this field are constantly changing. As new research and experience broaden our understanding, changes in research methods, professional practices, or medical treatment may become necessary.

Practitioners and researchers must always rely on their own experience and knowledge in evaluating and using any information, methods, compounds, or experiments described herein. In using such information or methods they should be mindful of their own safety and the safety of others, including parties for whom they have a professional responsibility.

To the fullest extent of the law, neither the Publisher nor the authors, contributors, or editors, assume any liability for any injury and/or damage to persons or property as a matter of products liability, negligence or otherwise, or from any use or operation of any methods, products, instructions, or ideas contained in the material herein.

ISBN: 978-0-323-95195-1

For information on all Elsevier publications
visit our website at https://www.elsevier.com/books-and-journals

Publisher: Matthew Deans
Acquisitions Editor: Ana Claudia Garcia
Editorial Project Manager: Soumya Yadav
Production Project Manager: Sharmila Kirouchenadassou
Cover Designer: Matthew Limbert

Typeset by VTeX

Contents

This page intentionally left blank

List of contributors

Alexander A. Antonov
Shubnikov Institute of Crystallography, FSRC "Crystallography and Photonics", Russian Academy of Sciences, Moscow, Russia

Viktoriia E. Babicheva
Department of Electrical and Computer Engineering, University of New Mexico, Albuquerque, NM, United States

Angela Barreda Gomez
Institute of Solid State Physics, Friedrich Schiller University Jena, Jena, Germany
Institute of Applied Physics, Abbe Center of Photonics, Friedrich Schiller University Jena, Jena, Germany
Group of Displays and Photonics Applications, Carlos III University of Madrid, Madrid, Spain

Ayesheh Bashiri
Institute of Solid State Physics, Friedrich Schiller University Jena, Jena, Germany
Institute of Applied Physics, Abbe Center of Photonics, Friedrich Schiller University Jena, Jena, Germany

Igal Brener
Center for Integrated Nanotechnologies, Sandia National Laboratories, Albuquerque, NM, United States
Sandia National Laboratories, Albuquerque, NM, United States

Evgeny Bulgakov
Kirensky Institute of Physics, Federal Research Center KSC SB RAS, Krasnoyarsk, Russia

Rocio Camacho Morales
ARC Centre of Excellence for Transformative Meta Optical Systems (TMOS), Research School of Physics, Australian National University, Canberra, ACT, Australia

Andrey B. Evlyukhin
Institute of Quantum Optics, Leibniz Universität Hannover, Hannover, Germany
Cluster of Excellence PhoenixD, Leibniz Universität Hannover, Hannover, Germany

Kebin Fan
School of Electronic Science and Engineering, Nanjing University, Nanjing, Jiangsu, China

Andrea Fratalocchi
PRIMALIGHT, Faculty of Electrical and Computer Engineering, Applied Mathematics and Computational Science, King Abdullah University of Science and Technology (KAUST), Thuwal, Saudi Arabia

Maxim V. Gorkunov
Shubnikov Institute of Crystallography, FSRC "Crystallography and Photonics", Russian Academy of Sciences, Moscow, Russia

Jeeyoon Jeong
Department of Physics and Institute of Quantum Convergence Technology, Kangwon National University, Gangwon, Republic of Korea

Mikhail F. Limonov
School of Physics and Engineering, ITMO University, St. Petersburg, Russia
Ioffe Institute, St. Petersburg, Russia

Sergey Makarov
Qingdao Innovation and Development Center, Harbin Engineering University, Qingdao, China
ITMO University, Saint Petersburg, Russia

Andrey Miroshnichenko
School of Engineering and Information Technology, University of New South Wales, Canberra, ACT, Australia

Dragomir Neshev
ARC Centre of Excellence for Transformative Meta Optical Systems (TMOS), Research School of Physics, Australian National University, Canberra, ACT, Australia

Andrey V. Novitsky
Department of Theoretical Physics and Astrophysics, Belarusian State University, Minsk, Belarus
ITMO University, St. Petersburg, Russia

Denis V. Novitsky
B.I. Stepanov Institute of Physics, National Academy of Sciences of Belarus, Minsk, Belarus

Willie J. Padilla
Department of Electrical and Computer Engineering, Duke University, Durham, NC, United States

Artem Pilipchuk
Kirensky Institute of Physics, Federal Research Center KSC SB RAS, Krasnoyarsk, Russia

Mohsen Rahmani
Advanced Optics & Photonics Laboratory, Nottingham Trent University, Nottingham, United Kingdom

Almas Sadreev
Kirensky Institute of Physics, Federal Research Center KSC SB RAS, Krasnoyarsk, Russia

Kirill B. Samusev
School of Physics and Engineering, ITMO University, St. Petersburg, Russia
Ioffe Institute, St. Petersburg, Russia

Alexander S. Shalin
Center for Photonics and 2D Materials, Moscow Institute of Physics and Technology, Dolgoprudny, Russia

Nikolay S. Solodovchenko
School of Physics and Engineering, ITMO University, St. Petersburg, Russia

Isabelle Staude
Institute of Solid State Physics, Friedrich Schiller University Jena, Jena, Germany
Institute of Applied Physics, Abbe Center of Photonics, Friedrich Schiller University Jena, Jena, Germany

Juan Sebastian Totero Gongora
Emergent Photonics Research Centre, Dept. of Physics, Loughborough University, Loughborough, England, United Kingdom
Emergent Photonics (EPic) Lab, Dept. of Physics and Astronomy, University of Sussex, Falmer, England, United Kingdom

Adrià Canós Valero
Institute of Physics, University of Graz, and NAWI Graz, Graz, Austria

Lei Xu
Advanced Optics & Photonics Laboratory, Nottingham Trent University, Nottingham, United Kingdom

Khosro Zangeneh Kamali
ARC Centre of Excellence for Transformative Meta Optical Systems (TMOS), Research School of Physics, Australian National University, Canberra, ACT, Australia

George Zograf
Chalmers University of Technology, Gothenburg, Sweden

1

Introduction

Andrey Miroshnichenko
School of Engineering and Information Technology, University of New South Wales, Canberra, ACT, Australia

All-dielectric nanophotonics is an emerging field that studies light-matter interactions at the nanoscale using high refractive index dielectric materials, which can manipulate light with unprecedented precision and efficiency. One of the most important applications of all-dielectric nanophotonics is the design and fabrication of metasurfaces, which are two-dimensional arrays of nanostructures that can control the phase, polarization, amplitude, and direction of light with subwavelength resolution. Metasurfaces have attracted considerable attention due to their potential to enable a wide range of advanced photonic devices, such as flat lenses, holograms, optical filters, and sensors, with high efficiency and compact size. Therefore, all-dielectric nanophotonics and metasurfaces play a crucial role in the development of next-generation optoelectronic technologies, making them suitable for a wide range of applications such as sensing, imaging, communication, and energy harvesting.

One of the fundamental characteristics of metasurfaces is wavefront control, which refers to altering the transmitted and/or reflected light by spatially modifying the metasurface properties, allowing for beam focusing, beam deflection, and holographic projections. Polarization control uses anisotropic meta-atoms to adjust the polarization of light waves, allowing for subwavelength polarization control in polarimetry and polarization imaging. Emission control, which includes adjusting the rate of spontaneous emission processes by Purcell enhancement, enables brighter LEDs, lasing action, and nonlinear frequency conversions. Managing the quantum qualities of light for novel quantum applications comprises increasing the generation of light with quantum properties, altering quantum states, and manipulating the state of quantum light once it is formed. Furthermore, detection control improves light absorption in ultra-thin layers, which can then be converted into heat, photocurrent, or hot carriers for plasmonic-enhanced photo thermoelectric conversion.

All-Dielectric Nanophotonics. https://doi.org/10.1016/B978-0-32-395195-1.00006-5
Copyright © 2024 Elsevier Ltd. All rights reserved.

All-dielectric metasurfaces are nanostructured surfaces with significant interaction with light, allowing for extraordinary miniaturization of optical components and unprecedented control over light wavefront, emission, and absorption. For more than a decade, the notion of meta-optics, based on metasurfaces, has been an active area of research, motivated by the need for advanced-vision technologies that necessitate completely new techniques for smart and miniaturized optical systems. By permitting the engineering of light's hidden qualities, such as phase, polarization, and angular momentum at the nanoscale, meta-optics provides a potential approach for developing sophisticated machine vision. Over the last ten years, the field of meta-optics has grown exponentially, with over 160 research groups working in the field worldwide. The development of metasurface-based devices with expanded functions, such as flat metalenses, polarization imaging, microscopy, and biosensing, has resulted in the formation of multiple startup companies, proving the technology's commercial viability. Meta-optical systems offer previously unimaginable applications such as the Internet of Things (IoT), self-driving cars, artificial intelligence (AI), wearable gadgets, augmented reality (AR), and remote sensing. The most significant driving force for the discipline is the incorporation of meta-optical elements and devices into optical systems, which provides prospects for extremely miniaturized consumer optoelectronics.

The Kerker effect, which is the phenomenon of the preferential scattering of light in a specific direction employing anisotropic scatterers, is one of the main elements of ADMs that enable their key capabilities. The Kerker effect has crucial implications for optical manipulation, sensing, and communication because it allows for high-efficiency and low-loss directional control of light. Recently, researchers have looked at using multipolar interference in ADMs to boost the Kerker effect and obtain more efficient and robust control over dispersed light. Multipolar interference is the interaction of different orders of multipole modes in scatterers, which can result in higher-order resonances and more complicated scattering patterns. This method has shown promise in producing more versatile and tunable ADMs with increased performance and functionality.

There has been progress in all-dielectric metasurfaces that enable high-Q resonances and bound states in the continuum (BICs) throughout the last decade. High-Q resonances allude to ADMs' capacity to confine light for an extended length of time, resulting in improved light-matter interactions and sensitivity. BICs, on the other hand, are a high-Q resonance that occurs due to mode interference in the ADMs and can result in complete suppression

of scattering in a specific frequency band. To create high-Q resonances and BICs, several ADM designs, such as photonic crystal slabs, nanopillars, and Mie resonators, have been used. New fabrication techniques such as electron beam lithography and focused ion beam milling have been adopted to generate increasingly complicated and accurate structures. Recent advances in high-Q ADMs and BICs have created new opportunities to achieve strong light-matter interactions and realize advanced optical functionalities. This has led to a variety of practical applications of high-Q ADMs and BICs, such as improving the sensitivity and selectivity of biochemical sensing, high-performance filtering, and lasing devices.

Nonlinear metasurfaces based on resonance effects are an intriguing new area in ADMs research with the potential to provide a new generation of extremely efficient and tunable nonlinear optical devices. Nonlinear materials respond to light intensity and can thus be used to change the parameters of ADMs actively. By incorporating nonlinear materials into the ADM design, tunable and efficient nonlinear optical phenomena, such as second harmonic generation, sum and difference frequency generation, and four-wave mixing, are made possible. Because of the improved light-matter interactions, the resonant nature of ADMs can considerably improve nonlinear optical response. The employment of high-Q resonant modes in ADMs, in particular, can greatly boost nonlinear conversion efficiency. This is known as nonlinear Fano resonance and occurs when the nonlinear process is accelerated by the interference between the resonant and non-resonant modes in the ADMs. Nonlinear metasurfaces based on resonance effects have significant implications for a variety of applications, including all-optical switching, frequency conversion, and high-speed, low-power optical signal processing. Nonlinear metasurfaces can also be utilized to generate new light frequencies, allowing the realization of novel optical sources and detectors.

Another interesting class of all-dielectric metasurfaces that has recently received a lot of attention are perfect absorbers. Perfect absorbers are metasurfaces that absorb all incident light at a certain frequency or range of frequencies, while reflecting little or no light at other frequencies. Perfect absorbers often consist periodic array of dielectric resonators or nanopillars that interact with incoming light to convert it to heat. Perfect absorbers have numerous applications, including energy harvesting, thermal imaging, and sensing. Perfect absorbers, for example, can boost solar cells' efficiency by absorbing more incident light and converting it into electricity.

Furthermore, by selectively absorbing light at specific wavelengths, perfect absorbers can improve the sensitivity and resolution of thermal imaging systems. Recent perfect absorber research has concentrated on improving their performance and utility through the use of sophisticated materials like graphene and transition metal dichalcogenides, as well as novel production techniques like nanoimprint lithography and roll-to-roll processing. Furthermore, using multipolar interference and Fano resonances in perfect absorbers enabled higher absorption efficiencies and tunable spectral selectivity.

Recent developments in all-dielectric metasurfaces have paved the way for new research areas in strong-coupling effects and chiral effects, which could lead to novel applications in quantum optics, sensing, and photonics. Strong-coupling effects are interactions at the quantum level between the electromagnetic field and matter that can produce hybrid states known as polaritons. Strong-coupling effects in all-dielectric metasurfaces can be achieved by coupling the metasurface's resonances with a quantum emitter such as a quantum dot or organic molecule, with potential applications in quantum information processing, sensing, and nonlinear optics. The interaction of light with chiral materials, which display asymmetry in their response to left- and right-circularly polarized light, is referred to as chiral effects. All-dielectric metasurfaces with strong chiral effects can be developed and employed for optical rotation, circular dichroism, and selective chiral sensing. Recent chiral metasurface research has concentrated on achieving high-quality chiral responses and comprehending the underlying physical principles.

It should be noted that tremendous development in the design, manufacture, and characterization of ADMs has been made. High-efficiency metasurfaces for polarization control, beam shaping, and wavefront engineering, for example, have been demonstrated employing a variety of dielectric materials, including silicon, germanium, gallium arsenide, titanium dioxide, and aluminum oxide. These metasurfaces have demonstrated extraordinary performance in terms of their ability to precisely modify the phase of light, which is crucial for obtaining high-quality imaging and sensing. ADMs have also been utilized to improve light absorption in thin-film solar cells and the efficiency of light-emitting diodes. Another significant advancement in ADM research is using nonlinear dielectric materials to create tunable and active metasurfaces, allowing for all-optical modulation and switching of light using ADM. Importantly, the combination of ADMs and plasmonic structures has resulted in the development of hybrid

metasurfaces with high field enhancement as well as strong light-matter interactions.

This page intentionally left blank

2

Theoretical background

Adrià Canós Valero[a] **and Alexander S. Shalin**[b]
[a] *Institute of Physics, University of Graz, and NAWI Graz, Graz, Austria.*
[b] *Center for Photonics and 2D Materials, Moscow Institute of Physics and Technology, Dolgoprudny, Russia*

2.1 Maxwell's equations

Consider a cavity embedded in free space, represented by a discontinuity in the dielectric permittivity $\Delta\varepsilon(\mathbf{r}) = \varepsilon(\mathbf{r}) - \varepsilon_0$, where $\varepsilon(\mathbf{r})$ is the permittivity of the cavity. Under the assumption that all fields are time-harmonic with the form $e^{-i\omega t}$ (this convention will be used throughout the chapter), the differential forms of the macroscopic curl Maxwell's equations read [1]:

$$\nabla \times \mathbf{E}(\mathbf{r};\omega) = \mathrm{i}\omega\mu_0\mathbf{H}(\mathbf{r};\omega), \tag{2.1}$$

$$\nabla \times \mathbf{H}(\mathbf{r};\omega) = -\mathrm{i}\omega\varepsilon(\mathbf{r})\mathbf{E}(\mathbf{r};\omega) + \mathbf{j}(\mathbf{r};\omega). \tag{2.2}$$

$\mathbf{j}(\mathbf{r};\omega)$ is the impressed current source generating the incident field, which can be potentially located at infinity in the case of a plane wave. From now on, the spatial dependence of the permittivity will be omitted for brevity. By making the substitution $\varepsilon = \varepsilon_0 + \Delta\varepsilon$ and rearranging, we write:

$$\nabla \times \mathbf{E}(\mathbf{r};\omega) = \mathrm{i}\omega\mu_0\mathbf{H}(\mathbf{r};\omega), \tag{2.3}$$

$$\nabla \times \mathbf{H}(\mathbf{r};\omega) = -\mathrm{i}\omega\varepsilon_0\mathbf{E}(\mathbf{r};\omega) + \mathbf{j}(\mathbf{r};\omega) - \mathrm{i}\omega\mathbf{P}(\mathbf{r};\omega), \tag{2.4}$$

with the *equivalent* polarization current $\mathbf{P}(\mathbf{r};\omega) = \Delta\varepsilon\mathbf{E}(\mathbf{r};\omega)$.

2.2 General concepts of scattering theory

The main problem that we will be dealing with in this book is illustrated in Fig. 2.1. In general, we will consider an incident wave interacting with one or more dielectric nanocavities. The latter will interact with the incident field and absorb or redirect the electromagnetic energy. Imagine that we place a detector D downstream from the particles. In the absence of them, the detector receives an input power P_b^D, corresponding to the integral of

All-Dielectric Nanophotonics. https://doi.org/10.1016/B978-0-32-395195-1.00007-7
Copyright © 2024 Elsevier Ltd. All rights reserved.

the Poynting vector of the incident field, $\mathbf{S}_b$, over the cross section of D:

$$P_b^D = -\int_{\partial D} \mathbf{S}_b \cdot \hat{\mathbf{n}}_A dA. \tag{2.5}$$

In the above, $\hat{\mathbf{n}}_A$ is a unit vector pointing upward, as shown in Fig. 2.1. In the presence of the particles, the Poynting vector is modified and D receives less power, P^D. This phenomenon is called *extinction*.

Let us now consider the general solution of Maxwell's equations for this case. The solution to Eqs. (2.3) can be formed via the Green's function approach [2,3] as a Fredholm integral equation of the second kind, or *Lippmann-Schwinger* equation:

$$\begin{aligned}\mathbf{E}(\mathbf{r};\omega) = &\underbrace{i\omega \int_{V_b} \bar{\bar{G}}_b\left(\mathbf{r},\mathbf{r}';\omega\right)\mathbf{j}\left(\boldsymbol{r}';\omega\right)d^3\boldsymbol{r}'}_{\text{Incident Field, } \mathbf{E}_b(\mathbf{r};\omega)} \\ &+\underbrace{\omega^2 \int_{V_s} \bar{\bar{G}}_b\left(\mathbf{r},\mathbf{r}';\omega\right)\mathbf{P}\left(\boldsymbol{r}';\omega\right)d^3\boldsymbol{r}'}_{\text{Scattered Field, } \mathbf{E}_s(\mathbf{r};\omega)},\end{aligned} \tag{2.6}$$

where the first integral on the right-hand side runs over the volume containing $\mathbf{j}(\mathbf{r};\omega)$, V_b, and the second integral is carried over the volume of the scatterer V_s. $\mathbf{E}_b(\mathbf{r};\omega)$ is an homogeneous solution to Maxwell's equations with $\Delta\varepsilon = 0$ (in the absence of the scatterer). $\mathbf{E}_s(\mathbf{r};\omega)$ is the *scattered* field generated by the polarization currents induced in the cavity. We say that the total field can be expressed as the sum of the *scattered* and *incident* fields. The main task of the scattering problem is to determine the scattered field, given some pre-specified incident field.

The Green's function $\bar{\bar{G}}_b\left(\mathbf{r},\mathbf{r}';\omega\right)$ is sometimes referred to as the electromagnetic propagator. Physically, it can be represented as a 3×3 matrix, where every column corresponds to the electric field radiated at $\mathbf{r}$ by point electric dipole sources oriented along x, y and z, respectively, located at $\mathbf{r}'$. In a homogeneous environment, for $\mathbf{r}\notin V_s$, it has the form:

$$\bar{\bar{G}}_b^N\left(\mathbf{r},\mathbf{r}'\right) = \left(-\mathbf{I} + 3\hat{\mathbf{n}}_R\otimes\hat{\mathbf{n}}_R\right)\mu_0\frac{e^{ikR}}{4\pi k^2R^3}, \tag{2.7}$$

$$\bar{\bar{G}}_b^I\left(\mathbf{r},\mathbf{r}'\right) = \left(\mathbf{I} - 3\hat{\mathbf{n}}_R\otimes\mathbf{n}_R\right)\mu_0\frac{ie^{ikR}}{4\pi kR^2}, \tag{2.8}$$

$$\bar{\bar{G}}_b^F\left(\mathbf{r},\mathbf{r}'\right) = \left(\mathbf{I} - \hat{\mathbf{n}}_R\otimes\hat{\mathbf{n}}_R\right)\mu_0\frac{e^{ikR}}{4\pi R}, \tag{2.9}$$

for the near, intermediate, and far field regions, respectively. In the above, $\mathbf{R} = \mathbf{r} - \mathbf{r}'$ and $\hat{\mathbf{n}}_R = \mathbf{R}/R$.

Both terms on the right-hand side of Eq. (2.6) are solutions to Maxwell's equations. By making the replacement $\mathbf{E} = \mathbf{E}_b + \mathbf{E}_s$ in Eq. (2.1), and subtracting the homogeneous solution in free space, Maxwell's equations can be rewritten to solve for the scattered field:

$$\nabla \times \mathbf{E}_s(\mathbf{r};\omega) = \mathrm{i}\omega\mu_0 \mathbf{H}_s(\mathbf{r};\omega), \tag{2.10}$$

$$\nabla \times \mathbf{H}_s(\mathbf{r};\omega) = -\mathrm{i}\omega\varepsilon(\mathbf{r})\mathbf{E}_s(\mathbf{r};\omega) - \mathrm{i}\omega\Delta\varepsilon(\mathbf{r})\mathbf{E}_b(\mathbf{r};\omega), \tag{2.11}$$

which shows that the scattered field corresponds to the fields generated by the source $\mathbf{J}_s(\mathbf{r};\omega) = -\mathrm{i}\omega\Delta\varepsilon\mathbf{E}_b(\mathbf{r};\omega)$.

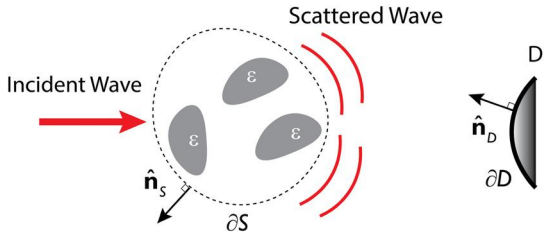

Figure 2.1. The scattering problem. An incident wave impinges on a collection of scatterers with permittivity ε, producing a scattered field. The intensity downstream in the direction of propagation is then recorded by a detector D.

The most common experimental figures of merit of the scattering process are the extinction, absorption and scattering *cross sections*. These are determined by performing an energy balance around a surface ∂S enclosing the particles, like the one shown in Fig. 2.1. The energy Q accumulated inside ∂S per unit time must be equal to the incoming minus the outgoing energy, so that

$$\frac{dQ}{dt} = -\int_{\partial S} \mathbf{S}\cdot\hat{\mathbf{n}}_A dA. \tag{2.12}$$

Note that, in the absence of gain, energy inside ∂S can only be constant or decrease with time. Therefore, dQ/dt is nothing more than the absorption power, P_a. The time-averaged Poynting vector is defined as $\mathbf{S} = \frac{1}{2}\mathrm{Re}(\mathbf{E}\times\mathbf{H}^*)$. However, the total electric and magnetic fields can be decomposed into scattered and incident fields. After this step, $\mathbf{S}$ can be rewritten as:

$$\mathbf{S} = \frac{1}{2}\mathrm{Re}(\mathbf{E}_b\times\mathbf{H}_b^*) + \frac{1}{2}\mathrm{Re}(\mathbf{E}_s\times\mathbf{H}_s^*) + \frac{1}{2}\mathrm{Re}(\mathbf{E}_b\times\mathbf{H}_s^* + \mathbf{E}_s\times\mathbf{H}_b^*).$$

We identify three contributions: from left to right, the first corresponds to the incident Poynting vector, the second is the scattered

Poynting vector, and the third mixes the incident and scattered fields. Integrating over ∂S, the first term gives 0 (since the incident field enters and leaves ∂S), the second yields *minus* the scattered power, $-P_s$, and we define the third term as the extinction power P_{ext}. After rearranging, we have:

$$P_{\text{ext}} = P_a + P_s. \tag{2.13}$$

Hence, the extinction power is the sum of the absorbed and scattered powers from the ensemble of particles. To render these quantities independent of the magnitude of the incident field, we normalize them by the incident field intensity I_b. In SI units, I_b is in W/m^2 while the powers are in W. The resulting quantities have the units of m^2:

$$\sigma_{\text{ext}} = \sigma_a + \sigma_s. \tag{2.14}$$

These are, from left to right, the extinction, absorption and scattering cross sections. By making use of the conjugated form of the reciprocity theorem, we can derive a more convenient expression for σ_{ext} [4]:

$$\sigma_{\text{ext}} = \frac{1}{2}\,\text{Re}\left(\int_{V_s} \mathbf{E}_b \cdot \mathbf{J}^* dV\right), \tag{2.15}$$

where the extinction can now be recovered with an integral over the scatterer volume. The integrand contains the induced current $J = -i\omega\Delta\varepsilon\mathbf{E}$.

2.3 Multipole decompositions

Multipoles are a central tool in the analysis and design of nanophotonic devices. They allow a deeper understanding of their behavior as well as physically intuitive explanations of important phenomena such as directional scattering, anapoles, or the transverse Kerker effect. In essence, a multipole decomposition consists in expanding some quantity of interest, e.g., the scattered electromagnetic fields, into a set of independent contributions. Often, however, one can find in the literature two approaches for performing the multipole decomposition, as shown in Fig. 2.2.

On the one hand, it is customary to perform a Taylor Series Expansion (TSE) of the induced current or the vector potential [5]. Within such approach, four kinds of terms are usually identified: electric, magnetic, magnetic Mean Square Radii (MSR), toroidal and toroidal MSR. The currents associated with the electric, toroidal and toroidal MSR all radiate fields such that $\mathbf{r} \cdot \mathbf{H} = 0$,

where $\mathbf{r}$ is a radial vector. These kinds of fields are usually termed transverse magnetic or *electric*. Oppositely, magnetic moments and magnetic MSR radiate with fields such that $\mathbf{r} \cdot \mathbf{E} = 0$, called transverse electric or *magnetic*.

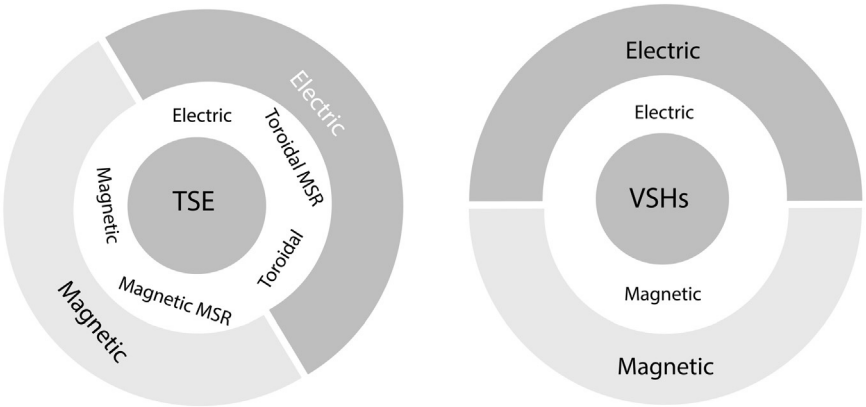

Figure 2.2. The multipole 'zoo'. This figure summarizes the differences and similarities between the two multipole expansions of the electromagnetic field radiated by a source. The inner white wheels show the types of multipoles that are identified in the expansions. The exterior wheel classifies the multipoles of the inner wheel into the two possible types of electromagnetic radiation in free space, i.e., electric or magnetic. More details can be found in the text.

On the other hand, it is also possible to directly expand the electromagnetic fields outside the source as a linear combination of transverse Vector Spherical Harmonic functions (VSHs), which fulfill either $\mathbf{r} \cdot \mathbf{H} = 0$ or $\mathbf{r} \cdot \mathbf{E} = 0$. Unlike the first approach, the VSH expansion yields only two kinds of moments: electric or magnetic, having a one-to-one relation with the electric or magnetic nature of the radiated fields. While the second approach is well documented in the literature, there are few textbooks discussing the TSE in detail. We dedicate this section to extensively discuss the origin of both expansions, present an approach to easily visualize multipoles, introduce the concept of toroidal multipoles, and examine the relation between the TSE and VSH expansions.

2.3.1 Taylor series expansion

Consider a dielectric material that has been polarized by some external electromagnetic field. The total polarization current is the sum over the contributions of all the microscopic currents in the object. Hence, we can write [5,6]:

$$\mathbf{P}(\mathbf{r}) = \int_{V_s} \mathbf{P}(\mathbf{r}')\delta(\mathbf{r} - \mathbf{r}')dV', \tag{2.16}$$

where V_s denotes the volume of the object (scatterer), under consideration and $\delta(\mathbf{r}-\mathbf{r}')$ is the Dirac delta distribution in three dimensions. To obtain the TSE, we expand $\delta(\mathbf{r}-\mathbf{r}')$ in a Taylor series over a point $\mathbf{r}_0$, which is typically chosen to be the center of charge:

$$\delta(\mathbf{r}-\mathbf{r}_0-\Delta r) \approx \delta(\mathbf{r}-\mathbf{r}_0) - (\Delta\mathbf{r}\cdot\nabla)\delta(\mathbf{r}-\mathbf{r}_0) + \frac{1}{2}(\Delta\mathbf{r}\cdot\nabla)^2\delta(\mathbf{r}-\mathbf{r}_0) + O(\Delta\mathbf{r}^3). \quad (2.17)$$

Inserting Eq. (2.17) in Eq. (2.16), we get:

$$\mathbf{P}(\mathbf{r}') \approx \int_{V_s} \mathbf{P}(\mathbf{r}')\delta(\mathbf{r}-\mathbf{r}_0)dV' - \int_{V_s} \mathbf{P}(\mathbf{r}')(\Delta\mathbf{r}\cdot\nabla)\delta(\mathbf{r}-\mathbf{r}_0)dV' + \frac{1}{2}\int_{V_s} \mathbf{P}(\mathbf{r}')(\Delta\mathbf{r}\cdot\nabla)^2\delta(\mathbf{r}-\mathbf{r}_0)dV'. \quad (2.18)$$

Starting from Eq. (2.18), we will now show how to retrieve expressions for the first multipoles. In particular, the zeroth-order contribution corresponds to the electric dipole (ED) contribution, the first-order term gives rise to magnetic dipole (MD) and electric quadrupole (EQ) moments, and the second-order term results in the electric octupole (EO) and magnetic quadrupole (MQ). Consider the expression $\mathbf{P}(\mathbf{r}')(\Delta\mathbf{r}\cdot\nabla)$ appearing in the integrand of the first-order term. For clarity, from now on we will omit the arguments in the polarization and the delta distribution, and we will only state them when they can arise confusion. Using the identity:

$$\mathbf{a}\times(\mathbf{b}\times\mathbf{c}) = \mathbf{b}(\mathbf{a}\cdot\mathbf{c}) - \mathbf{c}(\mathbf{a}\cdot\mathbf{b}), \quad (2.19)$$

with $\mathbf{a}=\nabla\delta$, $\mathbf{b}=\Delta\mathbf{r}$, $\mathbf{c}=\mathbf{P}$, we rearrange it as:

$$\nabla\delta\times(\Delta\mathbf{r}\times\mathbf{P}) = \Delta\mathbf{r}(\mathbf{P}\cdot\nabla\delta) - \mathbf{P}(\nabla\delta\cdot\Delta\mathbf{r}). \quad (2.20)$$

It is instructive to regard at the terms in Eq. (2.20) making use of Einstein's summation convention. In particular, we see that we have terms of the form $\mathbf{a}(\mathbf{b}\cdot\mathbf{c}) \to a_i(b_jc_j)$. In this notation, we immediately see that we can rearrange them as $a_i(b_jc_j) = (a_ib_j)c_j$, which in vector form can be written as $\mathbf{a}\otimes\mathbf{b}\cdot\mathbf{c}$, where the symbol $\otimes$ stems for outer product. Therefore, we have the identity $\mathbf{a}(\mathbf{b}\cdot\mathbf{c}) = \mathbf{a}\otimes\mathbf{b}\cdot\mathbf{c}$. Using this fact, and adding and subtracting $\mathbf{P}(\Delta\mathbf{r}\cdot\nabla)$, we can rewrite Eq. (2.20) as:

$$\nabla\delta\times(\Delta\mathbf{r}\times\mathbf{P}) = \Delta\mathbf{r}(\mathbf{P}\cdot\nabla\delta) + \mathbf{P}(\nabla\delta\cdot\Delta\mathbf{r}) - 2\mathbf{P}(\nabla\delta\cdot\Delta\mathbf{r}),$$
$$\nabla\delta\times(\Delta\mathbf{r}\times\mathbf{P}) = (\Delta\mathbf{r}\otimes\mathbf{P} + \mathbf{P}\otimes\Delta\mathbf{r})\cdot\nabla\delta - 2\mathbf{P}(\nabla\delta\cdot\Delta\mathbf{r}).$$

This finally leads to:

$$\mathbf{P}(\nabla\delta\cdot\Delta\mathbf{r}) = \frac{1}{2}(\Delta\mathbf{r}\otimes\mathbf{P}+\mathbf{P}\otimes\Delta\mathbf{r})\cdot\nabla\delta - \frac{1}{2}\nabla\delta\times(\Delta\mathbf{r}\times\mathbf{P}). \quad (2.21)$$

Plugging Eq. (2.21) in the first-order term of Eq. (2.18), we can manipulate the expression to yield the MD and EQ contributions:

$$\begin{aligned}-\int_{V_s}\mathbf{P}(\mathbf{r})(\nabla\delta\cdot\Delta\mathbf{r})dV' &= -\frac{1}{2}\int_{V_s}(\Delta\mathbf{r}\otimes\mathbf{P}+\mathbf{P}\otimes\Delta\mathbf{r})dV'\cdot\nabla\delta \\ &\quad -\frac{1}{2}\int_{V_s}(\Delta\mathbf{r}\times\mathbf{P})dV'\times\nabla\delta \\ &= -\frac{1}{6}\bar{\bar{Q}}\cdot\nabla\delta + \frac{i}{\omega}\left[-\frac{i\omega}{2}\int_{V_s}\Delta\mathbf{r}\times\mathbf{P}dV'\right]\times\nabla\delta.\end{aligned}$$

Here $\bar{\bar{Q}}$ is the EQ moment, defined as:

$$\bar{\bar{Q}} = 3\int\left[\Delta\mathbf{r}\mathbf{P}\left(\mathbf{r}'\right)+\mathbf{P}\left(\mathbf{r}'\right)\Delta\mathbf{r}\right]\mathrm{d}V'. \quad (2.22)$$

Notice that the delta distribution depends on $\mathbf{r}$, not $\mathbf{r}'$, and can thus be taken out of the integrals. The second term on the right-hand side can be identified as the MD moment, after noticing that $\nabla\delta\times(\Delta\mathbf{r}\times\mathbf{P}) = \nabla\times(\Delta\mathbf{r}\times\mathbf{P}\delta)$. The second term then gives $\nabla\times(\mathbf{m}\delta)$, with the MD moment $\mathbf{m}$ defined as:

$$\mathbf{m} = -\frac{i\omega}{2}\int_{V_s}\Delta\mathbf{r}\times\mathbf{P}dV'. \quad (2.23)$$

Summing up the contributions, to first order, the Taylor series of $\mathbf{P}$ yields:

$$\mathbf{P} = \mathbf{d}\delta(\mathbf{r}-\mathbf{r}_0) - \frac{1}{6}\bar{\bar{Q}}\cdot\nabla\delta(\mathbf{r}-\mathbf{r}_0) + \frac{i}{\omega}\nabla\times(\mathbf{m}\delta(\mathbf{r}-\mathbf{r}_0)) + O(\Delta\mathbf{r}^2). \quad (2.24)$$

$\mathbf{d}$ is the ED moment, defined as:

$$\mathbf{d} = \int_{V_s}\mathbf{P}(\mathbf{r}')dV'. \quad (2.25)$$

Similar steps to the ones above allow to obtain the EO and MQ moments from the second-order term, yielding additional contributions to the polarization, $\mathbf{P}_2(\mathbf{r})$:

$$\mathbf{P}_2(\mathbf{r}) = -\frac{i}{2\omega}\nabla\times\left[\bar{\bar{M}}\cdot\nabla\delta(\mathbf{r}-\mathbf{r}_0)\right] + \frac{1}{6}\hat{O}:\nabla\nabla\delta(\mathbf{r}-\mathbf{r}_0). \quad (2.26)$$

$\bar{\bar{M}}$ and $\hat{O}$ are, respectively, second and third rank tensors corresponding to the MQ and EO moments:

$$\bar{\bar{M}} = -\frac{2i\omega}{3}\int_{V_s}(\Delta\mathbf{r}\times\mathbf{P})\Delta\mathbf{r}dV', \tag{2.27}$$

$$\hat{O} = \int_{V_s}\Delta\mathbf{r}\Delta\mathbf{r}\Delta\mathbf{r}(\nabla\cdot\mathbf{P})dV'. \tag{2.28}$$

Eq. (2.23) and Eq. (2.26) together form the central result of this section, namely, an expansion of the polarization current into contributions of the individual multipoles. Starting from them, it is possible to determine the electromagnetic field outside the source by using Eq. (2.6). As an example, let us now obtain the far field behavior. In the far field, the Green's function is given by Eq. (2.9). As a result, the electric field is a spherical wave with the general form $\mathbf{E}(\mathbf{r}) = \frac{e^{ikr}}{r}\mathbf{E}_0(\hat{\mathbf{n}})$, where $\hat{\mathbf{n}}$ is a unit vector pointing in the radial direction, i.e. $\hat{\mathbf{n}} = \frac{\mathbf{r}}{|\mathbf{r}|}$. Inserting the TSE of Eq. (2.23) and Eq. (2.26) into Eq. (2.6), together with Eq. (2.9), the electric field produced by the scatterer is up to second order in the TSE:

$$\mathbf{E}_0(\hat{\mathbf{n}}) \approx \frac{k^2}{4\pi\varepsilon_0}\Big[\hat{\mathbf{n}}\times(\mathbf{d}\times\hat{\mathbf{n}}) + \frac{1}{c}(\mathbf{m}\times\hat{\mathbf{n}}) + \frac{ik}{6}\hat{\mathbf{n}}\times(\bar{\bar{Q}}\times\hat{\mathbf{n}}) + \frac{ik}{2c}\hat{\mathbf{n}}\times(\bar{\bar{M}}\cdot\hat{\mathbf{n}}) + \frac{k^2}{6}\hat{\mathbf{n}}\times[\hat{\mathbf{n}}\times(\hat{O}:\hat{\mathbf{n}}\otimes\hat{\mathbf{n}})]\Big]. \tag{2.29}$$

When making the change $\hat{\mathbf{n}}\to-\hat{\mathbf{n}}$ in Eq. (2.29), the electric field produced by the electric dipole does not change sign, while the electric field produced by the magnetic dipole is flipped. For quadrupoles, the opposite takes place, such that the magnetic quadrupole field is even while the electric quadrupole one is odd. The 'odd–even' behavior under space inversion is often referred to as the parity of the multipole field. This peculiar property is at the core of all multipolar interference effects.

2.3.1.1 Visualizing multipoles

In order to provide the reader with an intuitive picture of multipoles, we derive here a simple procedure to visualize the current distributions that would generate them. This procedure was originally proposed in Ref. [7] for visualizing electric multipoles of arbitrary order. Here, we adapt it also for magnetic ones. In what follows, it is perhaps more didactic to consider the induced currents, which are directly related to the polarization, as $\mathbf{J} = \frac{d\mathbf{P}}{dt} = -i\omega\mathbf{P}$.

Let us first consider the current distribution associated to an ED, i.e., $\mathbf{J}_d = -i\omega\mathbf{d}\delta(\mathbf{r}-\mathbf{r}_0)$. The latter is simply the first term

in Eq. (2.21) multiplied by $-i\omega$. In what follows, without loss of generality, we set $\mathbf{r}_0 = 0$. $\mathbf{J}_d$ has a clear physical interpretation: it corresponds to a linear current centered at $\mathbf{r}_0 = 0$, as depicted in Fig. 2.3a. However, higher order currents are not so clearly visualized. For instance, a current generating an EQ moment is $\mathbf{J}_Q = \frac{i\omega}{6}\bar{\bar{Q}} \cdot \nabla\delta(\mathbf{r})$. From this expression, one can understand that nonzero gradients of the field within the scatterer are necessary in order to excite quadrupolar moments. Let us now inspect in more detail a single component of the tensor, such as Q_{yx}. The associated current is

$$J_Q = \frac{i\omega}{6}\frac{d\delta}{dx} \approx \frac{i\omega Q_{yx}}{6}\frac{\delta(x+s/2)-\delta(x-s/2)}{s},$$

this approximate expression can be rewritten as:

$$J_Q \approx -i\omega[d_Q\delta(x+s/2) - d_Q\delta(x-s/2)], \tag{2.30}$$

with $d_Q = \frac{Q_{yx}}{6s}$. s is a small separation between the delta distributions. Hence, Eq. (2.30) tells us that Q_{yx} can be visualized as two effective ED moments displaced $\pm s/2$ from the origin, polarized along y, and out of phase with each other (Fig. 2.3b). Each component of the EQ tensor can be visualized in the same fashion. The approach can then be generalized to an arbitrary electric moment. Namely, one can use ED moments as building blocks to 'construct' the current distribution of higher order moments.

Magnetic moments are better visualized by defining a "magnetic current" $\mathbf{J}_H$ which obeys $\mathbf{J} = \nabla \times \mathbf{J}_H$. Considering only the magnetic moments, $\mathbf{J}_H$ is given by:

$$\mathbf{J}_H = \mathbf{m}\delta\mathbf{r} - \frac{1}{2}\bar{\bar{M}} \cdot \nabla\delta(\mathbf{r}). \tag{2.31}$$

It is then straightforward to apply the same procedure as for the electric moments. As in the case for the EQ, the M_{yx} component corresponds to two magnetic dipoles oriented along y, displaced in x and in antiphase with each other.

2.3.1.2 Irreducible multipoles and the toroidal dipole

The expressions for the multipole moments given above are not the most commonly used formulas in nanophotonic applications. The main reason for this is that certain combinations of the high-order moments, as defined above, can lead to radiation patterns identical to the low-order multipoles.

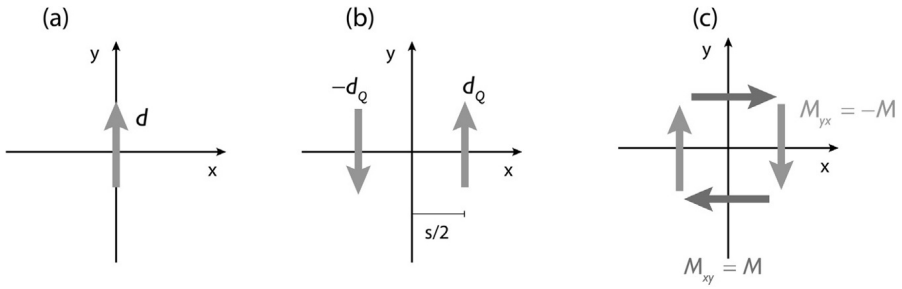

Figure 2.3. (a) A single point ED moment polarized along y, corresponding to the current distribution $\mathbf{J} = -i\omega d\hat{\mathbf{e}}_y \delta(\mathbf{r})$. (b) Representation of the Q_{yx} quadrupole moment. (c) Emergence of a z-polarized toroidal dipole moment from the antisymmetric part of the MQ tensor.

To see this, consider the MQ tensor given by:

$$\bar{\bar{M}} = \begin{pmatrix} 0 & M & 0 \\ -M & 0 & 0 \\ 0 & 0 & 0 \end{pmatrix}$$

Surprisingly, inserting $\bar{\bar{M}}$ into Eq. (2.29) can yield a contribution to the electric field:

$$\mathbf{E}_M \propto [\hat{\mathbf{n}} \times (0, 0, 2M)^T \times \hat{\mathbf{n}}], \tag{2.32}$$

which defines the same radiation pattern as an ED moment (compare with the first term of Eq. (2.29)). Therefore, to trace a one-to-one correspondence between the radiation patterns and the multipoles, it becomes necessary to determine a procedure for extracting all such terms from the high-order tensors and introduce them into the corresponding low-order multipoles. We call this procedure a *reduction*. We are looking for an *irreducible* multipole representation.

It can be shown that two conditions are sufficient for any multipole to be in its irreducible form: the tensor must be symmetric and also traceless. We will now illustrate the reduction procedure for the lowest order multipoles.

We start with the EQ moment. The latter is represented by a symmetric moment, but it is not traceless. This is a general rule for all high order electric moments. The opposite happens for magnetic moments.

We "detrace" $\bar{\bar{Q}}$ following Applequist [8]:

$$Q_{ij} = Q'_{ij} + \frac{1}{3}\delta_{ij} Q_{vv}. \tag{2.33}$$

Q_{vv} is the sum over the diagonal elements of the original tensor, and is given by:

$$Q_{vv} = 6 \int_{V_s} \mathbf{r}' \cdot \mathbf{P}(\mathbf{r}') dV'. \tag{2.34}$$

It can be shown that Q_{vv} only produces longitudinal fields, and thus cannot contribute to radiation. Therefore, it will be ignored in the following.

Similarly, the EO can be detraced:

$$O_{ijk} = O'_{ijk} + \frac{1}{5}\left[\delta_{ij} O_{vvk} + \delta_{ik} O_{vvj} + \delta_{kj} O_{vvi}\right], \tag{2.35}$$

with O_{vvk}:

$$O_{vvk} = \mathbf{W} = \int_{V_s} \left[2(\mathbf{r}' \cdot \mathbf{P})\mathbf{r}' + r^2 \mathbf{P}\right] dV'. \tag{2.36}$$

Further, we need to symmetrize the magnetic moments. For this purpose, we can use the fact that any arbitrary second rank tensor can be expressed as a sum of a symmetric and antisymmetric tensor:

$$A_{ij} = \underbrace{\frac{1}{2}(A_{ij} + A_{ji})}_{\text{Symmetric}} + \underbrace{\frac{1}{2}(A_{ij} - A_{ji})}_{\text{Antisymmetric}}. \tag{2.37}$$

We can see that the antisymmetric part is in fact defined by a vector, since:

$$A_{ij} - A_{ji} = \varepsilon_{vij}(\varepsilon_{\alpha\beta v} A_{\alpha\beta}) = \varepsilon_{vij} N_v, \tag{2.38}$$

where we have introduced the vector $N_v = \varepsilon_{\alpha\beta v} A_{\alpha\beta}$. ε_{ijk} is the Levi-Civita tensor. Particularizing for $\bar{\bar{M}}$, we get, for the symmetric part:

$$\bar{\bar{M}}' = \frac{\omega}{3i} \int_{V_s} [(\mathbf{r}' \times \mathbf{P})\mathbf{r}' + \mathbf{r}'(\mathbf{r}' \times \mathbf{P})] dV'. \tag{2.39}$$

And the vector $\mathbf{N}$ is:

$$\mathbf{N} = -\frac{2i\omega}{3} \int_{V_s} [\mathbf{r}'^2 \mathbf{P} - (\mathbf{r}' \cdot \mathbf{P})\mathbf{r}'] dV'. \tag{2.40}$$

Hence, $\bar{\bar{M}}$ can be decomposed as:

$$\bar{\bar{M}} = \bar{\bar{M}}' + \bar{\bar{M}}'' = \bar{\bar{M}}' + \frac{1}{2}\varepsilon_{vij}\mathbf{N}. \tag{2.41}$$

We can now introduce Eq. (2.41) to the electric field in Eq. (2.29). We get, for the $\bar{\bar{M}}$ term:

$$\hat{\mathbf{n}} \times (\bar{\bar{M}} \cdot \hat{\mathbf{n}}) = \hat{\mathbf{n}} \times (\bar{\bar{M}}' \cdot \hat{\mathbf{n}}) + \frac{1}{2}\hat{\mathbf{n}} \times (\bar{\bar{M}}'' \cdot \hat{\mathbf{n}}),$$

where $\bar{\bar{M}}''$ is the antisymmetric tensor defined as $\bar{\bar{M}}'' = \varepsilon_{vij} N_v$. The first term clearly retains the same functional form, however, the second term gives:

$$\frac{1}{2}\hat{\mathbf{n}} \times (\bar{\bar{M}}'' \cdot \hat{\mathbf{n}}) = -\frac{1}{2}\hat{\mathbf{n}} \times (\mathbf{N} \times \hat{\mathbf{n}}).$$

A similar procedure for the EO yields a second contribution to the ED fields. The sum of both contributions is then (taking into account the correct prefactors):

$$-\frac{1}{2}\frac{ik}{2c}\hat{\mathbf{n}} \times (\mathbf{N} \times \hat{\mathbf{n}}) - \frac{k^2}{6}\frac{1}{5}\hat{\mathbf{n}} \times (\mathbf{W} \times \hat{\mathbf{n}}) = \hat{\mathbf{n}} \times (\frac{ik}{c}\mathbf{T} \times \hat{\mathbf{n}}).$$

With $\mathbf{T}$ finally given by:

$$\mathbf{T} = \frac{i\omega}{10}\int_{V_s} [2r'^2\mathbf{P} - (\mathbf{r} \cdot \mathbf{P})\mathbf{r}']dV'. \tag{2.42}$$

$\mathbf{T}$ is the lowest order moment of the *toroidal* family, and is most often referred to as the *toroidal dipole moment* (TD).

We can visualize toroidal moments with the same trick illustrated previously. For instance, we can easily draw the current corresponding to the combination $T_z \propto M_{xy} - M_{yx}$. The first term leads to two antiparallel MD moments polarized along x and displaced in y, and vice versa for the second component (Fig. 2.3c). It turns out that the TD moment is characterized by a head-to-tail arrangement of MDs, separated by an infinitesimal distance from each other. In the limit of $s \to 0$, the latter can be seen as a continuous distribution of MD moments, i.e., as a current winding along a torus.

Since the radiation patterns of the ED and the TD are identical, they can interfere in the far field. If the two moments are out of phase, their radiation can be mutually canceled, leading to the anapole effect discussed in Chapter 6.

By performing the same process to high order terms in the TSE, it is possible to derive more contributions with the same radiation pattern [9]. These are the so-called toroidal MSR. The same procedure also leads to magnetic MSR, having the same radiation patterns as the magnetic moments.

2.3.2 Expansion in vector spherical harmonics

A second approach to derive the multipole decomposition of the scattered field is based on an expansion into vector spherical harmonics (VSHs) [1]. Since the latter is developed in detail in many standard textbooks, e.g., Ref. [1], (see also the excellent work [10]), we limit ourselves to the presentation of the main results.

VSHs form a complete and orthogonal basis set for any vector function defined on a spherical surface. We define the VSH $\mathbf{X}_{lm}$ as [1]:

$$\mathbf{X}_{lm} = -\frac{m}{\sqrt{l(l+1)}\sin\theta} Y_{lm}\hat{\boldsymbol{\theta}} - \frac{i}{\sqrt{l(l+1)}} \frac{\partial Y_{lm}}{\partial\theta}\hat{\boldsymbol{\phi}}, \tag{2.43}$$

where $\hat{\boldsymbol{\theta}}$ and $\hat{\boldsymbol{\phi}}$ are unit vectors along the polar and azimuthal directions in the spherical coordinate system. The quantum numbers l, m denote the angular momentum and its projection to the z-axis. The Y_{lm} are spherical harmonic functions. Within, or outside the smallest spherical surface surrounding the scatterer (or scatterers), the scattered field can be expanded as [1,7]:

$$\begin{aligned}\boldsymbol{E}_{\mathrm{s}}(r,\theta,\phi) = \sum_{l=1}^{\infty}\sum_{m=-l}^{l} C_l \Bigg\{ &\frac{1}{k} a_{lm} \nabla \times \left[h_l^{(1)}(kr)\boldsymbol{X}_{lm}(\theta,\phi) \right] \\ &+ b_{lm} h_l^{(1)}(kr)\boldsymbol{X}_{lm}(\theta,\phi) \Bigg\},\end{aligned} \tag{2.44}$$

with $C_l = \mathrm{i}^l E_0[\pi(2l+1)]^{1/2}$, where E_0 is the amplitude of the incident illumination, k is the wavevector, and $h_l^{(1)}(kr)$ is a spherical Hankel function of the first kind. The coefficients a_{lm} and b_{lm} are the electric and magnetic scattering coefficients, respectively. They can be calculated as an integral over a sphere surrounding the scatterer (or scatterers) [1]:

$$\begin{aligned} a_{lm} &= B_l \int_0^{2\pi}\int_0^{\pi} Y_{lm}^*(\theta,\phi)\mathbf{r}\cdot\mathbf{E}_{\mathrm{sca}}\sin\theta\,\mathrm{d}\theta\,\mathrm{d}\phi, \\ b_{lm} &= i Z_0 B_l \int_0^{2\pi}\int_0^{\pi} Y_{lm}^*(\theta,\phi)\mathbf{r}\cdot\mathbf{H}_{\mathrm{sca}}\sin\theta\,\mathrm{d}\theta\,\mathrm{d}\phi, \end{aligned} \tag{2.45}$$

where the prefactor B_l is:

$$B_l = \frac{(-i)^{l+1}k}{h_l^{(1)}(kr)E_0\sqrt{\pi(2l+1)l(l+1)}},$$

and Z_0 is the wave impedance in free space. The scattering cross section can then be presented as an incoherent sum of the electric

and magnetic contributions:

$$\sigma_s = \frac{\pi}{k^2}\sum_{l,m}(2l+1)[|a_{lm}|^2 + |b_{lm}|^2]. \tag{2.46}$$

The fields associated with the a_{1m} coefficient are identical to the ED moment as defined in the TSE. Notice that it also has three components a_{11}, a_{10}, a_{1-1}, and is thus a vector. Hence, it is usually referred to as ED coefficient. The same rule applies to higher order coefficients, i.e. a_{2m} is the EQ coefficient, etc. The magnetic coefficients follow the same rule.

2.3.2.1 Scattering from a sphere

Analytical solutions for the scattering coefficients (2.45) are available for spherical objects with isotropic permittivities under plane wave illumination. In this case, only the $m = 1, -1$ contributions are nonzero [11]:

$$\begin{aligned} a_{l,1} = -a_{l,-1} &= \frac{m\psi_l(mx)\psi_l'(x) - \psi_l(x)\psi_l'(mx)}{m\psi_l(mx)\xi_l'(x) - \xi_l(x)\psi_l'(mx)}, \\ b_{l,1} = b_{l,-1} &= \frac{m\psi_l(x)\psi_l'(mx) - \psi_l(mx)\psi_l'(x)}{m\xi_l(x)\psi_l'(mx) - \psi_l(mx)\xi_l'(x)}. \end{aligned} \tag{2.47}$$

In the above, the size parameter $x = kR_s$, where R_s is the sphere radius; $m = n_s/n_0$ is the ratio between the refractive indices of the sphere and the surrounding environment, $\psi_l(z), \xi_l(z) = \psi_l(z) - i\chi_l(z)$, $\psi_l(z) = zj_l(z)$ and $\chi_l(z) = -zy_l(z)$ are the Riccati-Bessel functions; $j_l(z)$, $y_l(x)$ stand for the spherical Bessel functions; and the prime ($'$) sign denotes derivative over the argument. Inserting Eqs. (2.47) into Eq. (2.46) allows to reconstruct the scattering cross section of a sphere of any size, provided that sufficient terms are included in the expansion. An example for the case of a dielectric sphere is shown in Fig. 2.4. With decreasing wavelength, the sphere is seen to support multipolar resonances of different kinds, both electric and magnetic.

A less known fact about Mie theory is that it allows finding the *resonance frequencies* of the *Quasinormal modes* (QNMs) of the sphere. QNMs are self-sustaining oscillations with outgoing boundary conditions that are responsible for the resonant features in the scattering spectra of each multipole coefficient. A rigorous discussion on QNMs can be found in section 2.4.

For a sphere, the QNMs are classified in electric and magnetic, with different l [12]. The eigenfrequencies correspond to the poles of Eqs. (2.47), which can be obtained by making the denominators

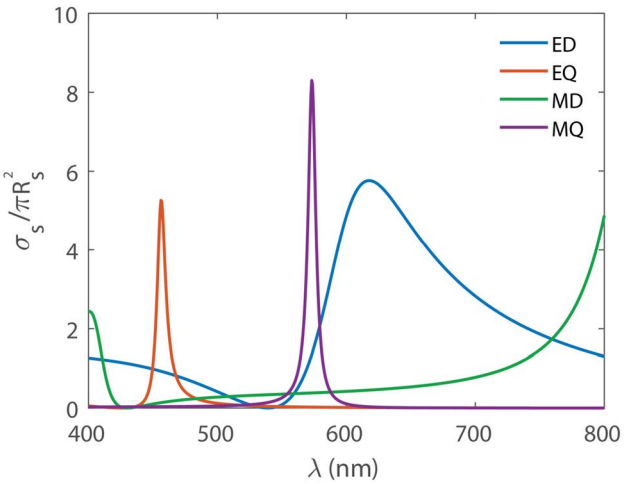

Figure 2.4. Multipole decomposition of the scattering cross section for a high-index dielectric sphere with $n = 3.87$ and radius $R_s = 100$ nm. The figure was produced with the help of Eqs. (2.47).

zero, giving the characteristic equations:

$$\frac{\left[x h_l^{(1)}(x)\right]'}{h_l^{(1)}(x)} = \frac{[m x j_l(mx)]'}{m^2 j_l(mx)}, \tag{2.48}$$

$$\frac{\left[x h_l^{(1)}(x)\right]'}{h_l^{(1)}(x)} = \frac{[m x j_l(mx)]'}{j_l(mx)}, \tag{2.49}$$

for the electric and magnetic modes, respectively.

2.3.3 Relations between the two decompositions

The TSE and the VSH expansions, when performed over the same center of charge, describe equivalently the scattered field, as long as sufficient terms are included. Until a few years ago, a straightforward connection between the two decompositions was not available. Recently, it was pointed out that the VSH expansion can be modified to yield exact multipole coefficients as volume integrals over the source in Cartesian coordinates [13]. The new formulae for the multipoles include all the terms in the TSE, which can be easily recovered from a Taylor series, as shown below. Here, we provide an outline of the derivation, following the approach in Ref. [4], which makes use of the Green's function. The reader is also invited to take a look at the original derivation in Ref. [14]. Let us start by regarding the expression for the scattered electric field in

the far field. From Eq. (2.6), the field radiated by a current $\mathbf{j}(\mathbf{r};\omega)$ can be evaluated as:

$$\mathbf{E}_F(\mathbf{r};\omega) = i\omega \int_{V_s} \bar{\bar{G}}_b^F\left(\mathbf{r},\mathbf{r}';\omega\right)\mathbf{j}\left(\boldsymbol{r}';\omega\right)d^3\boldsymbol{r}'. \tag{2.50}$$

In the far field, the observation point is very far from the source, so that $r >> r'$ and $r >> 1/k$. Using the identity $R = |\mathbf{r}-\mathbf{r}'| = [r^2 - 2\mathbf{r}\cdot\mathbf{r}' + (r')^2]^{1/2}$, rewriting it in the binomial form:

$$R \approx r\left[1 - \frac{2\mathbf{r}\cdot\mathbf{r}'}{r^2}\right]^{1/2},$$

and expanding the term in brackets to first order in a Taylor series with respect to $\mathbf{r}\cdot\mathbf{r}'/r^2$ leads to $R \approx r - \hat{\mathbf{n}}\cdot\mathbf{r}'$, with $\hat{\mathbf{n}} = \mathbf{r}/r$. Introducing the latter expression in Eq. (2.9) results in:

$$\bar{\bar{G}}_b^{\mathrm{F}}\left(\mathbf{r},\mathbf{r}';\omega\right) = \mu_0\frac{e^{ikr}}{4\pi r}(\bar{\bar{I}} - \hat{\mathbf{n}}\otimes\hat{\mathbf{n}})e^{-ik(\hat{\mathbf{n}}\cdot\mathbf{r}')}. \tag{2.51}$$

Introducing Eq. (2.51) in Eq. (2.50) yields:

$$\mathbf{E}_F(\mathbf{r};\omega) = i\omega\mu_0\frac{e^{ikr}}{4\pi r}(\bar{\bar{I}} - \hat{\mathbf{n}}\otimes\hat{\mathbf{n}})\int_{V_s} e^{-ik(\hat{\mathbf{n}}\cdot\mathbf{r}')}\mathbf{j}\left(\boldsymbol{r}';\omega\right)d^3\boldsymbol{r}'. \tag{2.52}$$

We can now expand the factor $e^{-ik(\hat{\mathbf{n}}\cdot\mathbf{r}')}$ in the Green's function with respect to a point $\mathbf{r}_0 \in V_s$ in spherical harmonics [1]:

$$e^{-ik(\hat{\mathbf{n}}\cdot\mathbf{r}')} = 4\pi\sum_{l=0}^{\infty}\sum_{m=-l}^{l}(-i)^l j_l\left(kr'\right)Y_{lm}^*(\theta,\varphi)Y_{lm}\left(\theta',\varphi'\right), \tag{2.53}$$

where $j_l\left(kr'\right)$ is the lth order spherical Bessel function, $Y_{lm}(\theta,\varphi)$ is a spherical harmonic, θ and φ $\left(\theta'\right.$ and $\left.\varphi'\right)$ are the polar and azimuthal angles of $\hat{\mathbf{n}}\left(\hat{\mathbf{n}}'\right)$ in the spherical coordinate system, and the asterisk $(*)$ denotes complex conjugation. The sum can be further reduced with the help of the addition theorem [1]:

$$P_l(\cos\gamma) = \frac{4\pi}{2l+1}\sum_{m=-l}^{l}Y_{lm}^*\left(\theta',\varphi'\right)Y_{lm}(\theta,\varphi), \tag{2.54}$$

where γ is defined such that $\cos\gamma = \hat{\mathbf{n}}\cdot\hat{\mathbf{n}}'$. Inserting the expansion in Eq. (2.52), we get:

$$\mathbf{E}_F(\mathbf{r};\omega) = i\omega\mu_0\frac{e^{ikr}}{4\pi r}(\bar{\bar{I}} - \hat{\mathbf{n}}\otimes\hat{\mathbf{n}})\sum_{l=0}^{\infty}\mathbf{S}_l, \tag{2.55}$$

with the $\mathbf{S}_l$ vectors defined as:

$$\mathbf{S}_l = (-i)^l (2l+1) \int_{V_s} j_l\left(kr'\right) P_l(\cos\gamma) \mathbf{j}\left(\mathbf{r}'\right) d\mathbf{r}'. \tag{2.56}$$

Applying detracing and symmetrization procedures to the $\mathbf{S}_l$ up to $l = 3$, similar to the ones in section 2.3.1.2 (refer to [4] for details), we can recover exact expressions for the dipole moments:

$$\mathbf{d} = \int \mathbf{P} j_0(kr) d^3\mathbf{r} + \frac{k^2}{10} \int \left\{ [\mathbf{r}\cdot\mathbf{P}]\mathbf{r} - \frac{1}{3} r^2 \mathbf{P} \right\} \frac{15 j_2(kr)}{(kr)^2} d^3\mathbf{r}, \tag{2.57}$$

$$\mathbf{m} = -\frac{3i\omega}{2} \int (\mathbf{r}\times\mathbf{P}) \frac{j_1(kr)}{kr} d^3\mathbf{r}, \tag{2.58}$$

while the EQ is:

$$\bar{\bar{Q}} = \int \{3(\mathbf{r}\otimes\mathbf{P} + \mathbf{P}\otimes\mathbf{r}) - 2[\mathbf{r}\cdot\mathbf{P}]\mathbf{I}\} \times \frac{3 j_1(kr)}{kr} d^3\mathbf{r} + 6k^2 \int \left\{ 5\mathbf{r}\otimes\mathbf{r}[\mathbf{r}\cdot\mathbf{P}] - (\mathbf{r}\otimes\mathbf{P} + \mathbf{P}\otimes\mathbf{r}) r^2 - r^2[\mathbf{r}\cdot\mathbf{P}]\mathbf{I} \right\} \frac{j_3(kr)}{(kr)^3} d^3\mathbf{r}, \tag{2.59}$$

and the MQ:

$$\bar{\bar{M}} = \frac{\omega}{3i} \int \{[\mathbf{r}\times\mathbf{P}]\otimes\mathbf{r} + \mathbf{r}\otimes[\mathbf{r}\times\mathbf{P}]\} \frac{15 j_2(kr)}{(kr)^2} d^3\mathbf{r}. \tag{2.60}$$

The radiated fields are identical to those of the TSE, [Eq. (2.29)]. The scattering cross section can then be evaluated as [6,13]:

$$\sigma_s = \frac{k^4}{6\pi\varepsilon_0^2 |\mathbf{E}_b|^2} \left[\sum_\alpha \left(|d_\alpha|^2 + \left| \frac{m_\alpha}{c} \right|^2 \right) + \frac{1}{120} \sum_{\alpha\beta} \left(\left| k Q_{\alpha\beta} \right|^2 + \left| \frac{k M_{\alpha\beta}}{c} \right|^2 \right) + \cdots \right], \tag{2.61}$$

where the α, β subscripts indicate summation over the tensor components of the multipoles. Up to $l = 2$, this expression for σ_s is exactly equivalent to Eq. (2.46).

The first term in the ED moment in Eq. (2.57) has a very similar functional form to its TSE counterpart in Eq. (2.25), but critically, it already includes the contributions of the toroidal dipole and the higher order MSR, as can be shown from a Taylor series of $j_0(kr)$ and $j_2(kr)$ with respect to kr [14]. In the small argument approximation, $j_0(kr) \approx 1 - (kr)^2/6$ and $j_2(kr) \approx (kr)^2/15$. This gives:

$$\mathbf{d} \approx \mathbf{d}_{\mathrm{TSE}} + \frac{ik}{c} \mathbf{T}_{\mathrm{TSE}}, \tag{2.62}$$

where $\mathbf{d}_{\mathrm{TSE}}$ and $\mathbf{T}_{\mathrm{TSE}}$ correspond to the ED moment in the TSE [Eq. (2.25)] and the TD moment [Eq. (2.42)]. Retaining higher order terms in the Taylor series, it is also possible to recover the expressions for the MSR.

2.4 Quasinormal modes

The multipolar framework introduced in section 2.2 provides the primary means to classify and control the far-field response of dielectric nanoresonators with relatively simple shapes, such as disks (cylinders with small height), spheres or cubes. In such cases, the radiation patterns of the particle resonances are mostly associated with a single dominant multipole. This is due to the fact that the solution to the scattering problem does not differ significantly from that of a sphere. However, once the particle shape becomes more complex, the electromagnetic resonances can radiate as mixtures of multipoles. In such cases, the multipolar picture often leads to confusion and misinterpretation of the underlying physics.

In order to properly describe the behavior of dielectric resonators of arbitrary shape, we must first put forward a general theory of electromagnetic resonances. The latter has been extensively developed in the last years, but its origins can be traced back to Gamow [15] and Zel'dovich [16] to describe solutions of the Schrodinger equation subject to outgoing boundary conditions. The main idea, (developed in the next section) consists in expanding an arbitrary solution of the scattering problem as the sum of the contributions of the so-called *Quasinormal modes* (QNMs) [17] or Resonant States [18], which correspond to self-sustaining oscillations of the resonator (i.e., resonant modes). In what follows, we will first summarize the main characteristics of QNMs and later proceed to derive them in more detail. The discussion is largely based in Refs. [17,19–21]. As in most of this book, we consider reciprocal, non-magnetic, isotropic materials. An extended theory that treats non-reciprocal materials can be found in Ref. [22]. We denote by $\mathbf{F}_m(\mathbf{r};\omega) = \left[\mathbf{E}_m(\mathbf{r};\omega) \quad \mathbf{H}_m(\mathbf{r};\omega)\right]^T$ the six-component vector combining the electric and magnetic fields of a QNM.

Formally, a QNM labeled m is a solution of Eqs. (2.1) with $\mathbf{j}(\mathbf{r};\omega) = \mathbf{0}$. The latter can be expressed as an eigenvalue equation:

$$\bar{\bar{D}}\mathbf{F}_m(\mathbf{r};\tilde{\omega}_m) = -i\omega_m \mathbf{F}_m(\mathbf{r};\tilde{\omega}_m), \tag{2.63}$$

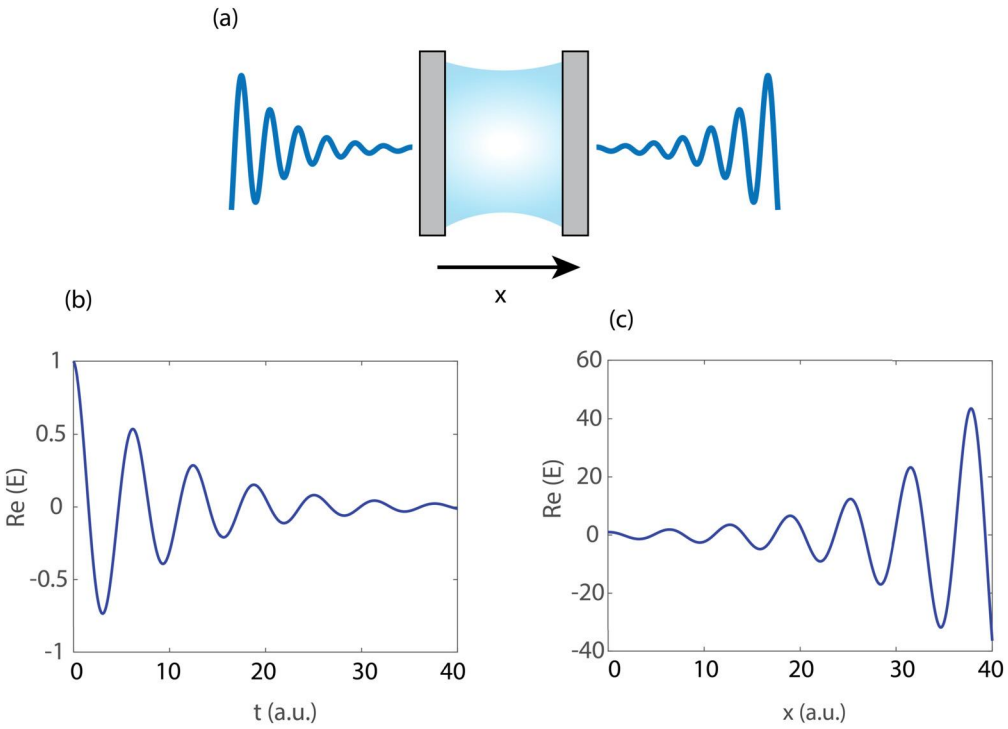

Figure 2.5. (a) Scheme depicting a QNM of a resonant Fabry-Perot cavity. In space, the fields (blue lines) diverge at increasing distance from the cavity. (b) Evolution of the QNM fields with time when the excitation has been turned off. (c) Divergence of the QNM fields in space.

subject to outgoing boundary conditions:

$$\lim_{r\to\infty} \mathbf{e}_r \times \mathbf{E}_m = Z_0 \mathbf{H}_m \tag{2.64}$$

$$\lim_{r\to\infty} \mathbf{e}_r \times Z_0 \mathbf{H}_m = -\mathbf{E}_m. \tag{2.65}$$

The matrix $\bar{\bar{D}}$ is given by:

$$\bar{\bar{D}} = \begin{pmatrix} 0 & \varepsilon^{-1}\nabla\times \\ -\mu_0^{-1}\nabla\times & 0 \end{pmatrix}. \tag{2.66}$$

Hence, to every QNM m we can associate a field $\mathbf{F}_m$ and an eigenfrequency ω_m. In an isolated cavity, such as a lossless Fabry-Perot resonator formed by two perfectly conducting walls, the resonances are perfectly bound within the resonator, implying that the light remains perfectly trapped for an infinite time. QNMs, on the other hand, progressively decay to the far field after their initial excitation. As a result, their eigenfrequencies become complex

$\omega_m = \mathrm{Re}\,\omega_m + i\,\mathrm{Im}\,\omega_m$. $\mathrm{Re}\,\omega_m$ is the resonance frequency (i.e., the optimal frequency of the excitation to drive the resonance), and $\mathrm{Im}\,\omega_m = -\gamma_m$, where γ_m is a positive real number representing the inverse lifetime.

To understand this and the origin of the negative sign in the imaginary part of ω_m, consider the time dependence of a single QNM, namely $\exp(-i\omega_m t) = \exp(-i\,\mathrm{Re}\,\omega_m t)\exp(-\gamma_m t)$. Due to radiation, the fields will now exponentially decay in time, while oscillating at the resonance frequency, as shown in Fig. 2.5b. Note that, unless we keep the negative sign in $\mathrm{Im}\,\omega_m$, the fields would exponentially increase instead of decay, which would violate energy conservation. Of course, γ_m also takes into account ohmic losses in the resonator and/or the environment. In the remaining of this discussion, we will neglect the latter, since radiation losses play the dominant role in dielectric materials. The exponential decay in time also creates a seeming paradox, shown in Fig. 2.5c and depicted also in Fig. 2.5a. In the far field, the fields of the QNM will have the spatial dependence $\mathbf{E}_m \propto \exp(i\omega_m/c)$. As a result, they will exponentially increase with increasing distance from the cavity. This effect can be understood when taking into account causality: at shorter times, the field that radiates away from the cavity has larger amplitudes than at longer times. In this section, we present a detailed derivation of the QNM expansion for mesoscopic dielectric cavities. We believe the QNM framework provides a much needed complementary analysis to multipole decompositions, as it allows to describe the resonant response of the system in a physically transparent fashion. Nowadays, the QNM expansion has been implemented in the freeware MAN [23] for the popular finite element software COMSOL Multiphysics©. MAN also comes with a variety of example models for both plasmonic and dielectric nanoresonators. Other options include the nanobem toolbox developed by Hohenester and co-workers in Matlab® [24].

2.4.1 Spectral theorem for open systems

Before discussing the QNM expansion in the context of electromagnetism, we dedicate this subsection to presenting key concepts on general spectral decompositions for non-Hermitian operators. These form the basic tools needed to derive the QNM expansion.

We consider a generalized eigenvalue problem with operators $\mathcal{A}$ and $\mathcal{B}$ of the form:

$$\mathcal{A}\mathbf{v}_n = -\lambda_n \mathcal{B}\mathbf{v}_n, \tag{2.67}$$

supplemented by some a priori unspecified boundary conditions that determine the domain D_L of the vector space where all eigenvectors are included. The subscript "n" denotes a specific eigenvector of the eigenvalue λ_n. In what follows, we assume that there is only one eigenvector for each eigenvalue (i.e., there are no degenerate eigenvalues). These can most of the times be treated through the Grahm-Schmidt orthogonalization procedure, except in very special cases, known as exceptional points. For a detailed discussion of the latter, we refer the reader to Chapter 8.

We can rewrite Eq. (2.67) in a more compact form by defining an operator $\mathcal{L}(\lambda_n) = \mathcal{A} + \lambda_n \mathcal{B}$:

$$\mathcal{L}(\lambda_n)\mathbf{v}_n = 0. \tag{2.68}$$

We refer to Eq. (2.68) as the *right* eigenvalue problem, for reasons that will become clear in the following.

We define an *inner product* for the vector space containing the vectors $\mathbf{v}_n$:

$$\langle \mathbf{y}|\mathbf{x}\rangle = \int_V \mathbf{y}^\dagger \mathbf{x} dV, \tag{2.69}$$

where $\mathbf{y}, \mathbf{x}$ are two arbitrary vectors in the space, and $\dagger$ denotes conjugate transpose. We also introduce an *adjoint* of the operator $\mathcal{L}$, denoted as $\mathcal{L}^\dagger$, determined by the relation:

$$\langle \mathbf{y}|\mathcal{L}\mathbf{x}\rangle = \langle \mathcal{L}^\dagger \mathbf{y}|\mathbf{x}\rangle. \tag{2.70}$$

An operator is called *hermitian* or *self-adjoint* when $\mathcal{L} = \mathcal{L}^\dagger$, and *non-hermitian* or *non-self-adjoint* otherwise. In open systems, particularly any kind of electromagnetic scatterer, we will see that we are dealing with non-Hermitian operators. In order for the right eigenvectors to be readily used in expansions of the quantities of interest, we need to prove some kind of orthogonality relation so that we can use them as a basis of the vector space. However, this is not straightforward to do for non-Hermitian operators. We require one more ingredient in our formulation, *left eigenvectors*, which are solutions to the left eigenvalue problem:

$$\mathcal{L}^\dagger(\tilde{\lambda}_n)\mathbf{w}_n = 0, \tag{2.71}$$

lying in some vector space with a domain $D_L^\dagger$. If the operator is Hermitian, the left eigenvalue problem is equivalent to the right eigenvalue one.

We further assume that we are dealing with an arbitrarily large, yet finite number of eigenvectors. In this case, it can be shown that

the eigenvalues of the left eigenvalue problem are the complex-conjugate of the right eigenvalue problem, i.e., $\tilde{\lambda}_n = \lambda_n^*$. Before proceeding, we show that the left and right eigenvectors obey a *bi-orthogonality* condition, which is nothing else than a relation between $\mathbf{v}_n$ and $\mathbf{w}_n$. Consider the products:

$$\left\langle \mathcal{L}^\dagger(\lambda_m)\mathbf{w}_m \middle| \mathbf{v}_n \right\rangle = 0, \tag{2.72}$$

$$\langle \mathbf{w}_m | \mathcal{L}(\lambda_n)\mathbf{v}_n \rangle = 0. \tag{2.73}$$

The latter two vanish since $\mathcal{L}(\lambda_n)\mathbf{v}_n = \mathcal{L}^\dagger(\lambda_m)\mathbf{w}_m = 0$. Since, by the definition of the adjoint operator in Eq. (2.70), we have $\left\langle \mathcal{L}^\dagger(\lambda_m)\mathbf{w}_m \middle| \mathbf{v}_n \right\rangle = \langle \mathbf{w}_m | \mathcal{L}(\lambda_m)\mathbf{v}_n \rangle$, then:

$$\langle \mathbf{w}_m | (\mathcal{A} + \lambda_m \mathcal{B})\mathbf{v}_n \rangle = \langle \mathbf{w}_m | (\mathcal{A} + \lambda_n \mathcal{B})\mathbf{v}_n \rangle ,$$

which can be rearranged to give:

$$(\lambda_m - \lambda_n) \langle \mathbf{w}_m | \mathcal{B}\mathbf{v}_n \rangle = 0. \tag{2.74}$$

Eq. (2.74) implies that the product $\langle \mathbf{w}_m | \mathcal{B}\mathbf{v}_n \rangle$ vanishes for all $m \neq n$. This result is known as the bi-orthogonality condition.

Our goal is to reach an expansion of the vector $\mathbf{u}$, which is a solution the inhomogeneous problem:

$$\mathcal{L}(\lambda)\mathbf{u} = \mathbf{S}, \tag{2.75}$$

where $\mathbf{S}$ corresponds to a source. We assume $\mathbf{u}$ can be expanded as a weighted sum of the right eigenvectors:

$$\mathbf{u} = \sum_n \alpha_n \mathbf{v}_n, \tag{2.76}$$

where the coefficients α_n are to be determined. Inserting Eq. (2.76) into Eq. (2.75) and taking the inner product of both sides with a left eigenvector $\mathbf{w}_m$, we get:

$$\sum_n \alpha_n \langle \mathbf{w}_m | \mathcal{L}(\lambda)\mathbf{v}_n \rangle = \langle \mathbf{w}_m | \mathbf{S} \rangle ,$$

$$\sum_n \alpha_n \langle \mathbf{w}_m | \mathcal{B}\mathbf{v}_n \rangle (\lambda - \lambda_n) = \langle \mathbf{w}_m | \mathbf{S} \rangle .$$

We can now use the bi-orthogonality condition to get rid of the summation, leading to an expression for the α_m coefficient:

$$\alpha_m = \frac{1}{\lambda - \lambda_m} \frac{\langle \mathbf{w}_m | \mathbf{S} \rangle}{\langle \mathbf{w}_m | \mathcal{B}\mathbf{v}_m \rangle}. \tag{2.77}$$

2.4.2 Quasinormal mode expansion

We are now ready to deal with the particular case of Maxwell's equations. Starting from Eqs. (2.1), there are many equivalent ways to choose the operators $\mathcal{A}$ and $\mathcal{B}$. Here, we follow Ref. [20] and define symmetric matrices:

$$\bar{\bar{A}} = -i \begin{pmatrix} 0 & \nabla\times \\ \nabla\times & 0 \end{pmatrix}, \tag{2.78}$$

$$\bar{\bar{B}} = \begin{pmatrix} \varepsilon & 0 \\ 0 & -\mu \end{pmatrix}. \tag{2.79}$$

In analogy with Eq. (2.75), we can rewrite Eqs. (2.1) as:

$$\left[-i \begin{pmatrix} 0 & \nabla\times \\ \nabla\times & 0 \end{pmatrix} + \omega \begin{pmatrix} \varepsilon & 0 \\ 0 & -\mu \end{pmatrix} \right] \mathbf{F} = \begin{pmatrix} -i\mathbf{J} \\ 0 \end{pmatrix}, \tag{2.80}$$

with $\lambda = \omega$, and $\mathbf{S} = \begin{pmatrix} -i\mathbf{J} & 0 \end{pmatrix}^T$. Our goal is now to find the adjoint $\mathcal{L}^\dagger$ and its associated left eigenvectors. To determine $\mathcal{L}^\dagger$, we impose Eq. (2.70). The term on the right-hand side gives:

$$\langle \mathbf{F}_1 | \mathcal{L}(\omega) \mathbf{F}_2 \rangle = \int_V \mathbf{F}_1^\dagger \mathcal{L}(\omega) \mathbf{F}_2 dV$$

$$= \int_V \left[-i(\nabla \times \mathbf{H}_2 \cdot \mathbf{E}_1^\dagger + \nabla \times \mathbf{E}_2 \cdot \mathbf{H}_1^\dagger) + \omega\varepsilon \mathbf{E}_1^\dagger \cdot \mathbf{E}_2 - \omega\mu \mathbf{H}_1^\dagger \cdot \mathbf{H}_2 \right] dV.$$

Here the volume V of the integral must include the resonator and its surroundings. To simplify the above expression, we can make use of the identity:

$$\nabla \cdot (\mathbf{A} \times \mathbf{B}) = \mathbf{B} \cdot (\nabla \times \mathbf{A}) - \mathbf{A} \cdot (\nabla \times \mathbf{B}), \tag{2.81}$$

in order to rearrange the first two terms:

$$\nabla \times \mathbf{H}_2 \cdot \mathbf{E}_1^\dagger = \mathbf{H}_2 \cdot \nabla \times \mathbf{E}_1^\dagger - \nabla \cdot (\mathbf{E}_1^\dagger \times \mathbf{H}_2),$$
$$\nabla \times \mathbf{E}_2 \cdot \mathbf{H}_1^\dagger = \nabla \times \mathbf{H}_1^\dagger \cdot \mathbf{E}_2 - \nabla \cdot (\mathbf{H}_1^\dagger \times \mathbf{E}_2).$$

With the help of the divergence theorem, this leads to:

$$\underbrace{\int_V \mathbf{F}_1^\dagger \mathcal{L}(\omega) \mathbf{F}_2 dV}_{\langle \mathbf{F}_1 | \mathcal{L} \mathbf{F}_2 \rangle} =$$

$$\underbrace{\int_V [\mathcal{L}(\omega) \mathbf{F}_1^\dagger] \cdot \mathbf{F}_2 dV}_{\langle \mathcal{L}^\dagger \mathbf{F}_1 | \mathbf{F}_2 \rangle} + \underbrace{i \int_{\partial V} (\mathbf{E}_1^\dagger \times \mathbf{H}_2 + \mathbf{H}_1^\dagger \times \mathbf{E}_2) \cdot \hat{\mathbf{n}} dS}_{I_{\partial V}}. \tag{2.82}$$

The surface integral $I_{\partial V}$ runs over the surface ∂V of the volume V. Suppose $I_{\partial V} = 0$ for some volume V. Then, $\mathcal{L}^\dagger$ is nothing else than the complex conjugate of $\mathcal{L}$. To make $I_{\partial V}$ vanish, we take a volume large enough to be considered in the far field so that the radiation conditions can be imposed. First, we rewrite each of the terms in the integrand of $I_{\partial V}$ separately:

$$(\mathbf{E}_1^\dagger \times \mathbf{H}_2) \cdot \hat{\mathbf{n}} = \mathbf{E}_1^\dagger \cdot (\mathbf{H}_2 \times \hat{\mathbf{n}}),$$
$$(\mathbf{H}_1^\dagger \times \mathbf{E}_2) \cdot \hat{\mathbf{n}} = \mathbf{E}_2 \cdot (\hat{\mathbf{n}} \times \mathbf{H}_1^\dagger).$$

In the far field, Eqs. (2.64) give $\hat{\mathbf{n}} \times \mathbf{H}_2 = -Z_0 \mathbf{E}_2$. Hence the integrand of $I_{\partial V}$ becomes:

$$\mathbf{E}_2 \cdot (\hat{\mathbf{n}} \times \mathbf{H}_1^\dagger + Z_0 \mathbf{E}_1^\dagger).$$

On the other hand, the fields $\mathbf{E}_1^\dagger$, $\mathbf{H}_1^\dagger$ fulfill the conjugate of Eqs. (2.64), so that $\hat{\mathbf{n}} \times \mathbf{H}_1^\dagger = -Z_0 \mathbf{E}_1^\dagger$. As a result, the integrand vanishes and $I_{\partial V} = 0$. The left eigenvectors $\mathbf{W}_n$ are found by solving the left eigenvalue problem:

$$\mathcal{L}^*(\omega)\mathbf{W}_n = 0, \tag{2.83}$$

which can be equivalently written as:

$$(\mathcal{A}^* + \omega^* \mathcal{B})\mathbf{W}_n = 0. \tag{2.84}$$

Note that $\mathcal{B}^* = \mathcal{B}$, since we have assumed the materials are lossless. Taking the complex conjugate of Eq. (2.84), it turns out that:

$$(\mathcal{A} + \omega \mathcal{B})\mathbf{W}_n^* = 0. \tag{2.85}$$

Since $\mathbf{W}_n^*$ is a solution to the right eigenvalue problem and $\mathbf{F}_n^*$ fulfills the conjugate of Eqs. (2.64), we can conclude that $\mathbf{W}_n = \mathbf{F}_n^*$.

We are now ready to calculate the expansion coefficients. Hereon, we assume that we can integrate over a domain large enough for the radiation conditions to be fulfilled so that we can get rid of $I_{\partial V}$. In numerical calculations, particularly the finite element method, it is possible to use perfectly-matched layers to achieve a fast convergence with the domain size [17]. An analytic normalization for any volume surrounding the scatterer is also possible by including the term $I_{\partial V}$. However, the derivation of the expansion coefficients is slightly more involved [22]. Taking into account these considerations, we can directly apply Eq. (2.77), which for our case gives:

$$\alpha_m = -\frac{i}{\omega - \omega_m} \frac{\int_V \mathbf{E}_m \cdot \mathbf{J} dV}{\int_V \mathbf{E}_m \varepsilon \mathbf{E}_m - \mathbf{H}_m \mu_0 \mathbf{H}_m dV}. \tag{2.86}$$

The normalization factor $\langle \mathbf{w}_m | \mathcal{B} \mathbf{v}_m \rangle$ is simply given by:

$$N_m = \int_V \mathbf{E}_m \varepsilon \mathbf{E}_m - \mathbf{H}_m \mu_0 \mathbf{H}_m dV. \tag{2.87}$$

We now proceed assuming all fields are normalized such that $N_m = 1$. The scattered field is produced by a current $\mathbf{J} = -i\omega\Delta\varepsilon\mathbf{E}_b$. Inserting the latter into the previous expression, we get:

$$\alpha_m = \frac{\omega}{\omega_m - \omega} \int_V \mathbf{E}_m \Delta\varepsilon \mathbf{E}_b dV. \tag{2.88}$$

We can now appreciate that the contribution of each individual QNM is just a Lorentzian centered at $\omega = \omega_m$. We can now calculate modal expansions for all quantities of interest. Since we have assumed lossless materials, the absorption cross section is 0. The extinction cross section can be directly computed as:

$$\sigma_{\text{ext}} = \frac{P_{\text{ext}}}{I_0} = \frac{\omega}{2I_0} \int_V \text{Im}[\Delta\varepsilon \mathbf{E}_b^* \cdot \mathbf{E}_s] dV = \sum_m \sigma_{\text{ext},m}, \tag{2.89}$$

where $\sigma_{\text{ext},m}$ is the contribution of each individual QNM:

$$\sigma_{\text{ext},m} = \frac{\omega}{2I_0} \int_V \alpha_m(\omega) \, \text{Im}[\Delta\varepsilon \mathbf{E}_b^* \cdot \mathbf{E}_m] dV. \tag{2.90}$$

It is also possible to calculate the multipolar content of a QNM to analyze the far-field behavior. This can be done by inserting the polarization current $\mathbf{P}_m = \Delta\varepsilon\mathbf{E}_m$ into Eqs. (2.57)–(2.60). We can also investigate the response of the cavity to a point source, or an arbitrary combination of multipoles, by inserting Eq. (2.24) into Eq. (2.77). For instance, consider a point ED source with $\mathbf{J} = -i\omega\mathbf{d}\delta(\mathbf{r} - \mathbf{r}_0)$. The total field inside the cavity and its vicinity can be decomposed as $\mathbf{E}_{\text{tot}} = \sum_m A_m(\omega)\mathbf{E}_m$, with $A_m(\omega) = \frac{\omega}{\omega_m - \omega}\mathbf{d} \cdot \mathbf{E}_m(\mathbf{r}_0)$, assuming again $N_m = 1$. It is then straightforward to calculate quantities such as the decay rate of a point ED emitter, which gives [17]:

$$\frac{\gamma}{\gamma_0} = -\frac{3}{4\pi^2} \sum_m \text{Im}\left(\frac{\omega}{\omega - \omega_m} \frac{\lambda^3}{2\tilde{V}_m} \right), \tag{2.91}$$

where $\tilde{V}_m$ is the complex mode volume, defined as:

$$\tilde{V}_m = \frac{1}{2\varepsilon_0 |\mathbf{E}_m(\mathbf{r}_0) \cdot \mathbf{u}|^2}, \tag{2.92}$$

and $\mathbf{u}$ is the dipole polarization direction, i.e., $\mathbf{d} = d\mathbf{u}$. In the previous we have assumed the cavity to be embedded in air.

2.5 Phenomenological models

2.5.1 Coupled harmonic oscillators

As has been shown in section 2.4, the response of a dielectric nanocavity can be synthesized as a sum of QNMs. Thus, as a first approximation to the more general QNM theory, it is reasonable to trace an analogy with a set of coupled mechanical oscillators. In many cases of interest, the dynamics of the resonator can be mapped to a simple model of two driven harmonic oscillators (Fig. 2.6a). Often one of the oscillators is strongly driven (a *bright* mode), while the other is only weakly driven or only excited due to the coupling with the bright mode (a *dark* mode).

To illustrate the idea, consider two oscillators with masses $m_1 = m_2 = m$, connected by a third spring, as shown in Fig. 2.6a. Oscillator 1 is driven by a harmonic force $f = f_0 e^{-i\omega t}$. First, we proceed to derive the equations of motion. Assume for the moment that there is no driving force. If we keep 2 fixed, and displace 1 by a distance x_1, the latter will feel a force $-k_1 x_1 - g x_1$, where k_1 is the spring constant and g is the spring constant of the connecting spring. Keeping x_1 fixed, but moving x_2, we also get a force on x_1, $+g x_2$. Newton's law gives:

$$m\ddot{x}_1 = -k_1 x_1 - g x_1 + g x_2.$$

We can also introduce a damping term $-\gamma_1 \dot{x}_1$, that would take into account losses due to radiation and dissipation. Finally, when adding the driving force, the equations of motion read:

$$\begin{aligned} \ddot{x}_1 + \gamma_1 \dot{x}_1 + (\omega_1^2 + g)x_1 - g x_2 &= f_0 e^{-i\omega t}, \\ \ddot{x}_2 + \gamma_1 \dot{x}_1 + (\omega_2^2 + g)x_2 - g x_1 &= 0. \end{aligned} \tag{2.93}$$

In the previous, we have made the choice $m = 1$ and assumed the second oscillator has no losses. ω_1 and ω_2 are the resonance frequencies of the uncoupled oscillators (i.e., if $g = 0$). Let us now find the stationary response of the system. Eqs. (2.93) can then be solved assuming solutions of the form:

$$\begin{aligned} x_1 &= c_1 e^{-i\omega t}, \\ x_2 &= c_2 e^{-i\omega t}. \end{aligned}$$

Inserting these ansatz into Eqs. (2.93), we can write down the following algebraic system of equations:

$$\underbrace{\begin{pmatrix} -\omega^2 + i\omega\gamma_1 - (\omega_1^2 + g) & g \\ g & -\omega^2 + i\omega\gamma_2 - (\omega_2^2 + g) \end{pmatrix}}_{\bar{\bar{M}}} \begin{pmatrix} c_1 \\ c_2 \end{pmatrix} = \begin{pmatrix} f_0 \\ 0 \end{pmatrix}. \tag{2.94}$$

The c_i coefficients give:

$$c_1 = \frac{f_0(\omega_2^2 - \omega^2)}{(\omega^2 - \omega_1^2 + 2i\gamma_1\omega)(\omega^2 - \omega_2^2) - g^2}, \tag{2.95}$$

$$c_2 = \frac{f_0 g}{(\omega^2 - \omega_1^2 + 2i\gamma_1\omega)(\omega^2 - \omega_2^2) - g^2}. \tag{2.96}$$

Using the expressions for $|c_i(\omega)|$, we can reproduce the lineshapes associated with interesting phenomena, such as Lorentz or Fano resonances, as shown in Fig. 2.6b,c. Let us now find the eigenmodes of the coupled system. For simplicity in the expressions, we assume small dissipation losses and neglect γ_1 unless stated in the text. The eigenmodes are self-sustaining oscillations in the absence of driving force. They can be found by setting $f_0 = 0$ in

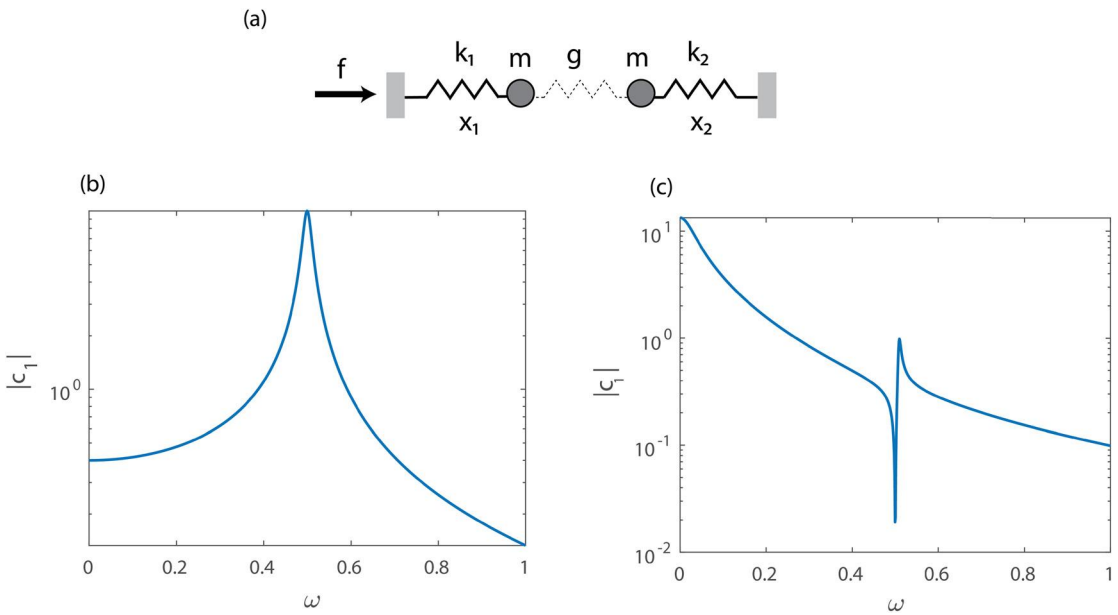

Figure 2.6. (a) Scheme depicting two coupled harmonic oscillators driven by a force f. The coupling constant g is usually assumed to be significantly weaker than k_1, k_2. (b) Lorentz profile obtained with $|c_1|$ with the following parameters: $\omega_1 = \omega_2 = 0.5$, $\gamma_1 = 0.01$, $f_0 = 0.1$, $g = 0$. (c) Fano resonance realized in the same fashion but with $\omega_1 = 0.05$, $\omega_2 = 0.5$, $\gamma_1 = 0.1$, $f_0 = 0.1$, $g = 0.05$.

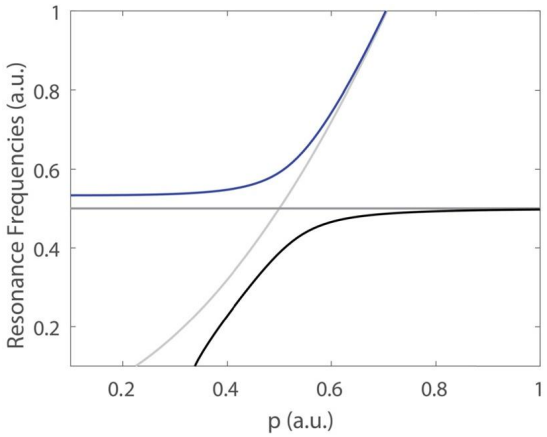

Figure 2.7. Resonance frequencies of the coupled system of oscillators obtained with Eqs. (2.97). Blue line corresponds to ω_+, while the black line is ω_-., as a function of a tuning parameter p. Gray lines show the uncoupled eigenfrequencies. We assume that $\omega_1 = 2p^2$, while $\omega_2 = 0.5$. In this example, we set $g = 0.1$.

Eq. (2.94) and solving for the nontrivial solutions, for instance, by finding $\det\left[\bar{\bar{M}}(\omega)\right] = 0$. The two eigenfrequencies are [25]:

$$\omega_\pm^2 = \frac{1}{2}[\omega_1^2 + \omega_2^2 \pm \sqrt{(\omega_1^2 - \omega_2^2)^2 + 4\Gamma^2\omega_1\omega_2}], \tag{2.97}$$

with $\Gamma = \frac{g}{\sqrt{\omega_1\omega_2}}$. We can now study their evolution with different values of the parameters. The most interesting behavior occurs when the original eigenfrequencies are nearly degenerate ($\omega_1 \approx \omega_2 \approx \omega_0$). Where the eigenfrequencies originally crossed, we now get:

$$\omega_\pm^2 = \frac{1}{2}[2\omega_0^2 \pm 2\Gamma\omega_0] = \omega_0^2 \pm g.$$

For $g << \omega_i$, a Taylor series yields $\omega_\pm = \omega_0 \pm \frac{g}{2\omega_0} + O(g^2)$. Hence, due to the coupling we get a splitting of

$$\omega_+ - \omega_- = \frac{g}{\omega_0} = \Gamma. \tag{2.98}$$

The eigenfrequencies of the toy model with and without coupling are plotted in Fig. 2.7. The eigenfrequencies are seen to "avoid" the crossing. If we had taken into account losses, the splitting would only be visible when $g/\gamma_1 >> 1$ [25]. The observation of avoided crossing is usually taken as the hallmark of *strong coupling*. In this regime, the energy per unit time exchanged between the two oscil-

lators is much larger than the energy dissipated by each of them. The new eigenmodes can be expressed as a linear combination of the original oscillators [25]:

$$\begin{pmatrix} c_+ \\ c_- \end{pmatrix} = \begin{pmatrix} \sin\theta_M & \cos\theta_M \\ \cos\theta_M & -\sin\theta_M \end{pmatrix} = \begin{pmatrix} c_1 \\ c_2 \end{pmatrix}, \tag{2.99}$$

where θ_M is the *mixing angle*, which, as its name indicates, determines the degree of mixing between the two original uncoupled oscillators. It is given by the equation:

$$\tan\theta_M = \frac{\omega_2^2 - \omega_+^2}{g}. \tag{2.100}$$

2.5.2 Temporal coupled mode theory

In the previous section, we have shown a simplified model of coupled oscillators allowing to capture the most essential qualitative features of electromagnetic resonators. This approach, however, has important shortcomings in practice. On the one hand, the equations become very cumbersome once the number of oscillators (number of resonances) in our system increases, complicating the physical interpretation. On the other hand, its parameters are only weakly constrained. In order to quantitatively describe a system, we are forced to rely on inaccurate multiparameter fitting procedures, which can lead to unphysical results.

Most importantly, the coupled oscillator model is not immediately suited to take into account energy transport into multiple channels of a continuum (e.g., several multipolar waves or diffraction orders). Here, we will introduce a powerful *general* method that, relying on a few approximations, can describe photonic systems of many different kinds, including dielectric metasurfaces and isolated dielectric nanoparticles.

This method is called the *Temporal Coupled Mode Theory*, or TCMT for short. The basic picture of TCMT is shown in Fig. 2.8a. We study an arbitrary electromagnetic resonator that exchanges energy with some environment through a set of incoming (+) and outgoing (−) "scattering channels" with amplitudes s_i. The choice of the scattering channels depends on the system. The most commonly used are plane waves (for planar systems such as metasurfaces [26]) or VSHs (for finite systems such as isolated nanoparticles [27]). They can also correspond to forward and backward propagating waveguide modes [28]. The s_i are normalized such that $|s_i^2|$ corresponds to the power carried by the ith channel. In what follows, we make 5 main assumptions about our system [29]:

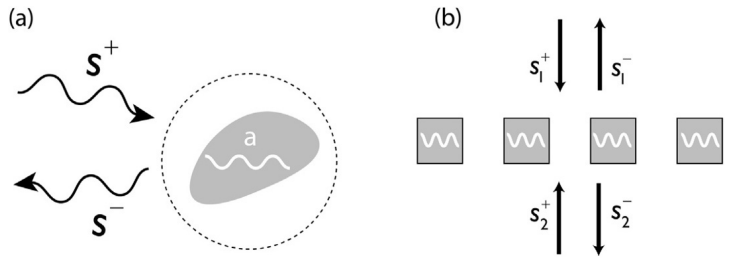

Figure 2.8. (a) A resonator supporting an excited mode with amplitude a exchanges energy with the environment through scattering channels. (b) A metasurface operating in the 0th diffraction order, modeled as a two-channel structure.

1. The resonant modes are only weakly coupled with the scattering channels.
2. The system is linear.
3. The system is time-invariant.
4. Energy conservation is satisfied.
5. The system obeys time-reversal invariance.

We want to investigate how the (complex) amplitude a of the resonant mode in the cavity changes with time. For simplicity, we can normalize a such that $|a|^2$ corresponds to the energy stored in the mode. With time, the fields must decay as $e^{-\omega_r t}e^{-t/\tau_0}$, where ω_r is the resonance frequency and $\tau_0 = 1/\gamma_0$ is the mode lifetime due to intrinsic (ohmic) losses and γ_0 is the intrinsic decay rate. This is a solution to the ordinary differential equation:

$$\frac{da}{dt} = -i(\omega_r - i\gamma_0)a.$$

However, we must also take into account that the mode can leak or be excited through the available scattering channels. Then, (i) the decay rate changes, and (ii) a must grow proportionally to the input power. With these two in mind, the "equation of motion" for the mode is modified to yield:

$$\frac{da}{dt} = -i(\omega_r - i\gamma_0 - i\sum_i \gamma_i)a + \sum_i \alpha_i s_i^+, \tag{2.101}$$

where α_i is a proportionality parameter that indicates how well light from the ith scattering channel is coupled to the mode. Consider now the relation between incoming and outgoing channels. In the absence of the resonator, the outgoing waves must be proportional to the incoming waves, i.e. $s_i^- = \beta_i s_i^+$. Once we introduce the resonator, the mode can also leak a fraction of its energy to the

outgoing channels. Hence:

$$s_i^- = \beta_i s_i^+ + d_i a. \tag{2.102}$$

Similar to the CO model, there appear to be several unknowns that require fitting. Now, we will show how to impose symmetry constraints to drastically reduce the number of unknowns. In this book, we will be dealing mostly with dielectrics with low ohmic losses. Therefore, from now on we set $\gamma_0 = 0$. Now, imagine all channels shut down (no incoming power). Further, assume the mode decays only through channel $i = 1$. Then, we know that energy from the mode must decay as:

$$\frac{d|a|^2}{dt} = -|s_1^-|^2. \tag{2.103}$$

Operating with Eq. (2.102) and its complex conjugate, we get:

$$-|s_1^-|^2 = -2\gamma_1 |a|^2.$$

Using Eq. (2.102) with $s_1^+ = 0$ we notice that $|s_1^-|^2 = |d_1|^2|a|^2$. Inserting this into the previous equation results in the relation $|d|_1^2 = 2\gamma_1$. This can be extended (to first order in $gamma_i$) to all channels, i.e. $|d_i|^2 = 2\gamma_i$. Since similar considerations can also be used in what follows, we will simplify our system and consider only one scattering channel, omitting the subscript, writing only $s^{\pm}$.

Next, we study the effect of time reversal symmetry. We have started with the mode amplitude $a(t)$, with the Fourier decomposition:

$$a(t) = \int_{-\infty}^{\infty} a(\omega) e^{-i\omega t} d\omega. \tag{2.104}$$

Time-reversal implies switching time such that we get the amplitudes:

$$\tilde{a}(t) := a(-t) = \int_{-\infty}^{\infty} a(\omega) e^{i\omega t} d\omega. \tag{2.105}$$

However, we stick to our original convention of $e^{-i\omega t}$. This is simply done by using the property that any real function fulfills $a(-\omega) = a^*(\omega)$, leading to:

$$\tilde{a}(t) = \int_{-\infty}^{\infty} a^*(\omega) e^{-i\omega t} d\omega. \tag{2.106}$$

It turns out that $\hat{a}(\omega)$ is nothing else than $a^*(\omega)$. Further, we can use Eq. (2.101) to write down expressions for each Fourier amplitude $a(\omega)$ and $\tilde{a}(\omega)$, after replacing the time derivatives by $-i\omega$:

$$a(\omega) = \frac{\alpha s^+}{-i(\omega - \omega_r) + \gamma}, \tag{2.107}$$

$$\tilde{a}(\omega) = \frac{\alpha \tilde{s}^+}{-i(\omega - \omega_r) + \gamma}, \tag{2.108}$$

where we have denoted by $\tilde{s}^+$ the time-reversed incoming wave. We want to study the time-reversed process of the mode decay in Eq. (2.103), where we had originally set $s^+ = 0$. In this first process, the mode decays at the frequency $\omega_r - i\gamma$, with amplitude $a(\omega)$, which from Eq. (2.107) is:

$$a(\omega) = \frac{\alpha s^+}{2\gamma}. \tag{2.109}$$

Analogously, the amplitude of the time-reversed process is given by:

$$\tilde{a}(\omega) = \frac{\alpha \tilde{s}^+}{2\gamma}. \tag{2.110}$$

With $\tilde{s}^- = 0$, we get:

$$\frac{d|\tilde{a}|^2}{dt} = 2\gamma|\tilde{a}|^2 = |\tilde{s}^+|^2 \tag{2.111}$$

But we know that if the system is time-reversal symmetric, the incoming power of the time-reversed process must be equal to the outgoing power of the original process, $|\tilde{s}^+|^2 = |s^-|^2$. Introducing Eq. (2.110) in Eq. (2.111), we get:

$$\alpha^* \alpha = 2\gamma. \tag{2.112}$$

A second consequence of the time-reversed process is that $\hat{s}^- = 0$, so:

$$0 = \beta s^+ + d\tilde{a},$$

as follows from Eq. (2.102). Since $\tilde{s}^+ = (s^-)^*$, and $s^- = da$, we can replace the latter in the previous expression. Recalling that $\tilde{a} = a^*$, we finally get:

$$\beta d^* = -d. \tag{2.113}$$

Summarizing all constraints:

$$\alpha^*\alpha = 2\gamma, \tag{2.114}$$
$$d^*d = 2\gamma, \tag{2.115}$$
$$\beta d^* = -d. \tag{2.116}$$

It is possible to introduce a last constraint due to reciprocity [28], which imposes $\alpha = d$. As long as we respect the weak coupling condition ($\omega_i >> \gamma_i$), all these results can be generalized to an arbitrary number of channels and resonant modes, leading to the system of equations [30]:

$$\frac{d\mathbf{a}}{dt} = -i\bar{\bar{H}}\mathbf{a} + \bar{\bar{D}}^T\mathbf{s}^+, \tag{2.117}$$
$$\mathbf{s}^- = \bar{\bar{B}}\mathbf{s}^+ + \bar{\bar{D}}\mathbf{a}. \tag{2.118}$$

$\mathbf{a}$ is a column vector containing the amplitudes of all the modes, while $\mathbf{s}^{\pm}$ contains the amplitudes of all incoming(outgoing) channels. The elements D_{ij} of the matrix $\bar{\bar{D}}$ determine the coupling of mode j with the scattering channel i, $\bar{\bar{B}}$ is the background scattering matrix and $\bar{\bar{H}} = \bar{\bar{\Omega}}_r - i\bar{\bar{\Gamma}}$ is often referred to as the *effective Hamiltonian*. $\bar{\bar{\Omega}}$ is a diagonal matrix with all the resonant frequencies in its diagonal, and $\bar{\bar{\Gamma}}$ contains the radiative losses.

In analogy to the simple case studied above, the matrices are constrained by:

$$\bar{\bar{D}}^\dagger\bar{\bar{D}} = 2\Gamma, \tag{2.119}$$
$$\bar{\bar{B}}\bar{\bar{D}}^* = -\bar{\bar{D}}, \tag{2.120}$$

where the superscript † indicates conjugate transpose. Eqs. (2.117)–(2.120) determine the scattering response of the system. In particular, they allow to reconstruct the so-called *scattering matrix* $\bar{\bar{S}}$, connecting incoming and outgoing channels for a fixed frequency of operation:

$$\mathbf{s}^- = \bar{\bar{S}}\mathbf{s}^+. \tag{2.121}$$

By imposing a time dependence of $e^{-i\omega t}$ in Eq. (2.117) and Eq. (2.118), $\bar{\bar{S}}$ can be directly found as:

$$\bar{\bar{S}} = \bar{\bar{B}} + i\bar{\bar{D}}(\omega\bar{\bar{I}} - \bar{\bar{H}})^{-1}\bar{\bar{D}}^T, \tag{2.122}$$

where $\bar{\bar{I}}$ is the identity matrix.

The TCMT formalism can be used to understand the coupling of multiple modes in a very simple way. Assume two modes can be described by the equations of motion:

$$\frac{da_1}{dt} = -i\omega_1 a_1,$$
$$\frac{da_2}{dt} = -i\omega_2 a_2.$$

In the above we have neglected the coupling with the scattering channels. This can be introduced later in the same way as previously.

We introduce some perturbation in the system and allow the modes to couple with some coefficients κ_{ij}. Then, the equations for the two modes read:

$$\frac{da_1}{dt} = -i\omega_1 a_1 + \kappa_{12} a_2, \tag{2.123}$$
$$\frac{da_2}{dt} = -i\omega_2 a_2 + \kappa_{21} a_1. \tag{2.124}$$

As before, the only assumption is that $\omega_1, \omega_2 >> \kappa_{12}, \kappa_{21}$. The latter could be called *weak coupling*. However, we know from Section 2.5.1 that weak coupling usually refers to the situation when $\omega_1 - \omega_2 << \kappa_{12}, \kappa_{21}$, while strong coupling corresponds to $\omega_1 - \omega_2 >> \kappa_{12}, \kappa_{21}$. It is important to emphasize that both regimes are accessible under the assumptions of TCMT.

If the closed system is energy conserving, there are strict constraints on the coupling coefficients. Consider that energy is present in the resonant system. In the steady state, the total energy in both modes must not change with time, so we must have:

$$\frac{d}{dt}(|a_1|^2 + |a_2|^2) = 0.$$

Operating with this expression and Eqs. (2.123)–(2.124), we get:

$$a_1^* \kappa_{12} a_2 + a_1 \kappa_{12}^* a_2^* + a_2^* \kappa_{21} a_1 + a_2 \kappa_{21}^* a_1^* = 0.$$

The latter condition must hold for *any* phase difference between a_1 and a_2. This can only happen when:

$$\kappa_{12} = -\kappa_{21}^*. \tag{2.125}$$

Using Eq. (2.125), we can now write down Eqs. (2.123)–(2.124) in matrix form as:

$$\frac{d\mathbf{a}}{dt} = -i\bar{\bar{H}}\mathbf{a}, \tag{2.126}$$

with $\bar{\bar{H}}$ now given by:

$$\bar{\bar{H}} = \begin{pmatrix} \omega_1 & \kappa \\ \kappa^* & \omega_2 \end{pmatrix}. \tag{2.127}$$

For a bimodal system, the most general form of the effective Hamiltonian (taking into account radiation losses and in the absence of ohmic losses) would read:

$$\bar{\bar{H}} = \begin{pmatrix} \omega_1 & \kappa \\ \kappa^* & \omega_2 \end{pmatrix} - i\frac{D^\dagger D}{2}. \tag{2.128}$$

2.5.2.1 Example

We will now show with a particular example how to derive a TCMT model from the general theory above. We choose a hypothetical dielectric metasurface supporting a single resonant mode, (Fig. 2.8b). As explained in section 2.6, only the zeroth diffraction order can carry energy to the far field. As a result,power can be exchanged with the environment through two channels $i = 1, 2$, corresponding to the plane waves propagating toward the upper and lower half-spaces.

We first determine the background scattering matrix. In the absence of the metasurface, incoming light from the top would be fully transmitted and vice versa, so that $B_{12} = B_{21} = 1$ and $B_{11} = B_{22} = 0$. Hence:

$$\bar{\bar{B}} = \begin{pmatrix} 0 & 1 \\ 1 & 0 \end{pmatrix}. \tag{2.129}$$

We have a single mode that can couple to two channels, so the matrix $\bar{\bar{D}} = \begin{pmatrix} d_1 & d_2 \end{pmatrix}^T$. We can then use Eq. (2.119) to determine the d_i up to a phase:

$$|d_1|^2 + |d_2|^2 = 2\gamma. \tag{2.130}$$

Since the system is symmetric to a mirror reflection from the $x - y$ plane, we know that $|d_1| = |d_2|$, and in combination with Eq. (2.130) we get $|d_1| = |d_2| = \sqrt{\gamma}$. To fix the phase, we use Eq. (2.120), which gives:

$$d_2^* = -d_1, \tag{2.131}$$

$$|d_2| \exp(-i\theta_2) = -\exp(i\theta_1). \tag{2.132}$$

Since there are no other constraints, we are free to set one of the phases. For instance, we set $\theta_1 = 0$, so that $\exp(i\theta_2) = -1$. The final

d_i are then $d_{1,2} = \pm\sqrt{\gamma}$. Our final equations look like:

$$\frac{da}{dt} = -i(\omega_0 - i\gamma)a + \sqrt{\gamma}s_1^+ - \sqrt{\gamma}s_2^+, \tag{2.133}$$

$$s_1^- = s_1^+ + \sqrt{\gamma}a, \tag{2.134}$$

$$s_2^- = s_2^+ - \sqrt{\gamma}a, \tag{2.135}$$

where ω_0 is the resonance frequency of the mode. To determine the reflection and transmission from the structure, we calculate the scattering matrix with Eq. (2.122):

$$\bar{\bar{S}} = \begin{pmatrix} 0 & 1 \\ 1 & 0 \end{pmatrix} + \frac{1}{\gamma - i(\omega - \omega_0)} \begin{pmatrix} \gamma & -\gamma \\ -\gamma & \gamma \end{pmatrix}. \tag{2.136}$$

The reflection r is nothing more than the $S_{11} = S_{22}$ coefficient, while transmission t is the $S_{21} = S_{12}$ coefficient:

$$\begin{aligned} r(\omega) &= \frac{\gamma}{\gamma - i(\omega - \omega_0)}, \\ t(\omega) &= 1 - \frac{\gamma}{\gamma - i(\omega - \omega_0)}. \end{aligned} \tag{2.137}$$

Reflectance and transmittance can be directly calculated as $R = |r|^2$ and $T = |t|^2$, as shown in Fig. 2.9a, where a dip in transmission centered at the resonance frequency can be appreciated. A plot of $\arg(r)$ (Fig. 2.9b) demonstrates how the model is also capable of reproducing the phase shift experienced by the incident light upon reflection.

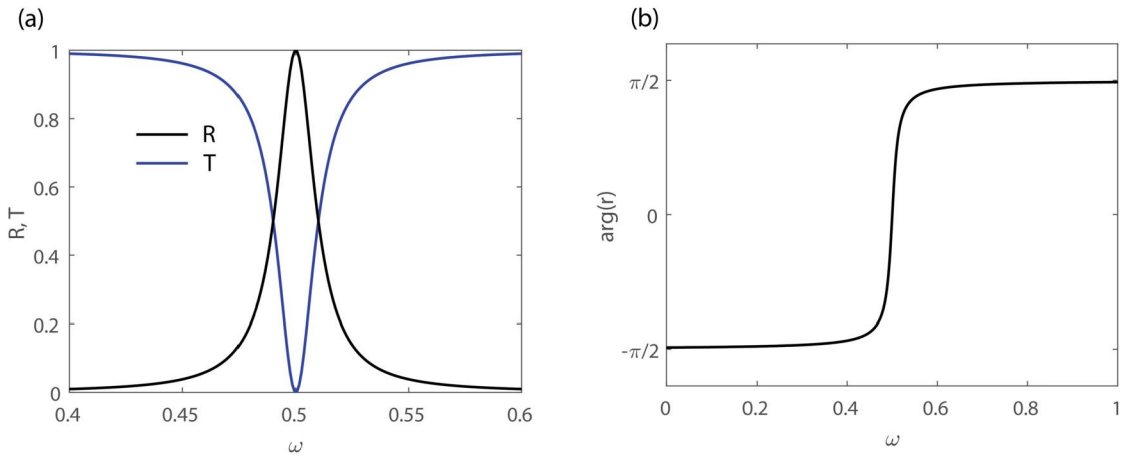

Figure 2.9. (a) Reflectance and transmittance calculated with Eqs. (2.137). Parameters: $\omega_0 = 0.5$, $\gamma = 0.01$. (b) Phase shift induced in the incident light after reflection.

2.6 General principles of periodic arrays

We dedicate this section to present basic concepts of periodic photonic structures. The discussion provided here is by no means complete. Extensive treatments can be found in well-established textbooks [29,31]. We limit ourselves to essential results derived from *Bloch's theorem* in one dimension, which are necessary to understand the working principle of dielectric metasurfaces.

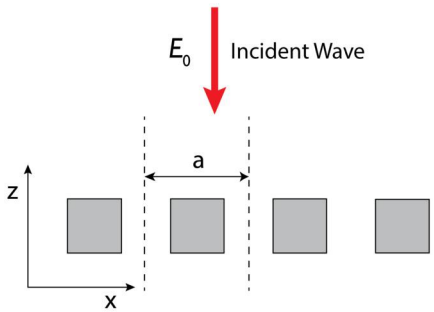

Figure 2.10. A periodic dielectric structure with period a is illuminated by an incident plane wave.

A prototypical one-dimensional periodic structure is depicted in Fig. 2.10. The latter is composed of identical dielectric cavities repeated with a period a. The smallest repetitive unit is called a *unit cell*. Consider an incident plane wave with wavevector $\mathbf{k}$. Upon interaction with the periodic array, a scattered field $\mathbf{E}_{t,r}$ will be produced, where the subscripts t, r denote transmitted or reflected fields, respectively. The periodicity imposes strict bounds on the spatial dependence of the scattered field. In particular, since the structure possesses a discrete translational symmetry (i.e., it repeats itself along x after a period a), the scattered fields can be expanded in a Fourier series in k-space, that obeys Bloch's theorem:

$$\mathbf{E}_{t,r}(x,z) = \sum_{m=-\infty}^{\infty} \mathbf{U}_m^{t,r}(z) e^{i(k_\parallel + mb)x}, \tag{2.138}$$

where $b = \frac{2\pi}{a}$ is the reciprocal vector and $k_\parallel$ is the in-plane component of the incident wavevector (in our case, the x-component). Eq. (2.138) tells us that the scattered fields are formed by a superposition of plane waves with increasing in-plane wavevectors. The contribution of each of these plane waves, distinguished by the index m, is called a *diffraction order*. They are illustrated in

Fig. 2.11 for the case of a normally incident plane wave. For the 0th diffraction order, light is reflected and transmitted without any additional in-plane wavevector. However, higher orders "tilt" light by an angle. To understand how the scattered light behaves in the far field, it suffices to realize that $\mathbf{U}_m^{t,r}(z)$ must behave as a plane wave in the limit of $z \to \infty$, so that $\mathbf{U}_m^{t,r}(z >> \lambda) \propto e^{ik_{z,m}z}$. Furthermore, due to energy conservation, we must have $k^2 = k_{\parallel,m}^2 + k_{z,m}^2$. We can then solve for $k_{z,m}$:

$$k_{z,m} = \pm\sqrt{k^2 - k_{\parallel,m}^2} = \pm\sqrt{k^2 - \left(k_\parallel + \frac{2\pi m}{a}\right)^2}. \tag{2.139}$$

If $k^2 \leq k_{\parallel,m}^2$, $k_{z,m}$ is purely imaginary or 0. Then, the mth diffraction order would correspond to an evanescent wave that would vanish in the far field, i.e. $\mathbf{U}_m^{t,r}(z >> \lambda) = 0$. It turns out that only the diffraction orders with $k^2 > k_{\parallel,m}^2$ can propagate to the far field. Noting that $\omega = ck$, we can rewrite this condition as $\omega > c|k_{\parallel,m}|$. The lines $\omega = \pm ck_{\parallel,m}$ define the so-called *light cone*. Diffraction orders with frequencies lying inside the light cone can propagate to the far field. Those lying outside the light cone correspond to evanescent waves.

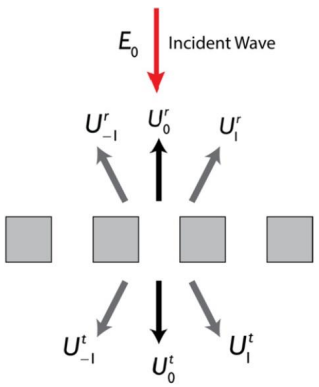

Figure 2.11. Illustration of the 0th and 1st diffraction orders produced in the scattering from a periodic dielectric structure.

A metasurface is a 2D periodic array where only the 0th diffraction order lies inside its light cone. All other orders must be evanescent. If we allow $m = 0$, we require that the $m = \pm 1$ orders are evanescent:

$$\pm k < k_\parallel + \frac{2\pi}{a}.$$

This implies the condition $|k - k_{\|}| < 2\pi$. For a normally incident plane wave, $k_{\|} = 0$ and we get $a < \lambda$. Thus, a metasurface must have a *subwavelength unit cell*. Consider now the coefficient $\mathbf{U}_0^s(z)$, where $s = t, r$. By definition of the zeroth Fourier coefficient [32]:

$$\mathbf{U}_0^s(z) = \int_{-a/2}^{a/2} \mathbf{E}_s(x, z) e^{-ik_{\|}x} dx. \tag{2.140}$$

Then, at normal incidence $k_{\|} = 0$, we get:

$$\mathbf{U}_0^s(z) = \int_{-a/2}^{a/2} \mathbf{E}_s(x, z) dx. \tag{2.141}$$

The zeroth order response is nothing more than the average response of the single unit cell. This result can be directly generalized to two-dimensional arrays, simply by replacing the line integral by a surface integral. Writing $\mathbf{U}_0^s(z >> \lambda) = \mathbf{U}^s e^{ik_{z,0}z}$, we can now define some reflection and transmission coefficients as $t = \frac{U^t}{E_0}$ and $r = \frac{U^r}{E_0}$, where E_0 is the amplitude of the incident wave. Hence, since no diffraction orders are "open", a metasurface reflects and transmits light in an analogous fashion as an homogeneous material slab would, despite being composed of an heterogeneous array of scatterers.

Acknowledgments

The authors gratefully acknowledge the financial support from the Ministry of Science and Higher Education of the Russian Federation (Agreement No. 075-15-2022-1150). Sections 2.2 and 2.3 are partially supported by the Russian Science Foundation grant 21-12-00151. Section 2.4 are partially supported by the Russian Science Foundation grant 23-72-00037. A.S.S. and A.C.V. gratefully acknowledge the support from the Latvian Council of Science, projects: NEO-NATE, No. lzp-2022/1-0553 and DNSSN, project No. lzp-2021/1-0048 for Sections 2.5 and 2.6.

References

[1] John David Jackson, Classical Electrodynamics, Wiley, 2021.
[2] Lukas Novotny, Bert Hecht, Principles of Nano-Optics, Cambridge University Press, 2012.
[3] Maurice I. Sancer, et al., On volume integral equations, IEEE Transactions on Antennas and Propagation 54 (5) (2006) 1488–1495.

[4] Andrey B. Evlyukhin, Boris N. Chichkov, Multipole decompositions for directional light scattering, Physical Review B 100 (12) (2019) 125415.
[5] Andrey B. Evlyukhin, et al., Multipole analysis of light scattering by arbitrary-shaped nanoparticles on a plane surface, Journal of the Optical Society of America B 30 (10) (2013) 2589–2598.
[6] Andrey B. Evlyukhin, et al., Optical theorem and multipole scattering of light by arbitrarily shaped nanoparticles, Physical Review B 94 (20) (2016) 205434.
[7] Patrick Grahn, Andriy Shevchenko, Matti Kaivola, Electromagnetic multipole theory for optical nanomaterials, New Journal of Physics 14 (9) (2012) 093033.
[8] Jon Applequist, Traceless Cartesian tensor forms for spherical harmonic functions: new theorems and applications to electrostatics of dielectric media, Journal of Physics. A, Mathematical and General 22 (20) (1989) 4303.
[9] Egor A. Gurvitz, et al., The high-order toroidal moments and anapole states in all-dielectric photonics, Laser & Photonics Reviews 13 (5) (2019) 1800266.
[10] Ferdinando Borghese, Paolo Denti, Rosalba Saija, Scattering from Model Nonspherical Particles: Theory and Applications to Environmental Physics, Springer Science & Business Media, 2007.
[11] Craig F. Bohren, Donald R. Huffman, Absorption and Scattering of Light by Small Particles, John Wiley & Sons, 2008.
[12] R. Fuchs, K.L. Kliewer, Optical modes of vibration in an ionic crystal sphere, Journal of the Optical Society of America 58 (3) (Mar. 1968) 319–330, https://doi.org/10.1364/JOSA.58.000319, http://www.osapublishing.org/abstract.cfm?URI=josa-58-3-319.
[13] Rasoul Alaee, Carsten Rockstuhl, Ivan Fernandez-Corbaton, Exact multipolar decompositions with applications in nanophotonics, Advanced Optical Materials 7 (1) (2019) 1800783.
[14] Ivan Fernandez-Corbaton, et al., Exact dipolar moments of a localized electric current distribution, Optics Express 23 (26) (2015) 33044–33064.
[15] George Gamow, Zur quantentheorie des Atomkernes, Zeitschrift für Physik 51 (3–4) (1928) 204–212.
[16] Ya B. Zel'Dovich, On the theory of unstable states, Soviet Physics, JETP 12 (1961) 542.
[17] Philippe Lalanne, et al., Light interaction with photonic and plasmonic resonances, Laser & Photonics Reviews 12 (5) (2018) 1700113.
[18] E.A. Muljarov, Full electromagnetic Green's dyadic of spherically symmetric open optical systems and elimination of static modes from the resonant-state expansion, Physical Review A 101 (5) (2020) 053854.
[19] Philip Trøst Kristensen, et al., Modeling electromagnetic resonators using quasinormal modes, Advances in Optics and Photonics 12 (3) (2020) 612–708.
[20] Minh Duy Truong, Théorie et modélisation numérique des résonances photoniques: expansion modale quasi-normale: applications en théorie électromagnétique, PhD thesis, Aix-Marseille, 2020.
[21] Adrià Canós Valero, et al., Theory, observation, and ultrafast response of the hybrid anapole regime in light scattering, Laser & Photonics Reviews 15 (10) (2021) 2100114.
[22] Egor A. Muljarov, Thomas Weiss, Resonant-state expansion for open optical systems: generalization to magnetic, chiral, and bi-anisotropic materials, Optics Letters 43 (9) (2018) 1978–1981.
[23] Tong Wu, et al., Modal analysis of electromagnetic resonators: user guide for the MAN program, Computer Physics Communications 284 (2023) 108627.
[24] Ulrich Hohenester, Nikita Reichelt, Gerhard Unger, Nanophotonic resonance modes with the nanobem toolbox, Computer Physics Communications 276 (2022) 108337.

[25] Lukas Novotny, Strong coupling, energy splitting, and level crossings: a classical perspective, American Journal of Physics 78 (11) (2010) 1199–1202.
[26] Maxim V. Gorkunov, Alexander A. Antonov, Yuri S. Kivshar, Metasurfaces with maximum chirality empowered by bound states in the continuum, Physical Review Letters 125 (9) (2020) 093903.
[27] Zhichao Ruan, Shanhui Fan, Superscattering of light from subwavelength nanostructures, Physical Review Letters 105 (1) (2010) 013901.
[28] Zhexin Zhao, Cheng Guo, Shanhui Fan, Connection of temporal coupled-mode-theory formalisms for a resonant optical system and its time-reversal conjugate, Physical Review A 99 (3) (2019) 033839.
[29] John D. Joannopoulos, et al., Molding the Flow of Light, Princet. Univ. Press, Princeton, NJ, 2008.
[30] Shanhui Fan, Wonjoo Suh, John D. Joannopoulos, Temporal coupled-mode theory for the Fano resonance in optical resonators, Journal of the Optical Society of America A 20 (3) (2003) 569–572.
[31] Charles Kittel, Introduction to Solid State Physics, Wiley, 2022.
[32] Mary L. Boas, Philip Peters, Mathematical Methods in the Physical Sciences, John Wiley & Sons, 1984.

This page intentionally left blank

3

Dielectric materials

George Zograf[b] **and Sergey Makarov**[a,c]
[a] *Qingdao Innovation and Development Center, Harbin Engineering University, Qingdao, China.* [b] *Chalmers University of Technology, Gothenburg, Sweden.* [c] *ITMO University, Saint Petersburg, Russia*

3.1 Introduction

3.1.1 Linear properties of dielectric materials

The key parameter defining the functionality of a resonant all-dielectric nanostructure (besides its geometry) is the value of the refractive index (n) and negligible, approaching zero, optical losses (k) of the material forming resonant nanoantennas. Indeed, the ratio between the nanostructure characteristic size and the resonant wavelength is proportional to $1/n$, while the quality factor of the fundamental Mie resonance scales as n^2. Thus, the increase in the refractive index supports both more pronounced and deeper subwavelength resonances in all-dielectric nanostructures.

On the other hand, the refractive index and energy band gap (E_g) of dielectrics and semiconductors are the two fundamental parameters that govern their optical response, which is crucial in the visible and infrared spectral ranges. The value of the refractive index of dielectrics and semiconductors is closely related to their electronic bandgap. Namely, according to the so-called Moss's law [1], the refractive index of a material decreases with the increase of its energy band gap. This correlation can be understood if we assume that electrons in a valence band of a semiconductor are considered similar to the case of bound electrons in a hydrogen atom. In this case, the energy needed to ionize the atom and allow a transition of the electron to the conduction band is defined as $E_g \sim 1/\epsilon^2$, where ϵ is the dielectric permittivity of the semiconductor. This scaling law is a very simple approximation for the static refractive index known as Moss's law [1] and reads:

$$n^4 E_g = 95 \text{ eV}, \tag{3.1}$$

All-Dielectric Nanophotonics. https://doi.org/10.1016/B978-0-32-395195-1.00008-9
Copyright © 2024 Elsevier Ltd. All rights reserved.

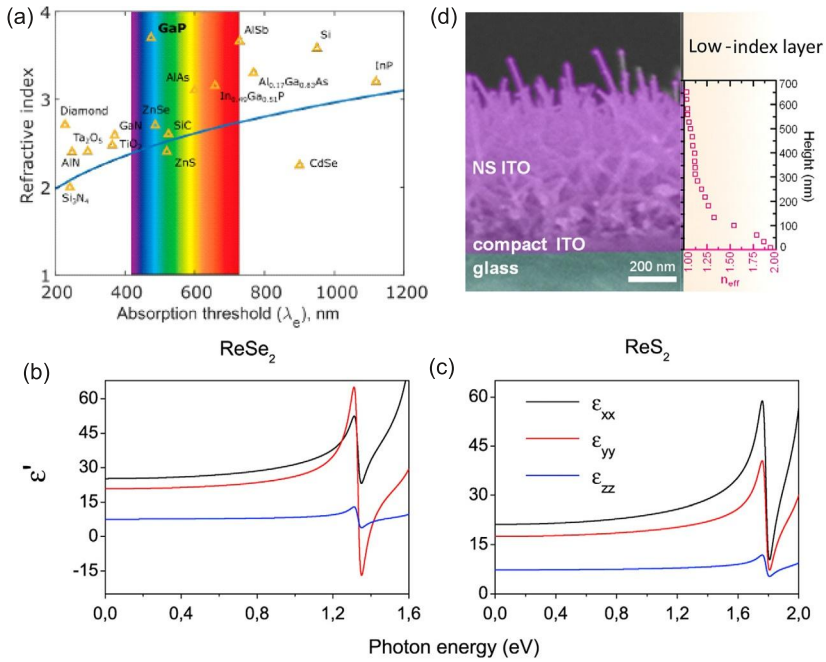

Figure 3.1. (a) Comparison of the refractive indices and bandgap absorption thresholds for different materials (triangles) and Moss relation (solid line). Reprinted (adapted) with permission from [3]. Copyright 2023 American Chemical Society. (b,c) Real parts of dielectric permittivity of the bulk $ReSe_2$ (left) and ReS_2 (right) for different light polarizations calculated within TDDFT. Adapted from [4] under CC BY 4.0. (d) Cross-sectional SEM image of the nanostructured ITO substrate and n_{eff} profile for the ITO layer. Adapted from [5] under CC BY 4.0.

or, in terms of absorption threshold wavelength,

$$n^4/\lambda_e = 77\ \mu\text{m}^{-1}. \tag{3.2}$$

This formula is a decent estimation for a huge variety of materials, see Fig. 3.1a. However, such materials as gallium phosphide (GaP) are among those that deviate from this law, exhibiting considerably higher refractive index [2] at a relatively large energy band gap.

From Moss's law, one can expect that the refractive index should be larger at lower frequencies of light. Indeed, the values $n > 10$ can be easily achieved in the wide frequency range from terahertz to mid-IR. In the near-IR and visible ranges, the refractive index values are currently limited by a value of approximately 4–5. According to Fig. 3.1a and literature [6], this is true for all well-known high-index reference materials like gallium arsenide ($n \approx 3.7$), silicon ($n \approx 4$), and germanium ($n \approx 4.5$). In visible and near-IR ranges, the broadband high refractive index is originated

from a strong interband polarization. Moreover, in the work [4], it was shown that such parameter (η) as the ratio between the sum of the widths of the conduction Δ_c and valence Δ_v bands to the bandgap E_g can contribute to high values of the off-resonant refractive index.

$$\eta = \frac{\Delta_c + \Delta_v}{E_g}. \tag{3.3}$$

Indeed, this key parameter defines the value of the refractive index for the frequencies slightly below the band gap. The refractive index can be increased if η is reduced, which can be achieved in materials with flattened conduction and valence bands. For example, such conditions can be observed in $ReSe_2$ or ReS_2, where for the photon energies around 1 eV, the real part of the refractive index can be larger than 5, whereas its imaginary part remains low (Fig. 3.1b,c). Moreover, one can observe extreme biaxial optical anisotropy in these materials. These theoretical calculations are confirmed experimentally [7]. In principle, the criterion in Eq. (3.3) can be used for the preliminary search of the prospective candidates for the novel high-index materials for all-dielectric nanophotonics based on their band structures known from the literature.

Another direction is the lowering refractive index of materials, which is needed for providing higher optical contrasts. Since air is the perfect "material" with refractive index $n = 1$, one of the options is to create a composite material where nanostructures are separated by air on a subwavelength scale, forming an effective medium. According to the Maxwell-Garnett model [8], one can introduce an averaged effective refractive index (n_{eff}) of such a medium, which usually possesses values between those for air and the nanomaterial. In Fig. 3.1d, an example of such effective low-index material is presented. Namely, it can be a layer of nanostructured indium-tin-oxide (ITO, $n \approx 2$), where a significant fraction of air results in a reduction of the effective refractive index from $n_{eff} \approx 2$ to $n_{eff} \approx 1$ across the thickness.

3.1.2 Nonlinear properties of dielectric materials

It states that the coefficient of the second-order electric susceptibility response (χ_2) is proportional to the product of the first-order susceptibilities (χ_1) at the three frequencies on which χ_2 depends [9]. The proportionality coefficient is known as Miller's coefficient δ, which variation is relatively small in most experiments [10].

$$\chi_2(\omega_1, \omega_2) = \delta \cdot \chi_1(\omega_1) \cdot \chi_1(\omega_2) \cdot \chi_1(\omega_1 + \omega_2). \tag{3.4}$$

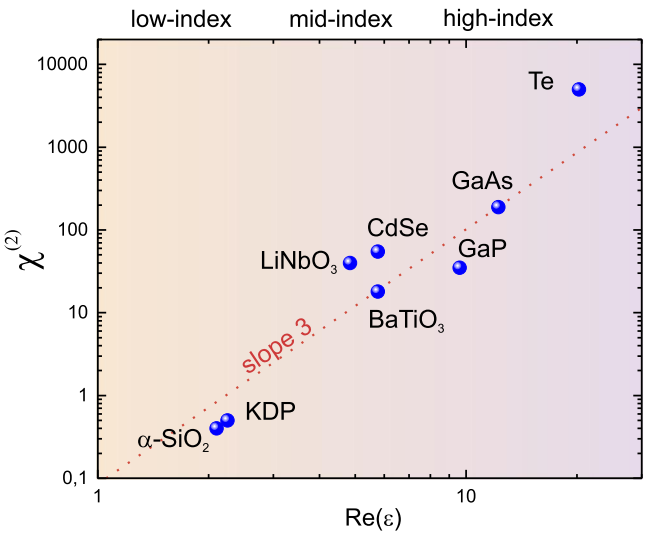

Figure 3.2. Second-order susceptibility dependence on dielectric permittivity. $\chi^{(2)}$ is shown in $\times 10^{-12}$ m/V units. The data are given for wavelgnth around 1 μm and taken from [11,12].

For the third-order susceptibility, there is the following connection between χ_3 and χ_1 values with new coefficient δ' [11]:

$$\chi_3(\omega_1, \omega_2, \omega_3) = \delta' \cdot \chi_1(\omega_1) \cdot \chi_1(\omega_2) \cdot \chi_1(\omega_3) \cdot \chi_1(\omega_1 + \omega_2 + \omega_3). \quad (3.5)$$

Therefore, the higher the refractive index of the dielectric material, the higher the high-order nonlinear response.

In Fig. 3.2, there is a summary of χ_2 values for materials, which are wide-spread in all-dielectric nanophotonics, depending on their dielectric permittivity. One can clearly see the general trend governed by Miller's rule, where χ_2 is proportional to the ϵ^3. Some deviations from this trend are originated from strong dispersion in some of these materials.

3.2 Conventional semiconductors

In the visible and near-IR spectral ranges, the highest known permittivities are possessed by materials such as Si, Ge, GaP, GaSb, and other narrow-band semiconductore (Fig. 3.3a). In the mid-IR spectral range, narrower-band semiconductors and polar crystals demonstrate even higher values, which were employed for the design of all-dielectric metasurfaces consisting of resonant particles made of Te [13] or SiC [14]. In such materials, the spectral regions corresponding to high refractive index originate from the

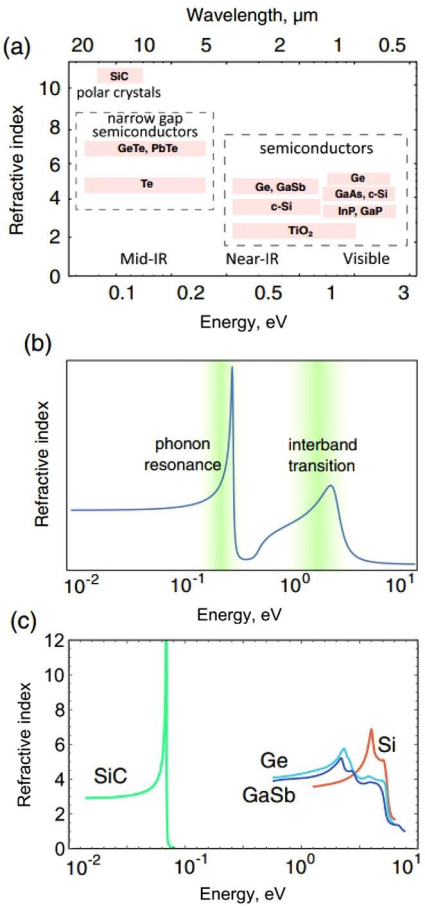

Figure 3.3. (a) Refractive indices of materials available for dielectric nanophotonics from visible to mid-IR spectral ranges. (b) A typical dielectric response of a high-index material exhibiting a series of resonances. The shaded area depicts two high-index plateaus related to material resonances. (c) The refractive index of several semiconductors and SiC shows behavior very similar to that of the generic material shown in (b). Reprinted/Adapted with permission from [19] © The Optical Society.

type of their electronic response, as shown in Fig. 3.3b, which are formed by interband and phonon resonances. In the low-frequency range, the response is purely dielectric (assuming that the material is not doped with free carriers); in the IR and visible spectral ranges, these materials exhibit a series of resonances. Due to the coupling of light to these resonances of the medium, the regions of increased refractive index appear in the spectrum. The low-frequency phonon–polariton resonance occurs due to

the coupling of light with optical phonons of the crystal lattice of polar crystals [15,16]. The higher frequency exciton–polariton resonance originates from interband transitions in semiconductors and forms a pronounced plateau in their dielectric function. As Fig. 3.3c shows, real semiconductors and polar materials indeed demonstrate qualitatively similar dispersions of the refractive index.

The high refractive index of these materials comes at a cost of increased absorption. According to the Kramers–Kronig relations [17], any dispersion of permittivity is related to dissipation. As it was pointed out above, the high-index regions of semiconductors and polar crystals stem from their exciton and phonon resonances, which bring optical absorption. This fundamental trade-off between absorption and high refractive index eventually sets the limit to all-dielectric resonator performance.

There is a significant difference between the behavior of refractive indices of semiconductors and polar crystals. In semiconductors, the high refractive index at below-band gap frequencies originates from a continuum of interband transitions [16], which allows one to have a high index and a relatively low absorption at the same time. In polar crystals, the high index is related to a single phonon resonance, so that it is accompanied by a large absorption coefficient [18].

Semiconductor materials may have either a direct or indirect bandgap, which has a profound implication on the absorbing properties. When light passes through a direct-band-gap semiconductor, a photon can be absorbed to the conduction band. At the same time, when light travels through an indirect-bandgap medium, due to the large mismatch between the electron and photon wavevectors, such process does not occur, which results in reduced optical absorption. Good examples of such materials are c-Si and Ge. Nevertheless, even direct-bandgap materials may demonstrate good performance if the operating frequency lies slightly below the bandgap.

3.3 Emerging materials

3.3.1 2D materials

Atomically thin or 2D semiconductor materials attracted major attention not only due to their outstanding conductive properties, but also for the ability to widely tune their optical properties depending on the material, number of layers, stacking, via electrical current running through the material, and even the mechanical

strain. In this section, we will focus on the most popular 2D materials for nanophotonics and their optical properties.

One of the most beneficial features of the 2D materials is the ability for stacking multiple different isolated monolayers into *van der Waals* heterostructures, revealing new phenomena and unusual properties [20]. Among the other, most popular from optical perspective are hBN and graphene family, 2D dichalcogenides and 2D oxides. By stacking those materials into van der Waals multilayers, one can achieve unconventional physical phenomena, including superconductivity [21–23], Moire excitons [24–26], broadband optoelectronics [27], light-emitting diodes [28], thin-film electronics [29], and many others [30]. Despite being attractive for such a broad range of applications, we will mostly focus on a family of transition-metal dichalcogenides (TMDs) as the most promising for high-index resonant nanophotonics. TMDs compounds MX_2, where M stands for metal (Mo, W, Re, Ta, etc.) and X for chalcogenide (S, Se, Te, etc.) possess high refractive index in the visible in bulk materials(see Fig. 3.5a), allow active light emission via bandgap engineering, and are highly nonlinear ($\chi^{(2)}$) and anisotropic (see Fig. 3.5a,b), therefore, we will cover below mostly them.

3.3.1.1 Linear properties

Owing to reduced spatial degrees of freedom and dominated direct transitions from conduction to valence band in the visible and near-IR range, some 2D materials, namely TMDs, become especially attractive for their exciton binding energies (E_B up to 1 eV) and high photoluminescence quantum yield [31–33]. These outstanding properties allow to host peculiar effects including the creation of bright and dark excitons [34], electrical tuning of exciton binding energy [35], bosonic condensation and valley-polarized exciton-polaritons [36–38], light-emitting diodes at room-temperature [39], and many others [40,41] including single-photon emission [42–45].

Others that do not exhibit high inherent QY may also be highly attractive for nanophotonics applications, like hexagonal boron nitride (hBN) [46]. Despite being a wide-gap indirect semiconductor, hBN serves great for a number of nanophotonics applications in UV and VIS optical ranges [47], namely atomically-thin structures based on hBN may preserve the graphene plasmon lifetime [48], may host point defects for single-photon emission [49–51], support resonant nonlinear phenomena in the surrounding structures [52] and also provide tools for tuning optical losses and optical response in a wide range [53,54].

3.3.1.2 Nonlinearities and anisotropy

Among other promising optical features in 2D materials, especially TMDs, is the inherent strong second-order nonlinearity and anisotropy.

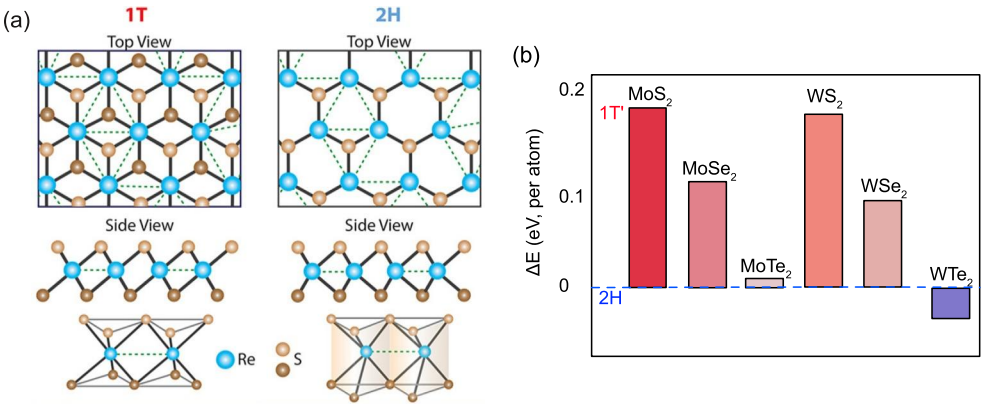

Figure 3.4. (a) Schematic of the crystalline structure of the ReS_2 monolayer for 1T and 2H phases. Reprinted with permission from [55]. Copyright 2023 American Chemical Society. (b) Energy differences of the phases in TMDs monolayers. Data used from [56].

In the ground state, TMD monolayers tend to possess certain in-plane crystalline symmetry. Schematic of the crystalline lattice of the ReS_2 is shown in Fig. 3.4a. One can clearly see that the 1T phase monolayer exhibits inverse symmetry, therefore, making, for instance, second-harmonic generation (SHG) forbidden. However, there have been more reports claiming that ReS_2 crystals tend to posses 1T' (distorted) ground state phase [57], or even 1T" (double distorted) that has been reported so far only numerically [56]. Contrary to that, a 2H phase has in-plane broken-inverse symmetry, demonstrating pronounced SHG response [55]. Indeed, most of the conventional TMDs monolayers, as depicted in Fig. 3.4b, have a 2H phase as the most energetically beneficial, therefore are very promising for nonlinear emission, as has been proven in a number of papers [58,59]. Moreover, TMDs enable highly efficient and strong tuning of the SHG emission via charge carriers [60–62]. On top of that, stacking the monolayers with specific rotational angles improves the SHG emission [63–65]. Additionally, one can tune the intensity at emission direction with mechanical strain, as it affects the crystalline lattice symmetry [66].

Owing to the peculiar crystalline structure–individual monolayers of TMDs combined into bulk crystals demonstrate unprecedented optical anisotropy for in- and out-of-plane refractive index, as depicted in Fig. 3.5a,b [7,67,69]. The difference in refractive

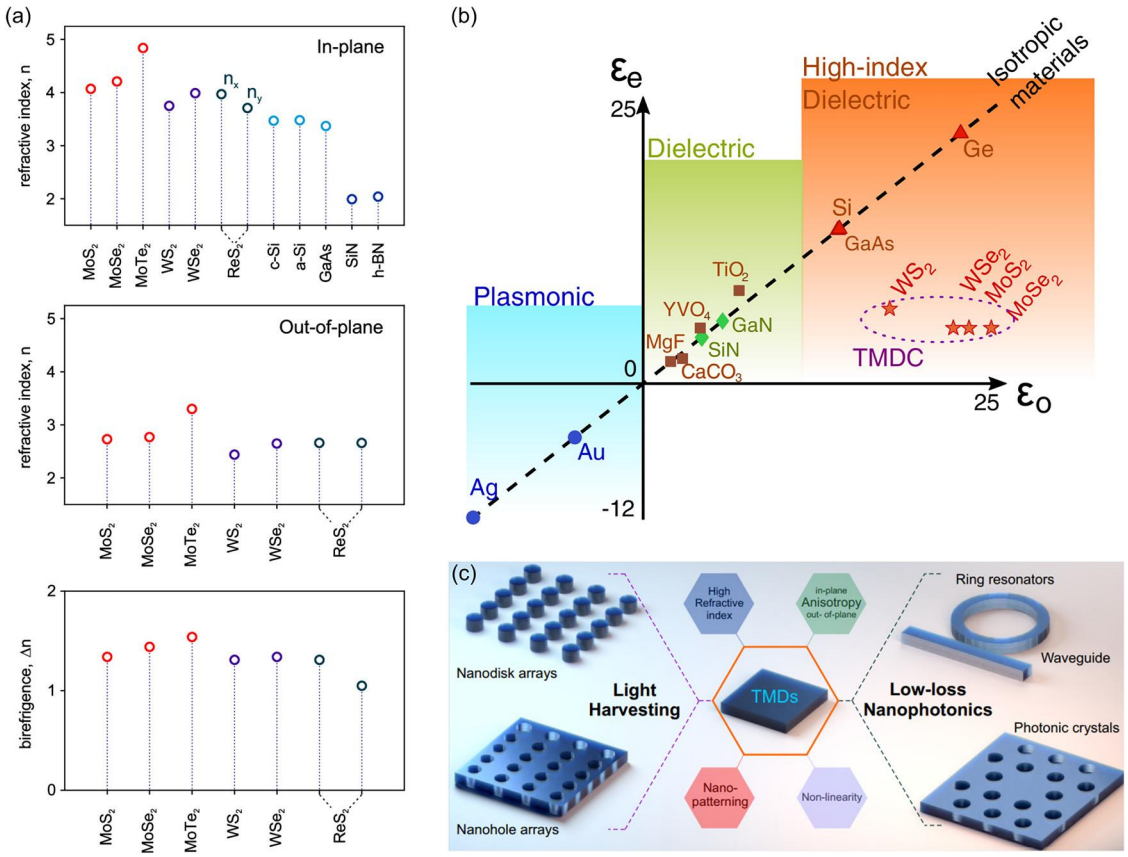

Figure 3.5. Bulk material properties. (a) represents high-anisotropy in refractive index between in-plane and out-of-plane of the TMDC materials. Reprinted with permission [7]. Copyright 2023 American Chemical Society (CC BY 4.0). (b) compares TMDC anisotropy with conventional materials. Reprinted/Adapted with permission from [67] © The Optical Society (CC BY 4.0). (c) depicts optically resonant nanostructures reflecting the beneficial sides of TMDC materials. Reprinted with permission from [68]. Copyright 2023 Wiley (CC BY 4.0).

index anisotropy is larger by order of magnitude compared to the widely used calcite. Such anisotropy is highly attractive for modern nanophotonics applications that will be described below in more detail.

3.3.1.3 Resonant structures

TMDs are highly attractive platforms for 2D technologies, however, they have proven to be efficient in resonant nanophotonics applications. Indeed, both calculations and experimental studies prove that bulk TMDs possess a very high in-plane refractive index in the visible ($n = 3.5 \div 5$), as shown in Fig. 3.5a. Such properties

enable the creation of optically resonant, subwavelength, high-quality, atomically precise, active, and highly nonlinear nanostructures.

The very first demonstration of TMDs-based single subwavelength nanoresonators that hosted Mie-modes was shown in 2019 [70], where Verre et al. also demonstrated strong coupling of anapole mode to exciton of WS_2 - the material of the nanoresonator itself. Anapole modes also serve to enhance SHG emission in single nanodisks [71].

The advances in fabrication techniques also allow producing periodic nanophotonics structures from TMDs for advanced light manipulation [72–75]. However, one of the most promising fabrication abilities was demonstrated recently by Munkhbat et al. [76], where TMD flakes can be chemically etched into atomically sharp periodic arrays of perfect hexagons down to several nanometers thickness. More and more different nanophotonic structures were demonstrated in [68] that support advanced light manipulation.

To wrap up, this section covered recent advances in 2D materials nanophotonics. This type of materials is widely used in various applications. For all-dielectric nanophotonics, high-index ($n > 3.5$) TMDs with huge optical anisotropy and active emission should be considered the most promising for the community in the upcoming years. As the most perspective platform in the upcoming years for resonant nonlinear TMD nanophotonics, we would like to highlight 3R-MoS_2 - a molybdenum disulfide stacked in a bulk crystal with $\chi^{(2)}$ magnitude of 10^{-7} m/V [58], which is 7 orders of magnitude higher than the 2H phase of MoS_2, and 3–4 orders of magnitude higher nonlinear susceptibility than that of $BaTiO_3$ or $LiNbO_3$. Such 3R-MoS_2 already demonstrated a vast range of applications in nanophotonics [77].

3.3.2 Halide perovskites

3.3.2.1 Linear properties

The high complexity of the methods for the creation and post-processing of semiconductor-based nanostructures is still time-consuming and expensive in most cases. Moreover, the samples based on GaAs are several orders of magnitude more expensive than those based on Si due to the high cost of the substrates, as well as the use of complex epitaxial growth methods and rarity of the material. Therefore, perovskite-based nanostructures are more affordable and cheaper for the production on large scales [78]. Using wet chemistry methods and roll-to-roll techniques [79], it is possible to create flexible, cheap and efficient all-dielectric nanophotonic devices. Also, recent progress in material

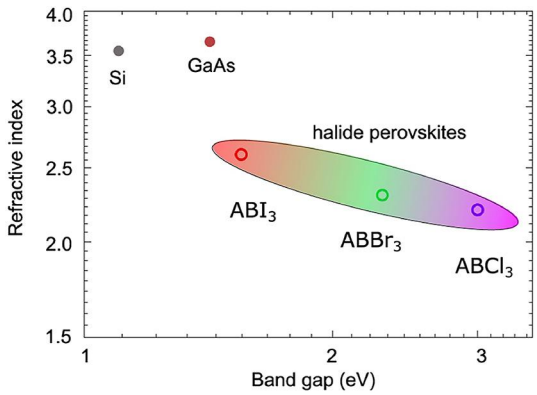

Figure 3.6. Comparison of the dependencies for refractive index on bandgap value for perovskites and different materials. Reprinted with permission from [80]. Copyright AIP Publishing.

sciences leads to the synthesis protocols, where halide perovskites are demonstrated to be stable for thousands of hours under conditions in a standard environment.

From the optical point of view, the real part of the refractive index of halide perovskites is significantly larger than that of SiO_2 or most polymers, making the perovskites suitable materials for all-dielectric nanophotonics, owing to sufficiently high optical contrast (see Fig. 3.6). Moreover, *in situ* chemical modification of the halide perovskite bandgap [81,82] and, thus, variation of their luminescence spectrum, opens up unprecedented opportunities for reconfigurable nanophotonic devices not achievable with the use of the conventional GaAs platform. As a result, halide perovskite nanoparticles [83], nanowires [84,85], microdisks [86], microplates [87], nanoscale gratings [88], and metasurfaces [89,90] are easy to fabricate and process, and they can become a convenient and cheap part of optical circuitry in the near future [91]. Nevertheless, the existing silicon-based platform is much more developed for on-chip integrated photonics [92], but it is expected to be outperformed by the perovskites in the future.

Halide perovskites can be considered as direct bandgap materials resembling GaAs. Ab initio calculations [93] show that the state contributed by the cation 'A' (e.g. Cs, MA, FA, etc.) is far from the band edges, which means that it does not play a significant role in determining the basic electronic structures in halide perovskites. In turn, the valence band has Pb *s* and X *p* anti-bonding character, whereas the conduction band is formed by the Pb *p* states. This is the unique dual nature (ionic and covalent) of halide perovskites electronic structure. In conventional semiconductors

such as GaAs, the conduction band primarily has *s* orbital character, whereas the valence band primarily has *p* orbital character. In contrast, halide perovskites exhibit an inverted band structure, and the conduction band is mainly composed of degenerate Pb *p* bands. The atomic *p* orbital is less dispersive than *s* orbitals, and the density of states in the lower conduction band of the halide perovskites is significantly higher than in GaAs, and it is several orders of magnitude stronger than in Si. As a result, halide perovskites have stronger the interband transition dipole moment, yielding a high absorption coefficient and high quantum yield in the emission of light.

Additionally, as compared to GaAs, halide perovskites also have a high tolerance to defects for luminescence [94], excitons at room temperature [95], the slightly lower refractive index in visible/near-infrared ranges, and reversibly tunable band gap from 1.5 eV up to 3 eV [81,82]. Due to these favorable characteristics, ease of processing and low price, perovskites are the promising family of materials for the next generation of optoelectronic and nanophotonic devices. Namely, there is an urgent necessity to create cheap, efficient, reliable and easy-to-manufacture solar cells, LEDs, ultracompact lasers, nonlinear optical devices and optical chips.

3.3.2.2 Nonlinearities and anisotropy

Nonlinear optical response of halide perovskites is superior to many conventional semiconductors [96,97]. For example, $CsPbX_3$ demonstrates efficient two-photon, three-photon, and even five-photon absorption [98], being sufficient for multiphoton pumping of lasing [99], which can be used for metasurfaces as well [100]. Third-harmonic generation has also been measured with high third-order susceptibilities $\chi^{(3)}$ exceeding 10^{-17} m^2V^{-2} [101]. Second-harmonic generation from halide perovskite ($CsPbX_3$ or $MAPbX_3$, where $MA=CH_3NH_3$) structures is not as effective on average due to the centrosymmetric crystalline structure. However, lead-free perovskites (such as $CsGeI_3$ and $MAGeI_3$) exhibit giant second-harmonic generation, with the second-order nonlinear coefficient $\chi^{(2)}$ exceeding the values of 150 pm V^{-1}, comparable with those for GaAs and many orders of magnitude larger than the coefficients observed for silicon [90,102], as well as better than most of the mid-index materials like CdSe, $LiNbO_3$, and $BaTiO_3$ (see Fig. 3.2).

Recently, strong anisotropy was observed in $CsPbX_3$ perovskites, where in-plane refractive index (n_{ab}) is larger than in perpendicular direction (Fig. 3.7a). Optical anisotropy in the single-crystal halide perovskite originates from an excitonic resonance, which

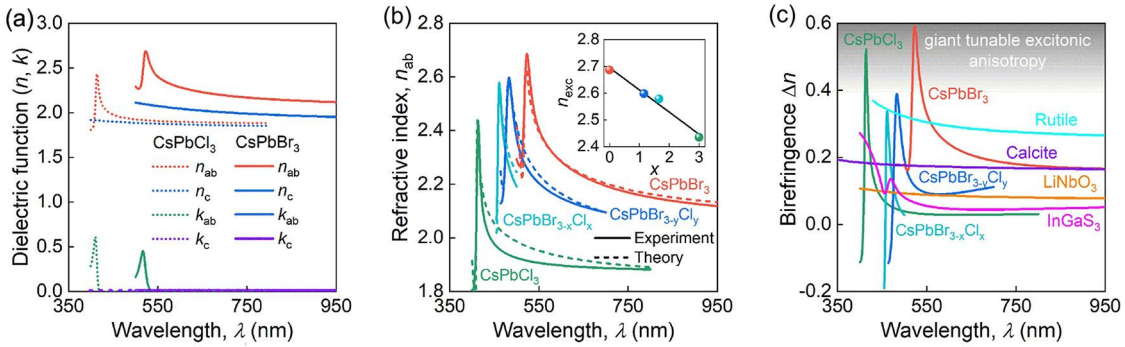

Figure 3.7. (a) Anisotropic complex refractive index of $CsPbCl_3$ and $CsPbBr_3$. (b) Tunable refractive index of halide perovskite microplates for crystallographic ab-plane. The inset shows the dependence of the refractive index at exciton resonance n_{exc} on stoichiometry number x of Cl atoms in mixed-halide composition $CsPbBr_{3-x}Cl_x$. (c) Tunable birefringence of halide perovskites compared with other widely used anisotropic materials: rutile, calcite, $LiNbO_3$, and $InGaS_3$. Reprinted/adapted with permission from [103]. Copyright 2023 American Chemical Society.

spectral position and strength are determined by the halogens composition. In particular, it is possible to gradually modify the optical anisotropy by 0.14, while optical anisotropy can be as high as $\Delta n = 0.6$ in the visible range, the largest value among non-van der Waals materials (see the comparison in Fig. 3.7c). Moreover, this anisotropy can be both in-plane and out-of-plane, depending on perovskite shape: rectangular or square. Hence, it can serve as an additional degree of freedom for anisotropy manipulation [103].

3.3.2.3 Resonant structures

Despite high sensitivity of the halide perovskite to polar liquids and various gases, which destroy their crystalline structure with ionic bounds, there are a lot of methods of their nanostructuring [83]. Such methods as nanoimprint lithography [104, 105], electron beam lithography [100,106], laser printing [83], laser projection lithography [107,108], and focused ion beam lithography [89,109] were successfully used for the fabrication of nanostructures and metasurfaces based on halide perovskites.

The relatively high refractive index of halide perovskites makes it possible to employ them for the creation of nanoparticles that support Mie resonances. This can result in enhancement of optical field inside the nanoparticle and improve optical characteristics of halide perovskites. In particular, this approach was used to enhance the photoluminescence [83], lasing [110], for optical cooling [111], as well as to modify extinction spectrum of the island-like perovskite films [112]. Importantly, perovskite

nanoparticles can be easily produced by relatively simple fabrication methods, such as laser ablation [83,112] and chemical synthesis [110] and do not require multi-stage lithography processes. Despite the wide range of potential applications for such single perovskite nanoparticles, the creation of metasurfaces of ordered meta-atoms can substantially expand their scope. One of the first applications of perovskite metasurfaces was surface coloration [89]. After this, reversible *in situ* tuning of surface color by a perovskite metasurface was demonstrated [113], which was further developed for switchable holography [106]. As a result, halide perovskite nanostructuring opened a new direction in all-dielectric nanophotonics [114], which found numerous applications in photovoltaics [115], optoelectronics [116] and laser technologies [117].

References

[1] T. Moss, Relations between the refractive index and energy gap of semiconductors, Physica Status Solidi B 131 (2) (1985) 415–427.
[2] D. Khmelevskaia, D. Markina, V. Fedorov, G. Ermolaev, A. Arsenin, V. Volkov, A. Goltaev, Y.M. Zadiranov, I. Tzibizov, A. Pushkarev, et al., Directly grown crystalline gallium phosphide on sapphire for nonlinear all-dielectric nanophotonics, Applied Physics Letters 118 (20) (2021) 201101.
[3] P. Trofimov, A.P. Pushkarev, I.S. Sinev, V.V. Fedorov, S. Bruyère, A. Bolshakov, I.S. Mukhin, S.V. Makarov, Perovskite–gallium phosphide platform for reconfigurable visible-light nanophotonic chip, ACS Nano 14 (7) (2020) 8126–8134.
[4] A.A. Shubnic, R.G. Polozkov, I.A. Shelykh, I.V. Iorsh, High refractive index and extreme biaxial optical anisotropy of rhenium diselenide for applications in all-dielectric nanophotonics, Nanophotonics 9 (16) (2020) 4737–4742.
[5] D.I. Markina, A.P. Pushkarev, I.I. Shishkin, F.E. Komissarenko, A.S. Berestennikov, A.S. Pavluchenko, I.P. Smirnova, L.K. Markov, M. Vengris, A.A. Zakhidov, et al., Perovskite nanowire lasers on low-refractive-index conductive substrate for high-q and low-threshold operation, Nanophotonics 9 (12) (2020) 3977–3984.
[6] E.D. Palik, Handbook of Optical Constants of Solids, vol. 3, Academic Press, 1998.
[7] B. Munkhbat, P. Wróbel, T.J. Antosiewicz, T.O. Shegai, Optical constants of several multilayer transition metal dichalcogenides measured by spectroscopic ellipsometry in the 300–1700 nm range: high index, anisotropy, and hyperbolicity, ACS Photonics 9 (7) (2022) 2398–2407.
[8] V.A. Markel, Introduction to the Maxwell Garnett approximation: tutorial, Journal of the Optical Society of America A 33 (7) (2016) 1244–1256.
[9] R.C. Miller, Optical second harmonic generation in piezoelectric crystals, Applied Physics Letters 5 (1) (1964) 17–19.
[10] F. Parsons, R. Chang, Measurement of the nonlinear susceptibility dispersion by dye lasers, Optics Communications 3 (3) (1971) 173–176.
[11] R.W. Boyd, Nonlinear Optics, Academic Press, 2020.
[12] N. Koroteev, I.L. Shumai, Physics of Intense Laser Radiation, Academic Press, 2020.

[13] J.C. Ginn, I. Brener, D.W. Peters, J.R. Wendt, J.O. Stevens, P.F. Hines, L.I. Basilio, L.K. Warne, J.F. Ihlefeld, P.G. Clem, et al., Realizing optical magnetism from dielectric metamaterials, Physical Review Letters 108 (9) (2012) 097402.
[14] J.A. Schuller, R. Zia, T. Taubner, M.L. Brongersma, Dielectric metamaterials based on electric and magnetic resonances of silicon carbide particles, Physical Review Letters 99 (10) (2007) 107401.
[15] C.F. Klingshirn, Semiconductor Optics, Springer Science & Business Media, 2012.
[16] M. Cardona, Y.Y. Peter, Fundamentals of Semiconductors, vol. 619, Springer, 2005.
[17] H.M. Nussenzveig, Causality and dispersion relations, Tech. Rep., 1972.
[18] J.D. Caldwell, L. Lindsay, V. Giannini, I. Vurgaftman, T.L. Reinecke, S.A. Maier, O.J. Glembocki, Low-loss, infrared and terahertz nanophotonics using surface phonon polaritons, Nanophotonics 4 (1) (2015) 44–68.
[19] D.G. Baranov, D.A. Zuev, S.I. Lepeshov, O.V. Kotov, A.E. Krasnok, A.B. Evlyukhin, B.N. Chichkov, All-dielectric nanophotonics: the quest for better materials and fabrication techniques, Optica 4 (7) (2017) 814–825.
[20] A.K. Geim, I.V. Grigorieva, Van der Waals heterostructures, Nature 499 (7459) (2013) 419–425.
[21] S. Kezilebieke, M.N. Huda, V. Vaňo, M. Aapro, S.C. Ganguli, O.J. Silveira, S. Głodzik, A.S. Foster, T. Ojanen, P. Liljeroth, Topological superconductivity in a van der Waals heterostructure, Nature 588 (7838) (2020) 424–428.
[22] E. Persky, A.V. Bjørlig, I. Feldman, A. Almoalem, E. Altman, E. Berg, I. Kimchi, J. Ruhman, A. Kanigel, B. Kalisky, Magnetic memory and spontaneous vortices in a van der Waals superconductor, Nature 607 (7920) (2022) 692–696.
[23] J.I.-J. Wang, D. Rodan-Legrain, L. Bretheau, D.L. Campbell, B. Kannan, D. Kim, M. Kjaergaard, P. Krantz, G.O. Samach, F. Yan, et al., Coherent control of a hybrid superconducting circuit made with graphene-based van der Waals heterostructures, Nature Nanotechnology 14 (2) (2019) 120–125.
[24] L. Zhang, F. Wu, S. Hou, Z. Zhang, Y.-H. Chou, K. Watanabe, T. Taniguchi, S.R. Forrest, H. Deng, Van der Waals heterostructure polaritons with moiré-induced nonlinearity, Nature 591 (7848) (2021) 61–65.
[25] Q. Tong, H. Yu, Q. Zhu, Y. Wang, X. Xu, W. Yao, Topological mosaics in moiré superlattices of van der Waals heterobilayers, Nature Physics 13 (4) (2017) 356–362.
[26] K. Tran, G. Moody, F. Wu, X. Lu, J. Choi, K. Kim, A. Rai, D.A. Sanchez, J. Quan, A. Singh, et al., Evidence for moiré excitons in van der Waals heterostructures, Nature 567 (7746) (2019) 71–75.
[27] N. Ubrig, E. Ponomarev, J. Zultak, D. Domaretskiy, V. Zólyomi, D. Terry, J. Howarth, I. Gutiérrez-Lezama, A. Zhukov, Z.R. Kudrynskyi, et al., Design of van der Waals interfaces for broad-spectrum optoelectronics, Nature Materials 19 (3) (2020) 299–304.
[28] F. Withers, D. Pozo-Zamudio, A. Mishchenko, A. Rooney, A. Gholinia, K. Watanabe, T. Taniguchi, S.J. Haigh, A. Geim, A. Tartakovskii, et al., Light-emitting diodes by band-structure engineering in van der Waals heterostructures, Nature Materials 14 (3) (2015) 301–306.
[29] Z. Lin, Y. Huang, X. Duan, Van der Waals thin-film electronics, Nature Electronics 2 (9) (2019) 378–388.
[30] Y. Liu, N.O. Weiss, X. Duan, H.-C. Cheng, Y. Huang, X. Duan, Van der Waals heterostructures and devices, Nature Reviews Materials 1 (9) (2016) 1–17.
[31] K.F. Mak, C. Lee, J. Hone, J. Shan, T.F. Heinz, Atomically thin MoS_2: a new direct-gap semiconductor, Physical Review Letters 105 (13) (2010) 136805.

[32] A. Splendiani, L. Sun, Y. Zhang, T. Li, J. Kim, C.-Y. Chim, G. Galli, F. Wang, Emerging photoluminescence in monolayer MoS_2, Nano Letters 10 (4) (2010) 1271–1275.
[33] A. Chernikov, T.C. Berkelbach, H.M. Hill, A. Rigosi, Y. Li, B. Aslan, D.R. Reichman, M.S. Hybertsen, T.F. Heinz, Exciton binding energy and nonhydrogenic Rydberg series in monolayer WS_2, Physical Review Letters 113 (7) (2014) 076802.
[34] M. Selig, G. Berghäuser, M. Richter, R. Bratschitsch, A. Knorr, E. Malic, Dark and bright exciton formation, thermalization, and photoluminescence in monolayer transition metal dichalcogenides, 2D Materials 5 (3) (2018) 035017.
[35] A. Chernikov, A.M. Van Der Zande, H.M. Hill, A.F. Rigosi, A. Velauthapillai, J. Hone, T.F. Heinz, Electrical tuning of exciton binding energies in monolayer WS_2, Physical Review Letters 115 (12) (2015) 126802.
[36] C. Anton-Solanas, M. Waldherr, M. Klaas, H. Suchomel, T.H. Harder, H. Cai, E. Sedov, S. Klembt, A.V. Kavokin, S. Tongay, et al., Bosonic condensation of exciton–polaritons in an atomically thin crystal, Nature Materials 20 (9) (2021) 1233–1239.
[37] Y.-J. Chen, J.D. Cain, T.K. Stanev, V.P. Dravid, N.P. Stern, Valley-polarized exciton–polaritons in a monolayer semiconductor, Nature Photonics 11 (7) (2017) 431–435.
[38] L. Sun, C.-Y. Wang, A. Krasnok, J. Choi, J. Shi, J.S. Gomez-Diaz, A. Zepeda, S. Gwo, C.-K. Shih, A. Alù, et al., Separation of valley excitons in a MoS_2 monolayer using a subwavelength asymmetric groove array, Nature Photonics 13 (3) (2019) 180–184.
[39] J. Gu, B. Chakraborty, M. Khatoniar, V.M. Menon, A room-temperature polariton light-emitting diode based on monolayer WS_2, Nature Nanotechnology 14 (11) (2019) 1024–1028.
[40] K.F. Mak, J. Shan, Photonics and optoelectronics of 2D semiconductor transition metal dichalcogenides, Nature Photonics 10 (4) (2016) 216–226.
[41] G. Wang, A. Chernikov, M.M. Glazov, T.F. Heinz, X. Marie, T. Amand, B. Urbaszek, Colloquium: excitons in atomically thin transition metal dichalcogenides, Reviews of Modern Physics 90 (2) (2018) 021001.
[42] C. Chakraborty, L. Kinnischtzke, K.M. Goodfellow, R. Beams, A.N. Vamivakas, Voltage-controlled quantum light from an atomically thin semiconductor, Nature Nanotechnology 10 (6) (2015) 507–511.
[43] Y.-M. He, G. Clark, J.R. Schaibley, Y. He, M.-C. Chen, Y.-J. Wei, X. Ding, Q. Zhang, W. Yao, X. Xu, et al., Single quantum emitters in monolayer semiconductors, Nature Nanotechnology 10 (6) (2015) 497–502.
[44] M. Koperski, K. Nogajewski, A. Arora, V. Cherkez, P. Mallet, J.-Y. Veuillen, J. Marcus, P. Kossacki, M. Potemski, Single photon emitters in exfoliated WSe_2 structures, Nature Nanotechnology 10 (6) (2015) 503–506.
[45] A. Srivastava, M. Sidler, A.V. Allain, D.S. Lembke, A. Kis, A. Imamoğlu, Optically active quantum dots in monolayer WSe_2, Nature Nanotechnology 10 (6) (2015) 491–496.
[46] J.D. Caldwell, I. Aharonovich, G. Cassabois, J.H. Edgar, B. Gil, D. Basov, Photonics with hexagonal boron nitride, Nature Reviews Materials 4 (8) (2019) 552–567.
[47] D. Grudinin, G. Ermolaev, D. Baranov, A. Toksumakov, K. Voronin, A. Slavich, A. Vyshnevyy, A. Mazitov, I. Kruglov, D. Ghazaryan, et al., Hexagonal boron nitride nanophotonics, arXiv preprint, arXiv:2303.02804, 2023.
[48] J.D. Caldwell, K.S. Novoselov, Mid-infrared nanophotonics, Nature Materials 14 (4) (2015) 364–366.

[49] T.T. Tran, K. Bray, M.J. Ford, M. Toth, I. Aharonovich, Quantum emission from hexagonal boron nitride monolayers, Nature Nanotechnology 11 (1) (2016) 37–41.

[50] G. Grosso, H. Moon, B. Lienhard, S. Ali, D.K. Efetov, M.M. Furchi, P. Jarillo-Herrero, M.J. Ford, I. Aharonovich, D. Englund, Tunable and high-purity room temperature single-photon emission from atomic defects in hexagonal boron nitride, Nature Communications 8 (1) (2017) 1–8.

[51] N. Mendelson, D. Chugh, J.R. Reimers, T.S. Cheng, A. Gottscholl, H. Long, C.J. Mellor, A. Zettl, V. Dyakonov, P.H. Beton, et al., Identifying carbon as the source of visible single-photon emission from hexagonal boron nitride, Nature Materials 20 (3) (2021) 321–328.

[52] V. Kravtsov, E. Khestanova, F.A. Benimetskiy, T. Ivanova, A.K. Samusev, I.S. Sinev, D. Pidgayko, A.M. Mozharov, I.S. Mukhin, M.S. Lozhkin, et al., Nonlinear polaritons in a monolayer semiconductor coupled to optical bound states in the continuum, Light: Science & Applications 9 (1) (2020) 1–8.

[53] M.A. El-Sayed, A.P. Tselin, G.A. Ermolaev, M.K. Tatmyshevskiy, A.S. Slavich, D.I. Yakubovsky, S.M. Novikov, A.A. Vyshnevyy, A.V. Arsenin, V.S. Volkov, Non-additive optical response in transition metal dichalcogenides heterostructures, Nanomaterials 12 (24) (2022) 4436.

[54] A.N. Toksumakov, G.A. Ermolaev, M.K. Tatmyshevskiy, Y.A. Klishin, A.S. Slavich, I.V. Begichev, D. Stosic, D.I. Yakubovsky, D.G. Kvashnin, A.A. Vyshnevyy, et al., Anomalous optical response of graphene on hexagonal boron nitride substrates, Communications Physics 6 (1) (2023) 13.

[55] B. Küçüköz, B. Munkhbat, T.O. Shegai, Boosting second-harmonic generation in monolayer rhenium disulfide by reversible laser patterning, ACS Photonics 9 (2) (2022) 518–526.

[56] M.N. Gjerding, A. Taghizadeh, A. Rasmussen, S. Ali, F. Bertoldo, T. Deilmann, N.R. Knøsgaard, M. Kruse, A.H. Larsen, S. Manti, et al., Recent progress of the Computational 2D Materials Database (C2DB), 2D Materials 8 (4) (2021) 044002.

[57] S. Tongay, H. Sahin, C. Ko, A. Luce, W. Fan, K. Liu, J. Zhou, Y.-S. Huang, C.-H. Ho, J. Yan, et al., Monolayer behaviour in bulk ReS_2 due to electronic and vibrational decoupling, Nature Communications 5 (1) (2014) 1–6.

[58] N. Kumar, S. Najmaei, Q. Cui, F. Ceballos, P.M. Ajayan, J. Lou, H. Zhao, Second harmonic microscopy of monolayer MoS_2, Physical Review B 87 (16) (2013) 161403.

[59] S. Klimmer, O. Ghaebi, Z. Gan, A. George, A. Turchanin, G. Cerullo, G. Soavi, All-optical polarization and amplitude modulation of second-harmonic generation in atomically thin semiconductors, Nature Photonics 15 (11) (2021) 837–842.

[60] K.L. Seyler, J.R. Schaibley, P. Gong, P. Rivera, A.M. Jones, S. Wu, J. Yan, D.G. Mandrus, W. Yao, X. Xu, Electrical control of second-harmonic generation in a WSe_2 monolayer transistor, Nature Nanotechnology 10 (5) (2015) 407–411.

[61] M. Taghinejad, Z. Xu, H. Wang, H. Taghinejad, K.-T. Lee, S.P. Rodrigues, A. Adibi, X. Qian, T. Lian, W. Cai, Photocarrier-induced active control of second-order optical nonlinearity in monolayer MoS_2, Small 16 (5) (2020) 1906347.

[62] C.T. Le, D.J. Clark, F. Ullah, J.I. Jang, V. Senthilkumar, Y. Sim, M.-J. Seong, K.-H. Chung, J.W. Kim, S. Park, et al., Impact of selenium doping on resonant second-harmonic generation in monolayer MoS_2, ACS Photonics 4 (1) (2017) 38–44.

[63] S. Shree, D. Lagarde, L. Lombez, C. Robert, A. Balocchi, K. Watanabe, T. Taniguchi, X. Marie, I.C. Gerber, M.M. Glazov, et al., Interlayer exciton mediated second harmonic generation in bilayer MoS_2, Nature Communications 12 (1) (2021) 1–9.
[64] S. Shabani, D. Halbertal, W. Wu, M. Chen, S. Liu, J. Hone, W. Yao, D.N. Basov, X. Zhu, A.N. Pasupathy, Deep moiré potentials in twisted transition metal dichalcogenide bilayers, Nature Physics 17 (6) (2021) 720–725.
[65] W.-T. Hsu, Z.-A. Zhao, L.-J. Li, C.-H. Chen, M.-H. Chiu, P.-S. Chang, Y.-C. Chou, W.-H. Chang, Second harmonic generation from artificially stacked transition metal dichalcogenide twisted bilayers, ACS Nano 8 (3) (2014) 2951–2958.
[66] L. Mennel, M. Paur, T. Mueller, Second harmonic generation in strained transition metal dichalcogenide monolayers: MoS_2, $MoSe_2$, WS_2, and WSe_2, APL Photonics 4 (3) (2019) 034404.
[67] T.D. Green, D.G. Baranov, B. Munkhbat, R. Verre, T. Shegai, M. Käll, Optical material anisotropy in high-index transition metal dichalcogenide Mie nanoresonators, Optica 7 (6) (2020) 680–686.
[68] B. Munkhbat, B. Küçüköz, D.G. Baranov, T.J. Antosiewicz, T.O. Shegai, Nanostructured transition metal dichalcogenide multilayers for advanced nanophotonics, arXiv preprint, arXiv:2202.04898, 2022.
[69] G. Ermolaev, D. Grudinin, Y. Stebunov, K.V. Voronin, V. Kravets, J. Duan, A. Mazitov, G. Tselikov, A. Bylinkin, D. Yakubovsky, et al., Giant optical anisotropy in transition metal dichalcogenides for next-generation photonics, Nature Communications 12 (1) (2021) 854.
[70] R. Verre, D.G. Baranov, B. Munkhbat, J. Cuadra, M. Käll, T. Shegai, Transition metal dichalcogenide nanodisks as high-index dielectric Mie nanoresonators, Nature Nanotechnology 14 (7) (2019) 679–683.
[71] S. Busschaert, R. Reimann, M. Cavigelli, R. Khelifa, A. Jain, L. Novotny, Transition metal dichalcogenide resonators for second harmonic signal enhancement, ACS Photonics 7 (9) (2020) 2482–2488.
[72] X. Zhang, C. De-Eknamkul, J. Gu, A.L. Boehmke, V.M. Menon, J. Khurgin, E. Cubukcu, Guiding of visible photons at the ångström thickness limit, Nature Nanotechnology 14 (9) (2019) 844–850.
[73] M. Nauman, J. Yan, D. de Ceglia, M. Rahmani, K. Zangeneh Kamali, C. De Angelis, A.E. Miroshnichenko, Y. Lu, D.N. Neshev, Tunable unidirectional nonlinear emission from transition-metal-dichalcogenide metasurfaces, Nature Communications 12 (1) (2021) 1–11.
[74] A.A. Popkova, I.M. Antropov, G.I. Tselikov, G.A. Ermolaev, I. Ozerov, R.V. Kirtaev, S.M. Novikov, A.B. Evlyukhin, A.V. Arsenin, V.O. Bessonov, et al., Nonlinear exciton-Mie coupling in transition metal dichalcogenide nanoresonators, Laser & Photonics Reviews (2022) 2100604.
[75] Z. Wang, G. Yuan, M. Yang, J. Chai, Q.Y. Steve Wu, T. Wang, M. Sebek, D. Wang, L. Wang, S. Wang, et al., Exciton-enabled meta-optics in two-dimensional transition metal dichalcogenides, Nano Letters 20 (11) (2020) 7964–7972.
[76] B. Munkhbat, A.B. Yankovich, D.G. Baranov, R. Verre, E. Olsson, T.O. Shegai, Transition metal dichalcogenide metamaterials with atomic precision, Nature Communications 11 (1) (2020) 1–8.
[77] X. Xu, C. Trovatello, F. Mooshammer, Y. Shao, S. Zhang, K. Yao, D.N. Basov, G. Cerullo, P.J. Schuck, Towards compact phase-matched and waveguided nonlinear optics in atomically layered semiconductors, Nature Photonics 16 (10) (2022) 698–706.
[78] H.J. Snaith, Present status and future prospects of perovskite photovoltaics, Nature Materials 17 (5) (2018) 372.

[79] B. Dou, J.B. Whitaker, K. Bruening, D.T. Moore, L.M. Wheeler, J. Ryter, N.J. Breslin, J.J. Berry, S.M. Garner, F.S. Barnes, et al., Roll-to-roll printing of perovskite solar cells, ACS Energy Letters 3 (10) (2018) 2558–2565.
[80] A.S. Berestennikov, P.M. Voroshilov, S.V. Makarov, Y.S. Kivshar, Active meta-optics and nanophotonics with halide perovskites, Applied Physics Reviews 6 (3) (2019) 031307.
[81] N. Pellet, J. Teuscher, J. Maier, M. Grätzel, Transforming hybrid organic inorganic perovskites by rapid halide exchange, Chemistry of Materials 27 (6) (2015) 2181–2188.
[82] D. Solis-Ibarra, I. Smith, H. Karunadasa, Post-synthetic halide conversion and selective halogen capture in hybrid perovskites, Chemical Science 6 (7) (2015) 4054–4059.
[83] E. Tiguntseva, G.P. Zograf, F.E. Komissarenko, D.A. Zuev, A.A. Zakhidov, S.V. Makarov, Y.S. Kivshar, Light-emitting halide perovskite nanoantennas, Nano Letters 18 (2) (2018) 1185–1190.
[84] H. Zhu, Y. Fu, F. Meng, X. Wu, Z. Gong, Q. Ding, M.V. Gustafsson, M.T. Trinh, S. Jin, X. Zhu, Lead halide perovskite nanowire lasers with low lasing thresholds and high quality factors, Nature Materials 14 (6) (2015) 636.
[85] J. Xing, X.F. Liu, Q. Zhang, S.T. Ha, Y.W. Yuan, C. Shen, T.C. Sum, Q. Xiong, Vapor phase synthesis of organometal halide perovskite nanowires for tunable room-temperature nanolasers, Nano Letters 15 (7) (2015) 4571–4577.
[86] P.J. Cegielski, A.L. Giesecke, S. Neutzner, C. Porschatis, M. Gandini, D. Schall, C.A.R. Perini, J. Bolten, S. Suckow, S. Kataria, B. Chmielak, T. Wahlbrink, A. Petrozza, M.C. Lemme, Monolithically integrated perovskite semiconductor lasers on silicon photonic chips by scalable top-down fabrication, Nano Letters 18 (11) (2018) 6915–6923.
[87] Q. Zhang, S.T. Ha, X. Liu, T.C. Sum, Q. Xiong, Room-temperature near-infrared high-Q perovskite whispering-gallery planar nanolasers, Nano Letters 14 (10) (2014) 5995–6001.
[88] E. Tiguntseva, Z. Sadrieva, B. Stroganov, Y.V. Kapitonov, F. Komissarenko, R. Haroldson, B. Balachandran, W. Hu, Q. Gu, A. Zakhidov, A. Bogdanov, S.V. Makarov, Enhanced temperature-tunable narrow-band photoluminescence from resonant perovskite nanograting, Applied Surface Science 473 (2019) 419–424.
[89] B. Gholipour, G. Adamo, D. Cortecchia, H.N. Krishnamoorthy, M. Birowosuto, N.I. Zheludev, C. Soci, Organometallic perovskite metasurfaces, Advanced Materials 29 (9) (2017).
[90] S.V. Makarov, M.I. Petrov, U. Zywietz, V. Milichko, D. Zuev, N. Lopanitsyna, A. Kuksin, I. Mukhin, G. Zograf, E. Ubyivovk, D.A. Smirnova, S. Starikov, B.N. Chichkov, Y.S. Kivshar, Efficient second-harmonic generation in nanocrystalline silicon nanoparticles, Nano Letters 17 (5) (2017) 3047–3053.
[91] S. Makarov, A. Furasova, E. Tiguntseva, A. Hemmetter, A. Berestennikov, A. Pushkarev, A. Zakhidov, Y. Kivshar, Halide-perovskite resonant nanophotonics, Advanced Optical Materials 7 (1) (2019) 1800784.
[92] W. Bogaerts, L. Chrostowski, Silicon photonics circuit design: methods, tools and challenges, Laser & Photonics Reviews 12 (4) (2018) 1700237.
[93] W.-J. Yin, J.-H. Yang, J. Kang, Y. Yan, S.-H. Wei, Halide perovskite materials for solar cells: a theoretical review, Journal of Materials Chemistry A 3 (17) (2015) 8926–8942.
[94] J. Kang, L.-W. Wang, High defect tolerance in lead halide perovskite $CsPbBr_3$, Journal of Physical Chemistry Letters 8 (2) (2017) 489–493.
[95] K. Tanaka, T. Takahashi, T. Ban, T. Kondo, K. Uchida, N. Miura, Comparative study on the excitons in lead-halide-based perovskite-type crystals

$CH_3NH_3PbBr_3$ $CH_3NH_3PbI_3$, Solid State Communications 127 (9–10) (2003) 619–623.
[96] A. Ferrando, J.P. Martínez Pastor, I. Suárez, Toward metal halide perovskite nonlinear photonics, Journal of Physical Chemistry Letters 9 (18) (2018) 5612–5623.
[97] J. Xu, X. Li, J. Xiong, C. Yuan, S. Semin, T. Rasing, X.-H. Bu, Halide perovskites for nonlinear optics, Advanced Materials (2019) 1806736.
[98] W. Chen, S. Bhaumik, S.A. Veldhuis, G. Xing, Q. Xu, M. Grätzel, S. Mhaisalkar, N. Mathews, T.C. Sum, Giant five-photon absorption from multidimensional core-shell halide perovskite colloidal nanocrystals, Nature Communications 8 (2017) 15198.
[99] Y. Xu, Q. Chen, C. Zhang, R. Wang, H. Wu, X. Zhang, G. Xing, W.W. Yu, X. Wang, Y. Zhang, M. Xiao, Two-photon-pumped perovskite semiconductor nanocrystal lasers, Journal of the American Chemical Society 138 (11) (2016) 3761–3768.
[100] Y. Fan, P. Tonkaev, Y. Wang, Q. Song, J. Han, S.V. Makarov, Y. Kivshar, S. Xiao, Enhanced multiphoton processes in perovskite metasurfaces, Nano Letters 21 (17) (2021) 7191–7197.
[101] I. Abdelwahab, G. Grinblat, K. Leng, Y. Li, X. Chi, A. Rusydi, S.A. Maier, K.P. Loh, Highly enhanced third-harmonic generation in 2D perovskites at excitonic resonances, ACS Nano 12 (1) (2017) 644–650.
[102] M. Cazzanelli, F. Bianco, E. Borga, G. Pucker, M. Ghulinyan, E. Degoli, E. Luppi, V. Véniard, S. Ossicini, D. Modotto, S. Wabnitz, R. Pierobon, L. Pavesi, Second-harmonic generation in silicon waveguides strained by silicon nitride, Nature Materials 11 (2) (2012) 148.
[103] G. Ermolaev, A.P. Pushkarev, A. Zhizhchenko, A.A. Kuchmizhak, I. Iorsh, I. Kruglov, A. Mazitov, A. Ishteev, K. Konstantinova, D. Saranin, et al., Giant and tunable excitonic optical anisotropy in single-crystal halide perovskites, Nano Letters 23 (7) (2023) 2570–2577, arXiv:2210.03541.
[104] S.V. Makarov, V. Milichko, E.V. Ushakova, M. Omelyanovich, A. Cerdan Pasaran, R. Haroldson, B. Balachandran, H. Wang, W. Hu, Y.S. Kivshar, A.A. Zakhidov, Multifold emission enhancement in nanoimprinted hybrid perovskite metasurfaces, ACS Photonics 4 (4) (2017) 728–735.
[105] H. Wang, R. Haroldson, B. Balachandran, A. Zakhidov, S. Sohal, J.Y. Chan, A. Zakhidov, W. Hu, Nanoimprinted perovskite nanograting photodetector with improved efficiency, ACS Nano 10 (12) (2016) 10921–10928.
[106] C. Zhang, S. Xiao, Y. Wang, Y. Gao, Y. Fan, C. Huang, N. Zhang, W. Yang, Q. Song, Lead halide perovskite-based dynamic metasurfaces, Laser & Photonics Reviews 13 (7) (2019) 1900079.
[107] A.Y. Zhizhchenko, P. Tonkaev, D. Gets, A. Larin, D. Zuev, S. Starikov, E.V. Pustovalov, A.M. Zakharenko, S.A. Kulinich, S. Juodkazis, et al., Light-emitting nanophotonic designs enabled by ultrafast laser processing of halide perovskites, Small 16 (19) (2020) 2000410.
[108] A. Zhizhchenko, A. Cherepakhin, M. Masharin, A. Pushkarev, S. Kulinich, A. Porfirev, A. Kuchmizhak, S. Makarov, Direct imprinting of laser field on halide perovskite single crystal for advanced photonic applications, Laser & Photonics Reviews 15 (8) (2021) 2100094.
[109] K. Baryshnikova, D. Gets, T. Liashenko, A. Pushkarev, I. Mukhin, Y. Kivshar, S. Makarov, Broadband antireflection with halide perovskite metasurfaces, Laser & Photonics Reviews 14 (12) (2020) 2000338.
[110] E. Tiguntseva, K. Koshelev, A. Furasova, P. Tonkaev, V. Mikhailovskii, E.V. Ushakova, D.G. Baranov, T. Shegai, A.A. Zakhidov, Y. Kivshar, S.V. Makarov, Room-temperature lasing from Mie-resonant nonplasmonic nanoparticles, ACS Nano 14 (7) (2020) 8149–8156.

[111] P. Tonkaev, G. Zograf, S. Makarov, Optical cooling of lead halide perovskite nanoparticles enhanced by Mie resonances, arXiv preprint, arXiv:1905.13093, 2019.
[112] E.Y. Tiguntseva, D.G. Baranov, A.P. Pushkarev, B. Munkhbat, F. Komissarenko, M. Franckevicius, A.A. Zakhidov, T. Shegai, Y.S. Kivshar, S.V. Makarov, Tunable hybrid Fano resonances in halide perovskite nanoparticles, Nano Letters 18 (9) (2018) 5522–5529.
[113] Y. Gao, C. Huang, C. Hao, S. Sun, L. Zhang, C. Zhang, Z. Duan, K. Wang, Z. Jin, N. Zhang, A.V. Kildishev, C.-W. Qiu, Q. Song, S. Xiao, Lead-halide perovskite nanostructures for dynamic color display, ACS Nano 12 (9) (2018) 8847–8854.
[114] C. Soci, G. Adamo, D. Cortecchia, K. Wang, S. Xiao, Q. Song, A.L. Schall-Giesecke, P.J. Cegielski, M.C. Lemme, D. Gerace, et al., Roadmap on perovskite nanophotonics, Optical Materials: X 17 (2023) 100214.
[115] A. Furasova, P. Voroshilov, M. Baranov, P. Tonkaev, A. Nikolaeva, K. Voronin, L. Vesce, S. Makarov, A. Di Carlo, Mie-resonant mesoporous electron transport layer for highly efficient perovskite solar cells, Nano Energy 89 (2021) 106484.
[116] M. Klein, Y. Wang, J. Tian, S.T. Ha, R. Paniagua-Domínguez, A.I. Kuznetsov, G. Adamo, C. Soci, Polarization-tunable perovskite light-emitting metatransistor, Advanced Materials 35 (1) (2023) 2207317.
[117] C. Huang, C. Zhang, S. Xiao, Y. Wang, Y. Fan, Y. Liu, N. Zhang, G. Qu, H. Ji, J. Han, et al., Ultrafast control of vortex microlasers, Science 367 (6481) (2020) 1018–1021.

This page intentionally left blank

4

Directional scattering of dielectric nanoantennas

Viktoriia E. Babicheva[a] **and Andrey B. Evlyukhin**[b,c]

[a]Department of Electrical and Computer Engineering, University of New Mexico, Albuquerque, NM, United States. [b]Institute of Quantum Optics, Leibniz Universität Hannover, Hannover, Germany. [c]Cluster of Excellence PhoenixD, Leibniz Universität Hannover, Hannover, Germany

4.1 First and second Kerker conditions

Mie solution for high-index all-dielectric spherical nanoparticles shows that such nanoparticles can support well-pronounced magnetic and electric multipole resonances with reasonable quality factor in the optical frequency range (in particular, visible and near-infrared), even in the case of the subwavelength size of the sphere. In a general case, multipole resonances depend on the size, shape, and composition of the nanoparticle as well as the frequency of the incident light. For a high-index nanoparticle with the refractive index $n_{\text{particle}} \approx 3.3$–4 and characteristic dimension $D \approx 150$ nm (e.g., sphere diameter) and surrounded by air or low-index dielectric, the wavelength of the first dipole resonance is $\lambda \approx n_{\text{particle}} D \approx 500$–600 nm [1]. Thus, the characteristic size of the nanoparticle required to support multipole resonances is several times smaller than the operating wavelength [2]. Most importantly, the high contrast between the nanoparticle and surrounding refractive indices results in a low-loss reflection of light inside the nanoparticle [3]. This reflection facilitates tight confinement of the mode and strong resonances with relatively low radiative losses (Fig. 4.1).

Practical high-index dielectric materials include silicon Si [4, 5], germanium Ge [6–8], or III-V compounds, which most commonly refer to gallium-indium-arsenide-antimonide-phosphide compounds [9–13]. These materials have near-zero absorption in some parts of the spectrum spanning the visible and infrared ranges. But all-dielectric nanoparticles are not necessarily made of such high-index materials. Based on the refractive index average value, one can identify other classes of materials: moderate-

All-Dielectric Nanophotonics. https://doi.org/10.1016/B978-0-32-395195-1.00009-0
Copyright © 2024 Elsevier Ltd. All rights reserved.

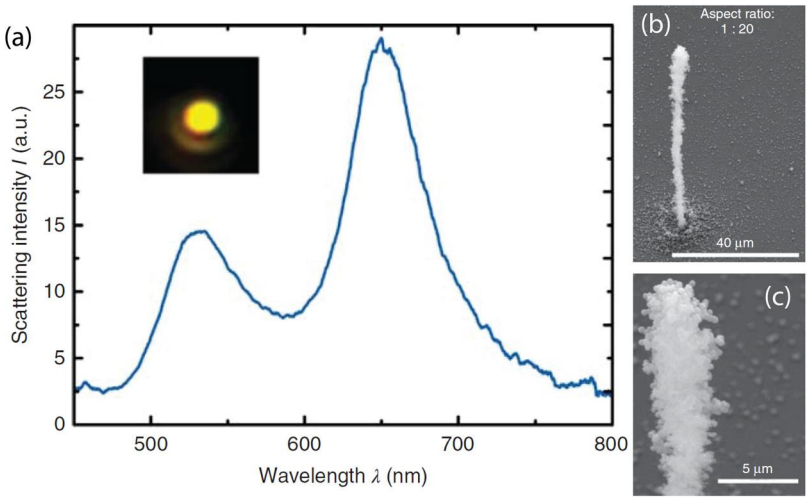

Figure 4.1. (a) Scattering intensity of a single spherical nanoparticle with a diameter of 160 nm made of silicon. The experimentally measured scattering spectrum showed well-pronounced electric and magnetic dipole resonances. Inset: dark-field microscopic image of these silicon nanoparticles. (b) and (c) Three-dimensional nanoparticle cluster consisting of several thousand silicon nanoparticles: scalar bars are (b) 40 µm and (c) 5 µm. The nanostructure was produced with laser printing [5,7]. Reproduced with permission from [7]. Copyright 2018 Wiley-VCH Verlag GmbH & Co. KGaA.

index materials, such as cupric oxide CuO_2 [14,15], titanium dioxide TiO_2 [16,17], selenium Se, and silicon oxynitride SiN_xO_y with $n_{\text{particle}} \approx 2$–$2.7$ [18], and low-index materials, such as silicon oxide SiO (dioxide SiO_2 in an ideal case) and polymers with $n_{\text{particle}} \approx 1.5$. Here, we limit our examples to non-absorbing materials or those with negligible losses. Nanoparticles made of moderate- and low-index materials can also support Mie resonances excited at the subwavelength scale, but light confinement in these cases is much weaker. This results in relatively high radiative losses and resonances that are not well-pronounced in the radiation spectrum. In the all-dielectric nanoparticles, the electromagnetic field of Mie resonances is mostly confined inside the nanoparticles. While the reflection at the boundaries affects the mode confinement, the surrounding medium index does not affect the optical properties to the same extent as it affects the properties of plasmonic nanoparticles. In what follows, we mainly focus on the high-index all-dielectric nanoparticle; but the same considerations can be extended to the nanoparticles with moderate or low refractive index.

The strong excitation of both magnetic and electric multipole resonances gives an additional degree to control light scattering using such high-index subwavelength nanoparticles [19], and these properties have been employed to improve the efficiency of

optical nanoantennas. In what follows, we refer to *forward scattering* as the one in the direction of the incident light propagation illuminating the nanoparticle. Correspondingly, the *back-scattered light* is the one in the direction opposite to the incident illuminating wave.

Kerker et al. [20] have theoretically analyzed the scattering from a single sphere and reported two scattering conditions where anomalous properties can be observed. The so-called *first Kerker condition* states that for the particle with relative permittivity $\varepsilon_{\text{particle}}$ and permeability μ_{particle} equal to each other ($\varepsilon_{\text{particle}} = \mu_{\text{particle}}$), the scattering in the backward direction can be reduced to zero. Similarly, the so-called *second Kerker condition* states that the forward scattering of the small particle can be zero when $a_1 = -b_1$, where a_1 and b_1 are the first order electric and magnetic Mie coefficients. It is equivalent to $\varepsilon_{\text{particle}} = (4 - \mu_{\text{particle}})/(2\mu_{\text{particle}} + 1)$ for a small particle.

As we mentioned earlier, a high-index nanoparticle supports not only electric multipoles but also magnetic ones. For a small particle, one can consider only dipole moments. One can show that the first Kerker condition is satisfied when the nanoparticle polarizabilities corresponding to the electric (ED) α_p and magnetic dipoles (MD) α_m are equal. We note that nanoparticle polarizability is a complex quantity, and the equality should be satisfied for the magnitude and phase value of the polarizability simultaneously. The suppression of back-scattering under the first Kerker condition is often called *Kerker effect*.

While the first Kerker condition can be satisfied with any values of ED and MD polarizabilities, a particular practical interest is drawn to the case when polarizabilities are large and at (or close to) their resonant values. This is commonly referred to as *resonant Kerker effect*.

One of the first demonstrations of the Kerker effect was performed for spherical nanoparticles with characteristic sizes ranging $D \approx 100$–200 nm, and it was shown that a forward-to-backward scattering ratio above six can be experimentally obtained [21]. The resulting radiation asymmetry of the forward and backward scattering components depends on the amplitudes and phases of the induced ED and MD moments: a representative example is shown for a spherical nanoparticle in Fig. 4.2 [22].

At the wavelengths λ_{K1} and λ_{K2} (Fig. 4.2), ED $\boldsymbol{p}$ and MD $\boldsymbol{m}$ moments induced in the nanoparticle are in-phase (zero phase difference) and equal in magnitude. Thus, the first Kerker condition is satisfied, and it suppresses the back-scattering and allows a high forward scattering. As the dipole moments are in-phase at λ_{K1} and λ_{K2}, the Poynting vector of the field scattered by dipoles $\boldsymbol{S} \propto$

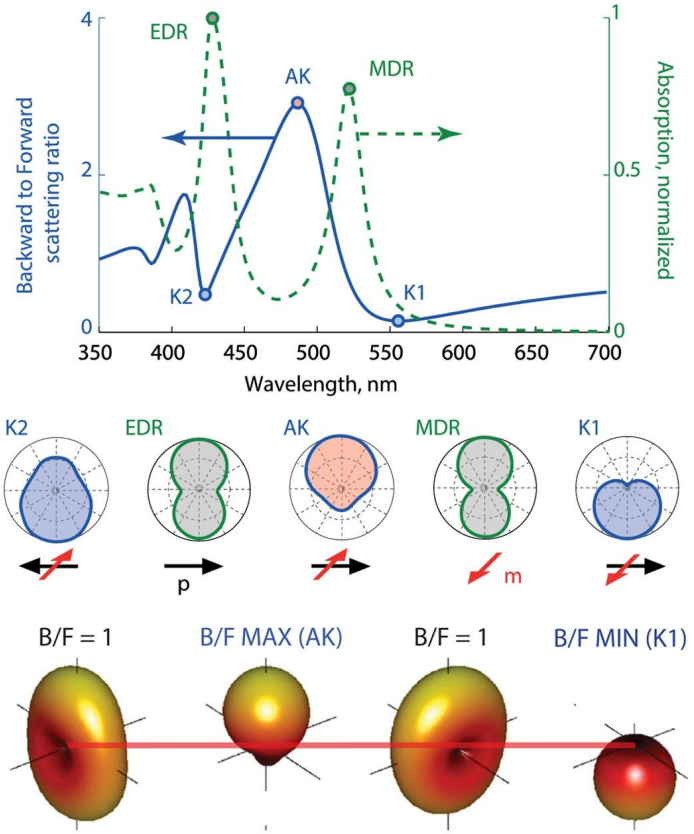

Figure 4.2. Ratio of backward to forward scattered energy of individual silicon nanoparticle with diameter $D = 120$ nm in the air compared to normalized absorption spectrum with the resonances of ED and MD multipoles. The middle row shows directivity plots for the different wavelengths of pronounced backward/forward scattering: the ratio is the highest in AK and the lowest in K1 and K2 points. The ratio is also small near the dipole resonances (denoted "EDR" and "MDR"), which do not necessarily coincide with K1 and K2 points. The bottom row shows three-dimensional schematics of far-field radiation patterns for various values of the backward-to-forward ratio. The scattering is calculated for an isolated silicon nanosphere with a diameter of $D = 150$ nm in free space. Analytical calculations are performed using Mie theory. Reproduced with permission from [22]. Copyright 2017 Optical Society of America.

$[\boldsymbol{p} \times \boldsymbol{m}]$ points downward, which means that the dipole efficiently scatters waves in the forward direction and no back-scattering is observed (see K1 and K2 points in Fig. 4.2). Furthermore, at the anti-Kerker (AK) wavelength, the backward-to-forward ratio is the highest. For the wavelength between the ED and MD resonances,

$\boldsymbol{p}$ and $\boldsymbol{m}$ have π phase difference, Poynting vector $\boldsymbol{S}$ points upward (see AK point in Fig. 4.2).

However, spherical nanoparticles have spectrally separated ED and MD resonances, and one can only observe the non-resonant Kerker effect in the scattering from such nanoparticles. In contrast, nanoparticles with spheroid, disk or cuboid shapes allow for independent changes of the geometrical parameters, and therefore, one can achieve an overlap of ED and MD resonances in such nanoparticles [23] and observe the resonant Kerker effect. As a downside, there are no general analytical solutions for disk or cuboid nanoparticles, and the analysis needs to be performed using electromagnetic simulations, possibly supplemented by multipole decomposition [24–28].

In this section, let us limit the consideration to the case of small nanoparticles and include only ED and MD in the calculations of the radiated far field of a nanoparticle. First, we assume that the induced ED moment is p_x and the induced MD moment is m_y. The backward scattering cross-section of the nanoparticle σ_{backward} is defined as:

$$\sigma_{\text{backward}} = \frac{k^4}{4\pi\varepsilon_0^2|\boldsymbol{E}_{\text{inc}}|^2}\left|p_x - \frac{\sqrt{\varepsilon_r}m_y}{c}\right|^2, \tag{4.1}$$

where ε_r is the relative permittivity of the surrounding medium ($\varepsilon_r = n_r^2$, both ε_r and n_r are considered real numbers throughout this chapter), c is the speed of light, $\boldsymbol{E}_{\text{inc}}$ is the vector of the incident electric field at the point of the ED and MD localization, k is the wavenumber of the incident light in the surrounding medium ($k = k_0\sqrt{\varepsilon_r}$), and ε_0 is vacuum permittivity.

From Eq. (4.1), the first Kerker condition can be written as:

$$p_x = \frac{\sqrt{\varepsilon_r}m_y}{c}. \tag{4.2}$$

The complex multipole moments can be expressed in a polar form as:

$$p_x = A_p e^{i\phi_p}, \;\; m_y = A_m e^{i\phi_m}, \;\; etc. \tag{4.3}$$

When we discuss the magnitudes and phases of the multipoles below, we refer to the values $A_{\text{multipole}}$ and $\phi_{\text{multipole}}$ (multipole = p, m, Q, M, O, or O^m). Some of the magnitude values need to be multiplied by a coefficient corresponding to the multipole term, e.g., $\sqrt{\varepsilon_r}/c$ for MD (see, Eq. (4.2)). Two multipole moments (including their corresponding coefficients) or polarizabilities being equal means that both real and imaginary parts or magnitude and phase values of two multipoles are equal simultaneously.

The forward scattering cross-section of the nanoantenna σ_{forward} is defined as:

$$\sigma_{\text{forward}} = \frac{k^4}{4\pi\varepsilon_0^2|\boldsymbol{E}_{\text{inc}}|^2}|p_x + \frac{\sqrt{\varepsilon_r}m_y}{c}|^2. \tag{4.4}$$

Similar to the concept existing in the field of microwaves and wireless communication [29], *the Huygens dipole source* antenna can be introduced as a small element that includes ED and MD response satisfying the first Kerker condition. In some sense, having equal ED and MD polarizabilities of the nanoparticle can be seen as having equal effective permittivity and permeability. If we replace the consideration of the isolated Huygens dipole source with an effective medium, the impedance of such an effective medium equals the impedance of the surrounding medium. If the effective impedance of these two media is equal, the back-scattering at the "interface" is zero and thus the first Kerker condition is satisfied.

We need to note that zero scattering in the backward (forward) direction does not automatically mean an increase of scattering in the forward (backward) direction. Excitation of electric and magnetic Mie resonances comes along with increased electromagnetic fields, and if nanoparticle material has an imaginary part of the permittivity $\varepsilon''_{\text{particle}} > 0$, the field increase results in non-radiative losses and heat dissipation. On one side, the material value of $\varepsilon''_{\text{particle}}$ can be small for the dielectric excited with the energy below the bandgap. On another side, resonant excitations greatly enhance light-matter interaction, and non-radiative losses increase accordingly. Thus, while the directionality of scattering can be increased by tailoring the nanoparticle properties to satisfy Kerker conditions, the total scattering can still suffer from non-radiative losses, absorption, and dissipation of energy into heat.

A recent analysis of nanoparticle scattering has been directed to survey materials with refractive indices in the range of $n_{\text{particle}} =$ 2–5 [30]. The theoretical Mie calculations have been performed for a lossless dielectric sphere, and the target has been to observe maximum forward and near-zero backward scattering components. The authors concluded that the optimum nanoparticle refractive index is $n_{\text{particle}} = 2.47$ and the total scattering cross-section can be several times larger than the geometrical cross-section of the nanoparticle ($\approx 3.5\pi D^2/4$). Interestingly, the authors also point out that there are a number of materials with refractive index in that range and negligible material losses: diamond, titanium dioxide TiO_2, and strontium titanate $SrTiO_3$. This makes it realistic to design nanostructures based on such nanoparticles

and apply them to practical devices. Of these three materials, titanium dioxide can be processed in nanofabrication facilities with well-established techniques and is commonly used for metasurfaces [16,17].

4.2 Generalized Kerker effect

The first Kerker condition was originally derived for particles with equal relative permittivity and permeability. It subsequently was formulated in terms of polarizabilities of ED and MD for the case of the optically small particle with dominating dipole moments. Earlier literature often uses the terms "electric resonance/mode" and "magnetic resonance/mode" assuming only dipole excitations make a significant contribution.

Advancing further the theoretical models and exploring the conditions for directional scattering, the researchers discovered the generalized Kerker condition that includes higher-order multipoles in the considerations [31,32]. In a more general case, the electric field radiated to the far-filed zone by several first multipole moments located at the origin of the coordinate system can be expressed through the following multipole superposition [24,33]:

$$\begin{aligned}\boldsymbol{E}(\boldsymbol{r}) = \frac{k_0^2 e^{ikr}}{4\pi\varepsilon_0 r}\Bigg(& [\boldsymbol{n}\times[\boldsymbol{p}\times\boldsymbol{n}]] + \frac{1}{c_r}[\boldsymbol{m}\times\boldsymbol{n}] + \frac{ik}{6}\left[\boldsymbol{n}\times\left[\boldsymbol{n}\times\hat{Q}\boldsymbol{n}\right]\right] \\ & + \frac{ik}{2c_r}\left[\boldsymbol{n}\times\left(\hat{M}\boldsymbol{n}\right)\right] + \frac{k^2}{6}\left[\boldsymbol{n}\times\left[\boldsymbol{n}\times\hat{O}(\boldsymbol{n}\boldsymbol{n})\right]\right] \\ & + \frac{k^2}{6c_r}\left[\boldsymbol{n}\times\hat{O}^m(\boldsymbol{n}\boldsymbol{n})\right] + \cdots\Bigg),\end{aligned} \tag{4.5}$$

where k_0 and k are the wavenumbers in vacuum and surrounding medium, respectively, ε_0 is the vacuum permittivity, c_r is the light speed in the surrounding medium, and $\boldsymbol{n} = \boldsymbol{r}/r$ is the unit vector towards the observation point. Here, we additionally introduced the tensors $\hat{Q}$, $\hat{M}$, $\hat{O}$, and $\hat{O}^m$ of electric (EQ) and magnetic (MQ) quadrupoles, and electric (EOC) and magnetic (MOC) octupole moments, respectively. The electric field irradiated to the far-field point $-\boldsymbol{r}$ (the opposite direction and the same absolute distance r) is directly obtained from Eq. (4.5) by replacing $\boldsymbol{r}$ and $\boldsymbol{n}$ with $-\boldsymbol{r}$ and $-\boldsymbol{n}$:

$$\begin{aligned}\boldsymbol{E}(-\boldsymbol{r}) = \frac{k_0^2 e^{ikr}}{4\pi\varepsilon_0 r}\Bigg(& [\boldsymbol{n}\times[\boldsymbol{p}\times\boldsymbol{n}]] - \frac{1}{c_r}[\boldsymbol{m}\times\boldsymbol{n}] - \frac{ik}{6}\left[\boldsymbol{n}\times\left[\boldsymbol{n}\times\hat{Q}\boldsymbol{n}\right]\right] \\ & + \frac{ik}{2c_r}\left[\boldsymbol{n}\times\left(\hat{M}\boldsymbol{n}\right)\right] + \frac{k^2}{6}\left[\boldsymbol{n}\times\left[\boldsymbol{n}\times\hat{O}(\boldsymbol{n}\boldsymbol{n})\right]\right]\end{aligned}$$

$$-\frac{k^2}{6c_r}\left[\boldsymbol{n}\times\hat{O}^m(\boldsymbol{nn})\right]+\cdots\Big). \tag{4.6}$$

Comparison of Eqs. (4.5) and (4.6) shows that ED, MQ, and EOC radiate an electric field in the directions $\boldsymbol{r}$ and $-\boldsymbol{r}$ with the same phase, while MD, EQ, and MOC with a phase difference equal to π. This means that the Kerker effect, leading to the suppression of backward or forward scattering, can only be realized with the simultaneous contribution of the multipole moments from both groups. Note that the first group includes multipole moments that change sign during the inversion of the coordinate system (odd multipoles), while the second group includes multipoles that do not change sign (even multipoles). Thus, ED (MD), MQ (EQ), and EOC (MOC) are the odd (even) multipole moments. The directional scattering with the participation of not only dipole terms, but also higher-order multipoles, can be called *a generalized Kerker effect*.

Various terminology has been used in the literature over the years, but in this chapter, we use terms in the following way. Term *condition* is used when we analyze only the forward or backward direction of light scattering with respect to the incident wave. Term *effect* is used when we describe directional scattering by a group of multipoles without specifying whether it occurs in the forward or backward direction.

Let us consider a particular case when only the first three multipoles are excited (ED, MD, and EQ). It has been first shown in [31] that one can achieve near-zero scattering in the backward direction in the case of comparable ED and EQ moments (Fig. 4.3).

For ED, MD, and EQ, contributing to the scattering cross-section, the backward scattering is defined as:

$$\sigma_{\text{backward}}=\frac{k^4}{4\pi\varepsilon_0^2|\boldsymbol{E}_{\text{inc}}|^2}\left|p_x-\frac{\sqrt{\varepsilon_r}m_y}{c}+\frac{ik}{6}Q_{xz}\right|^2, \tag{4.7}$$

where Q_{xz} is the EQ moment. In this case, EQ contribution needs to be included with a multiplier, which is related to the differences in units.

Thus, *the generalized first Kerker condition* of the zero backward scattering for the case limited to ED, MD, and EQ moment consideration is:

$$p_x-\frac{\sqrt{\varepsilon_r}m_y}{c}+\frac{ik}{6}Q_{xz}=0. \tag{4.8}$$

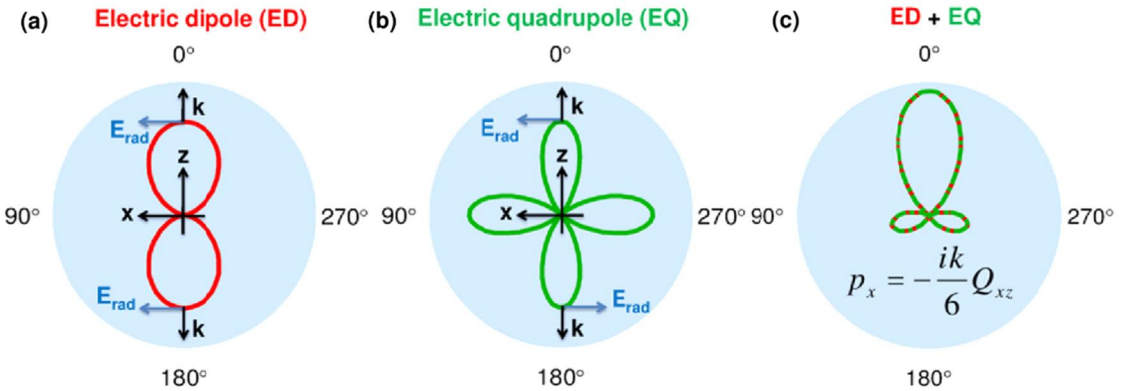

Figure 4.3. Radiation pattern for the case of ED and EQ multipole moments in the xz-plane. For simplicity, the contribution of MD is negligible in this example, e.g., plasmonic nanoparticle with a simple shape. In the diagram, the forward scattering corresponds to 0°, and the backward scattering corresponds to 180°. (a) Electric dipole moment p_x, and the radiated far field is $|\boldsymbol{E}_{\text{far}}|^2 \propto \cos^2\theta$. (b) Electric quadrupole moment Q_{xz}, and $|\boldsymbol{E}_{\text{far}}|^2 \propto \cos^2 2\theta$. The arrows E_{rad} denote the phase of the radiated field in panels (a) and (b). (c) Resulting radiation from the ED and EQ moments, when the generalized Kerker condition is fulfilled by satisfying the condition $p_x = -ikQ_{xz}/6$. The superposition of the ED and EQ moments results in the far field $|\boldsymbol{E}_{\text{far}}|^2 \propto (\cos 2\theta + \cos\theta)^2$, and can be canceled in the backward direction. Reproduced with permission from [31]. Copyright 2015 Optical Society of America.

Correspondingly, the forward scattering can be defined as:

$$\sigma_{\text{forward}} = \frac{k^4}{4\pi\varepsilon_0^2|\boldsymbol{E}_{\text{inc}}|^2}\left|p_x + \frac{\sqrt{\varepsilon_r}m_y}{c} - \frac{ik}{6}Q_{xz}\right|^2, \tag{4.9}$$

and the equation:

$$p_x + \frac{\sqrt{\varepsilon_r}m_y}{c} - \frac{ik}{6}Q_{xz} = 0, \tag{4.10}$$

corresponds to the case of zero forward scattering. These two conditions, Eqs. (4.8) and (4.10), can be straightforwardly extended to take into account higher-order multipole moments.

4.3 Non-diffractive arrays: Kerker effect, perfect reflection, and lattice anapole

Up to this point, we have discussed the directionality of radiation for the case of an isolated scatterer (single nanoparticle or nanoparticle cluster). One can extend similar considerations to the case of an infinite nanoparticle array. For the latter, we analyze reflection and transmission instead of the forward and backward

scattering, which cannot be defined any longer because the array is considered effectively infinite.

In this section, we consider a non-diffractive array, which we define as a lattice with a pitch smaller than the effective wavelength of light in the medium surrounding nanoparticles ($P_{x,y} < \lambda/n_r$, where $P_{x,y}$ are lattice pitches in the x- and y-directions, respectively, λ is the wavelength of light incident on the lattice, and n_r is the refractive index of the surrounding medium). In the next section, we discuss collective (or lattice) effects emerging in the case of $P_{x,y} \gtrsim \lambda/n_r$ and the impact of the resonance proximity to the diffraction wavelength. Here, it is important to note that nanoparticle polarizability needs to be described by an effective response of all nanoparticles in the lattice. Therefore, it requires accounting for the contribution of all nanoparticles in the array and calculating lattice sums. It is often assumed that the contribution from the array is significant only if the array period is equal to or smaller than the effective wavelength in the surrounding medium. The reason for identifying these regimes is the proximity to the emergence of the next diffraction order (in most cases the first diffraction order). However, even if the resonance of the single nanoparticle is excited at a wavelength longer than the lattice period, e.g., by 100–200 nm for the visible spectral range (dense array of nanoparticles), the nanoparticle interaction (same-multipole coupling) strongly affects the resonance shape and its spectral position [34].

The Kerker effect in the non-diffractive nanoparticle array can be defined as a near-zero reflection from the nanoparticle array resulting from the compensation of ED and MD contributions. Thus, Huygens dipole source (or Huygens element) is defined as a scatterer with spectrally overlapping ED and MD, and *Huygens metasurfaces* are introduced as metasurfaces made of such elements (Fig. 4.4). Reflection and transmission coefficients can be expressed either through ED and MD polarizabilities or multipole moments [35,36].

First, we discuss representation in terms of the multipole moments and then we move to the analysis of the nanoparticle polarizabilities. In the seminal work of Staude et al. [35], only ED and MD (Fig. 4.5) are discussed. In another example (Fig. 4.6), we can observe that for normal light incidence of a plane wave, the ED and MD resonances overlap when the silicon disk diameter is $d \approx 350$ nm and the height $h = 130$ nm. In turn, for larger diameters, ED resonance is excited at a wavelength λ_{EDR} longer than the one λ_{MDR} for MD resonance. It is the case opposite to the spherical nanoparticle, where $\lambda_{MDR} > \lambda_{EDR}$.

Similar to the case of the isolated scatterer, one can extend the definition to the compensation of ED and EQ contributions and introduce a broader concept of the generalized Kerker effect in a nanoparticle array. We present expressions through multipole moments up to EOC and expressions through nanoparticle polarizabilities up to MOC.

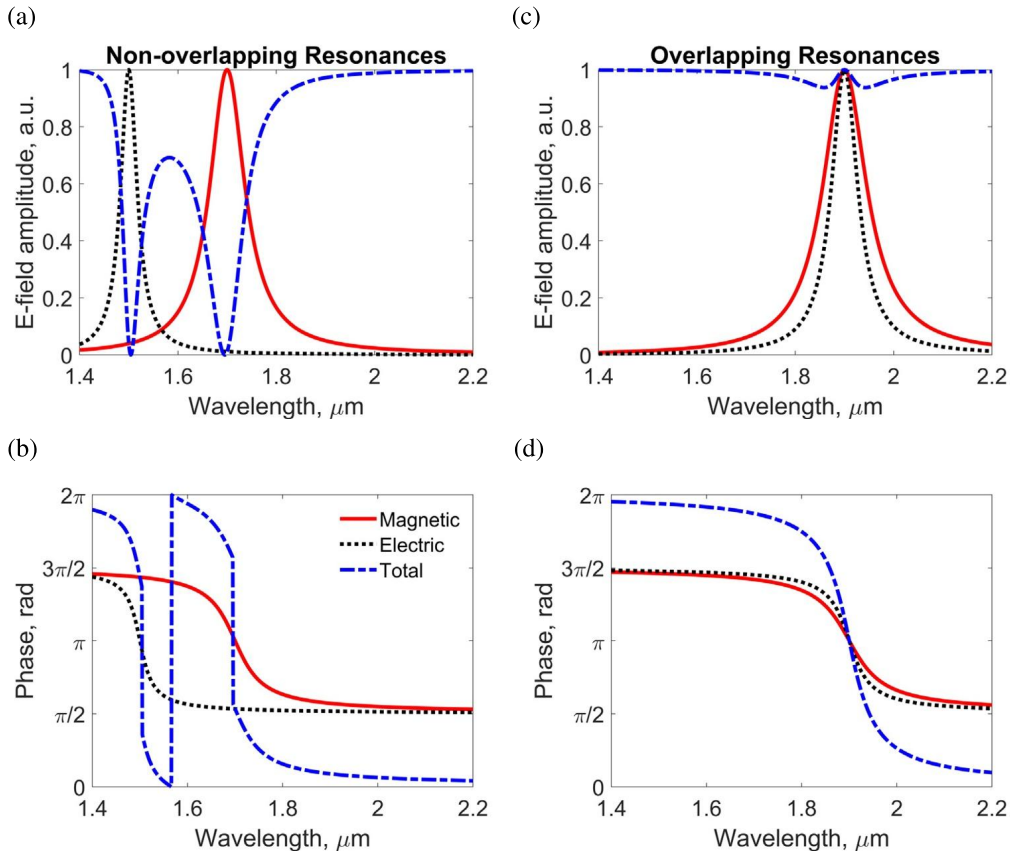

Figure 4.4. Non-overlapping ED and MD resonances: (a) E-field amplitude of ED resonance (dotted black), MD resonance (solid red), and total transmission (dot-dashed blue); (b) E-field phase. (c) and (d) same as (a) and (b), but for the case of spectrally overlapping ED and MD resonances. All results were obtained with analytical calculations.

Using the equations for the electric field reflection r and transmission t and the multipole representations, the contribution of the multipole moments to the reflection and transmission can be estimated. Here, we present them in the case of the normal light incidence on the nanoantenna array. Another assumption is that all nanoantennas are identical, respond with the same multipole moments, and form an infinite periodic lattice. Because of the

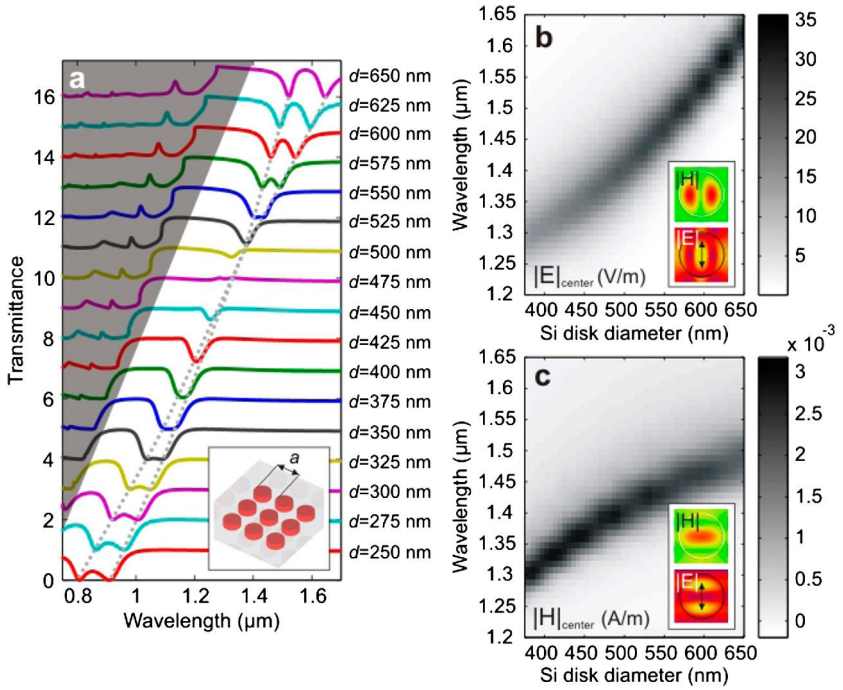

Figure 4.5. (a) Transmission through the silicon nanodisk arrays. The height is $h = 220$ nm, and the lattice period varies as $a = d + 200$ nm. One can observe a complete mode crossing for a diameter $d \approx 475$ nm and spectrally separated resonances on both sides of the overlap. For clarity, each transmission spectrum is vertically shifted by 1 when the disk changes by 25 nm. The dashed lines are guides for the eye, approximately corresponding to the dips in transmission. The gray area corresponds to the wavelength below the diffraction limit, and the spectral features in this region are not considered here. Inset: Schematics of silicon nanodisks arranged into a periodic array. (b) Electric and (c) magnetic-field magnitudes at the silicon nanodisk center for $d = 600$ nm and $a = 850$ nm. The insets in (b) and (c) panels show the electric and magnetic-field profiles corresponding to this case. The results in all panels are obtained by numerical simulations and correspond to the linear regime. The array of silicon nanodisks is embedded in a homogeneous surrounding environment with $n_r = 1.5$. Reproduced with permission from [35]. Copyright 2013 American Chemical Society.

translational symmetry of the lattice, such identical nanoparticles can be modeled using periodic boundary conditions in the numerical simulation domain.

Let us express the reflection and transmission coefficients considering the contribution of several first multipoles up to MOC: $\boldsymbol{p}$ and $\boldsymbol{m}$ are the vectors of ED and MD moments; $\hat{Q}$, $\hat{M}$, $\hat{O}$, and $\hat{O}^m$ are the tensors of the EQ, MQ, EOC, and MOC moments, respectively. For these conditions and for the x-polarized incident plane light waves propagating along the z-axis with the time dependence $e^{-i\omega t}$ (xy-plane is the array plane), the r and t coeffi-

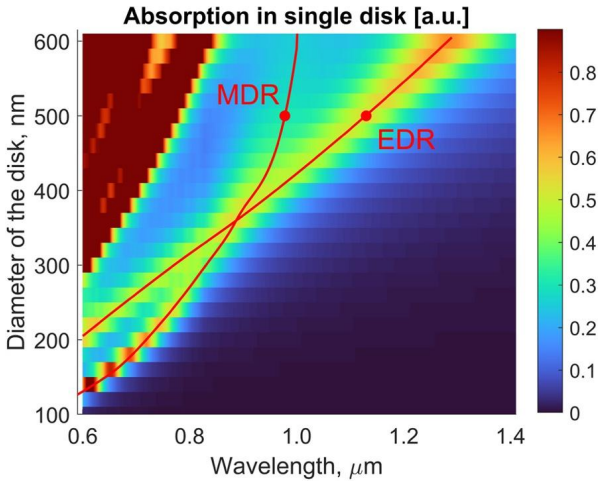

Figure 4.6. Absorption properties of a single silicon disk under normal light incidence and various disk diameters. The single disk has the height $h = 130$ nm and different diameters d. The silicon disk has a permittivity taken from the experimental data, while the surrounding material is air with a refractive index of $n_r = 1$. The red lines represent the electric and magnetic resonances, which correspond to the points of maximum absorption.

cients are [25]:

$$r = \frac{ik}{E_{\text{inc}} 2 S_L \varepsilon_0 \varepsilon_r} \left(p_x - \frac{1}{c_r} m_y + \frac{ik}{6} Q_{xz} - \frac{ik}{2c_r} M_{yz} - \frac{k^2}{6} O_{xzz} + \frac{k^2}{6c_r} O^{(m)}_{yzz} \right), \tag{4.11}$$

$$t = 1 + \frac{ik}{E_{\text{inc}} 2 S_L \varepsilon_0 \varepsilon_r} \left(p_x + \frac{1}{c_r} m_y - \frac{ik}{6} Q_{xz} - \frac{ik}{2c_r} M_{yz} - \frac{k^2}{6} O_{xzz} - \frac{k^2}{6c_r} O^{(m)}_{yzz} \right). \tag{4.12}$$

For the y-polarization, the coefficients are:

$$r = \frac{ik}{E_{\text{inc}} 2 S_L \varepsilon_0 \varepsilon_r} \left(p_y + \frac{1}{c_r} m_x + \frac{ik}{6} Q_{yz} + \frac{ik}{2c_r} M_{xz} - \frac{k^2}{6} O_{yzz} + \frac{k^2}{6c_r} O^{(m)}_{xzz} \right), \tag{4.13}$$

$$t = 1 + \frac{ik}{E_{\text{inc}} 2 S_L \varepsilon_0 \varepsilon_r} \left(p_y - \frac{1}{c_r} m_x - \frac{ik}{6} Q_{yz} + \frac{ik}{2c_r} M_{xz} - \frac{k^2}{6} O_{yzz} - \frac{k^2}{6c_r} O^{(m)}_{xzz} \right). \tag{4.14}$$

Here k is the wavenumber in the surrounding medium, S_L is the area of a lattice unit cell with $S_L = P_x P_y$, ε_0 is the vacuum permittivity, ε_r is the relative permittivity of surrounding medium, E_{inc} is the electric field of the normally incident plane waves in the array plane, and $c_r = 1/\sqrt{\mu_0 \varepsilon_0 \varepsilon_r}$ is the speed of light in the surrounding medium. For the case of x-polarized light, $E_{\text{inc}} = E_x$, and magnetic field of the incident field $H_y = \sqrt{\epsilon_0 \epsilon_r / \mu_0} E_x$, the effective polarizabilities of ED, MD, EQ, MQ, EOC, and MOC are related to multipoles as $\alpha_p = p_x/(\varepsilon_0 \varepsilon_r E_x)$, $\alpha_m = m_y/H_y$, $\alpha_Q = 2Q_{xz}/(ikE_x)$, $\alpha_M = 2M_{yz}/(ikH_y)$, $\alpha_{eo} = -3O_{xzz}/(k^2 E_x)$, and $\alpha_{mo} = -3O^{(m)}_{yzz}/(k^2 H_y)$, respectively.

The expressions (4.11)–(4.14) can be applied to an arbitrary nanoparticle providing the periodic array is infinite and nanoparticles are identical and the multipole moments can be calculated from numerical simulations by means of multipole decomposition (see, e.g., [25]). In contrast, for the spherical nanoparticle, the reflection and transmission coefficients can be expressed in terms of polarizabilities. For the dipole-quadrupole-octupole system, which includes six multipoles, the reflection and transmission coefficients (calculated with respect to the electric field and only for the zeroth-order diffraction) are:

$$r_0 = \frac{ik}{2S_L}\left[\alpha_p - \alpha_m - \frac{k_0^2}{12\varepsilon_0}\alpha_Q + \frac{k^2}{4}\alpha_M + \frac{k^4}{18\epsilon_0\epsilon_r}\alpha_{eo} - \frac{k^4}{18}\alpha_{mo}\right], \tag{4.15}$$

$$t_0 = 1 + \frac{ik}{2S_L}\left[\alpha_p + \alpha_m + \frac{k_0^2}{12\varepsilon_0}\alpha_Q + \frac{k^2}{4}\alpha_M + \frac{k^4}{18\epsilon_0\epsilon_r}\alpha_{eo} + \frac{k^4}{18}\alpha_{mo}\right]. \tag{4.16}$$

These expressions (4.15) and (4.16) can be obtained from Eqs. (4.11)–(4.12) for the x-polarization. To achieve this, it is necessary to express the multipole moments of spherical nanoparticles in terms of their corresponding polarizabilities [1,37–39].

Using the general expressions above, we can now discuss several particular cases that result in directional scattering (forward or backward) and even complete suppression of scattering (anapole state). In what follows, we use expressions for reflection and transmission coefficients that include effective possibilities of the nanoparticle corresponding to different multipoles.

4.3.1 Zero reflection and Kerker effect

Similar to the case of a single nanoparticle, one can specify the condition when reflection from the nanoparticle array is com-

pletely suppressed, that is, $r = 0$. If only ED and MD contribute to the nanoparticle scattering and the contributions of higher multipoles are negligible, the condition of $r = 0$ is either $p_x = m_y/c_r$ from Eq. (4.11) or $\alpha_p = \alpha_m$ from Eq. (4.15). Here, the main difference from the case of a single nanoparticle is that the quantities p_x, m_y, α_p, and α_m are effective ones. Thus, these quantities correspond to a nanoparticle in the array and take into account contributions of all other nanoparticles around, even for a non-diffractive array. As these quantities are complex, their equality requires that both real and imaginary parts be equal simultaneously (or magnitude and phase values for the polar representation). One can generalize the condition and replace MD with EQ (imposing $\alpha_p = \alpha_Q k_0^2/(12\varepsilon_0)$ condition) or include both MD and EQ contributions.

Earlier, analyzing expressions (4.5) and (4.6), we identified two groups of multipole: ED-MQ-EOC and MD-EQ-MOC. One can notice that multipoles from one group need to be compensated by multipoles from another group, e.g., ED compensated by MD or ED compensated by EQ, and it is not possible to compensate MD by EQ, and so on. Thus, most importantly, we see that at least one multipole from each group needs to be significant enough to compensate for the scattering of one or more multipoles from another group and achieve suppression of reflection (generalized Kerker effect). If absorption in the nanoparticles is negligible, zero reflection results in 100% light transmission through such a nanoparticle array.

4.3.2 Zero transmission and perfect reflection

Next, one can analyze the condition that is complementary to the one we discuss in Sec. 4.3.1 for the case of non-absorbing nanoparticles: transmission is completely suppressed (that is, equal to zero), and reflection is 100%. An example of such non-absorbing materials can be titanium dioxide, silicon nitride, other dielectrics, or silicon in the near-infrared spectral range.

Let us start with analyzing the case when only ED and MD are significant, and the contribution from other multipoles can be neglected. From Eq. (4.16), the transmission intensity is given by [40]:

$$|t_0|^2 = \left[1 - \frac{k}{2S_L}\left(\mathrm{Im}\left[\alpha_p\right] + \mathrm{Im}\left[\alpha_m\right]\right)\right]^2 + \frac{k^2}{4S_L^2}\left(\mathrm{Re}\left[\alpha_p\right] + \mathrm{Re}\left[\alpha_m\right]\right)^2 . \quad (4.17)$$

Analyzing Eq. (4.17), we observe that under the conditions

(i)

$$\frac{k}{2S_L}\left(\mathrm{Im}\left[\alpha_p\right]+\mathrm{Im}\left[\alpha_m\right]\right)\rightarrow 1 \tag{4.18}$$

and

(ii)

$$\frac{k}{2S_L}\left(\mathrm{Re}\left[\alpha_p\right]+\mathrm{Re}\left[\alpha_m\right]\right)\rightarrow 0 \tag{4.19}$$

the transmission is suppressed. One can see that whether both conditions are satisfied depends on the nanoparticle dipole polarizabilities and array period. The second condition (ii) in Eq. (4.19) can only be satisfied in the spectral region between ED and MD resonances, where the signs of the polarizability's real part of both ED and MD are opposite. However, to satisfy the first condition (i) in Eq. (4.18), the dipole scattering from the nanoparticle in the array should be sufficiently strong. Thus, significant suppression of light transmission can be expected in spectral regions close to the two dipole resonances for arrays with unit cells satisfying the estimate:

$$S_L \approx \frac{2\pi\,\mathrm{Im}\left[\alpha_R\right]}{\lambda_R}, \tag{4.20}$$

where α_R is the corresponding effective dipole polarizability (ED and MD) at the resonant wavelength λ_R.

Thus, the wave can be resonantly scattered forward by one or both ED and MD excitations of the nanoparticles and can destructively interfere with the incident wave [40]. This can significantly suppress the transmission of light propagating through the array and even result in zero transmission (Fig. 4.7).

For non-absorbing nanoparticles, suppressed transmission results in ideal 100% reflection depending on surrounding conditions [41,42]. Practical realization of such nanostructure and experimental confirmation of its optical properties have been demonstrated in Ref. [43]. There, the authors realized the perfect reflector operating in the telecom range with 99.7% reflection at the wavelength of 1530 nm, which exceeds the reflectance of metallic mirror. One can also see that the disorder originating from the self-assembly process insignificantly affects the reflection and introduces only minor deviations from the ideal theoretical value for perfectly arranged nanoparticles (Fig. 4.8).

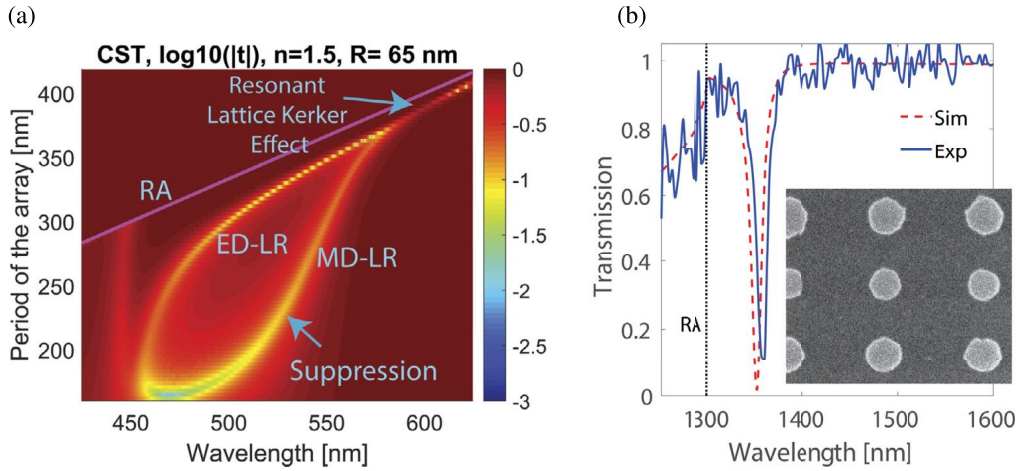

Figure 4.7. (a) The transmission coefficients of Si nanosphere arrays with a square elementary cell, calculated for various periods and presented in logarithmic form. The nanosphere radius is $R = 65$ nm, and the results were obtained by numerical simulations. The magenta lines mark the RA. The data in the diffraction regime (above the RA lines) are not shown. The surrounding medium has $n_r = 1.5$, and the wavelengths correspond to the free space wavelength (without dividing by the refractive index of the surrounding medium). (b) Experimental demonstration "Exp" (*vs.* corresponding numerical simulation "Sim") of near-zero transmission in Si nanodisk array. Disks have a radius of 150 nm and a height of 280 nm, and they are placed on a fused silica substrate ($n_r = 1.47$) and arranged in the lattice with periods of 690 nm and 895 nm. There is an index-matching liquid with $n_r = 1.47$ on top of the array. Inset: Scanning electron microscope (SEM) image of the array. Panel (a) reproduced with permission from [40]. Copyright 2018 Optical Society of America.

4.3.3 Lattice anapole state for non-spherical nanoparticles

The third special case is the formation of a non-radiating (radiationless, scatter-less) anapole state enabled by the nanoparticle array. The formation of anapole states in a single nanoparticle is described in detail elsewhere in this book (see, e.g., [44–49]). Here, we emphasize that one can obtain an anapole state by achieving a complete compensation of scattering from all significant multipoles, provided some conditions are satisfied: see Ref. [25] for non-diffractive array and Ref. [38] for array properties defined by the lattice spacing. It is another special case of directional scattering, and the compensation occurs between multipoles that have the same inverse-symmetry properties: either between ED, MQ, and EOC multipoles or between MD, EQ, and MOC multipoles. It is opposed to the Kerker effect we discussed above, which requires compensation from the multipoles with different parity (i.e., with even and odd symmetries).

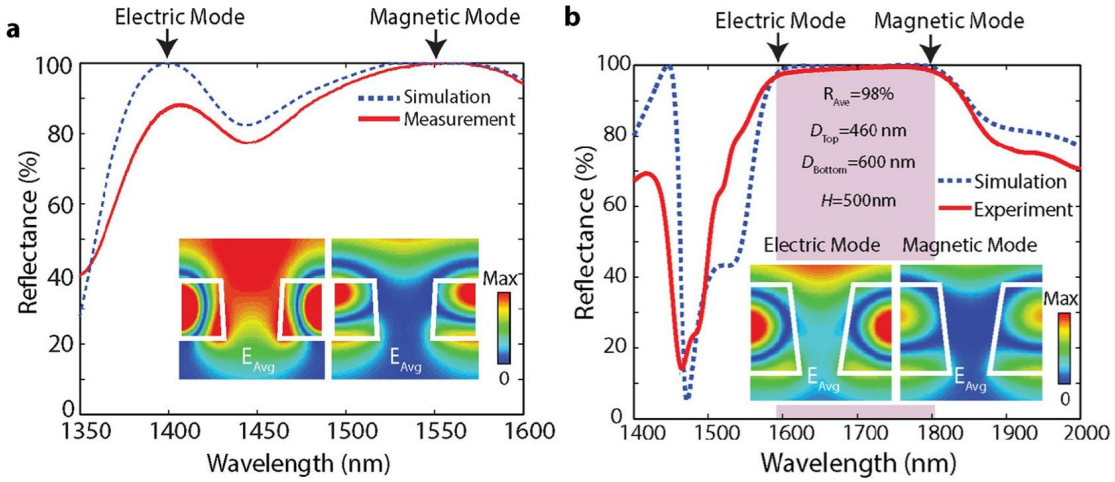

Figure 4.8. (a) Reflection of a periodic metamaterial: comparison of numerical simulations with perfectly periodic structures and measurements with 4% disorder in the lattice. Silicon nanoparticle array was fabricated using self-assembly-based nanosphere lithography. One can observe the higher tolerance to disorder of the MD mode compared to the ED one. Inset: Time-averaged electric fields obtained by numerical simulations for ED and MD. It shows that the electromagnetic field of ED mode is expanded outside of the nanoparticle in comparison to MD, and this results in lower tolerance of ED resonance to disorder. (b) Reflection spectra of a broadband mirror: numerical simulations and experimental measurements. The average reflection in the experiment is 98%, and it covers the bandwidth of ≈ 200 nm. The nanoparticle dimensions are $D_{\text{top}} = 460$ nm, $D_{\text{bottom}} = 600$ nm, $H = 500$ nm, and the periodicity of array is $P = 820$ nm. Inset: Time-averaged electric fields obtained by numerical simulations for ED and MD. The former experience tighter confinement within the nanoparticle. Reproduced with permission from [43]. Copyright 2015 American Chemical Society.

Light propagates through the nanoparticle lattice without changes in intensity or phase, but with the simultaneous excitation of nanoparticle multipole moments. Thus, the energy is localized within the nanoparticles or around them, but the light transmission is unperturbed and there is no reflection. For this reason, this effect is called *lattice invisibility*. We note that this effect should not be confused with the case when the interaction of light and nanoparticles is weak, multipoles are not excited, and therefore light propagation is only weakly affected by the lattice.

An example of a nanoparticle array supporting a lattice anapole state is shown in Figs. 4.9 and 4.10 [25]. The metasurface consists of silicon nanocubes with the side $a_p = 250$ nm, and they are arranged into the lattice with the same spacing $P = 400$ nm in both lateral directions. In the spectra in Fig. 4.9, we identify several wavelengths with particular properties. At $\lambda = 1200$ nm, ED and MD terms have equal magnitudes and phases (Fig. 4.10), which result in zero reflection and total transmission (Kerker effect in

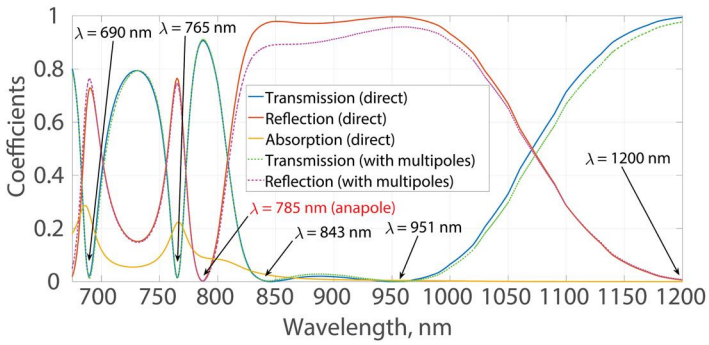

Figure 4.9. Spectra of the transmittance, reflectance, and absorbance of the silicon metasurfaces. It consists of cubes with the side $a_p = 250$ nm arranged in the square lattice with pitch $P = 400$ nm. The nanoparticles are placed in a homogeneous surrounding medium with $\varepsilon_r = 1$. Notations "(direct)" correspond to the results obtained directly from numerical simulations with the commercial package COMSOL. Notations "(with multipoles)" correspond to the values calculated from multipole moments using Eqs. (4.11) and (4.12) (up to EOC). One can notice a very good agreement between the spectra obtained in two different ways. However, we note that multipole moments were calculated from the same simulation run as the direct spectra. Reproduced with permission from [25]. Copyright 2019 American Physical Society.

non-absorbing metasurface, Fig. 4.9). In contrast, at $\lambda \approx 905$ nm, ED and MD terms have equal magnitudes, but different phases, which results in high reflection and near-zero transmission. The broadband increase in the reflection and near-zero transmission from $\lambda = 843$ nm to $\lambda = 951$ nm is realized due to the excitation of the strong ED and MD, and their scattering in the forward and backward directions. The destructive interference between the incident wave and the strong forward scattering provides transmission suppression. One can also observe the insignificant contribution of EQ at that long wavelength range ($\lambda > 900$ nm). The EOC contribution to reflection and transmission is very small for the entire considered spectral range and therefore it is not included in the subsequent multipole analysis.

Most importantly, at the wavelength $\lambda = 785$ nm, we observe the realization of lattice anapole. In Fig. 4.10, we see that the magnitudes and phases of the four significant multipoles (ED, MD, EQ, and MQ) are equal, while their excitation is reasonably strong. From Eqs. (4.11) and (4.12), we see that in this case, the multipole terms cancel each other out, and this results in zero reflection and total transmission of light through the array, which is confirmed by values of these quantities in the numerical simulations in Fig. 4.9.

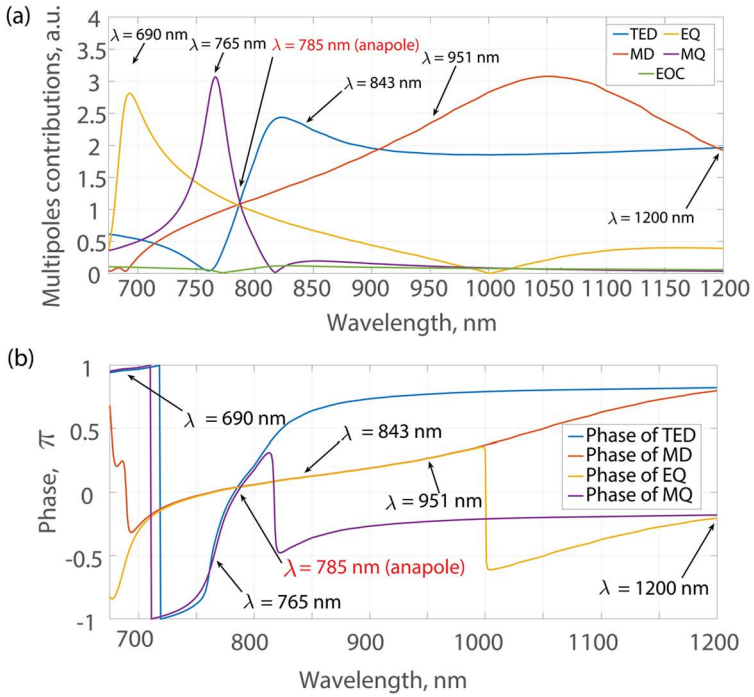

Figure 4.10. (a) Absolute values and (b) phases of the multipole contributions in the electric-field reflection and transmission coefficients for the metasurface in Fig. 4.9. Notation "TED" in the legend corresponds to the combined electric dipole and toroidal moment, which we abbreviate to "ED" throughout the chapter. Reproduced with permission from [25]. Copyright 2019 American Physical Society.

4.4 Lattice resonance effect

The coupling of dipoles in nanoparticle arrays of one and two dimensions generates narrow collective resonances manifested as features in light spectra, and the feature wavelengths depend on the array periods, surrounding medium, the angle of excitation, etc. In the electric dipole approximation, the lattice resonances of these collective modes involve only dipole moments of the nanoparticles perpendicular to the lattice wave propagation.

Let us take one step further and consider the case when effective polarizabilities of different multipoles are not just insignificantly affected, but strongly defined by the lattice arrangement. We further refer to it as *lattice* or *collective* effects. In the previous section, we discussed the case when multipole polarizabilities of the nanoparticle $\alpha_{\text{multipole}}$ (multipole = *p, m, Q*, etc.) are insignificantly affected by the presence of other nanoparticles in the array. Here, we extend the considerations up to MQ.

We operate with polarizabilities α_p^{eff}, α_m^{eff}, α_Q^{eff}, and α_M^{eff}, assuming all nanoparticles in the array are identical. In agreement with Ref. [38] and in contrast to Section 4.3, in this section, we consider ED polarizability defined as $\alpha_p = p_x/E_x$. The expressions in Eqs. (4.15) and (4.16) for reflection and transmission, respectively, can be rewritten as:

$$r_0 = \frac{ik}{2S_L}\left[\frac{1}{\varepsilon_0\varepsilon_r}\alpha_p^{\text{eff}} - \alpha_m^{\text{eff}} - \frac{k_0^2}{12\varepsilon_0}\alpha_Q^{\text{eff}} + \frac{k^2}{4}\alpha_M^{\text{eff}}\right], \tag{4.21}$$

$$t_0 = 1 + \frac{ik}{2S_L}\left[\frac{1}{\varepsilon_0\varepsilon_r}\alpha_p^{\text{eff}} + \alpha_m^{\text{eff}} + \frac{k_0^2}{12\varepsilon_0}\alpha_Q^{\text{eff}} + \frac{k^2}{4}\alpha_M^{\text{eff}}\right]. \tag{4.22}$$

The effective polarizabilities are defined as:

$$\begin{aligned} \frac{1}{\alpha_p^{\text{eff}}} &= \frac{1}{\alpha_p} - \frac{S_{pp}}{\varepsilon_0}, \quad \frac{1}{\alpha_m^{\text{eff}}} = \frac{1}{\alpha_m} - S_{mm}, \\ \frac{1}{\alpha_Q^{\text{eff}}} &= \frac{1}{\alpha_Q} - \frac{S_{QQ}}{2\varepsilon_0}, \quad \frac{1}{\alpha_M^{\text{eff}}} = \frac{1}{\alpha_M} - \frac{S_{MM}}{2}. \end{aligned} \tag{4.23}$$

These effective quantities include polarizabilities of a single nanoparticle α_p, α_m, α_Q, and α_M as well as lattice sums S_{pp}, S_{mm}, S_{QQ}, and S_{MM} corresponding to each multipole. One can perform derivations (see, e.g., [37–39]) and obtain lattice sums as follows:

$$S_{pp} = \frac{k_0^2}{4\pi}\sum_{l\neq 0}\frac{e^{ikr_l}}{r_l}\left(1 + \frac{i}{kr_l} - \frac{1}{k^2r_l^2} - \frac{x_l^2}{r_l^2} - \frac{i3x_l^2}{kr_l^3} + \frac{3x_l^2}{k^2r_l^4}\right), \tag{4.24}$$

$$S_{mm} = \frac{k^2}{4\pi}\sum_{l\neq 0}\frac{e^{ikr_l}}{r_l}\left(1 + \frac{i}{kr_l} - \frac{1}{k^2r_l^2} - \frac{y_l^2}{r_l^2} - \frac{i3y_l^2}{kr_l^3} + \frac{3y_l^2}{k^2r_l^4}\right), \tag{4.25}$$

$$\begin{aligned} S_{QQ} = \frac{k_0^2}{6}\frac{ik}{4\pi}\sum_{l\neq 0}\frac{e^{ikr_l}}{r_l^2}\Bigg(&-2 - i\frac{6+k^2x_l^2}{kr_l} + \frac{12+7k^2x_l^2}{k^2r_l^2} \\ &+ i\frac{12+27k^2x_l^2}{k^3r_l^3} - \frac{60x_l^2}{k^2r_l^4} - \frac{i60x_l^2}{k^3r_l^5}\Bigg), \end{aligned} \tag{4.26}$$

$$\begin{aligned} S_{MM} = \frac{k_0^2\varepsilon_r}{2}\frac{ik}{4\pi}\sum_{l\neq 0}\frac{e^{ikr_l}}{r_l^2}\Bigg(&-2 - i\frac{6+k^2y_l^2}{kr_l} + \frac{12+7k^2y_l^2}{k^2r_l^2} \\ &+ i\frac{12+27k^2y_l^2}{k^3r_l^3} - \frac{60y_l^2}{k^2r_l^4} - \frac{i60y_l^2}{k^3r_l^5}\Bigg), \end{aligned} \tag{4.27}$$

where $r_l = \sqrt{x_l^2+y_l^2}$ is the distance between the nanoparticle with number l and the origin of the coordinate system, and the sum runs over all nanoparticles except the nanoparticle at the origin of the coordinate system with $l = 0$.

Lattice resonances in plasmonic nanoparticles have been studied for a long time [37,50–62]. In plasmonic arrays, such as those made of silver, gold, or other low-loss materials, the lattice resonance is usually seen as an additional resonance appearing in proximity to the Rayleigh anomaly, while the single-particle resonance is affected insignificantly.

Arrays of high refractive index nanoparticles exhibit properties somewhat different from plasmonic nanoparticles, even though the processes are governed by the same equations. Electric dipole resonance in a single silicon nanoparticle is weaker than such resonance in a silver nanoparticle, provided that in both cases the characteristic nanoparticle size is approximately the same. As a result, the lattice effect is stronger and results in larger changes in polarizability.

For the silicon nanoparticle array, the lattice resonance becomes not just an additional one, but the main one, and it changes its position along with the change of Rayleigh anomaly (Fig. 4.11, [63]). In contrast, the initial single-particle resonance remains spectrally in place and gets substantially weaker once its spectral position at the wavelength is below the diffraction limit. In the recent work [63], we have demonstrated that one can control the position of ED lattice resonance and overlap its spectral position with MD. This results in the *resonant lattice Kerker effect* that is the near-zero reflection from the array facilitated by the compensation of ED and MD resonances (Fig. 4.11). An experimental demonstration of the effect has been reported in Ref. [64]. Under oblique incidence, lattice resonances in periodic structures are highly sensitive to the polarization and incident angle of the incoming light [65], leading to significant changes in the spectral response and field distribution.

Lattice resonances are excited only at the red side of the single-particle resonance, and thus, the shift is possible only into the longer wavelength range. Because of this, for the spherical silicon nanoparticles, it is possible to overlap only ED lattice resonance and MD. In contrast, for the nanoparticles in the shape of disk or cuboid, one can possibly achieve an overlap of MD lattice resonance and ED, provided that the aspect ratio of the nanoparticle is significantly changed and ED is excited at a longer wavelength than MD in the single nanoparticle constituting the array.

Further analysis of multipole lattices has shown that such periodic arrangement facilitates the coupling of multipoles of a dif-

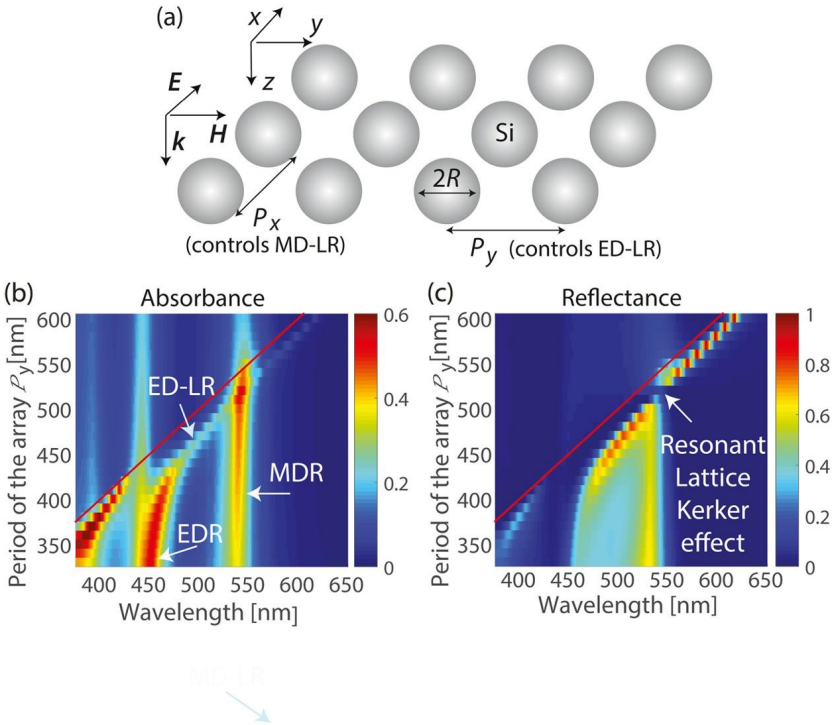

Figure 4.11. (a) Periodic array of spherical silicon nanoparticles with radius R in the air, periods P_x and P_y, and normal incidence of light with electric field E along the x-direction. (b) Absorption and (c) Reflection through the array. The change of peak resonance wavelength for various periods P_y and fixed $P_x = 220$ nm. The *EDR* and *MDR* notations correspond to ED and MD resonances, respectively, and *ED-LR* and *MD-LR* to their lattice resonances counterparts. ED-LR is controlled by P_y. Silicon nanoparticles have $R = 65$ nm, and the arrays are in the air. Red lines show the wavelength of RA. The overlap of ED-LR and MD resonances causes an increase in absorbance and a decrease in reflectance. Reproduced with permission from [63]. Copyright 2017 by WILEY-VCH Verlag GmbH & Co. KGaA, Weinheim.

ferent kind (*cross-multipole coupling*) in addition to the coupling of multipoles of the same kind described by Eqs. (4.23). In fact, accounting for cross-multipole coupling in the lattice, one can show that:

$$\frac{1}{\alpha_p^{\text{eff/coup}}} = \frac{1 - S_{Mp}\alpha_p^{\text{eff}} \cdot S_{pM}\alpha_M^{\text{eff}} k_0^2/(2\varepsilon_0)}{\alpha_p^{\text{eff}}\left[1 - S_{pM}\alpha_M^{\text{eff}} k^2/2\right]}, \tag{4.28}$$

$$\frac{1}{\alpha_m^{\text{eff/coup}}} = \frac{1 - S_{Qm}\alpha_m^{\text{eff}} \cdot S_{mQ}\alpha_Q^{\text{eff}} k_0^2/(2\varepsilon_0)}{\alpha_m^{\text{eff}}\left[1 + S_{mQ}\alpha_Q^{\text{eff}} k_0^2/(2\varepsilon_0)\right]}, \tag{4.29}$$

$$\frac{1}{\alpha_Q^{\text{eff/coup}}} = \frac{1 - S_{Qm}\alpha_m^{\text{eff}} \cdot S_{mQ}\alpha_Q^{\text{eff}} k_0^2/(2\varepsilon_0)}{\alpha_Q^{\text{eff}}\left[1 + S_{Qm}\alpha_m^{\text{eff}}\right]}, \tag{4.30}$$

$$\frac{1}{\alpha_M^{\text{eff/coup}}} = \frac{1 - S_{Mp}\alpha_p^{\text{eff}} \cdot S_{pM}\alpha_M^{\text{eff}} k_0^2/(2\varepsilon_0)}{\alpha_M^{\text{eff}}\left[1 - S_{Mp}\alpha_p^{\text{eff}}/(\varepsilon_0\varepsilon_r)\right]}, \tag{4.31}$$

and the sums S_{pM}, S_{Mp}, S_{mQ}, and S_{Qm} responsible for cross-multipole coupling are:

$$S_{pM} = \frac{-k^2}{8\pi}\sum_{l\neq 0}\frac{y_l^2 e^{ikr_l}}{r_l^3}\left(-1 - \frac{3i}{kr_l} + \frac{3}{k^2 r_l^2}\right), \tag{4.32}$$

$$S_{mQ} = \frac{1}{6}\frac{k^2}{4\pi}\sum_{l\neq 0}\frac{x_l^2 e^{ikr_l}}{r_l^3}\left(-1 - \frac{3i}{kr_l} + \frac{3}{k^2 r_l^2}\right), \tag{4.33}$$

$$S_{Mp} = 2S_{pM}, \quad S_{Qm} = 6S_{mQ}. \tag{4.34}$$

Using Eqs. (4.28)–(4.31), one can write reflection and transmission coefficients as:

$$r_0 = \frac{ik}{2S_L}\left[\frac{1}{\varepsilon_0\varepsilon_r}\alpha_p^{\text{eff/coup}} - \alpha_m^{\text{eff/coup}} - \frac{k_0^2}{12\varepsilon_0}\alpha_Q^{\text{eff/coup}} + \frac{k^2}{4}\alpha_M^{\text{eff/coup}}\right], \tag{4.35}$$

$$t_0 = 1 + \frac{ik}{2S_L}\left[\frac{1}{\varepsilon_0\varepsilon_r}\alpha_p^{\text{eff/coup}} + \alpha_m^{\text{eff/coup}} + \frac{k_0^2}{12\varepsilon_0}\alpha_Q^{\text{eff/coup}} + \frac{k^2}{4}\alpha_M^{\text{eff/coup}}\right]. \tag{4.36}$$

Earlier, analyzing expressions in Eqs. (4.5) and (4.6), we concluded that there are two groups of multipoles and directional scattering can be enabled by the compensation of multipoles from different groups. Now, analyzing cross-multipole coupling in the lattice in the form of Eqs. (4.28)–(4.31), we see that ED couples to MQ and MD couples to EQ. While exact analytical expressions for octupoles have not been reported in the literature because of very cumbersome derivations, similar considerations regarding the cross-multipole coupling can be extended to the case including octupoles [66]. Thus, we see that cross-multipole coupling occurs in the lattice for multipoles of one group with the same parity property. In other words, ED couples to MQ and EOC, and MQ couples to EQ and MOC.

4.4.1 Directional scattering facilitated by lattice

One of the most important consequences of cross-multipole coupling in the lattice, expressed by Eqs. (4.28)–(4.31), is that it can substantially enhance multipoles that are weak in the single nanoparticle. For example, MD lattice resonance can be excited in the array of nanoparticles without MD resonance due to the coupling to EQ [67]. Cross-multipole coupling in the array can facilitate the excitation of lattice resonances that correspond to weak multipoles. Excitation of strong EQ and MD lattice resonances can result in the compensation of ED and generalized Kerker effect facilitated by the lattice (Fig. 4.12).

One can consider a periodic nanoparticle array in a polarization, where only EQ and MD multipoles contribute to the lattice resonances, and ED is broad and falls outside the spectral range where the lattice resonances are excited. It has been demonstrated in Ref. [67] that these arrays can foster the excitation of lattice resonances in both homogeneous and inhomogeneous environments with higher-order cross-multipole coupling between nanoparticles. The authors have discovered that in the infinite periodic nanoparticle lattice, EQ and MD moments of nanoparticles are coupled and affect each other's resonant contributions. Even for very small, non-zero EQ and MD moments, their lattice resonances are strong enough to cause destructive interference with the electric dipole, resulting in zero reflectance. It has been explained by a resonant Kerker effect, where the generalized condition of directional scattering is satisfied.

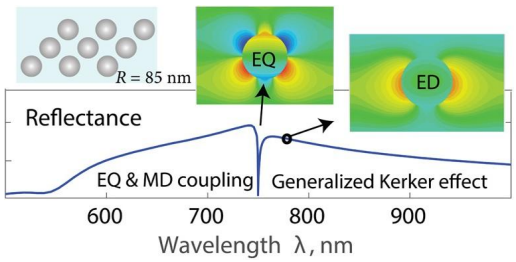

Figure 4.12. Lattice resonance: Zero-order coefficient of reflection from the array of nanospheres. Periods are $P_x = 510$ nm and $P_y = 250$ nm. A homogeneous environment with a refractive index of 1.47 surrounds the array. Light incidence is normal to the array, and electric field E is along the x-axis. Insets: (Left) Schematic view of the array with gold nanospheres of radius R. (Middle) EQ field distribution is well pronounced for the resonant wavelength. (Right) The field distribution drastically changes and resembles ED upon a small change in the wavelength. Reproduced with permission from [67]. Copyright 2018 American Chemical Society.

4.4.2 Lattice anapole states in spherical nanoparticle metasurfaces

In the previous section, we discussed that light can be scattered or transmitted almost unperturbed by the nanoparticles supporting resonant optical response. The ability to become invisible is achieved through the excitation with light and a specific combination of multipoles in the nanoparticles constituting the metasurface. This combination of multipoles significantly reduces both the forward and backward scattering of light, resulting in its propagation with minimal changes in amplitude and phase.

Now, let us consider an effect similar to light scattering by isolated nanoparticles or their non-diffractive array in anapole states. We refer to it as *lattice anapole effect* because of its similarity to the case without the lattice. In these states, nanoparticles do not provide the far-field scattering of light, and the incident wave remains unperturbed. In Ref. [38], the authors have shown that the lattice anapole effect can be realized in an array of spherical silicon nanoparticles due to interference of the fields related to ED, MD, EQ, and MQ moments excited in the array's nanoparticles. A demonstrative example is shown in Fig. 4.13 for silicon spherical nanoparticles with $R = 125$ nm arranged into a periodic lattice with $P_x = 530$ nm and $P_y = 410$ nm (Fig. 4.13). In this case, at the wavelength range 610–630 nm, the contributions of multipole moments to the reflection and transmission coefficients, defined by Eqs. (4.15) and (4.16), have comparable values. One can see from Fig. 4.13b that phases of ED and EQ terms are almost equal (and close to zero), and the same holds for MD and MQ, while the value is close to π.

In this wavelength range, reflection is near zero, transmission is close to 100% (Fig. 4.13c), and its phase does not change (Fig. 4.13d), indicating a lattice anapole state. The calculations of the field distribution confirm that the wave propagates through the array unperturbed at $\lambda = 629$ nm, where transmission is close to 100% and the phase change is zero [38]. In contrast, for the wavelength $\lambda = 580$ nm, the phase of the transmission field changes and one can see a significant reflection from the array and a phase shift of the transmitted wave compared with the free-space case. Note that from a comparison of the analytical and numerical curves presented in Fig. 4.13c, one can see that the analytical model, limited to ED, MD, EQ, and MQ multipole terms, describes well the optical properties of the arrays under consideration. Thus, we can see that one can design an array of spherical silicon nanoparticles where the propagating light excites multipoles moderately (as they are offset from the resonance peaks) and is not reflected. At the same time, the light is transmitted

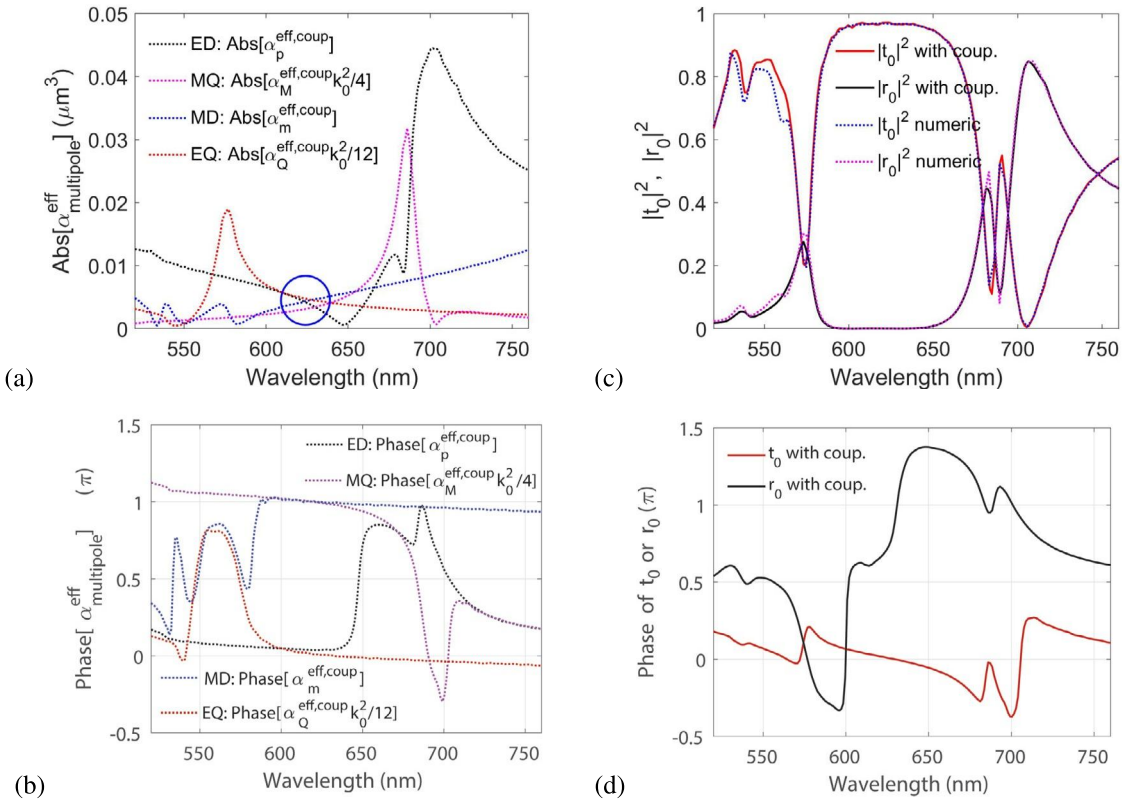

Figure 4.13. Multipole resonances and reflection and transmission through the periodic array of spheres. The lattice periods are $P_x = 530$ nm and $P_y = 410$ nm, and silicon nanoparticles have $R = 125$ nm. (a) Absolute values of each separate multipole term in the brackets of Eqs. (4.15) and (4.16) for the reflection and transmission coefficients (the effective polarizabilities of MQ and EQ are normalized to $k_0^2/4$ and $k_0^2/12$, respectively, and the polarizabilities of ED and EQ are divided by ε_0). (b) Corresponding phases of the multipole terms in Eqs. (4.15) and (4.16); (c) Intensity reflection and transmission coefficients; (d) Phases of the field reflection and transmission coefficients (4.15) and (4.16). Reproduced with permission from [38]. Copyright 2019 by American Physical Society.

with almost the same amplitude as the incident light and without phase change. As a result, this behavior can be associated with a lattice anapole state.

4.5 Finite-size arrays

So far, we discussed only hypothetical infinitely large periodic arrays of nanoparticles, assuming all nanoparticles are identical and experience the same external excitation – from the incident wave and all neighboring nanoparticles. While most practical nanostructures can be fabricated with a large number of nanopar-

ticles and be well described by the infinite array, there are some practical cases when the number of nanoparticles is on the order of tens or hundreds. In this case, the scattering properties of such finite-size arrays can be calculated either numerically (with full-wave electromagnetic simulations, e.g., [63]) or from analytical models accounting for all nanoparticles individually through direct summation. Numerical analysis is a valuable tool for designing and optimizing plasmonic metasurfaces for various applications, such as sensing and light manipulation. For the analytical techniques, we refer the reader to the discussion of the directional light scattering behavior of both single nanoparticles and nanoparticle structures within a finite spatial region in Ref. [24].

The only important parameter for the applicability of the long-wavelength approximation multipole decomposition is the small ratio of the scatterer's size (projected in the scattering direction) and the wavelength of light. The approach in Ref. [24] is based on multipole decomposition. The results demonstrate that even for relatively large scatterers, the multipole decomposition obtained in the long-wavelength approximation can achieve significantly better convergence compared to the multipole decomposition with exact multipoles obtained from the spherical harmonic expansion. It has been demonstrated that the required number of approximate multipoles for accurate results can be much smaller than the required number of exact multipoles for shape-anisotropic finite-size scatterers with different geometrical dimensions such as plates, rods, disks, and rings.

4.6 Unidirectional scattering near substrate

Unidirectional scattering related to the Kerker effect can be realized not only in a homogeneous medium with respect to ordinary (propagating) electromagnetic waves, but also in systems supporting surface electromagnetic waves in the form of surface plasmon polaritons (SPPs) propagating along the surface of metallic substrates [68]. The mechanism of the unidirectional and elastic SPP scattering by high refractive index dielectric nanoparticles (Fig. 4.14a) is related again to their ED and MD resonant response. As shown in [69], for the electric field $E_{\mathrm{SPP}z}$ (directed normally to the metal interface) of the scattered SPP, one can write in the dipole approximation:

$$E_{\mathrm{SPP}z} \sim p_z - \sqrt{\mu_0 \varepsilon_0}\, m_y \cos\varphi\,, \tag{4.37}$$

where p_z and m_y are the out-of-plane ED and in-plane MD components excited in the scatterer by incident SPPs propagating

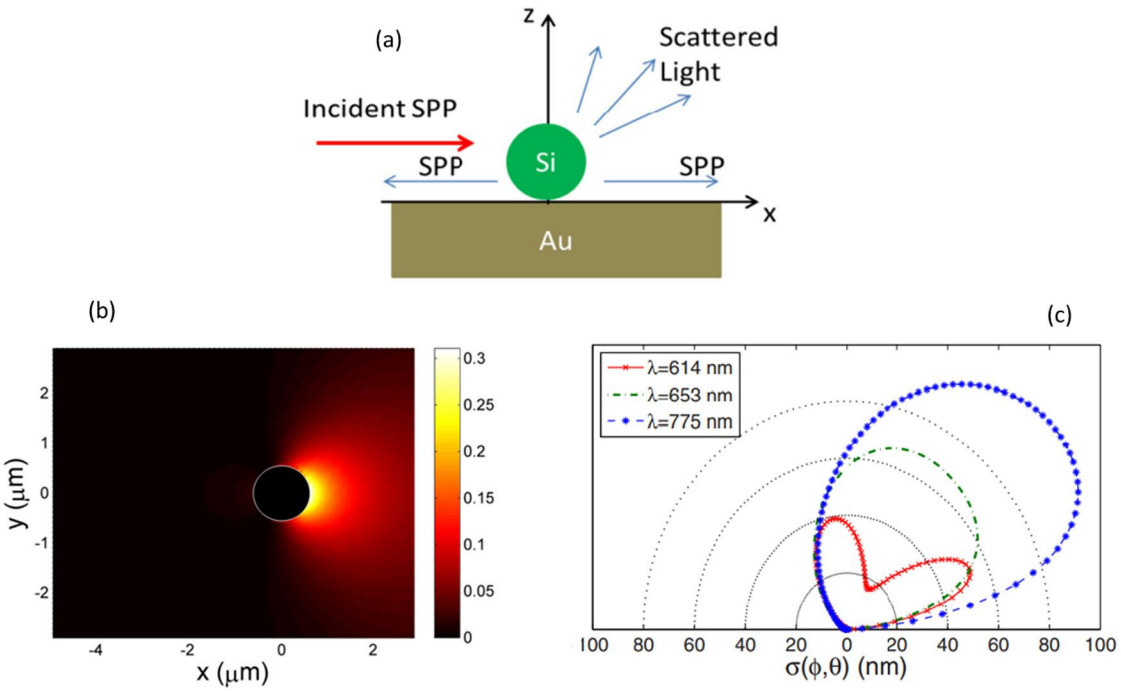

Figure 4.14. (a) Schematic presentation of SPP, scattered by an individual silicon nanoparticle placed on a gold substrate. Scattering channels include the SPP excitation and scattering into light propagating away from the substrate. (b) Scattered SPP electric-field intensity (arb. units) calculated 150 nm above the air-gold interface for the SPP plane wave (light wavelength $\lambda = 614$ nm) being incident on the oblate spheroid silicon nanoparticle with aspect ratio $q = 1.8$. The black circle indicates the nanoparticle position. (c) Differential scattering cross sections (scattering diagrams) of SPP-into-light scattering by the oblate spheroid silicon nanoparticle with aspect ratio $q = 1.8$, calculated in the xz-plane. The silicon nanospheroid has a volume equal to that of a spherical particle with a radius of 95 nm. Reproduced with permission from [69]. Copyright 2015 American Physical Society.

along x-axis (Fig. 4.14a), φ is the in-plane scattering angle ($\varphi = 0(\pi)$ corresponds to the forward (backward) scattering). Thus, the suppression of the SPP backward scattering (the Kerker effect) is realized under the condition $p_z = -\sqrt{\mu_0\varepsilon_0}\, m_y$. For simultaneous minimization of SPP scattering into the light waves, it has been suggested to use nanoparticles of oblate spheroid shapes [69]. Results of such optimization for Si nanoparticles located near a gold substrate are shown in Fig. 4.14b and Fig. 4.14c. One can see that for the wavelength $\lambda = 614$ nm the SPP scattering into the light is significantly decreased (Fig. 4.14c), and the resonant forward SPP-to-SPP scattering is realized (Fig. 4.14b). It is important to note that the substrate presence can initiate the bianisotropic response of the dielectric nanoparticles. In this case, ED and MD moments of the nanoparticles can be excited by both electric and

magnetic incident fields that can also lead to the suppression of the SPP-into-light scattering and realization of efficient unidirectional SPP-into-SPP scattering.

4.6.1 Channeling of light near metal surface

In the context of general beam steering, it is important to highlight the resonant channeling of light by dielectric nanoantennas near the metal surface. Recently, it has been theoretically studied the optical response of silicon nanospheres located above the gold substrate (Fig. 4.15) supporting the excitation and propagation of SPPs [70]. The authors have demonstrated and explained the influence of the particle ED and MD resonances on the channeling of scattered light into the two channels: light-to-light and light-to-SPPs. Scattering efficiencies of both channels have been calculated and compared for different gaps between the nanosphere

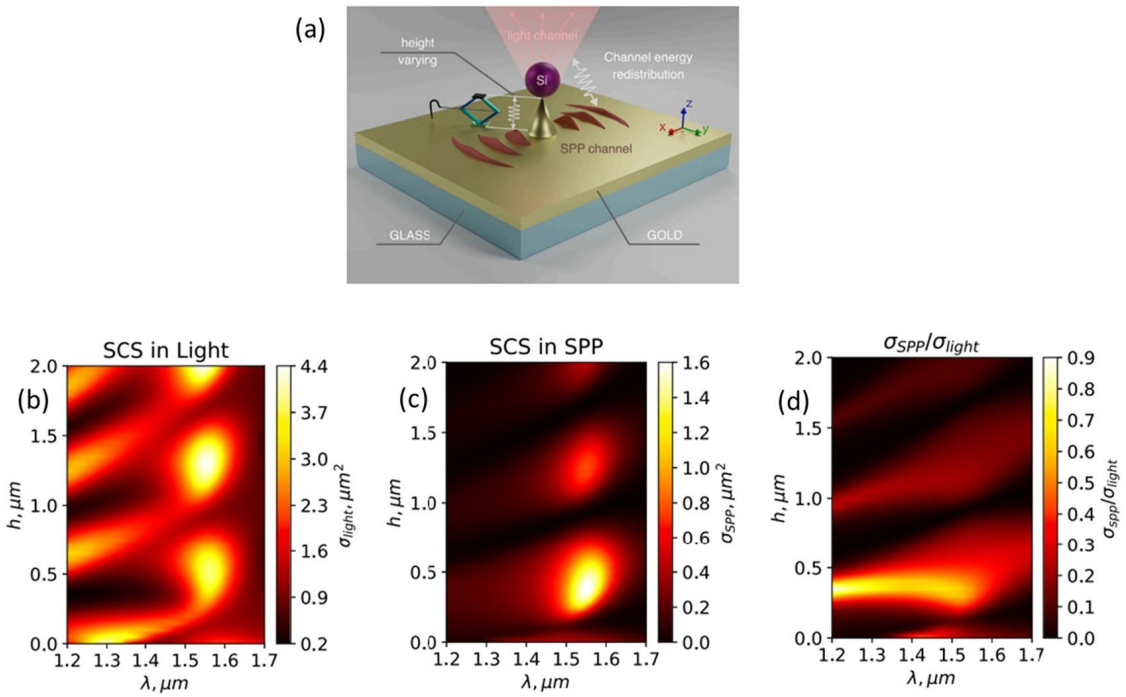

Figure 4.15. (a) The design of the system. The green lift jack symbolizes the importance of the gap height in the system for the energy distribution between light and SPP channels. (h, λ) maps of (b) the scattering cross section (SCS) into light, (c) the scattering cross section into SPP, and (d) the ratio between scattering cross sections into SPP and light. λ is the wavelength of the incident plane wave. Reproduced with permission from [70]. Copyright 2022 Elsevier B.V. All rights reserved.

and gold substrate. The authors analyze the dependencies on the height h and various wavelengths λ, referring to them as (h, λ) maps. Fig. 4.15 shows (h, λ) maps of the scattering cross sections (SCSs) calculated for the light- and SPP-channels (Fig. 4.15b and c, respectively), and their ratio (Fig. 4.15d). It has been established that (i) the maxima of both SCSs are observed at the wavelength of ≈ 1.55 μm, corresponding to the MD resonances, and (ii) the SCS of light-into-light is larger than the SCS of light-into-SPP for all considered distances h and λ. Note, however, approximately equal distribution of the scattered energy between two channels was observed only for the gap $h \approx 0.34$ μm, corresponding to the first appearance of MD resonance with respect to the gold surface. For all other h, the intensity of the light-into-light scattering is significantly higher than the intensity of the light-into-SPP scattering (see Fig. 4.15d). The computed directivity of light channels at the MD resonant wavelength for multiple heights indicates that the formation of scattering patterns results from the interplay of directly radiated waves by the MD and scattered waves reflected from the substrate surface through interference. Usually, diffraction governs the directivity patterns. Nevertheless, if the MD is closer to the substrate surface than half the wavelength, the diffraction only involves the zero-order beam.

4.6.2 Interference of multipoles and substrate

The interest in all-dielectric photonics for potential photonic applications and photovoltaics as an alternative optical technology to plasmonics leads to the comparison of the antireflective properties of plasmonic and all-dielectric nanoparticle coatings. The silicon coatings can exhibit zero reflectance due to the destructive interference of ED and MD responses of the nanoparticle array and the reflected wave from the substrate [22,71]. This reflection suppression is known as the substrate-mediated Kerker effect. By varying the size of the nanoparticles, the band position can be effectively tuned, allowing more than 60% increase in absorbance in a narrow band spectral range.

4.7 Transverse Kerker effect

Let us consider the case of a dipole, ED or MD, placed on a typical glass substrate, and refer to it as an *in-plane* dipole. Such in-plane dipole scatters predominantly in the optically denser medium, e.g. substrate, and the dipole emission is symmetric irrespective of the azimuth angle. Above, we considered the case of combining orthogonal in-plane ED and MD oscillating in phase,

and realizing the Huygens dipole source. A scatterer with such ED and MD satisfies the Kerker condition to achieve directional emission in the far field. Partial or full directional scattering (Huygens dipole source) can be obtained depending on the values of ED and MD. The dielectric antenna can be designed to support not only ED and MD multipole resonances, but also chiral dipole emitters, and a single subwavelength dielectric antenna can be utilized to achieve on-demand steering of radiation direction for a single photon source, which can facilitate on-chip quantum information processing [72].

Recently, transverse Kerker scattering, defined as scattering transverse to the direction of the illumination propagation, has been investigated in detail. As expected, multiple ways exist to design the system and observe the effect.

One way is to illuminate the nanoparticle with a conventional plane way, excite dipole moments in-plane (perpendicular to the direction of light illumination), excite quadrupole moments in addition to dipoles, and achieve a desirable compensation of contributions from different multipoles [73]. The authors have demonstrated transverse scattering while suppressing it in both forward and backward directions. It occurs when in-phase electric and magnetic dipoles are out of phase with corresponding quadrupoles. The crucial role of the ED Fano resonance and off-resonant quadrupoles in achieving transverse scattering has been identified. The authors have also demonstrated metasurfaces composed of nanoparticles with transverse scattering patterns and their periodicity-dependent zero reflection. Compared to conventional metasurfaces discussed above, which scatter light in forward and/or backward directions, the transverse scattering makes the nanoparticles in the metasurface almost invisible. It opens the possibilities for applications for efficient beam control, strong field enhancements in nonlinear interactions, and highly efficient sensing. This approach can also find applications in tweezer systems.

An alternative way to design the system exhibiting the transverse Kerker effect is to illuminate it with structured light and excite out-of-plane dipoles [74,75]. In particular, one can combine the in-plane magnetic (electric) dipole with the out-of-plane electric (magnetic) dipole. In particular, the authors have proposed a transverse Kerker scattering scheme, which comprises a tightly focused vector beam and a spherical dielectric nanoparticle. The authors have also extended the scheme for a more sophisticated experimental scenario, such as a particle on an interface, with an analytical model that can be applied to arbitrary excitation beams (structured light) and particle parameters, such as

size, refractive index, etc. The experimental results have demonstrated that after optimization, sub-angstrom accuracy can be achieved with individual nanoantenna displacement. The proposed scheme shows that nanoparticles' locations can be sensed with ultrahigh precision and accuracy, facilitating interesting applications such as the stabilization of positioning systems in microscopy and nanometrology. Additionally, a quadrant-detector-based signal detection would allow for an ultrafast time-resolved tracking of nanoscopic systems.

4.8 Superdirectivity

As we have discussed earlier, there is a connection between scattering directionality and multipole resonances of nanoparticles. In addition, superdirectivity can be achieved by exciting specific multipole resonances of the nanoparticle. The term "superdirectivity" refers to the fact that the scattered light is concentrated into a beam, much narrower than what is possible with conventional optical elements. This effect is due to the resonant properties of the nanoparticle, which can be tuned to interact strongly with light at specific frequencies. For example, a dielectric nanoparticle with a high refractive index can exhibit superdirectivity when we excite multipole resonances and engineer their scattering superposition. This occurs when the wavelength of the incident light is comparable to the size of the nanoparticle.

Yagi-Uda geometry allows for creating an optical Huygens source in which a small electric dipole operates at the magnetic resonance of a dielectric nanosphere [76]. This results in high directivity without backward scattering or polarization dependence, making it an appealing choice for compact and effective designs of optical nanoantennas. The authors have investigated an all-dielectric alternative to the plasmonic Yagi-Uda nanoantenna in the form of a nanoelement array and have demonstrated its high directivity. The electromagnetic field is localized within the nanoparticles, and with minimal dissipation losses, the distance between neighboring elements can be further decreased without compromising its performance.

The superdirectivity arises because the nanoparticle scatters light in a highly directional manner due to the constructive interference of the scattered waves [76], and different multipoles of the nanoparticle can contribute to superdirectivity. The multipole excitations are facilitated by the high refractive-index contrast between the nanoparticle and its surrounding medium.

Recently, electric and magnetic non-radiating sources have been proposed in Ref. [77] operating based on a single ultra-high permittivity dielectric hollow disk excited by electric or magnetic point-like dipole antennas. The authors have observed radiation suppression at the desired frequency by implementing the ED-ED-ETD anapole for the electric non-radiating source ('ETD' stands for electric toroidal dipole) and the MD-MD anapole state for the magnetic non-radiating source. They propose that these non-radiating sources can function as meta-elements in more complex systems with unique near-field properties, making them useful for practical applications in sensing, cloaking, secure communication, radio-frequency identification (RFID) tags, wireless power transfer, and other related fields.

The radiation properties of a small high-refractive-index nanoparticle with a notch have been theoretically analyzed in Ref. [78]. The authors have demonstrated that a point emitter (such as a quantum dot) placed in the notch effectively excites higher-order magnetic multipole moments in the nanoparticle. These magnetic moments are responsible for the subwavelength nanoantenna high directivity, which surpasses that attainable by any other method. This nanoantenna design demonstrates markedly reduced losses compared to traditional optical antennas and exhibits exceptional radiation efficiency, reaching up to 70%. The authors have also established that while the nanoantenna possesses high directivity in the transmission regime, it does not rely on intense near-field confinement and therefore avoids excessive losses during the reception stage.

Superdirectivity has many potential applications in areas such as optical sensing, communication, and imaging. For example, superdirective scattering can be used to enhance the sensitivity of optical sensors by increasing the amount of light that is collected in a specific direction. It can also be used to improve the resolution of optical imaging systems by enabling them to distinguish finer details.

4.9 Beam steering with nanoantennas

Gradient change of the individual scatterers incorporated in the nanoantenna properties, e.g. size, mainly defines the functionality of the conventional metasurfaces. To realize the gradient change, the design typically includes spatially-varying distribution of the phase of the waves scattered by each nanoantenna. Generating such non-uniform changes in the phase of scattered waves requires exact tuning of each building block and is limited

by nanofabrication constraints. However, even in the case when precise nanofabrication is realized, the large-angle beam routing is not fully implemented in high-index metasurfaces, and the resulting designs are not particularly efficient.

An alternative design can be based on a grating configuration and take advantage of the combination of multipole effects such as their interference, coupling through the lattice, and diffraction facilitated by the grating. Utilizing these effects, one can efficiently control optical waves and achieve perfect transmission, reflection, and large-angle beam steering. In such metal lattice, the angular scattering pattern of each unit cell is highly asymmetric, making an essential contribution to forming the large-angle beam steering [79]. We envision that including effects related to photonic bandgaps (periodic structures), Anderson localization (random structures), and topological engineering can be utilized in wavefront engineering and potentially increase the efficiency of beam steering metastructures.

In Ref. [78], it has been demonstrated that an effective beam-steering effect can be achieved by displacing the subwavelength source. The promising combination of superdirectivity and beam-steering capability exhibited by these results presents opportunities for various applications in nanophotonics. By comparing their all-dielectric nanoantennas with plasmonic nanoantennas of the same geometry, the authors in Ref. [78] have concluded that the superdirectivity effect is absent in the latter.

4.10 Nanoparticle chain waveguides

Nanostructures with nanoparticles have been shown to be efficient not only in manipulating the scattering of light in free space. It is also possible to engineer nanostructures for guiding electromagnetic energy with subwavelength confinement. The key principle involves the excitation of both ED and MD and the designing of the coupled-resonator optical system. These coupled-resonator systems can find applications as building blocks for photonic integrated circuits due to their small size and the ability to bend without any significant reduction of signal propagation.

Recent examples of novel ultra-compact waveguides based on nanoparticles with coupled high-Q resonances include chains of micro/nano cavities made of metal nanoparticles. In this case, subwavelength localized modes of surface plasmon are excited and transferred from one particle to another in the form of the guided wave [80] or involving adjacent guiding components, such as conducting or dielectric surfaces, hollow rectangular metallic

waveguides [81], and others. Theoretical models have been developed to account for various properties of nanoparticles, but in the approximation of lossless materials [80–82]. However, non-radiative losses (and heat dissipation) substantially hinder wave propagation, and the propagation length of the signals is limited to several microns.

In contrast to plasmonic nanostructures, using all-dielectric nanoparticles can result in very low non-radiative losses, and the chains of such particles have been shown to support waves with much longer propagation distances [83]. An all-dielectric nanoparticle waveguide can be considered as an infinite chain of EDs and MDs, and advanced models incorporate material losses and permeabilities [84,85]. For some high-index materials, such as silicon and III-V compounds, nanoparticle chains can guide waves over distances greater than tens of micrometers in the visible and near-infrared ranges [83]. Similar to plasmonic nanoparticle chains, the propagation properties of all-dielectric chains are greatly affected by non-quasistatic components of the dipole field. As one can expect, due to strong excitations of MD resonance in all-dielectric nanoparticles, it is important to account for both ED and MD components of nanoparticle response for an accurate estimate of the supported wave and the dispersion characteristics of complex dipole modes.

The resonant properties of the nanoparticle chain waveguide are paramount for integrated photonics beyond traditional or nanowire silicon waveguides [86]. Experimental measurement of guiding properties and near-field imaging of the modes provide an important insight into the waves supported by the nanoparticle chain (Fig. 4.16).

The calculation technique includes a theoretical model based on an ED and MD approximation for one-, two-, and three-dimensional arrays of nanoparticles. For the dense nanoparticle lattice and small array period, the ED and MD interference and coupling strongly affect the dispersion properties of guided and leaky waves. The nanoparticle chain waveguide can be engineered to allow energy transfer with nanoscale transverse confinement. As a result, propagating guided mode can bend around the corners and split into two waves by the Y-type design of the chain waveguide. Up to 180° bending with high efficiency is possible with strategically engineered nanoparticle positioning and tailoring scattering [83].

Surrounding medium properties, including the substrate underneath the nanoparticles, also play an important role in wave propagation along the nanoparticle chain. The guiding properties

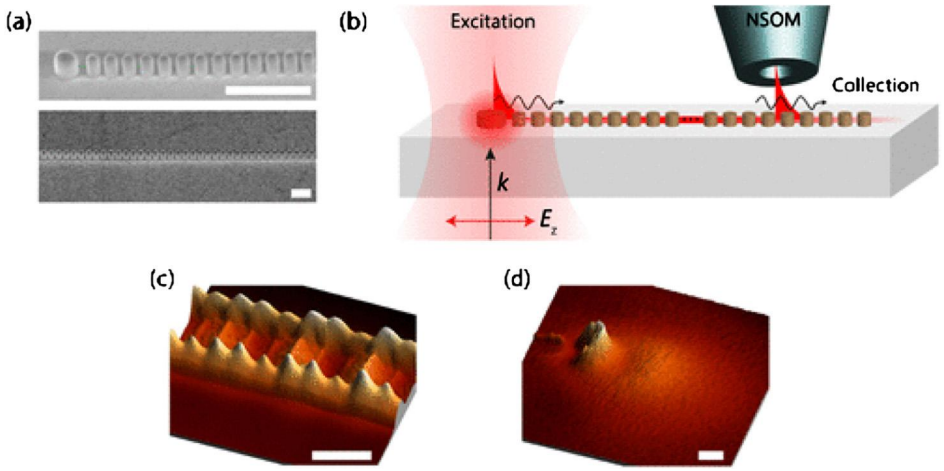

Figure 4.16. Experimental measurements and near-field imaging of nanoparticle chain waveguide. (a) Scanning electron microscope image of the silicon nanoparticle chain waveguide for the disks with a diameter of 150 nm. (b) Schematic of the measurements that include excitation of the waveguide with linearly polarized light. The incident light is focused on the origin of the chain waveguide, and the evanescent near fields are collected with a near-field scanning optical microscope at various points s of the waveguide. (c) Near-field microscopy image of the propagated mode supported by the chain waveguide. This image was taken at a wavelength of $\lambda = 720$ nm and at $s = 400$ μm away from the excitation point. (d) The same as (c) but for $s = 580$ μm, which is close to the end of the waveguide. Reproduced with permission from [86]. Copyright 2017 American Chemical Society.

of the dielectric nanoparticle chain are less susceptible to the refractive index of the surrounding medium than in the structures with plasmonic modes. It mainly stems from the confinement of the mode inside the nanoparticle. However, the refractive index of the surrounding medium affects the radiative losses of the nanoparticle and can result in modification of the guiding properties, including dispersion and signal decay.

4.11 Summary

The multipole resonances in all-dielectric nanoparticles can be excited in the visible or near-infrared spectral range, which makes them particularly useful for applications in nanophotonics. Dielectric materials have small losses at optical frequencies, and nanoparticles made of high-permittivity dielectrics can sustain both electric and magnetic multipole resonances. One important property of these resonances is that they can be tuned by adjusting the size and shape of the nanoparticle, making it possible to control the scattering properties of the nanoparticle.

One way to achieve scattering directivity is to design the dielectric nanoparticle to have a high refractive index contrast with its surrounding medium. As a result, nanoparticle multipoles are excited, and thus one can control their interplay. This causes the light to scatter in a highly directional manner, leading to a strong scattering peak. By tuning multipole resonances, it is possible to control the scattering properties of the nanoparticle and achieve highly directional scattering, which has important applications in areas such as sensing, imaging, and communication. Overall, control of directional scattering is an exciting area of research that has the potential to revolutionize the field of optics and enable the development of new and more advanced optical technologies.

4.12 Abbreviations

The following abbreviations are used in this work:
ED Electric Dipole
EOC Electric Octupole
EQ Electric Quadrupole
ETD Electric Toroidal Dipole
MD Magnetic Dipole
MOC Magnetic Octupole
MQ Magnetic Quadrupole
RA Rayleigh Anomaly
RFID Radio-Frequency Identification
SCS Scattering Cross Sections
SPP Surface Plasmon Polariton

Acknowledgments

V.E.B. acknowledges the support from the University of New Mexico Research Allocations Committee (Award No. RAC 2023) and WeR1: Investing in Faculty Success Programs PERC and SURF. This work was performed, in part, at the Center for Integrated Nanotechnologies, an Office of Science User Facility operated for the U.S. Department of Energy (DOE) Office of Science by Los Alamos National Laboratory (Contract 89233218CNA000001) and Sandia National Laboratories (Contract DE-NA-0003525). A.B.E. acknowledges the support from the Deutsche Forschungsgemeinschaft (DFG, German Research Foundation) under Germany's Excellence Strategy within the Cluster of Excellence PhoenixD (EXC 2122, Project ID 390833453).

References

[1] A.B. Evlyukhin, C. Reinhardt, A. Seidel, B.S. Luk'yanchuk, B.N. Chichkov, Optical response features of Si-nanoparticle arrays, Phys. Rev. B 82 (2010) 045404, https://doi.org/10.1103/PhysRevB.82.045404.

[2] A.I. Kuznetsov, A.E. Miroshnichenko, M.L. Brongersma, Y.S. Kivshar, B. Luk'yanchuk, Optically resonant dielectric nanostructures, Science 354 (2016) aag2472, https://doi.org/10.1126/science.aag2472.

[3] T.G. Habteyes, I. Staude, K.E. Chong, J. Dominguez, M. Decker, A. Miroshnichenko, Y. Kivshar, I. Brener, Near-field mapping of optical modes on all-dielectric silicon nanodisks, ACS Photonics 1 (2014) 794–798.

[4] A.B. Evlyukhin, S.M. Novikov, U. Zywietz, R.L. Eriksen, C. Reinhardt, S.I. Bozhevolnyi, B.N. Chichkov, Demonstration of magnetic dipole resonances of dielectric nanospheres in the visible region, Nano Lett. 12 (2012) 3749–3755.

[5] U. Zywietz, A.B. Evlyukhin, C. Reinhardt, B.N. Chichkov, Laser printing of silicon nanoparticles with resonant optical electric and magnetic responses, Nat. Commun. 5 (2014) 3402.

[6] L. Cao, J.-S. Park, P. Fan, B. Clemens, M.L. Brongersma, Resonant germanium nanoantenna photodetectors, Nano Lett. 10 (2010) 1229–1233.

[7] U. Zywietz, T. Fischer, A. Evlyukhin, C. Reinhardt, B. Chichkov, Laser printing of nanoparticles, in: A. Piqué, P. Serra (Eds.), Laser Printing of Functional Materials, Wiley, Hoboken, NJ, 2018.

[8] Zhong-Xing Zhou, M.-J. Ye, M.-W. Yu, J.-H. Yang, K.-L. Su, C.-C. Yang, C.-Y. Lin, V.E. Babicheva, I.V. Timofeev, K.-P. Chen, Germanium metasurfaces with lattice Kerker effect in near-infrared photodetectors, ACS Nano 16 (4) (2022) 5994–6001.

[9] S. Liu, P.P. Vabishchevich, A. Vaskin, J.L. Reno, G.A. Keeler, M.B. Sinclair, I. Staude, I. Brener, An all-dielectric metasurface as a broadband optical frequency mixer, Nat. Commun. 9 (2018) 2507.

[10] M.R. Shcherbakov, S. Liu, V.V. Zubyuk, A. Vaskin, P.P. Vabishchevich, G. Keeler, T. Pertsch, T.V. Dolgova, I. Staude, I. Brener, A.A. Fedyanin, Ultrafast all-optical tuning of direct-gap semiconductor metasurfaces, Nat. Commun. 8 (2017) 17.

[11] R. Sarma, N. Nookala, K.J. Reilly, S. Liu, D. de Ceglia, L. Carletti, M.D. Goldflam, S. Campione, K. Sapkota, H. Green, G.T. Wang, J. Klem, M.B. Sinclair, M.A. Belkin, I. Brener, Strong coupling in all-dielectric intersubband polaritonic metasurfaces, Nano Lett. 21 (2021) 367–374.

[12] R. Sarma, J. Xu, D. de Ceglia, L. Carletti, S. Campione, J. Klem, M.B. Sinclair, M.A. Belkin, I. Brener, An all-dielectric polaritonic metasurface with a giant nonlinear optical response, Nano Lett. 22 (2022) 896–903.

[13] V. Karimi, V.E. Babicheva, Semiconductor nanopillars for programmable directional lasing emissions, MRS Adv. 6 (2021) 234–240.

[14] S. Zhang, R. Jiang, Y.-M. Xie, Q. Ruan, B. Yang, J. Wang, H.-Q. Lin, Colloidal moderate-refractive-index Cu2O nanospheres as visible-region nanoantennas with electromagnetic resonance and directional light-scattering properties, Adv. Mater. 27 (2015) 7432–7439.

[15] S.B. Ramakrishnan, N. Khatri, R.T.A. Tirumala, F. Mohammadparast, K. Karuppasamy, A.K. Kalkan, M. Andiappan, Cupric oxide Mie resonators, J. Phys. Chem. C 126 (2022) 16272–16279.

[16] Y. Huang, H. Xu, Y. Lu, Y. Chen, All-dielectric metasurface for achieving perfect reflection at visible wavelengths, J. Phys. Chem. C 122 (2018) 2990–2996.

[17] J.A. Garcia, C. Hrelescu, X. Zhang, D. Grosso, M. Abbarchi, A.L. Bradley, Quasi-guided modes in titanium dioxide arrays fabricated via soft nanoimprint lithography, ACS Appl. Mater. Interfaces 13 (2021) 47860–47870.
[18] J.-H. Yang, V.E. Babicheva, M.-W. Yu, T.-C. Lu, T.-R. Lin, K.-P. Chen, Structural colors enabled by lattice resonance on silicon nitride metasurfaces, ACS Nano 14 (2020) 5678–5685.
[19] J.M. Geffrin, B. García-Cámara, R. Gómez-Medina, P. Albella, L.S. Froufe-Pérez, C. Eyraud, A. Litman, R. Vaillon, F. González, M. Nieto-Vesperinas, J.J. Sáenz, F. Moreno, Magnetic and electric coherence in forward- and back-scattered electromagnetic waves by a single dielectric subwavelength sphere, Nat. Commun. 3 (2012) 1171.
[20] M. Kerker, D.-S. Wang, C. Giles, Electromagnetic scattering by magnetic spheres, J. Opt. Soc. Am. A 73 (1983) 765.
[21] Y.H. Fu, A.I. Kuznetsov, A.E. Miroshnichenko, Y.F. Yu, B. Luk'yanchuk, Directional visible light scattering by silicon nanoparticles, Nat. Commun. 4 (2013) 1527.
[22] V.E. Babicheva, M.I. Petrov, K.V. Baryshnikova, P.A. Belov, Reflection compensation mediated by electric and magnetic resonances of all-dielectric metasurfaces [Invited], J. Opt. Soc. Am. B 34 (2017) D18–D28.
[23] A.B. Evlyukhin, C. Reinhardt, B.N. Chichkov, Multipole light scattering by nonspherical nanoparticles in the discrete dipole approximation, Phys. Rev. B 84 (2011) 235429.
[24] A.B. Evlyukhin, B.N. Chichkov, Multipole decompositions for directional light scattering, Phys. Rev. B 100 (2019) 125415.
[25] P.D. Terekhov, V.E. Babicheva, K. Baryshnikova, A. Shalin, A. Karabchevsky, A.B. Evlyukhin, Multipole analysis of dielectric metasurfaces composed of nonspherical nanoparticles and lattice invisibility effect, Phys. Rev. B 99 (2019) 045424.
[26] R. Alaee, C. Rockstuhl, I. Fernandez-Corbaton, Exact multipolar decompositions with applications in nanophotonics, Adv. Opt. Mater. 7 (2019) 1800783.
[27] R. Alaee, C. Rockstuhl, I. Fernandez-Corbaton, An electromagnetic multipole expansion beyond the long-wavelength approximation, Opt. Commun. 407 (2018) 17–21.
[28] A. Han, J.V. Moloney, V.E. Babicheva, Applicability of multipole decomposition to plasmonic- and dielectric-lattice resonances, J. Chem. Phys. 156 (2022) 114104.
[29] W. Lin, R.W. Ziolkowski, J. Huang, Electrically small, low-profile, highly efficient, Huygens dipole rectennas for wirelessly powering Internet-of-things devices, IEEE Trans. Antennas Propag. 67 (6) (2019) 3670–3679.
[30] Y. Zhang, M. Nieto-Vesperinas, J.J. Sáenz, Dielectric spheres with maximum forward scattering and zero backscattering: a search for their material composition, J. Opt. 17 (2015) 105612.
[31] R. Alaee, R. Filter, D. Lehr, F. Lederer, C. Rockstuhl, A generalized Kerker condition for highly directive nanoantennas, Opt. Lett. 40 (2015) 2645–2648.
[32] W. Liu, Y.S. Kivshar, Generalized Kerker effects in nanophotonics and meta-optics [Invited], Opt. Express 26 (2018) 13085–13105.
[33] A.B. Evlyukhin, C. Reinhardt, E. Evlyukhin, B.N. Chichkov, Multipole analysis of light scattering by arbitrary-shaped nanoparticles on a plane surface, J. Opt. Soc. Am. B 30 (2013) 2589.
[34] V.E. Babicheva, J.V. Moloney, Lattice effect influence on the electric and magnetic dipole resonance overlap in a disk array, Nanophotonics 7 (2018) 1663–1668.

[35] I. Staude, A.E. Miroshnichenko, M. Decker, N.T. Fofang, S. Liu, E. Gonzales, J. Dominguez, T.S. Luk, D.N. Neshev, I. Brener, Y. Kivshar, Tailoring directional scattering through magnetic and electric resonances in subwavelength silicon nanodisks, ACS Nano 7 (2013) 7824–7832.
[36] M. Decker, I. Staude, M. Falkner, J. Dominguez, D.N. Neshev, I. Brener, T. Pertsch, Y.S. Kivshar, High-efficiency dielectric Huygens' surfaces, Adv. Opt. Mater. 3 (2015) 813–820.
[37] A.B. Evlyukhin, C. Reinhardt, U. Zywietz, B. Chichkov, Collective resonances in metal nanoparticle arrays with dipole-quadrupole interactions, Phys. Rev. B 85 (24) (2012) 245411.
[38] V.E. Babicheva, A.B. Evlyukhin, Analytical model of resonant electromagnetic dipole-quadrupole coupling in nanoparticle arrays, Phys. Rev. B 99 (19) (2019) 195444.
[39] V.E. Babicheva, A.B. Evlyukhin, Multipole lattice effects in high refractive index metasurfaces, J. Appl. Phys. 129 (2021) 040902.
[40] V.E. Babicheva, A.B. Evlyukhin, Resonant suppression of light transmission in high-refractive-index nanoparticle metasurfaces, Opt. Lett. 43 (21) (2018) 5186–5189.
[41] A.B. Evlyukhin, M. Matiushechkina, V.A. Zenin, M. Heurs, B.N. Chichkov, Lightweight metasurface mirror of silicon nanospheres, Opt. Mater. Express 10 (2020) 2706–2716.
[42] M. Matiushechkina, A.B. Evlyukhin, V.A. Zenin, M. Heurs, B.N. Chichkov, High-efficiency silicon metasurface mirror on a sapphire substrate, Opt. Mater. 138 (2023) 113618.
[43] P. Moitra, B.A. Slovick, W. Li, I.I. Kravchencko, D.P. Briggs, S. Krishnamurthy, J. Valentine, Large-scale all-dielectric metamaterial perfect reflectors, ACS Photonics 2 (6) (2015) 692–698.
[44] A.E. Miroshnichenko, A.B. Evlyukhin, Y.F. Yu, R.M. Bakker, A. Chipouline, A.I. Kuznetsov, B. Luk'yanchuk, A.V. Zayats, Nonradiating anapole modes in dielectric nanoparticles, Nat. Commun. 6 (2015) 8069.
[45] R. Wang, L. Dal Negro, Engineering non-radiative anapole modes for broadband absorption enhancement of light, Opt. Express 24 (2016) 19048–19062.
[46] L. Wei, A.E. Miroshnichenko, Y.S. Kivshar, Excitation of the radiationless anapole mode, Optica 3 (2016) 799–802.
[47] F. Monticone, C. Argyropoulos, A. Alu, Can a nonradiating mode be externally excited? Nonscattering states versus embedded eigenstates, ACS Photonics 6 (2019) 3108–3114.
[48] K.V. Baryshnikova, D.A. Smirnova, B.S. Luk'yanchuk, Y.S. Kivshar, Optical anapoles: concepts and applications, Adv. Opt. Mater. 7 (2019) 1801350.
[49] E. Díaz-Escobar, T. Bauer, E. Pinilla-Cienfuegos, et al., Radiationless anapole states in on-chip photonics, Light: Sci. Appl. 10 (2021) 204, https://doi.org/10.1038/s41377-021-00647-x.
[50] M. Meier, A. Wokaun, P.F. Liao, Enhanced fields on rough surfaces: dipolar interactions among particles of sizes exceeding the Rayleigh limit, J. Opt. Soc. Am. B 2 (6) (1985) 931–949.
[51] S. Zou, N. Janel, G.C. Schatz, Silver nanoparticle array structures that produce remarkably narrow plasmon lineshapes, J. Chem. Phys. 120 (23) (2004) 10871–10875.
[52] S. Zou, G.C. Schatz, Silver nanoparticle array structures that produce giant enhancements in electromagnetic fields, Chem. Phys. Lett. 403 (1–3) (2005) 62–67.
[53] B. Auguie, W.L. Barnes, Collective resonances in gold nanoparticle arrays, Phys. Rev. Lett. 101 (14) (2008) 143902.

[54] V.G. Kravets, A.V. Kabashin, W.L. Barnes, A.N. Grigorenko, Plasmonic surface lattice resonances: a review of properties and applications, Chem. Rev. 118 (12) (2018) 5912–5951.
[55] S. Rodriguez, M. Schaafsma, A. Berrier, J.G. Rivas, Collective resonances in plasmonic crystals: size matters, Physica B, Condens. Matter 407 (20) (2012) 4081–4085.
[56] A.D. Humphrey, W.L. Barnes, Plasmonic surface lattice resonances on arrays of different lattice symmetry, Phys. Rev. B 90 (7) (2014) 075404.
[57] R. Guo, T.K. Hakala, P. Torma, Geometry dependence of surface lattice resonances in plasmonic nanoparticle arrays, Phys. Rev. B 95 (15) (2017) 155423.
[58] L. Michaeli, S. Keren-Zur, O. Avayu, H. Suchowski, T. Ellenbogen, Nonlinear surface lattice resonance in plasmonic nanoparticle arrays, Phys. Rev. Lett. 118 (24) (2017) 243904.
[59] D. Khlopin, F. Laux, W.P. Wardley, J. Martin, G.A. Wurtz, J. Plain, N. Bonod, A.V. Zayats, W. Dickson, D. Gerard, Lattice modes and plasmonic linewidth engineering in gold and aluminum nanoparticle arrays, J. Opt. Soc. Am. B 34 (3) (2017) 691–700.
[60] V.E. Babicheva, A.B. Evlyukhin, Interplay and coupling of electric and magnetic multipole resonances in plasmonic nanoparticle lattices, MRS Commun. 8 (2018) 712–717.
[61] A. Han, C. Dineen, V.E. Babicheva, J.V. Moloney, Second harmonic generation in metasurfaces with multipole resonant coupling, Nanophotonics 9 (11) (2020) 3545–3556.
[62] D. Bosomtwi, M. Osiński, V.E. Babicheva, Lattice effect for enhanced hot-electron generation in nanoelectrodes, Opt. Mater. Express 11 (2021) 3232.
[63] V.E. Babicheva, A.B. Evlyukhin, Resonant lattice Kerker effect in metasurfaces with electric and magnetic optical responses, Laser Photonics Rev. 11 (2017) 1700132.
[64] C.Y. Yang, J.H. Yang, Z.Y. Yang, Z.X. Zhou, M.G. Sun, V.E. Babicheva, K.P. Chen, Nonradiating silicon nanoantenna metasurfaces as narrow-band absorbers, ACS Photonics 5 (11) (2018) 2596–2602.
[65] V.E. Babicheva, Lattice effect in Mie-resonant dielectric nanoparticle array under the oblique light incidence, MRS Commun. 8 (4) (2018) 1455–1462.
[66] A.V. Prokhorov, P.D. Terekhov, M.Yu. Gubin, A.V. Shesterikov, X. Ni, V.R. Tuz, A.B. Evlyukhin, Resonant light trapping via lattice-induced multipole coupling in symmetrical metasurfaces, ACS Photonics 9 (12) (2022) 3869–3875.
[67] V.E. Babicheva, A.B. Evlyukhin, Metasurfaces with electric quadrupole and magnetic dipole resonant coupling, ACS Photonics 5 (2018) 2022.
[68] A.V. Zayats, I.I. Smolyaninov, A.A. Maradudin, Nano-optics of surface plasmon polaritons, Phys. Rep. 408 (3–4) (2005) 131–314.
[69] A.B. Evlyukhin, S.I. Bozhevolnyi, Resonant unidirectional and elastic scattering of surface plasmon polaritons by high refractive index dielectric nanoparticles, Phys. Rev. B 92 (2015) 245419.
[70] V. Yaroshenko, D. Zuev, A.B. Evlyukhin, Resonant channeling of light near metal surface by passive and active silicon nanoparticles, Surf. Interfaces 34 (2022) 102344.
[71] K. Baryshnikova, M. Petrov, V. Babicheva, P. Belov, Plasmonic and silicon spherical nanoparticle antireflective coatings, Sci. Rep. 6 (2016) 22136, https://doi.org/10.1038/srep22136.
[72] F. Qin, Z. Zhang, K. Zheng, Y. Xu, S. Fu, Y. Wang, Y. Qin, Transverse Kerker effect for dipole sources, Phys. Rev. Lett. 128 (2022) 193901.

[73] H.K. Shamkhi, K.V. Baryshnikova, A. Sayanskiy, P. Kapitanova, P.D. Terekhov, P. Belov, A. Karabchevsky, A.B. Evlyukhin, Y. Kivshar, A.S. Shalin, Transverse scattering and generalized Kerker effects in all-dielectric Mie-resonant metaoptics, Phys. Rev. Lett. 122 (2019) 193905.
[74] A. Bag, M. Neugebauer, P. Woźniak, G. Leuchs, P. Banzer, Transverse Kerker scattering for angstrom localization of nanoparticles, Phys. Rev. Lett. 121 (2018) 193902.
[75] S. Nechayev, J.S. Eismann, M. Neugebauer, P. Wozniak, A. Bag, G. Leuchs, P. Banzer, Huygens' dipole for polarization-controlled nanoscale light routing, Phys. Rev. A 99 (2019) 041801(R).
[76] A.E. Krasnok, A.E. Miroshnichenko, P.A. Belov, Y.S. Kivshar, All-dielectric optical nanoantennas, Opt. Express 20 (2012) 20599–20604.
[77] E. Zanganeh, A.B. Evlyukhin, A.E. Miroshnichenko, M. Song, E. Nenasheva, P. Kapitanova, Anapole meta-atoms: nonradiating electric and magnetic sources, Phys. Rev. Lett. 127 (2021) 096804.
[78] A.E. Krasnok, C.R. Simovski, P.A. Belov, Y.S. Kivshar, Superdirective dielectric nanoantennas, Nanoscale 6 (2014) 7354–7361.
[79] W. Liu, A.E. Miroshnichenko, Beam steering with dielectric metalattices, ACS Photonics 5 (2018) 1733–1741.
[80] R. Shore, A. Yaghjian, Travelling electromagnetic waves on linear periodic arrays of lossless spheres, Electron. Lett. 41 (2005) 578.
[81] P.A. Belov, C.R. Simovski, Subwavelength metallic waveguides loaded by uniaxial resonant scatterers, Phys. Rev. E 72 (2005) 036618.
[82] A.B. Evlyukhin, S.I. Bozhevolnyi, Surface plasmon polariton guiding by chains of nanoparticles, Laser Phys. Lett. 3 (2006) 396–400.
[83] R.S. Savelev, A.P. Slobozhanyuk, A.E. Miroshnichenko, Y.S. Kivshar, P.A. Belov, Subwavelength waveguides composed of dielectric nanoparticles, Phys. Rev. B 89 (2014) 035435.
[84] R. Shore, A. Yaghjian, Complex waves on periodic arrays of lossy and lossless permeable spheres: 1. Theory, Radio Sci. 47 (2012) RS2014.
[85] R. Shore, A. Yaghjian, Complex waves on periodic arrays of lossy and lossless permeable spheres: 2. Numerical results, Radio Sci. 47 (2012) RS2015.
[86] R.M. Bakker, Y.F. Yu, R. Paniagua-Domínguez, B. Luk'yanchuk, A.I. Kuznetsov, Resonant light guiding along a chain of silicon nanoparticles, Nano Lett. 17 (2017) 3458–3464.

This page intentionally left blank

5

Fano resonances in all-dielectric nanostructures

Nikolay S. Solodovchenko[a], **Kirill B. Samusev**[a,b], **and Mikhail F. Limonov**[a,b]

[a] *School of Physics and Engineering, ITMO University, St. Petersburg, Russia.*
[b] *Ioffe Institute, St. Petersburg, Russia*

5.1 Theory of Fano resonances

If a physicist is asked a question which resonance is the most famous, he is most likely to answer that it is the Fano resonance [1–3], and this applies not only to physics. The Fano resonance is also well-known in chemistry, biology and other sciences. As far as physics is concerned, the Fano resonance is actively studied and used in practice in various fields [4–7], and all-dielectric photonics is no exception [8–10].

This unique commonality is due to the nature of the Fano resonance, which is simply the result of the interference of two waves corresponding to resonant states with different quality factors. As was emphasized in a recent review [10], the Fano resonance is not a conventional resonance and is called so only by tradition. Fano resonance does not require an ordinary resonator, and a spectroscopic situation constantly arises when a narrow line is superimposed on a broad one and interferes with it. Accordingly, all-dielectric nanostructures, which are characterized by a whole bunch of different resonances, including the most famous resonances such as Mie and Fabry–Pérot, as well as the recently actively studied bound states in the continuum [11–13], anapole modes [14], Purcell effect [15] and a number of others, are ideal objects for observing and studying Fano resonances.

The history of the successful description of asymmetric lines in experimentally observed spectra began in 1935 when Ugo Fano explained sharp peaks in the absorption spectra of noble gasses during the photoionization of atoms. This process can occur through two channels: when an electron in the inner shell is excited above the ionization threshold, and when an atom is excited to a quasi-discrete level, which spontaneously ionizes with the

All-Dielectric Nanophotonics. https://doi.org/10.1016/B978-0-32-395195-1.00010-7
Copyright © 2024 Elsevier Ltd. All rights reserved.

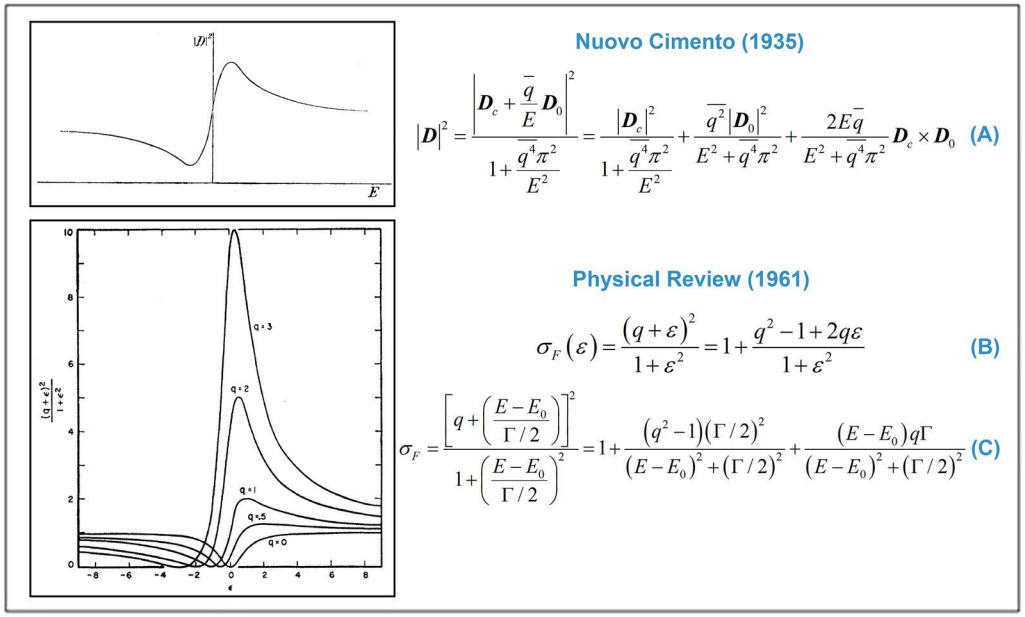

Figure 5.1. (a) Asymmetric profile of $|D|^2$ calculated by formula (A), shown on the right [1]. (b) Fano line shapes for different values of Fano parameter q, calculated by formula (B), shown on the right [2] in the normalized frequency axis $\epsilon = 2(E - E_0)/\Gamma$. *(a) Reproduced with permission from: U. Fano, Sullo spettro di assorbimento dei gas nobili presso il limite dello spettro d'arco, Nuovo Cimento, N. S. 12 (1935) 154-161 (in Italian) [1]. (b) Reproduced with permission from: U. Fano, Effects of configuration interaction on intensities and phase shifts, Phys. Rev. 124 (6) (1961) 1866-1878 [2].*

electron leaving for the continuum. As a result of the analysis, the first image of the asymmetric contour was obtained, shown in Fig. 5.1a, which was described by formula (A), containing a term in the blue frame, describing the interaction between the term itself and the continuum. The term in the blue frame causes the absorption to be not just a superposition of the absorptions due to the discrete and continuous terms, it reduces the intensity on one side of the position of the discrete term $E = 0$ and increases it by the same amount on the other side, which is determined by the change in the sign of E.

This result and publication [1] did not receive wide recognition, since the article was published in Italian. In 1961, Fano published another paper with an updated theory [2], which brought him universal recognition. The asymmetric contours shown in Fig. 5.1b are now known as the Fano profiles and Eq. (B) as the Fano formula. The Fano parameter $q = \cot\delta$ appears in this equation, where δ is the phase shift of the background continuum, $\epsilon = 2(E_0 - E)/\Gamma$, where Γ and E_0 are the resonance width and energy, respectively. To demonstrate the analogy of the formulas given in

the papers of 1935 and 1961 and to explain the physical meaning of formula (B), this formula is decomposed into three terms (Eq. (C)) [10]. The broad scattering component is described by a constant infinite background with normalized amplitude equal to 1. A relatively narrow line is described by a Lorentzian contour; this is the second term. As in the case of Eq. (A) from the 1935 paper, the key term is the third term, highlighted in the blue frame. This is also a key alternating term, but if the third term in Eq. (A) changes sign at $E = 0$, then Eq. (C) describes the general case and the sign changes at resonant frequency of the narrow line $E = E_0$.

In literature, there are different normalization coefficients for formula (B) in Fig. 5.1 as well as different descriptions of the broad background, including those consisting of several components interfering or not interfering with a narrow line. We will use a simple form of the Fano formula [4,8,10], which makes it easy to represent all the main contours of the spectroscopic lines that this formula describes:

$$\sigma(E) = D^2 \frac{(q+\Omega)^2}{1+\Omega^2}. \tag{5.1}$$

In this formula, E is the energy or normalized frequency, $q = \cot\delta$ is the Fano parameter that determines the shape of the narrow line contour, δ is the phase shift between a broad background and a narrow resonance line, $\Omega = 2(E - E_0)/\Gamma$, where Γ and E_0 are the width and energy of the resonance, respectively, and $D^2 = 4\sin^2\delta$.

Notably, the theory does not impose any restrictions on the value and sign of the Fano parameter q. In real structures, the value of the Fano parameter is determined by geometric and material parameters and, according to the cotangential dependence, can change monotonously from plus infinity to minus infinity passing through zero. The schematic Fig. 5.2 shows this cotangential behavior of q and the corresponding forms of narrow resonant lines, which can be of three types. At the edges of a broadband line, where the narrow line does not couple to the continuum and the Fano parameter tends to infinity $q \to \pm\infty$, the Fano line shape becomes a symmetric Lorentzian $\sigma_L(\Omega) \sim \frac{1}{1+\Omega^2}$. Another important special case corresponds to the zero value of the Fano parameter q, when the narrow line becomes a symmetric quasi-Lorentzian anti-resonance in the continuum spectrum $\sigma_L(\Omega) \sim \frac{\Omega^2}{1+\Omega^2}$. In all intermediate cases, the shape of the narrow line will be asymmetric and described by the Fano formula (5.1).

As follows from Eq. (5.1), the Fano profile always vanishes at frequency $q + \Omega = 0$. If there is only one broadband profile in the observed spectrum, then the Fano resonance determines the true zero in scattering. Such an effect can be observed experimen-

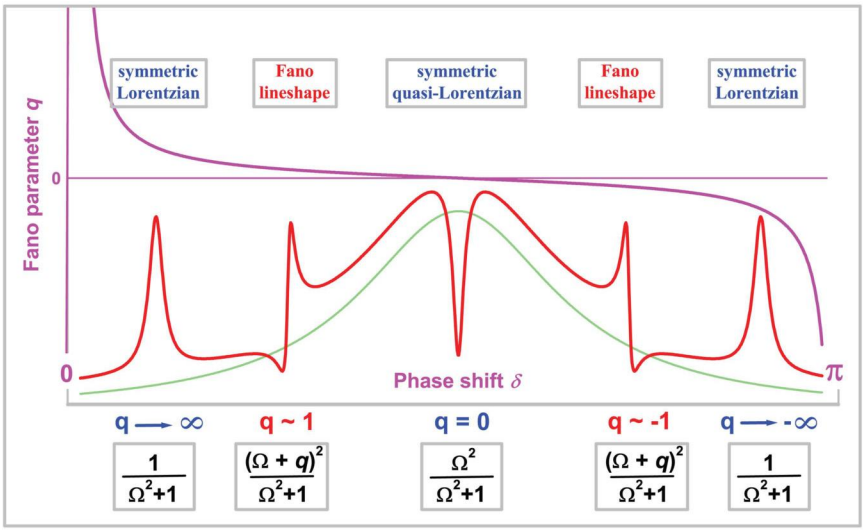

Figure 5.2. The shape of the characteristic Fano profiles (red curve, compilation of five lines) depending on Fano parameter $q = \cot\delta$ (magenta curve) and the corresponding Fano-formulas (in square frames). The green curve is the symmetrical Lorentzian profile that plays a role of the background. *Adapted with permission: M.F. Limonov, Fano resonance for applications, Adv. Opt. Photon. 13 (3) (2021) 703-771 [10].*

tally. Fig. 5.3 presents the experimental and calculated scattering spectrum of the dielectric ring of an outer diameter of 115 mm, an inner diameter of 93 mm, and a height of 7 mm, made of low-loss Ti-Ca-based microwave ceramics with relative dielectric permittivity of 43 and a loss tangent 10^{-4} [16]. The scattering cross-section spectra of the ring and the distributions of the field were measured at microwave frequencies in far-field and near-field zones, respectively, in an anechoic chamber. The spectral region of the Fano resonance was studied in detail, where a complete suppression of the scattering intensity is observed, i.e., the object becomes invisible to an outside observer. The results of the near-field study indicate that at frequency 5 GHz neither the amplitude nor the phase of the H_z component of the TE polarized field around and inside the ring are not distorted, the electromagnetic wave passes through the ring unchanged, remaining an ordinary plane wave, Fig. 5.3d-f.

Finally, we will determine the place of the Fano resonance among other resonances observed in photonics. The Fano resonance corresponds to the weak-coupling regime and can be described in terms of the two coupled oscillators model [8,17,18]. Two coupled driven oscillators (Fig. 5.4) are described by the fol-

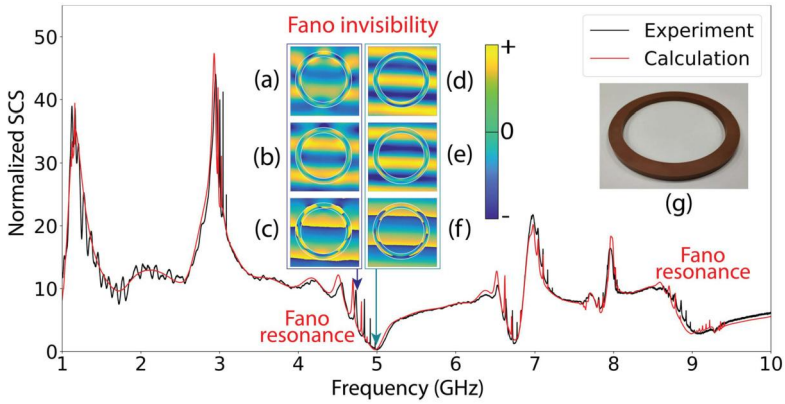

Figure 5.3. Experimental far-field normalized scattering cross-section spectra (black curve) and calculated spectra (red curve) for ring. (a-f) Field patterns in the near-field zone. Shown are: the spatial distribution of the real [(a), (d)] and imaginary [(b), (e)] H_z magnetic component of the TE polarized electromagnetic field and its phase [(c), (f)] for two frequencies 4.75 and 5 GHz, respectively. The insert (g) shows a photograph of the examined sample. *Adapted with permission from: N. Solodovchenko et al., Cascades of Fano resonances in light scattering by dielectric particles, Mater. Today 60 (2022) 69-78. [16].*

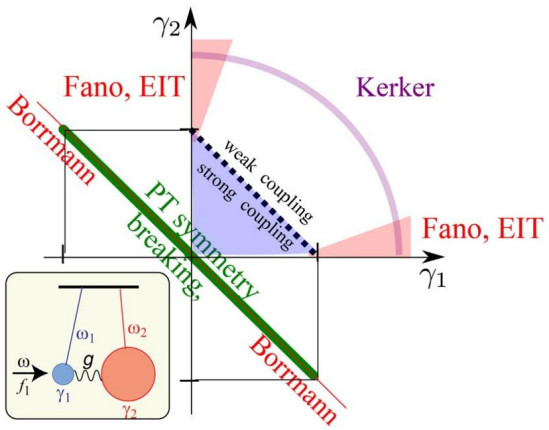

Figure 5.4. Phase diagram for the Fano resonance as well as other photonic resonances (electromagnetically-induced transparency, Kerker effect, Borrmann effect, parity-time symmetry) in the damping constants (γ_1, γ_2) plane. In the lower left corner: schematic view of two coupled damped oscillators with a driving force f1 applied to one of them. *Adapted with permission from: M.F. Limonov et al., Fano resonances in photonics, Nat. Photonics 11 (9) 543–554 (2017) [8].*

lowing matrix equation [8]:

$$\begin{pmatrix} \omega_1 - \omega - i\gamma_1 & g \\ g & \omega_2 - \omega - i\gamma_2 \end{pmatrix} \begin{pmatrix} x_1 \\ x_2 \end{pmatrix} = i \begin{pmatrix} f_1 \\ f_2 \end{pmatrix}, \qquad (5.2)$$

where x_1 and x_2 are the oscillator amplitudes, ω_1 and ω_2 are the resonant frequencies, γ_1 and γ_2 are the damping terms, and f_1 and f_2 are the external forces with the driving frequency ω. The coupling constant g describes the interaction between the oscillators. The Fano resonance occurs when only one of the oscillators (with larger damping) is driven ($f_1 \neq 0,\ f_2 = 0$). The key condition for the occurrence of the Fano resonance is a strong difference in damping rates $\gamma_1 \gg \gamma_2$ to realize narrow and broad spectral lines. For the weak-coupling regime, coupling constant g should be less than the greater damping γ_1, that is, $\gamma_1 \gg g \gg \gamma_2$. The phase of the undamped oscillator changes by π at the resonance, while the phase of the strongly damped oscillator varies slowly. As a result of interference, the resulting spectra show a typical Fano asymmetry.

The phase diagram in the damping constants ($\gamma_1,\ \gamma_2$) plane (Fig. 5.4) shows the region of Fano resonance existence together with other photonic resonances [8].

5.2 Disorder-induced Fano resonances

Among the many mechanisms for the Fano resonance to occur [1–10], the most mysterious is probably the mechanism associated with the disorder of the structure. Fano resonances are usually associated with coherent scattering in regular systems, and the Fano parameter q depends on precisely known dielectric and structural parameters. In the case of a disordered structure, in addition to the averaged values of the parameters, their dispersion characteristics are added, and the theoretical problem becomes much more complicated. However, disorder provides an additional degree of freedom to control the spectroscopic properties of the structures, and new, unexpected properties can be observed, which is impossible in the case of ordered objects. In particular, it becomes possible to control the Fano parameter over a wide range, including tuning it from extremely large values to zero, which corresponds to a complete flip of the Bragg band and the transition from the reflection regime to the transmission regime. The source of the unique transmutability of the Bragg band in the spectra of dielectric photonic structures is the Fano interference between multiple Bragg scattering and single disorder-induced Fabry–Pérot scattering. This Fano resonance and the Anderson localization phenomenon have the same physical origin, namely the interference between different paths due to the multiple scattering of photons by imperfections in the structure [19,20].

Next, nontrivial properties associated with the Fano resonance in disordered photonic crystals will be demonstrated using one-

dimensional (1D) and three-dimensional (3D) structures as examples.

5.2.1 Fano resonances in 1D dielectric structures

In this section, the main features of the transmission spectra of 1D photonic crystals (PhCs) with different types of disorder are discussed. Following the works [19,20], let us consider 1D PhCs consisting of a sequence of A and B layers. The A layers are assumed to be identical with permittivity ε_A and thickness w_A. The B layers are allowed to possess some degree of disorder both in permittivity (ε_B^i for i-th layer, mean value $\bar{\varepsilon}_B$), referred to as *ε-disorder*, and in thickness (w_B^i for i-th layer, mean value $\bar{w}_B$), referred to as *w-disorder*. The variations are described by the normal distribution with half-width normalized to maximum position as σ_ε and σ_w. An average lattice constant of 1D PhCs is $a = w_A + \bar{w}_B$. The transmission coefficients of 1D PhCs are evaluated with the use of the transfer matrix technique. Then, spectra are averaged for a sufficient number of realizations M.

Fig. 5.5 demonstrates the qualitative difference between the geometric (w) and compositional (ε) disorder. A classical Bragg stop-band (Fig. 5.5a, red line) is observed in an ordered 1D PhCs (Fig. 5.5c). Such a Bragg stop-band is surrounded by the fringes associated with Fabry–Pérot-type interference on PhCs boundaries. The effect of w-disorder (Fig. 5.5e) on the transmission spectra of 1D PhCs gives rise to the well-known broadening and degradation of fringes, while outside the Bragg bands the transmittance can reach nearly 100% (Fig. 5.5a, black line). The introduction of ε-disorder (Figs. 5.5f, 5.6) leads to a different transformation behavior of the transmission spectra of 1D PhCs. This new behavior is characterized by the asymmetric shape of the Bragg bands and the appearance of additional "background" scattering outside the Bragg bands (Fig. 5.5b, black line).

An ordered 1D PhCs ($\sigma_{w_B} = \sigma_{\varepsilon_B} = 0$, Fig. 5.6a, black line) is optically transparent in the whole spectral range, except for narrow h-order Bragg stop-bands at frequencies ω_h, determined by the condition:

$$\frac{\omega_h \bar{n} a}{c} = \pi h, \qquad h = 1, 2, \ldots \tag{5.3}$$

where $\bar{n} = (w_A\sqrt{\varepsilon_A} + w_B\sqrt{\varepsilon_B})/a$ is the average refractive index. Novel and unexpected effects are discovered when the disorder is introduced to the permittivity of the layers B. The disorder destroys perfect transmittance within the background regions, transforming it into a relatively slowly changing Fabry–Pérot spectrum.

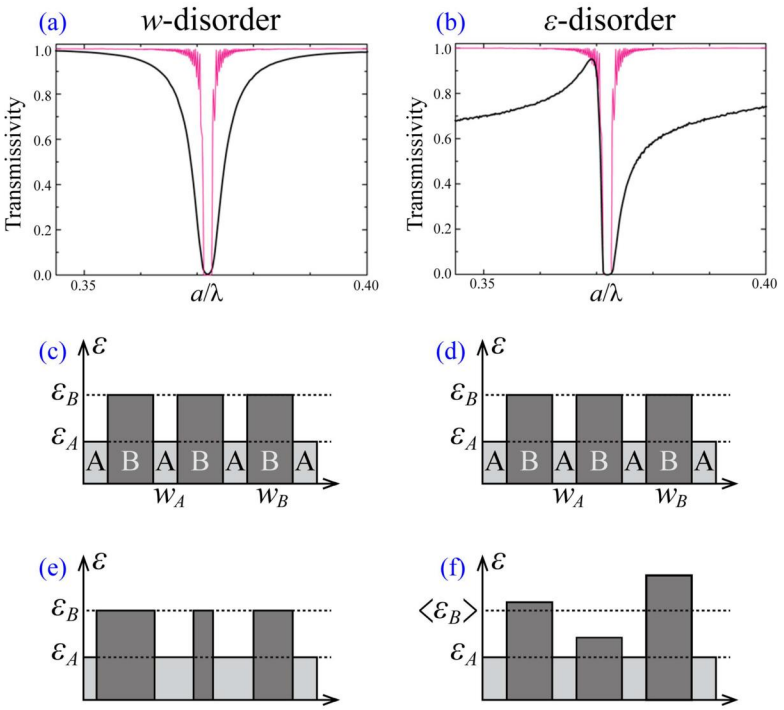

Figure 5.5. Averaged transmission spectra of one-dimensional photonic crystals for different types of disorder. (a) Spectra of an ordered PhC (red) and of PhC with w-disorder (black). (b) Spectra of an ordered PhC (red) and of PhC with ε-disorder. (c, d) Schematic illustration of the spatial dependence of permittivity ε of an ordered 1D PhC. (e) Schematic illustration of the spatial dependence of permittivity ε of PhC with w-disorder. (f) Schematic illustration of the spatial dependence of permittivity ε of PhC with ε-disorder.

Light transport can be conveniently quantified by extinction χ, related to the transmission coefficient T as $T = \exp(-Na\chi)$, where $a = w_A + w_B$. For a 1D PhCs with ε-disorder, the following expression is obtained [20]:

$$\chi \approx \frac{\sigma_{\varepsilon_B}}{4a\varepsilon_A} \sin^2\left(\frac{\omega\sqrt{\varepsilon_A}w_B}{c}\right). \tag{5.4}$$

This background extinction is determined by uncompensated scattering on different layers B and the spectral dependence of Eq. (5.4) reflects the Fabry–Pérot interference on layer B with the width w_B and variable permittivity ε_B. Increase in σ_{ε_B} results in a gradual increase in modulation of a spectrum with a period of Fabry–Pérot resonance T_{FP}. In addition to the detected Fabry–Pérot scattering, the results demonstrate unexpected changes in

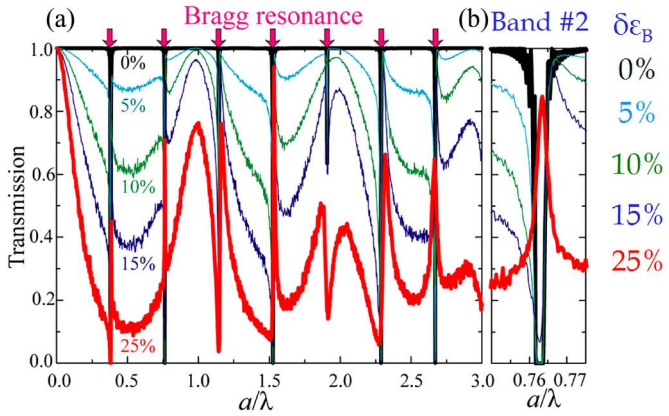

Figure 5.6. (a) Transmission spectra of 1D PhCs with ε-disorder as a function of degree of disorder σ_ε. The bands corresponding to the h-order Bragg resonance are shown by the red arrows at the top of the figure. (b) Evolution of the second-order Bragg band of 1D PhCs given in a larger scale for different values of disorder σ_ε, indicated by the corresponding color to the right of the figure. Calculation parameters: $\varepsilon_A = 1.70$, $w_B^i = 1.75$, $w_B = 0.38a$, $N = 1000$ (the number of pairs of AB layers), $M = 5000$ (number of random realizations). *Adapted with permission from: M.V. Rybin et al., Optical properties of 1D disordered photonic structures, in: M.F. Limonov and R.M. De La Rue (Eds.), Optical properties of photonic structures: interplay of order and disorder, p. 14, CRC Press, Taylor & Francis Group, Boca Raton, London, New York, 2012 [19].*

the amplitude and shape of the spectrum at Bragg frequencies, Fig. 5.6. When weak disorder is introduced ($\delta\varepsilon_B = 5\%$), the symmetric contour of Bragg bands of ordered 1D PhCs becomes asymmetric. A further increase in the degree of disorder ($\delta\varepsilon_B = 10$–15%) causes an increasingly asymmetric shape of the Bragg line. The spectrum marked with a thick red line in Fig. 5.6 ($\delta\varepsilon_B = 25\%$) illustrates the most impressive effect: band reversal and the transformation of the *Bragg stop-band* into the *Bragg pass-band*. Thus, in the 1D PhCs with ε-disorder, the Fano–Bragg band goes through a complete cycle with a contour flip.

Fig. 5.7 demonstrates the impressive transformation of the Bragg stop-band in ordered (a) and Bragg pass-band in disordered (b) 1D PhCs depending on the number of unit cells N. For a disordered 1D PhCs, the degree of disorder was fixed $\sigma_\varepsilon = 10$. Quite unexpectedly, with increase in N the line-width of the pass-band strongly decreases and becomes much less than the width of the stop-band that becomes finite and unchangeable at $N > 10^4$. In this case, the disorder leads to the formation of ultra-narrow bands at the Bragg frequency. In the limit $N \to \infty$, these bands become very narrow, while their intensity remains the same [19].

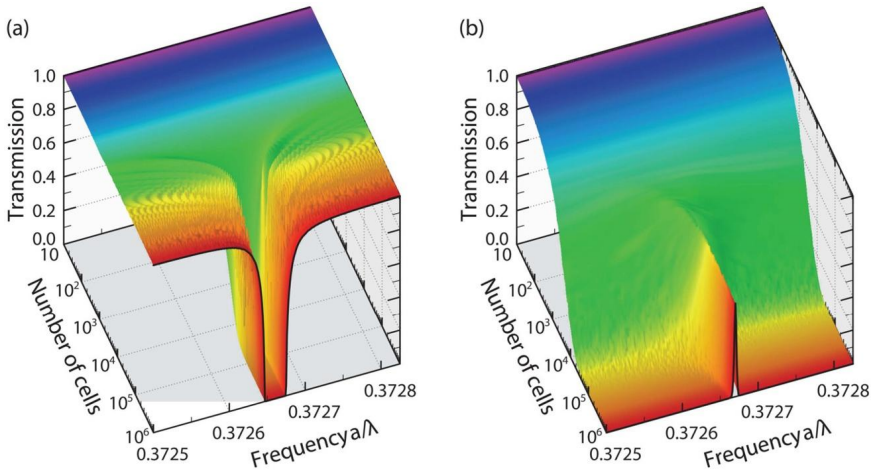

Figure 5.7. Bragg stop-band in transmission spectra of ordered 1D PhCs (a) and Bragg pass-band in transmission spectra of 1D PhCs with ε-disorder (b) as a function of the number of unit cells N. *Adapted with permission from: M.V. Rybin et al., Optical properties of 1D disordered photonic structures, in: M.F. Limonov and R.M. De La Rue (Eds.), Optical properties of photonic structures: interplay of order and disorder, p. 14, CRC Press, Taylor & Francis Group, Boca Raton, London, New York, 2012 [19].*

A theoretical model was developed to verify the existence of Fano-type interference between narrow Bragg bands and the Fabry–Pérot background [20]. Based on the transfer matrix method [21], extinction χ was determined from the Fokker-Planck equations for the distribution of the electric field phase. The spectral range close to the given Bragg frequency ω_h and the case of weak dielectric contrast are considered. These two conditions are sufficient for an analytical description of the results of numerical simulation. The average phase incursion $\Phi_h = \omega_h \sqrt{\varepsilon_A} w_B / c \geq 1$ is introduced that characterizes the average phase shift in the layers at Bragg resonance. As a result, it was shown that, under the assumptions made, the extinction can be expressed as a Fano function [20]:

$$\chi(\Omega) = \frac{\sin^2 \Phi_h \sigma_{\varepsilon_B}^2}{4a\varepsilon_A^2} \frac{(\Omega + q)^2}{\Omega^2 + 1}. \tag{5.5}$$

The formula includes dimensionless frequency of the Bragg line $\Omega = (\omega - \omega_h)/\Gamma_h$ and the Fano parameter:

$$q = -\left(1 + \frac{|\bar{\varepsilon}_B - \varepsilon_A|^2}{\sigma_{\varepsilon_B}^2}\right) \cot \Phi_h - \frac{1}{\Phi_h} \frac{2\varepsilon_A |\bar{\varepsilon}_B - \varepsilon_A|}{\sigma_{\varepsilon_B}^2}. \tag{5.6}$$

As in the main Fano formula (5.1), in Eq. (5.6) the Fano parameter has a cotangential dependence. Notably, Eq. (5.6) includes the parameter σ_{ε_B}, which describes the ε-disorder, and does not include the parameter σ_{w_B}, which characterizes the w-disorder, in accordance with the results of numerical calculations, Fig. 5.5. It follows directly from formula (5.6) that by changing the magnitude of the ε-disorder, one can change the Fano parameter q, and control the shape of the Fano line.

5.2.2 Fano resonances in 3D dielectric structures

In this section, we continue the discussion of the optical properties of disordered PhCs in which the Fano resonance is observed. The object of research is 3D PhCs based on synthetic opals [22–29]. The structural parameters and physical properties of opals make these gemstones not only beautiful decorations but also perfect objects for optical studies. Opals are built up of quasi-spherical particles of amorphous silica $a-SiO_2$ (Fig. 5.8a), each particle having a rather hard coat and porous nucleus, which contains randomly located spherical pores 7–15 nm in diameter (Fig. 5.8c,d). Porosity of the $a-SiO_2$ particles produces inhomogeneity of dielectric permittivity of a single $a-SiO_2$ particle and of the opal structure as a whole. As a result, opals always have a disordered structure that can be described as face-centered cubic (fcc) only as a rough approximation.

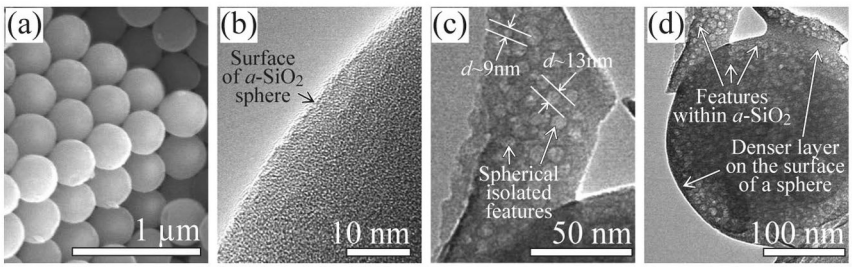

Figure 5.8. (a) Scanning electron microscopy images of opals. (b)-(d) Transmission electron microscopy images of $a-SiO_2$ particles. *Adapted with permission from: M.V. Rybin et al., Selective manipulating the stop-bands in multi-component photonic crystals: opals as an example, Phys. Rev. B 77(20), 205106 (2008) [22].*

Opals have an overlapping net of air voids in between the $a-SiO_2$ particles (Fig. 5.8a), which allows infilling the voids with various materials, including repeatedly filling the sample with liquids. The average permittivity of each individual $a-SiO_2$ particle is 1.8–2.0 depending on the sample [22,27]. This value is excellent for studying different effects in the optical spectra of 3D PhCs. For

example, by filling opals voids with a mixture of distilled water ($\varepsilon = 1.78$) and propylene glycol ($\varepsilon = 2.05$) in various proportions, one can scan the average dielectric constant of opals, including passing the point of the assumed complete transparency of the sample.

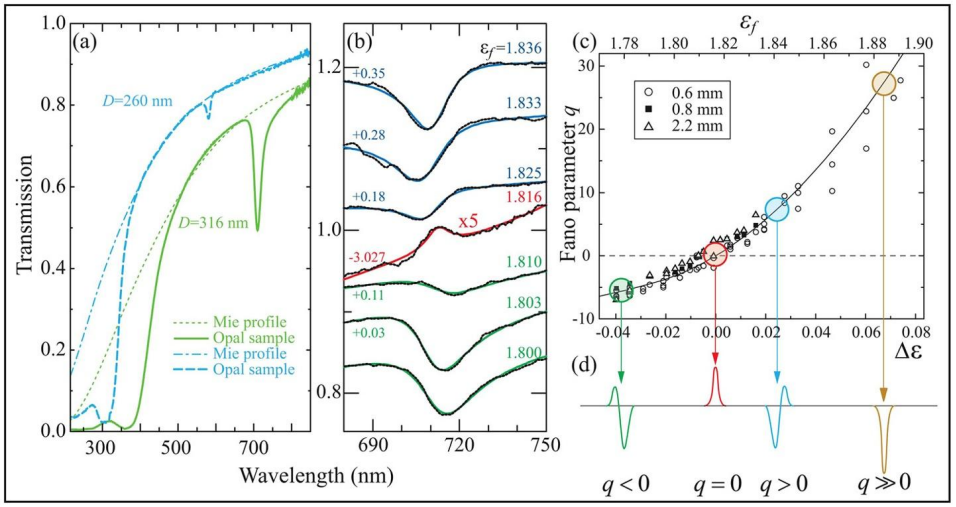

Figure 5.9. (a) Transmission spectra of two opal samples for the $\Gamma \rightarrow$ L geometry and the results of calculations of the transmission spectra of an disordered ensemble of isolated spherical particles with $D = 260$ nm and $D = 316$ nm with the use of Mie theory. (b) The transmission spectra of an opal sample ($D = 316$ nm, thickness ~ 0.6 nm) as a function of the filler permittivity ε_f in the region of the (111) photonic band (black dotted curves). The color curves (red solid, blue solid, and green dashed) are the results of fitting with a Fano function. (c) The Fano asymmetry parameter q that changes continuously from negative to positive values with filler permittivity ε_f increasing for three samples with different thickness of 0.6, 0.8, and 2.2 mm, respectively, $D = 316$ nm. The solid line is a guide for the eyes only. Below: Schematic of the Bragg band shape observed in the transmission spectra on changes in the filler permittivity ε_f, which, in turn depends on Fano parameter q. *Adapted with permission from: M.V. Rybin et al., Fano resonance between Mie and Bragg scattering in photonic crystals, Phys. Rev. Lett. 103(2), 023901 (2009) [29].*

Fig. 5.9a shows the transmission spectra of two oriented samples of high quality opals. The spectrum is determined by two mechanisms. First, broadband defect-induced Mie scattering due to ε-disorder in individual $a-SiO_2$ particles, and second, narrow Bragg stop band from the (111) planes of the fcc opal lattice. The key experimental result is shown in Fig. 5.9b, which demonstrates a surprising transformation of the transmission spectra of opal with a change in the dielectric permittivity of the filler, starting from small values. At first, the well-known effect of diminishing of the Bragg stop band intensity is observed when the filler permittivity ε_f approaches a certain value, which was determined for the family of (111) stop band of the 316 nm opal sample to

be $\varepsilon_f^0 = 1.816$ (Fig. 5.9b, the green curves). It should be emphasized that there is no value of ε_f at which the (111) Bragg band disappears. When the filler permittivity is $\varepsilon_f = \varepsilon_f^0$ (the red curve), a transmission Bragg rise is observed instead of the conventional transmission Bragg dip. This means that for some parameters of the disordered 3D structure the *Bragg-stop band* is transformed into the *Bragg pass-band*, similar to the case described above for the 1D disordered structure. The turning point of the Bragg band corresponds to the Fano parameter $q = 0$, Fig. 5.9c. With a further increase in filler permittivity ε_f, the reverse transformation of the Bragg pass-band into the Bragg stop-band occurs (blue lines in Fig. 5.9b). Note that below and above point $\varepsilon_f = \varepsilon_f^0$, the Bragg lines have the opposite asymmetry (Fig. 5.9b), which is expressed by the sign change of the Fano parameter q at this point (Fig. 5.9c).

Thus, it was demonstrated that in both 1D PhCs and 3D PhCs ε-disorder leads to Fano interference and a surprising transformation of the stop band into the transmission band. In both cases the Bragg resonance plays a role of the narrow line demonstrating the flip, and the broad defective background has a different nature: in 1D this is Fabry–Pérot scattering, in 3D this is Mie scattering.

In the classic work by S. John "Strong localization of photons in certain disordered dielectric superlattices", [30], it was predicted that strong Anderson localization of photons can be achieved due to Bragg resonances in disordered dielectric superlattices with a real positive dielectric constant. Therefore, the interference between Bragg diffraction and disorder-induced scattering is usually considered a way to localize light and a mechanism capable of suppressing transmission and increasing backscattering. It appears that the opposite situation exists, and Fano interference between defective background scattering and Bloch waves, under certain conditions, leads to an anomalous increase in transmission at Bragg frequencies.

5.3 Cascades of Fano resonances

A single Fano resonance results from the interference of two spectrally wide and narrow lines, as discussed in Section 5.1. The Fano profile can be either asymmetric or symmetric, and its shape is determined by the Fano parameter q. However, if in the region of sufficiently broad background scattering there are several interfering narrow lines, then a number of resonance lines with different Fano contours are observed in the spectrum. If the mechanism of the appearance of narrow resonances leads to an infinite series, then an infinite cascade of Fano resonances arises. Such a strik-

ing example has been studied in detail in atomic spectroscopy, where infinite cascades of asymmetric Fano lines were thoroughly studied for Rydberg series of autoionization resonances [4]. Rydberg resonances may or may not overlap in energy, interacting with a continuum of varying phase shift and demonstrating all possible Fano shapes, Fig. 5.10b. Noteworthy, atomic physics is directly related to the theory of Ugo Fano, who created his own model for describing unusual sharp asymmetric peaks in the absorption spectra of noble gasses [1,2]. Fig. 5.10a from the classic article by Ugo Fano presents the experimental data on the inelastic scattering of electrons by helium (circles) and the results of fitting at different values of the spectral width of the autoionized state.

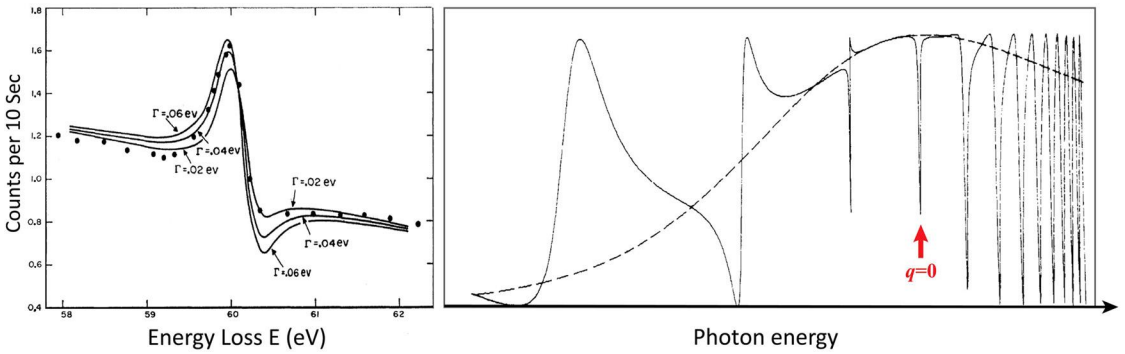

Figure 5.10. (a) Experimental data on the inelastic scattering of electrons by He (circles) and three fitting curves. The intermediate value $\Gamma = 0.04$ eV gives the best overall fit. (b) Calculation of the cross section of a Rydberg–Fano series interacting with a giant resonance in the limit of weak coupling. *(a) Adapted with permission from: U. Fano, Effects of configuration interaction on intensities and phase shifts, Phys. Rev. 124, 1866–1878 (1961) [2]. (b) Adapted with permission from: J.-P. Connerade and A.M. Lane, Interacting resonances in atomic spectroscopy, Rep. Prog. Phys. 51, 1439-1478 (1988) [4].*

As in the case with Rydberg series in atomic physics, in optics the full Mie and Fabry–Perot manifold comprises an infinite sequences of narrow resonances in all-dielectric structures. As a result, cascades of Fano resonances can be observed in the far field. In optics, Fano resonance cascades were first discovered and analyzed theoretically in detail in the spectra of light scattering by a dielectric cylinder [31]. By employing the exact solution of the Maxwell's equations, it was demonstrated that the Lorentz–Mie coefficients of the Mie problem can be expressed as infinite cascades of Fano profiles. Mathematically, the Lorentz–Mie coefficients describe the interference between the background radiation of an incident wave scattered by the cylinder as a whole and narrow Mie resonances, which corresponds to the physical conditions for the occurrence of Fano resonances. When the position of the narrow Mie line was changed relative to the broad background

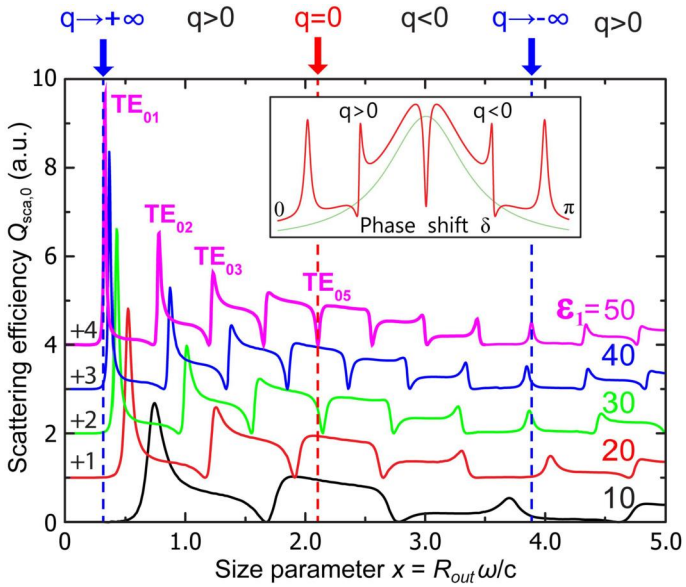

Figure 5.11. Spectral dependence of the amplitude of the Mie scattering efficiency $Q_{\mathrm{sca},0}$ for dipole mode TE_{0k} for a single dielectric cylinder and different values of real dielectric permittivity ε_1. Spectra are shifted vertically by the values shown. The cylinder is embedded in air, $\varepsilon_2 = 1$. The behavior of Fano parameter q is shown above the figure. Insert: The shape of the characteristic Fano profiles (red curve compiling five lines) depends on Fano parameter $q = \cot\delta$ (red curve) and the symmetrical Lorentzian profile (green curve). *Adapted with permission from: M.V. Rybin et al., Mie scattering as a cascade of Fano resonances, Opt. Express 21, 30107–30113 (2013) [31].*

spectrum, the resonance line shape periodically transforms from the Lorentzian contour ($q \to \pm\infty$) to the Fano contour, then to the quasi-Lorentzian dip ($q = 0$) and vice versa. Fig. 5.11 demonstrates this strict periodicity using the spectral dependence of Mie scattering efficiency $Q_{\mathrm{sca},0}$ for the dipole mode TE_{0k}. It is important to note that the position of the singular points of the $q(x)$ function does not depend on the dielectric permittivity of the resonator. As a result of the numerical fitting of the functions $Q_{\mathrm{sca},0}(x)$ for a dielectric cylinder (Fig. 5.12a), the spectral dependences of the Fano parameter $q(x)$ were obtained, which fully correspond to the cotangential theoretical dependence $q = \cot\delta$ following from Fano theory [1,2].

Light scattering by a single homogeneous spherical dielectric particle with a high refractive index and low losses based on the exact Mie solution, which included the study of Fano resonances, is analytically studied [32]. In this case, far-field scattering can be

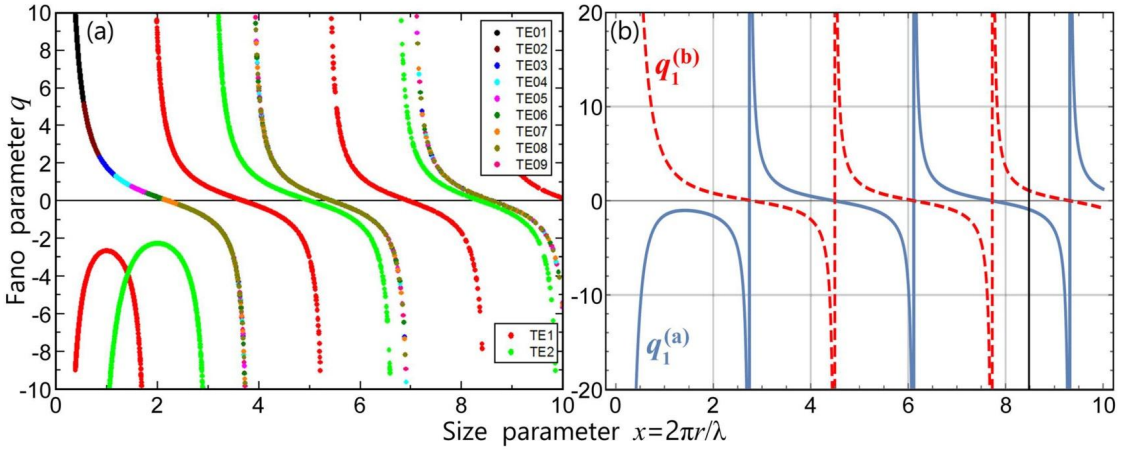

Figure 5.12. (a) Dependence of Fano parameter q on size parameter x for dipole mode TE_{0k} and multipole modes TE_{1k} (red) and TE_{2k} (green) for a cylinder. (b) Dependences of Fano parameter q on size parameter x: $q_1^{(a)}$ (solid blue line for magnetic modes) and $q_1^{(b)}$ (dashed red line for electric modes) for a sphere. *(a) Adapted with permission from M. F. Limonov, Adv. Opt. Photon. 13, 703-771 (2021) [10]. (b) Adapted with permission from: M.I. Tribelsky and A.E. Miroshnichenko, Giant in-particle field concentration and Fano resonances at light scattering by high-refractive-index particles, Phys. Rev. A 93, 053837 (2016) [32].*

decomposed into orthogonal electromagnetic dipolar and multipolar terms with spherical Lorentz–Mie coefficients a_n and b_n. It was demonstrated that, as in the case with a cylinder, each partially scattered wave is represented as a sum of two terms. One of them plays the role of a broadband background, the other the role of a narrow resonance and is associated with the excited Mie mode. Term interference leads to Fano resonance with all possible line shapes. For the Mie scattering efficiencies of the electric modes $|a_n|^2$ and magnetic modes $|b_n|^2$, the conventional Fano profile normalized to its maximal value was obtained with the Fano parameters $q_n^{(a)}$ and $q_n^{(b)}$ respectively:

$$|a_n|^2 = \frac{1}{\left(1+q_n^{(a)2}\right)}\frac{\left(\Omega_n^{(a)}+q_n^{(a)}\right)^2}{\left(1+\Omega_n^{(a)2}\right)},$$
$$|b_n|^2 = \frac{1}{\left(1+q_n^{(b)2}\right)}\frac{\left(\Omega_n^{(b)}+q_n^{(b)}\right)^2}{\left(1+\Omega_n^{(b)2}\right)}. \tag{5.7}$$

It is important that the Fano parameters for electric and magnetic modes were analytically determined. The parameters depend only on the multipolarity of the scattered partial wave n and

do not depend on the particle refractive index:

$$q_n^{(a)} = \frac{\chi_n'(x)}{\psi_n'(x)}, \qquad q_n^{(b)} = \frac{\chi_n(x)}{\psi_n(x)}, \tag{5.8}$$

where x is the size parameter, $\chi_n(x)$ and $\psi_n(x)$ are the Riccati–Bessel functions. The corresponding dependencies of the Fano parameters, which are exactly reminiscent of the cotangent function of the phase shift from Ref. [2], are shown in Fig. 5.12b.

The transformation of the calculated normalized scattering cross-section (SCS) spectra as the shape changes from a cylinder to a ring with an increase in the inner radius of the ring was analyzed in detail in Ref. [18]. As a result of numerical calculations, it was shown that the Mie modes of the cylinder are transformed into broad transverse modes of the ring, to which new longitudinal modes are added due to the presence of two side walls. At the same time, the transverse modes of the ring, genetically related to the Mie modes of the cylinder, which exhibit cascades of Fano resonances in scattered light, also retain this property, but in a nontrivial sequence. In the SCS spectra of the ring, as well as the split ring and, unexpectedly, the rectangular cuboid, the identical strict alternation of line shapes in the cascade of transverse resonances in the Lorentzian-Fano- Lorentzian-Fano-... sequence is observed, Fig. 5.13. Note that the spectral position of intense lines is almost the same in the spectra of three structures of different shapes, which is associated with the transverse type of these modes in resonators with the same width, and this effect is retained with transformation from a ring to a cuboid. In this case, narrow longitudinal resonances have different amplitudes and shapes in the scattering spectra of different structures. In particular, in the spectra of a split ring (Fig. 5.13b), all narrow lines have pronounced Fano profiles, which is associated with additional interference due to the presence of an air gap.

Let us discuss in more detail the scattering spectrum of a ring with a rectangular cross-section and a very high dielectric permittivity $\varepsilon = 200$, when all the spectral features are clearly visible [16]. In three-dimensional structures with axial symmetry, such as a disk and a ring, the eigenfunctions can be characterized by the azimuthal (m), radial (r), and axial (z) mode indices, forming an ordered triple (m, r, z). The SCS spectrum of a ring is divided into separate spectral regions, which begin with a broad transverse resonance of the Lorentz- or Fano-type and continue with a gallery of longitudinal modes, Fig. 5.14. This is an alternation of galleries with different transverse field distributions: either an integer or a

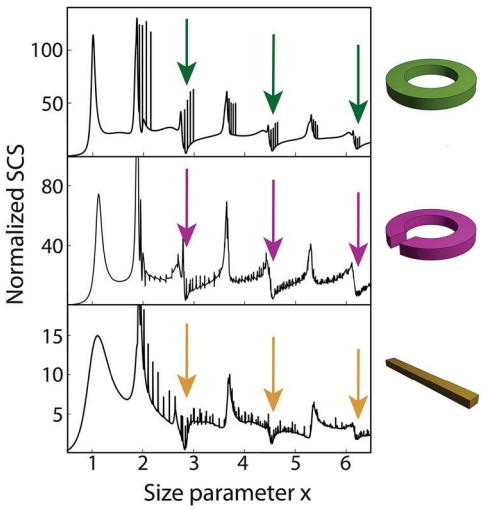

Figure 5.13. Normalized SCS spectra of dielectric resonators with a rectangular cross-section. (a) ring, (b) split ring, (c) cuboid. The colored arrows mark cascades of Fano resonances formed by intense transverse Fabry–Perot modes. TE polarization, $\varepsilon = 80$, $\varepsilon_{air} = 1$. Size parameter $x = R_{out}\omega/c$ for all structures except the cuboid, for which $x = L\omega/c$, $L = \pi(R_{out} + R_{in})$. *Adapted with permission from: N. Solodovchenko et al., Cascades of Fano resonances in light scattering by dielectric particles, Mater. Today 60 (2022) 69-78 [16].*

half-integer number of waves fit across the resonator width, which corresponds to either even or odd radial index r. The Fano resonance heads the galleries with even radial photonic indices, while the Lorentz resonance heads the galleries with odd radial indices. The analysis performed by calculating SCS spectra of the dielectric ring resonator at excitation by partial harmonics indicates that the partial spectra change strictly periodically, retaining in general the characteristic Fano properties of the Mie scattering for dipole modes TE_{0k} by a dielectric cylinder, Fig. 5.11. Indeed, let us consider the SCS spectral dependence at excitation by partial cylindrical harmonics with $n = \pm 1$, marked in Fig. 5.14 with the bold blue line. The spectrum is strictly periodic with maxima in the region of odd galleries and minima in the region of even galleries (marked in pink).

Thus, Fano resonance cascades are a general property of the light scattering spectra by all-dielectric particles with Mie or Fabry–Pérot type resonances [16]. This effect is associated, in particular, with the periodic behavior of the Fano parameter q in the spectral domain, as follows from Fig. 5.12.

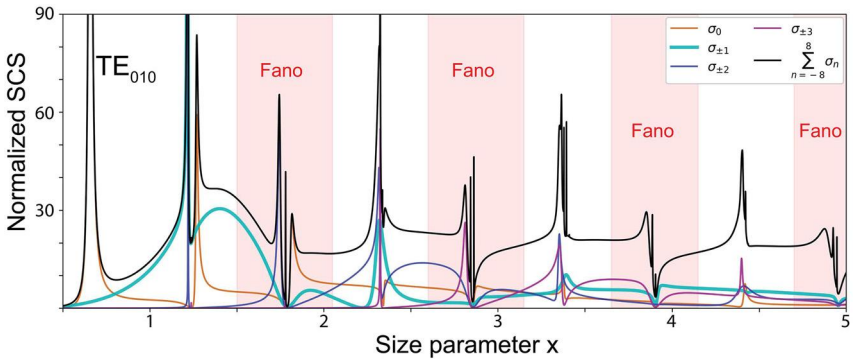

Figure 5.14. Total normalized scattering cross-section spectrum of dielectric ring (black curve) and SCS spectra at excitation by partial cylindrical harmonics with modal number $n = 0, \pm 1, \pm 2, \pm 3$. Most of the narrow lines of longitudinal modes forming the galleries are not shown in the black curve for better visibility of the plot. $R_{in}/R_{out} = 0.6$, TE polarization, $\varepsilon = 200$. The normalized size parameter $x = R_{out}\omega/c$. *Adapted with permission from: N. Solodovchenko et al., Cascades of Fano resonances in light scattering by dielectric particles, Mater. Today 60 (2022) 69-78 [16].*

5.4 Fano resonance and Purcell effect

The spontaneous emission rate of an emitter in a cavity may be enhanced or inhibited compared to emission in free space. The spontaneous emission modification factor, also known as the Purcell factor, scales inversely with the cavity mode volume. In his seminal paper of less than one page, which nevertheless laid the foundation for a new direction in solid state physics, E.M. Purcell gives the following formula for the spontaneous emission probability that can be increased, and the relaxation time reduced, by a factor [33]:

$$F_{\mathrm{p}} = 3Q\lambda^3/4\pi^2 V, \tag{5.9}$$

where V is the volume of the resonator. This result was obtained for the probability of spontaneous emission for nuclear magnetic moment transitions at radio frequencies when the Purcell factor F_{p} is scaled as the ratio of the cavity quality factor Q to volume V with a certain coefficient. There are a number of works where the analysis and calculation of the Purcell factor for a specific resonant structure with an emitter is carried out [15,34–40]. According to quantum theory [41], spontaneous emission occurs when an emitter relaxes from an excited state to its ground state by photon emission into an optical mode. The rate of this transition is determined by the photonic density of states and the electric-field strength at the position of the emitter. The Purcell effect implies the resonator influence on the spontaneous emission rate of an emitter is observed in systems of different scales and configura-

tions. In particular, homogeneous and inhomogeneous broadenings result in much lower overall spontaneous emission rates than might be the case if all emitters exactly matched the cavity resonance. Therefore, when trying to manipulate spontaneous emission, it is important to control the number of optical modes and their spatial distribution with respect to the emitter [34].

An important feature of complex dielectric structures consisting of several elements, such as a resonator and an emitter, is the presence of a number of spectroscopic effects, including the coexistence of the Purcell effect and the Fano resonance [15,37–40]. The Fano resonance, with its nontrivial spectral dependence, can provide an additional degree of freedom for controlling the rate of spontaneous emission. Let us recall that the Fano resonance has a simple optical interpretation as the result of the interference of two waves corresponding to resonant states with different quality factors [10]. In the same way, a change of the emission rate of an emitter caused by an environment has a classical counterpart [15,35]. For the Purcell effect and the Lamb shift [42], which are usually discussed in the context of quantum electrodynamics, it is possible to find classical counterparts in photonics and explain their physics through the interference wave phenomenon. As an example, a waveguide in a planar photonic crystal with a side-coupled defect was considered, the coincidence of the results obtained on the basis of quantum and classical approaches was demonstrated, and their connection with the Fano resonance was revealed [15].

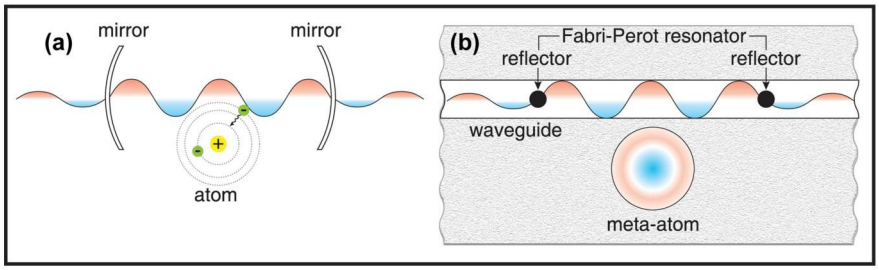

Figure 5.15. Schematic of quantum and classical systems demonstrating the Purcell effect and Lamb shift. In case (a), a quantum particle is placed into a resonator. In case (b), a photonic cavity is placed in a close proximity to a Fabry–Pérot resonator waveguide in a planar photonic crystal described by Maxwell's equations. *Adapted from: M.V. Rybin et al., Purcell effect and Lamb shift as interference phenomena, Sci. Rep. 6, 20599 (2016) [15].*

For a quantum particle (an atom) placed in the middle of a resonator (Fig. 5.15a), the quantum electrodynamics approach predicts two effects: Purcell effect and the Lamb shift [43]. The Lamb shift corresponds to a shift in the transition energy due to the

perturbation of stationary modes by the zero-vibrations of electromagnetic field. As a classical analogue of a quantum system, a microcavity is considered, which is called a meta-atom instead of a quantum particle, Fig. 5.15b. Two subsystems are considered, namely, a low-Q Fabry–Pérot resonator associated with a pair of partially reflecting defects, and a meta-atom characterized by a narrow Lorentzian spectrum. The transmission spectrum of such a classical structure is calculated using the transfer matrix approach and, after mathematical transformations, the transmission intensity is represented in the form of the Fano formula [15]:

$$T = \left| \frac{1 - r^2}{r^2 e^{ikd} - e^{-ikd}} \right|^2 \frac{(q + \Omega)^2}{1 + \Omega^2}, \tag{5.10}$$

where $\Omega = (\omega - \omega_c)/\gamma_c$ is the dimensionless frequency, $q = -2r \times \sin\delta/(1 - r^2)$ is the Fano parameter, r is the reflection coefficient, $k = \omega/c$ is the wavenumber, d is the Fabry–Pérot resonator length. Eq. (5.10) shows that the transmission intensity is determined by two terms. The first term defines the transmission in the absence of the meta-atom (only the Fabry–Pérot resonator), and the second term describes the interaction with the meta-atom through the Fano interference.

Fig. 5.16 shows the dependencies of the Purcell factor F_p, the Lamb shift Δ_c/γ_0 and the Fano parameter q on the length of the Fabry–Pérot resonator d (distance between reflectors), obtained on the basis of the analytical theory (the curves) and numerical calculations (the dots). As seen, the results of ab-initio calculations are in good agreement with the analytical data. An important result of the analytical theory is the discovery of a linear relationship between the Purcell factor and the Lamb shift, in which the proportionality factor is the Fano parameter:

$$\Delta_p = q \cdot F_\mathrm{p}. \tag{5.11}$$

The role of the parity of the Fabry–Pérot resonator modes was also established. Note that the sequence of maximum values of the Purcell factor (Fig. 5.16b) corresponds to the Fano parameter $q = 0$ (Fig. 5.16d), which determines the maximum of the symmetrical transmission band of the even Fabry–Pérot modes (Eq. (5.10), Fig. 5.16a). Even Fabry–Pérot modes correspond to a strong Lamb shift and larger values of the Purcell factor (short lifetime) due to a large local density of states and a larger overlap integral since both modes are even. Odd Fabry–Pérot modes correspond to a small Lamb shift and Purcell factor less than unity (low decay rate), Fig. 5.16.

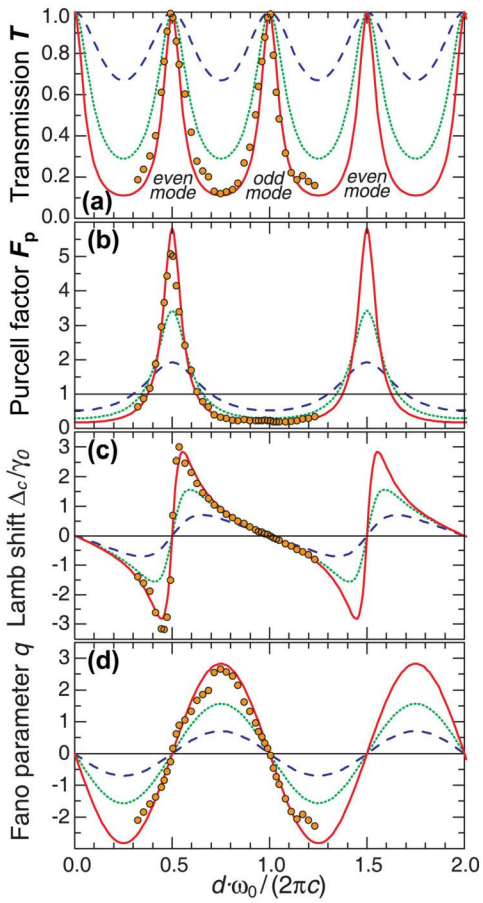

Figure 5.16. Photonic properties of the resonant dielectric structure with the side-coupled defect depending on the length of the Fabry–Pérot resonator d. (a) Transmission intensity, (b) Purcell factor F_{p}, (c) Lamb shift, (d) Fano parameter. Curves are calculated depending on the square of the reflection coefficient $r^2 = 0.1$ (dashed blue), $r^2 = 0.3$ (dotted green), and $r^2 = 0.5$ (solid red) on the basis of analytical theory, dots are the result of numerical calculations. ω_0 is the resonant frequency of the defect mode. *Adapted from: M.V. Rybin et al., Purcell effect and Lamb shift as interference phenomena, Sci. Rep. 6, 20599 (2016) [15].*

Optical phenomena associated with the coexistence of the Fano resonance and the Purcell effects have been studied in dielectric structures formed by the same elements, such as dimers and oligomers. In particular, the near-field enhancement of dielectric homodimers (a dimer consisting of two identical subunits) and oligomers composed of high-refractive-index spherical particles has been theoretically studied [38]. Figs. 5.17a,c present

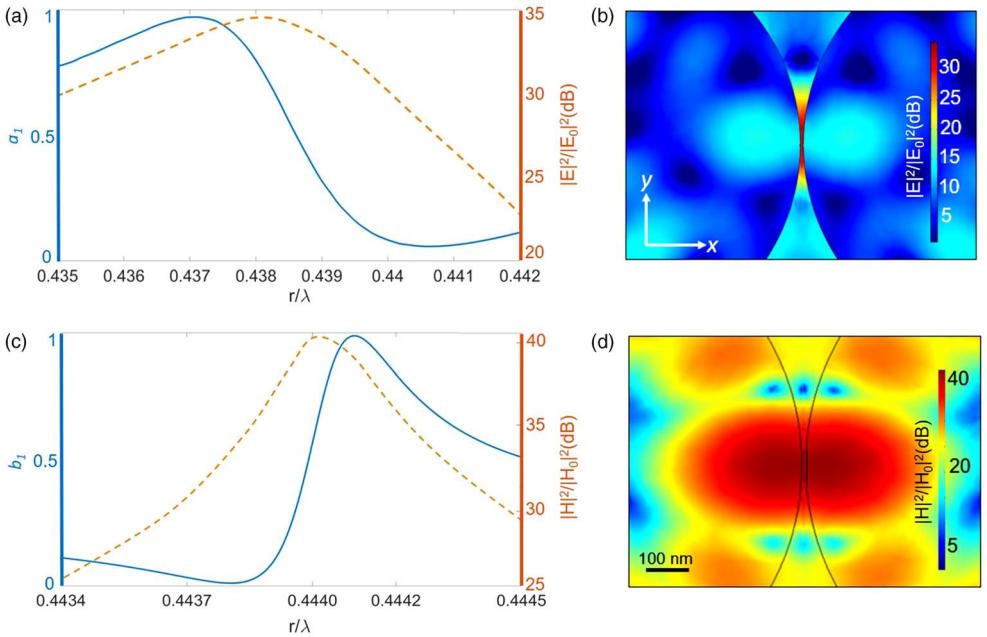

Figure 5.17. (a) Normalized electric dipole, a_1, contribution of the dimer (blue curve) and electric field intensity enhancement (orange curve) in the middle of the gap. (b) Zoom of the electric field intensity enhancement (dB scale) for a homodimer with $r/\lambda = 0.4383$. (c) Normalized magnetic dipole, b_1, contribution of the dimer (blue curve) and magnetic field intensity enhancement (orange curve) in the middle of the gap. (d) Zoom of the magnetic field intensity enhancement (dB scale) for a homodimer with $r/\lambda = 0.444$. *Reproduced with permission from: D. Rocco et al., Giant electric and magnetic Purcell factor in dielectric oligomers, JOSA B. 37, 2738 (2020) [38].*

the normalized electric dipole in the spheres, a_1, and magnetic dipole contribution, b_1, by changing r/λ for a fixed gap between the spheres $g/\lambda = 0.0645$ for the two orthogonal pump excitations. A strong electric or magnetic field enhancement is associated with a Fano-like resonance of the electric or magnetic dipole coefficient, respectively. The normalized radius at which Fano resonance occurs coincides with the maximum of field enhancement. The interference of the incident light and re-emitted light creates a complex near-field pattern and results in either strong enhancement (constructive interference) or strong suppression (destructive interference) of the electromagnetic field.

For the homodimer (Fig. 5.17), in the case of spheres with a gap of 10 nm and $r/\lambda = 0.4383$ excited by an electric point dipole polarized along the x axis and placed in the middle of the gap, electric Purcell factor achieves the maximum value of 1256. In the case of a magnetic dipole, the magnetic Purcell factor achieves the record value of 3250 for $r/\lambda = 0.444$.

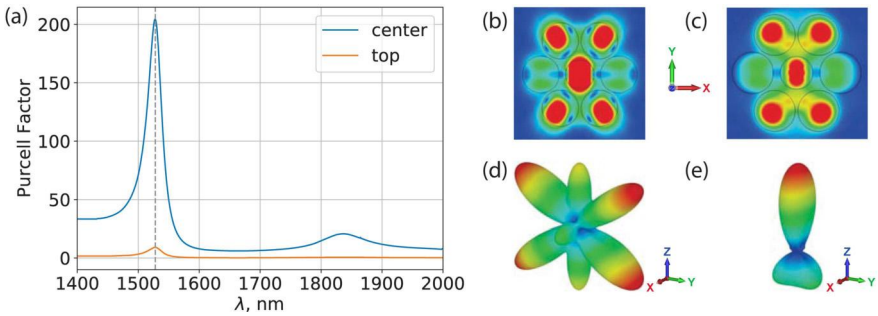

Figure 5.18. (a) Numerically calculated Purcell factor showing the shape of the Fano line for a silicon oligomer (heptamer, gray insert) for two positions of the magnetic dipole: in the center (the blue Fano line) and 20 nm from the top surface of the central nanocylinder (the orange line). The gray dashed line is the standard telecommunication wavelength (1540 nm). The magnetic field distribution and directivity patterns for the dipole placed in the center (b, d) and 20 nm from the top surface (c,e). *Adapted with permission from: V. Yaroshenko et al., Purcell effect control in oligomer based active nanoantenna for the near-IR wavelength range, AIP Conf. Proceedings 2300, 020133 (2020) [39].*

The theoretical study of four types of oligomers (tetramer, pentamer, hexamer, and heptamer) made of silicon nano-cylinders are presented in Ref. [39]. For the heptamer, a Fano resonance is observed on the wavelength of 1540 nm. When estimating the Purcell factor, it was taken into account that there are no losses in silicon in the wavelength range from 1400 to 2000 nm, therefore the radiative Purcell factor is equal to the total Purcell factor, and the following equation was used [35]:

$$F_{\mathrm{p}} = P/P_0, \tag{5.12}$$

where P is the power radiated by a dipole in the presence of the oligomer and P_0 - in the absence of the oligomer. In calculations, a 10 nm dipole was placed in the center of the oligomer along the Y axis. For the heptamer, the highest Purcell factor of 200 was obtained (Fig. 5.18a). For other cases, the Purcell factor is 2-3 times lower and demands additional optimizations of geometrical parameters to tune the resonance on the wavelength of 1540 nm. The shift of the dipole close to the surface of the central nanocylinder along the z-axes causes a dramatic decrease of the Purcell factor to the value of 10 and changes the directivity pattern, Fig. 5.18b-e.

The study of the Purcell effect and Fano resonance is not limited to photonic structures. An instructive example is provided by mechanical modes in optomechanical resonators [37]. There are analogies between optics and mechanics, where the equations for acoustic waves are given in terms of pressure and velocity fields [44], rather than electromagnetic fields for optics. Note that optomechanical structures can support coupling between mechan-

ical and optical modes, offering a wide range of applications in optomechanics [45].

For optomechanical resonators, a quasi-normal-mode theory of mechanical open-cavity modes was developed and the importance of using a complex effective mode volume and the phase of the quasi-normal mode was demonstrated [37]. The normal-mode theories of the elastic Purcell factor were generalized, and a striking example of coupled quasi-normal modes leading to a pronounced Fano resonance was demonstrated. The theory is exemplified by full three-dimensional calculations of optomechanical beams, but the general findings apply to a wide range of mechanical cavity modes. To validate the theory, an analytical Green function expansion was performed using quasi-normal modes with the Purcell elastic factor expression, and excellent agreement was obtained with numerical simulations for 3D optomechanical beams. The elastic Purcell factor evaluated at the resonant mode Ω_{m} at the source point $\mathbf{r}_0$ can be written as:

$$F_{\mathrm{p}}(\mathbf{r}_0) = \eta_{\mathrm{n}} \frac{6\pi\,\Omega_{\mathrm{m}}}{\Omega_{\mathrm{m}}^3 \alpha\, V_{\mathrm{eff,m}}(\mathbf{r}_0)}, \tag{5.13}$$

in which it is assumed that the Green function's response is dominated by a single mode, and the response is on-resonance $\Omega = \Omega_{\mathrm{m}}$. Here η_{n} is a numerically determined constant to account for elastic anisotropy of the medium; $\alpha = 0.5 v_l^{-3} + v_s^{-3}$ where v_l and v_s are the scalar longitudinal and shear speed of sound in the material; $V_{\mathrm{eff,m}}$ is the real part of the effective mode volume. Eq. (5.13) is the elastic Purcell factor evaluated at the resonant mode Ω_{m} at the source point.

Fig. 5.19 shows the results of numerical calculations for a 3D optomechanical beam for coupled quasi-normal modes. The crystal beam consists of a five-hole and a three-hole cavities separated by 4 µm. According to the calculations, two resonant quasi-normal modes are close in frequency with the spectral overlap. The first QNM 1 (Fig. 5.19a) with eigenfrequency $\Omega/2\pi = 5.172 - i0.012$ GHz and quality factor $Q_1 = 216$, is dominated by the three-hole cavity. The second QNM 2 (Fig. 5.19b, $\Omega/2\pi = 5.171 - i0.002$ GHz) with a higher quality factor $Q_2 = 1293$ is dominated by the five-hole cavity. The closeness of the frequencies of two modes with different Q leads to a striking Fano resonance that results in an interference effect in the total decay rate, Fig. 5.19d.

The presented analysis should serve as a reliable and valuable tool for understanding and developing emerging optomechanical technologies.

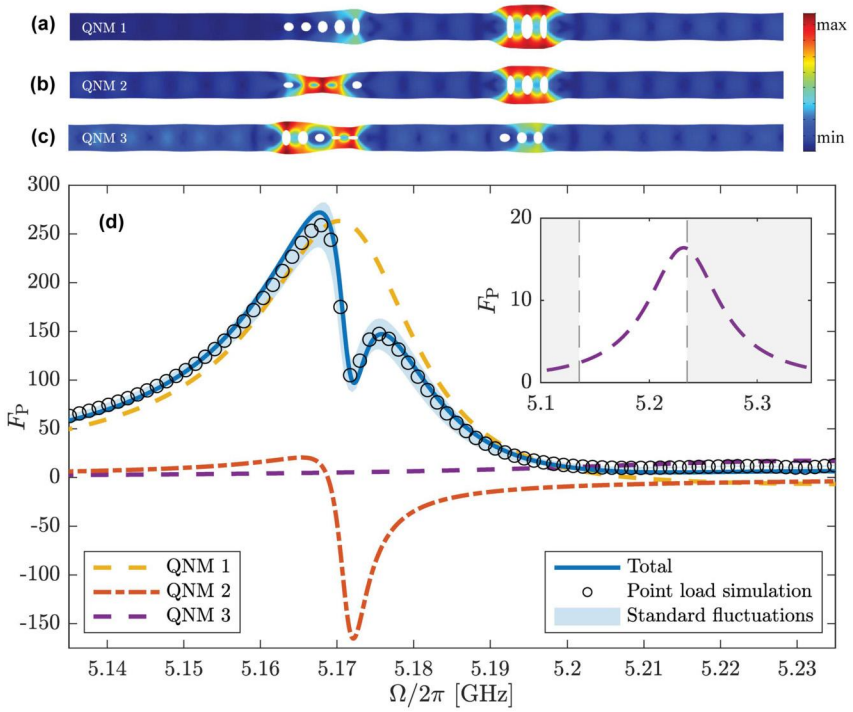

Figure 5.19. The Fano resonance in the total decay rate. (a-c) Three quasi-normal mode profiles of an optomechanical crystal beam. (d) Elastic Purcell factor simulation with a three-mode approximation of the total decay rate (using an isotropic material approximation $\eta_n = 1$). Contributions from each individual mode are shown with dashed lines. The inset shows a clearer view of quasinormal modes 3 (c), where the unshaded region indicates the frequency range of the main plot. *Adapted from: A.-W. El-Sayed and S. Hughes, Quasinormal-mode theory of elastic Purcell factors and Fano resonances of optomechanical beams, Phys. Rev. Res., 2, 043290 (2020) [37].*

5.5 Dynamical scattering effects at the Fano resonances

Like other resonant effects, Fano resonances have some response when the excitation signal changes. As already shown in the previous sections of this chapter, the Fano resonance has been observed in a wide range of different physical systems, and the same should be true for *dynamic Fano resonances* (DFRs).

It is noteworthy that autoionization processes in noble gasses have dominated the pioneering work on Fano resonances for more than 80 years. In 1935, U. Fano published his pioneering work on the theoretical interpretation of the absorption spectra of Ar, Kr, and Xe [1]. In 1961, a seminal paper presented the results of fitting the shape of the He resonance observed in inelastic

electron scattering, Fig. 5.10a [2]. Recently, the next key step has been taken: the experiments demonstrating the dynamics of the shaping of a Fano contour in the time domain were published in 2016 [46]. To measure the time-dependent formation of the Fano resonance in He, a transient buildup of the 2s2p doubly excited state was observed using the extreme ultraviolet (XUV) absorption spectroscopy. Monitoring the formation of the Fano lineshape was achieved by rapidly terminating the coherent dipole response of the He atom via saturated strong-field ionization by using an intense near-infrared (NIR) laser pulse. Upon excitation, the XUV pulse triggers the dynamic buildup of the Fano resonance, while the time-delayed NIR pulse depletes the autoionization level and ends the buildup process of the Fano spectral line. The evolution of the Fano line shape in real time was tracked due to the change in the time delay between the XUV and NIR pulses with subfemtosecond precision. Thus, the possibility of dynamic control of the shape of the Fano line in the absorption spectrum was demonstrated experimentally [46].

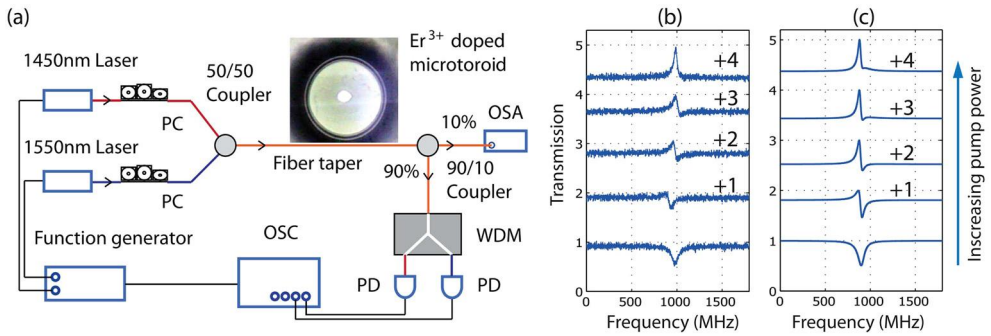

Figure 5.20. (a) Experimental setup and (b) normalized transmission spectra obtained from experiments and (c) numerical simulations at different powers of pump laser. The spectra are shifted as shown in the figure. The scanning speed and the power of probe laser were 1.2 THz/s and 1 μW, respectively. From bottom to top, the pump power was set at 0, 5, 20, 50 and 100 μW. *Adapted with permission from: F. Lei et al., Dynamic Fano-like resonances in erbium-doped whispering-gallery-mode microresonators, Applied Physics Letters, 105(10), 101112 (2014) [47].*

The DFR can also be observed in dielectric particles, for example, in a microtoroidal resonator with a diameter of 90 μm fabricated from Er^{3+} - doped sol-gel silica film on a silicon wafer [47]. Fig. 5.20a depicts schematics of the experimental setup. Two tunable lasers with an external cavity were used to create the DFR: one in the 1450 nm band and another in the 1550 nm band, where the first laser is a pump and the second one is a probe laser. To achieve stable pumping, the pump laser frequency was thermally locked to a resonant mode at 1434.6 nm, and the probe laser was continuously scanned to obtain transmission spectra around

a mode at 1538.2 nm. While the pump laser excites the erbium ions to a metastable state, the probe laser knocks down ions from the metastable state, decreasing the population of excited ions in the metastable state. Note that erbium ions emit photons in the 1550 nm band when pumped with a light in the 1450 nm band.

However, the population of the metastable state is changed by changing the power of the pump laser. Thus, a Lorentzian dip is observed at zero pumping. As the pump laser power is increased from 0 to 100 μW, a transition from the Lorentzian dip (0 μW) to the Lorentzian peak (100 μW) with intermediate Fano contours is observed in the transmission spectrum of the probe laser, Fig. 5.20b. There is a competition between the pump and probe lasers. As a result, as the pump power is increased, the transmission spectra exhibit a transformation from the Lorentzian dip to all intermediate asymmetric Fano contours and further to the Lorentzian peak at saturation. Moreover, such an evolution can be observed when changing the scanning speed in the frequency domain or changing the power of the probe laser. In the case of an increase in the power of the probe laser, the mechanism described above is valid. If the probing laser power is much less than the pump power, then a Lorentz peak is observed in the transmission spectrum, and with increasing power it gradually takes the Fano contour shape, and eventually transform into a Lorentz dip. In another case, when the scan speed is increased, the probe does not stay on-resonance long enough to cause a significant decrease in gain so the pump can provide enough gain to transform the Lorentzian dip into a Lorentzian peak.

DFRs can be also observed in the scattering by single dielectric particles [48], for example, in Mie scattering of a time-modulated, linearly polarized plane electromagnetic wave on a circular cylinder. For instance, consider a cylinder irradiated by a TE-polarized electromagnetic wave with a wave vector k perpendicular to the cylinder axis and a vector **E** oscillating in the base plane of cylinder, Fig. 5.21a. To study transient effects, let us to consider a square incident pulse, which duration is much longer than the transition time to a stationary process. This choice is due to the desire to separate the transient processes occurring at the beginning and at the end of the incident electromagnetic wave pulse.

The stationary problem of electromagnetic wave scattering on a cylinder of radius R has an exact solution [49]. In this case, the solution is represented as an infinite series of multipole contributions. In TE polarization, the field (with time dependence $\exp(-i\omega t)$) is described by two well-known coefficients: a_l and d_l, which correspond to the field outside and inside the cylinder, respectively [49]. Ordinary calculations lead to the following expres-

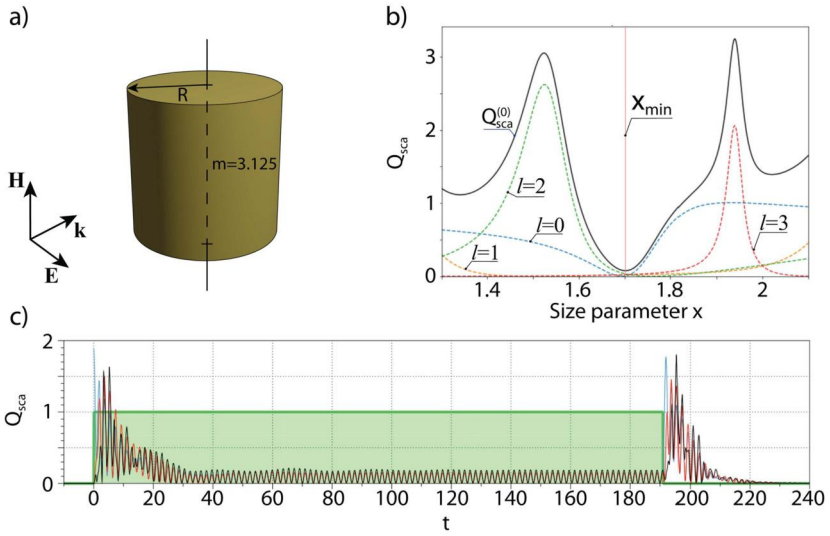

Figure 5.21. Dynamic scattering on a cylinder. a) The orientation of the cylinder and an incident TE-linearly polarized plane electromagnetic wave. b) The spectrum of the total scattering efficiency (black line) and the first four partial modes (colored lines) as a function of the dimensionless size parameter x. The corresponding indices of partial contributions are signed in the figure. c) Dynamics of the scattering efficiency of a cylinder, under the condition of destructive Fano resonance ($x = x_{min} = 1.702$). The black line is the numerical results, the blue line obtained from the temporal coupled-mode theory, and the red one obtained using the harmonic oscillators method. *Adapted with permission from: M.I. Tribelsky, A.E. Miroshnichenko, Two tractable models of dynamic light scattering and their application to Fano resonance, Nanophotonics, 10, 4357-4371 (2021) [48].*

sions [50]:

$$Q_{sca} = Q_{sca}^{(0)} + Q_{sca}^{(osc)} = \sum_{l=-\infty}^{\infty} \left[Q_{sca(l)}^{(0)} + Q_{sca(l)}^{(osc)} \right],$$
$$Q_{sca(l)}^{(0)} = \frac{2}{x} |a_l|^2; \quad Q_{sca(l)}^{(osc)} = -\frac{i}{x} \left[a_l^2 e^{2i(kr-\omega t)} - c.c. \right], \tag{5.14}$$

where l is the order of the multipole (dipole, quadrupole, etc.). $Q_{sca}^{(0)}$ is the conventional scattering efficiency, $Q_{sca}^{(osc)}$ is an additional zero-mean term that rapidly oscillates in time and space and lies in the far field $kr \gg 1$. The coefficients are interconnected by the identity relation:

$$a_l \equiv a_l^{PEC} - \frac{J_l'(mx)}{H_l^{(1)'}(x)} d_l, \qquad a_l^{PEC} \equiv \frac{J_l'(x)}{H_l^{(1)'}(x)}, \tag{5.15}$$

where $x = kR$, m is a refractive index of a cylinder. For Fano resonances in light scattering by a cylinder, a_l^{PEC} plays the role of the

background component, and $\frac{J_l'(mx)}{H_l^{(1)'}(x)}d_l$ plays the role of the resonant one.

To clearly distinguish stationary scattering from transient, it is necessary to find such x and m, so that:

1. Partial modes exhibited destructive Fano interference.
2. Value $\left|a_l^{PEC}\right|^2$ was as large as possible, which should correspond to the beginning of scattering, when resonances have not been excited yet.
3. The contribution of non-resonant multipoles to total scattering should be minimal.

Considering the NIR range of the spectrum, it is possible to choose $m = 3.125$, which corresponds to the refractive index of such semiconductors as Si, GaAs, and GaP. For chosen refractive index m, a good choice would be $x = x_F \cong 1.702$. This corresponds to the minimum of $Q_{sca}^{(0)} = \sum Q_{sca(l)}^{(0)} = 0.076$, which is due to turning to zero the first four partial modes: $Q_{sca(0)}^{(0)}$ and $Q_{sca(l)}^{(0)} + Q_{sca(-l)}^{(0)}$ for $l \neq 0$ (Fig. 5.21b). When a_0 and a_2 are replaced by the corresponding a_l^{PEC}, the value of $Q_{sca}^{(0)} = 1.290$. Thus, the criteria are fulfilled.

For the modulation of the incident electromagnetic radiation, it is necessary to turn to one of the modeling approaches based on time-dependent differential equations: the harmonic oscillators method or the temporal coupled-mode theory. Both models can be successfully used for characterization and show good accuracy (Fig. 5.21c).

The first spike is explained by the rapid excitation of non-resonant modes, while the resonant ones are not yet excited yet (as in the case of replacing a_l with a_l^{PEC}, a large scattering value $Q_{sca}^{(0)}$ was obtained). Thus, the spike amplitude is determined by the amplitudes of the non-resonant modes. Gradually, resonant modes are excited and destructive Fano interference turns on, the scattering passes into a stationary mode. In the second case, the non-resonant components decay rapidly, while the resonant components still retain their stationary amplitudes. Thus, the second spike is determined by the output of the resonant components. The stepped shape of the incident electromagnetic pulse is chosen for simplicity, the phenomenon remains the same for any rapidly changing (compared to the reciprocal width of the resonant components) pulse shape. Thus, DRF can be detected in a wide range of physical systems, many of which are yet to be explored.

5.6 Fano resonance in metasurfaces

Metasurfaces have been the subject of intensive research in the last decade, since these compact objects can be used to effectively manipulate light beams and obtain a wide range of optical characteristics. Metasurfaces based on dielectric resonators were introduced to overcome the ohmic losses characteristic of metal element metasurfaces. An important step in the design of all-dielectric metasurfaces was the creation of structures with Fano resonances or electromagnetically induced transparency [51–54]. Such structures have intense narrow optical resonances and further expand the possibilities of their application [9].

A number of all-dielectric metasurfaces with Fano resonances have been created, in which the structural elements support both "bright" and "dark" resonances. The incident optical field is directly couples to the bright resonance. With the right design, it is possible to introduce a weak coupling between the two resonances, and as a result of the interference, Fano resonances arise, which can be tuned over a wide spectral range.

In a short review, it is impossible to describe in detail, or even simply list, all currently known areas of creation, research, and application of metasurfaces. We will start with a discussion of structural coloration, an interference phenomenon where colors emerge when visible light interacts with a nanostructured material, which can be a metasurface formed by metallic [55] or dielectric [56] elements. These papers describe structures in which structural colors are generated due to Fano resonance, which is a result of interference between the broad resonance of the individual nanoantenna and the sharp lattice resonance of the array. In Ref. [56], all-dielectric metasurfaces formed by a periodic set of high-index silicon nanoantennas in the form of a rod on glass and elastic polydimethylsiloxane substrates were created. The Fano resonance maxima predicted in the calculations were observed in the reflection spectra with a weak angular dependence. In addition, dynamical color control was achieved by isotropically stretching the elastic substrates with the fabricated Fano structure, resulting in a shift of reflection peaks in agreement with simulation.

A significant area in the study of Fano-metasurfaces is occupied by works that use great flexibility in manipulating the shape of the Fano contour for enhancement and controlling light-matter interaction. Of particular interest are the effects in the spectral region of frequency $\Omega = -q$, where the object becomes nonradiating, $\sigma(E) = 0$, as follows from Eq. (5.1) due to destructive interference in the far field. Nonradiative energy sources, such as photonic bound states in the continuum, have recently attracted

much attention due to the possibility of effectively localizing high-intensity electromagnetic fields in small volumes of matter [57]. Note that a close connection between Fano resonances and bound states in the continuum excited in trapezoidal dielectric nanodisks has recently been experimentally demonstrated [58], which once again emphasizes the potential of Fano devices for applications in nanophotonics.

A striking example of the effects determined by the light-matter interaction is the all-dielectric Fano-metasurface, which demonstrates over three-orders photoluminescence enhancement [59]. The metasurface consists of a periodic lattice of asymmetric air holes in a Si-on-insulator slab, embedded with four layers of self-assembled Ge quantum dots (Fig. 5.22). The asymmetric air hole is composed of a semicircle and a semiellipse, and the hole is etched through the top layer of the structure. Symmetry breaking of the dielectric metasurface due to the asymmetric shape of air holes leads to the appearance of Fano resonances arising due to destructive interference of antiphased electric or magnetic dipoles and collective coherent oscillations. High-Q Fano resonances with an asymmetric line shape are clearly visible in Fig. 5.22b. The presence of the Fano-metasurface leads to a significant intensity enhancement as well as spectral narrowing of the Ge quantum dots photoluminescence. The gain estimate is given by the ratio of photoluminescence intensity of the quantum dots coupled into the metasurface to the photoluminescence collected from unstructured regions of the wafer (gray area in Fig. 5.22c). The intensity of the M_{M1} peak is enhanced by a factor of up to 1097, and the FWHM of M_{M1} is only 1.28 nm, Fig. 5.22b. The Fano-amplification mechanism is confirmed by the coincidence of the resonant photoluminescence peak in frequency with the midpoint of the Fano-shaped dip in the transmission spectrum, where the best suppression of antiphased dipole radiation is achieved.

Another field of study of Fano-metasurfaces, related to the resonance-induced electromagnetic field enhancement, is the topic of small-scale nonlinear photonics and higher harmonic generation [54,60–63]. For nanoscale metasurfaces, phase matching is not required, and the generation of n-th order harmonic is proportional to the integration of induced electric dipoles over the volume of the unit cell of the metasurface [60]:

$$\mathbf{P}^{(n)} \propto \int_V \chi^{(n)} \left[\mathbf{E}_{\text{loc}}(\mathbf{r}, \omega)\right]^n \mathrm{d}V, \tag{5.16}$$

where $\chi^{(n)}$ is the intrinsic n-th order nonlinear susceptibility, $\mathbf{E}_{\text{loc}}(\mathbf{r}, \omega)$ is the local electric field, and V is the volume of a unit

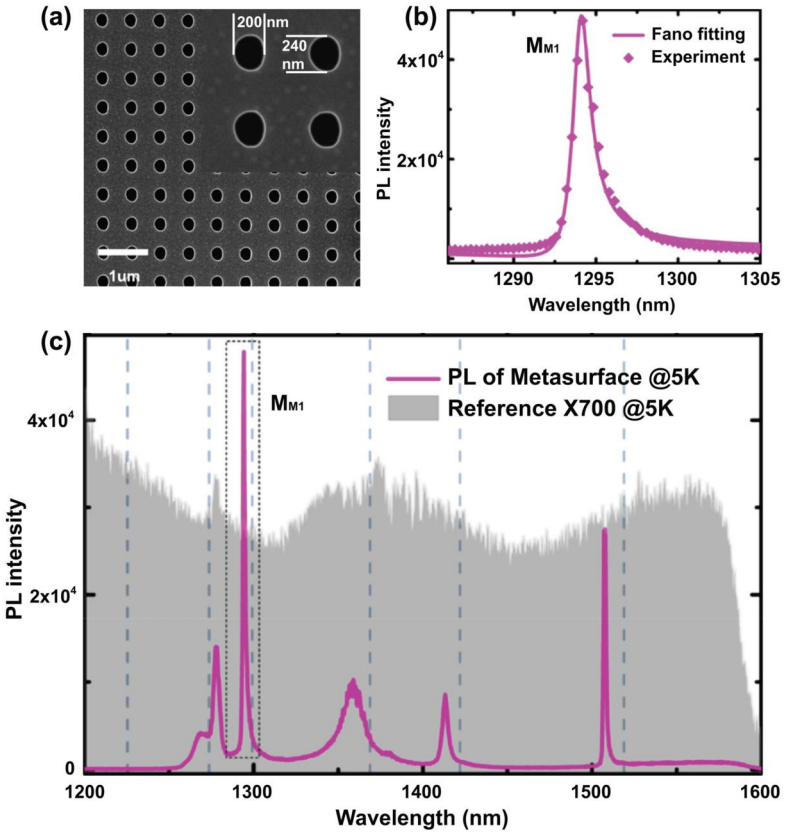

Figure 5.22. Strong photoluminescence enhancement in all-dielectric Fano metasurface. (a) Scanning electron microscope image of a fabricated metasurface. Inset: Enlarged image of four unit cells. (b) Fano fitting of the peak M_{M1} (solid line) at 1294 nm. (c) Photoluminescence spectra of the fabricated sample at 5°K. Photoluminescence spectrum of bare Ge quantum dots in pattern-free region at 5°K is indicated by the light gray area and magnified by 700 times. *Adapted with permission from: S. Yuan et al., Strong photoluminescence enhancement in all-dielectric Fano metasurface with high quality factor, ACS Nano, 11, 10704 (2017) [59].*

cell. As an example, localized surface plasmon resonances can be utilized to substantially enhance $\mathbf{E}_{\text{loc}}(\mathbf{r}, \omega)$ by efficiently tunneling light from the far-field to a deep subwavelength scale.

For all-dielectric structures, the near field of the Fano-metasurface can be enhanced due to the destructive interference of resonant and non-resonant modes, which leads to enhanced light-matter interaction and nonlinear effects. Fig. 5.23a shows a schematic of a Fano nonlinear all-dielectric metasurface consisting of a periodical array of rod resonators Si (blue) supporting the

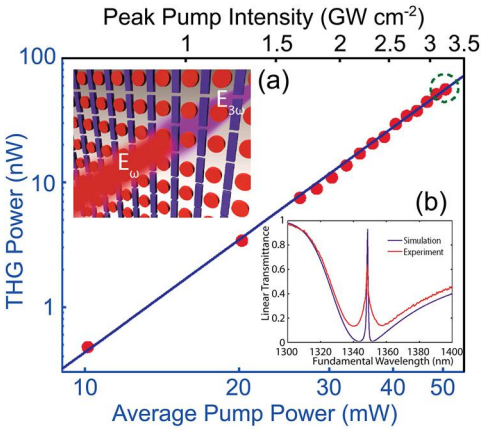

Figure 5.23. Nonlinear Fano-resonant all-dielectric metasurface. Log-log plot of the third harmonic power as a function of the pump power and the peak pump intensity with illumination by an optical parametric oscillator. The red circles indicate the measured data, and the blue line is a numerical fit to the data. The inset (a) shows a schematic of Fano nonlinear metasurface. The inset (b) shows simulated (blue) and experimentally measured (red) transmittance spectra of the metasurface. *Adapted with permission from: Y. Yang at al., Nonlinear Fano-resonant dielectric metasurfaces, Nano Lett. 15, 7388 (2015) [60].*

bright mode and Si resonant nanodisks (red) supporting the dark mode. Their combination realizes a Fano metasurface with measured third-harmonic generation enhancement factor of 1.5×10^5 with respect to an unpatterned silicon film and an absolute conversion efficiency of 1.2×10^{-6} with a peak pump intensity of $3.2\,\mathrm{GW\,cm^{-2}}$ [60].

Fig. 5.24 demonstrates another example of third harmonic generation in a dielectric Fano metasurface [61]. The metasurface consists of a square array of symmetric clusters of four a-Si:H nanodisks supporting high-quality collective modes associated with the magnetic Fano resonance. The pronounced Fano dip near $1.34\,\mu\mathrm{m}$ originates from the destructive far-field interference of two A_{2g} modes (magnetic and electric) strongly coupled through the near-field interaction. The A_{2g} magnetic mode is formed by four magnetic dipoles co-oriented out of the sample plane, and the A_{2g} electric mode is constructed by electric dipoles excited in the plane, which constitute a circular displacement current over the four disks, Fig. 5.24b. Generation of the third harmonic from quadrumeric clusters is achieved due to the strong Fano-localization of the field inside the nanodisks and the high third-order nonlinear susceptibility $\chi^{(3)}$ of a-Si:H.

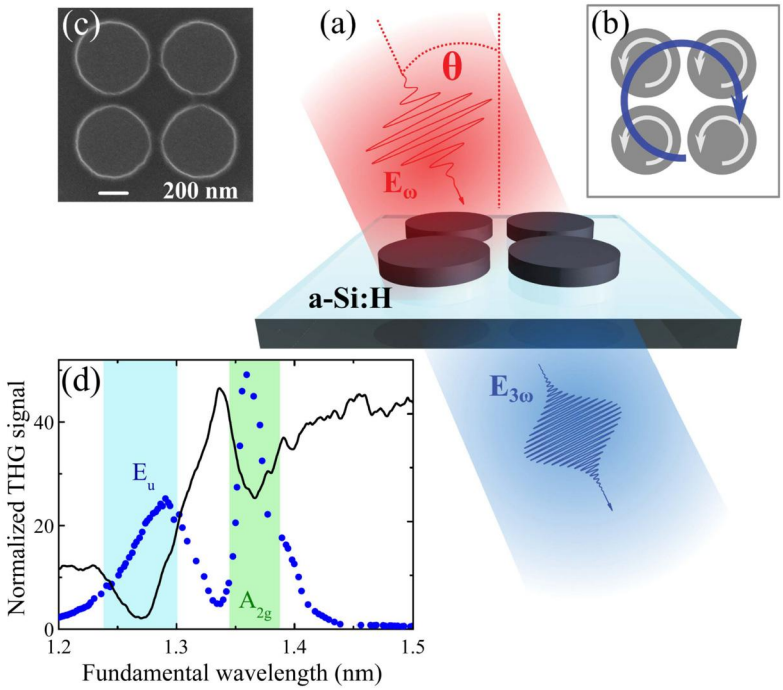

Figure 5.24. The resonant third-harmonic generation in silicon quadrumers metasurfaces. (a) Quadrumers are excited by an oblique plane wave in the vicinity of the magnetic dipole resonance. (b) Origin of the magnetic Fano resonance in quadrumers: interference of two A_{2g} modes. (c) SEM image of the cluster of four a-Si:H nanodisks. (d) Experimental transmission (black line) and third harmonic generation spectra (blue dots) of the sample for the incident angle of 45 degrees. *Adapted with permission from: A.S. Shorokhov et al., Multifold enhancement of third-harmonic generation in dielectric nanoparticles driven by magnetic Fano resonances, Nano Lett. 16, 4857 (2016) [61].*

The idea of using a dielectric Fano-metasurface for image processing and edge detection was implemented in Ref. [64]. It should be noted that the optical computing dates back to the 1960s and pioneering work that used the concepts of Fourier optics [65,66]. Unfortunately, these solutions require bulky optical components that cannot be integrated into a modern nanophotonic system. Computing metasurfaces can benefit from the speed and low power consumption of optics, while still allowing on-chip integration.

Dielectric Fano metasurfaces that perform optical image edge detection in the analog domain using a subwavelength geometry that can be easily integrated with detectors have been created and investigated experimentally [64]. The metasurface consists of an

array of nanobeams, which perform spatial differentiation of the first or second order. The authors tailor the spatial dispersion of the metasurface by controlling the leaky modes guided along the surface. When the frequency and in-plane wave vector of incident light match one of these guided modes, an asymmetric Fano line shape appears in the transmission spectrum due to interference with the broad Fabry–Pérot resonance determined by the geometry of the metasurface. Due to Fano interference, the transmission ranges from 0 to 1 in a narrow bandwidth. The 2D image was also processed by performing the second derivative line by line.

The imaging function of a Fano-resonant metasurface formed by asymmetric silicon nanodisks with a circular notch cut from the edge and coated with a $Ge_2Sb_2Te_5$ layer is calculated and discussed [67]. $Ge_2Sb_2Te_5$ is a phase-change material with a significant difference in dielectric constants in the amorphous and crystalline phases [68]. When analyzing the transmission properties of the Si/GST metasurface, a 40×40 array was used to produce transmitted target images by selectively changing the $Ge_2Sb_2Te_5$ phase states in different units from amorphous and crystalline phases, which reconstruct the corresponding targets well. The results pave the way for imaging and spatial light modulation based on Fano-metasurfaces from phase-change materials.

We note a number of other interesting results obtained during the creation and study of all-dielectric Fano-metasurfaces [69–71]. The idea of broken symmetry is used in the design of a metasurface, consisting of a two-dimensional periodic array of split asymmetric silicon arcs on a silica substrate [69]. The maximum achieved spectral contrast of the Fano resonance peak is 99%. Such a metasurface is proposed for refractive index sensing with calculated sensitivity, Q-Factor and figure of merit of 324 nm/RIU, 8720 and 2465, respectively [70]. The Fano-metasurface, whose unit cell consists of a silicon elliptical disk and an elliptical ring, can also be used as a refractive index sensor with sensitivity and quality factor of up to 392 nm/RIU and 3001 [71].

Thus, breaking the symmetry of individual dielectric elements allows the creation of various Fano-metasurface configurations with promising prospects for various applications [9].

5.7 Summary

The number of publications on the study of the Fano resonance in various all-dielectric structures and their applications in practice is constantly increasing, so it can be assumed that devices based on the Fano resonance will play an increasingly important role in the near future. We are witnessing a gradual replacement of

electronic processing, transmission and storage of information by optical technologies. Dielectric structures with directional Fano resonances [72–74] can play an essential role in these processes. An analytical theory of spatial Fano resonances in antennas was developed, which describes the experimentally observed switching of the radiation pattern between the forward and reverse directions [73]. The Fano parameter q, which determines the shape of the radiation pattern, becomes spatially dependent in the case of a Fano antenna.

A fascinating technological challenge is the creation of devices for slowing down light. Slow light is important for all-optical tunable delays for routers and data synchronization, for optical buffering and switching, improved light-matter interaction and nonlinear effects, and for quantum networks [10]. It is believed that devices associated with the phenomenon of electromagnetically induced transparency, which is a particular case of the Fano resonance, will play an important role in the implementation of the slow light regime [75].

We also note the impressive growth of quantum technologies and informatics, a significant interest in the development of quantum networks [76]. Optical photons are convenient for transmitting information over large quantum networks, and atoms are physical systems capable of processing and storing information. One of the most promising methods to efficiently couple single photons with atomic media is cavity quantum electrodynamics [77], where the confinement of photons inside an optical resonator with a high Q factor can significantly improve the interaction with material systems [78]. When creating basic elements for quantum technologies, the properties of the optical resonator play one of the key roles. Among various systems, resonators are considered, in which one of the mirrors is characterized by the properties of the Fano resonance [79–81].

References

[1] U. Fano, Sullo spettro di assorbimento dei gas nobili presso il limite dello spettro d'arco, Nuovo Cimento, N. S. 12 (1935) 154–161 (in Italian).
[2] U. Fano, Effects of configuration interaction on intensities and phase shifts, Phys. Rev. 124 (6) (1961) 1866–1878.
[3] U. Fano, G. Pupillo, A. Zannoni, C.W. Clark, On the absorption spectrum of noble gases at the arc spectrum limit, J. Res. Natl. Inst. Stand. 110 (6) (2005) 583–587.
[4] J.-P. Connerade, A.M. Lane, Interacting resonances in atomic spectroscopy, Rep. Prog. Phys. 51 (1988) 1439–1478.
[5] A.E. Miroshnichenko, S. Flach, Y.S. Kivshar, Fano resonances in nanoscale structures, Rev. Mod. Phys. 82 (3) (2010) 2257–2298.

[6] B. Luk'yanchuk, N.I. Zheludev, S.A. Maier, N.J. Halas, P. Nordlander, H. Giessen, C.T. Chong, The Fano resonance in plasmonic nanostructures and metamaterials, Nat. Mater. 9 (9) (2010) 707–715.
[7] Y. Francescato, V. Giannini, S.A. Maier, Plasmonic systems unveiled by Fano resonances, ACS Nano 6 (2) (2012) 1830–1838.
[8] M.F. Limonov, M.V. Rybin, A.N. Poddubny, Y.S. Kivshar, Fano resonances in photonics, Nat. Photonics 11 (9) (2017) 543–554.
[9] E. Kamenetskii, A. Sadreev, A. Miroshnichenko (Eds.), Fano Resonances in Optics and Microwaves. Physics and Applications, Springer Series in Optical Sciences, vol. 219, Springer, 2018.
[10] M.F. Limonov, Fano resonance for applications, Adv. Opt. Photonics 13 (3) (2021) 703–771.
[11] C.W. Hsu, B. Zhen, A.D. Stone, J.D. Joannopoulos, M. Soljacic, Bound states in the continuum, Nat. Rev. Mater. 1 (2016) 1–13.
[12] A. Bogdanov, K. Koshelev, P. Kapitanova, M. Rybin, S. Gladyshev, Z. Sadrieva, K. Samusev, Y. Kivshar, M. Limonov, Bound states in the continuum and Fano resonances in the strong mode coupling regime, Adv. Photon. 1 (1) (2019) 016001.
[13] N. Solodovchenko, K. Samusev, D. Bochek, M. Limonov, Bound states in the continuum in strong-coupling and weak-coupling regimes under the cylinder - ring transition, Nanophotonics 10 (17) (2021) 4347–4355.
[14] A.E. Miroshnichenko, A.B. Evlyukhin, Y.F. Yu, R.M. Bakker, A. Chipouline, A.I. Kuznetsov, B. Luk'yanchuk, B.N. Chichkov, Y.S. Kivshar, Nonradiating anapole modes in dielectric nanoparticles, Nat. Commun. 6 (2015) 8069.
[15] M.V. Rybin, S.F. Mingaleev, M.F. Limonov, Yu.S. Kivshar, Purcell effect and Lamb shift as interference phenomena, Sci. Rep. 6 (2016) 20599.
[16] N. Solodovchenko, M. Sidorenko, T. Seidov, I. Popov, E. Nenasheva, K. Samusev, M. Limonov, Cascades of Fano resonances in light scattering by dielectric particles, Mater. Today 60 (2022) 69–78.
[17] Y.S. Joe, A.M. Satanin, C.S. Kim, Classical analogy of Fano resonances, Phys. Scr. 74 (2006) 259–266.
[18] M.I. Tribelsky, Linear and Nonlinear Evolution in Time and Space, RITS Lecture Notes Dec. 15.2014, The Research Institute for Time Studies Yamaguchi University, 2014, https://www.researchgate.net/publication/273693137_Linear_and_Nonlinear_Evolution_in_Time_and_Space.
[19] M.V. Rybin, M.F. Limonov, A.B. Khanikaev, C.M. Soukoulis, Optical properties of 1D disordered photonic structures, in: M.F. Limonov, R.M. De La Rue (Eds.), Optical Properties of Photonic Structures: Interplay of Order and Disorder, CRC Press, Taylor & Francis Group, Boca Raton, London, New York, 2012, pp. 9–22.
[20] A.N. Poddubny, M.V. Rybin, M.F. Limonov, Yu.S. Kivshar, Fano interference governs wave transport in disordered systems, Nat. Commun. 3 (2012) 914.
[21] P. Yeh, A. Yariv, C.-S. Hong, Electromagnetic propagation in periodic stratified media. I. General theory, J. Opt. Soc. Am. 67 (4) (1977) 423–437.
[22] M.V. Rybin, A.V. Baryshev, A.B. Khanikaev, M. Inoue, K.B. Samusev, A.V. Sel'kin, G. Yushin, M.F. Limonov, Selective manipulating the stop-bands in multi-component photonic crystals: opals as an example, Phys. Rev. B 77 (20) (2008) 205106.
[23] Y.A. Vlasov, V.N. Astratov, O.Z. Karimov, A.A. Kaplyanskii, V.N. Bogomolov, A.V. Prokofiev, Existence of a photonic pseudogap for visible light in synthetic opals, Phys. Rev. B 55 (20) (1997) R13357.
[24] Y.A. Vlasov, X.Z. Bo, J.C. Sturm, D.J. Norris, On-chip natural assembly of silicon photonic bandgap crystals, Nature 414 (2001) 289–293.

[25] C. López, Materials aspects of photonic crystals, Adv. Mater. 15 (20) (2003) 1679–1704.
[26] A.V. Baryshev, A.B. Khanikaev, M. Inoue, P.B. Lim, A.V. Sel'kin, G. Yushin, M.F. Limonov, Resonant behavior and selective switching of stop bands in three-dimensional photonic crystals with inhomogeneous components, Phys. Rev. Lett. 99 (6) (2007) 063906.
[27] R.K. Iler, The Chemistry of Silica, John Wiley & Sons, New York, 1979.
[28] A.A. Kaplyanskii, A.V. Baryshev, M.V. Rybin, A.V. Sel'kin, M.F. Limonov, Optical properties of low contrast opal-based photonic crystals, in: M.F. Limonov, R.M. De La Rue (Eds.), Optical Properties of Photonic Structures: Interplay of Order and Disorder, CRC Press, Taylor & Francis Group, Boca Raton, London, New York, 2012, pp. 249–274.
[29] M.V. Rybin, A.B. Khanikaev, M. Inoue, K.B. Samusev, M.J. Steel, G. Yushin, M.F. Limonov, Fano resonance between Mie and Bragg scattering in photonic crystals, Phys. Rev. Lett. 103 (2) (2009) 023901.
[30] S. John, Strong localization of photons in certain disordered dielectric superlattices, Phys. Rev. Lett. 58 (23) (1987) 2486–2489.
[31] M.V. Rybin, K.B. Samusev, I.S. Sinev, G. Semouchkin, E. Semouchkina, Yu.S. Kivshar, M.F. Limonov, Mie scattering as a cascade of Fano resonances, Opt. Express 21 (24) (2013) 30107–30113.
[32] M.I. Tribelsky, A.E. Miroshnichenko, Giant in-particle field concentration and Fano resonances at light scattering by high-refractive-index particles, Phys. Rev. A 93 (5) (2016) 053837.
[33] E.M. Purcell, Spontaneous emission probabilities at radio frequencies, Phys. Rev. 69 (11–12) (1946) 681.
[34] S. Noda, M. Fujita, T. Asano, Spontaneous-emission control by photonic crystals and nanocavities, Nat. Photonics 1 (8) (2007) 449–458.
[35] A.E. Krasnok, A.P. Slobozhanyuk, C.R. Simovski, S.A. Tretyakov, A.N. Poddubny, A.E. Miroshnichenko, Y.S. Kivshar, P.A. Belov, An antenna model for the Purcell effect, Sci. Rep. 5 (1) (2015) 12956.
[36] A. Zalogina, R. Saveliev, E.V. Ushakova, G. Zograf, P. Komissarenko, V. Milichko, S. Makarov, D. Zuev, I. Shadrivov, Purcell effect in active diamond nanoantennas, Nanoscale 10 (2018) 8721–8727.
[37] A.-W. El-Sayed, S. Hughes, Quasinormal-mode theory of elastic Purcell factors and Fano resonances of optomechanical beams, Phys. Rev. Res. 2 (4) (2020) 043290.
[38] D. Rocco, A. Lamprianidis, A.E. Miroshnichenko, C. De Angelis, Giant electric and magnetic Purcell factor in dielectric oligomers, J. Opt. Soc. Am. B 37 (2020) 2738–2744.
[39] V. Yaroshenko, A. Larin, E. Ageev, D. Zuev, Purcell effect control in oligomer based active nanoantenna for the near-IR wavelength range, AIP Conf. Proc. 2300 (2020) 020133.
[40] H.M. Doeleman, C.D. Dieleman, C. Mennes, B. Ehrler, A.F. Koenderink, Observation of cooperative Purcell enhancements in antenna-cavity hybrids, ACS Nano 14 (9) (2020) 12027–12036.
[41] R. Loudon, The Quantum Theory of Light, Oxford University Press, New York, 2000 (Chapter 2).
[42] W.E. Lamb, R.C. Retherford, Fine structure of the hydrogen atom by a microwave method, Phys. Rev. 72 (3) (1947) 241–243.
[43] A. Kavokin, J.J. Baumberg, G. Malpuech, F.P. Laussy, Microcavities, Oxford University Press, 2011.
[44] K.Y. Bliokh, F. Nori, Spin and orbital angular momenta of acoustic beams, Phys. Rev. B 99 (17) (2019) 174310.

[45] E. Verhagen, S. Deléglise, S. Weis, A. Schliesser, T.J. Kippenberg, Quantum-coherent coupling of a mechanical oscillator to an optical cavity mode, Nature 482 (2012) 63–67.
[46] A. Kaldun, A. Blättermann, V. Stooß, S. Donsa, H. Wei, R. Pazourek, S. Nagele, C. Ott, C.D. Lin, J. Burgdörfer, T. Pfeifer, Observing the ultrafast buildup of a Fano resonance in the time domain, Science 354 (6313) (2016) 738–741.
[47] F. Lei, B. Peng, S.K. Özdemir, G. Long, L. Yang, Dynamic Fano-like resonances in erbium-doped whispering-gallery-mode microresonators, Appl. Phys. Lett. 105 (10) (2014) 101112.
[48] M.I. Tribelsky, A.E. Miroshnichenko, Two tractable models of dynamic light scattering and their application to Fano resonance, Nanophotonics 10 (17) (2021) 4357–4371.
[49] C.F. Bohren, D.R. Huffman, Absorption and Scattering of Light by Small Particles, Wiley, New York, 2008.
[50] M.I. Tribelsky, A.E. Miroshnichenko, Dynamics of destructive Fano resonances, Phys. Rev. A 100 (5) (2019) 053824.
[51] H.-T. Chen, A.J. Taylor, N. Yu, A review of metasurfaces: physics and applications, Rep. Prog. Phys. 79 (7) (2016) 076401.
[52] H. Jeong, Y. Yang, H. Cho, T. Badloe, I. Kim, R.-M. Ma, J. Rho, Emerging advanced metasurfaces: alternatives to conventional bulk optical devices, Microelectron. Eng. 220 (2020) 111146.
[53] A. Krasnok, M. Krasnok, A. Tymchenko, A. Alù, Nonlinear metasurfaces: a paradigm shift in nonlinear optics, Mater. Today 21 (1) (2018) 8–21.
[54] B. Sain, C. Meier, T. Zentgraf, Nonlinear optics in all-dielectric nanoantennas and metasurfaces: a review, Adv. Photon. 1 (2) (2019) 024002.
[55] K. Kumar, H. Duan, R.S. Hegde, S.C.W. Koh, J.N. Wei, J.K.W. Yang, Printing colour at the optical diffraction limit, Nat. Nanotechnol. 7 (9) (2012) 557–561.
[56] Y. Shen, V. Rinnerbauer, I. Wang, V. Stelmakh, J.D. Joannopoulos, M. Soljačić, Structural colors from Fano resonances, ACS Photonics 2 (1) (2015) 27–32.
[57] K. Koshelev, G. Favraud, A. Bogdanov, Y. Kivshar, A. Fratalocchi, Nonradiating photonics with resonant dielectric nanostructures, Nanophotonics 8 (5) (2019) 725–745.
[58] E. Melik-Gaykazyan, K. Koshelev, J.-H. Choi, S.S. Kruk, A. Bogdanov, H.-G. Park, Y. Kivshar, From Fano to quasi-BIC resonances in individual dielectric nanoantennas, Nano Lett. 21 (4) (2021) 1765–1771.
[59] S. Yuan, X. Qiu, C. Cui, L. Zhu, Y. Wang, Y. Li, J. Song, Q. Huang, J. Xia, Strong photoluminescence enhancement in all-dielectric Fano metasurface with high quality factor, ACS Nano 11 (11) (2017) 10704–10711.
[60] Y. Yang, W. Wang, A. Boulesbaa, I.I. Kravchenko, D.P. Briggs, A. Puretzky, D. Geohegan, J. Valentine, Nonlinear Fano-resonant dielectric metasurfaces, Nano Lett. 15 (11) (2015) 7388–7393.
[61] A.S. Shorokhov, E.V. Melik-Gaykazyan, D.A. Smirnova, B. Hopkins, K.E. Chong, D.-Y. Choi, M.R. Shcherbakov, A.E. Miroshnichenko, D.N. Neshev, A.A. Fedyanin, Y.S. Kivshar, Multifold enhancement of third-harmonic generation in dielectric nanoparticles driven by magnetic Fano resonances, Nano Lett. 16 (8) (2016) 4857–4861.
[62] M.R. Shcherbakov, A.S. Shorokhov, D.N. Neshev, B. Hopkins, I. Staude, E.V. Melik-Gaykazyan, A.A. Ezhov, A.E. Miroshnichenko, I. Brener, A.A. Fedyanin, Y.S. Kivshar, Nonlinear interference and tailorable third-harmonic generation from dielectric oligomers, ACS Photonics 2 (5) (2015) 578–582.
[63] J.S. Ginsberg, A.C. Overvig, M.M. Jadidi, S.C. Malek, G.N. Patwardhan, N. Swenson, N. Yu, A.L. Gaeta, Enhanced harmonic generation in gases using an all-dielectric metasurface, Nanophotonics 10 (1) (2021) 733–740.

[64] A. Cordaro, H. Kwon, D. Sounas, A.F. Koenderink, A. Alù, A. Polman, High-index dielectric metasurfaces performing mathematical operations, Nano Lett. 19 (12) (2019) 8418–8423.
[65] L.J. Cutrona, E.N. Leith, L.J. Porcello, W.E. Vivian, On the application of coherent optical processing techniques to synthetic-aperture radar, Proc. IEEE 54 (8) (1966) 1026–1032.
[66] R. Athale, D. Psaltis, Optical computing: past and future, Opt. Photonics News 27 (6) (2016) 32–39.
[67] C. Zhou, X. Qu, S. Xiao, M. Fan, Imaging through a Fano-resonant dielectric metasurface governed by quasi-bound states in the continuum, Phys. Rev. Appl. 14 (4) (2020) 044009.
[68] D.V. Bochek, N.S. Solodovchenko, D.A. Yavsin, A.B. Pevtsov, K.B. Samusev, M.F. Limonov, Bound states in the continuum versus material losses: Ge2Sb2Te5 as an example, Phys. Rev. B 105 (16) (2022) 165425.
[69] S. Campione, S. Liu, L.I. Basilio, L.K. Warne, W.L. Langston, T.S. Luk, J.R. Wendt, J.L. Reno, G.A. Keeler, I. Brener, M.B. Sinclair, Broken symmetry dielectric resonators for high quality factor Fano metasurfaces, ACS Photonics 3 (12) (2016) 2362–2367.
[70] K.S. Modi, J. Kaur, S.P. Singh, U. Tiwari, R.K. Sinha, Extremely high figure of merit in all-dielectric split asymmetric arc metasurface for refractive index sensing, Opt. Commun. 462 (2020) 125327.
[71] W. Su, X. Chen, Z. Geng, Y. Luo, B. Chena, Multiple Fano resonances in all-dielectric elliptical disk-ring metasurface for high-quality refractive index sensing, Results Phys. 18 (2020) 103340.
[72] M.I. Tribelsky, S. Flach, A.E. Miroshnichenko, A.V. Gorbach, Y.S. Kivshar, Light scattering by a finite obstacle and Fano resonances, Phys. Rev. Lett. 100 (2008) 043903.
[73] M.V. Rybin, P.V. Kapitanova, D.S. Filonov, A.P. Slobozhnanyuk, P.A. Belov, Yu.S. Kivshar, M.F. Limonov, Fano resonances in antennas: general control over radiation pattern, Phys. Rev. B 88 (2013) 205106 (1-8).
[74] M.I. Tribelsky, J.-M. Geffrin, A. Litman, C. Eyraud, F. Moreno, Directional Fano resonances in light scattering by a high refractive index dielectric sphere, Phys. Rev. B 94 (2016) 121110(R).
[75] Q. Xu, P. Dong, M. Lipson, Breaking the delay-bandwidth limit in a photonic structure, Nat. Phys. 3 (2007) 406–410.
[76] S. Wehner, D. Elkouss, R. Hanson, Quantum internet: a vision for the road ahead, Science 362 (2018) eaam9288.
[77] H. Walther, B.T.H. Varcoe, B-G. Englert, T. Becker, Cavity quantum electrodynamics, Rep. Prog. Phys. 69 (2006) 1325–1382.
[78] A. Reiserer, G. Rempe, Cavity-based quantum networks with single atoms and optical photons, Rev. Mod. Phys. 87 (2015) 1379.
[79] J. Li, R. Yu, J. Liu, C. Ding, Y. Wu, Fano line-shape control and superluminal light using cavity quantum electrodynamics with a partially transmitting element, Phys. Rev. A 93 (2016) 053814.
[80] E.V. Denning, J. Iles-Smith, J. Mørk, Quantum light-matter interaction and controlled phonon scattering in a photonic Fano cavity, Phys. Rev. B 100 (2019) 214306.
[81] M. Yamaguchi, A. Lyasota, T. Yuge, Theory of Fano effect in cavity quantum electrodynamics, Phys. Rev. Res. 3 (2021) 013037.

This page intentionally left blank

6

Non-radiating sources

Fundamental and higher-order anapole states in all-dielectric nanostructures

Juan Sebastian Totero Gongora[a,b] **and Andrea Fratalocchi**[c]

[a] *Emergent Photonics Research Centre, Dept. of Physics, Loughborough University, Loughborough, England, United Kingdom.* [b] *Emergent Photonics (EPic) Lab, Dept. of Physics and Astronomy, University of Sussex, Falmer, England, United Kingdom.* [c] *PRIMALIGHT, Faculty of Electrical and Computer Engineering, Applied Mathematics and Computational Science, King Abdullah University of Science and Technology (KAUST), Thuwal, Saudi Arabia*

Non-radiating sources are radiationless electromagnetic states that do not propagate in the far field. Historically, quantum mechanics and astrophysics introduced radiationless conditions to describe elementary particles non-interacting with the electromagnetic field. Thanks to recent theoretical and experimental developments in nanophotonics, researchers have demonstrated that the optical equivalent of non-radiating sources can be excited in high-index dielectric nanostructures. A quintessential example of photonic non-radiating sources is the so-called anapole state, which originates from the complex superposition and interaction of different nanostructure-supported modes. Modal interactions can suppress any coupling with far-field propagating modes for specific illumination and geometrical configurations while sustaining a high degree of near-field localization. Robust field localization makes them remarkably fit to engineer near-field applications in all-dielectric metamaterials, akin to plasmonic near-field enhancement but in lossless media.

This chapter overviews the theoretical foundations and experimental milestones in investigating radiationless states in dielectric nanostructures. The chapter is organized as follows. Section 6.1 provides an intuitive theoretical description of optical anapole states through the multipole decomposition of the electromagnetic fields. It discusses the definition of anapole states as the dynamical superposition of electric and toroidal dipole moments (6.1.1), their higher-order counterparts (6.1.2), and the effect of losses on the formation of anapole states (6.1.3). Section 6.2

All-Dielectric Nanophotonics. https://doi.org/10.1016/B978-0-32-395195-1.00011-9
Copyright © 2024 Elsevier Ltd. All rights reserved.

explains the formation of anapole states through Fano–Feshbach partitioning and Generalized Maxwell projectors (6.2.1), two theoretical frameworks originating from the field of open quantum systems. The section exemplifies the Fano–Feshbach analysis for two-dimensional nanodisks (6.2.2) to illustrate the formation of anapole states of multiple orders as the non-resonant superposition of orthogonal eigenmodes of the open system. Finally, Section 6.3 presents a selection of experimental milestones in studying anapole states and their application in multiple-anapole systems.

6.1 Multipole analysis of radiationless states

6.1.1 Toroidal moments and fundamental anapole states

When dealing with microstructures with characteristic sizes comparable with the incident wavelength, it is possible to describe the electromagnetic response of the system through multipole expansions of the electromagnetic fields [1]. There are three fundamental families of multipole excitations corresponding to electric, magnetic, and toroidal multipoles [2]. Fig. 6.1 shows the elementary dipole members of these families. The three families of multipoles are commonly regarded as complementary, as they represent distinct physical symmetry properties of the scattered field [2,3]. For instance, electric dipoles appear even under time reversal while odd under spatial inversion; magnetic dipoles are odd under time reversal but even under spatial inversion. Toroidal modes turn odd under both time and spatial inversion. As such, for a given spatial representation of the scattering problem, the different multipoles generally contribute as expansion terms in perturbative expressions for the scattered and internal fields [3].

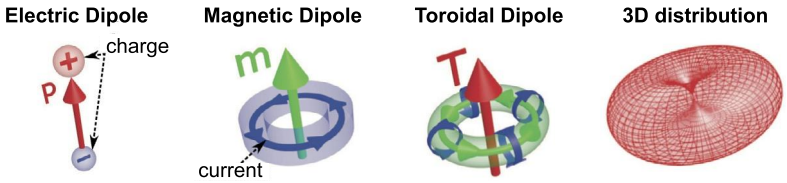

Figure 6.1. Fundamental Multipole families. The electromagnetic field scattered by a nanostructure can be expressed in electric, magnetic, and toroidal dipoles. The different multipoles comprise distinct near-field and current distributions but similar 3D far-field distributions. Adapted with permission from [4], Copyright (2014) by the American Physical Society.

For generic resonator structures, low-order radiation modes such as "bright modes" or "leaky resonances" with relatively small Q-factors dominate the electromagnetic response of the system [5]. These modes couple quite efficiently to far-field radiating waves. The scattered field comprises low-order electric and magnetic dipole contributions for structures with characteristic sizes comparable to optical wavelengths. These states manifest through localized scattering or absorption cross-section peaks at specific wavelengths. Non-radiating forms, on the contrary, can be phenomenologically identified by the simultaneous suppression of the scattering efficiency and enhancement of the total internal energy [6]. Since causality forbids ideal non-scattering objects [7], scientists argued that the suppression of the scattered field must originate from structural peculiarities of the leading multipole, as best exemplified by the concept of optical anapole state [8].

The first introduction of Anapoles was in the late 1950s to describe families of elementary particles non-interacting with the electromagnetic fields [9]. Since then, classical dark matter theories have extensively employed this concept to explain various cosmological phenomena [10]. It took more than 40 years to develop the optical counterpart of anapole in terms of an ideal superposition of toroidal dipole modes oscillating out-of-phase to single electric dipoles [11,12]. In this configuration, the far-field radiation patterns of the two fundamental modes cancel each other due to destructive interference. Experimental results implemented in high-index dielectric nanostructures came after 30 years, leading to the first demonstration of optical anapole states [8]. In close analogy with their elementary counterpart, the microscopic origin of optical anapoles is a superposition effect between different multipolar excitations in the structure.

An effective way to derive this result is through standard Mie Theory calculations. Initially introduced in 1908, Mie Theory provides an exact analytical description of the electromagnetic scattering of a spherical particle in terms of electric and magnetic scattering amplitudes a_l, b_l. The scattering amplitudes correspond to the expansion coefficients required to solve Maxwell's equations in spherical coordinates as partial spherical waves [5]. By matching the resonant electromagnetic waves in the particle's interior with an incident plane wave, it is possible to obtain full analytical expressions. For a given particle of radius R, the modal amplitudes a_l, b_l consist of combinations of special functions (e.g., Bessel, Neumann), and the orbital mode-index l identifies different multipole solutions, namely $l = 1, 2, 3$ corresponding to dipolar, quadrupolar, and octupolar modes. In terms of the electric and magnetic amplitudes, one can define the three fundamental

quantities characterizing the response of the particle: the scattering Q_{sca}, extinction Q_{ext}, and absorption Q_{abs} efficiencies, defined as follows:

$$Q_{sca} = \frac{2}{x^2}\sum_{l=1}^{L}(2l+1)(|a_l|^2 + |b_l|^2), \tag{6.1}$$

$$Q_{ext} = \frac{2}{x^2}\sum_{l=1}^{L}(2l+1)\mathrm{Re}(a_l + b_l), \quad Q_{abs} = Q_{ext} - Q_{sca}, \tag{6.2}$$

where $x = \frac{2\pi R}{\lambda}$ is the size parameter of the particle, and the efficiencies are defined in terms of the geometrical cross-section $\sigma = \pi R^2$. The Mie Theory description of the electromagnetic interactions in terms of electric and magnetic amplitudes enables observing the formation of radiationless states directly. Fig. 6.2a shows the electric dipole contribution to the scattering efficiency (blue line) of a silicon sphere ($n = 3.5$) as a function of the sphere diameter. The partial scattering efficiency is computed by considering only the contributions from the electric dipole a_l, namely $C_{sca} \propto |a_1|^2$ [8] that in this regime dominates the structure response. As illustrated in the figure, it is possible to identify a specific geometric condition that leads to a vanishing scattering efficiency even for a simple spherical object. Quite interestingly, however, the corresponding electric energy, corresponding to the volume integral of the electromagnetic energy density, is generally characterized by non-zero values, suggesting that an appreciable amount of electromagnetic energy concentrates inside the particle despite suppressing the scattering field [2,13].

It is possible to obtain a clearer picture of the mechanism that suppresses the electric dipole contribution to the far field by introducing different representations of the electromagnetic fields. As an alternative to the traditional spherical coordinate description of Mie theory, the multipolar decomposition can be effectively carried out also in cartesian coordinates [8]. In practical terms, the cartesian representation relies on the expansion of the light-induced displacement current in the interior of the resonator $\mathbf{J}(\mathbf{x})$ in a multipole series. The light-induced displacement current is defined as follows:

$$\mathbf{J}(\mathbf{x}) = -i\omega\mathbf{P}(\mathbf{x}) = -i\omega\varepsilon_0(\varepsilon_r - 1)\mathbf{E}_{int}(\mathbf{x}), \tag{6.3}$$

where ω is the electromagnetic wave frequency, ε_r is the relative dielectric permittivity, and $\mathbf{E}_{int}(\mathbf{x})$ is the total electromagnetic field inside the resonator. The emergence of toroidal modes is obtained by expanding the electromagnetic field in terms of the canonical

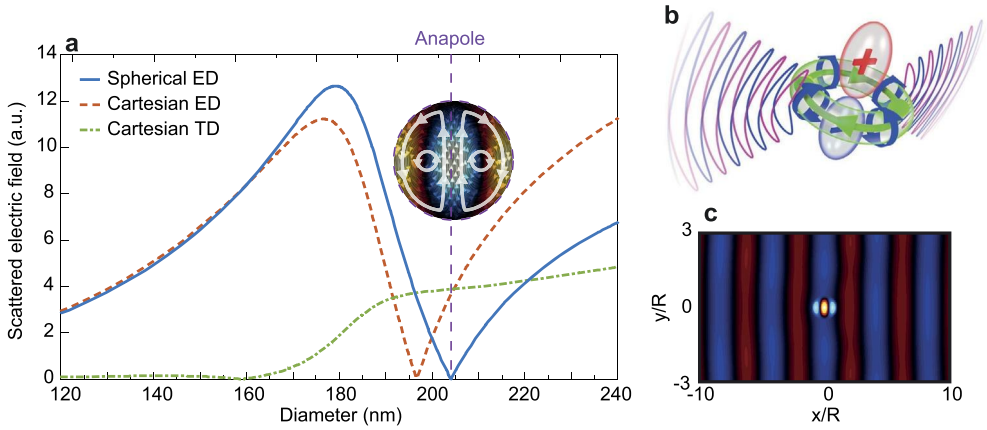

Figure 6.2. Fundamental anapole states. a) Electric dipole contribution to the scattering cross section (blue line) for a silicon sphere at $\lambda = 550$ nm as a function of the particle diameter. The suppression of the scattering cross-section identifies the anapole state (dashed gray line), and it originates from the superposition of a cartesian electric dipole (red dashed line) and toroidal dipole (green dashed line). Adapted from Ref. [8] and reused under the Creative Commons Attribution 4.0. b) Anapole state as the superposition of electric and toroidal dipoles. Adapted from [13], and re-used under the Creative Commons Attribution 4.0. c) Electromagnetic energy distribution for a silicon disk, illustrating the suppression of the scattered field at the anapole wavelength. Adapted with permission from [14], ©IOP Publishing Ltd.

spherical basis (as in the case of Mie theory), but defined on a cartesian representation. In this case, for example, the scattered field $\mathbf{E}_{sca}(\mathbf{x})$ is expressed as [2,8]:

$$\mathbf{E}_{sca}(\mathbf{n}) = \frac{k_0^2}{4\pi\varepsilon_0}\frac{e^{ik_0 r}}{r}\left([\mathbf{n}\times[\mathbf{p}\times\mathbf{n}]] + \frac{\mathbf{m}\times\mathbf{n}}{c} - \frac{ik_0}{6}[\mathbf{n}\times(Q^{(e)}\mathbf{n}\times\mathbf{n})] - \frac{ik_0}{2c}[(Q^{(m)}\mathbf{n}\times\mathbf{n})] + \cdots\right), \quad (6.4)$$

where $\mathbf{p}$, $\mathbf{m}$, $Q^{(e)}\mathbf{n}$, $Q^{(m)}\mathbf{n}$ correspond to the spherical multipole moments (electric dipole, magnetic dipole, electric quadrupole, and magnetic quadrupole) expressed in cartesian coordinates [15]. By expanding each multipole term with respect to kr, the standard spherical electric dipole $\mathbf{p}$ is expressed as a superposition of a cartesian electric $\mathbf{p}_{car}$ and cartesian toroidal $\mathbf{T}_{car}$ dipoles as $\mathbf{p} \approx \mathbf{p}_{car} + i\mathbf{T}_{car}$ [2,8]. As mentioned above, the different families of multipoles possess specific physical symmetries [2,3]. In terms of fundamental symmetries, $\mathbf{p}_{car}$ appears even under time reversal, while odd under spatial inversion, $\mathbf{m}_{car}$ is odd under time reversal, but even under spatial inversion, and $\mathbf{T}_{car}$ turns odd under both time and spatial inversion.

The expansion of the spherical electric dipole in cartesian dipole and toroidal dipole unveils the physical mechanism underlying the vanishing of the electric dipole's contribution to the far-field scattering, as shown in Fig. 6.2a. For small particle sizes, the far-field response of the particle is dominated by electric dipole contributions. The spherical and cartesian dipole components (blue and dashed red lines, respectively) are almost indistinguishable, and the toroidal dipole contribution (dashed green line) is practically non-existing. Conversely, the cartesian toroidal contribution to the spherical electric dipole becomes increasingly relevant for larger diameters. In this scenario, the vanishing of the spherical electric dipole corresponds to the condition $\mathbf{p}_{car} = -i\mathbf{T}_{car}$ (dashed gray line), leading to the established definition of the optical anapole as a non-resonant, out of phase superposition of cartesian electric and toroidal dipoles (Fig. 6.2b).

We stress here that the analysis in Fig. 6.2 focuses only on the spherical electric dipole contributions to the far-field scattering of the particle. Analogous calculations for the spherical magnetic dipole lead to the definition of a magnetic anapole [16]. While electric and magnetic anapole states originate from an identical mechanism, their electromagnetic configuration differs significantly. While the electric anapole possesses an electromagnetic energy distribution tightly localized inside the particle, magnetic anapoles tend to concentrate the energy in the outer region of the particle, leading to a near-field enhancement distribution similar to that usually associated with plasmonic particles. Analogously, radiationless states corresponding to the simultaneous excitation of electric and magnetic anapoles lead to the formation of hybrid anapole states [17]. For spherical particles, however, partial contributions from higher-order modes (quadrupolar, octupolar) hinder this effect, and pure hybrid anapole states do not exist. In generic structures such as disks or core-shell structures [18], the broader range of degrees of freedom enables fine-tuning of the dielectric and magnetic dipole contributions, leading to the observation of pure electric, magnetic, and hybrid optical anapoles. As will be further discussed in Section 6.3, the transition from spherical to nanodisk geometries enabled observing anapole states in real-life experiments.

6.1.2 Higher-order and hybrid anapole states

While the previous section focused on the electric and magnetic dipoles, we here discuss the concept of anapole as a peculiar combination of higher-order dipole moments. The superposition of higher-order cartesian electric and toroidal dipoles can

lead to the formation of higher-order anapole states [3,19]. Such analysis is presented in [20], where the authors extended the standard set of electric, magnetic, and toroidal dipoles (cf., Fig. 6.1) to include higher-order toroidal moments. More specifically, the authors extend the Cartesian multipole expansion introduced in the previous subsection (cf., Eq. (6.4)) up to the fifth order, including magnetic 16-poles and electric 32-poles. In comparison to earlier approximations of the Cartesian multipole decomposition, the results in Ref. [20] enabled the detailed and exact analysis of light scattering due to the additional degrees of freedom provided by new electric, magnetic, and toroidal multipoles contributions (Fig. 6.3a).

Fig. 6.3b-d illustrates the formation of three anapole states of increasing order. The authors compare the total scattering efficiency calculated through Finite-Element methods (COMSOL) with the cartesian dipole with (dashed lines) and without (solid lines) the higher-order toroidal contributions. The minima of all the dashed lines correspond to the different anapole states, whose electric and magnetic field profiles are shown in Fig. 6.3e-h. At these points, the fundamental and toroidal multipoles have the same amplitude, but π-shifted phases give rise to destructive interference. As a final observation, in Fig. 6.3c and 6.3d, it is possible to see that at $kr = 1.468$, there is the simultaneous vanishing of the total magnetic dipole and full electric quadrupole and at $kr = 1.769$ for the magnetic quadrupole and electric octupole. These states closely approximate a pure hybrid anapole state composed of higher-order anapole contributions. The versatility offered by structures supporting hybrid anapole states was recently leveraged by Kutsenov et al. to control the amplitude and phase response of dielectric metasurfaces with negligible reflection [21]. In their theoretical work, the authors demonstrate that the excitation of hybrid anapole states can open to the control of the scattered field phase up to a meta-atom level (i.e., up to a single structure composing the metasurface) thanks to the vanishing coupling between neighboring structures. Quite remarkably, the authors also show how to exploit a controllable amount of positional and configurational disorder to achieve coherent control of the phase of an ultrafast pulse (linearly polarized Gaussian pulse with a duration of 400 fs) while retaining a transmission efficiency above 85%.

6.1.3 Anapoles states in lossy media

A final observation on the physics of anapole states concerns the effect of material losses. While most theoretical analyses focus on purely dielectric media, the role of material losses in real-life

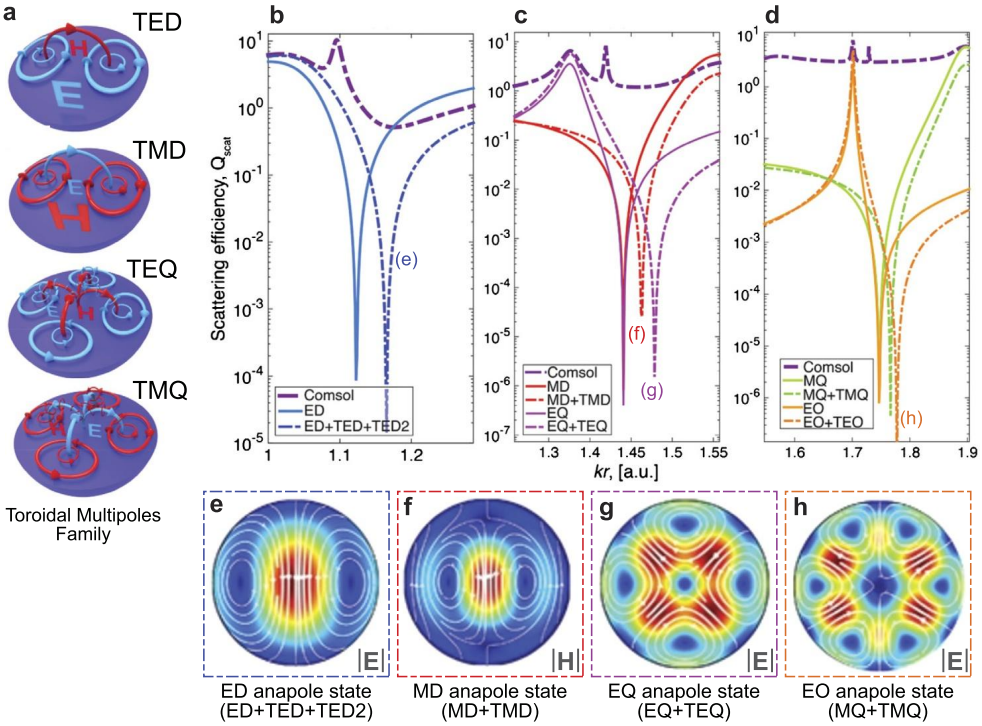

Figure 6.3. Multipole description of higher-order anapole states. a) Toroidal multipoles family, as introduced in Ref. [20], including the toroidal electric dipole (TED), the toroidal magnetic dipole (TMD), the toroidal electric quadrupole (TEQ), the toroidal magnetic quadrupole (TMQ). b-c) Scattering efficiency Q_{sca} for the fundamental dipole and quadrupole contributions, as calculated with Eqs. (6.1). The different types of anapole states are identified by vanishing the scattering efficiency for individual combinations of electric, magnetic, and toroidal multipoles. e-h) Electric $|\mathbf{E}|$ (panels e, g, h) and magnetic $|\mathbf{H}|$ (panel f) field distribution for each anapole state in panels (b-d). Figure adapted with permission from Ref. [20], ©WILEY-VCH.

experiments must be duly taken into account [23]. A relevant example of such analysis can be found in [22], a theoretical work that introduced a new type of integrated nanolaser emitting at the anapole frequency. The authors considered an InGaAs nanodisk as an active lasing cavity whose geometry was optimized to support the formation of a fundamental anapole state in correspondence with the gain medium emission frequency ($\lambda \approx 950$ nm). Fig. 6.4 illustrates the multipole components of the internal field in the resonator for varying values of the material losses κ in the medium and as a function of the incident wavelength. Losses' effect slightly reduces the overall scattering efficiency, which, however, maintains values very close to experimental results in Si and Ge nanostructures [8,24]. As shown in Fig. 6.4f, the energy difference that does not couple to electromagnetic components

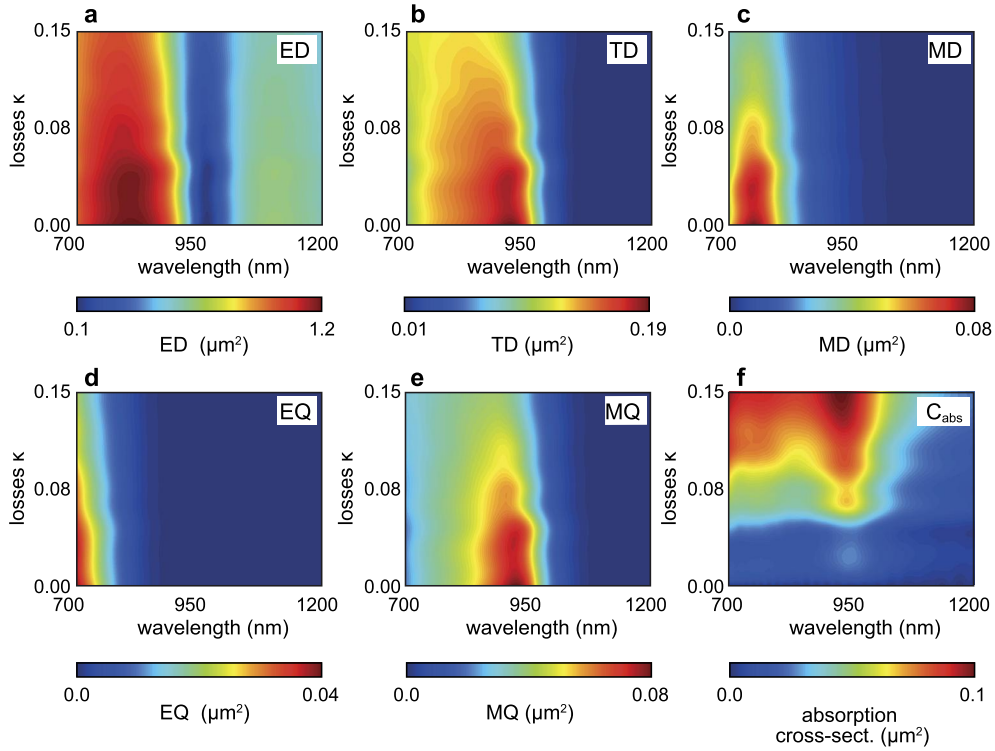

Figure 6.4. Losses and higher-order dipoles in anapole states. a-e) Multipole decomposition for an InGaAs cylinder of height $h = 100$ nm and radius $r = 220$ nm as a function of the incident wavelength and the imaginary part of the refractive index k. The multipole components are (a) electric dipole, (b) toroidal dipole, (c) magnetic dipole, (d) electric quadrupole, and (e) electric octupole. f) Corresponding absorption cross-section. Adapted from [22] and reused under the Creative Commons Attribution 4.0.

contributes to the increase in the absorption cross-section of the nanodisk, and does not significantly affect the properties of the fundamental anapole state. This result also suggests that nonlinear amplification via stimulated emission is a viable solution to excite almost ideal anapole states in realistic lossy structures [22].

6.2 Fano–Feshbach description of radiationless states

6.2.1 Fano–Feshbach partitioning and generalized Maxwell projectors

Considering these unique features and applications, the possibility of engineering integrated sources with anapole states ap-

pears counter-intuitive. Differently from dark modes and plasmons, anapole states constitute a non-resonant superposition of multipole components which appears unsuitable to sustain localized enhancement of the electromagnetic energy [2,25]. The anapole state appears as a dynamic "equilibrium state" of the electromagnetic fields and is generally not associated with a finite Q-factor [6]. Said differently, such a dynamic state exists only under stationary illumination and disappears as soon as the external illumination is removed [25]. However, one can disentangle this apparent contradiction by looking at the fundamental properties of the anapole states beyond standard multipole expansions.

The description of anapole states within a more rigorous theoretical framework was initially developed in [14], where the authors redefined the anapole state in terms of a complete set of orthogonal, resonant states. Since dielectric resonators are, by definition, open electromagnetic cavities, one cannot directly solve Maxwell's equations by defining a set of orthogonal eigenmodes [26]. Even when applying Mie theory, which is mathematically exact, the expansion in partial waves accurately represents the fields. Still, the partial spherical waves do not form an orthogonal basis of Maxwell's eigenmodes inside and outside the resonator [5].

A rigorous approach to overcome this limitation is to apply a Fano–Feshbach projection scheme to describe the electromagnetic interactions in the resonator. This technique, which originates from the field of open quantum systems [27,28], relies on the definition of a generic dielectric cavity $\mathcal{A}$ delimited by a boundary $\partial\mathcal{A}$, with a spatially-dependent dielectric function $\varepsilon(\mathbf{x})$ defining its optical properties. The definition of the resonator boundary is entirely general: it can either represent the boundary of a complex dielectric object or a region containing several resonators (see Fig. 6.5). A common way to solve Maxwell's equations in this type of system is by defining a set of resonance modes $\psi(\mathbf{x})$ of the photonic cavity. The latter are the solutions of the Helmholtz eigenproblem associated with the standard Maxwell's equations, which read:

$$\mathcal{L}\psi(\mathbf{x}) = \frac{\varepsilon(\mathbf{x})\Omega^2}{c^2}\psi(\mathbf{x}), \tag{6.5}$$

where we introduced the differential operator $\mathcal{L} = \nabla \times \nabla\times$ and its eigenvalues Ω. Whenever it is possible to obtain a complete set of eigenmodes for Eq. (6.5), the eigenbasis $\psi(\mathbf{x})$ can be employed to expand all the electromagnetic quantities of the system. By definition, however, a dielectric resonator is an open cavity; therefore, it is impossible to define a set of orthogonal eigenmodes [29].

The Fano–Feshbach partitioning scheme circumvents this limitation by splitting all the electromagnetic quantities into "resonator" and "environment" contributions, with the only condition that all the projection components preserve their hermiticity [30–33]. In practice, the total space divides into an internal resonator space A and an external area B, separated by the boundary of the dielectric cavity ∂A (Fig. 6.5a). Following the mathematical partitioning of the eigenspace of Eq. (6.5), the system expands in terms of a discrete set of internal $\mu_m(\mathbf{x})$ and a continuum of radiative scattering eigenmodes $\nu(\mathbf{x}, \omega)$, as illustrated in Fig. 6.5b. By coupling the two domains through *ad-hoc* boundary conditions, it is possible to describe the electromagnetic scattering from the resonator in terms of internal and external resonant eigenmodes [14], defined as the solution of the following independent eigenproblems:

$$\nabla \times \nabla \times \mu_m(\mathbf{x}) = \frac{\omega_m^2}{c^2} \varepsilon \mu_m(\mathbf{x}), \tag{6.6}$$

$$\nabla \times \nabla \times \mu(\mathbf{x}, \omega) = \frac{\omega^2}{c^2} \varepsilon \nu(\mathbf{x}, \omega), \tag{6.7}$$

with the following boundary conditions:

$$\begin{aligned} \mathbf{n} \times \nabla \times \mu_m(\mathbf{x})|_{\partial \mathcal{A}} &= 0, \\ \mathbf{n} \times \nu(\mathbf{x}, \omega)|_{\partial \mathcal{A}} &= 0, \end{aligned} \tag{6.8}$$

being $\mathbf{n}$ the normal unit vector to the surface $\partial \mathcal{A}$. The internal and external eigenmodes are mutually orthogonal by definition, and they separately form a complete set of eigenmodes for the resonator and the environment subspaces. Therefore, they coincide with the closed-cavity modes of the system. These modes describe the system without interacting with the resonator and the external environment. In the realistic case of an open cavity, the Fano–Feshbach eigenmodes $\mu_m(\mathbf{x})$ and $\nu(\mathbf{x}, \omega)$ are connected by *ad hoc* coupling terms, rigorously defined on the resonator boundary, which rules the resonant interaction between the internal and external eigenspaces. Ultimately, the Fano–Feshbach partitioning scheme defines a set of dynamical equations akin to time-dependent Coupled-mode-theory (TD-CMT). However, one of the key challenges in applying Fano–Feshbach partitioning schemes is that the calculation of the system eigenmodes and their coupling at the cavity boundary leads to cumbersome algebraic expressions, as discussed in [14] and references therein. In addition, the standard Fano–Feshbach partitioning scheme relies on a single resonator space containing the totality of dielectric resonators composing the system.

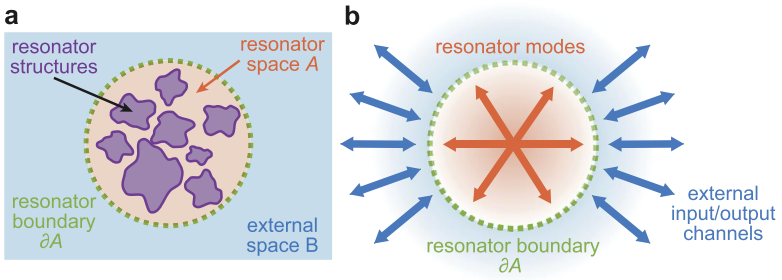

Figure 6.5. Fano–Feshbach partitioning scheme. a) External and internal partitioning. The boundary ∂A is not fixed and is the boundary of a region containing all the dielectric objects composing the resonator. b) The electromagnetic dynamics are expanded separately in the resonator space (resonator modes) and the external space (input/output channels). The internal and external modes couple at the boundary of the resonator region ∂A.

An equivalent, more straightforward approach to the calculation of the internal and external eigenmodes of the system is to integrate the Fano–Feshbach partitioning with the theory of generalized functions applied to multiple projection spaces [34]. This approach, introduced in [35,36], provides an intuitive description of Maxwell's equations in terms of propagating and resonant effects. Moreover, the temporal electromagnetic field dynamics follow a rigorous but straightforward set of coupled equations that are particularly convenient for analytical descriptions and numerical analysis. Rather than dividing the total space into only two regions (resonator and external space), the generalized Maxwell projections scheme splits the entire space Ω into a set of adjoined regions (Fig. 6.6a). Within each sub-region, the dynamical equations describing the evolution of the electromagnetic fields are in terms of orthogonal eigenmodes. More specifically, within each set Ω_n, Maxwell's equations are decomposed through the theory of generalized functions [34] using the generalized differential operator ∇, defined as follows:

$$\nabla = \{\nabla\} + \mathbf{n}_{S_n} \cdot \delta_{S_n}, \tag{6.9}$$

where $\{\nabla\}$ is the standard nabla operator evaluated for each point within the volume V_n, $\mathbf{n}_{S_n}$ the unit vector normal to the surface S_n, and $\delta_{S_n} = \delta(\mathbf{x} - \mathbf{x}_{S_n})$ a three-dimensional Dirac delta function centered on the surface $\mathbf{x} \in S_n$. By substituting Eq. (6.9) in Maxwell's equations and imposing the absence of any singular terms in the dynamics of the resonator space, one finds that the whole resonator space $\Omega_r = \cup_n \Omega_n$ appears as a Perfect Electric Conductor (PEC) material from the external area. Similarly, the exterior space

appears from within each resonator region Ω_n as a Perfect Magnetic Conductor (PMC) material, leading to the following set of partitioned Maxwell's equations [35]:

$$\Omega_n : \begin{cases} \{\nabla\} \times \mathbf{E}_n = -\mu(\mathbf{x}) \frac{\partial}{\partial t} \mathbf{H}_n, \\ \{\nabla\} \times \mathbf{H}_n - \delta_{S_{n-}} \mathbf{n}_{S_n} \times \mathbf{H}_e = \epsilon_0 \epsilon_r(\mathbf{x}) \frac{\partial}{\partial t} \mathbf{E}_n + \mathbf{J}_\Delta, \\ \{\nabla\} \cdot \mathbf{D}_n - \delta_{S_{n-}} \mathbf{n}_{S_n} \cdot \mathbf{D}_e = 0, \\ \{\nabla\} \cdot \mathbf{B}_n = 0 \end{cases}$$
$$\Omega_e : \begin{cases} \{\nabla\} \times \mathbf{E}_e + \delta_{S_{n+}} \mathbf{n}_{S_n} \times \mathbf{E}_n = -\mu(\mathbf{x}) \frac{\partial}{\partial t} \mathbf{H}_e, \\ \{\nabla\} \times \mathbf{H}_e = \epsilon(\mathbf{x}) \frac{\partial}{\partial t} \mathbf{E}_e, \\ \{\nabla\} \cdot \mathbf{D}_e = 0, \\ \{\nabla\} \cdot \mathbf{B}_e + \delta_{S_{n+}} \mathbf{n}_{S_n} \cdot \mathbf{B}_n = 0 \end{cases} \tag{6.10}$$

coupled with the following set of boundary conditions:

$$\text{PMC} : \begin{cases} \mathbf{n}_{S_n} \times \mathbf{H}_n|_{S_n} = 0, \\ \mathbf{n}_{S_n} \cdot \mathbf{D}_n|_{S_n} = 0, \end{cases} \qquad \text{PEC} : \begin{cases} \mathbf{n}_{S_n} \times \mathbf{E}_e|_{S_n} = 0, \\ \mathbf{n}_{S_n} \cdot \mathbf{H}_e|_{S_n} = 0. \end{cases} \tag{6.11}$$

The advantage of the splitting described by Eqs. (6.10)–(6.11), when compared with the standard Fano–Feshbach partitioning, is the electromagnetic problem defined within independent spatial regions terminated by well-defined and ideal PEC/PMC boundary conditions. In analogy with the Fano–Feshbach partitioning in Fig. 6.5, all the electromagnetic quantities of interest are expressed through a complete eigenbasis of purely orthogonal modes. Such modes, however, correspond to the eigenmodes of ideal metallic resonators and, for simple choices of the resonator boundaries, can be analytically expressed in closed form [37]. With this position, the electromagnetic field inside the resonator expands in terms of resonator modes (*c.c.* stands for complex conjugate):

$$\begin{aligned} \mathbf{E}_n(\mathbf{x}, t) &= \sum_{m=1}^{M} \frac{a_m(t)}{2} \mathbf{E}_{nm}(\mathbf{x}) + c.c., \\ \mathbf{H}_n(\mathbf{x}, t) &= \sum_{m=1}^{M} \frac{a_m(t)}{2} \mathbf{H}_{nm}(\mathbf{x}) + c.c. \end{aligned} \tag{6.12}$$

Similarly, the time-averaged electromagnetic energy $\langle \mathcal{E}(t) \rangle$ dissipated inside the resonator space for monochromatic excitation at frequency ω is expressed as the sum of the energy of each mode:

$$\langle \mathcal{E}(t) \rangle = \int_{V_n} dV_n \left\langle \epsilon_0 \epsilon_r \mathbf{E}_n^2 + \mu \mathbf{H}_n^2 \right\rangle = \sum_m |\tilde{a}_m(\omega)|^2 = \tilde{\mathbf{a}}^2, \tag{6.13}$$

with $a_m(t) = \tilde{a}(\omega)e^{i\omega t}$ and $\tilde{\mathbf{a}} = \left[\tilde{a}_1(\omega), \ldots, \tilde{a}_M(\omega)\right]$ defining the vector of amplitudes of the internal modes in the frequency domain. External modes in the outer region Ω_e consist of a series of ingoing and outgoing scattered waves. As the radiation spectrum is typically continuous, it is convenient to carry out the mode expansion in the frequency domain $\mathbf{E}_e(\mathbf{x}, t) = \tilde{\mathbf{E}}_e(\mathbf{x}, \omega)e^{i\omega t}$, $\mathbf{H}_e(\mathbf{x}, t) = \tilde{\mathbf{H}}_e(\mathbf{x}, \omega)e^{i\omega t}$:

$$\begin{cases} \tilde{\mathbf{E}}_e = \sum_{h=1}^{H} \tilde{s}_{h+}(\omega)\mathbf{E}_{h+} + \tilde{s}_{h-}(\omega)\mathbf{E}_{h-} \\ \tilde{\mathbf{H}}_e = \sum_{h=1}^{H} \tilde{s}_{h+}(\omega)\mathbf{H}_{h+} + \tilde{s}_{h-}(\omega)\mathbf{H}_{h-} \end{cases}, \quad \text{PEC}: \begin{cases} \mathbf{n}_{S_n} \times \tilde{\mathbf{E}}_e\Big|_{S_n} = 0, \\ \mathbf{n}_{S_n} \cdot \tilde{\mathbf{H}}_e\Big|_{S_n} = 0, \end{cases} \tag{6.14}$$

with time-varying amplitude coefficients $s_{m\pm}(t) = \tilde{s}_{m\pm}(\omega)e^{i\omega t}$, which describe the time evolution of incoming $\mathbf{E}_{m+}$, $\mathbf{H}_{m+}$ and outgoing $\mathbf{E}_{m-}$, $\mathbf{H}_{m-}$ waves through $m = 1, ..., M$ different scattering channels. Traveling waves $\mathbf{E}_{m\pm}$, $\mathbf{H}_{m\pm}$ depend in general on ω through their wavevector $\mathbf{k}$ as, e.g., in the case of plane waves $e^{\pm i\mathbf{k}\cdot\mathbf{r}}$, spherical waves $e^{\pm ikr}/r$ or other types of traveling waves in free space. The mode expansions carried out in Eqs. (6.13) and (6.14) reduce the time dynamics of Maxwell's equations to an exact set of spatio-temporal coupled-mode equations, which relate the time evolution of the amplitudes of internal modes $a_m(t)$, with outgoing scattered waves $s_{h-}(t)$ for a given set of impinging sources $s_{h+}(t)$. The mode expansions in Eqs. (6.12) and Eqs. (6.14) express the corresponding spatial distribution of the field, providing a complete solution to the problem. In the external space Ω_e, due to the absence of any source $\mathbf{J}_\Delta = 0$, Maxwell's equations are linear, and the scattered modes $s_{h-}(t)$ follow a linear evolution as a function of modes $a_m(t)$ and impinging fields $s_{h+}(t)$. The time dynamics of the scattered field $\mathbf{s}_-(\omega)$ in the frequency domain is then expressed as a linear superposition of $\tilde{\mathbf{a}}(\omega)$ and $\tilde{\mathbf{s}_+}(\omega)$:

$$\tilde{\mathbf{s}}_-(\omega) = \tilde{D}(\omega) \cdot \tilde{\mathbf{a}}(\omega) + \tilde{C}(\omega) \cdot \tilde{\mathbf{s}}_+(\omega), \tag{6.15}$$

with $\tilde{D}(\omega)$, $\tilde{C}(\omega)$ being linear matrices. The dynamics of $\mathbf{a}(t)$, conversely, follow from the most general form of the linear time evolution equation for the modes $a_m(t)$, with input sources corresponding to impinging waves $\mathbf{s}_+$:

$$\dot{\mathbf{a}}(t) = \int_{t_0}^{t} \mathrm{d}t' \left[H\left(t - t'\right) \cdot \mathbf{a}\left(t'\right) + K\left(t - t'\right) \cdot \mathbf{s}_+\left(t'\right)\right]. \tag{6.16}$$

In close analogy with standard energy conservation considerations, the following self-consistency relations must be satisfied:

$$\begin{cases} \tilde{C}(\omega)^{\dagger}\tilde{C}(\omega) = 1 \\ 2\tilde{\Gamma}(\omega) = \tilde{K}(\omega)\tilde{K}^{\dagger}(\omega) \\ \tilde{D}(\omega) = -\tilde{C}(\omega)\tilde{K}^{\dagger}(\omega) \end{cases} \tag{6.17}$$

where $\tilde{\Gamma}(\omega)$ is the Fourier transform of Γ. The conditions imposed by Eqs. (6.17) solve Eqs. (6.15)–(6.16) in the frequency domain:

$$\begin{cases} \tilde{\mathbf{a}}(\omega) = \frac{\tilde{K}}{i(\omega - W) + \frac{\tilde{K}\tilde{K}^{\dagger}}{2}}\tilde{\mathbf{s}}_{+}, \\ \tilde{\mathbf{s}}_{-}(\omega) = \tilde{C}\left(\tilde{\mathbf{s}}_{+} - \tilde{K}^{\dagger}\cdot\tilde{\mathbf{a}}\right), \end{cases} \tag{6.18}$$

with $1/\tilde{X}$ being shorthand notation for the inverse matrix $\tilde{X}^{-1}$. Eqs. (6.18) are similar to the time-dependent coupled-mode equations written in the frequency domain and originally introduced in [38,39]. However, there are also differences. In the traditional set [38,39], all the linear matrices C, K, Γ are frequency independent, and $a_m(t)$ are the amplitudes of traditional electromagnetic modes with radiating boundary conditions.

Fig. 6.6b shows a block diagram representation of Eqs. (6.18). In the absence of any resonance, $\tilde{\mathbf{a}} = 0$ and the system output is characterized by the open-loop response $\tilde{\mathbf{s}}_{-} = \tilde{C}(\omega)\cdot\tilde{\mathbf{s}}_{+}$. This contribution arises from propagation effects and not from a resonant light-matter interaction. When $\tilde{\mathbf{a}} \neq 0$, the system response is characterized by a second term represented by the closed-loop feed-

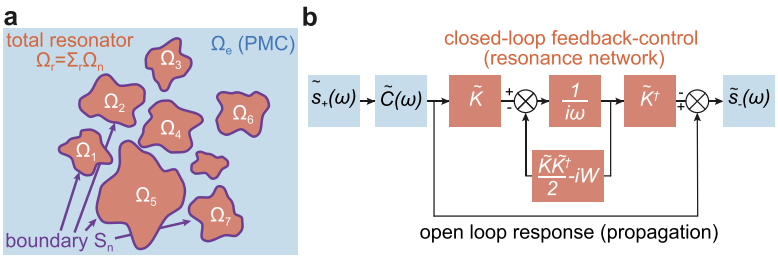

Figure 6.6. Generalized Maxwell Projections. a) Conceptual view of the Generalized Maxwell Projections scheme. The total space divides into external Ω_e and internal Ω_r regions. The outer region is a perfect magnetic conductor (PMC), while the internal region is divided into resonator subregions Ω_n with boundaries S_n. b) Block diagram representation of the dynamical equations from Eq. (6.18). The total electromagnetic dynamics are decomposed into propagation (open-loop) and resonance effects (closed-loop feedback control). Adapted from [35] and reused under the Creative Commons Attribution 4.0.

back unit of Fig. 6.6b, which forms the contribution of resonances. In a generic resonator, the superposition of radiative and resonant contributions naturally leads to the formation of Fano–Feshbach resonances (also known simply as Fano resonances), which represent the characteristic signature of the interaction among localized resonances and a slowly-varying background [40,41].

6.2.2 Fano–Feshbach description of anapole states

Fano–Feshbach partitioning schemes provide fundamental insights into the microscopic origin of the anapole state. In [14], the authors investigated the formation of anapole states in circular two-dimensional cavities of radius R and dielectric function under plane wave illumination $\varepsilon(\mathbf{x}) = n^2$. In the two-dimensional space, Mie theory is replaced by the analogous Mie–Lorentz formalism [5]. The closed cavity limit computes the external eigenmodes by solving Eq. (6.6) in the external space, obtaining:

$$v_m(\mathbf{x}, \omega) = \sqrt{\frac{k}{8\pi}} \left[H_m^{(1)}(k\rho) - R_m^0(kR) H_n^{(2)}(k\rho) \right] e^{jm\phi}, \tag{6.19}$$

where $H^{(1,2)}$ are Hankel functions of the first and second type, respectively, and $R^0 = -\partial_\rho H^1(k\rho)/\partial_\rho H^2(k\rho)\big|_{\rho=R}$ was obtained by means of Eq. (6.8). In close analogy with the generalized Maxwell projections, such a set of external eigenmodes correspond to the electromagnetic field produced by a TM-polarized plane wave impinging on an ideal metallic cylinder. The internal eigenmodes correspond to the solution of Helmholtz equation (6.6) in the resonator space, obtaining:

$$\mu_{ml}(\mathbf{x}, \omega) = \frac{e^{jm\theta} J_m(nk_{ml}\rho)}{\sqrt{\pi} n R J_{m+1}(x_{ml})}, \tag{6.20}$$

where the internal resonance frequencies $x_{ml} = k_{ml} R$ coincide with the l-th zero of the Bessel function $J_m(\rho)$. In analogy with the angular momentum formalism, the additional discrete index l distinguishes the eigenmodes with the same order m but a different number of zeros [28]. As a first example, the authors considered the scattering from a disk of silicon ($n = 3.5$) with a radius of $R =$ 150 nm (Fig. 6.7). Fig. 6.7a illustrates the total Mie–Lorentz scattering efficiency $Q_{sca}(x)$ as a function of the size parameter $x = kR$, being k the wavenumber of the incident plane wave. The vertical dotted lines correspond to the internal resonances x_{ml} as computed from Eq. (6.20). Even for such a simple geometry, it is pos-

sible to identify a first fundamental anapole state at $x = 1.525$ (see Fig. 6.7a). The Fano–Feshbach partitioning unveils the presence of two distinct resonances generating the anapole state: a first one, corresponding to the cavity mode $|\mu_{02}\rangle$, with $m = 0$ and $l = 2$ and a higher-order mode with $m = 2$ and $l = 1$ (Fig. 6.7e,f). These resonances couple to different external channels and, therefore, they are mutually independent, provided that the coupling amplitudes $\Gamma_{mll'}$ connect only states with the same angular momentum index $m' = m$. However, both these resonances are individually characterized by Fano-shaped profiles, as can be evinced by inspecting their scattering response separately (Fig. 6.7b,c). The $m = 0$ mode, which possesses a significant and positive Fano parameter ϕ_0 in the proximity of the resonance (Fig. 6.7b, green line), provides for a quasi-Lorentzian dip (Fig. 6.7b, orange line). The $m = 2$ mode, conversely, presents a small and negative Fano parameter (Fig. 6.7c, green line), yielding an almost symmetric Fano profile (Fig. 6.7c, violet line). When these resonances are close to each other, their superposition substantially cancels the total scattering efficiency. As a further confirmation that the superposition of two distinct resonances generates the anapole state, we compare the exact electric field distribution computed from Lorentz–Mie theory (Fig. 6.7d) with the distribution of the internal modes for the two resonances (Fig. 6.7e,f). Remarkably, their superposition (Fig. 6.7g), as computed from the Fano–Feshbach approach, strongly agrees with the exact solution from Maxwell's equations. Interestingly, this geometry's fundamental anapole state at $x = 1.525$ is the only scattering reduction state. In a two-dimensional structure, the strong scattering suppresses higher-order anapole states from nearby resonances [23,42]. As a result, no additional anapole states can be identified for larger values of x.

Interestingly, the Fano–Feshbach partitioning scheme to dielectric cylinders can identify the formation of higher-order anapole states [14]. Fig. 6.8 illustrates the results of a dielectric disk with the same geometry as in Fig. 6.7, but refractive index $n = 8$. Such a high value for the refractive index is available in experiments by considering, e.g., the refractive index of water in the microwave spectrum [42]. As the total scattering efficiency shows (Fig. 6.8a), in this case, the resonances are much narrower and closer, producing a significantly more detailed Mie–Lorentz scattering profile characterized by distinct Fano-shaped profiles. Even in this scenario, it is possible to identify three anapole states, occurring at $x = 0.49$, $x = 1.495$, and $x = 1.896$, respectively (Fig. 6.8a, gray bars). Such states are the result of the competition of multiple Fano–Feshbach resonances: in the first case ($x = 0.49$, cf. Fig. 6.8b), the invisibility state is due to the excitation of a sin-

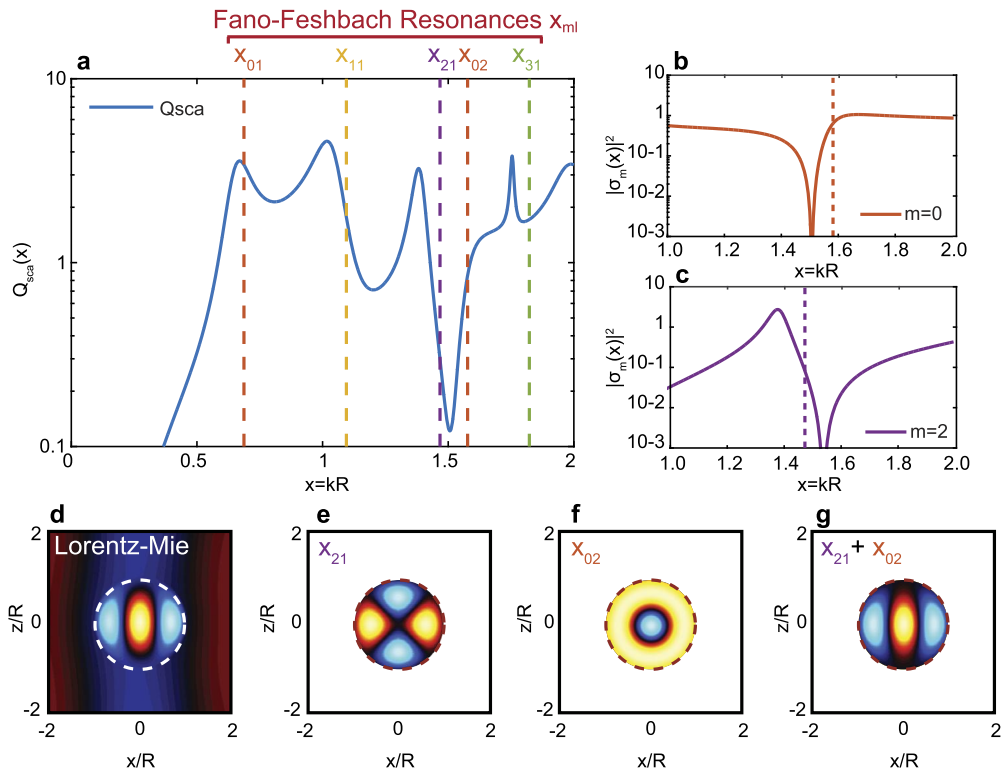

Figure 6.7. Fano–Feshbach description of anapole state. Anapole states in a silicon resonator ($n = 3.5$). a) Total scattering efficiency $Q_{sca}(x)$ and internal resonances (dotted vertical lines) as computed from the Fano–Feshbach partitioning scheme. The anapole state occurring at $x = 1.595$ appears a superposition between the μ_{21} and μ_{02} modes. b-c) Partial scattering intensity $|\sigma_m(x)|^2$ and Fano coefficient $\phi_m(x)$ for (b) $m = 0$ and (c) $m = 2$. d) Electric field distribution of the anapole state as computed from Lorentz–Mie theory. e-f) Spatial distributions of the μ_{21} (e) and μ_{02} (f) resonances as computed with the Fano–Feshbach formalism. Their superposition (g) is in excellent agreement with the exact case. Adapted with permission from [14], ©IOP Publishing Ltd.

gle internal mode μ_{01}, with $m = 0, l = 1$ mode (yellow dashed line). The higher-order anapole states, conversely, are characterized by the mutual interaction between states with $m = 0$ (orange dashed lines), and $m = 2$ (violet dashed lines) with different values of l (Fig. 6.8c,d). As in the case of the silicon resonator, the spatial distributions for the internal modes responsible for the anapole state formation (Fig. 6.8a, inset) are in excellent agreement with the results from Lorentz–Mie theory (insets of Fig. 6.8b,d). The additional anapole states, unveiled by the Fano–Feshbach description, cannot be represented in terms of fundamental anapole states. They are analogous to the higher-order anapoles described in Section 6.1.2. The Fano–Feshbach description of the formation of

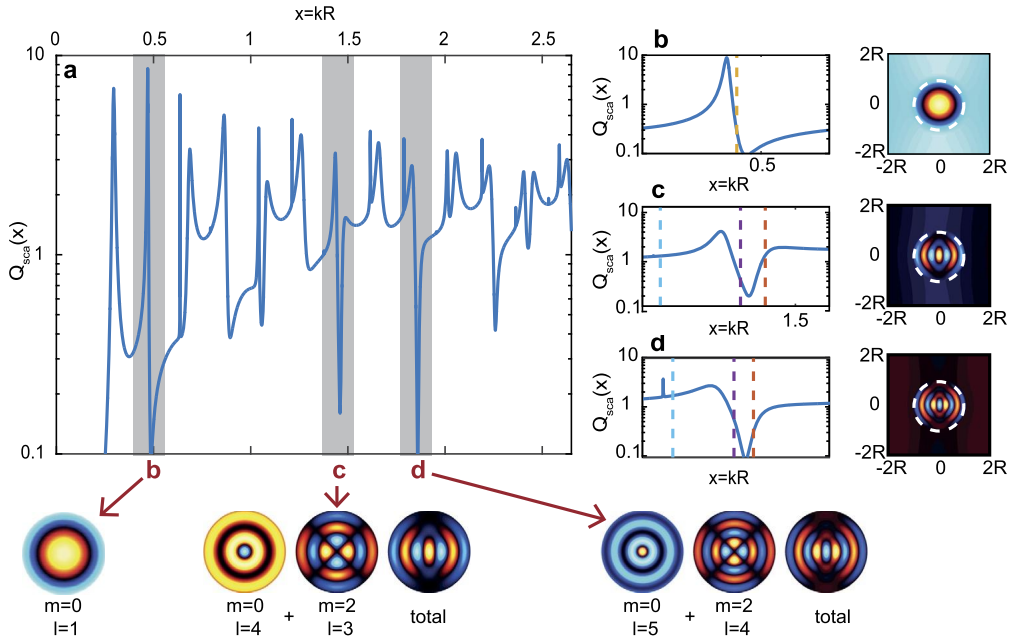

Figure 6.8. Fano–Feshbach description of higher-order anapole states. Higher-order anapole states in a high-index resonator ($n = 8$). a) Total scattering efficiency $Q_{sca}(x)$. Three non-radiating states appear (gray areas), which originate from different superpositions of internal modes (inset). b, d) As in the silicon case, the non-radiating states are characterized by a different superposition of internal and external channels. While in the first state at $x = 0.495$ (b) the invisibility is due to a pure state ($m = 0, l = 1$), in the higher order non-radiating states, the internal field is characterized by the superposition of two different internal modes, with $m = 0$ and $m = 2$ and different values of l (c,d). Adapted with permission from [14], ©IOP Publishing Ltd.

fundamental and higher-order anapole states in terms of quasi-overlapping orthogonal resonances is beneficial for comparing the critical properties of anapole states with other families of radiationless states.

Another family of non-radiating states supported by all-dielectric nanostructures are the so-called bound states in the continuum (BICs), initially introduced in the context of the Schrödinger equation in 1929 by von Neumann and Wigner [43]. BIC states correspond to peculiar resonances localized within the radiation continuum spectrum without energy decay. The work of [6] proposed the first direct link between anapoles and BIC states, where the authors demonstrated that the anapole states constitute the non-resonant counterpart of a specific type of cavity super-mode known as Friedrich–Wintgen Bound states In the Continuum (FW-BIC).

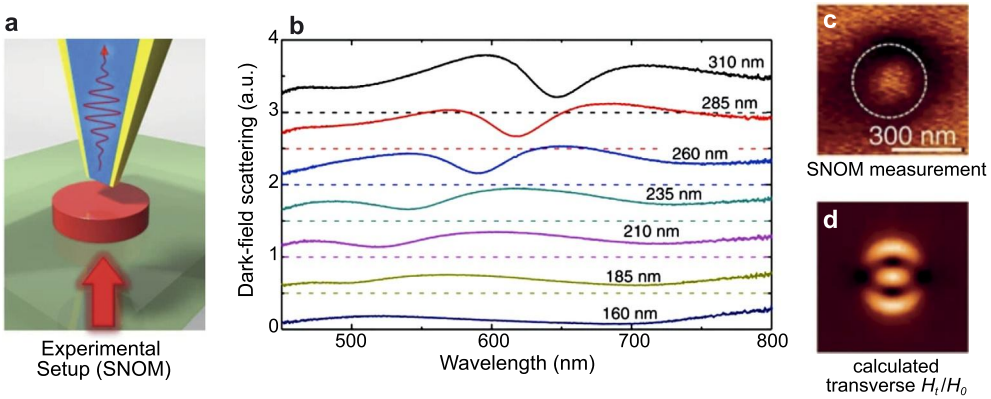

Figure 6.9. First experimental observation of anapole states. a) Experimental configuration. b) Experimental dark-field scattering spectra of silicon nanodisks with a height of 50 nm and a diameter ranging from 160 to 310 nm. c) SNOM electric field distribution (horizontal polarization), illustrating the near-field enhancement around the silicon nanodisk with a diameter of 310 nm. d) Corresponding calculated transverse magnetic field distribution on top of the disk, 10 nm above surface. Adapted from [8] and reused under the Creative Commons Attribution 4.0.

6.3 Selected experiments and applications

As discussed in Section 6.1, in generic structures such as disks or core-shell structures, the broader range of degrees of freedom opens to the manipulation of the multipole response of the system and engineer pure anapole states [44,45]. The seminal work by Miroshnichenko et al. [8] exemplifies best such a possibility, where the authors provided the first experimental demonstration of the existence of anapole states in silicon nanodisks. Fig. 6.9 shows a summary of the experimental results. The authors performed scanning near-field optical microscope (SNOM) experiments on silicon nanodisks with a thickness of 50 nm and varying diameters in the range from 200 to 400 µm (Fig. 6.9b). Far-field scattering spectra, collected through single nanoparticle dark-field spectroscopy, showed the formation of a radiationless state (identified by the suppression of the far-field scattering), for nanodisks with diameters above 200 µm (Fig. 6.9 b), in perfect agreement with the cartesian multipole decomposition described in Section 6.1.1. The formation of an anapole state was confirmed by mapping the near-field distribution of the scattered field, as illustrated in Fig. 6.9c,d.

Several experimental works hinted at their existence even before the theoretical formalization of higher-order anapole states, most notably in [46]. In this work, the authors extensively mapped silicon dielectric disks' far-field and near-field responses. As illustrated in Fig. 6.10a, the authors considered silicon nanodisks

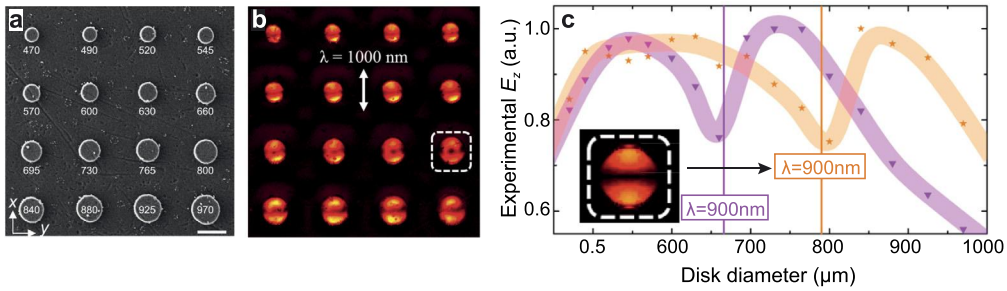

Figure 6.10. Experimental observation of higher-order anapole states. a) SEM picture of the array of silicon nanodisks of 80 nm thickness and diameters varied from 470 to 970 nm. b) Corresponding SNOM maps of the near-field electric field amplitude under linearly-polarized illumination (the vertical arrows denote the polarization direction). The resonator encircled with a white dashed line corresponds to a second-order anapole state. c) Average near-field amplitude measured at two different wavelengths of $\lambda = 900$ nm (pink triangles) and $\lambda = 1000$ nm (orange triangles). The figure includes shaded regions for eye guidance. The vertical lines identify the nanodisks with lower scattering and correspond to second-order anapole states. Adapted with permission from [46], Copyright (2017) American Chemical Society.

of 80 nm thickness and diameters varied from 470 to 970 nm fabricated on a fused silica substrate and arranged in a four-by-four array with a period of 2 μm. The authors collected near-field electric field distribution with the scattering-type amplitude- and phase-resolved scanning near-field microscope (SNOM) at 900 to 1640 nm. Fig. 6.10b clearly illustrates that a disk with a diameter of 800 nm (white dashed block) corresponds to the minimum average near-field amplitude for an incident wavelength of $\lambda = 1000$ nm (6.10b, orange stars, thick line added for eye guidance). This state corresponds to a second-order anapole state by comparing numerical simulations (vertical solid lines).

Reports of fundamental and high-order anapole states also appear in dynamic metasurfaces and metamaterials. In a recent work by Tian et al., the authors demonstrated the dynamical transition from radiating to radiationless conditions in phase-changing materials at infrared wavelengths [47]. The authors considered nanostructures composed of a phase-changing alloy Ge2Sb2Te5 (GST), a material whose optical properties can be finely thermally tuned. The ability to actively control the optical response of the structure enabled the authors to observe the transition from radiative electric dipoles to radiationless anapole states (Fig. 6.11a). The experimental extinction spectra of GST disks with a diameter of 2 μm and a height of 220 nm are shown in Fig. 6.11b. The different curves correspond to nanodisks thermally exposed to a fixed temperature (145 degrees) for different amounts of time. The GST disks support notable extinction

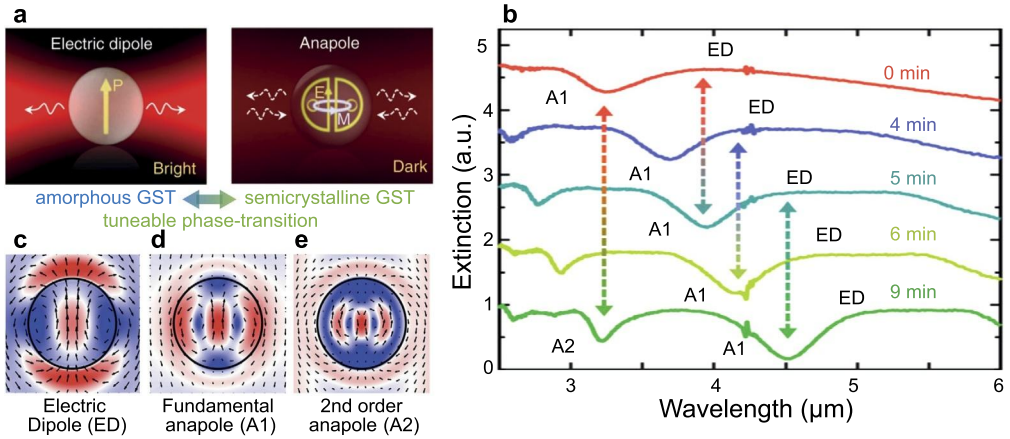

Figure 6.11. Anapole states in dynamic metamaterials. a) Tunable transition from electric dipole (bright state) to anapole (dark state) via thermal tuning of phase-changing GST microdisks. b) Experimental extinction spectra of GST disks with radius R = 1 μm and height H = 220 nm. ED, A1, and A2 denote the electric dipole, first- and second-order anapole states, respectively. c-e) Near field distributions for the ED, A1, and A2 states in the middle plane of the disk. Adapted with permission from [47], Copyright (2019) American Chemical Society.

maxima and minima with evident shifting as a function of the temperature. Multipole decomposition of the extinction spectra, supported by full numerical simulations, confirmed that the maxima and minima exactly correlate with the electric dipole (ED), fundamental anapole states (A1), and second-order anapoles (A2) (Fig. 6.11c-e).

An interesting question is whether the near-field coupling properties of the anapole can provide an edge to engineer advanced devices based on complex interactions between different anapole states. To answer this question, in [48] Mazzone et al. investigated the mutual coupling of passive anapole nanoparticles. Fig. 6.12a-c reports the results of their analysis on Si nanodisks. The figure confirms how the mutual coupling of different anapole states is strongly dependent on both their position (Fig. 6.12a) and orientation (Fig. 6.12b), as initially suggested in [22]. As a direct application, the authors demonstrated that the non-radiating state could efficiently transfer across chains of nanoparticles (Fig. 6.12c), and that the guiding properties of the anapole chains were robust against bends and splitting [48].

The work of [49] experimentally confirmed the mutual coupling of chains and arrays of anapole states. In this work, the authors fabricated and characterized rectangular arrays of amorphous GaP nanodisks 6.12d. Each nanodisk, characterized by a 130 nm radius and 50 nm height, individually supports an anapole

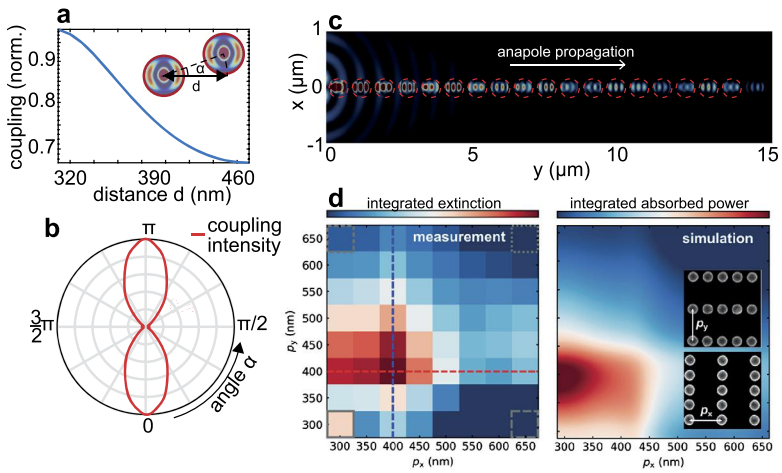

Figure 6.12. Multiple-anapole coupling and its applications. a,b) Coupling efficiency between anapole nanoparticles as a function of (a) the lateral displacement and (b) rotation angle. c) Electromagnetic energy distribution along a chain of silicon nanoparticles excited at the anapole wavelength. The near-field coupling allows transferring the radiationless state across ensembles of resonators, allowing the design of unconventional waveguides and splitters [48]. d) Integrated extinction and calculated absorbed power for arrays of amorphous GaP nanodisks that support anapole excitations at 600 nm. The lateral coupling between the resonators enables engineering the absorption properties of the sample. The inset illustrates SEM images of fabricated samples illustrating the displacements p_x and p_y [49]. Adapted from [48,49] and reused under the Creative Commons Attribution 4.0.

excitation at $\lambda = 600$ nm, a condition within the lossy region of the amorphous GaP substrate. Interestingly, the mutual coupling of the anapole states leads to drastic changes in the absorbed power. Fig. 6.12 d illustrates such results, where the experimental integrated extinction as a function of the horizontal p_x and vertical p_y array periods for an x-polarized incident wave. The experimental results (left) are in excellent agreement with numerical simulations of the nanoarrays. These results show that the overall absorption of the anapole nanoarray can be maximized for a specific array period of $p_x = p_y = 400$ nm, corresponding to a grating resonance of the collective structure. Quite interestingly, maintaining $p_y = 400$ nm stabilizes high extinction for small and intermediate values of p_x, an asymmetric behavior that is direct evidence of the different coupling strengths along the x- and y-axis initially predicted in [48].

Acknowledgments

JSTG acknowledges support from The Leverhulme Trust (Leverhulme Early Career Fellowship ECF-2020-537). This work was supported by the UK Engineering and Physical Sciences Research Council (EPSRC) [Grant number EP/W028344/1].

References

[1] N. Papasimakis, V.A. Fedotov, V. Savinov, T.A. Raybould, N.I. Zheludev, Electromagnetic toroidal excitations in matter and free space, Nature Materials 15 (3) (2016) 263–271, https://doi.org/10.1038/nmat4563.
[2] K.V. Baryshnikova, D.A. Smirnova, B.S. Lukyanchuk, Y.S. Kivshar, Optical anapoles: concepts and applications, Advanced Optical Materials 7 (14) (2019) 1801350, https://doi.org/10.1002/adom.201801350.
[3] S. Nanz, Toroidal Multipole Moments in Classical Electrodynamics, Springer Fachmedien Wiesbaden, Wiesbaden, 2016.
[4] V. Savinov, V.A. Fedotov, N.I. Zheludev, Toroidal dipolar excitation and macroscopic electromagnetic properties of metamaterials, Physical Review B 89 (20) (2014) 205112, https://doi.org/10.1103/PhysRevB.89.205112.
[5] C.F. Bohren, D.R. Huffman, Absorption and Scattering of Light by Small Particles, John Wiley & Sons, 2008.
[6] K. Koshelev, G. Favraud, A. Bogdanov, Y. Kivshar, A. Fratalocchi, Nonradiating photonics with resonant dielectric nanostructures, Nanophotonics 8 (5) (2019) 725–745, https://doi.org/10.1515/nanoph-2019-0024.
[7] E. Wolf, T. Habashy, Invisible bodies and uniqueness of the inverse scattering problem, Journal of Modern Optics 40 (5) (1993) 785–792, https://doi.org/10.1080/09500349314550821.
[8] A.E. Miroshnichenko, A.B. Evlyukhin, Y.F. Yu, R.M. Bakker, A. Chipouline, A.I. Kuznetsov, B. Luk'yanchuk, B.N. Chichkov, Y.S. Kivshar, Nonradiating anapole modes in dielectric nanoparticles, Nature Communications 6 (2015) 8069, https://doi.org/10.1038/ncomms9069.
[9] I.B. Zel'Dovich, Electromagnetic interaction with parity violation, Journal of Experimental and Theoretical Physics (U.S.S.R.) 33 (1957) 1531–1533.
[10] C.M. Ho, R.J. Scherrer, Anapole dark matter, Physics Letters B 722 (4) (2013) 341–346, https://doi.org/10.1016/j.physletb.2013.04.039.
[11] A. Costescu, E.E. Radescu, Induced toroid structures and toroid polarizabilities, Physical Review D 35 (11) (1987) 3496–3499, https://doi.org/10.1103/PhysRevD.35.3496.
[12] G.N. Afanasiev, Y.P. Stepanovsky, The electromagnetic field of elementary time-dependent toroidal sources, Journal of Physics. A, Mathematical and General 28 (16) (1995) 4565–4580, https://doi.org/10.1088/0305-4470/28/16/014.
[13] V. Savinov, N. Papasimakis, D.P. Tsai, N.I. Zheludev, Optical anapoles, Communications Physics 2 (1) (2019) 69, https://doi.org/10.1038/s42005-019-0167-z.
[14] J.S.T. Gongora, G. Favraud, A. Fratalocchi, Fundamental and high-order anapoles in all-dielectric metamaterials via Fano–Feshbach modes competition, Nanotechnology 28 (10) (2017) 104001, https://doi.org/10.1088/1361-6528/aa593d.
[15] R. Alaee, C. Rockstuhl, I. Fernandez-Corbaton, Exact multipolar decompositions with applications in nanophotonics, Advanced Optical Materials 7 (1) (2019) 1800783, https://doi.org/10.1002/adom.201800783.

[16] P. Kapitanova, E. Zanganeh, N. Pavlov, M. Song, P. Belov, A. Evlyukhin, A. Miroshnichenko, Seeing the unseen: experimental observation of magnetic anapole state inside a high-index dielectric particle, Annalen der Physik 532 (12) (2020) 2000293, https://doi.org/10.1002/andp.202000293.

[17] B. Luk'yanchuk, R. Paniagua-Domínguez, A.I. Kuznetsov, A.E. Miroshnichenko, Y.S. Kivshar, Hybrid anapole modes of high-index dielectric nanoparticles, Physical Review A 95 (6) (2017) 063820, https://doi.org/10.1103/PhysRevA.95.063820.

[18] E. Zanganeh, A. Evlyukhin, A. Miroshnichenko, M. Song, E. Nenasheva, P. Kapitanova, Anapole meta-atoms: nonradiating electric and magnetic sources, Physical Review Letters 127 (9) (2021) 096804, https://doi.org/10.1103/PhysRevLett.127.096804.

[19] W.-C. Zhai, T.-Z. Qiao, D.-J. Cai, W.-J. Wang, J.-D. Chen, Z.-H. Chen, S.-D. Liu, Anticrossing double Fano resonances generated in metallic/dielectric hybrid nanostructures using nonradiative anapole modes for enhanced nonlinear optical effects, Optics Express 24 (24) (2016) 27858–27869, https://doi.org/10.1364/OE.24.027858, http://www.osapublishing.org/abstract.cfm?uri=oe-24-24-27858.

[20] E.A. Gurvitz, K.S. Ladutenko, P.A. Dergachev, A.B. Evlyukhin, A.E. Miroshnichenko, A.S. Shalin, The high-order toroidal moments and anapole states in all-dielectric photonics, Laser & Photonics Reviews 13 (5) (2019) 1800266, https://doi.org/10.1002/lpor.201800266.

[21] A.V. Kuznetsov, A.C. Valero, M. Tarkhov, V. Bobrovs, D. Redka, A.S. Shalin, Transparent hybrid anapole metasurfaces with negligible electromagnetic coupling for phase engineering, Nanophotonics 10 (17) (2021) 4385–4398, https://doi.org/10.1515/nanoph-2021-0377.

[22] J.S. Gongora, A.E. Miroshnichenko, Y.S. Kivshar, A. Fratalocchi, Anapole nanolasers for mode-locking and ultrafast pulse generation, Nature Communications 8 (2017) 15535, https://doi.org/10.1038/ncomms15535.

[23] M.I. Tribelsky, A.E. Miroshnichenko, Giant in-particle field concentration and Fano resonances at light scattering by high-refractive-index particles, Physical Review A 93 (5) (2016) 053837, https://doi.org/10.1103/PhysRevA.93.053837.

[24] G. Grinblat, Y. Li, M.P. Nielsen, R.F. Oulton, S.A. Maier, Enhanced third harmonic generation in single germanium nanodisks excited at the anapole mode, Nano Letters 16 (7) (Jun. 2016) 4635–4640, https://doi.org/10.1021/acs.nanolett.6b01958.

[25] F. Monticone, D. Sounas, A. Krasnok, A. Alù, Can a nonradiating mode be externally excited? Nonscattering states versus embedded eigenstates, ACS Photonics 6 (12) (2019) 3108–3114, https://doi.org/10.1021/acsphotonics.9b01104.

[26] O. Zaitsev, L. Deych, Recent developments in the theory of multimode random lasers, Journal of Optics 12 (2) (2010) 024001, https://doi.org/10.1088/2040-8978/12/2/024001.

[27] G. Hackenbroich, C. Viviescas, F. Haake, Field quantization for chaotic resonators with overlapping modes, Physical Review Letters 89 (8) (2002) 083902, https://doi.org/10.1103/PhysRevLett.89.083902.

[28] C. Viviescas, G. Hackenbroich, Quantum theory of multimode fields: applications to optical resonators, Journal of Optics. B, Quantum and Semiclassical Optics 6 (4) (2004) 211, https://doi.org/10.1088/1464-4266/6/4/004.

[29] P.T. Kristensen, S. Hughes, Modes and mode volumes of leaky optical cavities and plasmonic nanoresonators, ACS Photonics 1 (1) (2014) 2–10.

[30] P.M. Morse, H. Feshbach, Methods of Theoretical Physics, McGraw-Hill, 1953.
[31] U. Fano, Effects of configuration interaction on intensities and phase shifts, Physical Review 124 (6) (1961) 1866–1878, https://doi.org/10.1103/PhysRev.124.1866, http://link.aps.org/doi/10.1103/PhysRev.124.1866.
[32] C. Chin, R. Grimm, P. Julienne, E. Tiesinga, Feshbach resonances in ultracold gases, Reviews of Modern Physics 82 (2) (2010) 1225–1286, https://doi.org/10.1103/RevModPhys.82.1225, http://link.aps.org/doi/10.1103/RevModPhys.82.1225.
[33] D. Chruściński, A. Kossakowski, Feshbach projection formalism for open quantum systems, Physical Review Letters 111 (5) (2013) 050402, https://doi.org/10.1103/PhysRevLett.111.050402, http://link.aps.org/doi/10.1103/PhysRevLett.111.050402.
[34] R.P. Kanwal, Generalized Functions Theory and Applications, Springer, London, 2004.
[35] M. Makarenko, A. Burguete-Lopez, F. Getman, A. Fratalocchi, Generalized Maxwell projections for multi-mode network Photonics, Scientific Reports 10 (1) (2020) 9038, https://doi.org/10.1038/s41598-020-65293-6.
[36] F. Getman, M. Makarenko, A. Burguete-Lopez, A. Fratalocchi, Broadband vectorial ultrathin optics with experimental efficiency up to 99% in the visible region via universal approximators, Light: Science & Applications 10 (1) (2021) 47, https://doi.org/10.1038/s41377-021-00489-7.
[37] J.D. Jackson, Classical Electrodynamics, 3rd edition, Wiley, New York, NY, 1999.
[38] H.A. Haus, Waves and Fields in Optoelectronics, Prentice Hall, London, 1983.
[39] Wonjoo Suh, Zheng Wang, Shanhui Fan, Temporal coupled-mode theory and the presence of non-orthogonal modes in lossless multimode cavities, IEEE Journal of Quantum Electronics 40 (10) (2004) 1511–1518, https://doi.org/10.1109/JQE.2004.834773.
[40] Z. Ruan, S. Fan, Temporal coupled-mode theory for Fano resonance in light scattering by a single obstacle†, The Journal of Physical Chemistry C 114 (16) (2010) 7324–7329, https://doi.org/10.1021/jp9089722, http://pubs.acs.org/doi/abs/10.1021/jp9089722.
[41] S. Fan, W. Suh, J.D. Joannopoulos, Temporal coupled-mode theory for the Fano resonance in optical resonators, Journal of the Optical Society of America A 20 (3) (2003) 569, https://doi.org/10.1364/JOSAA.20.000569, https://www.osapublishing.org/josaa/abstract.cfm?uri=josaa-20-3-569.
[42] M.V. Rybin, D.S. Filonov, P.A. Belov, Y.S. Kivshar, M.F. Limonov, Switching from visibility to invisibility via Fano resonances: theory and experiment, Scientific Reports 5 (2015) 8774, https://doi.org/10.1038/srep08774, http://www.nature.com/articles/srep08774.
[43] C.W. Hsu, B. Zhen, A.D. Stone, J.D. Joannopoulos, M. Soljačić, Bound states in the continuum, Nature Reviews Materials 1 (9) (2016) 16048, https://doi.org/10.1038/natrevmats.2016.48.
[44] P.C. Wu, C.Y. Liao, V. Savinov, T.L. Chung, W.T. Chen, Y.-W. Huang, P.R. Wu, Y.-H. Chen, A.-Q. Liu, N.I. Zheludev, D.P. Tsai, Optical anapole metamaterial, ACS Nano 12 (2) (2018) 1920–1927, https://doi.org/10.1021/acsnano.7b08828.
[45] A. Tripathi, H.-R. Kim, P. Tonkaev, S.-J. Lee, S.V. Makarov, S.S. Kruk, M.V. Rybin, H.-G. Park, Y. Kivshar, Lasing action from anapole metasurfaces, Nano Letters 21 (15) (2021) 6563–6568, https://doi.org/10.1021/acs.nanolett.1c01857.
[46] V.A. Zenin, A.B. Evlyukhin, S.M. Novikov, Y. Yang, R. Malureanu, A.V. Lavrinenko, B.N. Chichkov, S.I. Bozhevolnyi, Direct amplitude-phase

near-field observation of higher-order anapole states, Nano Letters 17 (11) (2017) 7152–7159, https://doi.org/10.1021/acs.nanolett.7b04200.

[47] J. Tian, H. Luo, Y. Yang, F. Ding, Y. Qu, D. Zhao, M. Qiu, S.I. Bozhevolnyi, Active control of anapole states by structuring the phase-change alloy Ge2Sb2Te5, Nature Communications 10 (1) (2019) 396, https://doi.org/10.1038/s41467-018-08057-1.

[48] V. Mazzone, J.S. Totero Gongora, A. Fratalocchi, Near-field coupling and mode competition in multiple anapole systems, Applied Sciences 7 (6) (2017) 542, https://doi.org/10.3390/app7060542.

[49] L. Hüttenhofer, A. Tittl, L. Kühner, E. Cortés, S.A. Maier, Anapole-assisted absorption engineering in arrays of coupled amorphous gallium phosphide nanodisks, ACS Photonics 8 (5) (2021) 1469–1476, https://doi.org/10.1021/acsphotonics.1c00238.

This page intentionally left blank

7

Bound states in the continuum in dielectric resonators embedded into metallic waveguide

Evgeny Bulgakov, Artem Pilipchuk, and Almas Sadreev
Kirensky Institute of Physics, Federal Research Center KSC SB RAS, Krasnoyarsk, Russia

7.1 Introduction

Since the famous paper by Gustav Mie [1], engineering of dielectric cavities in optics and photonics has long been an area of implementation various ideas and approaches to enhance the quality factor Q due to its paramount importance in both applied and fundamental research. Conventionally, light can be confined in closed or Hermitian system where access to radiation channels is prohibited due to, for example, metallic cover or embedding the resonant frequencies of cavity in the bandgap of photonic crystal [2]. However, this way conflicts with necessity of easy manipulation of light confined in the cavity. On the other hand, the compact dielectric resonator in air can be easily manipulated by external sources of coherent light, but its Q-factor is very restricted due to its embedding in the radiation continuum whose spectrum is given by light cone $\omega = ck$ with no cutoff. In principle, the problem can be solved cardinally when dealing with infinite periodical structures, for example, gratings. The periodicity quantizes the directions of radiation leakage by means of diffraction orders and brings cutoffs. As a result, the periodical structures support bound states in the radiation continuum (BICs) [3–18]. In the first part of this chapter, we reproduce comprehensive analytical insight into the origin of BICs in two limiting cases. In the first case, we consider a dielectric homogeneous slab with periodical slits whose thickness is much less than the period $h \ll L$, as shown in Fig. 7.1. BICs in general case of a high-contrast grating with arbitrary h were considered in Refs. [12,16,19–24]. The low-contrast case of periodic modulation of refractive index $n(z) =$

All-Dielectric Nanophotonics. https://doi.org/10.1016/B978-0-32-395195-1.00012-0
Copyright © 2024 Elsevier Ltd. All rights reserved.

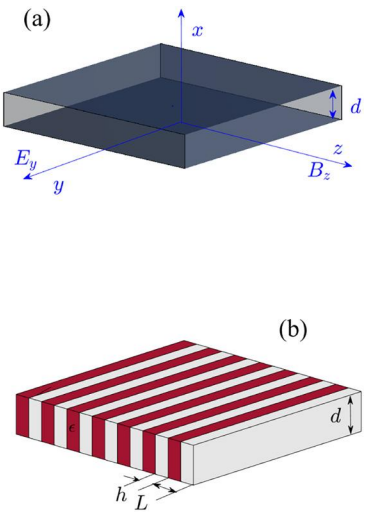

Figure 7.1. (a) Infinite dielectric slab with refractive index $n^2 = \epsilon$ and (b) grating slab with stepwise dependence $n(z)$.

$n + \delta n \cos(2\pi z/L)$, $\delta n \ll n$ presents the second case which allows analytical consideration of Bloch BICs [16,23,24].

However, in practice an increasing of the number of cavities in periodical arrays is limited by material losses [25] and structural fluctuations [26]. Moreover, grating slabs yield isolated dielectric cavities in compact form. In view of this, a breakthrough in the engineering of dielectric cavities was achieved by avoiding crossing of resonances of single cavity [27–31] or different cavities [32,33]. In spite of reporting unprecedent values of the Q-factor in these cavities that cannot achieve infinity because the isolated cavity in air cannot support the true BICs [34,35]. In other words, although the multipolar radiation with low orders of orbital momentum can be suppressed due to avoided crossing of resonances, the higher-order multipolar radiation still remains [31,32,36,37]. Hence, the second basic part of the chapter considers a compromise solution of the problem by restricting the radiation space by two parallel metallic planes separated by a distance d. Then, for instance, the single dielectric cylinder inserted between the planes, as depicted in Fig. 7.6 (a), is equivalent to the infinite periodical array of cylinders with the period d in which BICs were considered by many scholars [8,11,13,14,17,38–46]. The equivalency follows from the Dirichlet boundary conditions at perfectly conducting metal surface for the TM solutions of the Maxwell's equations. Respectively, two identical cavities between the planes are equivalent to two periodical arrays of rods which support Fabry–Perot BICs [9,47].

7.2 BICs in periodical arrays and gratings

In this sector, we formulate basic principles and mechanisms for electromagnetic bound states embedded into radiation continuum with discrete eigenfrequencies above light line. Let us consider first the textbook eigenvalue problem of the Maxwell equations in dielectric slab of thickness d [48] and refractive index $\epsilon = n^2$ as sketched in Fig. 7.1 (a).

7.2.1 Mechanism of light trapping by one-dimensional periodic dielectric structures

Slab is homogeneous along the y and z directions. Therefore, for the TE solutions in which electric field is directed along the y direction and transverse to the propagation direction z, we can write the Maxwell equations as follows:

$$-\frac{\partial^2 E_y}{\partial x^2} - \frac{\partial^2 E_y}{\partial z^2} = n^2 \frac{\omega^2}{c^2} E_y, \tag{7.1}$$

inside the slab at $|x| < d/2$. Here c is the light velocity, n is the refractive index of slab. Outside the slab we have the same equation, however, with $n = 1$. A free wave propagation along the y direction gives the solution of Eq. (7.1) as $E_y(x, z) = E_y(x)e^{ik_z z}$. While a stepwise behavior of refractive index for $x > 0$ direction allows to write for the symmetric solutions:

$$E_y(x) = \begin{cases} A\cos(q_x x), & |x| < d/2 \\ B\exp(-k_x|x|), & |x| > d/2, \end{cases} \tag{7.2}$$

where

$$k_x = \sqrt{k_z^2 - \omega^2/c^2}, \quad q_x = \sqrt{n^2\omega^2/c^2 - k_z^2}. \tag{7.3}$$

The magnetic field:

$$B_z = \frac{i}{\omega}\frac{\partial E_y}{\partial x}. \tag{7.4}$$

The continuity for the EM fields gives us the dispersion equation:

$$k_x = q_x \tan(q_x d/2). \tag{7.5}$$

From Eq. (7.3), we have:

$$k_x^2 + q_x^2 = \frac{\omega^2}{c^2}(n^2 - 1). \tag{7.6}$$

Introducing dimensionless variables $k_x d \to k_x$, $q_x d \to q_x$, $\nu = \omega d/c$, Eqs. (7.5) and (7.6) take the following form:

$$k_x^2 + q_x^2 = \nu^2(n^2 - 1),$$
$$k_x = q_x \tan(q_x). \tag{7.7}$$

The dispersion curves for the first three TE solutions $E_y(x, z)$ are shown in Fig. 7.2.

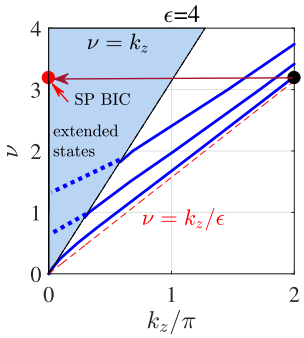

Figure 7.2. Dispersion curves $\nu(k_z) = \omega(k_z)d/c$ of the first 3 TE solutions (7.2) of slab with refractive index $n = 2$. Solid lines show the real eigenfrequencies of non radiative TE modes propagating along the slab below light line. Dotted lines show complex eigenfrequencies above light line, leaking into radiation space.

Consider now the case of slab with refractive index n with periodical slits of thickness h as shown in Fig. 7.1 (b). If radiation can leak from slab in arbitrary directions, in periodical one-dimensional grating light can leak only in discrete directions defined by ratio $\sin\theta_n = k_m/k = k_m c/\nu$, $k_m = 2\pi m/L$, and integers $m = 0, \pm 1, \pm 2$ enumerate the diffraction orders. As a result, grating can support BICs as was notified by many scholars [4,6–8,10–13, 16–18]. Fig. 7.3 shows by the gray shading where the first radiation channel in the continuum is open, namely, $|k_z - 2\pi/L| > n\nu > |k_z|$.

The case of photonic crystal grating gives easy understanding of origin of symmetry protected BICs in the limit of narrow slits, $h \to 0$ [49]. For the case $h = 0$, we have multiple TE bound states below the light line shown by solid lines in Fig. 7.2. These solutions at $k_z = 2\pi/L$ take the following form:

$$u_j(x)\cos(2\pi z/L), \tag{7.8}$$

$u_j(x)$ describes the even and odd TE solutions across the slab. On the one hand, the solutions of grating are very close to the solution (7.8) for $h \to L$. On the other hand, the grating even with very narrow slits can radiate only into the diffraction channel $m = 0$ if

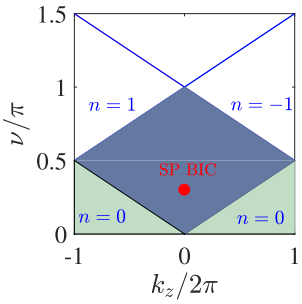

Figure 7.3. Band structure of grating given by dispersion curves $\nu(k_z)$.

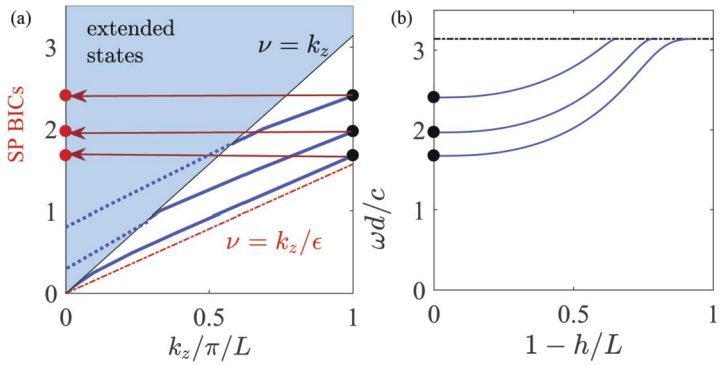

Figure 7.4. (a) Frequency of the TE SP BICs $\nu = \omega d/c$ vs the thickness of slits h in terms of the period L for $n = 2$. Closed red circle marks the BIC shown in Figs. 7.2 and 7.3. (b) Frequencies of SP BICs vs the thickness of slits.

the frequency of the solution is below the second diffraction cutoff given by the orders $m = \pm 1$, as shown in Fig. 7.3. Therefore, the solution (7.8) becomes the SP BIC at Γ-point $k_z = 0$ of grating. With extension of slit the frequency of SP BIC is increasing compared to the case $h \to 0$ because of squeezing of the solution inside each rod of thickness l_h along the z-axis, as demonstrated in Fig. 7.4. With further squeezing, the frequency of BIC passes the cutoff of the next diffraction channel, which destroys SP BIC. Therefore, there is a threshold in thickness of rods $L - h$ below which BIC vanishes in dependence of the refractive index. This approach of increasing the dimensions of periodical slits can be applied to dielectric waveguides of arbitrary cross-section, in particular to cylindrical waveguides to form SP BICs in an array of coaxial disks [49].

Now we demonstrate that BICs can occur in low-contrast gratings in refractive index of dielectric slab, weakly modulated

along the z-axis. That can be done by illuminating the slab by two counter-propagating monochromatic laser beams along z-direction with wavelength λ, leading to:

$$n(x,z) = n(x)n(z), \quad n(z) = n + n_2 I_0 \cos^2(2\pi z/\lambda), \tag{7.9}$$

where n_2 is the nonlinear refractive index, I_0 is the total intensity of two laser beams. The case of low-grating contrast allows BICs to be treated analytically in two-wave coupling approach [12,16, 19,21–24]. We reproduce this approach below in tutorial aim.

Following Refs. [23,24,50], we write the even solutions:

$$\psi_s(x,z) = e^{ik_z z} \sum_l \begin{cases} C_n u_l(z) \frac{\cos(q_{x,l}x)}{\cos(q_{x,l}d/2)}, & |x| < d/2 \\ t_l e^{ik_z z} \exp(-ik_{x,l}(x - d/2)), & |x| > d/2, \end{cases} \tag{7.10}$$

where a set of local modes $u_l(z) = u_l(z + L)$ in the slab satisfies:

$$\left\{ \left(\frac{\partial}{\partial z} + ik_z \right)^2 + \nu^2 n^2(z) \right\} u_l(z) = \kappa_l^2 u(z), \tag{7.11}$$

where κ_l will be determined later. For homogeneous slab $\kappa_l^2 = q_{x,l}^2$, we have:

$$\begin{aligned} &q_{x,l}^2 = \nu^2 n^2 - (k_z + k_l)^2, \quad k_{x,l}^2 = \nu^2 - (k_z + k_l)^2, \\ &k_l = 2\pi l/L, \quad l = 0, \pm 1, \pm 2, \ldots \end{aligned} \tag{7.12}$$

where ϵ_c is the relative permittivity of the slab. Here the wave numbers $k_{x,l}$ and $q_{x,l}$ have the same meaning as the wave numbers k_x and q_x in the homogeneous slab (see, Eq. (7.3)). All quantities in Eq. (7.12) are dimensionless via the slab thickness d.

The low-grating contrast suggests that we can calculate the leaky resonant modes and in particular the BIC based on resonant modes of a homogeneous slab without grating. Then we can leave only the terms $l = 0$ and $l = -1$ [23,24,50] for the eigenfrequency frequency ν below the first diffraction order $l = -1$ $k_z < \nu < 2\pi/L - k_z$ (see Fig. 7.3). We can approximate the local modes (7.10) as follows:

$$u_l(z) \approx u_0 + u_{-1} e^{-ik_1 z}. \tag{7.13}$$

That gives us closed system of two algebraic equations:

$$\begin{aligned} &(n^2\nu^2 - k_z^2)u_0 + \delta n \nu^2 u_{-1} = \kappa_n^2 u_0, \\ &2\delta n \nu^2 u_0 - (k_z - k_1)^2 u_{-1} + n^2 \nu^2 u_{-1} = \kappa_n^2 u_{-1}, \end{aligned} \tag{7.14}$$

where δn is weak perturbation amplitude of modulation of refractive index. For the laser-induced modulation (7.9), $\delta n = n_2 I_0/2$

with period $L = \lambda/2$. This equation has the solution when the determinant equals zero, which gives us two roots:

$$q_{x,0}^2 = \epsilon_d \nu^2 - k_z^2 - \frac{\delta n \nu^4}{(k_z - k_1)^2 - k_z^2},$$
$$q_{x,-1}^2 = \epsilon_d \nu_2^2 - (k_z - k_1)^2 + \frac{\delta \epsilon^2 \nu^4}{(k_z - k_1)^2 - k_z^2}, \tag{7.15}$$

where $q_{x,0}$ and $q_{x,-1}$ have a meaning of the eigenvalues of Eq. (7.14). Respectively, for each root we obtain the solution (7.14) $u_0 = -\sigma u_1$ and $u_0 = \frac{1}{\sigma} u_1$ where $\sigma = \frac{\delta \epsilon \nu^2}{(k_z - k_1)^2 - k_z^2}$. A substitution of these relations into Eq. (7.10) allows to write analytically particular solutions inside the slab:

$$E_y(x, z) \approx e^{ik_z z}(1 - \sigma e^{-ik_1 z}) \frac{\cos(q_{x,0} x)}{\cos(q_{x,0} d/2)},$$
$$E_y(x, z) \approx e^{ik_1 z})(\sigma + e^{-ik_1 z}) \frac{\cos(q_{x,-1} x)}{\cos(q_{x,-1} d/2)}. \tag{7.16}$$

The general solution inside the slab can therefore be presented as superposition of these particular solutions through coefficients C_0 and C_{-1}. A continuity condition for electric field E_y at $x = d/2$ with the solution outside slab $t_0 e^{ik_z z} e^{-ik_1(x-d/2)}$ gives:

$$C_0 + C_{-1} 1\sigma = t_0,$$
$$-C_0 \sigma + C_{-1} 1 = t_{-1}, \tag{7.17}$$

and for magnetic field B_z, (7.4) gives

$$J_0 C_0 + J_1 C_{-1} 1\sigma = i k_z t_0,$$
$$J_0 C_0 \sigma - J_1 C_{-1} 1 = i(k_z + k_1) t_{-1}, \tag{7.18}$$

where $J_p = q_{x,p} \tan(q_{x,p} d/2)$ even for the solutions and $J_p = -q_{x,p} \cot(q_{x,p} d/2)$, relative to $x \to -x$.

From Eq. (7.17), we have

$$\begin{pmatrix} C_0 \\ C_{-1} \end{pmatrix} = \frac{1}{1 + \sigma^2} \begin{pmatrix} 1 & -\sigma \\ \sigma & 1 \end{pmatrix}. \tag{7.19}$$

Substituting this equation into Eq. (7.18), we obtain

$$\begin{pmatrix} J_0 + J_1 \sigma^2 + (1 + \sigma^2) i k_{z,0} & \sigma(J_1 - J_0) \\ \sigma(J_1 - J_0) & J_0 + J_1 \sigma^2 + (1 + \sigma^2) i k_{z,-1} \end{pmatrix} \begin{pmatrix} t_0 \\ t_1 \end{pmatrix} = 0. \tag{7.20}$$

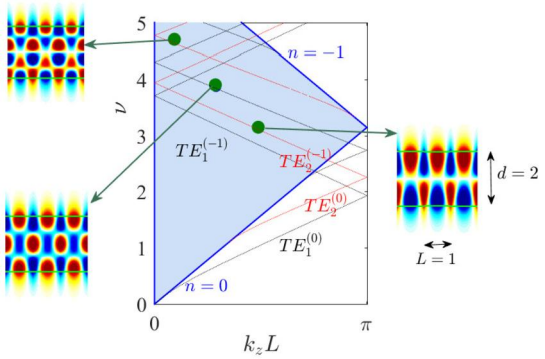

Figure 7.5. Dispersion curves of TE solutions around which the Bloch BICs, marked by closed green circles, are positioned. Patterns of BICs show E_y. $n=\sqrt{3}$, $\delta n=0.2$.

In order the frequency of the BIC solution was embedded in the first diffraction continuum but below the next diffraction continuum with dispersion $k_0=k_z-k_1$ we are to null a leakage by setting $t_0=0$ [23,24]. As a result, we obtain the BICs for different TE solutions, whose dispersion curves are shown by thin lines in Fig. 7.5. Note that the SP BICs originated from the first TE_1 solution in slab, even relative to $x\to -x$ does not exist, at least not for $\epsilon=3$. Examples of SP BICs corresponding to higher solutions TE_j, $j=2,3,4$ are shown by closed green circles with patterns E_y in insets of Fig. 7.5. In contrast to high-contrast grating, which supports SP BICs (see, Fig. 7.4), the low-contrast grating supports only Bloch BICs, as shown in Fig. 7.5, which were shown in the arrays of dielectric cylinders [10,11,51]. Therefore, similar to homogeneous slab, in TE electromagnetic waves can propagate below the light line, as demonstrated in Fig. 7.2. In the slab with periodic modulation of refractive index over slab, waves can propagate above light line.

7.3 Dielectric rods inserted into radiation space restricted by metal planes

BICs in great variety of PhCs provide unique opportunity to confine and manipulate electromagnetic wave within the radiative continuum (see, numerous reviews: [10,29,52–63]). However, in practice, theoretical results of BICs resonant states with infinite quality factor (Q-factor), are bumping into a few unavoidable obstacles. First of all, the number of elements in periodic structures is finite, which transforms BICs into quasi-BICs. Secondly,

Q-factor is limited by the material losses and structural fluctuations [25,26,64–66]. Although magnificent values of the Q-factor in isolated dielectric cavity were reported through whispering gallery modes [67,68] or avoided crossing of resonances [27,33], which cannot achieve infinity because the isolated cavity in open 3d radiation space air cannot support the true BICs [34,35].

In the present paper, we propose compromise solution to the problem by restriction of radiation space by two parallel metallic planes separated by a distance d. Then, for instance, the single dielectric cylinder inserted between the planes, as depicted in Fig. 7.6 (a), is equivalent to the infinite periodical array of cylinders with the period d in which BICs have been considered by many scholars [8,11,13,14,17,40–46]. The equivalency follows from the Dirichlet boundary conditions on a perfectly conducting metal surface for the TM solutions of the Maxwell equations. Respectively, two identical cavities between the planes are equivalent to two periodical arrays of rods, which support Fabry–Perot BICs [9,47].

In practice, material losses and structural fluctuations restrict the number of cavities transforming these BICs into quasi-BICs with although small but finite resonant widths [25,26,64]. Moreover, this way of engineering quasi-BICs leads to dielectric structures (DS) not being compact. For example, to achieve the Q-factor 10^5 of quasi-BIC, we need at least a few tens of silicon disks [25,65,69] or silicon cuboids [70]. The best results for the Q-factor were reported by Taghizadeh and Chung [71] with $Q = 10^5$ for 10 long silicon rods. In general, all the ways to achieve the extremely high Q-factor listed above require extended DS, in which the mode volume grows as well [23,72].

As considered in the previous section, BICs can exist in extended dielectric periodical gratings embedded in a three-dimensional radiation space. In the present section, we show that BICs can exist even in one or two dielectric rods embedded in a two-dimensional radiation space. The dimensions of radiation space can be easily reduced by two metallic planes parallel to each other, as shown in Fig. 7.6 (a) and (b). Moreover, in the case of a metallic waveguide with rectangular cross-section, the dimension of radiation space reduces to one and allows to remove another typical theoretical approximation of infinitely long cylinders rods, as shown in Fig. 7.6 (c) and (d). In fact, owing to boundary conditions at surface of perfectly conducting metallic surface, such systems are equivalent to arrays of dielectric cavities, as sketched in Fig. 7.8. Thus, the metallic waveguide with one or two dielectric insets is converted into a desktop laboratory for a variety of BICs. While reaching the BICs in gratings often requires tuning of geo-

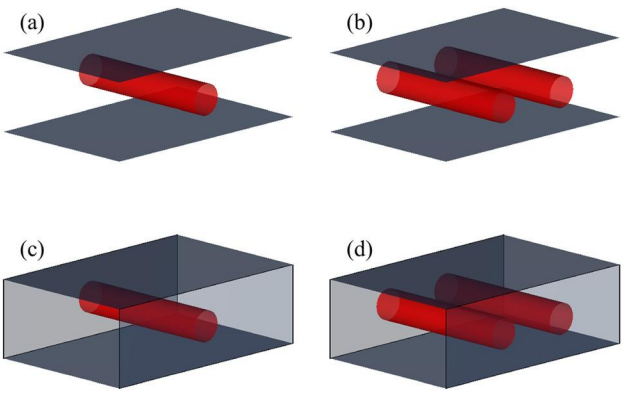

Figure 7.6. Single (a) and two parallel (b) infinitely long dielectric cylinders between two metallic planes. The same for cylinders of finite length inside waveguide of rectangular cross-section (c) and (d).

metrical parameters, in the present case of the desktop laboratory, BICs can be achieved by simply varying the width of the waveguide, the position or orientation of the dielectric inset within the waveguide. However, the main advantage of this laboratory is related to material losses and structural fluctuations, which rapidly saturate growth of the Q-factor with the number of cavities in periodic arrays [25,26,66], which prevents to clearly unveil the BICs.

The existence of symmetry protected (SP) BICs near rigid cylinder placed symmetrically in between parallel walls with Neumann or Dirichlet boundary conditions imposed upon them was shown by Evans and Porter [73]. After, Linton et al. [74] and Duan et al. [75] have examined the cases of accidental BICs for slender rods of arbitrary cross-section arranged asymmetrically in a waveguide. We develop these results for the case of dielectric rods of circular and rectangular cross-sections and find a threshold for dimensions and permittivity of the rod below which the BICs do not exist. Once the rod is shifted relative to center line, we obtain equivalent dimerized chain of rods, as shown in Fig. 7.8 (c). There are only a few reports of BICs in dimerized arrays of dielectric cavities [76,77]. Moreover, the rectangular rod inserted between metallic planes brings new parameter to vary, namely the angle of orientation of the rod, as shown in Fig. 7.8 (d). That, in turn, opens a way for realization of topologically protected BICs with winding numbers $m = \pm 1$ in two-parametric space of angle and frequency or angle and distance between rods.

7.3.1 One rod above one metallic plane

Although this case reduces the radiation space twice, still BICs can exist only in infinite periodical gratings. Nevertheless, this case is interesting in terms of enhancing the Q-factor due to avoided crossing of resonant modes of cylindrical rod with modes of image of the rod below the metal surface. This phenomenon was considered in Ref. [78] for dielectric sphere above the metal surface. Fig. 7.7 shows resonant modes at two distances: $h = 0$ the rod lies close to metal surface and $h = 0.976$ at which the Q-factor is maximal, where $Q = -\frac{\mathrm{Re}(\omega)}{2\mathrm{Im}(\omega)}$ and ω is the complex resonant eigenfrequency of the system. As inset shows, this is the result of avoided crossing of Mie resonance with azimuthal number $m = 6$ of the cylinder with the same resonances of its image on metal surface. This Mie resonant mode is hybridized to form symmetric or anti symmetric modes. As distance between cylinder and metal surface increase, the coupling between cylinder and its image behaves as $\frac{1}{L}e^{ikL}$ [79]. As a result, we observe regular oscillations of the Q-factor in Fig. 7.7. However, as this figure illustrates, the Q-factor is always finite, although can reach rather large values for variation of distance between surface and rod. Thereby, let us address the case of single cylinder inside two metallic planes.

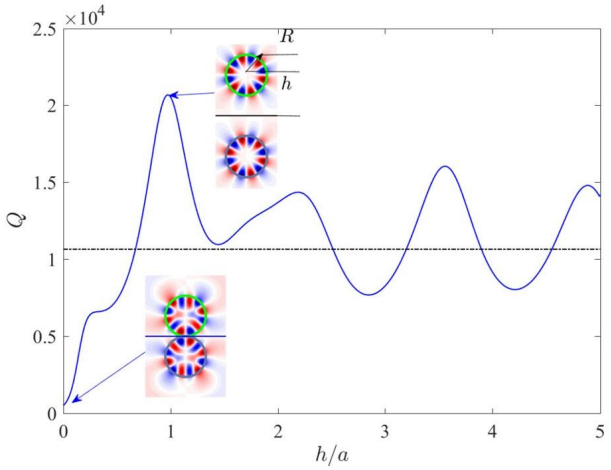

Figure 7.7. Dielectric rod with refractive index $n = 3.48$ above the metal surface. Mie resonant mode $m = 6$ of cylinder hybridizes with the same mode of image cylinder due to avoided crossing. Insets show the TE solutions for resonant modes with boundary conditions at metal surface which are equivalent to the solutions of two cylinders: $h = 0$ with the complex frequency $kR = 5.102 - 0.0051$ and $h = 0.976a$ with $kR = 5 - 0.00012i$. Dot-dashed line shows the Q-factor of Mie resonant mode of isolated cylinder with the azimuthal index $m = 6$.

7.3.2 Cylinder between two metallic planes

We start consideration with single dielectric cylinder of the radius R inserted parallel to metallic planes, as depicted in Fig. 7.6 (a). In what follows, all quantities are measured in terms of the distance between plates d, with x-axis directed along the waveguide and z-axis directed along the rod. Because of boundary conditions for the electric field $E_z(x = 0, d) = 0$, the solutions of the Maxwell equations of the system are equivalent to the solutions in periodical infinite array of rods at the Γ- or X-point, as sketched in Fig. 7.8 (a).

There are two distinct cases for these solutions. The case of dielectric inset symmetrically disposed between two parallel metallic planes is equivalent to periodical array of rods with the period d, as shown in Fig. 7.8 (a) and (b). Fig. 7.8 (c) presents the case of cylinder shifted from the center line of waveguide by distance Δ. Then the TM solutions of the system coincide with the solutions of the binary array of cylinders with double period $2d$. The equivalence of the solutions allows us to use well-known analytical approaches developed for periodical arrays of dielectric resonators [80,81]. We complete these approaches by COMSOL MultiPhysics numerical calculations for the rods with circular and rectangular cross-sections.

In Fig. 7.9, we show typical examples of the SP BICs with azimuthal indices $m = 1$ and $m = 2$ for the case of symmetrical position of dielectric cylinder with the refractive index n (Fig. 7.8 (a)). It is clear that for the dielectric rod to trap the EM wave with definite wavelength $\frac{2\pi}{k}$, its radius R has to be comparable or exceed the characteristic wavelength inside the rod $\frac{2\pi}{nk}$. Therefore, the curve of existence of the SP BICs can be evaluated as:

$$Rnk_{BIC} \geq 1/2\pi, \tag{7.21}$$

where the frequency of SP BIC k_{BIC} depend on the refractive index n and the radius of cylindrical rod R. Note, the light velocity is taken equaled to unit. Precise value of the frequency of BIC can be found numerically, e.g., by means of Comsol Multiphysics, however, the inequality (7.21) allows us to rewrite it as:

$$Rnk_{BIC} = C, \tag{7.22}$$

where the constant C is to be fitted to specific SP BIC. Numerical behavior and comparison of evaluation of the SP BIC's frequency with formula (7.22) is shown in Fig. 7.9, which demonstrates excellent agreement. Since the diameter of rod cannot exceed distance between mirrors, we obtain that SP BICs cannot

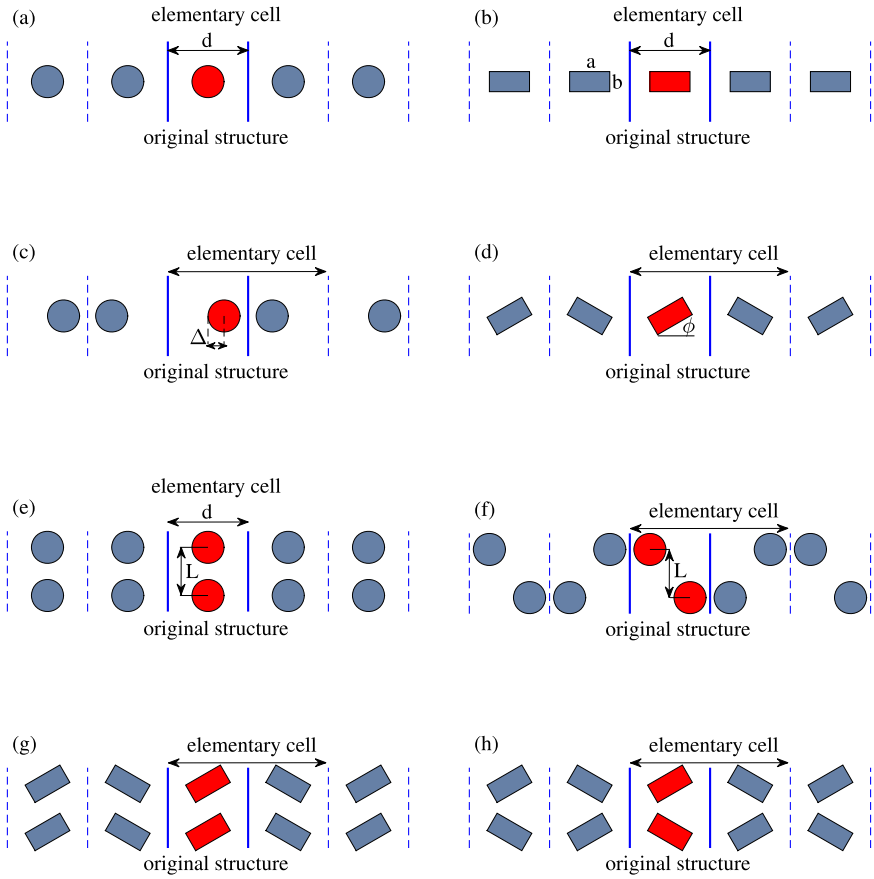

Figure 7.8. Periodical arrays of dielectric rods whose solutions at the Γ-point are equivalent to the solutions of Maxwell equations of rods placed between two parallel metallic planes, shown by solid thick lines. The original rod is shown in red, while its images in the metallic planes are shown in gray. Cylindrical (a) and rectangular (b) rods positioned symmetrically between planes are equivalent to the periodical array of rods with period d. Cylindrical rod shifted by distance y_0 from center line (c) and rectangular rod rotated by the angle ϕ make the system equivalent to dimerized chain. (e) Two rods positioned symmetrically make the system equivalent to double array of rods that can support FPR BICs. Two circular rods positioned asymmetrically (f) or two rotated rectangular rods (g) and (h) are equivalent to two dimerized chains.

exist for $nk_{BIC} \geq 2$. For non-symmetric position of the rod inside the waveguide the SP BICs. When the rod is positioned asymmetrically inside the waveguide, SP BICs transform to accidental BICs at tuned rod's radius or refractive index. In the equivalent system of binary periodical array of rods (see, Fig. 7.8 (c)), these BICs correspond to the BICs at Γ-point. Phase diagrams of existence of the accidental BICs are plotted in Fig. 7.10.

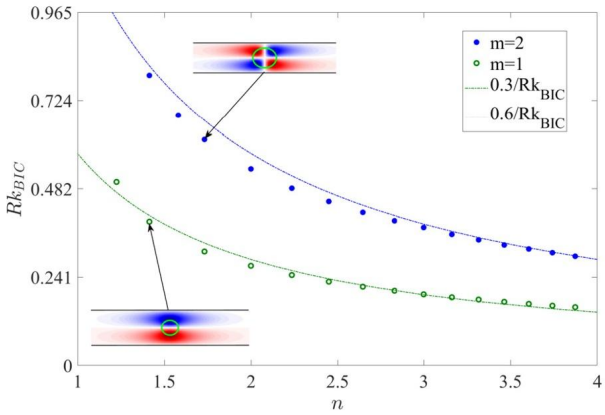

Figure 7.9. Curves of existence of the SP BICs vs refractive index and radius of circular rod.

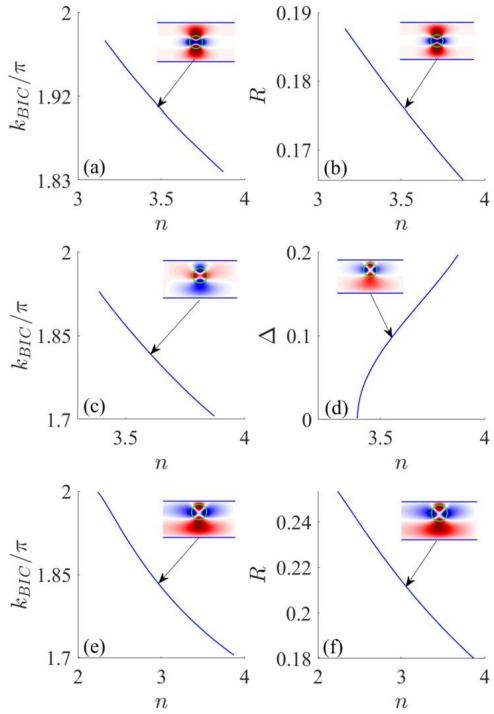

Figure 7.10. Curves of existence of accidental BICs in two-parametric space of refractive index of the rod and (a) frequency, (b) radius of the rod for $\Delta = 0$; (c) frequency, (d) displacement of the rod for $R = 0.18$; (e) frequency, (f) radius of the rod for $\Delta = 0.3$. Insets show the accidental BICs for certain parameters.

7.4 Rectangular rod between two metallic planes

First of all, the rectangular rod is interesting by that Linton et al. [74] have shown existence of accidental BICs under assumption that the aspect ratio a/b is sufficiently large and the rod is metallic. Moreover, rectangular rod brings new parameter to vary, rotation angle relative to the frame of metallic waveguide, as shown in Fig. 7.8 (d). Fig. 7.11 (a) shows curves of accidental BICs versus dimensions of rectangular quartz rod $a \times b$. Insets show evolution of two accidental BIC modes (electric field E_z directed along the rod). In fact, there are more curves which differ by number of nodal lines that cross the waveguide. TM propagation channels are given by simple formula $k^2 = k_x^2 + \pi^2 p^2$, $p = 1, 2, 3, \ldots$, where k_x is the wave vector of TM waves along the waveguide. We consider only the BICs embedded into the continuum of the first propagation channel of the waveguide with $p = 1$ and frequencies below the cutoff of the second propagation channel $\pi < k < 2\pi$.

First, one can see that the curves of BICs follow to analysis of Linton et al. obtained by different mathematical techniques [74] for the case of Dirichlet BC at the walls of rectangular rod, i.e., metallic rod. These accidental BICs shown in Fig. 7.11 (a) have clear physical origin. Far from the rod, accidental BICs follow to the evanescent mode $p = 2$, which is orthogonal to the first propagation channel $p = 1$ and therefore cannot go out. The dielectric rod perturbs the evanescent mode and the perturbation strength depends on size and refractive index of the rod. The larger the index and size, the stronger the perturbation. Despite the difference between the metallic and dielectric rods, the accidental BIC exists at $b \to 0$. However, BIC's frequency is limited by the cutoff 2π of the second channel and the localization range diverges for $k \to 2\pi$, as insets in Fig. 7.11 (b) show.

7.5 Fabry–Perot BICs: two rods inside waveguide

Two identical circular rods inserted symmetrically inside the waveguide, as shown in Fig. 7.6 (e), make the system equivalent to periodic double arrays of subwavelength dielectric cylinders. Such arrays were studied by Ndangali and Shabanov with analytic TM solutions for BICs in the limit of thin cylinders [47]. Underlying physical mechanism for BICs is the Fabry–Perot one [82], in which each array perfectly reflects electromagnetic waves at definite frequency k_c. Then, two arrays serve as ideal mirrors which are able

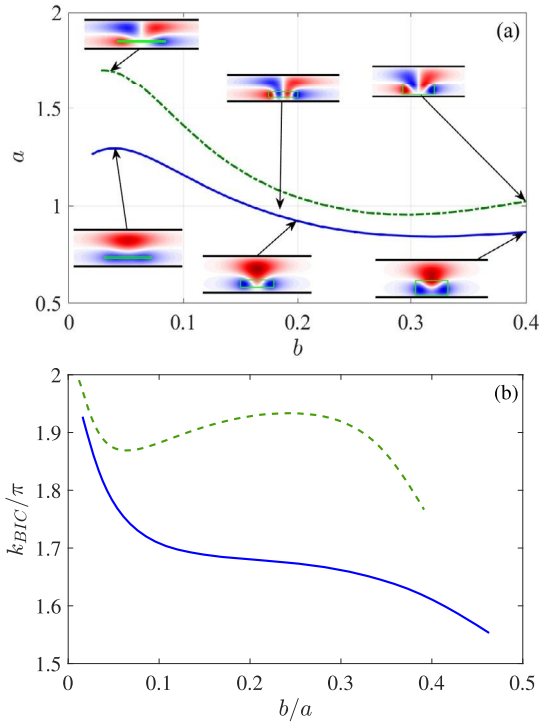

Figure 7.11. Curves of existence of the accidental BICs. (a) As a function of the cross-section of rectangular quartz rod $a \times b$ at $\Delta = 0.25$ with refractive index $n = 2.05$. (b) The frequency of BICs vs aspect ratio of rectangular rod.

to capture electromagnetic wave with frequency k_c at discrete distances roughly equal to integer number of half wavelength π/k_c. Fig. 7.12 demonstrates the effect of total reflection of TM waves by (a) cylindrical and (b) rectangular rods positioned symmetrically inside the waveguide. The effect of total reflection by rod inserted into waveguide exists irrespective to position of the rod inside the waveguide. In Fig. 7.12 (b) one can see the well-known effect of collapse of Fano resonance for $\phi \to 0$ and $\Delta = 0$, at which the scattering function tends to the SP BIC [83]. Fig. 7.12 (c) shows that total reflection ($T = 0$) is achieved owing to variation of cylindrical rod radius. However, the variation of the rod size is difficult in the experiment. Fig. 7.12 (d) demonstrates that the problem can be easily solved by orientation of rectangular rod relative to waveguide.

In Fig. 7.13 (a), we show results of numerical calculations for the case of two circular quartz rods inserted symmetrically (see, Fig. 7.8 (c)) with patterns of Fabry–Perot BICs for different dis-

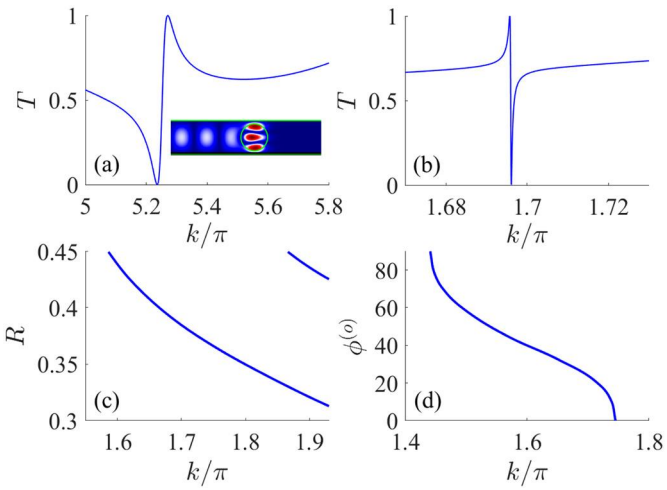

Figure 7.12. Transmittance vs frequency (upper panels) for (a) cylindrical rod with $R = 0.4$, $\Delta = 0$, (b) rectangular rod with cross-section 0.6×0.3 and $\Delta = 0.01$. Transmittance zeros (bottom panels) vs frequency of incident wave and (c) radius of cylindrical rod, (d) orientation angle of rectangular rod for $\Delta = 0$. The refractive index of the rods is $n = 2.05$ in all cases.

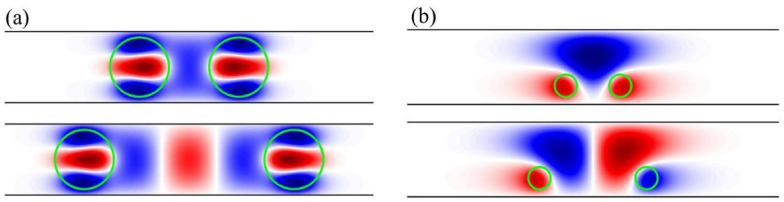

Figure 7.13. Patterns of Fabry–Perot BICs for the case of two cylindrical rods (shown by green circles) positioned (a) symmetrically ($R = 0.4, n = 2.05$) and (b) shifted cross to the waveguide inside the waveguide by $\Delta = 0.25$, $R = 0.15$.

tances between cylindrical rods. This case is equivalent to the case of two periodic arrays considered in Refs. [47,84]. It is interesting that similar type of BICs exist even for asymmetrical position of circular rods, as one can see from Fig. 7.13 (b). In Fig. 7.14 we show curves of the Fabry–Perot BICs in two-parametric space of the rotation angle of rods ϕ and distance between them L for two distinct cases of rod rotation: in-phase and anti-phase.

One of the ways to experimentally confirm BICs is observation of singularities in the wave transmission in waveguide. At the BIC point, the total reflection coalesces with the full transmission

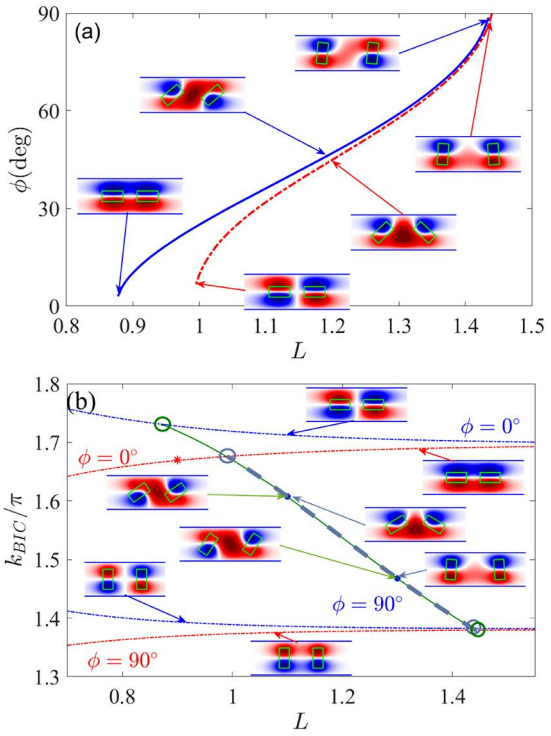

Figure 7.14. Curves of existence of topologically protected BICs for two rectangular rods inside the waveguide. (a) Vs distance between rectangular rods and angle of rotation, (b) vs frequency and distance between insets at $\Delta = 0$. Points of merging are marked by open circles.

[85], which can be defined as collapse of Fano resonance [83]. In Fig. 7.15 we present typical examples of such singular points in parametric space of incident light frequency and orientation angle of rectangular rods. Moreover, one can see that the transmission peaks follow the resonant frequencies of the system, shown by solid lines in Fig. 7.15. There are two equivalent cases $\phi = 0$ and $\phi = \pi/2$ which were considered in Refs. [9,86]. In both cases, we observe two solutions for BICs whose frequencies are considered as splittings due to interaction of rods. As a result, we obtain the symmetric and anti symmetric hybridized solutions, shown in insets of Fig. 7.15. If the rods were in air, the splitting of frequencies would decrease as $1/L^2$ [79]. However, a presence of parallel metal planes cardinally changes the interaction between two rods and cancels L-dependence.

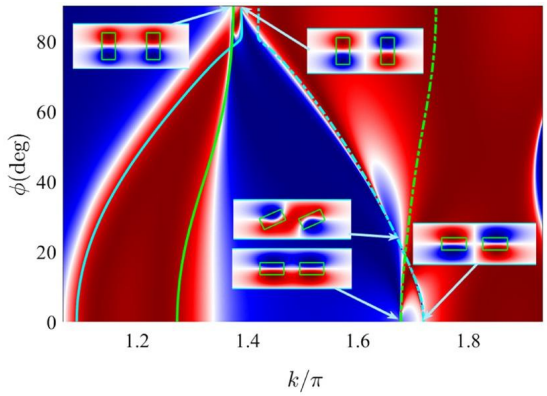

Figure 7.15. Transmittance of electromagnetic waves across the waveguide vs frequency and rotation angle of rods, as shown in insets. Lines show resonant frequencies as function of the rotation angle ϕ. The parameters are $a = 0.6$, $b = 0.3L = 1$.

7.6 Topologically protected BICs merge into SP or accidental BICs

Topologically protected (TP) BICs were reported by many scholars [41,87–92] which originate from the merging of several BICs in the momentum space. Recently, Huang et al. [93] have demonstrated TP BICs in coupled acoustic resonators which arise from the merging of BICs in parametric space of frequency and coupling strength. The importance of the TP BICs is that they are robust to the fabrication imperfection, and that the degree of enhancement of the Q-factor of quasi-BICs changes from standard quadratic to the fourth or even to the sixth degree. Here we demonstrate the cases of merging of two accidental BICs with winding numbers $m = \pm 1$ into one non-robust accidental BIC with $m = 0$. The phase singularities arise if some complex function $\Psi(x, y) = u(x, y) + iv(x, y) = |\Psi(x, y)| \exp(i\theta(x, y))$ has nodal point in some two-dimensional parametric space (x, y). Then the winding number of the singularity is given by:

$$m = \text{sgn}\left(\frac{\partial u}{\partial x}\frac{\partial v}{\partial y} - \frac{\partial u}{\partial y}\frac{\partial v}{\partial x}\right) \tag{7.23}$$

or

$$m = \oint d\vec{l}\,\nabla\theta. \tag{7.24}$$

As the parametric space we have chosen the frequency k and the angle of rotation ϕ while for the function Ψ we have chosen $\frac{1}{E_z}$.

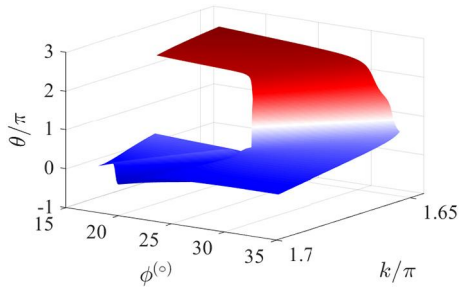

Figure 7.16. The phase of function $\frac{1}{E_z}$ vs frequency and the rotation angle of dielectric rectangular rod 0.6×0.3.

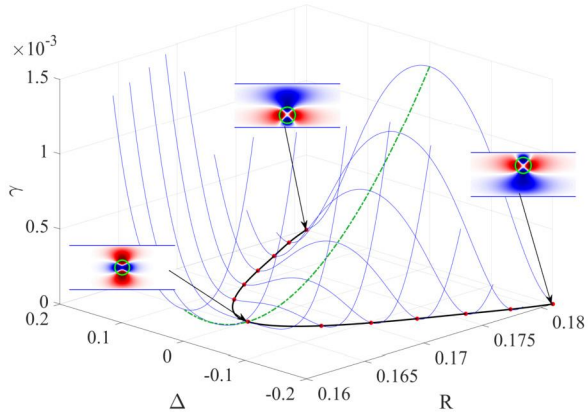

Figure 7.17. Half width of resonances vs shift of cylindrical rod relative to center of waveguide and radius of rod for $n = 3.87$. Insets show patterns of BICs (E_z of electric field).

Fig. 7.16 shows as the phase of this function in an anticlockwise sense, i.e., gives us $m = 1$. The merging is shown in Fig. 7.17, in which evolution of TP BIC with $m = \pm 1$ in two-parametric space of radius and shift of dielectric cylinder is plotted by solid green line, while the accidental BIC with $m = 0$ occurs only at $R = 0.1656$ and $\Delta = 0$.

These two TP BICs with $m = \pm 1$ are not distinguishable because are related by the inverse $y \to -y$. However, Fig. 7.18 (a) brightly demonstrates effect of annihilation of two TP BICs which merge into the SP BIC with zero winding number when rod with the critical radius $R_c = 0.1656$ takes the symmetrical position $\Delta \to 0$. Owing to log-log scale of dependence, we obtain that $Q \sim \frac{1}{\Delta^4}$. If the radius of rod were different from the critical one we would have standard quadratic behavior $Q \sim \frac{1}{\Delta^2}$.

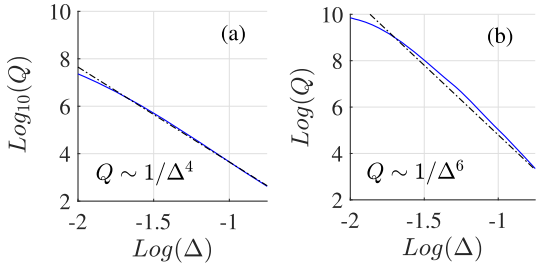

Figure 7.18. Dependence of Q-factor vs position of rod in waveguide in Log Log scale at the points of merging of topologically protected BICs. (a) The case of circular rod shown in Fig. 7.17 and (b) the case of rectangular rod with cross-section $a = 0.3, b = b_c = 0.911$, shown in Fig. 7.19.

First, this phenomenon was demonstrated in periodical array of cylindrical rods, in which two off-Γ BICs with winding numbers $m = \pm 1$ were merged into the SP BIC at Γ point with $m = 0$ [41]. This phenomenon is similar to the case of merging BICs observed in the photonic system, where topological charges move toward the Γ-point in the first Brillouin zone at momentum space [40,87,90,94,95]. It is important to note that the merging of BICs does not imply that two BICs exist at the same point of parametric space, i.e., degeneracy of BICs. In fact, when approaching the merging point, accidental BICs vanish compared to the SP BIC.

Fig. 7.19 demonstrates similar effects for the case of rectangular rod $a \times b$ in two-parametric space of its length a and position Δ. At the merging point of two TP BICs with SP BIC, the behavior of Q-factor turns into $Q \sim \frac{1}{\Delta^6}$, as shown in Fig. 7.18 (b).

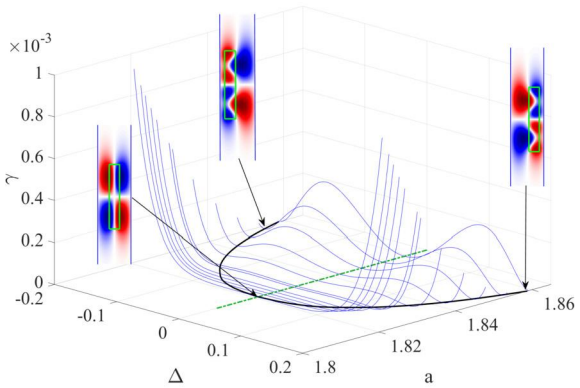

Figure 7.19. Half width of resonances vs shift of rectangular rod $a \times b$ with $n = 2.05$ and length a at $b = 0.3$. Insets show patterns of BICs (E_z of electric field).

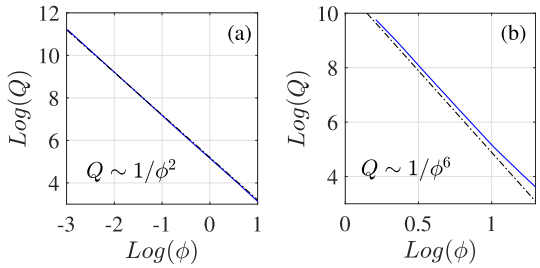

Figure 7.20. Dependence of Q-factor vs rotation angle of two rectangular rods with $a = 0.6, b = 0.3$ positioned symmetrically in waveguide in log-log scale at the points (a) beyond merging of topologically protected BICs marked by star in Fig. 7.14 (b) at $L = 0.9$ and (b) at the point of merging marked by open green circle in Fig. 7.14 (b) at $L = 0.989$.

The case of two rectangular rods brings a novelty of the merging of three BICs, two Fabry–Perot BICs with winding numbers $m = \pm 1$ and one SP BIC with $m = 0$. Respectively, beyond the point of merging (marked by star in Fig. 7.14 (b)), we have standard quadratic behavior of the Q-factor, as demonstrated in Fig. 7.20 (a). However, at the points of merging marked by open circles in Fig. 7.14 (b), we obtain strong dependence $Q \sim \frac{1}{\Delta^6}$, as Fig. 7.20 (b) shows. The degree of enhancement of the Q-factor is related to bifurcation of imaginary parts of TP BICs, as Fig. 7.17 and 7.19 show. This result follows from the algebra of bifurcation [41,90,93,96,97].

One can see in Fig. 7.14 points in which SP BICs at $\phi = 0, 90^o$ (dash-dot blue lines) coalesce with Fabry–Perot BICs evolving with angle of in-phase or anti-phase rotation of rods shown by solid green and dash gray lines. These Fabry–Perot BICs have morphology cardinally different from the SP BICs, as seen from insets in Fig. 7.14. For each angle $\phi \neq 0$ the Fabry–Perot BIC has to be tuned by distance between rods L, making an analogy with accidental BICs.

Fig. 7.21 demonstrates rich variety of merging effects of BICs with different winding numbers in the three-parametric space of frequency, distance between the rectangular rods and rotation angle.

7.7 Conclusions and discussion

A simple system of plane waveguide consisted of two parallel metal planes with inserted one or two dielectric quartz or silicon rods demonstrates abundance of various BICs, classified as

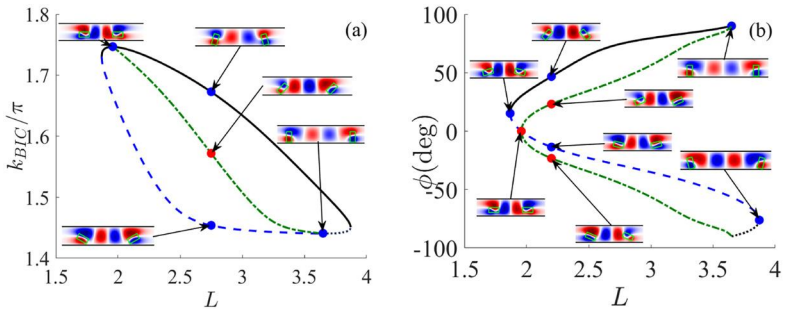

Figure 7.21. Curves of existence of the Fabry–Perot BICs vs (a) distance between rectangular rods and frequency and (b) angle of rotation and distance between rods at $\Delta = 1/2$. Dash-dotted line show curves of Fabry–Perot SP BICs at $\phi = 0, 90°$. Green solid line and dash gray lines show topologically protected in-phase BICs and anti-phase BICs, respectively. Points of BICs merging are marked by open circles.

symmetry-protected, accidental, Friedrich–Wintgen, and Fabry–Perot [82]. Moreover, we show numerous points of merging of different topologically protected BICs in two-parametric space. These events give rise to change the power degree in asymptotic behavior of the Q-factor, which has principal importance for numerous applications of BICs. First, this phenomenon of BICs merging was observed in the photonic system, where topological charges move toward the Γ-point in the first Brillouin zone at momentum space [40,87,90,94,95]. Recently, the two-parametric space was expanded onto the frequency and coupling strength of two acoustic resonators [93]. In the present paper, we go further by introducing parameters that determine the position of rods, distance between them, orientation of rectangular shaped rods, and frequency. It is important that all parameters can be easily varied experimentally in comparison to the case of topologically protected BICs in momentum space in the one- and two-dimensional periodical arrays of dielectric particles. It is clear that one can consider three-parametric space in which we can observe the lines of TP BICs.

Acknowledgments

We are grateful to Andrey Bogdanov, Lujun Huang, Dmitrii Maksimov, Andrey Miroshnichenko, Aleksandr Shalin and Yi Xu for discussions. Our special thanks to Konstantin Pichugin for calculation of Fig. 7.4. The research was supported by Russian Science Foundation with grant number 22-12-00070.

References

[1] G. Mie, Beiträge zur Optik trüber Medien, speziell kolloidaler Metallösungen, Annalen der Physik 330 (3) (1908) 377–445.
[2] J.D. Joannopoulos, S.G. Johnson, J.N. Winn, R.D. Meade, Photonic Crystals: Molding the Flow of Light, Princeton Univ. Press, Princeton, NJ, 1995.
[3] R. Kazarinov, Z. Sokolova, R. Suris, Planar distributed-feedback optical resonators, Soviet Physics. Technical Physics 21 (1976) 130–136.
[4] P. Vincent, M. Nevière, Corrugated dielectric waveguides: a numerical study of the second-order stop bands, Applied Physics 20 (4) (1979) 345–351.
[5] A.S. Bonnet-Bendhia, F. Starling, Guided waves by electromagnetic gratings and non-uniqueness examples for the diffraction problem, Mathematical Methods in the Applied Sciences 17 (5) (1994) 305–338.
[6] V.N. Astratov, J.S. Culshaw, R.M. Stevenson, D.M. Whittaker, M.S. Skolnick, T.F. Krauss, et al., Resonant coupling of near-infrared radiation to photonic band structure waveguides, Journal of Lightwave Technology 17 (11) (1999) 2050–2057.
[7] S.G. Tikhodeev, A.L. Yablonskii, E.A. Muljarov, N.A. Gippius, T. Ishihara, Quasiguided modes and optical properties of photonic crystal slabs, Physical Review B 66 (4) (2002).
[8] S.P. Shipman, S. Venakides, Resonant transmission near nonrobust periodic slab modes, Physical Review E 71 (2005) 026611.
[9] D.C. Marinica, A.G. Borisov, S.V. Shabanov, Bound states in the continuum in photonics, Physical Review Letters 100 (18) (2008) 183902.
[10] Chia Wei Hsu, Bo Zhen, Jeongwon Lee, S.G. Johnson, J.D. Joannopoulos, M. Soljačić, Observation of trapped light within the radiation continuum, Nature 499 (2013) 188.
[11] E.N. Bulgakov, A.F. Sadreev, Bloch bound states in the radiation continuum in a periodic array of dielectric rods, Physical Review A 90 (5) (2014) 053801.
[12] Yi Yang, Chao Peng, Yong Liang, Zhengbin Li, S. Noda, Analytical perspective for bound states in the continuum in photonic crystal slabs, Physical Review Letters 113 (3) (2014) 037401, https://doi.org/10.1103/PhysRevLett.113.037401.
[13] D.A. Bykov, L.L. Doskolovich, $\omega - kx$ Fano line shape in photonic crystal slabs, Physical Review A 92 (1) (2015).
[14] Z. Hu, Y.Y. Lu, Standing waves on two-dimensional periodic dielectric waveguides, Journal of Optics 17 (6) (2015) 065601.
[15] C.W. Hsu, B. Zhen, S.L. Chua, S.G. Johnson, J.D. Joannopoulos, M. Soljačić, Bloch surface eigenstates within the radiation continuum, Light: Science & Applications 2 (7) (2013) e84.
[16] X. Gao, C.W. Hsu, B. Zhen, X. Lin, J.D. Joannopoulos, M. Soljačić, et al., Formation mechanism of guided resonances and bound states in the continuum in photonic crystal slabs, Scientific Reports 6 (1) (2016).
[17] Z.F. Sadrieva, I.S. Sinev, K.L. Koshelev, A. Samusev, I.V. Iorsh, O. Takayama, et al., Transition from optical bound states in the continuum to leaky resonances: role of substrate and roughness, ACS Photonics 4 (4) (2017) 723–727, https://doi.org/10.1021/acsphotonics.6b00860.
[18] S.G. Lee, R. Magnusson, Band flips and bound-state transitions in leaky-mode photonic lattices, ArXiv preprint, arXiv:1804.02598, 2018.
[19] C.J. Chang-Hasnain, W. Yang, High-contrast gratings for integrated optoelectronics, Advances in Optics and Photonics 4 (3) (2012) 379.
[20] V. Karagodsky, C.J. Chang-Hasnain, Physics of near-wavelength high contrast gratings, Optics Express 20 (10) (2012) 10888.
[21] Y. Liang, C. Peng, K. Sakai, S. Iwahashi, S. Noda, Three-dimensional coupled-wave analysis for square-lattice photonic crystal surface emitting

lasers with transverse-electric polarization: finite-size effects, Optics Express 20 (14) (2012) 15945.
[22] Z. Wang, H. Zhang, L. Ni, W. Hu, C. Peng, Analytical perspective of interfering resonances in high-index-contrast periodic photonic structures, IEEE Journal of Quantum Electronics 52 (7) (2016) 1–9.
[23] X. Gao, B. Zhen, M. Soljačić, H. Chen, C.W. Hsu, Bound states in the continuum in fiber Bragg gratings, ACS Photonics 6 (11) (2019) 2996–3002.
[24] E.N. Bulgakov, D.N. Maksimov, Avoided crossings and bound states in the continuum in low-contrast dielectric gratings, Physical Review A 98 (2018).
[25] Z.F. Sadrieva, M.A. Belyakov, M.A. Balezin, P.V. Kapitanova, E.A. Nenasheva, A.F. Sadreev, et al., Experimental observation of a symmetry-protected bound state in the continuum in a chain of dielectric disks, Physical Review A 99 (2019) 053804.
[26] E.E. Maslova, M.V. Rybin, A.A. Bogdanov, Z.F. Sadrieva, Bound states in the continuum in periodic structures with structural disorder, Nanophotonics 10 (17) (2021) 4313–4321.
[27] M.V. Rybin, K.L. Koshelev, Z.F. Sadrieva, K.B. Samusev, A.A. Bogdanov, M.F. Limonov, et al., High-Q supercavity modes in subwavelength dielectric resonators, Physical Review Letters 119 (2017) 243901.
[28] A.A. Bogdanov, K.L. Koshelev, P.V. Kapitanova, M.V. Rybin, S.A. Gladyshev, Z.F. Sadrieva, et al., Bound states in the continuum and Fano resonances in the strong mode coupling regime, Advanced Photonics 1 (2019) 1.
[29] K. Koshelev, G. Favraud, A. Bogdanov, Y. Kivshar, A. Fratalocchi, Nonradiating photonics with resonant dielectric nanostructures, Nanophotonics 8 (5) (2019) 725–745.
[30] M. Odit, K. Koshelev, S. Gladyshev, K. Ladutenko, Y. Kivshar, A. Bogdanov, Observation of supercavity modes in subwavelength dielectric resonators, Advanced Materials (2020) 2003804.
[31] L. Huang, L. Xu, M. Rahmani, D. Neshev, A.E. Miroshnichenko, Pushing the limit of high-Q mode of a single dielectric nanocavity, Advanced Photonics 3 (01) (2021).
[32] E. Bulgakov, K. Pichugin, A. Sadreev, Mie resonance engineering in two disks, MDPI Photonics 8 (2021) 49.
[33] K. Pichugin, A. Sadreev, E. Bulgakov, Ultrahigh-Q system of a few coaxial disks, Nanophotonics 10 (17) (2021) 4341–4346.
[34] D. Colton, R. Kress, Inverse Acoustic and Electromagnetic Scattering Theory, 2nd ed., Springer, Berlin, 1998.
[35] M.G. Silveirinha, Trapping light in open plasmonic nanostructures, Physical Review A 89 (2) (2014) 023813.
[36] K. Koshelev, A. Bogdanov, Y. Kivshar, Meta-optics and bound states in the continuum, Science Bulletin 17 (2018) 065601.
[37] W. Chen, Y. Chen, W. Liu, Multipolar conversion induced subwavelength high-Q Kerker supermodes with unidirectional radiations, Laser & Photonics Reviews 13 (9) (2019) 1900067.
[38] Lijun Yuan, Ya Yan Lu, Perturbation theories for symmetry-protected bound states in the continuum on two-dimensional periodic structures, Physical Review A 101 (2020) 043827.
[39] Lijun Yuan, Ya Yan Lu, Bound states in the continuum on periodic structures: perturbation theory and robustness, Optics Letters 42 (21) (2017) 4490.
[40] Lijun Yuan, Mingyang Zhang, Ya Yan Lu, Real transmission and reflflection zeros of periodic structures with a bound state in the continuum, Physical Review A 106 (2022) 013505.
[41] E.N. Bulgakov, D.N. Maksimov, Bound states in the continuum and polarization singularities in periodic arrays of dielectric rods, Physical Review A 96 (6) (2017) 063833.

[42] E.N. Bulgakov, D.N. Maksimov, Light enhancement by quasi-bound states in the continuum in dielectric arrays, Optics Express 25 (2017) 14134.
[43] Lijun Yuan, Ya Yan Lu, Bound states in the continuum on periodic structures surrounded by strong resonances, Physical Review A 97 (4) (2018) 043828.
[44] D.R. Abujetas, J.J. Sáenz, J.A. Sánchez-Gil, Narrow Fano resonances in Si nanocylinder metasurfaces: refractive index sensing, Journal of Applied Physics 125 (18) (2019) 183103.
[45] Z. Hu, L. Yuan, Y.Y. Lu, Resonant field enhancement near bound states in the continuum on periodic structures, Physical Review A 101 (4) (2020).
[46] Z. Hu, L. Yuan, Y.Y. Lu, Bound states with complex frequencies near the continuum on lossy periodic structures, Physical Review A 101 (1) (2020).
[47] R.F. Ndangali, S.V. Shabanov, Electromagnetic bound states in the radiation continuum for periodic double arrays of subwavelength dielectric cylinders, Journal of Mathematical Physics 51 (10) (2010) 102901, https://doi.org/10.1063/1.3486358.
[48] H. Kogelnik, Theory of dielectric waveguides, in: Topics in Applied Physics, Springer Berlin Heidelberg, 1975, pp. 13–81.
[49] E.N. Bulgakov, A.F. Sadreev, Bound states in the continuum with high orbital angular momentum in a dielectric rod with periodically modulated permittivity, Physical Review A 96 (2017) 013841.
[50] O. Cohen, B. Freedman, J.W. Fleischer, M. Segev, D.N. Christodoulides, Grating-mediated waveguiding, Physical Review Letters 93 (10) (2004).
[51] Z. Hu, Y.Y. Lu, Resonances and bound states in the continuum on periodic arrays of slightly noncircular cylinders, Journal of Physics. B, Atomic, Molecular and Optical Physics 51 (2017) 035402.
[52] G. Quaranta, G. Basset, O.J.F. Martin, B. Gallinet, Recent advances in resonant waveguide gratings, Laser & Photonics Reviews 12 (9) (2018) 1800017.
[53] A. Krasnok, D. Baranov, H. Li, M.A. Miri, F. Monticone, A. Alú, Anomalies in light scattering, Advances in Optics and Photonics 11 (4) (2019) 892.
[54] S.I. Azzam, A.V. Kildishev, Photonic bound states in the continuum: from basics to applications, Advanced Optical Materials 9 (1) (2020) 2001469.
[55] L. Huang, L. Xu, M. Woolley, A.E. Miroshnichenko, Trends in quantum nanophotonics, Advanced Quantum Technologies 3 (4) (2020) 1900126.
[56] S. Joseph, S. Pandey, S. Sarkar, J. Joseph, Bound states in the continuum in resonant nanostructures: an overview of engineered materials for tailored applications, Nanophotonics 10 (17) (2021) 4175–4207.
[57] K.L. Koshelev, Z.F. Sadrieva, A.A. Shcherbakov, Y.S. Kivshar, A.A. Bogdanov, Bound states of the continuum in photonic structures, Physics Uspekhi 93 (2021).
[58] E.D. Tommasi, E. Esposito, S. Romano, A. Crescitelli, V.D. Meo, V. Mocella, et al., Frontiers of light manipulation in natural, metallic, and dielectric nanostructures, La Rivista del Nuovo Cimento 44 (1) (2021) 1–68.
[59] S. Both, T. Weiss, Resonant states and their role in nanophotonics, Semiconductor Science and Technology 37 (1) (2021) 013002.
[60] F. Wang, X. Yin, Z. Zhang, Z. Chen, H. Wang, P. Li, et al., Fundamentals and applications of topological polarization singularities, Frontiers in Physics 10 (2022).
[61] P. Hu, C. Xie, Q. Song, A. Chen, H. Xiang, D. Han, et al., Bound states in the continuum based on the total internal reflection of Bloch waves, National Science Review (2022).
[62] M.S. Hwang, K.Y. Jeong, J.P. So, K.H. Kim, H.G. Park, Nanophotonic nonlinear and laser devices exploiting bound states in the continuum, Communications Physics 5 (1) (2022).

[63] G.J. Tang, X.T. He, F.L. Shi, J.W. Liu, X.D. Chen, J.W. Dong, Topological photonic crystals: physics, designs, and applications, Laser & Photonics Reviews 16 (4) (2022) 2100300.
[64] Liangfu Ni, Jicheng Jin, Chao Peng, Zhengbin Li, Analytical and statistical investigation on structural fluctuations induced radiation in photonic crystal slabs, Optics Express 25 (5) (2017) 5580–5593.
[65] E.N. Bulgakov, A.F. Sadreev, High-Q resonant modes in a finite array of dielectric particles, Physical Review A 99 (2019) 033851.
[66] M.S. Sidorenko, O.N. Sergaeva, Z.F. Sadrieva, C. Roques-Carmes, P.S. Muraev, D.N. Maksimov, et al., Observation of an accidental bound state in the continuum in a chain of dielectric disks, Physical Review Applied 15 (3) (2021) 034041.
[67] V.B. Braginsky, M.L. Gorodetsky, V.S. Ilchenko, Quality-factor and nonlinear properties of optical whispering-gallery modes, Physics Letters A 137 (7–8) (1989) 393.
[68] M.L. Gorodetsky, V.S. Ilchenko, Optical microsphere resonators: optimal coupling to high-Q whispering-gallery modes, Journal of the Optical Society of America. B 16 (1999) 147.
[69] E.N. Bulgakov, D.N. Maksimov, Q-factor optimization in dielectric oligomers, Physical Review A 100 (2019).
[70] D.F. Kornovan, R.S. Savelev, Y.S. Kivshar, M.I. Petrov, High-Q localized states in finite arrays of subwavelength resonators, arXiv:2011.11791v2.
[71] A. Taghizadeh, I.S. Chung, Quasi bound states in the continuum with few unit cells of photonic crystal slab, Applied Physics Letters 111 (2017) 031114.
[72] J. Zhou, J. Zheng, Z. Fang, P. Xu, A. Majumdar, Ultra-low mode volume on-substrate silicon nanobeam cavity, Optics Express 27 (21) (2019) 30692.
[73] D. Evans, R. Porter, Trapped modes embedded in the continuous spectrum, Quarterly Journal of Mechanics and Applied Mathematics 52 (1998) 263–274.
[74] C.M. Linton, M. McIver, P. McIver, K. Ratcliffe, J. Zhang, Trapped modes for off-centre structures in guides, Wave Motion 36 (2002) 67–85.
[75] Y. Duan, W. Koch, C.M. Linton, M. McIver, Complex resonances and trapped modes in ducted domains, Journal of Fluid Mechanics 571 (2007) 119–147.
[76] A.C. Overvig, S. Shrestha, N. Yu, Dimerized high contrast gratings, Nanophotonics 7 (2018) 1157–1168.
[77] Q. Song, M. Zhao, L. Liu, J. Chai, G. He, H. Xiang, et al., Observation of bound states in the continuum in the dimerized chain, Physical Review A 100 (2019) 023810.
[78] E. Bulgakov, K. Pichugin, A. Sadreev, Resonant binding of dielectric particles to a metal surface without plasmonics, Physical Review A 103 (2021) L051501.
[79] E.N. Bulgakov, K.N. Pichugin, A.F. Sadreev, Evolution of the resonances of two parallel dielectric cylinders with distance between them, Physical Review A 100 (2019) 043806.
[80] K. Yasumoto, H. Jia, Modeling of photonic crystals by multilayered periodic arrays of circular cylinders, in: K. Yasumoto (Ed.), Electromagnetic Theory and Applications for Photonic Crystals, MIT Press, Cambridge, MA, 2006, pp. 527–579.
[81] T. Kushta, K. Yasumoto, Electromagnetic scattering from periodic arrays of two circular cylinders per unit cell, Progress in Electromagnetics Research 29 (2000) 69–85.
[82] A.F. Sadreev, Interference traps waves in an open system: bound states in the continuum, Reports on Progress in Physics 84 (5) (2021) 055901.
[83] C.S. Kim, A.M. Satanin, Y.S. Joe, R.M. Cosby, Resonant tunneling in a quantum waveguide: effect of a finite-size attractive impurity, Physical Review B 60 (15) (1999) 10962.

[84] V. Liu, M. Povinelli, S. Fan, Resonance-enhanced optical forces between coupled photonic crystal slabs, Optics Express 17 (24) (2009) 21897, https://doi.org/10.1364/OE.17.021897.
[85] A.F. Sadreev, E.N. Bulgakov, I. Rotter, Bound states in the continuum in open quantum billiards with a variable shape, Physical Review B 73 (23) (2006) 235342.
[86] H. Chen, H. Wang, K.-yin Wong, D. Lei, High-Q localized surface plasmon resonance based on bound states in the continuum for enhanced refractive index sensing, Optics Letters 47 (3) (2022) 609.
[87] E.N. Bulgakov, D.N. Maksimov, Topological bound states in the continuum in arrays of dielectric spheres, Physical Review Letters 118 (26) (2017) 267401.
[88] S. Mukherjee, J. Gomis-Bresco, P. Pujol-Closa, D. Artigas, L. Torner, Topological properties of bound states in the continuum in geometries with broken anisotropy symmetry, Physical Review A 98 (6) (2018).
[89] W. Liu, B. Wang, Y. Zhang, J. Wang, M. Zhao, F. Guan, et al., Circularly polarized states spawning from bound states in the continuum, Physical Review Letters 123 (11) (2019).
[90] J. Jin, X. Yin, L. Ni, M. Soljačić, B. Zhen, C. Peng, Topologically enabled ultrahigh-Q guided resonances robust to out-of-plane scattering, Nature 574 (7779) (2019) 501–504.
[91] T. Yoda, M. Notomi, Generation annihilation of topologically protected bound states in the continuum and circularly polarized states by symmetry breaking, Physical Review Letters 125 (5) (2020).
[92] M.S. Hwang, H.C. Lee, K.H. Kim, K.Y. Jeong, S.H. Kwon, K. Koshelev, et al., Ultralow-threshold laser using super-bound states in the continuum, Nature Communications 12 (1) (2021).
[93] L. Huang, B. Jia, Y.K. Chiang, S. Huang, C. Shen, F. Deng, et al., Topological supercavity resonances in the finite system, Advanced Science 9 (2022) 2200257.
[94] Bo Zhen, Chia Wei Hsu, Ling Lu, A.D. Stone, M. Soljačić, Strong resonances on periodic arrays of cylinders and optical bistability with weak incident waves, Physical Review Letters 113 (2014) 257401.
[95] Y. Zeng, G. Hu, K. Liu, Z. Tang, C.W. Qiu, Dynamics of topological polarization singularity in momentum space, Physical Review Letters 127 (17) (2021).
[96] Lijun Yuan, Ya Yan Lu, Strong resonances on periodic arrays of cylinders and optical bistability with weak incident waves, Physical Review A 95 (2017) 023834.
[97] H.M. Doeleman, F. Monticone, W. den Hollander, A. Alù, A.F. Koenderink, Experimental observation of a polarization vortex at an optical bound state in the continuum, Nature Photonics 12 (2018) 397.

8

Exceptional points

Denis V. Novitsky[a] **and Andrey V. Novitsky**[b,c]

[a] *B.I. Stepanov Institute of Physics, National Academy of Sciences of Belarus, Minsk, Belarus.* [b] *Department of Theoretical Physics and Astrophysics, Belarusian State University, Minsk, Belarus.* [c] *ITMO University, St. Petersburg, Russia*

8.1 Introduction

Among the recent trends in optical science, non-Hermitian photonics seems to be one of the most intriguing and promising. Generally speaking, it considers interaction of photonic structures as open dynamic systems with light. This approach allows one to look at the problem of light-matter interaction from another angle providing a different treatment even for well-known optical systems, such as lasers and coupled resonators. On the other hand, the non-Hermitian photonics has put forward the structures (for example, $\mathcal{PT}$-symmetric ones) that could not even be imagined before. As a result, a number of unusual, entirely unexpected features and effects due to the non-Hermiticity of photonic structures have been predicted and experimentally observed.

Non-Hermitian matrices describing Hamiltonians and scattering operators are at the heart of the non-Hermitian physics. They admit a distinctive type of degeneracy at the exceptional point (EP) when both eigenvalues and eigenvectors coalesce, so that the set of eigenfunctions becomes defective. It should be stressed that this type of degeneracy is impossible in the Hermitian case. The principles of non-Hermitian physics and exceptional points as their manifestation proved to be fruitful in various branches of classical and quantum physics, including optics, acoustics, mechanics, electronics, and even biophysics [1].

In this chapter, we start with the basic theoretical premises for the EPs, describe their properties, and then illustrate them with the examples of EPs in nanophotonics. In particular, we demonstrate the appearance of EPs in passive systems with purely radiative losses and in structures with spatially distributed gains and losses, including $\mathcal{PT}$-symmetric ones. We discuss topological properties of EPs, their application to sensing, and connection

All-Dielectric Nanophotonics. https://doi.org/10.1016/B978-0-32-395195-1.00013-2
Copyright © 2024 Elsevier Ltd. All rights reserved.

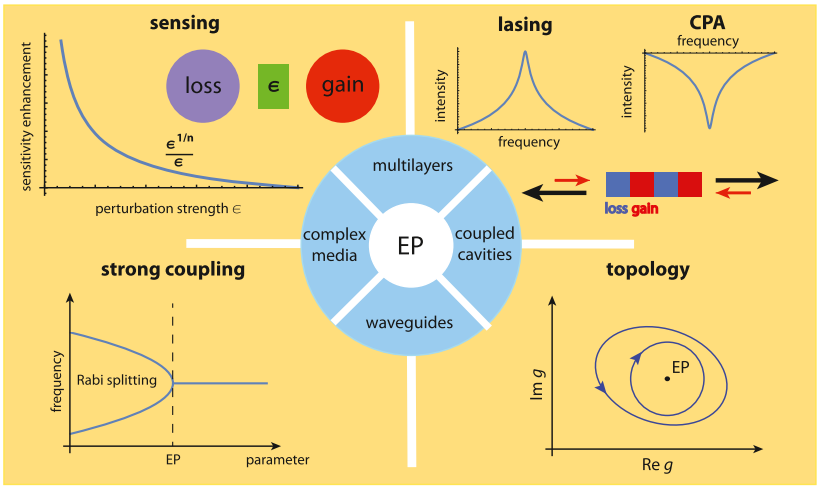

Figure 8.1. Roadmap on exceptional points (EP) within this chapter. Inner blue ring demonstrates four types of systems often used for investigation of EPs. In this chapter, we discuss the EP-based sensors, lasers, and coherent perfect absorbers (CPA), as well as perspectives of the EPs for polaritonic physics and topology.

with the strong-coupling physics (Fig. 8.1). There are a number of books [2–4] and review articles [5–8] on non-Hermitian physics and its application to photonics, while different aspects of EPs are discussed in [9,10]. We do not aim to compete with this literature in completeness and breadth of coverage. Instead, we try to make a general educational introduction to the subject of EPs for the dielectric photonics community and, especially, for beginners in non-Hermitian photonics. Readers interested in more details and examples may consult references herein.

8.2 General theory of exceptional points

8.2.1 The eigenvalue problem

Many physical systems are governed by a set of linear differential equations of the first order in the form of the non-stationary Schrödinger equation:

$$i\frac{d\psi}{d\tau} = \hat{H}(\vec{\alpha})\psi, \tag{8.1}$$

where τ is the evolution variable (either time or coordinate), $\psi(\tau,\vec{\alpha})$ and $\hat{H}(\vec{\alpha})$ are n-dimensional vector (wave function) and matrix (Hamiltonian), respectively, and $\vec{\alpha} = (\alpha_1,\ldots,\alpha_m)$ is a vector of m parameters. Here we assume that the Hamiltonian $\hat{H}$

can be either Hermitian ($\hat{H} = \hat{H}^{\dagger}$, where the superscript † stands for the Hermitian conjugate) as in quantum mechanics or non-Hermitian ($\hat{H} \neq \hat{H}^{\dagger}$). Eq. (8.1) emerges in many areas of physics, including quantum mechanics, acoustics, photonics, and classical electrodynamics. The simplest type of a system obeying Eq. (8.1) is the two-state one. It is described by the 2×2 Hamiltonian as follows:

$$i\frac{d}{d\tau}\begin{pmatrix}\psi_1\\ \psi_2\end{pmatrix} = \begin{pmatrix}H_{11} & H_{12}\\ H_{21} & H_{22}\end{pmatrix}\begin{pmatrix}\psi_1\\ \psi_2\end{pmatrix}. \tag{8.2}$$

Such an equation describes the evolution of two coupled optical or acoustic modes with the diagonal elements of the Hamiltonian corresponding to the complex resonant frequencies and the non-diagonal elements representing coupling strength between the modes. Generalization of Eq. (8.2) to higher dimensions is straightforward.

In electrodynamics of complex media, the propagation of stationary electromagnetic waves can be often considered in one dimension and described by the four-dimensional vector, comprising independent transverse field components $\mathbf{H}_t$ and $\mathbf{E}_t$ as:

$$\frac{d}{dz}\begin{pmatrix}\mathbf{H}_t\\ \mathbf{E}_t\end{pmatrix} = i\frac{\omega}{c}\begin{pmatrix}M_{11} & M_{12}\\ M_{21} & M_{22}\end{pmatrix}\begin{pmatrix}\mathbf{H}_t\\ \mathbf{E}_t\end{pmatrix}, \tag{8.3}$$

where M_{ij} are the 2×2 block matrices depending on material parameters, ω is the angular frequency and c is the speed of light in vacuum.

Fundamental solution of Eq. (8.1) can be formally written as:

$$\psi(\tau, \vec{\alpha}) = \exp[-i\hat{H}(\vec{\alpha})\tau]\psi(0, \vec{\alpha}). \tag{8.4}$$

Here exponential of matrix $\hat{H}$ is defined through a corresponding Taylor series. The Hamiltonian matrix can be spectrally decomposed,

$$\hat{H} = \sum_{j=1}^{n} \lambda_j \hat{P}_j, \tag{8.5}$$

where λ_j are the eigenvalues of $\hat{H}$ forming its spectrum and $\hat{P}_j = \mathbf{v}_j \otimes \mathbf{u}_j$ are the projectors onto the corresponding eigenvectors with the property $\hat{P}_j^2 = \hat{P}_j$. The tensor product of two vectors $\mathbf{u}$ and $\mathbf{v}$ is defined as a matrix $n \times n$ with elements $(\mathbf{u} \otimes \mathbf{v})_{jk} = u_j v_k$, where $j, k = 1, \ldots n$. Right $\mathbf{v}_j$ and left $\mathbf{u}_j$ eigenvectors are defined in accordance with

$$\hat{H}\mathbf{v}_j = \lambda_j \mathbf{v}_j, \qquad \mathbf{u}_j \hat{H} = \lambda_j \mathbf{u}_j, \tag{8.6}$$

and satisfy the orthonormality condition $\mathbf{u}_j\mathbf{v}_k = \delta_{jk}$ providing orthogonality of the projectors $\hat{P}_j\hat{P}_k = \hat{P}_j\delta_{jk}$. Here δ_{jk} is the Kronecker delta defined as usual: $\delta_{jk} = 1$ for $j = k$ and $\delta_{jk} = 0$ for $j \neq k$. If the matrix is symmetric, $\hat{H} = \hat{H}^T$, then the right and left eigenvectors coincide, $\mathbf{v}_j = \mathbf{u}_j^T$, where the superscript T stands for the transpose.

Eigenvalues λ meet the characteristic equation $\det(\hat{H} - \lambda I_n) = 0$ and can be written by means of n matrix invariants, e.g., the traces of matrix powers $\mathrm{tr}(\hat{H}) = \sum_{j=1}^{n}\lambda_j$, …, $\mathrm{tr}(\hat{H}^{n-1}) = \sum_{j=1}^{n}\lambda_j^{n-1}$ and the determinant $\det(\hat{H}) = \lambda_1 \ldots \lambda_n$, where I_n is the $n \times n$ unit matrix. The projectors can be determined from the system of n equations including the completeness condition $I_n = \sum_{j=1}^{n}\hat{P}_j$ and the condition for the Hamiltonian powers: $\hat{H} = \sum_{j=1}^{n}\lambda_j\hat{P}_j$, …, $\hat{H}^{n-1} = \sum_{j=1}^{n}\lambda_j^{n-1}\hat{P}_j$.

Using the spectral decomposition, we arrive at the fundamental solution (8.4) in the following form:

$$\psi(\tau, \vec{\alpha}) = \sum_{j=1}^{n}\exp[-i\lambda_j(\vec{\alpha})\tau]\hat{P}_j(\vec{\alpha})\psi(0, \vec{\alpha}). \tag{8.7}$$

The spectral decomposition can be used to solve the Schrödinger differential equation with a source **J**, e.g., a dipole. For the stationary wave function ψ and the source **J** proportional to $\exp(-i\lambda\tau)$, this equation reads:

$$\hat{H}\psi + \mathbf{J} = \lambda\psi. \tag{8.8}$$

Substituting decomposition $\psi = \sum_m a_m\mathbf{v}_m$ into the above equation and accounting for $\hat{H}\mathbf{v}_m = \lambda_m\mathbf{v}_m$, we arrive at the equation for a_m: $\sum_m a_m(\lambda - \lambda_m)\mathbf{v}_m = \mathbf{J}$. The wave function takes the form:

$$\psi = G\mathbf{J}, \qquad G = \sum_m \frac{1}{\lambda - \lambda_m}\frac{\mathbf{v}_m \otimes \mathbf{u}_m}{(\mathbf{u}_m\mathbf{v}_m)}. \tag{8.9}$$

Here G is the dyadic Green function.

8.2.2 Definition of exceptional points

When we change the parameters $\vec{\alpha}$, some eigenvalues may turn out to be equal. Generally, we can have M sets of equal eigenvalues as $\lambda_1 = \ldots = \lambda_{n_1} = \tilde{\lambda}_1$, $\lambda_{n_1+1} = \ldots = \lambda_{n_2} = \tilde{\lambda}_2$, $\ldots \lambda_{n_{M-1}} = \ldots = \lambda_n = \tilde{\lambda}_M$. A unique eigenvalue $\tilde{\lambda}$ corresponds to a block in the matrix $\hat{H}$. It is instructive to focus further on the Hamiltonian possessing a single degenerate eigenvalue.

Assume that the eigenvalues of the n-dimensional matrix $\hat{H}$ at the point $\vec{\alpha}_0$ in the parameter space $(\alpha_1, \ldots, \alpha_m)$ are equal, $\lambda_1 = \ldots = \lambda_n = \lambda$. Depending on the Hamiltonian Hermiticity, the point $\vec{\alpha}_0$ is called either diabolic or exceptional.

(i) At the *diabolic point*, the matrix $\hat{H}$ is diagonalizable, so that it can be represented as:

$$\hat{H}(\vec{\alpha}_0) = h\hat{I}_n. \tag{8.10}$$

The degenerate eigenvalues $\lambda = h$ correspond to the orthogonal eigenvectors and the fundamental solution $\psi(\tau, \vec{\alpha}_0) = \exp(\lambda\tau) \times \psi(0, \vec{\alpha}_0)$ is trivial.

(ii) At the *exceptional point*, the matrix is non-diagonalizable, so that

$$\hat{H}(\vec{\alpha}_0) = h\hat{I}_n + \hat{N}, \tag{8.11}$$

where $\hat{N}$ is a nilpotent matrix defined as $\hat{N}^n = 0$ with $\hat{N}^j \neq 0$ for $j < n$. Adding the nilpotent matrix to the diagonal one does not affect the degenerate eigenvalue $\lambda = h$, but drastically influences the eigenvectors. As well as the eigenvalues, the eigenvectors at the EP are degenerate, i.e., there is a single eigenvector at the EP, satisfying the equation $\hat{H}\mathbf{v}_1 = \lambda\mathbf{v}_1$, with the left eigenvector orthogonal to it, as $\mathbf{u}_1\mathbf{v}_1 = 0$. As a result, the basis set of orthogonal eigenvectors cannot be established, but one can introduce the set of non-orthogonal *generalized eigenvectors* using the following procedure. Equation for the degenerate eigenvector $(\hat{H} - \lambda)\mathbf{v}_1 = 0$ can be rewritten as $\hat{N}\mathbf{v}_1 = 0$ after substitution of Eq. (8.11). Generalized eigenvectors do not satisfy this equation, that is $\hat{N}\mathbf{v}_2 \neq 0$. Instead, the first generalized eigenvector satisfies equation:

$$\hat{N}\mathbf{v}_2 = \mathbf{v}_1, \qquad \text{or} \qquad (\hat{H} - \lambda)\mathbf{v}_2 = \mathbf{v}_1. \tag{8.12}$$

After multiplying both sides of this equation by the nilpotent matrix $\hat{N}$, we obtain $\hat{N}^2\mathbf{v}_2 = 0$ or $(\hat{H} - \lambda)^2\mathbf{v}_2 = 0$. The second generalized eigenvector is defined in the similar manner as:

$$\hat{N}\mathbf{v}_3 = \mathbf{v}_2, \qquad \text{or} \qquad (\hat{H} - \lambda)\mathbf{v}_3 = \mathbf{v}_2. \tag{8.13}$$

Multiplication by the matrix $\hat{N}^2$ yields $\hat{N}^3\mathbf{v}_2 = 0$ or $(\hat{H} - \lambda)^3\mathbf{v}_2 = 0$. Thus, the generalized eigenvectors are defined by the chain rule $\hat{N}\mathbf{v}_j = \mathbf{v}_{j-1}$, where $j = 2, \ldots, n$. This chain rule allows us to determine the form of the nilpotent matrix $\hat{N}$. It is quite easy to notice that the chain rule is valid if

$$\hat{N} = \sum_{j=1}^{n-1} \mathbf{v}_j \otimes \mathbf{u}_{n-j}, \tag{8.14}$$

where $\mathbf{u}_{n-j}\mathbf{v}_k = \delta_{j,k-1}$ or $\mathbf{u}_j\mathbf{v}_k = \delta_{n-j,k-1}$. Generalized left eigenvectors $\mathbf{u}_j$ can be found from the chain rule $\mathbf{u}_j\hat{N} = \mathbf{u}_{j-1}$ ($j = 2,\ldots,n$) consistent with the dyadic decomposition (8.14) of $\hat{N}$. The degenerate left eigenvector satisfies the equation $\mathbf{u}_1\hat{N} = 0$.

The Hamiltonian matrix can be presented in the Jordan canonical form, assuming non-zero elements on the superdiagonal $(k, k+1)$ of the nilpotent matrix ($k = 1,\ldots,n-1$), as follows:

$$\hat{H}(\vec{\alpha}_0) = \begin{pmatrix} \lambda & 1 & 0 & 0 & 0 & \ldots \\ 0 & \lambda & 1 & 0 & 0 & \ldots \\ 0 & 0 & \lambda & 1 & 0 & \ldots \\ \ldots & \ldots & \ldots & \ldots & \ldots & \ldots \end{pmatrix}. \tag{8.15}$$

To obtain other forms of the Hamiltonian matrix at the EP, one should exploit a similarity transformation S in the n-dimensional space. Then the Hamiltonian reads $\hat{H}'(\vec{\alpha}_0) = \hat{S}(h\hat{I}_n + \hat{N})\hat{S}^{-1} = h\hat{I}_n + \hat{N}'$, where $\hat{N}' = \hat{S}\hat{N}\hat{S}^{-1}$.

At the EP, the fundamental solution (8.4) of differential equations (8.1) reads:

$$\psi(\tau, \vec{\alpha}_0) = \exp(-i\lambda\tau)\exp(-i\hat{N}\tau)\psi(0, \vec{\alpha}_0). \tag{8.16}$$

Exponential of the nilpotent matrix is defined as a truncated Taylor series due to $\hat{N}^k = 0$ for $k \geq n$. Therefore, we get:

$$\psi(\tau, \vec{\alpha}_0) = \exp(-i\lambda\tau)\left[\sum_{k=0}^{n-1}\frac{(-i\tau)^k}{k!}\hat{N}^k\right]\psi(0, \vec{\alpha}_0). \tag{8.17}$$

This means that the solution is not just an exponential at the EP. Using decomposition over the basis of generalized eigenvectors for the initial wave function $\psi(0, \vec{\alpha}_0) = \sum_{j=1}^{n} c_j\mathbf{v}_j$, we can notice that the action of the nilpotent matrix reduces to $\hat{N}\psi(0, \vec{\alpha}_0) = \sum_{j=2}^{n} c_j\mathbf{v}_{j-1} = \sum_{j=1}^{n-1} c_{j+1}\mathbf{v}_j$ and the solution (8.17) reads:

$$\psi(\tau, \vec{\alpha}_0) = \exp(-i\lambda\tau)\sum_{k=0}^{n-1}\frac{(-i\tau)^k}{k!}\sum_{j=1}^{n-k} c_{j+k}\mathbf{v}_j. \tag{8.18}$$

The EPs are known to exist for electromagnetic waves in (bi)anisotropic crystals whose evolution is described with 4×4 Jordan matrices, as in Eq. (8.3). Since the nilpotent matrix is 4-dimensional, one is able to distinguish waves with exponential-linear (Voigt waves), exponential-quadratic and exponential-cubic dependence on the coordinate instead of regular plane-wave solutions [11]. Recently, a concept of Dyakonov–Voigt surface waves

was introduced, which propagate only in certain directions at the interface of anisotropic medium and decay away from the interface as a product of linear and exponential functions [12].

Hermitian Hamiltonians with degenerate spectrum can support only diabolic points, so that the set of orthogonal eigenvectors can be always found. Since the Hamiltonian at the EP (8.15) is clearly non-Hermitian, the EPs emerge exclusively for non-Hermitian Hamiltonians. Although non-Hermiticity can be arbitrary, the most curious cases correspond to certain symmetries, for example, $\mathcal{PT}$ and anti-$\mathcal{PT}$ symmetries, as it will be discussed further.

The Green function at the exceptional point λ_{EP} can be found as follows (see [13,14]). Subtracting the term $\lambda_{EP}\psi$ from the left and right hand sides of Eq. (8.8), we write:

$$(\hat{H}_0 - \lambda_{EP} I_n)\psi + \mathbf{J} = (\lambda - \lambda_{EP})\psi \tag{8.19}$$

or

$$\psi = \frac{1}{\lambda - \lambda_{EP}} \left(I_n - \frac{\hat{N}}{\lambda - \lambda_{EP}} \right)^{-1} \mathbf{J}. \tag{8.20}$$

Exploiting the Taylor series of this matrix function, the Green function defined as $\psi = G_{EP}\mathbf{J}$ can be presented in the form:

$$G_{EP} = \frac{1}{\lambda - \lambda_{EP}} \sum_{k=0}^{\infty} \frac{\hat{N}^k}{(\lambda - \lambda_{EP})^k}. \tag{8.21}$$

The series is truncated due to the property of the nilpotent matrix $\hat{N}^n = 0$, yielding:

$$\begin{aligned} G_{EP} &= \frac{1}{\lambda - \lambda_{EP}} \sum_{k=0}^{n-1} \frac{\hat{N}^k}{(\lambda - \lambda_{EP})^k} \\ &= \frac{I_n}{\lambda - \lambda_{EP}} + \frac{\hat{N}}{(\lambda - \lambda_{EP})^2} + \ldots + \frac{\hat{N}^{n-1}}{(\lambda - \lambda_{EP})^n}. \end{aligned} \tag{8.22}$$

Note that the leading-order term of the Green function at the EP is the last one, proportional to $(\lambda - \lambda_{EP})^{-n}$, if λ is close to λ_{EP}.

8.2.3 Exceptional points of two-state Hamiltonians

Consider a non-Hermitian Hamiltonian $\hat{H}(\vec{\alpha})$ that can be described by the 2×2 matrix. It governs evolution of the system given by Eq. (8.2) with the fundamental solution (8.4). Spectrum of the Hamiltonian $\hat{H}$ consists of a couple of eigenvalues λ_1 and λ_2 and

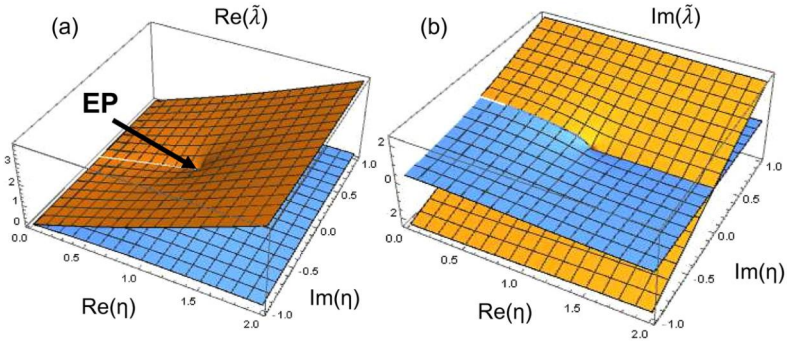

Figure 8.2. The EP of a two-state Hamiltonian. The real (a) and imaginary (b) parts of the normalized eigenvalues (8.23), $\lambda_{1,2}/\sqrt{\det(\hat{H})}$, as a function of complex parameter $\eta = \mathrm{tr}(\hat{H})/2\sqrt{\det(\hat{H})}$. The EP is observed at $\mathrm{Re}(\eta) = 1$ and $\mathrm{Im}(\eta) = 0$.

the Hamiltonian can be presented as $\hat{H} = \lambda_1 \hat{P}_1 + \lambda_2 \hat{P}_2$ with the projectors $\hat{P}_1$ and $\hat{P}_2$. The eigenvalues can be written by means of the matrix invariants $\mathrm{tr}(\hat{H}) = \lambda_1 + \lambda_2$ and $\det(\hat{H}) = \lambda_1 \lambda_2$ as:

$$\lambda_{1,2} = \frac{\mathrm{tr}(\hat{H}) \pm \sqrt{[\mathrm{tr}(\hat{H})]^2 - 4\det(\hat{H})}}{2}. \tag{8.23}$$

The equations $\hat{P}_1 + \hat{P}_2 = \hat{I}_2$ and $\lambda_1 \hat{P}_1 + \lambda_2 \hat{P}_2 = \hat{H}$ yield the projecting matrices:

$$\hat{P}_1 = \frac{1}{\lambda_1 - \lambda_2}\left(\hat{H} - \lambda_2 \hat{I}_2\right), \qquad \hat{P}_2 = \frac{1}{\lambda_2 - \lambda_1}\left(\hat{H} - \lambda_1 \hat{I}_2\right). \tag{8.24}$$

At the point $\vec{\alpha}_0$ of the parameter space, where the square root in Eq. (8.23) vanishes, the eigenvalues coalesce, $\lambda = \lambda_1 = \lambda_2 = \mathrm{tr}(\hat{H})/2$. If the eigenvectors also coalesce at this point, we have the EP of the second order. The eigenvalues of a generic two-dimensional system are shown in Fig. 8.2. One can see that to reach the EP, one has to tune two parameters: the real and imaginary parts of the value $\eta = \mathrm{tr}(\hat{H})/2\sqrt{\det(\hat{H})}$.

In the case of real-valued $\mathrm{tr}(\hat{H})$ and $\det(\hat{H})$, the eigenvalues are real at the EP independent of Hermiticity. The EP then lies on the line $[\mathrm{tr}(\hat{H})]^2 = 4\det(\hat{H})$ separating two phases, the first one being symmetric ($[\mathrm{tr}(\hat{H})]^2 > 4\det(\hat{H})$), while the second one being symmetry-broken ($[\mathrm{tr}(\hat{H})]^2 < 4\det(\hat{H})$). There is a single real-valued parameter η to be tuned, as shown Fig. 8.3. In the symmetric phase of the non-Hermitian Hamiltonian, the evolution

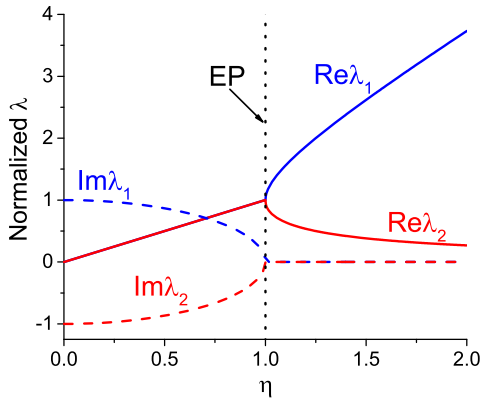

Figure 8.3. The EP of a two-state Hamiltonian. The normalized eigenvalues (8.23), $\lambda_{1,2}/\sqrt{\det(\hat{H})}$, as a function of real-valued $\eta = \mathrm{tr}(\hat{H})/2\sqrt{\det(\hat{H})}$. The EP is observed at $\eta = 1$.

of the system resembles that of a Hermitian system characterized by real eigenvalues. Symmetric phase requires symmetry of the non-Hermitian Hamiltonian and hence of the system itself. In the symmetry-broken phase, the eigenvalues are the complex-conjugate pair corresponding to the amplifying and decaying solutions. For the complex invariants $\mathrm{tr}(\hat{H})$ and $\det(\hat{H})$, the eigenvalues are complex in both phases, but the Hamiltonian matrix still has the Jordan form at the EP, when $[\mathrm{tr}(\hat{H})]^2 = 4\det(\hat{H})$.

At the EP, the Hamiltonian may be written in the canonical Jordan form:

$$\hat{H}(\vec{\alpha}_0) = \lambda \hat{I}_2 + \hat{N} = \begin{pmatrix} \lambda & 1 \\ 0 & \lambda \end{pmatrix}. \tag{8.25}$$

The two-dimensional nilpotent matrix satisfies $\hat{N}^2 = 0$. Using the similarity transformation $\hat{S} = \mathrm{diag}(s_1, s_2)$, we can present the nilpotent matrix as $\hat{N}' = \hat{S}\hat{N}\hat{S}^{-1} = (s_1/s_2)\hat{N}$. Using an orthogonal matrix $\hat{S}(\alpha) = \begin{pmatrix} \cos\alpha & \sin\alpha \\ -\sin\alpha & \cos\alpha \end{pmatrix}$ to transform the nilpotent matrix yields a wide class of non-Hermitian Hamiltonians, which at the EP have the form:

$$\hat{H}(\vec{\alpha}_0) = \lambda \hat{I}_2 + \hat{S}(\alpha)\hat{N}\hat{S}^{-1}(\alpha) = \begin{pmatrix} \lambda + \sin\alpha\cos\alpha & \cos^2\alpha \\ -\sin^2\alpha & \lambda - \sin\alpha\cos\alpha \end{pmatrix}. \tag{8.26}$$

When $\alpha = i\beta$, the Hamiltonian at the EP is:

$$\hat{H}(\vec{\alpha}_0) = \begin{pmatrix} \lambda + i\sinh\beta\cosh\beta & \cosh^2\beta \\ \sinh^2\beta & 1 - i\sinh\beta\cosh\beta \end{pmatrix}, \tag{8.27}$$

which is a symmetric matrix, when $\cosh\beta = \sinh\beta$. The fundamental solution (8.17) at the EP can be written for any Hamiltonian we mentioned before. In the case of Hamiltonian (8.25), the fundamental solution at the EP reads:

$$\begin{aligned} \begin{pmatrix} \psi_1(\tau) \\ \psi_2(\tau) \end{pmatrix} &= e^{-i\lambda\tau} \begin{pmatrix} 1 & -i\tau \\ 0 & 1 \end{pmatrix} \begin{pmatrix} \psi_1(0) \\ \psi_2(0) \end{pmatrix} \\ &= e^{-i\lambda\tau} \begin{pmatrix} \psi_1(0) - i\tau\psi_2(0) \\ \psi_2(0) \end{pmatrix}. \end{aligned} \tag{8.28}$$

Now we determine the generalized eigenvectors of the Hamiltonian (8.25). In the case of two coalescing eigenvectors, $n = 2$ and the nilpotent matrix $\hat{N} = \mathbf{v}_1 \otimes \mathbf{u}_1$ defined by Eq. (8.14) is a dyad. The normal right eigenvector $\mathbf{v}_1 = (1, 0)^T$ follows from the equation $(\hat{H} - \lambda\hat{I}_2)\mathbf{v}_1 = 0$. Single generalized eigenvector $\mathbf{v}_2 = (a_2, b_2)^T$ for the 2×2 Hamiltonian satisfies equation:

$$\begin{pmatrix} 0 & 1 \\ 0 & 0 \end{pmatrix} \begin{pmatrix} a_2 \\ b_2 \end{pmatrix} = \begin{pmatrix} 1 \\ 0 \end{pmatrix}, \tag{8.29}$$

yielding $\mathbf{v}_2 = (w, 1)^T$, where w is a constant that can be found from a normalization condition. Similarly, we can determine the left eigenvector $\mathbf{u}_1 = (0, 1)$ and the generalized eigenvector $\mathbf{u}_2 = (1, -w)$ consistent with orthonormalization conditions $\mathbf{u}_1\mathbf{v}_1 = 0$, $\mathbf{u}_1\mathbf{v}_2 = 1$, $\mathbf{u}_2\mathbf{v}_1 = 1$, and $\mathbf{u}_2\mathbf{v}_2 = 0$. One can directly verify that a kind of completeness condition $\mathbf{v}_1 \otimes \mathbf{u}_2 + \mathbf{v}_2 \otimes \mathbf{u}_1 = I_2$ holds true.

8.2.4 Symmetry and the EP order

The EP of the rth order emerges, when r eigenvalues become equal. The order of the EP is limited not only by dimensionality n of the system of Eqs. (8.1), but also by the number of parameters. Suppose we have the EP of the rth order and m parameters $\vec{\alpha} = (\alpha_1, \ldots, \alpha_m)^T$. Then we have $r - 1$ equations $\lambda_1(\vec{\alpha}_0) = \lambda_2(\vec{\alpha}_0)$, $\ldots$, $\lambda_1(\vec{\alpha}_0) = \lambda_r(\vec{\alpha}_0)$ for real (imaginary) eigenvalues, which can be consistently satisfied only if the number of equations is not greater than the number of parameters, i.e., $r - 1 \leq m$. The statement that the order of the EP is limited by the number of parameters as $r \leq m + 1$ is similar to the Gibbs phase rule for the systems in thermodynamic equilibrium. In the case of a single parameter α, $m = 1$

and the maximal order of the EP is $r = 2$ even if $n > 2$. In the case of complex eigenvalues, the number of equations doubles and the order of the EP should be within the range $2 \leq r \leq m/2 + 1$. Thus, the EP can exist only if the number of parameters $m \geq 2$.

Since, generally (for the complex eigenvalues), the minimal number of parameters is $2(r-1)$ for the r-th order EP, one should simultaneously tune $2(r-1)$ parameters that might be inconvenient and hardly realizable in practice. If the system satisfies some symmetries, the parameter space can be significantly reduced [15,16]. The most popular symmetries are parity ($\mathcal{P}$), parity–time ($\mathcal{PT}$), and charge-conjugation–parity ($\mathcal{CP}$) ones able to decrease the number of tuned parameters to $r-1$ [16]. For example, for the second order EP, one has to tune a single parameter instead of two parameters. The higher-order EPs can be realized due to increasing the number of channels in the system. In the optical context, this means that one should increase the number of coupled waveguides or cavities [17,18] or excite additional modes [19]. The order of EPs can be also doubled in the system consisting of two subsystems with identical degenerate eigenvalues. In this case, the merger of two individual EPs occurs only if the unidirectional coupling takes place [20].

Symmetric non-Hermitian Hamiltonians attract particular attention, because they can also provide a real spectrum of eigenvalues. If the symmetry is described by the linear operator $\hat{S}$, then it should commute with a symmetric Hamiltonian as $[\hat{H}, \hat{S}] = \hat{H}\hat{S} - \hat{S}\hat{H} = 0$. In the case of an anti-symmetric Hamiltonian, one should write the anti-commutation relation, $\{\hat{H}, \hat{S}\} = \hat{H}\hat{S} + \hat{S}\hat{H} = 0$.

One of the most studied symmetries is the parity–time ($\mathcal{PT}$) symmetry $\hat{S} = \hat{P}\hat{T}$, where $\hat{P}$ and $\hat{T}$ are the parity and time operators, respectively. The parity operator inverts spatial coordinates $\mathbf{r} \to -\mathbf{r}$. The time operator reverses time $t \to -t$, what is equivalent to the complex conjugate. The $\mathcal{PT}$-symmetric Hamiltonian $\hat{H}(\mathbf{r}, t)$ satisfies the commutation condition $\hat{P}\hat{T}\hat{H}(\mathbf{r}, t)\psi(\mathbf{r}, t) = \hat{H}(\mathbf{r}, t)\hat{P}\hat{T}\psi(\mathbf{r}, t)$ for an arbitrary wave function $\psi(\mathbf{r}, t)$. Since operators $\hat{P}$ and $\hat{T}$ act on the right-standing quantities, we arrive at $\hat{H}(-\mathbf{r}, -t)\psi(-\mathbf{r}, -t) = \hat{H}(\mathbf{r}, t)\psi(-\mathbf{r}, -t)$. Excluding arbitrary wave function ψ, we conclude that the Hamiltonian is $\mathcal{PT}$-symmetric, if $\hat{H}(-\mathbf{r}, -t) = \hat{H}(\mathbf{r}, t)$. For time-independent Hamiltonians, this condition reads $\hat{H}^*(-\mathbf{r}) = \hat{H}(\mathbf{r})$. For a quantum particle in potential $V(\mathbf{r})$, the condition of $\mathcal{PT}$ symmetry is valid, when $V^*(-\mathbf{r}) = V(\mathbf{r})$. The Maxwell equations can be recast in the form of the

Schrödinger equation (8.1) with the Hamiltonian:

$$H(\mathbf{r}) = \begin{pmatrix} 0 & -i\mu^{-1}(\mathbf{r})\nabla\times \\ i\varepsilon^{-1}(\mathbf{r})\nabla\times & 0 \end{pmatrix}, \tag{8.30}$$

$\tau = ct$, and the wave function $\psi(\mathbf{r},t) = (\mathbf{H}(\mathbf{r},t), \mathbf{E}(\mathbf{r},t))^T$. Here $\mathbf{H}$ and $\mathbf{E}$ are the magnetic- and electric-field strengths, and ε and μ are the permittivity and permeability tensors, respectively. $\mathcal{PT}$ symmetry then demands spatial distribution of material parameters according to $\varepsilon(\mathbf{r}) = \varepsilon^*(-\mathbf{r})$ and $\mu(\mathbf{r}) = \mu^*(-\mathbf{r})$, i.e., the permittivity and permeability play similar role as the potential in the context of quantum mechanics. Practical realization of the optical $\mathcal{PT}$ symmetry imposes severe restrictions on the choice of materials with gain and loss. To relax these requirements, an approach of the gain-free $\mathcal{PT}$ symmetry for input evanescent electromagnetic waves is proposed in Ref. [21].

Using the Fourier sum, a wave function in the box $L \times L \times L$ can be decomposed over countable number of orthogonal functions $f_{\mathbf{k}} = L^{-3/2}\exp(i\mathbf{kr})$ as $\psi(\mathbf{r}) = \sum_{\mathbf{k}} \psi_{\mathbf{k}} f_{\mathbf{k}}$. Then the wave function in the basis $\{f_{\mathbf{k}}\}$ can be presented as a vector $\psi = (\psi_{\mathbf{k}_n}, \psi_{\mathbf{k}_{n-1}}, \ldots, \psi_{-\mathbf{k}_n})^T$, where n is any integer number including infinity. From two expressions $\psi(-\mathbf{r}) = \hat{P}\psi(\mathbf{r})$ and $\psi(-\mathbf{r}) = \sum_{\mathbf{k}} \psi_{\mathbf{k}} f_{-\mathbf{k}} = \sum_{\mathbf{k}} \psi_{-\mathbf{k}} f_{\mathbf{k}}$ we can define the parity operator $\hat{P}$ as a matrix that should exchange the components $\psi_{\mathbf{k}_m}$ and $\psi_{-\mathbf{k}_m}$ of the wave function. That is why the parity operator for the two-state Hamiltonian reads:

$$\hat{P} = \begin{pmatrix} 0 & 1 \\ 1 & 0 \end{pmatrix}. \tag{8.31}$$

The $\mathcal{PT}$-symmetric two-state Hamiltonian satisfies $\hat{P}\hat{T}\hat{H}\psi = \hat{H}\hat{P}\hat{T}\psi$, or $\hat{P}\hat{H}^*\psi^* = \hat{H}\hat{P}\psi^*$ for any wave function ψ. Therefore, $\hat{P}\hat{H}^* = \hat{H}\hat{P}$. For the two-dimensional matrices $\hat{P}$ and $\hat{H}$, $\mathcal{PT}$-symmetry imposes the restrictions on the Hamiltonian matrix elements as $H_{12} = H_{21}^*$ and $H_{11} = H_{22}^*$. The invariants $\mathrm{tr}(\hat{H}) = 2\mathrm{Re}(H_{11})$ and $\det(\hat{H}) = |H_{11}|^2 - |H_{12}|^2$ appear to be real-valued, as do the eigenvalues of the non-Hermitian Hamiltonian, shown in Fig. 8.3.

Anti-$\mathcal{PT}$ symmetry arises when $\hat{P}\hat{T}\hat{H} = -\hat{H}\hat{P}\hat{T}$. For the two-state Hamiltonian, we have $\hat{P}\hat{H}^* = -\hat{H}\hat{P}$, so that the matrix elements are $H_{12} = -H_{21}^*$ and $H_{11} = -H_{22}^*$. This drastically changes the invariants of the matrix $\hat{H}$: $\mathrm{tr}(\hat{H}) = 2i\,\mathrm{Im}(H_{11})$ and $\det(\hat{H}) = |H_{12}|^2 - |H_{11}|^2$. The eigenvalues are no longer real, but the EP still exists at $\det(\hat{H}) = (\mathrm{tr}(\hat{H}))^2/4$, as demonstrated for a generic system in Fig. 8.2.

Although the discussion in this section concerns the EPs in the spectra of Hamiltonians, the similar regularities hold true for other matrices describing physical systems, too. One such matrix is the scattering matrix widely used in photonics. In particular, the scattering matrix is highly convenient for the analysis of optical multilayer structures. The study of EPs using scattering matrices can be found in many publications, see, e.g., Refs. [22,23].

8.3 Exceptional points in isolated and coupled dielectric resonators

We start discussion of specific realizations of exceptional points with the photonic systems consisting of ordinary dielectric materials. Although non-Hermitian effects are usually associated with the presence of losses and gains, the non-Hermiticity can be provided solely by the radiative energy exchange with environment, without intrinsic absorption or amplification of radiation. In general, the eigenvalues (frequencies or wavevectors of the eigenmodes) remain complex even at the EP due to uncompensated radiative losses.

One of the first examples of the EPs in such all-dielectric structures was reported in Ref. [24]. The authors considered a pair of infinitely-long circular waveguides of different radii. In accordance with the discussion above, the lack of symmetry in such a system implies that one has to tune two independent parameters in order to reach the EP of the second order in the complex plane. For the two cylinders, one can use the radius of one of the cylinders (another has a fixed radius) and the distance between them as the tuned parameters [Fig. 8.4(a)]. For the rectangular lattice of four identical cylinders, it is convenient to exploit the distances between the cylinders in two orthogonal directions [Fig. 8.4(b)]. The third-order EP can be found in the system of three different cylinders by tuning four independent parameters, for example, two radii (eigenfrequencies of resonators) and two distances between the cylinders (coupling coefficients) [Fig. 8.4(c)].

It was shown further that a single dielectric resonator is enough to observe the EP, if it has an asymmetric (non-spherical) shape. For example, in the dielectric spheroidal particle [Fig. 8.4(d)], the EP can be caught in tuning the permittivity of the material and the aspect ratio of the radii along two orthogonal axes [25]. The same reasoning is true for the dielectric disc with the permittivity and the thickness-to-radius ratio as the parameters [26]. A system of dimers composed of discs can be more practical for observation of the EPs, because distances between the dimers and between

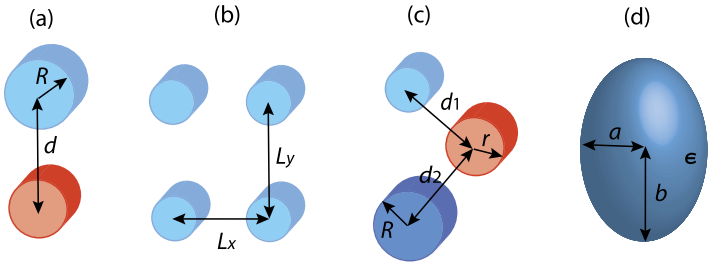

Figure 8.4. Types of resonators lacking a symmetry with the possible parameters for tuning. (a) Two cylinders, (b) two-dimensional array of cylinders, (c) three cylinders, and (d) spheroidal particle.

the separate discs in the dimers are the parameters allowing easier control [26]. Note that in all cases mentioned above, the quality (Q) factor is strongly enhanced at the EP, what is important for various applications.

It seems that introduction of the asymmetry or deformation is the general method for reaching EPs in dielectric resonators caused by the control of modes evolution. As further examples, we mention the whispering-gallery modes cavities either having non-circular (quad-cosine [27] or limaçon [28]) shape or perturbed by additional scatterers [29].

8.4 Exceptional points in non-Hermitian systems with gain and loss

Although non-Hermitian physics describes any open photonic system, it has been proved to be especially fruitful, when applied to active systems containing loss and gain components. Perhaps, the most intriguing class of such non-Hermitian systems possesses $\mathcal{PT}$ symmetry. The idea of the optical $\mathcal{PT}$ symmetry was adopted directly from quantum mechanics. In the pioneer work [30], it was shown that the $\mathcal{PT}$-symmetric Hamiltonian, commuting simultaneously with the parity and time reversal operators, has real eigenvalues. Since the stationary Schrödinger equation:

$$\frac{d^2\psi}{dx^2} - \frac{2m}{\hbar^2}[V(x) - E] = 0, \tag{8.32}$$

for the quantum particle in the potential $V(x)$ is mathematically equivalent to the Helmholtz equation:

$$\frac{d^2u}{dx^2} + \frac{\omega^2}{c^2}\varepsilon(x)u = 0, \tag{8.33}$$

for electromagnetic field in the medium with permittivity $\varepsilon(x)$, the transfer of $\mathcal{PT}$-symmetry to the optics domain is straightforward [5]. Obviously, the permittivity in optics plays the role of the potential in quantum mechanics. The $\mathcal{PT}$ symmetry condition for the potential $V(x) = V^*(-x)$ is then recast to $\varepsilon(x) = \varepsilon^*(-x)$. This means that $\mathcal{PT}$ symmetry can be realized in photonic structures with specific distributions of loss [$\mathrm{Im}(\varepsilon) > 0$] and gain [$\mathrm{Im}(\varepsilon) < 0$] over the media. The $\mathcal{PT}$-symmetric optical systems were realized using coupled waveguides [31,32], coupled cavities [33,34], and multilayer structures [35,36].

An EP in a $\mathcal{PT}$-symmetric photonic system can be defined as a point of spontaneous symmetry breaking. In other words, despite the condition $\varepsilon(x) = \varepsilon^*(-x)$ always holds true, the commutation of the Hamiltonian with the $\hat{P}$ and $\hat{T}$ operators is violated at the EP. One can introduce two phases touching at the EP: the first phase is $\mathcal{PT}$-symmetric with real eigenfrequencies and $\mathcal{PT}$-symmetric eigenmodes characterized by the balanced distribution of light energy over loss and gain components; the second phase is $\mathcal{PT}$-symmetry-broken with the complex eigenfrequencies and asymmetric eigenmodes demonstrating either strong amplification or attenuation of light. Exactly such a behavior of the modes is presented in Fig. 8.3. We should also emphasize that, as already discussed above, the $\mathcal{PT}$ symmetry diminishes the number of parameters needed to tune the system towards the EP.

Let us consider the archetypal case of a loss-gain multilayer structure. Interaction of light with such non-Hermitian structures can be conveniently described by the scattering matrix formalism. The proper expression for the scattering matrix can be derived from the Hamiltonian, similar to (8.30) and reads [23]:

$$\hat{S} = \begin{pmatrix} t & r_R \\ r_L & t \end{pmatrix}, \tag{8.34}$$

where t, r_R, and r_L are the transmission and reflection coefficients, which can be readily calculated with the well-known transfer matrix approach [37]. The eigenvalues of the matrix (8.34) are $s_{1,2} = t \pm \sqrt{r_R r_L}$, so that the EP corresponds to the situation when either r_R or r_L vanishes and $|t| = 1$ (Fig. 8.5). This is exactly the condition for the so-called anisotropic transmission resonances with the unitary transmission and the one-sided reflectionlessness [22]. If the multilayer structure is $\mathcal{PT}$-symmetric, i.e., consists of the balanced sequence of loss and gain layers, then the EP lies at the border between the $\mathcal{PT}$-symmetric phase with $|s_{1,2}| = 1$ and the $\mathcal{PT}$-symmetry-broken phase with $|s_1| = 1/|s_2| < 1$.

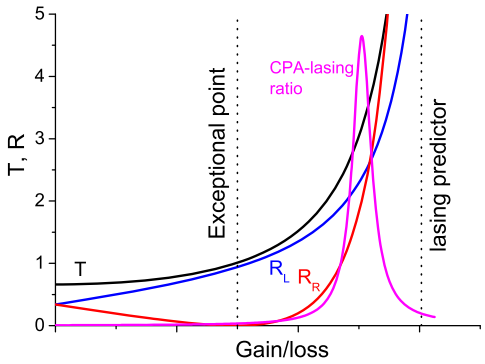

Figure 8.5. The EP of a $\mathcal{PT}$-symmetric multilayer structure. The EP corresponds to the unity transmission and zero reflection from one side. The lasing predictor corresponds to sharp increase of reflection and transmission. The ratio of output power in the cases corresponding to lasing and CPA reaches maximum between the EP and lasing predictor.

Another definition of the scattering matrix used in literature [22] reads as:

$$\hat{S}' = \begin{pmatrix} r_L & t \\ t & r_R \end{pmatrix}. \tag{8.35}$$

The exchange of matrix elements in comparison to Eq. (8.34) may seem to be inessential, but actually it results in a dramatic change of the eigenvalues which now take the form $s'_{1,2} = (r_R + r_L)/2 \pm \sqrt{t^2 + (r_L - r_R)^2/4}$. The exceptional point also changes its position being observed at $|r_L + r_R| = 2$. Since $\hat{S}'$ does not follow from the $\mathcal{PT}$-symmetric Hamiltonian, the corresponding EP is not a true EP, but it is not meaningless as well. It makes sense as a lasing predictor showing the level of loss and gain just below the lasing threshold (Fig. 8.5). This interpretation was proved with the calculations based on the Maxwell–Bloch equations for realistic loss and gain media [23]. The Maxwell–Bloch approach, as opposed to the usual phenomenological consideration based on complex permittivity, allows to take nonlinear saturation into account and describe behavior in the lasing regime with the intriguing propagation-locking effect [38]. It should be also noted that the EP as a lasing prethreshold was discussed in Ref. [39].

$\mathcal{PT}$ symmetry in photonic systems imposes tough limitations on loss and gain distribution raising a question of practical realization. That is why the non-Hermitian systems possessing EPs with relaxed demands on loss and gain are of great interest. As an example, we can spotlight anti-$\mathcal{PT}$-symmetric systems. In one-dimensional case, the anti-$\mathcal{PT}$-symmetry implies the permittiv-

ity of the form $\varepsilon(x) = -\varepsilon^*(-x)$. Since the imaginary part of the permittivity is either positive or negative in the entire space, the variety of passive materials can be employed in practice. However, this platform has a noticeable flaw preventing from the real-life application: it requires the utilization of exotic negative-refractive-index media [40]. More popular approach is based on the dissipative coupling of optical elements such as waveguides or cavities [41]. The dissipative coupling brings us to the special form of the Hamiltonian matrix that has real frequencies on the diagonal and complex coupling coefficients off the diagonal. The EPs in such anti-$\mathcal{PT}$-symmetric systems behave in the same way as for $\mathcal{PT}$-symmetric systems demarcating symmetric and symmetry-broken phases. The anti-$\mathcal{PT}$-symmetric EPs were reported in electric circuit resonators [42], optical fibers [43], and integrated-optics structures [44].

Passive analogue of the $\mathcal{PT}$-symmetric system is a promising paradigm for getting around the gain issues. Absorption modulation may emulate the true $\mathcal{PT}$ symmetry if a constant shift of permittivities of all components in the system is made [5]. In this case, the less absorbing parts of the structure play the role of gain, whereas the more absorbing parts can be considered as loss. In other words, the Hamiltonian matrix can be treated as a sum of the constant matrix and $\mathcal{PT}$-symmetric one. However, dissipative systems are dramatically different from those with balanced loss and gain, since the EPs are not necessary for $\mathcal{PT}$-symmetry-breaking transitions anymore [45]. A curious design of the passive $\mathcal{PT}$-symmetric structure is proposed in Ref. [46], where a mirror image supplements a passive structure instead of the real gain.

The unique features of EPs turned out to be extremely relevant for lasing as one of the typical non-Hermitian phenomena justified for the new class of $\mathcal{PT}$-symmetric lasers [47]. When the $\mathcal{PT}$ symmetry breaking at the EP violates balance between the modes, one of the modes becomes amplified and the other is attenuated. As a result, above the EP, which in this case is simultaneously the lasing threshold, the robust single-mode lasing is established. This idea, being of high demand for applications, was experimentally demonstrated with the microring lasers [48,49]. If the EP is above the lasing threshold, additional intriguing features emerge. For instance, the laser is able to turn off at the EP due to the coalescence of attenuating and amplifying modes [50,51]. The EP was predicted to be an on-off switching point also in the anti-$\mathcal{PT}$-symmetric lasing systems [52].

Sometimes a $\mathcal{PT}$-symmetric system can be simultaneously a coherent perfect absorber (CPA) and a laser. The CPA can be also called a time-reversed laser, or anti-laser, in the sense that incom-

ing waves are fully absorbed in the medium due to their interference [53]. The CPA-lasing effect in $\mathcal{PT}$-symmetric systems was theoretically predicted in Ref. [54]. It showed up in the scenario of two counter-propagating waves impinging the system, which behaves as a CPA or a laser depending on the phase difference between the waves [36]. The CPA-lasing conditions are not directly connected with emergence of the EPs. However, the optimal contrast between absorption and amplification appears to be reached above the EP, but below the lasing predictor point, as shown for multilayer structures (Fig. 8.5) [55]. This result, supported by the time-domain Maxwell–Bloch simulations, means that the CPA-lasing does not imply true lasing, because the latter is independent of the phase difference between the input waves [55].

8.5 Topological properties of exceptional points

Topology studies invariant, persistent properties of objects. These properties remain intact under perturbations or deformations of the object. The topological ideas penetrated first into condensed-matter physics, where they were fruitful in explaining the features of quantum Hall effect and topological insulators. They proved to be extremely beneficial for description of optical systems (especially periodic, such as photonic crystals and metamaterials) giving rise to the field of topological photonics [56–58]. The key parameter characterizing the system from the viewpoint of topology is the topological invariant. Perhaps the most widely used invariant is the Chern number, which is the integral characteristic expressing the properties of the band structure of a complex photonic system in just one integer [59].

Not pretending to cover all aspects of topological non-Hermitian systems [60,61], we limit our discussion to the specific problem of topological properties of EPs. The topology of any singular point, including the EP, can be characterized by the phase change under encircling this point in the parameter (or phase) space. The phase change under the closed path around the singular point defines the winding number:

$$q = \frac{1}{2\pi} \oint d\phi. \tag{8.36}$$

The winding number q has the meaning of the topological charge of the singular point, the point being topologically nontrivial if $q \neq 0$.

The topology of EPs is governed by geometry of the Riemannian surfaces formed by eigenvalues in the parameter space. An example of the Riemannian surfaces for the second-order EP is shown in Fig. 8.2. One can note that a single closed loop is not enough to return to the starting point on these surfaces and the second loop is needed. In this case, the EP's topological charge is $q = 1/2$, in contrast to the integer winding numbers in the topological systems supporting edge states. For the rth-order EP, one has r Riemannian surfaces and needs r loops to return to the starting point.

Moreover, the result of encircling the EP depends on the way it is performed. There are static and dynamic approaches to encircle the EP. For static encircling, the eigenmode swaps with another one at the different Riemannian surface gaining an additional (geometric) phase after returning to the starting point [62]. This is a direct consequence of the half-integer topological charge of the EP and the geometry of the Riemannian surfaces discussed above, so that the system does not return to the initial state at the end of the cycle. Perhaps, the first experimental observation of such a topological behavior was reported in 2001 for the two coupled microwave cavities perturbed by the semicircle scatterer [63]. Changing the position of the scatterer and coupling between the cavities, one can encircle the EP in the two-dimensional parameter space. The authors clearly observe the interchange of eigenvalues (complex frequencies) and eigenmodes (field distributions, see, Fig. 8.6(a)) at the final point of the circle [63]. The swap of the eigenvalues was reported also for the coupled waveguides with purely radiative losses (see Section 8.3), including the case of higher-order EPs with multiple participating eigenmodes [24]. Static encircling the EP was also realized for the deformed optical microcavity [64] and the exciton-polariton microcavity with changing dimensions [65].

Totally different situation occurs for dynamic encircling, when the measurements for the successive values of parameters are not independent. Changing characteristics of the system (e.g., its geometrical parameters or coupling strength with the environment) along the propagation direction provides the means to emulate the EP encircling in the parameter space. In this case, the process turns out to be non-adiabatic and allows jumps between the Riemannian surfaces [66,67]. Non-adiabaticity yields the chiral mode switching, when the final state depends on the encircling direction (clockwise or counter-clockwise), see Fig. 8.6(b). This effect was experimentally observed as an asymmetric light propagation in curved microwave waveguides [68] and in coupled photonic waveguides [69]. Dynamic effect of the moving EP and its encir-

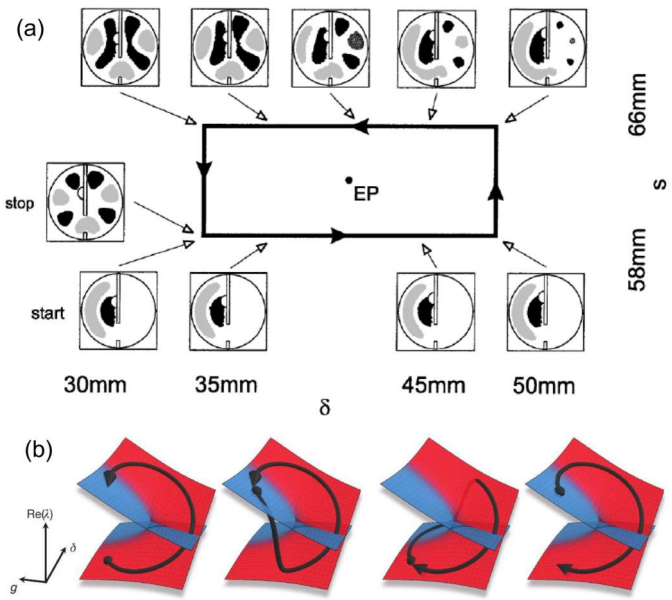

Figure 8.6. Topological features of the EPs. (a) Change of the field distribution for static encircling the EP. Adapted with permission from Ref. [63]. (b) Final state of a system depends on dynamic encircling direction (counter-clockwise for the two left panels, clockwise for the two right panels), but not on the starting point. Non-adiabatic jumps between the surfaces are clearly seen. Adapted with permission from Ref. [68].

cling by the pair of waveguides was realized in Ref. [70]. Interestingly, the chiral mode switching is possible even if the loop does not encircle the EP itself, but is only situated nearby sensing the details of Riemannian surfaces [71,72]. In the case of multiple EPs, the dynamics of encircling become even richer, since the loops with the common starting points and encircling direction are not always topologically equivalent (homotopic) [73]. The multiple EP encircling was experimentally observed in the non-Hermitian waveguide arrays fabricated in glass [74].

In the presence of symmetries (for example, $\mathcal{PT}$ symmetry), additional features of encircling dynamics can be highlighted. In particular, the chirality of the dynamics remarkably depends on the starting point of encircling. If the starting point in the parameter space corresponds to the symmetric phase, the chiral switching depends on the encircling direction. On the contrary, the dynamics are nonchiral (that is, the final state is the same for any direction of encircling) if the starting point is in the broken-symmetry phase. A pronounced role of the starting point was demonstrated using a system of coupled waveguides made of fer-

romagnetic material, which is well controlled by magnetic field [75]. The chiral switching in anti-$\mathcal{PT}$-symmetric systems was reported in Ref. [76].

The chiral mode switching is able to control the state of radiation polarization. It helps to design an optical omnipolarizer converting any input polarization into the desired one [77]. One more type of the chiral polarizer performed on the basis of anti-$\mathcal{PT}$-symmetric platform for waveguides was reported in Ref. [78].

8.6 Enhanced sensitivity at the EP

One of the most well studied and practically appealing effects observed in the EP vicinity is the sharp increase of system's sensitivity to an external perturbation. This effect allows using non-Hermitian systems as sensors to detect small changes of environment caused, e.g., by biomolecules. Enhanced sensitivity near the EP can be readily proved for the two-state Hamiltonian. Consider a non-Hermitian Hamiltonian $\hat{H}(\vec{\alpha}) = \hat{H}_0(\vec{\alpha}) + \varepsilon\hat{H}_1(\vec{\alpha})$, where $\varepsilon \ll 1$ is a dimensionless small parameter and $\varepsilon\hat{H}_1$ is a perturbation operator. The eigenvalues (8.23) of the non-perturbed system are degenerate at the EP, $\vec{\alpha} = \vec{\alpha}_0$, so that $f(0) = [\mathrm{tr}(\hat{H}_0)]^2 - 4\det(\hat{H}_0) = 0$, where $f(\varepsilon) = [\mathrm{tr}(\hat{H})]^2 - 4\det(\hat{H})$. When degeneracy is lifted due to the perturbation, the function takes the form $f(\varepsilon) \approx \varepsilon f'(0)$, where $f' = df/d\varepsilon$, and the eigenvalues (8.23) are equal to:

$$\lambda_\pm = \frac{\mathrm{tr}(H_0) + \varepsilon\mathrm{tr}(\hat{H}_1) \pm \sqrt{\varepsilon f'(0)}}{2} \approx \lambda \pm \sqrt{\varepsilon}\frac{\sqrt{f'(0)}}{2}. \tag{8.37}$$

Square root of the small perturbation parameter is the leading order for the second-order EP. Owing to this fact, the sensitivity at the EP is enhanced in comparison to the usual situation of the linear relation between perturbation and response.

In general, the eigenvalues and eigenvectors can be presented as a Puiseux series in the EP vicinity:

$$\lambda_\pm = \sum_{k=0}^{\infty}(\pm 1)^k \varepsilon^{k/2}\lambda_k, \qquad \mathbf{v}_\pm = \sum_{k=0}^{\infty}(\pm 1)^k \varepsilon^{k/2}\tilde{\mathbf{v}}_k, \tag{8.38}$$

where λ_0 and $\tilde{\mathbf{v}}_0 = \mathbf{v}_1$ are the degenerate eigenvalues and eigenvectors at the EP, respectively. As shown in Ref. [79], in the leading order, the perturbed quantities can be written as $\lambda_\pm \approx \lambda_0 \pm \sqrt{\varepsilon}\lambda_1$, $\mathbf{v}_\pm \approx \mathbf{v}_1 \pm \sqrt{\varepsilon}\lambda_1\mathbf{v}_2$, and $\mathbf{u}_\pm \approx \mathbf{u}_1 \pm \sqrt{\varepsilon}\lambda_1\mathbf{u}_2$, where $\lambda_1 = \sqrt{(\mathbf{u}_1 H_1 \mathbf{v}_1)}$ and $\mathbf{v}_2$ ($\mathbf{u}_2$) is the right (left) generalized eigenvector. Adopting $(\mathbf{u}_1\mathbf{v}_2) = (\mathbf{u}_2\mathbf{v}_1) = 1$, the above approximations in the EP vicinity

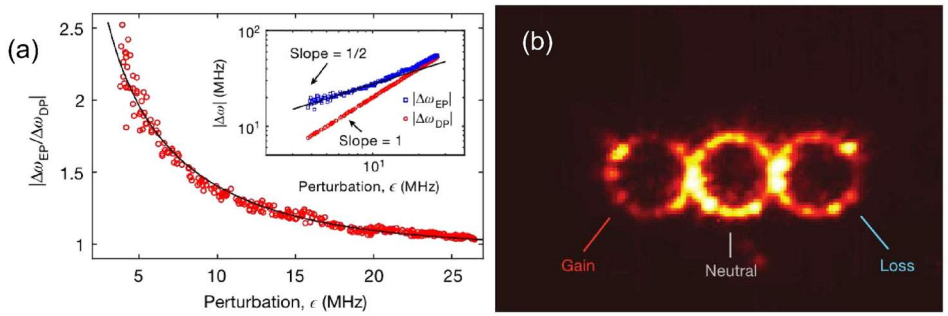

Figure 8.7. Sensing applications of the EPs. (a) Enhancement of the perturbation-induced frequency splitting of the cavity mode at the EP in comparison with the diabolic point (DP). Adapted with permission from Ref. [86]. (b) Intensity profile of the lasing mode at the 3rd order EP of the $\mathcal{PT}$-symmetric system consisting of three (loss, gain, and neutral) cavities. Adapted with permission from Ref. [87].

after substitution to (8.9) bring us to the dyadic Green function at the EP:

$$G_{EP} = \frac{\mathbf{v}_1 \otimes \mathbf{u}_1}{(\lambda - \lambda_0)^2} + \frac{\mathbf{v}_2 \otimes \mathbf{u}_1 + \mathbf{v}_1 \otimes \mathbf{u}_2}{\lambda - \lambda_0}. \tag{8.39}$$

This equation is equivalent to the Green function at the EP in Eq. (8.22), because $\mathbf{v}_1 \otimes \mathbf{u}_1 = \hat{N}$ and $\mathbf{v}_1 \otimes \mathbf{u}_2 + \mathbf{v}_2 \otimes \mathbf{u}_1 = I_2$. Imaginary part of the Green function can be used to calculate the local density of states that behaves as the squared Lorentzian function that is drastically different from the usual (non-degenerate) resonances and ensures stronger response with narrower spectrum.

As for the rth-order EP, the leading order of the response is $\varepsilon^{1/r}$ [80]. Generally, the response strongly depends on the properties of perturbation Hamiltonian $\hat{H}_1$ and is proportional to $\varepsilon^{k/r}$, where k is an integer number up to r. For details, a reader is referred to literature on the perturbation theory near EPs [81–83].

Let us illustrate the general features discussed above with several specific examples. First of all, we should mention the idea of single-particle detection proposed and substantiated in Refs. [84, 85]. The enhanced sensitivity at the EP for the single-particle detection in comparison to the Hermitian degeneracy at the diabolic point was experimentally demonstrated using the microtoroid whispering-gallery-mode cavity, see Fig. 8.7(a) [86]. Coupled loss-gain microring cavities were reported to provide thermal sensing [87]. $\mathcal{PT}$-symmetric system with the gain, loss, and neutral cavities demonstrated in Fig. 8.7(b) exhibits the cubic-root sensitivity to perturbation at the third-order EP [87]. Anti-$\mathcal{PT}$-symmetric scheme based on cavity-waveguide coupling was real-

ized in Ref. [88] for detecting weak effect of mode anharmonicity. The EP-enhanced sensing proved to be especially useful for detecting rotations. The non-Hermitian gyroscopes exploiting the stimulated Brillouin scattering in the microresonator [89] and the ring laser [90] were reported to enhance the Sagnac effect. The anti-$\mathcal{PT}$-symmetric gyroscopes can be advantageous compared to the $\mathcal{PT}$-symmetric ones in accuracy and ease of realization [91,92]. The most exotic proposal, which is of fundamental importance, is the search for the hypothetical axions using the $\mathcal{PT}$-symmetry-improved sensors [93,94].

We should note that the term "sensitivity" is used here to characterize the connection between the perturbation (input) and the response (output). However, this does not guarantee the enhanced signal-to-noise ratio, which is often more important for sensing applications. This fact has stirred up a discussion on the role of noise (both classical and quantum) in the non-Hermitian sensing. For more information on these debates and examples of specific EP sensors, we refer a reader to the recent papers [95,96].

8.7 EPs and strong coupling

Let us look at Fig. 8.3 once again and think about it from the other side. The real and imaginary parts of eigenvalues can be associated with the resonant frequencies and widths of the resonances, respectively. Then, for $\eta < 1$, we see a single resonance, which splits into two resonances at $\eta > 1$. Such a splitting (so-called Rabi splitting) is characteristic of the strong-coupling regime of light-matter interaction, when both radiation and matter cease to be independent entities and exist in the form of part-matter–part-light polaritons [97,98]. From this point of view, the EP is the point of transition between the weak- and strong-coupling regimes or transition from modes crossing (overlapping) to anti-crossing (splitting). The parameter η can be interpreted as the strength of the light-matter interaction, governed by system's parameters, such as distances between waveguides or cavities.

There is a number of reports on strong coupling in the non-Hermitian context making emphasis on behaviors in the EP vicinity. One of the first such reports has substantiated applicability of the $\mathcal{PT}$ symmetry to the polaritonic domain by considering coupling between photonic and excitonic modes, e.g., in a semiconductor-quantum-well structure [99]. The EP originates from merging the polaritonic modes at some level of pumping below the lasing threshold. Moreover, encircling the EP results in

switching the content of polaritons from pure photons to pure excitons and vice versa, which seems to be intriguing for controlling light-matter interaction [99]. Polaritons may also stem from the plasmon and phonon modes coupled in the structure containing graphene and polar dielectric [100]. The transition between the weak and strong coupling regimes in these systems was shown to be controllable simply by light's angle of incidence [100]. The strong coupling regime in the non-Hermitian context was experimentally realized due to interaction of excitons with either photons or plasmons. In the first case [101], the polaritons emerge due to the excitons in the semiconductor GaN coupled to the whispering-gallery modes of the hexagonal microcavity. In the second case [102], the excitons in the transition metal dichalcogenide (in particular, tungsten disulfide WS_2) monolayer were coupled to plasmons of the silver nanogroove to form the polaritonic non-Hermitian system. The magnon-photon coupling in the system composed of the nitrogen centers in diamond and waveguide resonator was studied in Ref. [103].

8.8 Conclusion

In this chapter, we have outlined the range of issues essential for the area of non-Hermitian photonics with the particular emphasis on the physics at the exceptional points. We have limited our discussion to the most basic and general properties of EPs originating from the non-Hermitian nature of Hamiltonian. We have illustrated the physics of EPs with a variety of examples from the optics and photonics literature. For the sake of brevity and clarity, we intentionally left aside many advanced topics and generalizations, such as exceptional rings [104] and surfaces [105,106], to name a few. Nevertheless, we strongly believe that this chapter will be of interest to everyone (especially beginners) interested in the non-Hermitian physics and its photonic applications.

Acknowledgment

A.V.N. was supported by the Belarusian Republican Foundation for Fundamental Research (Project No. F21ISR-003). D.V.N. is grateful to the State Program for Scientific Research "Photonics and Electronics for Innovations" (Task 1.5). General theory of exceptional points was supported by the Russian Science Foundation (Project No. 21-12-00383).

References

[1] Y. Ashida, Z. Gong, M. Ueda, Non-Hermitian physics, Adv. Phys. 69 (2020) 249–435.
[2] N. Moiseyev, Non-Hermitian Quantum Mechanics, Cambridge University Press, Cambridge, 2011.
[3] C.M. Bender, PT Symmetry in Quantum and Classical Physics, World Scientific, Singapore, 2019.
[4] D. Christodoulides, J. Yang (Eds.), Parity-Time Symmetry and Its Applications, Springer, 2018.
[5] A.A. Zyablovsky, A.P. Vinogradov, A.A. Pukhov, A.V. Dorofeenko, A.A. Lisyansky, $\mathcal{PT}$ symmetry in optics, Phys. Usp. 57 (2014) 1063–1082.
[6] L. Feng, R. El-Ganainy, L. Ge, Non-Hermitian photonics based on parity-time symmetry, Nat. Photonics 11 (2017) 752–762.
[7] R. El-Ganainy, K.G. Makris, M. Khajavikhan, Z.H. Musslimani, S. Rotter, D.N. Christodoulides, Non-Hermitian physics and $\mathcal{PT}$ symmetry, Nat. Phys. 13 (2018) 11–19.
[8] S.K. Özdemir, S. Rotter, F. Nori, L. Yang, Parity-time symmetry and exceptional points in photonics, Nat. Mater. 18 (2019) 783–798.
[9] M.-A. Miri, A. Alù, Exceptional points in optics and photonics, Science 363 (2019) eaar7709.
[10] A. Krasnok, N. Nefedkin, A. Alù, Parity-time symmetry and exceptional points, IEEE Antennas Propag. Mag. 63 (2021) 110–121.
[11] G.N. Borzdov, Waves with linear, quadratic and cubic coordinate dependence of amplitude in crystals, Pramana 46 (1996) 245–257.
[12] T.G. Mackay, C. Zhou, A. Lakhtakia, Dyakonov–Voigt surface waves, Proc. R. Soc. A 475 (2019) 20190317.
[13] W.D. Heiss, Green's functions at exceptional points, Int. J. Theor. Phys. 54 (2015) 3954–3959.
[14] J. Wiersig, Response strengths of open systems at exceptional points, Phys. Rev. Res. 4 (2022) 023121.
[15] I. Mandal, E.J. Bergholtz, Symmetry and higher-order exceptional points, Phys. Rev. Lett. 127 (2021) 186601.
[16] P. Delplace, T. Yoshida, Y. Hatsugai, Symmetry-protected multifold exceptional points and their topological characterization, Phys. Rev. Lett. 127 (2021) 186602.
[17] X. Zhou, S.K. Gupta, Z. Huang, Z. Yan, P. Zhan, Z. Chen, M. Lu, Z. Wang, Optical lattices with higher-order exceptional points by non-Hermitian coupling, Appl. Phys. Lett. 113 (2018) 101108.
[18] S.M. Zhang, X.Z. Zhang, L. Jin, Z. Song, High-order exceptional points in supersymmetric arrays, Phys. Rev. A 101 (2020) 033820.
[19] A.V. Hlushchenko, D.V. Novitsky, V.I. Shcherbinin, V.R. Tuz, Multimode $\mathcal{PT}$-symmetry thresholds and third-order exceptional points in coupled dielectric waveguides with loss and gain, J. Opt. 23 (2021) 125002.
[20] Q. Zhong, J. Kou, K. Özdemir, R. El-Ganainy, Hierarchical construction of higher-order exceptional points, Phys. Rev. Lett. 125 (2020) 203602.
[21] H. Li, A. Mekawy, A. Alù, Gain-free parity-time symmetry for evanescent fields, Phys. Rev. Lett. 127 (2021) 014301.
[22] L. Ge, Y.D. Chong, A.D. Stone, Conservation relations and anisotropic transmission resonances in one-dimensional $\mathcal{PT}$-symmetric photonic heterostructures, Phys. Rev. A 85 (2012) 023802.
[23] A. Novitsky, D. Lyakhov, D. Michels, A.A. Pavlov, A.S. Shalin, D.V. Novitsky, Unambiguous scattering matrix for non-Hermitian systems, Phys. Rev. A 101 (2020) 043834.

[24] A. Abdrabou, Y.Y. Lu, Exceptional points for resonant states on parallel circular dielectric cylinders, J. Opt. Soc. Am. B 36 (2019) 1659–1667.
[25] E. Bulgakov, K. Pichugin, A. Sadreev, Exceptional points in a dielectric spheroid, Phys. Rev. A 104 (2021) 053507.
[26] K. Pichugin, A. Sadreev, E. Bulgakov, Exceptional points through variation of distances between four coaxial dielectric disks, Photonics 8 (2021) 460.
[27] T. Jiang, Y. Xiang, Perfectly-matched-layer method for optical modes in dielectric cavities, Phys. Rev. A 102 (2020) 053704.
[28] S.-J. Park, I. Kim, S. Rim, M. Choi, Chiral exceptional point in transformation cavity, Opt. Lett. 47 (2022) 1705–1708.
[29] S. Ramezanpour, A. Bogdanov, A. Alù, Y. Ra'di, Generalization of exceptional point conditions in perturbed coupled resonators, Phys. Rev. B 104 (2021) 205405.
[30] C.M. Bender, S. Boettcher, Real spectra in non-Hermitian Hamiltonians having $\mathcal{PT}$ symmetry, Phys. Rev. Lett. 80 (1998) 5243–5246.
[31] C.E. Rüter, K.G. Makris, R. El-Ganainy, D.N. Christodoulides, M. Segev, D. Kip, Observation of parity-time symmetry in optics, Nat. Phys. 6 (2010) 192–195.
[32] M. Kremer, T. Biesenthal, L.J. Maczewsky, M. Heinrich, R. Thomale, A. Szameit, Demonstration of a two-dimensional $\mathcal{PT}$-symmetric crystal, Nat. Commun. 10 (2019) 435.
[33] B. Peng, Ş.K. Özdemir, F. Lei, F. Monifi, M. Gianfreda, G.L. Long, S. Fan, F. Nori, C.M. Bender, L. Yang, Parity–time-symmetric whispering-gallery microcavities, Nat. Phys. 10 (2014) 394–398.
[34] L. Chang, X. Jiang, S. Hua, C. Yang, J. Wen, L. Jiang, G. Li, G. Wang, M. Xiao, Parity–time symmetry and variable optical isolation in active–passive-coupled microresonators, Nat. Photonics 8 (2014) 524–529.
[35] L. Feng, Y.-L. Xu, W.S. Fegadolli, M.-H. Lu, J.E.B. Oliveira, V.R. Almeida, Y.-F. Chen, A. Scherer, Experimental demonstration of a unidirectional reflectionless parity-time metamaterial at optical frequencies, Nat. Mater. 12 (2013) 108–113.
[36] Z.J. Wong, Y.-L. Xu, J. Kim, K. O'Brien, Y. Wang, L. Feng, X. Zhang, Lasing and anti-lasing in a single cavity, Nat. Photonics 10 (2016) 796–801.
[37] M. Born, E. Wolf, Principles of Optics, 7th ed., Cambridge University Press, Cambridge, 1999.
[38] D.V. Novitsky, A. Karabchevsky, A.V. Lavrinenko, A.S. Shalin, A.V. Novitsky, $\mathcal{PT}$ symmetry breaking in multilayers with resonant loss and gain locks light propagation direction, Phys. Rev. B 98 (2018) 125102.
[39] A.A. Zyablovsky, I.V. Doronin, E.S. Andrianov, A.A. Pukhov, Yu.E. Lozovik, A.P. Vinogradov, A.A. Lisyansky, Exceptional points as lasing prethresholds, Laser Photonics Rev. 15 (2021) 2000450.
[40] L. Ge, H.E. Türeci, Antisymmetric $\mathcal{PT}$-photonic structures with balanced positive- and negative-index materials, Phys. Rev. A 88 (2013) 053810.
[41] F. Yang, Y.-C. Liu, L. You, Anti-$\mathcal{PT}$ symmetry in dissipatively coupled optical systems, Phys. Rev. A 96 (2017) 053845.
[42] Y. Choi, C. Hahn, J.W. Yoon, S.H. Song, Observation of an anti-$\mathcal{PT}$-symmetric exceptional point and energy-difference conserving dynamics in electrical circuit resonators, Nat. Commun. 9 (2018) 2182.
[43] A. Bergman, R. Duggan, K. Sharma, M. Tur, A. Zadok, A. Alù, Observation of anti-parity-time-symmetry, phase transitions and exceptional points in an optical fibre, Nat. Commun. 12 (2021) 486.
[44] H. Fan, J. Chen, Z. Zhao, J. Wen, Y.-P. Huang, Antiparity-time symmetry in passive nanophotonics, ACS Photonics 7 (2020) 3035.

[45] Y.N. Joglekar, A.K. Harter, Passive parity-time-symmetry-breaking transitions without exceptional points in dissipative photonic systems, Photon. Res. 6 (2018) A51–A57.
[46] F. Yang, A. Hwang, C. Doiron, G.V. Naik, Non-Hermitian metasurfaces for the best of plasmonics and dielectrics, Opt. Mater. Express 11 (2021) 2326–2334.
[47] B. Qi, H.-Z. Chen, L. Ge, P. Berini, R.-M. Ma, Parity–time symmetry synthetic lasers: physics and devices, Adv. Opt. Mater. 7 (2019) 1900694.
[48] L. Feng, Z.J. Wong, R.-M. Ma, Y. Wang, X. Zhang, Single-mode laser by parity-time symmetry breaking, Science 346 (2014) 972–975.
[49] H. Hodaei, M.-A. Miri, M. Heinrich, D.N. Christodoulides, M. Khajavikhan, Parity-time–symmetric microring lasers, Science 346 (2014) 975–978.
[50] M. Liertzer, L. Ge, A. Cerjan, A.D. Stone, H.E. Türeci, S. Rotter, Pump-induced exceptional points in lasers, Phys. Rev. Lett. 108 (2012) 173901.
[51] M. Brandstetter, M. Liertzer, C. Deutsch, P. Klang, J. Schöberl, H.E. Türeci, G. Strasser, K. Unterrainer, S. Rotter, Reversing the pump dependence of a laser at an exceptional point, Nat. Commun. 5 (2014) 4034.
[52] Y. Duan, X. Zhang, Y. Ding, X. Ni, Single-cavity bi-color laser enabled by optical anti-parity-time symmetry, Photon. Res. 9 (2021) 1280–1288.
[53] Y.D. Chong, Li Ge, Hui Cao, A.D. Stone, Coherent perfect absorbers: time-reversed lasers, Phys. Rev. Lett. 105 (2010) 053901.
[54] S. Longhi, $\mathcal{PT}$-symmetric laser absorber, Phys. Rev. A 82 (2010) 031801(R).
[55] D.V. Novitsky, CPA-laser effect and exceptional points in $\mathcal{PT}$-symmetric multilayer structures, J. Opt. 21 (2019) 085101.
[56] L. Lu, J.D. Joannopoulos, M. Soljačić, Topological photonics, Nat. Photonics 8 (2014) 821–829.
[57] T. Ozawa, H.M. Price, A. Amo, N. Goldman, M. Hafezi, L. Lu, M.C. Rechtsman, D. Schuster, J. Simon, O. Zilberberg, I. Carusotto, Topological photonics, Rev. Mod. Phys. 91 (2019) 015006.
[58] G.-J. Tang, X.-T. He, F.-L. Shi, J.-W. Liu, X.-D. Chen, J.-W. Dong, Topological photonic crystals: physics, designs, and applications, Laser Photonics Rev. 16 (2022) 2100300.
[59] D. Bisharat, R. Davis, Y. Zhou, P. Bandaru, D. Sievenpiper, Photonic topological insulators: a beginner's introduction, IEEE Antennas Propag. Mag. 63 (2021) 112–124.
[60] H. Wang, X. Zhang, J. Hua, D. Lei, M. Lu, Y. Chen, Topological physics of non-Hermitian optics and photonics: a review, J. Opt. 23 (2021) 123001.
[61] M. Parto, Y.G.N. Liu, B. Bahari, M. Khajavikhan, D.N. Christodoulides, Non-Hermitian and topological photonics: optics at an exceptional point, Nanophotonics 10 (2021) 403–423.
[62] A.A. Mailybaev, O.N. Kirillov, A.P. Seyranian, Geometric phase around exceptional points, Phys. Rev. A 72 (2005) 014104.
[63] C. Dembowski, H.-D. Gräf, H.L. Harney, A. Heine, W.D. Heiss, H. Rehfeld, A. Richter, Experimental observation of the topological structure of exceptional points, Phys. Rev. Lett. 86 (2001) 787–790.
[64] S.-B. Lee, J. Yang, S. Moon, S.-Y. Lee, J.-B. Shim, S.W. Kim, J.-H. Lee, K. An, Observation of an exceptional point in a chaotic optical microcavity, Phys. Rev. Lett. 103 (2009) 134101.
[65] T. Gao, E. Estrecho, K.Y. Bliokh, T.C.H. Liew, M.D. Fraser, S. Brodbeck, M. Kamp, C. Schneider, S. Höfling, Y. Yamamoto, F. Nori, Y.S. Kivshar, A.G. Truscott, R.G. Dall, E.A. Ostrovskaya, Observation of non-Hermitian degeneracies in a chaotic exciton-polariton billiard, Nature 526 (2015) 554–558.

[66] R. Uzdin, A. Mailybaev, N. Moiseyev, On the observability and asymmetry of adiabatic state flips generated by exceptional points, J. Phys. A 44 (2011) 435302.
[67] T.J. Milburn, J. Doppler, C.A. Holmes, S. Portolan, S. Rotter, P. Rabl, General description of quasiadiabatic dynamical phenomena near exceptional points, Phys. Rev. A 92 (2015) 052124.
[68] J. Doppler, A.A. Mailybaev, J. Böhm, U. Kuhl, A. Girschik, F. Libisch, T.J. Milburn, P. Rabl, N. Moiseyev, S. Rotter, Dynamically encircling an exceptional point for asymmetric mode switching, Nature 537 (2016) 76–79.
[69] J.W. Yoon, Y. Choi, C. Hahn, G. Kim, S.H. Song, K.-Y. Yang, J.Y. Lee, Y. Kim, C.S. Lee, J.K. Shin, H.-S. Lee, P. Berini, Time-asymmetric loop around an exceptional point over the full optical communications band, Nature 562 (2018) 86–90.
[70] Q. Liu, S. Li, B. Wang, S. Ke, C. Qin, K. Wang, W. Liu, D. Gao, P. Berini, P. Lu, Efficient mode transfer on a compact silicon chip by encircling moving exceptional points, Phys. Rev. Lett. 124 (2020) 153903.
[71] A.U. Hassan, G.L. Galmiche, G. Harari, P. LiKamWa, M. Khajavikhan, M. Segev, D.N. Christodoulides, Chiral state conversion without encircling an exceptional point, Phys. Rev. A 96 (2017) 052129.
[72] H. Nasari, G. Lopez-Galmiche, H.E. Lopez-Aviles, A. Schumer, A.U. Hassan, Q. Zhong, S. Rotter, P. LiKamWa, D.N. Christodoulides, M. Khajavikhan, Chiral state conversion without encircling an exceptional point, Nature 605 (2022) 256–261.
[73] Q. Zhong, M. Khajavikhan, D.N. Christodoulides, R. El-Ganainy, Winding around non-Hermitian singularities, Nat. Commun. 9 (2018) 4808.
[74] F. Yu, X.-L. Zhang, Z.-N. Tian, Q.-D. Chen, H.-B. Sun, General rules governing the dynamical encircling of an arbitrary number of exceptional points, Phys. Rev. Lett. 127 (2021) 253901.
[75] X.-L. Zhang, S. Wang, B. Hou, C.T. Chan, Dynamically encircling exceptional points: in situ control of encircling loops and the role of the starting point, Phys. Rev. X 8 (2018) 021066.
[76] X.-L. Zhang, T. Jiang, C.T. Chan, Dynamically encircling an exceptional point in anti-parity-time symmetric systems: asymmetric mode switching for symmetry-broken modes, Light: Sci. Appl. 8 (2019) 88.
[77] A.U. Hassan, B. Zneh, M. Soljačić, M. Khajavikhan, D.N. Christodoulides, Dynamically encircling exceptional points: exact evolution and polarization state conversion, Phys. Rev. Lett. 118 (2017) 093002.
[78] Y. Wei, H. Zhou, Y. Chen, Y. Ding, J. Dong, X. Zhang, Anti-parity-time symmetry enabled on-chip chiral polarizer, Photon. Res. 10 (2022) 76–83.
[79] A. Pick, B. Zhen, O.D. Miller, C.W. Hsu, F. Hernandez, A.W. Rodriguez, M. Soljačić, S.G. Johnson, General theory of spontaneous emission near exceptional points, Opt. Express 25 (2017) 12325–12348.
[80] Y. Wu, P. Zhou, T. Li, W. Wan, Y. Zou, High-order exceptional point based optical sensor, Opt. Express 29 (2021) 6080–6091.
[81] V. Lidskii, Perturbation theory of non-conjugate operators, USSR Comput. Math. Math. Phys. 6 (1966) 73–85.
[82] J. Moro, J.V. Burke, M.L. Overton, On the Lidskii-Vishnik-Lyusternik perturbation theory for eigenvalues of matrices with arbitrary Jordan structure, SIAM J. Matrix Anal. Appl. 18 (1997) 793–817.
[83] Y. Ma, A. Edelman, Nongeneric eigenvalue perturbations of Jordan blocks, Linear Algebra Appl. 273 (1998) 45–63.
[84] J. Wiersig, Enhancing the sensitivity of frequency and energy splitting detection by using exceptional points: application to microcavity sensors for single-particle detection, Phys. Rev. Lett. 112 (2014) 203901.

[85] J. Wiersig, Sensors operating at exceptional points: general theory, Phys. Rev. A 93 (2016) 033809.
[86] W. Chen, Ş.K. Özdemir, G. Zhao, J. Wiersig, L. Yang, Exceptional points enhance sensing in an optical microcavity, Nature 548 (2017) 192–196.
[87] H. Hodaei, A.U. Hassan, S. Wittek, H. Garcia-Gracia, R. El-Ganainy, D.N. Christodoulides, M. Khajavikhan, Enhanced sensitivity at higher-order exceptional points, Nature 548 (2017) 187–191.
[88] J.M.P. Nair, D. Mukhopadhyay, G.S. Agarwal, Enhanced sensing of weak anharmonicities through coherences in dissipatively coupled anti-PT symmetric systems, Phys. Rev. Lett. 126 (2021) 180401.
[89] Y.-H. Lai, Y.-K. Lu, M.-G. Suh, Z. Yuan, K. Vahala, Observation of the exceptional-point-enhanced Sagnac effect, Nature 576 (2019) 65–69.
[90] M.P. Hokmabadi, A. Schumer, D.N. Christodoulides, M. Khajavikhan, Non-Hermitian ring laser gyroscopes with enhanced Sagnac sensitivity, Nature 576 (2019) 70–74.
[91] M. De Carlo, F. De Leonardis, L. Lamberti, V.M.N. Passaro, High-sensitivity real-splitting anti-$\mathcal{PT}$-symmetric microscale optical gyroscope, Opt. Lett. 44 (2019) 3956–3959.
[92] H. Qin, Y. Yin, M. Ding, Sensing and induced transparency with a synthetic anti-$\mathcal{PT}$ symmetric optical resonator, ACS Omega 6 (2021) 5463–5470.
[93] X. Li, M. Goryachev, Y. Ma, M. Tobar, C. Zhao, R.X. Adhikari, Y. Chen, Broadband sensitivity improvement via coherent quantum feedback with $\mathcal{PT}$-symmetry, Proc. SPIE 11700 (2021) 117002H.
[94] Y. Chen, M. Jiang, Y. Ma, J. Shu, Y. Yang, Axion haloscope array with $\mathcal{PT}$ symmetry, Phys. Rev. Res. 4 (2022) 023015.
[95] J. Wiersig, Review of exceptional point-based sensors, Photon. Res. 8 (2020) 1457–1467.
[96] R. Duggan, S.A. Mann, A. Alù, Limitations of sensing at an exceptional point, ACS Photonics 9 (5) (2022) 1554–1566, https://doi.org/10.1021/acsphotonics.1c01535.
[97] F.J. Garcia-Vidal, C. Ciuti, T.W. Ebbesen, Manipulating matter by strong coupling to vacuum fields, Science 373 (2021) eabd0336.
[98] D.G. Baranov, M. Wersäll, J. Cuadra, T.J. Antosiewicz, T. Shegai, Novel nanostructures and materials for strong light–matter interactions, ACS Photonics 5 (2018) 24–42.
[99] J.B. Khurgin, Exceptional points in polaritonic cavities and subthreshold Fabry–Perot lasers, Optica 7 (2020) 1015–1023.
[100] S.H. Park, S. Xia, S.-H. Oh, P. Avouris, T. Low, Accessing the exceptional points in a graphene plasmon–vibrational mode coupled system, ACS Photonics 8 (2021) 3241–3248.
[101] H.G. Song, M. Choi, K.Y. Woo, C.H. Park, Y.-H. Cho, Room-temperature polaritonic non-Hermitian system with single microcavity, Nat. Photonics 15 (2021) 582–587.
[102] Y. Sang, C.-Y. Wang, S.S. Raja, C.-W. Cheng, C.-T. Huang, C.-A. Chen, X.-Q. Zhang, H. Ahn, C.-K. Shih, Y.-H. Lee, J. Shi, S. Gwo, Tuning of two-dimensional plasmon–exciton coupling in full parameter space: a polaritonic non-Hermitian system, Nano Lett. 21 (2021) 2596–2602.
[103] G.-Q. Zhang, Z. Chen, D. Xu, N. Shammah, M. Liao, T.-F. Li, L. Tong, S.-Y. Zhu, F. Nori, J.Q. You, Exceptional point and cross-relaxation effect in a hybrid quantum system, PRX Quantum 2 (2021) 020307.
[104] B. Zhen, C.W. Hsu, Y. Igarashi, L. Lu, I. Kaminer, A. Pick, S.-L. Chua, J.D. Joannopoulos, M. Soljačić, Spawning rings of exceptional points out of Dirac cones, Nature 525 (2015) 354–358.

[105] Q. Zhong, J. Ren, M. Khajavikhan, D.N. Christodoulides, Ş.K. Özdemir, R. El-Ganainy, Sensing with exceptional surfaces in order to combine sensitivity with robustness, Phys. Rev. Lett. 122 (2019) 153902.
[106] G.-Q. Qin, R.-R. Xie, H. Zhang, Y.-Q. Hu, M. Wang, G.-Q. Li, H. Xu, F. Lei, D. Ruan, G.-L. Long, Experimental realization of sensitivity enhancement and suppression with exceptional surfaces, Laser Photonics Rev. 15 (2021) 2000569.

9

Rational design of maximum chiral dielectric metasurfaces

Maxim V. Gorkunov and Alexander A. Antonov
Shubnikov Institute of Crystallography, FSRC "Crystallography and Photonics", Russian Academy of Sciences, Moscow, Russia

9.1 Introduction

Chirality, as non-identity to mirror image, is attributed to objects of omnifarious sizes and natures, from particles and molecules to all known life forms. Qualitative differences between the left and right variants of such an object seem obvious. However, an attempt to characterize them by a quantitative chiral measure can easily lead to confusion and ambiguity [1]. Much more productive is a utilitarian approach, when the chirality is evaluated based on specific properties of an object that are manifested in its interaction with other chiral entities.

Peculiar chiral light-matter interactions attracted prominent researchers of the 19th century [2,3] long before the concept of chirality itself was rigorously introduced by Lord Kelvin [4]. As we know now, light can be shaped in numerous chiral states, all of which can eventually probe the chirality of matter. The first known and primary are the circularly polarized plane waves. When they encounter chiral, optically isotropic media, such waves with opposite handedness are differently refracted and absorbed, giving rise to the two fundamental chiral optical phenomena: optical rotation (OR) and circular dichroism (CD), correspondingly. The effects produced by natural molecular-scale chirality are very subtle and require light to travel long paths. Nevertheless, the convenience and precision of light-based instruments motivate their ongoing improvement for the chirality detection, which is essential in very diverse fields from drug design to extraterrestrial life search [5].

Pioneering works on artificial chiral electromagnetic materials date back to the turn of the 20th century [6,7], and their main goal was to understand and reproduce the chiral light-matter interactions in scaled-up experiments conducted in microwave and

All-Dielectric Nanophotonics. https://doi.org/10.1016/B978-0-32-395195-1.00014-4
Copyright © 2024 Elsevier Ltd. All rights reserved.

radio ranges. Now, a century later, with the advent of metamaterials and metasurfaces [8], much broader ambitions and numerous concrete practical motives are driving the ongoing surge in research on artificial chiral optical nanostructures [9,10]. They can efficiently perform versatile chiral light processing, beam shaping, and detection required for the emerging technologies of chiral quantum informatics [11,12], optical telecommunications [13], biomedical enantioselective optical microscopy [14], as well for probing natural chirality at the nanoscale [15].

Chiral metasurfaces – subwavelength arrays of complex-shaped elements (meta-atoms) – are capable of very different, arbitrarily strong chiral light transformations within the distances smaller and even much smaller than the wavelength. The palette of available chiral effects and their strength greatly exceed those of natural materials even in conventional transmission-reflection experiments: while some chiral metasurfaces exhibit extremely strong OR and CD by transmitting waves of one circular polarization and absorbing those of the opposite polarization, others reflect waves of the blocked polarization, while still others invert the circular polarization of transmitted light. The type and extent of such discrimination between different circular polarizations is determined by the meta-atom material, shape, and the symmetry of packing into a metasurface.

Following general trends in the metamaterial research, first, various metallic metastructures were explored for gigantic electromagnetic chirality in the microwave [16–19] and then in the infrared [20,21] and visible [22–24] ranges. Disadvantages associated with strong optical absorption in metals were quickly identified. For example, although arrays of chiral silver holes resonantly block one circular polarization and deliver OR and CD spanning between the most extreme possible maximum/minimum values, the transmittance of the opposite circular polarization is also suppressed to several percent [23,25]. Losing the most part of incident light to absorption limits the potential practical value of such photonic components.

Transition to all-dielectric metasurfaces built from highly refracting transparent materials (not necessarily dielectric in the strict sense) has opened bright prospects for flexible engineering of flat optical elements with numerous electromagnetic functionalities [26,27]. As, in parallel, the corresponding precise nanofabrication techniques have become broadly available, the first commercial consumer devices are expected to enter the market soon [28]. The field of chiral metasurfaces has greatly benefited from such progress and many practically important chiral light trans-

formations have been proposed and realized within several years [29–54].

The rational approach to design has been the great strength of the metamaterial/metasurface concept since its inception. One can literally tailor the electromagnetic properties by choosing the appropriate type of metastructure and adjusting all its design parameters. For the recent chiral dielectric metasurfaces, the common design method includes selecting the structure of appropriate symmetry and then subjecting all its parameters to elaborate numerical optimization. The type of symmetry breaking, implicated at the beginning, is critical to the final chiral performance and, as a rule, is chosen precisely according to the clear guidelines based on the fundamental principles of symmetry, reciprocity, and causality [55,56]. The success of the latter numerical optimization stage is more vague, as one typically tunes the parameters until reaching a certain local optimum. Global capabilities of a particular metasurface type remain unspecified, and one can always suspect that a better performance is feasible upon somewhat different preconditions.

In this context, ultimate goals for the chiral metasurface design are set by the unique upper limit termed *maximum chirality* [57], implying that a maximum chiral metasurface remains fully transparent to the waves of one circular polarization and totally blocks those of the opposite circular polarization. It is unlikely that such exceptional performance can be eventually achieved in the course of multiparametric numerical optimization of an arbitrary metasurface. Instead, specific recipes are required that precisely indicate the direction to the maximum chirality. Such recipes have been recently formulated [44,45] in terms of the phenomenological coupled mode theory (CMT), which allows one to express observable optical chirality parameters through the properties of metasurface eigenstates and, especially, through their coupling with circularly polarized plane waves. Knowing the desired eigenstate properties, one can search for particular meta-atoms hosting such eigenstates and only at this last stage perform a few numerical optimization steps to adjust the metasurface exactly to the maximum chiral regime.

As we show in this chapter, this strategy can be successfully applied to chiral metasurfaces of different types, and, upon proper eigenstate engineering, they become maximum chiral. For an illustration of the potential approach extension, we also apply it to formally achiral planar metasurfaces and clarify the origin of their performance as helicity-preserving chiral mirrors that are ultimately selective with respect to circularly polarized light.

We restrict ourselves to non-diffracting metasurfaces operating in linear-optical regime, leaving the analysis of more sophisticated diffractive and non-linear maximum chiral light transformations to future works. Also, we consider metasurfaces operating with normally incident and outgoing light waves, excluding the effects of extrinsic chirality [18], occurring for light obliquely incident from specific directions onto achiral metasurfaces. Note that one can maximize the extrinsic chirality of almost arbitrary metasurface by simply choosing an appropriate direction of light incidence [58].

In the next section, we introduce the general theoretical background, starting in Section 9.2.1 with categorizing different types of chiral metasurfaces according to their point symmetry. We pay our special attention to the possibilities of ultimately selective interaction with circularly polarized waves. To reveal specific routes towards practical realization, in Section 9.2.2 we develop a general CMT of chiral metasurface-light interactions, which is then further applied to metasurfaces of different types. As discussed in Section 9.3, the chirality in its strict geometrical sense is not ultimately required for a metasurface to perform chiral light transformations. Even though the considered chiral mirrors possess symmetry planes, they can selectively reflect and transmit circularly polarized light, provided that their eigenstates are precisely oriented and spectrally adjusted. Truly chiral rotationally symmetric metasurfaces, as accounted in Section 9.4, achieve the maximum chirality of absorptive type analogous to isotropic natural chiral media when their degenerate eigenstates are adjusted to the chiral quasi-bounded state in the continuum (quasi-BIC) regime. Metasurfaces, which completely lack point symmetries, are much less restricted and usually perform all possible polarization transformations with moderate efficiency. However, as we show in Section 9.5, engineering a non-degenerate eigenstate to the chiral quasi-BIC regime drastically simplifies the optical properties: the metasurface becomes a lossless maximum chiral filter, which fully reflects one circular polarization and fully transmits its counterpart. Finally, in Section 9.6 we summarize the main conclusions and discuss future trends and prospective applications.

9.2 Theoretical background

9.2.1 Limits of chirality imposed by symmetry

Consider the most general linear interaction of a subwavelength periodic metasurface with normally incident circularly polarized light, shown schematically in Fig. 9.1(a). The complex unit

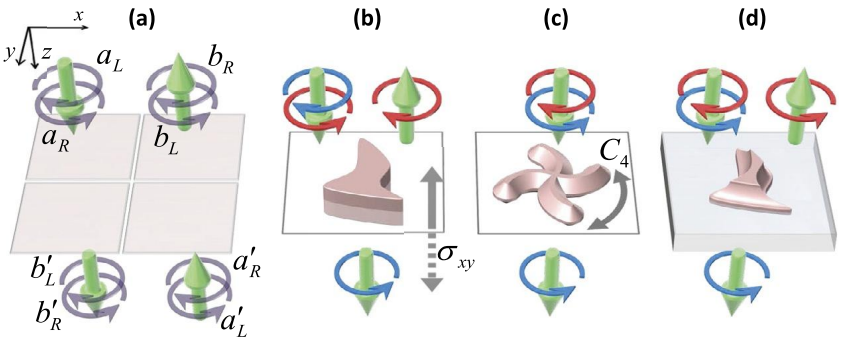

Figure 9.1. Interaction of metasurfaces of different point symmetry with normally incident circularly polarized light: (a) general transmission-reflection problem described by S-matrix equation (9.2); (b) planar metasurface possessing σ_{xy} symmetry plane and operating as chiral mirror; (c) maximum chiral absorber based on rotationally symmetric metasurface; (d) lossless maximum chiral filter based on metasurface without point symmetry elements.

vectors of circular polarizations are expressed by the Cartesian unit vectors as:

$$\mathbf{e}_{\pm} = \frac{1}{\sqrt{2}}(\mathbf{e}_x \pm i\mathbf{e}_y), \tag{9.1}$$

and for waves propagating in the positive z direction, $\mathbf{e}_+$ and $\mathbf{e}_-$ correspond to the left circularly polarized (LCP) and right circularly polarized (RCP) waves, respectively. For the negative z direction, the opposite is true.

Mathematically, the most general description of such a transmission-reflection problem is formulated in terms of an S-matrix equation:

$$\mathbf{b} = \mathbf{S} \cdot \mathbf{a}, \tag{9.2}$$

relating the vectors composed of the amplitudes of all incident and outgoing circularly polarized waves:

$$\mathbf{a} = \begin{bmatrix} a_R \\ a_L \\ a'_R \\ a'_L \end{bmatrix}, \ \mathbf{b} = \begin{bmatrix} b_R \\ b_L \\ b'_R \\ b'_L \end{bmatrix}, \tag{9.3}$$

with the primes distinguishing waves on the back metasurface side.

The corresponding S-matrix consists of the coefficients r and t of polarized reflections and transmissions respectively:

$$\mathbf{S} = \begin{bmatrix} r_{RR} & r_{RL} & t'_{RR} & t'_{RL} \\ r_{LR} & r_{LL} & t'_{LR} & t'_{LL} \\ t_{RR} & t_{RL} & r'_{RR} & r'_{RL} \\ t_{LR} & t_{LL} & r'_{LR} & r'_{LL} \end{bmatrix} \tag{9.4}$$

where the indices indicate the final and initial polarization states, and the primes denote scattering of light incident on the back metasurface side. For the vast majority of optical metasurfaces consisting of electromagnetically reciprocal materials, the Lorentz theorem implies that certain coefficients are equal:

$$r_{RL} = r_{LR},\ r'_{RL} = r'_{LR},\ t_{RR} = t'_{RR},\ t_{LL} = t'_{LL},\ t_{RL} = t'_{LR},\ t_{LR} = t'_{RL}, \tag{9.5}$$

which makes the S-matrix symmetric in this notation.

Naturally, the $R \leftrightarrow L$ asymmetry of the remaining 10 independent S-matrix elements can be used to quantify the metasurface optical chirality. Although a formal measure accounting for the asymmetry of all reflection and transmission processes can be generally formulated [59], its evaluation requires simultaneous knowledge of all S-matrix elements. Much more practical are simpler quantities depending on a few transmission characteristics obtained when a metasurface is exposed to LCP and RCP waves incident on its particular side. Thus, one can consider the CD, defined by the co-polarized transmissions, as:

$$CD = \frac{|t_{RR}|^2 - |t_{LL}|^2}{|t_{RR}|^2 + |t_{LL}|^2}, \tag{9.6}$$

i.e., similar to the CD characterizing chiral light absorption asymmetry of a natural isotropic media. Note that it is independent of the side of incidence due to Lorentz reciprocity, see Eq. (9.5).

Depending on their symmetry, metasurfaces are capable of circular polarization conversion in transmission. Therefore, evaluating a simpler version accounting for the total transmission upon LCP or RCP illumination, regardless of the outgoing wave polarization, provides a different CD:

$$\overline{CD} = \frac{|t_{RR}|^2 + |t_{LR}|^2 - |t_{LL}|^2 - |t_{RL}|^2}{|t_{RR}|^2 + |t_{LR}|^2 + |t_{LL}|^2 + |t_{RL}|^2}, \tag{9.7}$$

which is not necessarily equal for different sides of incidence. In certain cases, when the transmission is dominated by circular polarization conversion, the so-called circular conversion dichroism

(CCD) [19], defined as:

$$CCD = \frac{|t_{LR}|^2 - |t_{RL}|^2}{|t_{LR}|^2 + |t_{RL}|^2}, \tag{9.8}$$

can be remarkably strong. Reciprocity Eq. (9.5) requires this quantity to invert its sign when the side of incidence is flipped.

To explicitly characterize metasurfaces approaching the maximum chirality, it is more appropriate to consider transmittance differences [60]. Thus, instead of the CD (9.6), one evaluates:

$$\Delta T = |t_{RR}|^2 - |t_{LL}|^2, \tag{9.9}$$

to specifically characterize the proximity to maximum chirality: while the CD tends to ± 1 as the waves of a certain circular polarization are fully blocked, the difference ΔT approaches ± 1 only if, additionally, the waves of the opposite polarization are fully transmitted. Similarly, instead of the CCD (9.8), the conversion transmittance difference:

$$\Delta CT = |t_{LR}|^2 - |t_{RL}|^2, \tag{9.10}$$

characterizes the situation more precisely when a metasurface blocks one circular polarization and transmits the opposite, flipping its handedness.

Many useful S-matrix properties, which clarify the limits of optical chirality, can be derived if a metasurface possesses certain point symmetry elements. Thus, if it has an *out-of-plane mirror symmetry* (a vertical mirror plane parallel to the z-axis in Fig. 9.1), all the coefficients have to be invariant with respect to the $R \leftrightarrow L$ interchange. This, obviously, eliminates the optical chirality defined by the selectivity with respect to circular polarizations.

Notably, an *in-plane mirror symmetry* (a horizontal mirror plane parallel to the xy-plane in Fig. 9.1) though makes a metasurface geometrically achiral, leaves a possibility for optical chirality. Indeed, a mirror reflection from such a plane produces simultaneous $R \leftrightarrow L$ interchange supplemented by a metasurface side interchange. Combined with Eqs. (9.5), this implies the identities:

$$\begin{aligned} &r_{RL} = r_{LR} = r'_{LR} = r'_{RL},\ r_{RR} = r'_{LL},\ r_{LL} = r'_{RR}, \\ &t_{RR} = t_{LL} = t'_{LL} = t'_{RR}, \end{aligned} \tag{9.11}$$

which eliminate the conventional CD (9.6) and ΔT (9.9). At the same time, the CCD (9.8) can remain strong if ΔCT (9.10) is allowed to approach the limiting ± 1 values.

Therefore, although it is impossible for such a metasurface to attain the true maximum of chirality, it can maximum selectively

interact with circularly polarized light in the regime termed as chiral mirror [61]. Such ideal performance is shown in Fig. 9.1(b) and is characterized by $\Delta CT = -1$ due to a specific set of the S-matrix elements, all of which become zero apart from:

$$|r_{RR}| = |r'_{LL}| = |t_{RL}| = |t'_{LR}| = 1. \tag{9.12}$$

If a metasurface possesses a *rotational symmetry axis* $C_{\mathcal{N}}$, the S-matrix equation (9.2) should be invariant upon rotation of the coordinate frame by an angle $\phi = 2\pi/\mathcal{N}$ about the z-axis. Such rotation shifts complex phases of the unit vectors (9.1), transforming them into $\tilde{\mathbf{e}}_{\pm} = \mathbf{e}_{\pm}e^{\mp i\phi}$. Accordingly, the wave amplitudes (9.3) in the rotated coordinate frame are expressed as:

$$\tilde{\mathbf{a}} = \begin{bmatrix} a_R e^{-i\phi} \\ a_L e^{i\phi} \\ a'_R e^{i\phi} \\ a'_L e^{-i\phi} \end{bmatrix}, \quad \tilde{\mathbf{b}} = \begin{bmatrix} b_R e^{i\phi} \\ b_L e^{-i\phi} \\ b'_R e^{-i\phi} \\ b'_L e^{i\phi} \end{bmatrix}, \tag{9.13}$$

and obey the same S-matrix equation (9.2) with:

$$\tilde{\mathbf{S}} = \begin{bmatrix} r_{RR}e^{-2i\phi} & r_{RL} & t'_{RR} & t'_{RL}e^{-2i\phi} \\ r_{LR} & r_{LL}e^{2i\phi} & t'_{LR}e^{2i\phi} & t'_{LL} \\ t_{RR} & t_{RL}e^{2i\phi} & r'_{RR}e^{2i\phi} & r'_{RL} \\ t_{LR}e^{-2i\phi} & t_{LL} & r'_{LR} & r'_{LL}e^{-2i\phi} \end{bmatrix}. \tag{9.14}$$

The requirement of identity of the S-matrices in both frames clearly separates two cases: first-order (trivial) or second-order C_2 rotational symmetry with $\phi = \pi$ imposing no additional restrictions on $\mathbf{S}$; and rotational symmetry with $\mathcal{N} \geq 3$ explicitly implying that:

$$r_{RR} = r'_{RR} = r_{LL} = r'_{LL} = t_{RL} = t_{RL} = t'_{RL} = t'_{RL} = 0. \tag{9.15}$$

Note that the latter conclusion represents a particular example of the general crystallographic Hermann's theorem [62]: a rotationally symmetric metasurface with $\mathcal{N} \geq 3$ performs identically to a slab of isotropic chiral material. Combined with the reciprocity implications for reflections from Eqs. (9.5), the conditions (9.15) determine that the reflection by such metasurface is polarization independent. Accordingly, the CD (9.6) may occur here only due to different absorption of LCP and RCP waves, and the maximum chirality with, for instance, $\Delta T = 1$ is established when the metasurface performs as a maximum chiral absorber, as depicted in

Fig. 9.1(c), which is characterized by zero values of all S-matrix elements except for:

$$|t_{RR}| = |t'_{RR}| = 1. \tag{9.16}$$

From a practical point of view, dissipation of blocked circular polarization is not always of advantage. The lossless maximum chiral regime sketched in Fig. 9.1(d) is characterized by the nonzero S-matrix elements:

$$|t_{RR}| = |t'_{RR}| = |r_{LL}| = |r'_{LL}| = 1. \tag{9.17}$$

As follows from the above analysis, it is incompatible with the considered point symmetry elements. However, as we show in Section 9.5, a specific phenomenological approach can be used to design a metasurface without point symmetry elements, performing as a maximum chiral filter.

9.2.2 Chiral CMT phenomenology

As the optical response of most metasurfaces is determined by sets of resonances arising due to excitation of specific eigenstates, CMT has been widely used for the phenomenological description since the pioneering work by S. Fan et al. [63]. One can derive its basic relations by adapting the Fano–Feshbach partitioning scheme for Maxwell's equations, as described in Section 6.2.1 of Chapter 6.

When applying CMT to a particular metasurface, one begins by postulating a number and type of relevant eigenstates, keeping in mind that their eigenfrequencies, quality factors, spatial symmetry, and eventual degeneracy are of key importance [64]. Notably, the particular nature of the eigenstates can be arbitrary: plasmonic, guided mode or Mie-type resonances inherent to metasurfaces of absolutely different types can all be treated within the same theoretical formalism. Recently, CMT modifications describing chiral optical properties of metasurfaces of various point symmetry have been developed [25,44,45,52].

In this subsection, we summarize the CMT basis, which will later be applied to describe optically chiral metasurfaces. Within a CMT, one eventually chooses a number N of relevant eigenstates, each of them having a slow-varying complex amplitude p_n, $n = 1, \ldots, N$. Introducing a vector of the amplitudes $\mathbf{p} = [p_1, ..., p_N]^T$ one describes its time evolution as an oscillator-like behavior driven by the incident waves represented by the vector of amplitudes $\mathbf{a}$ same as in Eq. (9.3):

$$\frac{d\mathbf{p}}{dt} = (i\boldsymbol{\Omega} - \boldsymbol{\Gamma}) \cdot \mathbf{p} + \mathbf{M}^T \cdot \mathbf{a}. \tag{9.18}$$

Here the $4 \times N$ matrix $\mathbf{M}$ consists of coupling parameters of a particular eigenstate (subscript $n = 1, \ldots, N$) to the light of a particular circular polarization (subscripts R or L) incident on a particular metasurface side (the back one indicated by the prime):

$$\mathbf{M} = \begin{bmatrix} m_{1R} & \ldots & m_{NR} \\ m_{1L} & \ldots & m_{NL} \\ m'_{1R} & \ldots & m'_{NR} \\ m'_{1L} & \ldots & m'_{NL} \end{bmatrix}. \tag{9.19}$$

The coupling parameters can be expressed by the integrals over the structure volume [44,65]:

$$m_{n\ R,L} \propto \int_V dV\ \left(\mathbf{J}_n(\mathbf{r}) \cdot \mathbf{e}_{\mp}\right)\ e^{ikz}, \tag{9.20}$$

$$m'_{n\ R,L} \propto \int_V dV\ \left(\mathbf{J}_n(\mathbf{r}) \cdot \mathbf{e}_{\pm}\right)\ e^{-ikz}, \tag{9.21}$$

where $\mathbf{J}_n(\mathbf{r})$ is the displacement current density of an nth eigenstate, k is the free-space wavenumber $k = \omega/c$, and where ω is the frequency of incident light waves.

The main diagonals of the matrices $\mathbf{\Omega}$ and $\mathbf{\Gamma}$ contain the detuning of the complex eigenstate eigenfrequencies from the external excitation frequency ω. Generally, non-diagonal elements of $\mathbf{\Omega}$ and $\mathbf{\Gamma}$ can be introduced to account for the internal coupling between eigenstates of compatible symmetry [66]. Throughout this chapter, we consider combinations of non-interacting eigenstates and, therefore, assume that:

$$\mathbf{\Omega} = \begin{bmatrix} \omega - \omega_1 & & \\ & \ddots & \\ & & \omega - \omega_N \end{bmatrix}, \ \mathbf{\Gamma} = \begin{bmatrix} \gamma_1 & & \\ & \ddots & \\ & & \gamma_N \end{bmatrix}. \tag{9.22}$$

Emission of waves by a metasurface is described as a multichannel process by a linear algebraic equation:

$$\mathbf{b} = \mathbf{M} \cdot \mathbf{p} + \mathbf{C} \cdot \mathbf{a}, \tag{9.23}$$

where the vector of outgoing wave amplitudes $\mathbf{b}$ is the same as in Eq. (9.3). The former term accounts for the contributions of all eigenstates, while the latter term describes a background nonresonant scattering pathway. To ensure the reciprocity, the matrix of coupling parameters $\mathbf{M}$ here is the same as in Eq. (9.18), while the background matrix $\mathbf{C}$ is symmetric.

In a steady state, all time derivatives in Eq. (9.18) are zero and it becomes algebraic. Solving it together with Eq. (9.23) one can

exclude the amplitudes $\mathbf{p}$ and obtain the S-matrix as:

$$\mathbf{S} = \mathbf{C} - \mathbf{M} \cdot [i\boldsymbol{\Omega} - \boldsymbol{\Gamma}]^{-1} \cdot \mathbf{M}^T. \tag{9.24}$$

Although the role of electromagnetic energy loss to dissipation in the metasurface material is not always negligible, one can take it into account iteratively. Assuming that the dissipation does not substantially affect the internal eigenstate structure and the coupling parameters (9.20) and (9.21), one can first neglect it and derive very useful general relations between the phenomenological parameters requiring that the CMT equations are invariant with respect to the time reversal and the total electromagnetic energy is conserved. In such approximation, the corresponding decay rates are purely radiative, $\gamma_n = \gamma_n^{\text{rad}}$, as the eigenstates lose their energy only by emitting the outgoing waves. In the next step, one takes the dissipation into account by including its contribution to the eigenstate decay as $\gamma_n = \gamma_n^{\text{rad}} + \gamma_n^{\text{dis}}$.

Reversibility in the absence of dissipation determines energy conservation, which requires S-matrices to be unitary. Indeed, in the general S-matrix problem (9.4), the energy of incoming and outgoing light waves is constituted by the sums $|a_R|^2 + |a_L|^2 + |a'_R|^2 + |a'_L|^2$ and $|b_R|^2 + |b_L|^2 + |b'_R|^2 + |b'_L|^2$, correspondingly. With no energy lost, these sums, i.e., the magnitudes of vectors $\mathbf{a}$ and $\mathbf{b}$ should be equal for any combination of incident waves. This means that $\mathbf{S}$ acts as an isometric operator, $\mathbf{S}^\dagger\mathbf{S} = \mathbf{1}$, and its matrix is unitary. In particular, reversible background scattering is described by a unitary matrix $\mathbf{C}$, and, as it is symmetric, $\mathbf{C}^{-1} = \mathbf{C}^*$.

Further, if a set $\mathbf{a}$, $\mathbf{b}$, and $\mathbf{p}$ satisfies Eqs. (9.18) and (9.23), so should do their time-reversed counterparts $\tilde{\mathbf{a}}$, $\tilde{\mathbf{b}}$, and $\tilde{\mathbf{p}}$, expressed as:

$$\tilde{\mathbf{a}} = \mathbf{b}^*, \ \tilde{\mathbf{b}} = \mathbf{a}^*, \ \tilde{\mathbf{p}} = \mathbf{p}^*. \tag{9.25}$$

Substituting them into Eq. (9.23) yields upon complex conjugation:

$$\mathbf{a} = \mathbf{M}^* \cdot \mathbf{p} + \mathbf{C}^* \cdot \mathbf{b}, \tag{9.26}$$

and, as $\mathbf{C}^* = \mathbf{C}^{-1}$, one can write:

$$\mathbf{b} = -\mathbf{C} \cdot \mathbf{M}^* \cdot \mathbf{p} + \mathbf{C} \cdot \mathbf{a}. \tag{9.27}$$

By comparing this with Eq. (9.23), one obtains an important relation:

$$\mathbf{C} \cdot \mathbf{M}^* = -\mathbf{M}. \tag{9.28}$$

On the other hand, the set of time-reverse amplitudes (9.25) also should obey Eq. (9.18), with the sign of time derivative in-

verted. After a complex conjugation it reads:

$$-\frac{d\mathbf{p}}{dt} = (-i\boldsymbol{\Omega} - \boldsymbol{\Gamma}) \cdot \mathbf{p} + \mathbf{M}^{\dagger} \cdot \mathbf{b}. \tag{9.29}$$

By substituting here $\mathbf{b}$ from Eq. (9.23), one obtains:

$$\frac{d\mathbf{p}}{dt} = \left(i\boldsymbol{\Omega} + \boldsymbol{\Gamma} - \mathbf{M}^{\dagger}\mathbf{M}\right) \cdot \mathbf{p} - \mathbf{M}^{\dagger} \cdot \mathbf{C} \cdot \mathbf{a}. \tag{9.30}$$

As follows from Eq. (9.28), in the latter term the matrix product is $\mathbf{M}^{\dagger} \cdot \mathbf{C} = -\mathbf{M}^{T}$, and by comparing with Eq. (9.18), one concludes that:

$$2\boldsymbol{\Gamma} = \mathbf{M}^{\dagger} \cdot \mathbf{M}. \tag{9.31}$$

As in this approximation the decay rates are purely radiative, this equality determines that:

$$\gamma_n^{\mathrm{rad}} = \frac{1}{2}\left(|m_{nR}|^2 + |m_{nL}|^2 + |m'_{nR}|^2 + |m'_{nL}|^2\right), \tag{9.32}$$

and also that for the nth and lth eigenstates, the columns of their coupling parameters are orthogonal vectors:

$$m_{nR}m^{*}_{lR} + m_{nL}m^{*}_{lL} + m'_{nR}m'^{*}_{lR} + m'_{nL}m'^{*}_{lL} = 0. \tag{9.33}$$

Finally, let us consider the practically important case of isotropic background producing unpolarized scattering, when one can write:

$$\mathbf{C} = \begin{bmatrix} 0 & \rho & \tau & 0 \\ \rho & 0 & 0 & \tau \\ \tau & 0 & 0 & \rho \\ 0 & \tau & \rho & 0 \end{bmatrix}. \tag{9.34}$$

The unitarity, $\mathbf{C}^{-1} = \mathbf{C}^{\dagger}$, can be fulfilled only if:

$$|\rho|^2 + |\tau|^2 = 1, \tag{9.35}$$

and if the complex phases are constrained by:

$$\arg(\rho) = \arg(\tau) \pm \frac{\pi}{2}. \tag{9.36}$$

It is convenient to introduce two real parameters, the phase $\alpha \in [0, 2\pi]$, and the merit of background transparency $\beta \in [-\pi/2, \pi/2]$, and to explicitly express the background coefficients as:

$$\tau = e^{i\alpha}\cos\beta, \;\; \rho = ie^{i\alpha}\sin\beta. \tag{9.37}$$

To summarize, in terms of CMT, one can express the S-matrix, and, correspondingly, all reflection and transmission coefficients, by the model parameters according to the following matrix equation:

$$\begin{bmatrix} r_{RR} & r_{RL} & t'_{RR} & t'_{RL} \\ r_{LR} & r_{LL} & t'_{LR} & t'_{LL} \\ t_{RR} & t_{RL} & r'_{RR} & r'_{RL} \\ t_{LR} & t_{LL} & r'_{LR} & r'_{LL} \end{bmatrix} = \begin{bmatrix} 0 & \rho & \tau & 0 \\ \rho & 0 & 0 & \tau \\ \tau & 0 & 0 & \rho \\ 0 & \tau & \rho & 0 \end{bmatrix} - \sum_{n=1}^{N} \frac{1}{i(\omega-\omega_n)-\gamma_n} \begin{bmatrix} m_{nR}^2 & m_{nR}m_{nL} & m_{nR}m'_{nR} & m_{nR}m'_{nL} \\ m_{nL}m_{nR} & m_{nL}^2 & m_{nL}m'_{nR} & m_{nL}m'_{nL} \\ m'_{nR}m_{nR} & m'_{nR}m_{nL} & {m'_{nR}}^2 & m'_{nR}m'_{nL} \\ m'_{nL}m_{nR} & m'_{nL}m_{nL} & m'_{nL}m'_{nR} & {m'_{nL}}^2 \end{bmatrix}, \tag{9.38}$$

where γ_n generally includes dissipative and radiative parts, the latter determined by the coupling parameters as in Eq. (9.32); the background can be parameterized by Eqs. (9.37) and related to the coupling parameters by Eq. (9.28).

Deriving more specific S-matrix forms is possible for metasurfaces possessing particular symmetry elements. In the subsequent sections, we provide several examples illustrating how CMT can be applied to clarify the key properties of eigenstates required for a desired optical functionality and to design the corresponding metasurfaces.

9.3 Chiral mirrors

9.3.1 State of the art

The vast majority of modern nanofabrication techniques are based on cutting, etching, or milling of diverse nano-scale elements from layers (stacks of layers) of various materials. Therefore, planar arrays of dielectric elements with unbroken in-plane mirror symmetry constitute the most extensively studied class of metasurfaces. In the context of chiral light transformations, they can potentially perform as planar chiral mirrors that ideally fully reflect waves of one circular polarization preserving the helicity, and transmit those of the opposite polarization, flipping the helicity, see Eqs. (9.11) and Fig. 9.1(b).

As transmission experiments are more convenient, most of the works are focused on enhancing cross-polarized transmission [29,38,40,46–49]. Nevertheless, remarkably efficient helicity-preserving reflection has also been realized by Semnani et al. [39],

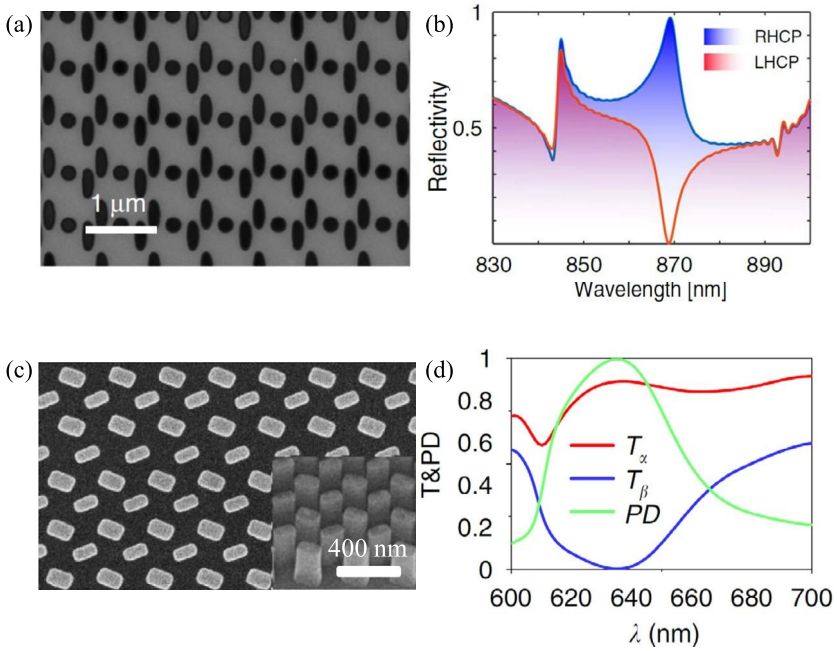

Figure 9.2. Dielectric metasurfaces performing as close-to-ideal chiral mirrors. (a) SEM-image of the chiral mirror based on perforated silicon nitride membrane and (b) its simulated co-polarized reflection spectra. *Adapted from [39] and re-used under the Creative Commons Attribution 4.0.* (c) SEM-image of the metasurface built of silicon nanopillars of two different types rotated by $\pi/4$ with respect to each other, and (d) the calculated power transmission spectra for the incident RCP (α) and LCP (β) light together with the polarization dichroism spectrum (PD defined identically to CCD). *Adapted from [50] and re-used under the Creative Commons Attribution 4.0.*

see Figs. 9.2(a) and 9.2(b). At the target wavelength of 870 nm, this metasurface operates as a helicity-preserving mirror for the RCP light. At the same wavelength, LCP waves are fully transmitted as RCP waves. The metasurface structure is based on silicon nitride membrane perforated by tripartite array of through holes having a C_{2h} point group symmetry. The chiral optical response is determined by a guided-mode resonance with simultaneous excitation of leaky transverse electric (TE-like) and transverse magnetic (TM-like) Bloch modes of the membrane, which is considered as a photonic crystal slab. The dimensions of the metasurface unit cell are precisely tuned to allow the leaky modes to be excited by normally incident waves at the target wavelength. The authors explain the chiral mirror performance by different irradiation of waves by electric and magnetic dipole moments associated with the TE and TM guided waves, correspondingly. Unfortunately, they do not provide quantitative information on the relative orientation of these dipole moments, although one can expect that

they are diverged by an angle close to $\pi/4$, as the reported reflection and transmission spectra are very similar to those suggested by the CMT phenomenology developed below in Section 9.3.3.

Recently, extensive research has been carried out on planar metasurfaces built of two different types of rotated dielectric birefringent nanopillars optimized for maximum selective cross-polarized transmission of RCP/LCP waves [29,32,35,38,41,50]. Essentially, the main idea of all designs is to combine in each unit cell two waveguide-like pillars producing different phase delays of transmitted waves polarized along their principal axes diverged by $\pi/4$ from each other. Straightforward Jones calculus provides a solution for the perfect circular polarization converter, which can be divided in two terms, physically realized by the two types of nanopillars. The desirable phase delays are set by the appropriate nanopillar dimensions, while their positions are chosen to minimize the near-field coupling.

Apart from the precise circular polarization filtering by metasurfaces with identical unit cells, the two-pillar design allows building versatile chiral refractive elements and holograms by applying gradual relative rotation to the pillars in adjacent cells. The functionality is based on shaping the cross-polarized transmission phase by the geometric Pancharatnam–Berry phase, determined by the relative unit cell orientation. Therefore, one can smoothly modulate the outgoing wave phase profile in an arbitrary manner and achieve precise polarization-determined refraction [35], focusing [46], vortex-beam formation, and holography [32,41]. Notably, deviating the diverging angle of the pillars from $\pi/4$, one can precisely locally suppress the outgoing light intensity thus enabling full control over both the phase and the amplitude of circularly polarized transmitted light [38]. Reciprocally, using the angles other than $\pi/4$ enables similar transformations of light of arbitrary ellipticity [35,38,41,50].

An exemplary planar metasurface built as a combination of two types of dielectric pillars, as studied in Ref. [50], is shown in Fig. 9.2(c). The silicon pillars are diverged by $\pi/4$ and their height and dimensions are optimized to provide near-unitary ΔCT at a 633 nm wavelength, see the transmission spectra in Fig. 9.2(d).

9.3.2 CMT of planar metasurface

Let us consider the application of CMT to a metasurface possessing an in-plane mirror symmetry plane, recently suggested in Ref. [52], with the aim of designing a chiral helicity-preserving mirror similar to the one studied in Ref. [39]. The mirror symmetry implies metasurface invariance with respect to the $z \leftrightarrow -z$

interchange. Correspondingly, the eigenstates can be categorized as even and odd: the x- and y-components of the current densities $\mathbf{J}_n(\mathbf{r})$ are either even or odd functions of z. Then, according to Eqs. (9.20) and (9.21), the coupling parameters of even states are related as:

$$m'_{\mathrm{e}R} = m_{\mathrm{e}L},\ m'_{\mathrm{e}L} = m_{\mathrm{e}R}, \tag{9.39}$$

while for the odd states:

$$m'_{\mathrm{o}R} = -m_{\mathrm{o}L},\ m'_{\mathrm{o}L} = -m_{\mathrm{o}R}, \tag{9.40}$$

and interactions of each eigenstate with the free-space light waves are described by only 2 independent parameters.

For an isotropic background, substituting Eq. (9.39) into Eq. (9.28) allows obtaining relations between the parameters of an even eigenstate:

$$m_{\mathrm{e}R} = -m^*_{\mathrm{e}L}(\tau+\rho),\ m_{\mathrm{e}L} = -m^*_{\mathrm{e}R}(\tau+\rho), \tag{9.41}$$

while for an odd one, similarly using Eq. (9.40) yields:

$$m_{\mathrm{o}R} = m^*_{\mathrm{o}L}(\tau-\rho),\ m_{\mathrm{o}L} = m^*_{\mathrm{o}R}(\tau-\rho). \tag{9.42}$$

Next, expressing ρ an τ by Eqs. (9.37), one further obtains that:

$$m_{\mathrm{e}L} = -m^*_{\mathrm{e}R}e^{i(\alpha+\beta)}, \tag{9.43}$$

$$m_{\mathrm{o}L} = m^*_{\mathrm{o}R}e^{i(\alpha-\beta)}, \tag{9.44}$$

which means, in particular, that all eigenstates are equally strongly coupled to the waves of both circular polarizations as $|m_{\mathrm{e,o}R}| = |m_{\mathrm{e,o}L}|$. According to Eq. (9.32), their absolute values determine the radiative decay rates:

$$\gamma^{\mathrm{rad}}_{\mathrm{e,o}} = 2|m_{\mathrm{e,o}R}|^2 = 2|m_{\mathrm{e,o}L}|^2. \tag{9.45}$$

To specify the complex phases of the coupling parameters, one can formally introduce angles $\theta_{\mathrm{e,o}}$ and explicitly express the coupling parameters as:

$$m_{\mathrm{e}R} = i\sqrt{\frac{\gamma^{\mathrm{rad}}_{\mathrm{e}}}{2}}e^{i\frac{\alpha+\beta}{2}-i\theta_{\mathrm{e}}},\ m_{\mathrm{e}L} = i\sqrt{\frac{\gamma^{\mathrm{rad}}_{\mathrm{e}}}{2}}e^{i\frac{\alpha+\beta}{2}+i\theta_{\mathrm{e}}}, \tag{9.46}$$

$$m_{\mathrm{o}R} = \sqrt{\frac{\gamma^{\mathrm{rad}}_{\mathrm{o}}}{2}}e^{i\frac{\alpha-\beta}{2}-i\theta_{\mathrm{o}}},\ m_{\mathrm{o}L} = \sqrt{\frac{\gamma^{\mathrm{rad}}_{\mathrm{o}}}{2}}e^{i\frac{\alpha-\beta}{2}+i\theta_{\mathrm{o}}}. \tag{9.47}$$

Notably, the angles $\theta_{\mathrm{e,o}}$ have clear physical meaning. To clarify it, we consider the definitions of the coupling parameters by the

eigenstate currents as in Eqs. (9.20) and (9.21). For an even eigenstate, they can be reduced to:

$$m_{eR,L} \propto \mathbf{e}_{\mp} \cdot \bar{\mathbf{J}}_e = \frac{1}{\sqrt{2}}(\bar{J}_{ex} \mp i\bar{J}_{ey}), \tag{9.48}$$

where the complex vector of the integrated current is defined as:

$$\bar{\mathbf{J}}_e = \int_{z>0} dV\ \mathbf{J}_e(\mathbf{r})\ \cos kz, \tag{9.49}$$

along with its x and y components, $\bar{J}_{ex}$ and $\bar{J}_{ey}$ respectively. Comparing with Eq. (9.46) reveals that these components are equal to:

$$\bar{J}_{ex} = ie^{i(\alpha+\beta)/2}|\bar{J}|\cos\theta_e,\ \ \bar{J}_{ey} = ie^{i(\alpha+\beta)/2}|\bar{J}|\sin\theta_e, \tag{9.50}$$

where $|\bar{J}_e|^2 = |\bar{J}_{ex}|^2 + |\bar{J}_{ey}|^2$. Accordingly, the angle θ_e describes the orientation of the vector of integrated current (9.49) in the xy-plane.

Considering in the same manner an odd eigenstate, one can show that the angle θ_o plays a similar role and describes the orientation of the vector of integrated current:

$$\bar{\mathbf{J}}_o = \int_{z>0} dV\ \mathbf{J}_o(\mathbf{r})\ \sin kz. \tag{9.51}$$

The physical meaning of these angles is most apparent for the electric-dipole and magnetic-dipole eigenstates. For the former, θ_e is the angle between the vector of dipole moment and the x-axis, while for the latter, the in-plane magnetic moment is aligned perpendicular to the direction characterized by θ_o.

9.3.3 Exemplary chiral mirror design

Although many useful relations linking different parameters of the CMT phenomenology can be drawn based on the metasurface symmetry, to derive a particular form of the S-matrix (9.24), one has to specify the number and parity of relevant eigenstates, as well as presume a certain background matrix **C**. Let us show how one can achieve the specific functionality of chiral mirror, which S-matrix has zero elements apart from those listed in Eq. (9.12).

In the simplest case of isotropic background described by Eq. (9.34), a single eigenstate of either parity is insufficient because it is equally strongly coupled to all circularly polarized waves on all sides with $|m_R| = |m_L| = |m'_R| = |m'_L|$. Then, for example, as co-polarized reflections are not performed by the isotropic background, suppressing r_{LL} is only possible by setting $m_L = 0$.

This, however sets to zero all coupling parameters and leads to a full isolation of the eigenstate from all free-space waves.

The next more complex arrangement involves a pair of eigenstates of different parity. By the symmetry, they can be independently excited and cannot intrinsically exchange the energy [64]. The corresponding CMT can be developed according to the general approach presented in Section 9.2.2 by considering two eigenstates with $n = \mathrm{e}, \mathrm{o}$. Accordingly, substituting the background matrix (9.34) together with the coupling parameters given by Eqs. (9.46) and (9.47) into Eq. (9.24), one obtains according to Eq. (9.38):

$$\begin{aligned} r_{RL} &= r_{LR} = r'_{RL} = r'_{LR} \\ &= ie^{i\alpha}\sin\beta + \frac{e^{i(\alpha+\beta)}}{2}\frac{\gamma_{\mathrm{e}}^{\mathrm{rad}}}{i(\omega-\omega_{\mathrm{e}})-\gamma_{\mathrm{e}}} - \frac{e^{i(\alpha-\beta)}}{2}\frac{\gamma_{\mathrm{o}}^{\mathrm{rad}}}{i(\omega-\omega_{\mathrm{o}})-\gamma_{\mathrm{o}}}, \end{aligned} \tag{9.52}$$

$$\begin{aligned} t_{RR} &= t'_{RR} = t_{LL} = t'_{LL} \\ &= e^{i\alpha}\cos\beta + \frac{e^{i(\alpha+\beta)}}{2}\frac{\gamma_{\mathrm{e}}^{\mathrm{rad}}}{i(\omega-\omega_{\mathrm{e}})-\gamma_{\mathrm{e}}} + \frac{e^{i(\alpha-\beta)}}{2}\frac{\gamma_{\mathrm{o}}^{\mathrm{rad}}}{i(\omega-\omega_{\mathrm{o}})-\gamma_{\mathrm{o}}}. \end{aligned} \tag{9.53}$$

$$r_{LL} = r'_{RR} = \frac{e^{i\alpha}}{2}\left[\frac{\gamma_{\mathrm{e}}^{\mathrm{rad}}e^{2i\theta_{\mathrm{e}}+i\beta}}{i(\omega-\omega_{\mathrm{e}})-\gamma_{\mathrm{e}}} - \frac{\gamma_{\mathrm{o}}^{\mathrm{rad}}e^{2i\theta_{\mathrm{o}}-i\beta}}{i(\omega-\omega_{\mathrm{o}})-\gamma_{\mathrm{o}}}\right], \tag{9.54}$$

$$r_{RR} = r'_{LL} = \frac{e^{i\alpha}}{2}\left[\frac{\gamma_{\mathrm{e}}^{\mathrm{rad}}e^{-2i\theta_{\mathrm{e}}+i\beta}}{i(\omega-\omega_{\mathrm{e}})-\gamma_{\mathrm{e}}} - \frac{\gamma_{\mathrm{o}}^{\mathrm{rad}}e^{-2i\theta_{\mathrm{o}}-i\beta}}{i(\omega-\omega_{\mathrm{o}})-\gamma_{\mathrm{o}}}\right], \tag{9.55}$$

$$t_{LR} = t'_{RL} = \frac{e^{i\alpha}}{2}\left[\frac{\gamma_{\mathrm{e}}^{\mathrm{rad}}e^{-2i\theta_{\mathrm{e}}+i\beta}}{i(\omega-\omega_{\mathrm{e}})-\gamma_{\mathrm{e}}} + \frac{\gamma_{\mathrm{o}}^{\mathrm{rad}}e^{-2i\theta_{\mathrm{o}}-i\beta}}{i(\omega-\omega_{\mathrm{o}})-\gamma_{\mathrm{o}}}\right], \tag{9.56}$$

$$t_{RL} = t'_{LR} = \frac{e^{i\alpha}}{2}\left[\frac{\gamma_{\mathrm{e}}^{\mathrm{rad}}e^{2i\theta_{\mathrm{e}}+i\beta}}{i(\omega-\omega_{\mathrm{e}})-\gamma_{\mathrm{e}}} + \frac{\gamma_{\mathrm{o}}^{\mathrm{rad}}e^{2i\theta_{\mathrm{o}}-i\beta}}{i(\omega-\omega_{\mathrm{o}})-\gamma_{\mathrm{o}}}\right]. \tag{9.57}$$

Consider first the feasibility of the lossless chiral mirror regime, when all the coefficients turn to zero apart from those listed in Eq. (9.12). Vanishing the cross-polarized reflection coefficients (9.52) and co-polarized transmission coefficients (9.53) is indeed possible if $\omega = \omega_{\mathrm{e}} = \omega_{\mathrm{o}}$ and $\gamma_{\mathrm{e,o}} = \gamma_{\mathrm{e,o}}^{\mathrm{rad}}$, i.e., if both eigenstates are precisely tuned to the same desired eigenfrequency and the dissipation is absent. Upon such conditions, the co-polarized reflection coefficients (9.54) and cross-polarized transmission coefficients (9.56) can also be zero if and only if:

$$\beta = \pm\frac{\pi}{4}, \quad \theta_{\mathrm{o}} - \theta_{\mathrm{e}} = \pm\frac{\pi}{4} + \pi l, \tag{9.58}$$

with an integer l. In this case, the absolute values of the coefficients (9.55) and (9.57) are unitary as required for the conditions (9.12). Note that such values of β determine a half-transparent background according to Eq. (9.37).

Therefore, we obtain that a planar metasurface can indeed perform as a lossless chiral mirror if it:

- **(i)** is composed of material with negligible dissipation;
- **(ii)** hosts a pair of eigenstates with identical eigenfrequency, opposite parity, and diverged by $\pi/4$;
- **(iii)** is characterized by an isotropic background with equal reflectance and transmittance, $|\tau|^2 = |\rho|^2 = 1/2$.

Upon all these conditions, the remaining model parameters such as the radiative decay rates $\gamma_{\mathrm{e,o}}^{\mathrm{rad}}$ or, equivalently, the quality factors, $Q_{\mathrm{e,o}} = \omega_{\mathrm{e,o}}/2\gamma_{\mathrm{e,o}}^{\mathrm{rad}}$, as well as the common phase α can be arbitrary.

To illustrate the applicability and potential accuracy of the CMT phenomenology, we consider an exemplary chiral mirror based on a perforated slab of transparent dielectric with refractive index $n = 4$. Its design is similar to that studied in Ref. [39], while the particular structure is somewhat different having been optimized to operate at the target wavelength of 800 nm [52]. The optimization was performed using a particle swarm algorithm employing a finite-difference time domain (FDTD) commercial solver (Lumerical) to evaluate the transmission and reflection coefficients. The set of optimal structure dimensions include: thickness $H = 142$ nm, unit cell size $L = 366$ nm, $r_c = 90$ nm, $r_x = 89$ nm, $r_y = 34$ nm, $C_x = 59$ nm, $C_y = 104$ nm, see the schematic in Fig. 9.3. Such parameters indeed ensure nearly perfect chiral mirror performance described by Eqs. (9.12) around the 800 nm wavelength, as is evident from the spectra of transmission and reflection coefficients shown by solid lines in Fig. 9.3.

To assess the extent to which this optical behavior is in-line with the phenomenological CMT, we fitted all spectra with Eqs. (9.52)–(9.57), varying only 4 parameters: the common resonant wavelength $\lambda_{\mathrm{e}} = \lambda_{\mathrm{o}}$, the two quality factors, Q_{e} and Q_{o}, and the common phase α. The corresponding fitting routine accounts for the wavelength range between 780 nm and 820 nm about the resonance and finds the values of these parameters providing the least mean-square error for the absolute differences between all reflection and transmission coefficients numerically calculated and evaluated by the CMT. As seen in Fig. 9.3, this yields the CMT parameters that allow Eqs. (9.52)–(9.57) to accurately reproduce the numerical data quantitatively in the resonance vicinity. From the optimal fitting parameters, one concludes that the even (electric) eigenstate of the mirror exhibits a considerably lower quality

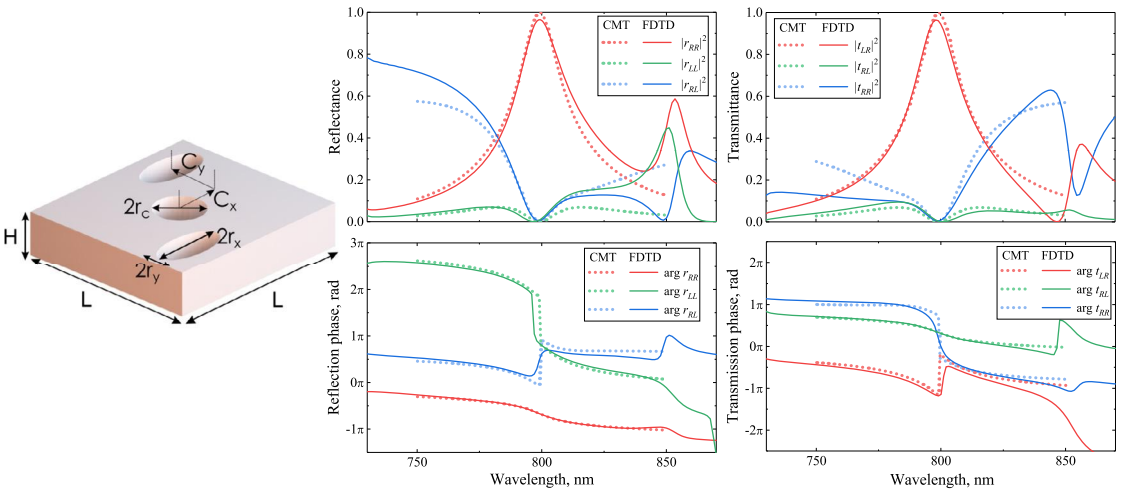

Figure 9.3. Optical chiral mirror performance obtained by numerical simulations and fitted by the CMT phenomenology. The schematic metasurface unit cell with the key structure parameters used for numerical optimization (see the optimal values listed in the text). Spectra of the power reflection and transmission coefficients, as well as the phases of complex reflection and transmission coefficients of circularly polarized light simulated using FDTD are plotted as solid lines. Those obtained by the CMT Eqs. (9.52)–(9.57) are plotted by the dotted lines for a superposition of odd and even eigenstates with equal eigenfrequencies corresponding to the resonant wavelength $\lambda = 799.1$ nm, aligned with $\theta_e = \pi/4$ and $\theta_o = 0$, having different quality factors $Q_e = 13.5$ and $Q_o = 43.3$, and supported by a semi-reflective background characterized by $\beta = -\pi/4$ and $\alpha = 3.40$ rad. *Adapted from [52] and re-used under the Creative Commons Attribution 4.0.*

factor than the odd (magnetic) one. This illustrates that a CMT can be used not only to analyze the optical chirality limits, but also to reproduce very accurately the whole optical observable datasets and to reveal intimate details of the actual mechanism of formation of strong optical chirality.

9.4 Rotationally symmetric chiral metasurfaces

9.4.1 State of the art

As discussed in Section 9.2.1, the optical chirality of metasurfaces possessing rotational symmetry of the order $\mathcal{N} \geq 3$ is relatively simple: they transmit circularly polarized waves without polarization conversion and reflect waves as an ordinary mirror, i.e., they invert the circular polarization but do not distinguish between RCP and LCP waves. The main chirality characteristic is the CD (9.6) and, as discussed in Section 9.2.1, it is determined by the

difference in absorption of RCP and LCP waves, while the ultimate maximum chirality is exhibited by a maximum chiral absorber depicted in Fig. 9.1(c).

Practical realization of such metasurfaces is challenging, as it requires fabricating structures of complex shapes without mirror symmetry planes and, therefore, not compatible with one-step planar nanofabrication techniques. Formally, the presence of a substrate breaks the in-plane mirror symmetry, however, the associated effects are weak and the related optical chirality typically appears as a result of asymmetric chiral diffraction [31,51].

Nevertheless, experimental non-diffracting chiral rotationally symmetric dielectric metasurfaces were successfully fabricated using non-standard approaches [34,42]. Thus, using digitally controlled focused ion beam (FIB) lithography, it was possible to pattern a monocrystalline silicon-on-sapphire film with a chiral surface relief [34], see Fig. 9.4(a). Although severe damage of silicon by the ions has required subjecting the sample to annealing with oxidation, the curved grooves milled in silicon withstood the treatment and provided the metasurface with remarkably strong CD up to 0.5 in the visible range, see Fig. 9.4(b). Notably, the strong chirality is accompanied by relatively good transparency. For example, a narrow CD peak about a 755 nm wavelength is caused by the LCP absorptance reaching 0.8, while the RCP absorptance remains about 0.4.

Another design of rotationally symmetric chiral metasurface proposed and realized by Tanaka et al. [42] is based on bilayer structure of silicon nanopillars embedded in glass, see Figs. 9.4(c) and 9.4(d). Comparing similar structures having C_2 and C_4 rotational symmetry axes, the authors found out that the latter is much more optically chiral. The strong chirality of the C_4-symmetric structure was found to be underpinned by a specific eigenstate "chiral supermode" comprising magnetic resonances in each pillar excited with a regular phase delay and revolving together with circular polarization unit vectors. Upon illumination with LCP or RCP light, the supermodes are excited very differently, which determines the difference in the absorptance: at a wavelength of 1.49 μm, about 0.8 of the RCP light energy is absorbed, while the transmission of the LCP light remains near-unitary, and the CD reaches 0.7, see Fig. 9.4(e).

A very different rotationally-symmetric structure, exhibiting strongly chiral optical performance, was recently proposed by Dyakov et al. [43]. The considered chiral silicon membrane of a complex shape depicted in Fig. 9.4(f) belongs to the D_4 point symmetry group. The authors have identified that the optical chirality here also is governed by a specific asymmetry of coupling of

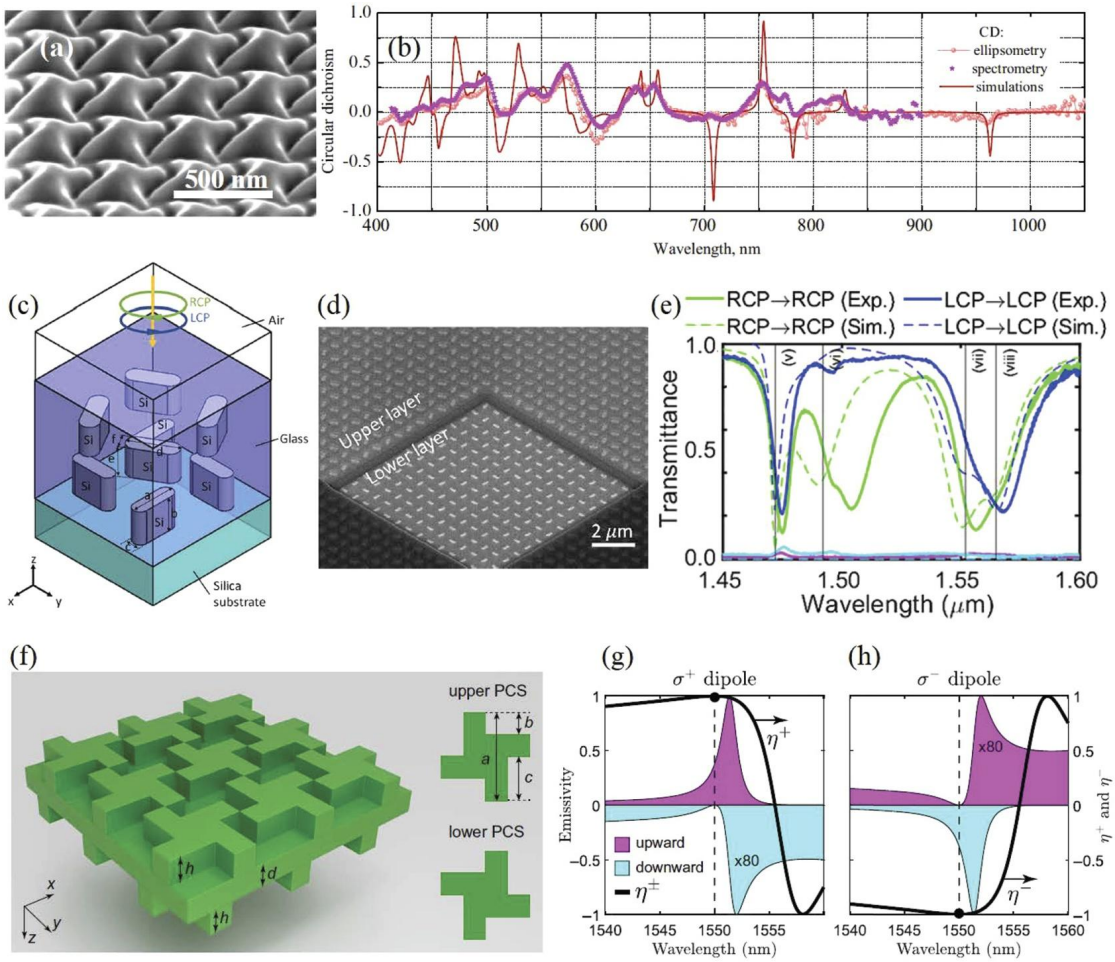

Figure 9.4. Rotationally symmetric chiral silicon metasurfaces. (a) SEM-image of a silicon layer patterned by FIB and (b) its measured and simulated CD spectra upon annealing with oxidation. *Adapted from [34] and re-used under the Creative Commons Attribution 4.0.* Schematic of the unit cell (c) and SEM-image of a cut (d) of bilayer metasurface and its measured and simulated RCP/LCP transmission spectra (e). *Adapted with permission from [42], © 2020 American Chemical Society.* Schematic of a silicon membrane (f) and normalized spectra of upward and downward emission of electric dipoles spinning in the opposite directions in (g) and (h), respectively. The normalized asymmetry $\eta^{\pm}$ of the radiated power is shown by black lines. *Adapted with permission from [43], © 2020 American Physical Society.*

modes guided by the silicon membrane with the far-field plane waves. Upon appropriate optimization, the coupling becomes unidirectional: electric dipoles rotating in the opposite directions emit circularly polarized light only upward or only downward, see Figs. 9.4(g) and 9.4(h). The authors proposed to employ such

structures as chiral routers. Although they refrained from evaluating the transmission and reflection characteristics, one can expect, based on the CMT formulated below, that such a structure can perform as a maximum-chiral absorber, provided that the dissipation in its material is appropriately adjusted.

9.4.2 CMT of rotationally symmetric chiral metasurface

To reveal the mechanism of optical chirality of rotationally symmetric metasurfaces, we apply the general CMT presented in Section 9.2.2, taking into account specific symmetry implications for the properties of optical eigenstates – quasi-normal modes (QNMs) of an open resonator [67]. The latter can be formally obtained as solutions of source-free Maxwell's equations:

$$\nabla \times \nabla \times \mathbf{E}^{(j)}(\mathbf{r}) - \varepsilon(\mathbf{r}) \frac{(\omega_j - i\gamma_j)^2}{c^2} \mathbf{E}^{(j)}(\mathbf{r}) = 0, \tag{9.59}$$

with outgoing wave conditions at $z \to \pm\infty$ imposed on $\mathbf{E}^{(j)}$, while the index j enumerates the states. The eigenfrequencies $(\omega_j - i\gamma_j)$ are complex due to dissipative and radiative energy losses determining the decay rates γ_j. The metasurface structure is described by inhomogeneous permittivity $\varepsilon(\mathbf{r})$ and its rotational symmetry defines the eigenstate $\mathbf{E}^{(j)}(\mathbf{r})$ symmetry. The connection is universally described by the group theory apparatus involving appropriate irreducible point group representations [68].

Consider, for example, a C_4 symmetric metasurface invariant upon rotation operation $\hat{R}$ by an angle $\pi/2$ about the z-axis, characterized by a coordinate transform matrix $\mathbf{R}$. It transforms a radius vector $\mathbf{r}$ into $\mathbf{r}' = \mathbf{R} \cdot \mathbf{r}$, or by coordinates as $x' = y$, $y' = -x$ and $z' = z$, preserves the permittivity $\varepsilon(\mathbf{r}) = \varepsilon(\mathbf{R} \cdot \mathbf{r})$, and transforms a vector field as $\hat{R}\mathbf{A}(\mathbf{r}) = \mathbf{R} \cdot \mathbf{A}(\mathbf{R}^{-1} \cdot \mathbf{r})$. Metasurface eigenstates can be categorized by irreducible representations of this rotation group as acquiring complex phases upon the rotation:

$$\hat{R}\mathbf{E}^{(j)} = e^{i\pi j/2} \mathbf{E}^{(j)} \tag{9.60}$$

where only integer j can ensure that repeating the rotation 4 times yields the initial state, and only the numbers $j = -1, 0, 1, 2$ are meaningful.

As eigenstates of a planar open resonator, in the far field, $\mathbf{E}^{(j)}(\mathbf{r})$ tend to transversal plane waves outgoing in the $z \to \pm\infty$ directions with only $E_x^{(j)}(z)$ and $E_y^{(j)}(z)$ nonzero components depending only on the z-coordinate. Not all j-numbers are compatible with this:

for $j = 0$, one must simultaneously satisfy $E_x^{(0)}(z) = E_y^{(0)}(z)$ and $E_x^{(0)}(z) = -E_y^{(0)}(z)$; while for $j = 2$, $E_x^{(2)}(z) = -E_y^{(2)}(z)$ and $E_x^{(2)}(z) = E_y^{(2)}(z)$, must hold true. Therefore, the eigenstates with $j = 0, 2$ cannot emit free-space waves and represent perfect BICs fully isolated by the symmetry. The eigenstates with $j = \pm 1$ (we denote them as '$\pm$'-modes), on the contrary, asymptotically tend to plane waves obeying the relations $E_x^{\pm}(z) = \pm i E_y^{\pm}(z)$, i.e., are circularly polarized along the unit vectors (9.1).

One can generally derive from the Lorentz reciprocity theorem that '$\pm$'-modes are degenerate: $\omega_{\pm} = \omega_r$ and $\gamma_{\pm} = \gamma$ [68]. For metasurfaces build of isotropic dielectrics, as described by Eq. (9.59), one can show this by constructing the modes directly. Consider an arbitrary eigenstate $\mathbf{E}_0(\mathbf{r})$, obeying Eq. (9.59) and having nonzero far-field asymptotics. Then, one can build two linear combinations:

$$\mathbf{E}^{\pm} = \mathbf{E}_0 \mp i\hat{R}\mathbf{E}_0 - \hat{R}^2\mathbf{E}_0 \pm i\hat{R}^3\mathbf{E}_0, \tag{9.61}$$

and easily check that they constitute the required eigenstates. Indeed, applying $\hat{R}$ to them and taking into account that $\hat{R}^4 = \hat{1}$ one can see that they obey Eq. (9.60) with $j = \pm 1$. As each term here is a solution of Eq. (9.59) with the same eigenfrequency, so are both $\mathbf{E}^+$ and $\mathbf{E}^-$.

Applying the general CMT apparatus to describe the contributions of degenerate modes $\mathbf{E}^{\pm}$ to the optical transmission and reflection is surprisingly nontrivial. Usually, the nature and spatial field distribution of a particular eigenstate are of minor importance to its role in the CMT phenomenology. One can derive the S-matrix knowing only the leaking eigenstate far-field asymptotics, regardless of the normalization [69]. However, the eigenstate norm is not allowed to identically vanish, which is the case for $\mathbf{E}^{\pm}$ states. One can verify this by expressing $\mathbf{E}^{\pm} = (1 - \hat{R}^2)(1 \mp i\hat{R})\mathbf{E}_0$, evaluating the norms as integrals without complex conjugation [67,70], and obtaining $\langle\langle \mathbf{E}^+|\mathbf{E}^+\rangle\rangle = \langle\langle \mathbf{E}^-|\mathbf{E}^-\rangle\rangle = 0$. The result is somehow intuitively clear, as the far-field asymptotics of the states also obey the same rule: $(\mathbf{e}_+ \cdot \mathbf{e}_+) = (\mathbf{e}_- \cdot \mathbf{e}_-) = 0$.

Fortunately, it is easy to write a pair of linearly independent combinations of the states $\mathbf{E}^{\pm}$:

$$\mathbf{E}_{\mathrm{I}} = \frac{1}{\sqrt{2}}\left(\mathbf{E}^+ + \mathbf{E}^-\right), \ \mathbf{E}_{\mathrm{II}} = \frac{1}{\sqrt{2}i}\left(\mathbf{E}^+ - \mathbf{E}^-\right), \tag{9.62}$$

having equal finite norms: $\langle\langle \mathbf{E}_{\mathrm{I}}|\mathbf{E}_{\mathrm{I}}\rangle\rangle = \langle\langle \mathbf{E}_{\mathrm{II}}|\mathbf{E}_{\mathrm{II}}\rangle\rangle = \langle\langle \mathbf{E}^+|\mathbf{E}^-\rangle\rangle$.

Accordingly, CMT equations (9.18) and (9.23) for a rotationally-symmetric metasurface are to be written for the vector of ampli-

tudes $\mathbf{p} = [p_{\mathrm{I}}, p_{\mathrm{II}}]^T$ of the states (9.62) with the matrices:

$$\mathbf{M} = \frac{1}{\sqrt{2}} \begin{bmatrix} m_- & im_- \\ m_+ & -im_+ \\ m'_+ & -im'_+ \\ m'_- & im'_- \end{bmatrix}, \quad i\boldsymbol{\Omega} - \boldsymbol{\Gamma} = [i(\omega - \omega_r) - \gamma] \begin{bmatrix} 1 & 0 \\ 0 & 1 \end{bmatrix}. \tag{9.63}$$

Here in $\mathbf{M}$, the coupling parameters for the states $\mathbf{E}_{\mathrm{I,II}}$ are expressed by those of the states $\mathbf{E}^{\pm}$. As the latter are decoupled from the waves polarized along the opposite unit vectors $\mathbf{e}_{\mp}$ (one can check by evaluating the coupling parameters using Eqs. (9.20) and (9.21) for these states), we omit the indices R and L.

Substituting the background matrix (9.34) and matrices (9.63) into Eq. (9.24) yields, fully in-line with the general symmetry consequences implied by Eq. (9.15), that the co-polarized reflection and cross-polarized transmission vanish, while the remaining non-zero coefficients are expressed as:

$$t_{RR} = t'_{RR} = \tau - \frac{m_- m'_+}{i(\omega - \omega_r) - \gamma}, \; t_{LL} = t'_{LL} = \tau - \frac{m_+ m'_-}{i(\omega - \omega_r) - \gamma}, \tag{9.64}$$

$$r_{RL} = r_{LR} = \rho - \frac{m_+ m_-}{i(\omega - \omega_r) - \gamma}, \; r'_{RL} = r'_{LR} = \rho - \frac{m'_+ m'_-}{i(\omega - \omega_r) - \gamma}. \tag{9.65}$$

To analyze this result, we again assume first that the eigenstate decay occurs only due to radiative losses and represent the decay rate $\gamma = \gamma^{\mathrm{rad}}$ as defined by the eigenstate leaking into the free-space waves. Then the condition Eq. (9.31) is applicable, and substituting the matrices (9.63) into it, we obtain:

$$2\gamma^{\mathrm{rad}} = |m_+|^2 + |m'_+|^2 = |m_-|^2 + |m'_-|^2, \tag{9.66}$$

which, therefore, implies additional restraints on the coupling coefficients of the degenerate eigenstates. For the isotropic lossless background S-matrix (9.34), deploying the matrix $\mathbf{M}$ from (9.63) into the condition (9.28) also yields other useful relations:

$$-m_{\pm} = \rho m^*_{\mp} + \tau m'^*_{\mp}, \; -m'_{\pm} = \tau m^*_{\mp} + \rho m'^*_{\mp}. \tag{9.67}$$

Next, to take the absorption into account, one includes the corresponding additional contribution to the decay rate as $\gamma = \gamma^{\mathrm{rad}} + \gamma^{\mathrm{dis}}$. To clearly manifest the general connection of the transmission circular dichroism of rotationally symmetric metasurfaces

with absorption, formulated in Section 9.2.1, we evaluate the difference in LCP and RCP power transmission (9.9). Taking the absolute values of coefficients (9.64) and using the relations (9.67) yields:

$$\Delta T = 2\gamma^{\mathrm{dis}} \frac{|m_+|^2 - |m_-|^2}{(\omega - \omega_r)^2 + (\gamma^{\mathrm{rad}} + \gamma^{\mathrm{dis}})^2}. \tag{9.68}$$

Apart from emphasizing the crucial role of absorption, this relation also shows that the optical chirality indeed stems from the asymmetry of excitation of '+' and '−' eigenstates, empirically called "chiral supermodes" by Tanaka et al. [42]. We see also that the ΔT spectrum has a characteristic resonant Lorentzian shape reaching its maximum at $\omega = \omega_r$.

9.4.3 Feasibility of maximum-chiral absorber

Let us consider how the optical chirality of rotationally-symmetric metasurface can be enhanced to the maximum-chiral absorber regime discussed in Section 9.2.1 and sketched there in Fig. 9.1(c). For definiteness, we choose to sustain the transparency to RCP waves, while LCP waves are fully resonantly absorbed. As follows from Eq. (9.64), the ultimate value of $|t_{RR}| = 1$ requires that $|\tau| = 1$ and that $m_- m'^*_+ = 0$. The former condition describes a fully transparent non-resonant background with $\beta = 0$, while the latter one shows that a certain coupling parameter has to vanish, i.e., that either of '±' eigenstates has to be fully uncoupled on the corresponding metasurface side.

Setting $\beta = 0$ in ρ and τ and choosing, for definiteness, that $m_- = 0$, one obtains from Eq. (9.67) that then also $m'_+ = 0$, and $m'_- = -e^{i\alpha} m^*_+$. Substituting these values into Eq. (9.64) yields:

$$t_{RR} = t'_{RR} = e^{i\alpha},\ t_{LL} = t'_{LL} = e^{i\alpha}\left(1 + \frac{2\gamma^{\mathrm{rad}}}{i(\omega - \omega_r) - (\gamma^{\mathrm{rad}} + \gamma^{\mathrm{dis}})}\right), \tag{9.69}$$

where we have also used that the coupling determines the radiative decay rate by Eq. (9.66).

Then the LCP power transmittance can be expressed as:

$$|t_{LL}|^2 = 1 - \frac{4\gamma^{\mathrm{dis}}\gamma^{\mathrm{rad}}}{(\omega - \omega_r)^2 + (\gamma^{\mathrm{rad}} + \gamma^{\mathrm{dis}})^2}, \tag{9.70}$$

and at $\omega = \omega_r$ it reaches the minimum value of:

$$\min |t_{LL}|^2 = \frac{(\gamma^{\mathrm{rad}} - \gamma^{\mathrm{dis}})^2}{(\gamma^{\mathrm{rad}} + \gamma^{\mathrm{dis}})^2}. \tag{9.71}$$

The ultimate limit of $\min |t_{LL}|^2 = 0$ is achieved when:

$$\gamma^{\text{rad}} = \gamma^{\text{dis}}. \tag{9.72}$$

This classical critical coupling condition [71] is typical for absorbers and describes a resonator receiving exactly the amount of external power it can dissipate.

In summary, for rotationally symmetric metasurface to perform as a maximum-chiral absorber it has to:

(i) host eigenstates uncoupled from particular circularly polarized waves on either metasurface sides: e.g., "$-$" state uncoupled from RCP waves incident on one side and "$+$" state uncoupled from RCP waves incident on the other side;

(ii) fully absorb the light of the opposite circular polarization in the critical coupling regime.

Note that the CMT also requires that this metasurface performs identically from its both sides: e.g., $m_- = 0$ and $|m_+|^2 = 2\gamma^{\text{dis}}$ on one side, and $m'_+ = 0$ and $|m'_-|^2 = 2\gamma^{\text{dis}}$ on the other side. To automatically ensure this, one can further narrow the metasurface symmetry group to D_4, which includes a flipping symmetry in addition to the C_4 rotational axis.

9.4.4 Quasi-BIC metasurface as maximum-chiral absorber

Adjusting a metasurface resonance to the maximum-chiral absorber regime requires precise engineering of the coupling of optical eigenstates to the free-space waves. For an arbitrary chiral metasurface composed of complex-shaped elements, this is a difficult, if not impossible, task, as the relations between the coupling parameters and the practically variable meta-atom shape and arrangement can be very sophisticated. Fortunately, recent advances in dielectric metasurfaces have elucidated broad availability of specific optical bound states in the continuum (BICs) [72]. Of particular interest here is the class of quasi-BICs stemming from symmetry-protected BICs hosted by metasurfaces with specifically perturbed structure.

While a symmetry-protected BIC is an eigenstate which interaction with the free-space waves is forbidden by its symmetry (see, e.g., $j = 0, 2$ states in Section 9.4.2), one can introduce symmetry-breaking perturbations and transform a BIC into a leaky quasi-BIC [65,73]. On this path, the arising coupling to free-space waves is controlled by the degree and character of asymmetry introduced into the metasurface structural elements. Let us illustrate how such a quasi-BIC can be tuned to the maximum chiral ab-

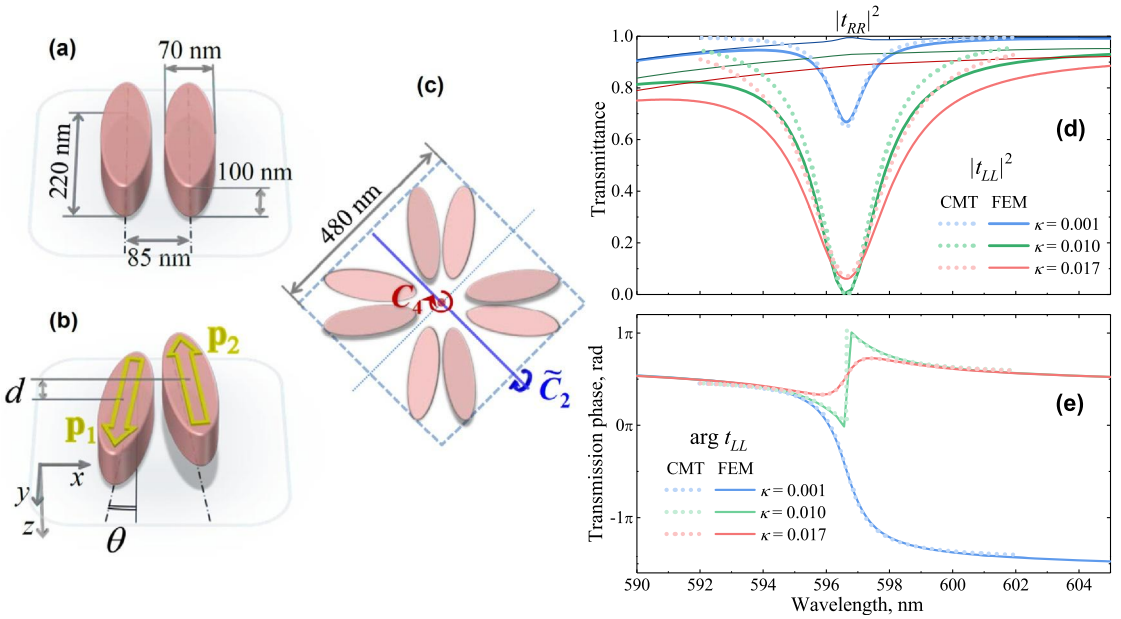

Figure 9.5. Maximum-chiral absorber, based on pairs of elliptical silicon bars hosting an antiparallel electric dipole BIC which is transformed into a chiral quasi-BIC by symmetry-breaking perturbations. (a) Symmetric pair of bars and (b) a pair of bars vertically displaced by d and diverged by angle θ. (c) Square unit cell of rotationally symmetric metasurface built of four perturbed bar pairs with the retained symmetry elements indicated. Spectra of power transmission coefficients (d) and transmission phases (e), illustrating how the maximum optical chirality is achieved by adjusting the material extinction coefficient κ to the value corresponding to the critical coupling regime after the symmetry perturbations of $d = 10$ nm and $\theta = 3.5°$ are set to suppress RCP transmission resonance. The best fit by CMT dependences is shown in (d) and (e) by dotted lines for the parameters $\alpha = 1.67$, $\lambda_r = 596.6$ nm, $Q^{\text{rad}} = 534$ and $Q = 483,\ 267,\ 196$ for $\kappa = 0.001,\ 0.010,\ 0.017$ correspondingly.

sorber regime by a sequence of precise symmetry-breaking perturbations.

Consider a pair of parallel dielectric bars shown in Fig. 9.5(a), possessing a C_2 rotation axes and three orthogonal mirror symmetry planes. In this perfectly symmetric situation, eigenstates transform according to irreducible representations of the C_2 group and, among these, there is a symmetric A-representation. A particular realization of such eigenstate is the antiparallel electric dipole state, which can be represented by a pair of electric dipole moments $\mathbf{p}_1 = -\mathbf{p}_2$ hosted by each bar and having equal absolute values and opposite directions. The coupling parameters of this state evaluated by Eqs. (9.20) and (9.21) identically vanish, as the integral over each bar reduces to the corresponding dipole mo-

ment:

$$m_{R,L},\ m'_{L,R} \propto \mathbf{p}_1 \cdot \mathbf{e}_{\mp} + \mathbf{p}_2 \cdot \mathbf{e}_{\mp} = 0. \tag{9.73}$$

Perturbing the symmetry by diverging the bars in-plane by an angle θ and shifting them vertically by an offset d, as shown in Fig. 9.5(b), eliminates all mirror symmetry planes and enables the quasi-BIC coupling to circularly polarized waves:

$$m_{R,L} \propto \mathbf{p}_1 \cdot \mathbf{e}_{\mp} + \mathbf{p}_2 \cdot \mathbf{e}_{\mp} e^{ikd} \propto e^{ikd/2} \sin\left(kd/2 \pm \theta\right), \tag{9.74}$$

$$m'_{R,L} \propto \mathbf{p}_1 \cdot \mathbf{e}_{\pm} + \mathbf{p}_2 \cdot \mathbf{e}_{\pm} e^{-ikd} \propto e^{-ikd/2} \sin\left(kd/2 \pm \theta\right). \tag{9.75}$$

Remarkably, a simple adjustment of d and θ to the proportion:

$$\theta = kd/2, \tag{9.76}$$

fully decouples the state from RCP waves incident on both sides, while the remaining coupling parameters:

$$m_L,\ m'_L \propto e^{i\theta} \sin(2\theta) \tag{9.77}$$

are controlled by the small perturbation θ and can be continuously tuned.

To take the advantage of the peculiar properties of perturbed pairs of dielectric bars, one can arrange a rotationally symmetric metasurface as a square lattice of unit cells, as depicted in Fig. 9.5(c). Each cell consists of 4 pairs symmetrically arranged about the center to ensure the rotational symmetry, and also diverged and vertically offset to achieve the proportionality (9.76). In such a case, each pair is isolated from RCP waves and the same is true for the $\pm$-eigenstates, build as linear combinations of such excitations with the relative phase shifts to establish Eq. (9.60). To adjust such metasurface to the regime of maximum-chiral absorber, it is sufficient to adjust d and θ to the condition (9.76) and also to ensure the critical coupling to LCP waves by appropriate value of θ in Eq. (9.77).

For an exemplary illustration, we simulate using finite element method (FEM) in COMSOL Multiphysics a metasurface built of bars of material with complex refractive index $n = 4 + i\kappa$ with small extinction coefficient κ, which is typical for silicon or germanium in the visible and infrared ranges, correspondingly. For simplicity, we set the background refractive index to unity. The dimensions of the bars and their periodic arrangement, as shown in Fig. 9.5, are chosen to ensure the appearance of the antiparallel electric dipole BIC at about a 596 nm wavelength, while the period is short enough to exclude the diffraction. For this wavelength, the condition (9.76) suggests that uncoupling the quasi-BICs of all pairs of

RCP waves requires, e.g., setting $d = 10$ nm and $\theta = 3.0°$. Numerically evaluating the spectra of transmission coefficients, we obtain the ideal uncoupling for $\theta = 3.5°$ [44], and attribute the small mismatch to a slight misalignment of the bar dipole moment from its geometric shape.

For this combination of θ and d, one can verify the main CMT conclusions and adjust the quasi-BIC to maximum chiral absorber regime. While the quasi-BIC radiative decay rate γ^{rad} is eventually determined by the coupling of dipole pairs to LCP waves (9.77), the dissipative decay rate γ^{dis} is determined by the small extinction coefficient κ. Accordingly, to ensure the critical coupling, we keep all other parameters fixed and simulate the transmission of structures with different κ, as illustrated in Figs. 9.5(d) and 9.5(e). For insufficiently small κ, the $|t_{LL}|^2$ dip is very shallow, while increasing κ too far again increases it. Setting $\kappa = 0.01$ yields the optimum critical coupling, and at the resonance one achieves exactly the performance depicted in Fig. 9.1(c).

To illustrate the applicability of the CMT phenomenology and to reveal the actual values of its parameters, we fit the numerically obtained complex transmission coefficients using the model Eqs. (9.69) with the resonant wavelength $\lambda_r = 2\pi c/\omega_r$, common phase α, radiative quality factor $Q^{\text{rad}} = \omega_r/2\gamma^{\text{rad}}$ and full quality factor $Q = \omega_r/2\gamma$ being the only fitting parameters. As seen in Figs. 9.5(d) and 9.5(e), the numerical data can be very well approximated by the analytical model relations. Varying the extinction coefficient affects only the full quality factor Q leaving other model parameters unchanged. The maximum-chiral absorber regime corresponds to $Q^{\text{rad}} = 2Q$ fully in-line with the critical coupling condition (9.72).

9.5 Asymmetric metasurfaces

9.5.1 State of the art

Objects without point symmetry elements are chiral by definition. Peculiar asymmetric configurations of nanoobjects, such as nanoparticle trimers [74,75] or crossed-bowtie shaped nanostructures [37] are intensively studied as chiral nanoantenas, which can also be optically reconfigurable [76]. Importantly, metasurfaces composed as arrays of such objects are formally capable of all chiral light transformations described by the S-matrix (9.4). Being all simultaneously present, such transformations are typically characterized by moderate optical chirality. In the general case, it

is unclear how to suppress certain processes and to enhance the others to maximize the optical chirality.

A representative example is the metasurface built of flat L-shaped silicon meta-atoms studied by Koshelev et al. [54], see Fig. 9.6(a,b). The mirror symmetry plane is broken by the presence of substrate and the metasurface exhibits experimental CD up to 0.3, see Fig. 9.6(c). The optical chirality is underpinned by several quasi-BIC modes whose spectral positions can be adjusted by varying the meta-atom shape parameters. The authors also report on broader Mie-type resonances, which are more convenient for establishing the specific critical coupling regime of third-harmonic generation yielding large nonlinear CD.

Arrays of helices constitute a large class of chiral metastructures without point symmetry elements [78]. Intuitively, one can expect that helically twisted fields of circularly polarized waves should selectively couple to such structures, provided that the wavelength is matched to the helix pitch. Then the periodicity gives rise to photonic crystal bandgaps at normal incidence [79,80], which was experimentally demonstrated by Thiel et al. [81], as the array of helices completely blocked infrared light of one circular polarization remaining fully transparent to its counterpart. Along this path, however, a substantial optical chirality can be achieved only by structures containing sufficient number of pitches, i.e., by those much thicker than the wavelength. Metasurfaces consisting of single-pitch nanohelices manifest rather moderate optical chirality [82].

A peculiar example of a thin helix-based metasurface without point symmetry and showing remarkably strong optical chirality was proposed by Karakasoglu et al. [36], as they have theoretically studied monolayers of silicon nanohelices with respect to light propagating perpendicular to their axis, see Fig. 9.6(d). When the wavelength of light is about half the distance between the helices, the structure operates as a maximum-chiral filter, remaining transparent to RCP waves and reflecting LCP ones, see the corresponding spectra of reflectance in Fig. 9.6(e) and transmittance in Fig. 9.6(f). The authors discuss the origin of optical chirality in terms of the stop bands inherited by a monolayer from an analogous multilayer array of helices. By starting from a monolayer of straight silicon rods and introducing the helicity as a perturbation, they also point out the crucial role of hybridization of TE and TM modes supported by the rods.

Due to a wider range of compatible fabrication techniques, very different asymmetric chiral metasurfaces have been fabricated from metals [83]. Whereas in the visible range, strong absorption accompanies their plasmon resonances, and in the

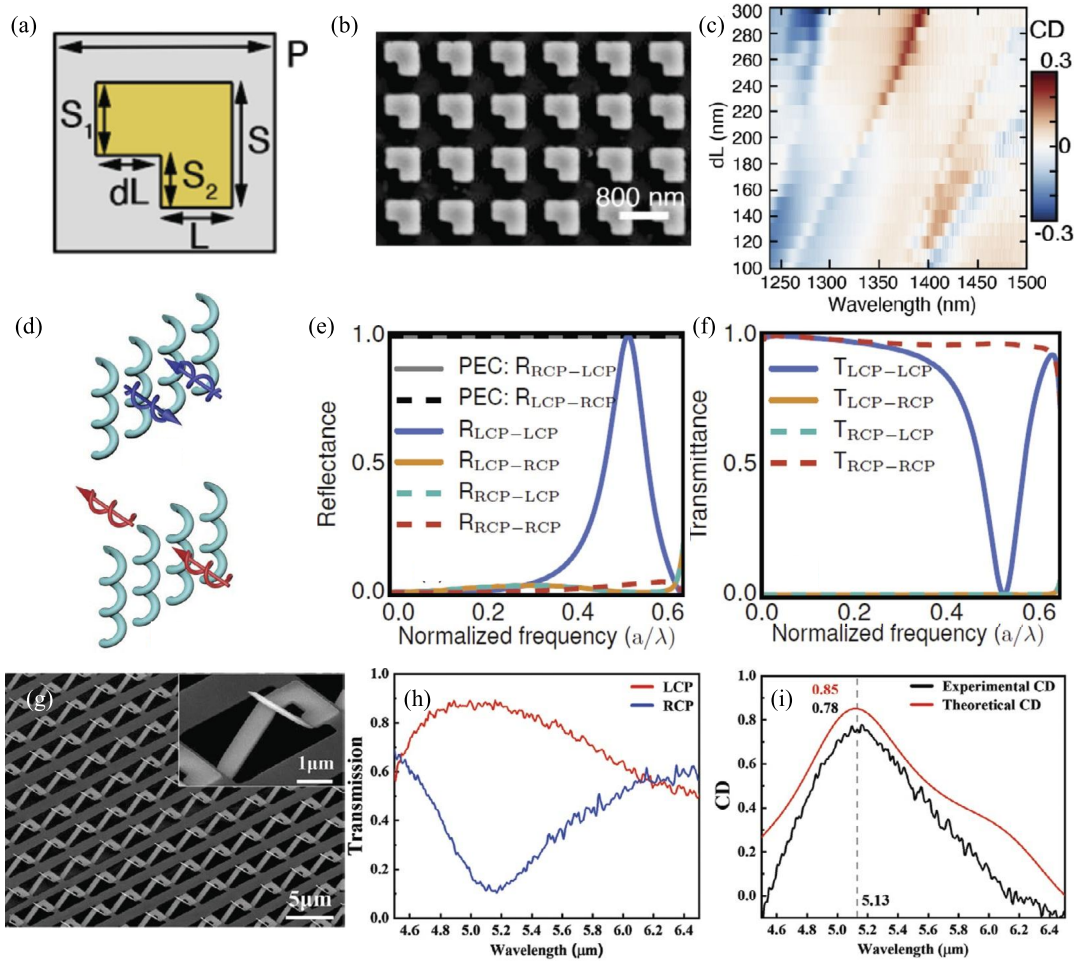

Figure 9.6. Examples of chiral metasurfaces without point symmetry elements. Silicon L-shaped meta-atom (a) composing a metasurface (b), which exhibits CD spectra combined in a colormap (d) for various dL. *Adapted with permission from [54] © 2023 American Chemical Society.* Schematic of silicon helix metasurface (d) and its simulated reflectance (e) and transmittance (f) as functions of wavelength normalized by the distance a between the helices. *Adapted with permission from [36] © 2018 The Optical Society.* SEM-image of Al/SiN_x chiral origami metasurface (g) and measured spectra of its transmittance (h) and CD (i). *Used with permission of © 2022 Wiley-VCH GmbH, from [77] conveyed through Copyright Clearance Center, Inc.*

infrared range, the dissipation effects are considerably weaker. A notable example of strongly chiral low-loss asymmetric metallic metasurface was provided by Zheng et al. [77]. Applying the advanced FIB-induced origami technique to bilayer Al/SiN_x membranes, they have created a chiral metasurface consisting of bidirectional folded split ring resonators, as seen in Fig. 9.6(g).

Experimental transmittance spectra in Fig. 9.6(h) demonstrate that such metasurface is almost transparent to LCP light and resonantly blocks RCP light in the mid-infrared range. The maximum CD value of 0.78 is reached at a 5.13 μm wavelength, see Fig. 9.6(i). The simulations revealed how the strong chirality can be explained by the distribution of currents in the main magnetic eigenmode of the folded split rings: the currents flow in the opposite directions of the folded metal arms and, if certain geometrical conditions are met, the state can be uncoupled from one circular polarization. Note that similarly shaped metallic origami metasurfaces have also been fabricated for the near-infrared range, but the absorption in metal has a much stronger negative effect there [84].

9.5.2 Near-lossless maximum chirality

As discussed in Section 9.2.1, a lossless or near-lossless maximum chiral performance, sketched in Fig. 9.1(d), is incompatible with rotational symmetry axes or mirror planes. In the absence of symmetry restrictions, all elements of the S-matrix (9.4) are allowed to be nonzero, and, therefore, such metasurfaces are relatively rarely studied. However, analyzing the phenomenological form of the S-matrix (9.24), expressed by its elements as in Eq. (9.38), one can notice a straightforward possibility to establish the lossless maximum-chiral regime by fulfilling a few simple conditions [45].

First, one assumes that the metasurface is lossless and hosts a single non-degenerate eigenstate producing a resonance in a spectral range where the background is perfectly transparent, i.e., characterized by $\beta = 0$ in Eq. (9.37). Then the condition (9.28) relates the coupling parameters on different metasurface sides as:

$$m'_R = -m^*_R e^{i\alpha},\ m'_L = -m^*_L e^{i\alpha}, \tag{9.78}$$

while the radiative decay rate (9.32) is expressed by:

$$\gamma^{\mathrm{rad}} = |m_R|^2 + |m_L|^2 = |m'_R|^2 + |m'_L|^2. \tag{9.79}$$

Now, if the metasurface eigenstate is isolated from RCP waves incident on the front, i.e., if $m_R = 0$, then on the back side also $m'_R = 0$, and one can express the remaining coupling parameters as:

$$m_L = i\sqrt{\gamma^{\mathrm{rad}}}e^{i\alpha/2+i\delta},\ m'_L = i\sqrt{\gamma^{\mathrm{rad}}}e^{i\alpha/2-i\delta}, \tag{9.80}$$

where the complex phase δ describes the difference in wave coupling on different metasurface sides. Evaluating the reflection and

transmission coefficients in Eq. (9.38), one obtains that most of them completely vanish in such case, while the remaining ones read as:

$$r_{LL} = \frac{\gamma^{\mathrm{rad}} e^{i\alpha+2i\delta}}{i(\omega-\omega_r)-\gamma},\ r'_{LL} = \frac{\gamma^{\mathrm{rad}} e^{i\alpha-2i\delta}}{i(\omega-\omega_r)-\gamma}, \tag{9.81}$$

$$t_{RR} = t'_{RR} = e^{i\alpha}, \tag{9.82}$$

$$t_{LL} = t'_{LL} = e^{i\alpha}\left(1+\frac{\gamma^{\mathrm{rad}}}{i(\omega-\omega_r)-\gamma}\right). \tag{9.83}$$

In the absence of absorption in metasurface material, $\gamma = \gamma^{\mathrm{rad}}$, and the absolute values of coefficients (9.81)–(9.83) all reach at the resonance their ultimate values envisioned by Eq. (9.17).

In contrast to rotationally symmetric metasurfaces, where the dissipation is a key necessary ingredient of maximum chirality, in the asymmetric case, its role is always negative. To clarify it, one can again assume that weak dissipation negligibly affects the eigenstate coupling, but contributes to the decay rate $\gamma = \gamma^{\mathrm{rad}} + \gamma^{\mathrm{dis}}$. In such case, at the resonance, the coefficients deviate from their ultimate values as:

$$\min|t_{LL}| = \frac{\gamma^{\mathrm{dis}}}{\gamma^{\mathrm{rad}}+\gamma^{\mathrm{dis}}},\ \max|r_{LL}| = \frac{\gamma^{\mathrm{rad}}}{\gamma^{\mathrm{rad}}+\gamma^{\mathrm{dis}}}. \tag{9.84}$$

Therefore, CMT allows formulating simple principles for the design of metasurfaces with resonant, near-lossless maximum chirality. It is sufficient that such a metasurface:

(i) manifests a resonance on a transparent background;
(ii) this resonance is isolated from one circular polarization;
(iii) dissipation in the metasurface material is negligible.

If the latter condition is weakly violated, the metasurface approaches maximum chirality in a near-lossless regime that is qualitatively different from the maximum-chiral absorber.

9.5.3 Exemplary design of lossless maximum chiral filter

Realizing the formulated phenomenological conditions of lossless maximum chirality requires precise control over the eigenstate coupling to free-space waves. Similarly to the design of the maximum-chiral absorber, one can also rely here on the quasi-BICs concept to tailor a non-degenerate spectrally isolated eigenstate for the maximum chirality. For a particular illustration, we

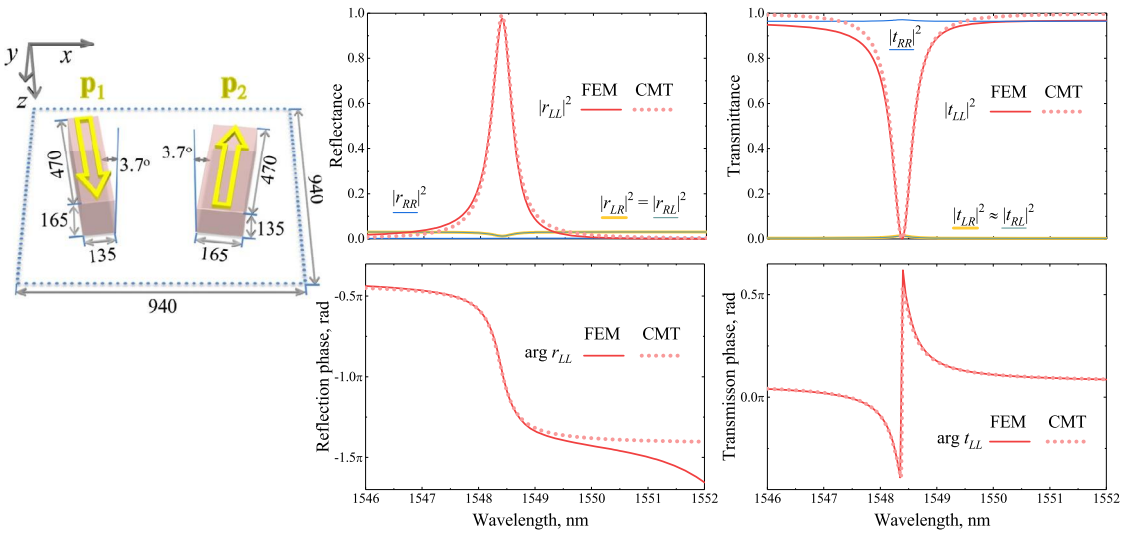

Figure 9.7. Near-lossless maximum-chiral metasurface based on pairs of identical rectangular silicon bars placed on different facets and diverged by a small angle. Key structure parameters of the metasurface unit cell are indicated in nanometers. Spectra of the power reflection and transmission coefficients, as well as the phases of complex reflection and transmission coefficients of circularly polarized light were obtained by FEM simulations (solid lines) and by fitting with CMT Eqs. (9.81) and (9.83) (dotted lines). CMT parameters are: resonant wavelength 1548.4 nm, radiative quality factor $Q^{\mathrm{rad}} = 3687$, total quality factor $Q = 3673$, common phase $\alpha = 0.2179$ rad, and the coupling phase $\delta = 0.0132$ rad.

again employ the antiparallel electric-dipole BIC of pairs of dielectric bars. As long as the bars are identically oriented and parallel, the eigenstate is fully isolated from all normally incident plane waves. Breaking the symmetry, one can precisely couple the state to the wave continuum and transform it into a chiral quasi-BIC.

In theory, one can vertically displace every other bar again and diverge the pairs. For better compatibility with planar fabrication techniques, we consider rectangular bars and let them all lie on the same plane. Turning every other bar on its side results in effective shift of the bar center of mass along the z-axis by a half difference of the bar cross section sides, which should produce a comparable vertical shift d of the dipole moment. Next, by diverging the pairs by a small angle θ, as shown in Fig. 9.7, one can again fulfill the condition (9.76) and eliminate the coupling parameters m_R and m'_R according to Eqs. (9.74) and (9.75), keeping control over m_L and m'_L according to Eq. (9.77).

To illustrate the capabilities of this design approach, we simulate using COMSOL Multiphysics polarized light transmission and reflection by exemplary metasurface built as array of differently aligned, identical rectangular silicon bars (the refractive in-

dex spectra taken from [85]). To minimize the background reflections, we suppose that the bars are supported by a transparent substrate and are covered by a transparent material with the same refractive index, i.e., they are effectively immersed in a transparent homogeneous background with the refractive index $n = 1.5$. The obtained spectra of transmission and reflection of circularly polarized waves, shown in Fig. 9.7, demonstrate that the simple model relation (9.76) provides a very accurate guidance. Antiparallel electric dipole BIC, arising around a wavelength of $\lambda = 1549$ nm, indeed is transformed into a chiral quasi-BIC. While the equality $|r_{LR}| = |r_{RL}|$ required by the reciprocity remains strictly valid, the difference between the metasurface sides is determined by a small relative vertical displacement of the bar centers and the cross-polarized transmission coefficients remain very close too, $|t_{LR}| \simeq |t_{RL}|$. For the diverging angle precisely adjusted to $\theta = 3.7°$, the metasurface optical chirality reaches its maximum, and the structure indeed performs very close to the regime depicted in Fig. 9.1(d): The main characteristic parameter of the maximum optical chirality ΔT reaches a numerical value of 0.97 at the top of the resonance, and the maximum chirality is practically lossless, as 97.5% of the energy of incident LCP waves is reflected. This illustrates that a lossless maximum chirality, generally forbidden in symmetric metasurfaces, is feasible in structures without point symmetry elements.

To extract the actual values of the CMT phenomenological parameters, we fit the numerically obtained complex transmission coefficients using the model Eqs. (9.81) and (9.83), see Fig. 9.7. Indeed, the dissipation produces almost negligible effect, as the total quality factor is practically equal to the radiative one. We also obtain that the phase δ, describing the difference of coupling of light on different metasurface sides, is fairly small.

9.6 Conclusions and outlook

As in other nanophotonic research areas, transition to the all-dielectric platform has enabled drastic reduction of light energy dissipation in chiral metasurfaces. Strategically even more important is that this transition facilitated rational design of artificial chirality. By adjusting optical eigenstates hosted by dielectric meta-atoms to specific configurations, one can precisely tailor their interaction with circularly polarized light to establish maximum-selective chiral regimes. Depending on the metasurface symmetry, such regimes can be very different: mirror-symmetric planar metasurfaces become chiral mirrors, rotationally-symmet-

ric ones operate as maximum-chiral absorbers, while asymmetric metasurfaces perform as lossless maximum-chiral filters.

Phenomenological CMT, describing light scattering by metasurfaces as excitation and irradiation of optical eigenstates, is a very convenient tool for the rational design of chiral metasurfaces. Fundamental restrictions imposed by the symmetry, electromagnetic reciprocity, and time reversibility (when the absorption is negligible) allow reducing the number of relevant phenomenological constants in each case, and identifying the particular combinations of eigenstates required for the target chiral optical functionality.

Thus, a chiral helicity-preserving mirror can be realized by a pair of eigenstates of opposite parity supported by an isotropic half-transparent background. For a maximum chiral absorber, the optimum path is to employ degenerate eigenstates of rotationally symmetric metasurfaces and to tune them to chiral quasi-BICs isolated from waves of certain circular polarization. Very peculiar performance is achieved when a single non-degenerate eigenstate is tuned to a chiral quasi-BIC. Then most of the chiral transmissions and reflections are suppressed and the metasurface operates as a lossless chiral filter. Certainly, several design examples considered in this chapter do not exhaust the manifold of arising opportunities as one can extend the number of relevant eigenstates, introduce background anisotropy, account for more incoming/outgoing channels in diffractive setups, etc. All this can be assisted by straightforward generalization of the theoretical background accounted in Section 9.2.

Diverse intriguing possibilities emerge when flat-optical chiral components are combined into chiral cavities supporting helical eigenmodes – standing waves with uniform chirality density. Thus, for instance, stacks of planar mirror-symmetric metasurfaces, selectively reflecting one circular polarization and transmitting the opposite reversing its helicity, support helical Fabry–Perot eigenstates coupled to normally incident/outgoing circularly polarized waves [52]. Apart from efficient generation and sensitive detection of chiral light, such cavities expand our set of tools for mastering chiral light-matter interaction: They open a door to chiral polaritonics and chiral electromagnetic vacuum prospectively facilitating chiral chemistry [86].

Resonant dielectric metasurfaces are capable of highly efficient nonlinear light transformations: harmonic generation and wave-mixing, accounted in Chapter 11, as well as single- and multi-photon luminescence and lasing [87,88]. A substantial extension of the theory is required to cover the nonlinear chirality. By analogy, one can attempt to design metasurfaces operat-

ing in maximum-chiral nonlinear regimes, i.e., those exhibiting ultimate chiral selectivity with respect to circularly polarized incoming (pumping) light, or generating circularly polarized output light, or combining both input and output selectivity in various combinations.

Whereas excitation of highly confined eigenstates is accompanied by strong near-field enhancement, quasi-BICs are known to provide metasurfaces with unprecedentedly high nonlinearity [89]. On the other hand, the maximum chirality relies on quasi-BICs which are fully uncoupled from light of a particular circular polarization but can be very efficiently excited by light of the opposite circular polarization. Therefore, one can expect the dielectric chiral quasi-BIC metasurfaces to be the optimal platform for realizing the maximum-chiral optical nonlinearity. First reported achievements of chiral quasi-BIC photonics [53,54] indicate huge potential of such approach.

Acknowledgments

The work was supported by the Russian Science Foundation (project 23-42-00091, https://rscf.ru/project/23-42-00091/).

References

[1] A.B. Harris, R.D. Kamien, T.C. Lubensky, Molecular chirality and chiral parameters, Reviews of Modern Physics 71 (5) (1999) 1745–1757, https://doi.org/10.1103/revmodphys.71.1745.

[2] A.-J. Fresnel, Considérations théoriques sur la polarisation de la lumière, Bull. Sci. Soc. Philomath. (1824) 147–158.

[3] L. Pasteur, Recherches sur les relations qui peuvent exister entre la forme crystalline, la composition chimique et le sens de la polarisation rotatoire', Annales de Chimie et de Physique 24 (1848) 442–459.

[4] W.T.B. Kelvin, The Molecular Tactics of a Crystal, Robert Boyle lecture, Clarendon Press, 1894.

[5] P. Polavarapu, Chiral Analysis: Advances in Spectroscopy, Chromatography and Emerging Methods, Elsevier, Amsterdam, Netherlands, 2018.

[6] J.C. Bose, On the rotation of plane of polarisation of electric waves by a twisted structure, Proceedings of the Royal Society of London 63 (1898) 146–152, http://www.jstor.org/stable/115973.

[7] K.F. Lindman, Über eine durch ein isotropes System von spiralförmigen Resonatoren erzeugte Rotationspolarisation der elektromagnetischen Wellen, Annalen der Physik 368 (23) (1920) 621–644, https://doi.org/10.1002/andp.19203682303.

[8] N.I. Zheludev, Y.S. Kivshar, From metamaterials to metadevices, Nature Materials 11 (11) (2012) 917–924, https://doi.org/10.1038/nmat3431.

[9] M. Schäferling, Chiral Nanophotonics, Springer International Publishing, 2017, https://doi.org/10.1007/978-3-319-42264-0.

[10] Y. Chen, W. Du, Q. Zhang, O. Ávalos-Ovando, J. Wu, Q.-H. Xu, N. Liu, H. Okamoto, A.O. Govorov, Q. Xiong, C.-W. Qiu, Multidimensional nanoscopic chiroptics, Nature Reviews Physics 4 (2) (2021) 113–124, https://doi.org/10.1038/s42254-021-00391-6.
[11] P. Lodahl, S. Mahmoodian, S. Stobbe, A. Rauschenbeutel, P. Schneeweiss, J. Volz, H. Pichler, P. Zoller, Chiral quantum optics, Nature 541 (7638) (2017) 473–480, https://doi.org/10.1038/nature21037.
[12] H. Hübener, U.D. Giovannini, C. Schäfer, J. Andberger, M. Ruggenthaler, J. Faist, A. Rubio, Engineering quantum materials with chiral optical cavities, Nature Materials 20 (4) (2020) 438–442, https://doi.org/10.1038/s41563-020-00801-7.
[13] L. Chenhao, S.A. Maier, R. Haoran, Optical vortices in nanophotonics, Chinese Optics 14 (4) (2021) 1–20, https://doi.org/10.37188/co.en.2021-0066.
[14] P. Stachelek, L. MacKenzie, D. Parker, R. Pal, Circularly polarised luminescence laser scanning confocal microscopy to study live cell chiral molecular interactions, Nature Communications 13 (1) (2022), https://doi.org/10.1038/s41467-022-28220-z.
[15] L.A. Warning, A.R. Miandashti, L.A. McCarthy, Q. Zhang, C.F. Landes, S. Link, Nanophotonic approaches for chirality sensing, ACS Nano 15 (10) (2021) 15538–15566, https://doi.org/10.1021/acsnano.1c04992.
[16] Y. Svirko, N. Zheludev, M. Osipov, Layered chiral metallic microstructures with inductive coupling, Applied Physics Letters 78 (4) (2001) 498–500, https://doi.org/10.1063/1.1342210.
[17] E. Plum, V.A. Fedotov, A.S. Schwanecke, N.I. Zheludev, Y. Chen, Giant optical gyrotropy due to electromagnetic coupling, Applied Physics Letters 90 (22) (2007) 223113, https://doi.org/10.1063/1.2745203.
[18] E. Plum, V.A. Fedotov, N.I. Zheludev, Extrinsic electromagnetic chirality in metamaterials, Journal of Optics. A, Pure and Applied Optics 11 (7) (2009) 074009, https://doi.org/10.1088/1464-4258/11/7/074009.
[19] E. Plum, V.A. Fedotov, N.I. Zheludev, Planar metamaterial with transmission and reflection that depend on the direction of incidence, Applied Physics Letters 94 (22) (2009) 131901, https://doi.org/10.1063/1.3109780.
[20] J.K. Gansel, M. Thiel, M.S. Rill, M. Decker, K. Bade, V. Saile, G. von Freymann, S. Linden, M. Wegener, Gold helix photonic metamaterial as broadband circular polarizer, Science 325 (5947) (2009) 1513–1515, https://doi.org/10.1126/science.1177031.
[21] M. Decker, R. Zhao, C.M. Soukoulis, S. Linden, M. Wegener, Twisted split-ring-resonator photonic metamaterial with huge optical activity, Optics Letters 35 (10) (2010) 1593, https://doi.org/10.1364/ol.35.001593.
[22] K. Dietrich, C. Menzel, D. Lehr, O. Puffky, U. Hübner, T. Pertsch, A. Tünnermann, E.-B. Kley, Elevating optical activity: efficient on-edge lithography of three-dimensional starfish metamaterial, Applied Physics Letters 104 (19) (2014) 193107, https://doi.org/10.1063/1.4876964.
[23] M.V. Gorkunov, A.A. Ezhov, V.V. Artemov, O.Y. Rogov, S.G. Yudin, Extreme optical activity and circular dichroism of chiral metal hole arrays, Applied Physics Letters 104 (22) (2014) 221102, https://doi.org/10.1063/1.4880798.
[24] M. Esposito, V. Tasco, F. Todisco, M. Cuscunà, A. Benedetti, D. Sanvitto, A. Passaseo, Triple-helical nanowires by tomographic rotatory growth for chiral photonics, Nature Communications 6 (1) (2015) 6484, https://doi.org/10.1038/ncomms7484.
[25] A.V. Kondratov, M.V. Gorkunov, A.N. Darinskii, R.V. Gainutdinov, O.Y. Rogov, A.A. Ezhov, V.V. Artemov, Extreme optical chirality of plasmonic nanohole arrays due to chiral Fano resonance, Physical Review B 93 (19) (2016) 195418, https://doi.org/10.1103/physrevb.93.195418.

[26] A.B. Evlyukhin, C. Reinhardt, A. Seidel, B.S. Luk'yanchuk, B.N. Chichkov, Optical response features of Si-nanoparticle arrays, Physical Review B 82 (4) (2010) 045404, https://doi.org/10.1103/physrevb.82.045404.
[27] A.I. Kuznetsov, A.E. Miroshnichenko, M.L. Brongersma, Y.S. Kivshar, B. Luk'yanchuk, Optically resonant dielectric nanostructures, Science 354 (6314) (2016) aag2472, https://doi.org/10.1126/science.aag2472.
[28] W.T. Chen, F. Capasso, Will flat optics appear in everyday life anytime soon?, Applied Physics Letters 118 (10) (2021) 100503, https://doi.org/10.1063/5.0039885.
[29] M. Kenney, S. Li, X. Zhang, X. Su, T.-T. Kim, D. Wang, D. Wu, C. Ouyang, J. Han, W. Zhang, H. Sun, S. Zhang, Pancharatnam–Berry phase induced spin-selective transmission in herringbone dielectric metamaterials, Advanced Materials 28 (43) (2016) 9567–9572, https://doi.org/10.1002/adma.201603460.
[30] J.B. Mueller, N.A. Rubin, R.C. Devlin, B. Groever, F. Capasso, Metasurface polarization optics: independent phase control of arbitrary orthogonal states of polarization, Physical Review Letters 118 (11) (2017) 113901, https://doi.org/10.1103/physrevlett.118.113901.
[31] A.Y. Zhu, W.T. Chen, A. Zaidi, Y.-W. Huang, M. Khorasaninejad, V. Sanjeev, C.-W. Qiu, F. Capasso, Giant intrinsic chiro-optical activity in planar dielectric nanostructures, Light: Science & Applications 7 (2) (2017) 17158, https://doi.org/10.1038/lsa.2017.158.
[32] F. Zhang, M. Pu, X. Li, P. Gao, X. Ma, J. Luo, H. Yu, X. Luo, All-dielectric metasurfaces for simultaneous giant circular asymmetric transmission and wavefront shaping based on asymmetric photonic spin-orbit interactions, Advanced Functional Materials 27 (47) (2017) 1704295, https://doi.org/10.1002/adfm.201704295.
[33] R. Verre, L. Shao, N.O. Länk, P. Karpinski, A.B. Yankovich, T.J. Antosiewicz, E. Olsson, M. Käll, Metasurfaces and colloidal suspensions composed of 3D chiral Si nanoresonators, Advanced Materials 29 (29) (2017) 1701352, https://doi.org/10.1002/adma.201701352.
[34] M.V. Gorkunov, O.Y. Rogov, A.V. Kondratov, V.V. Artemov, R.V. Gainutdinov, A.A. Ezhov, Chiral visible light metasurface patterned in monocrystalline silicon by focused ion beam, Scientific Reports 8 (1) (2018) 11623, https://doi.org/10.1038/s41598-018-29977-4.
[35] E. Arbabi, S.M. Kamali, A. Arbabi, A. Faraon, Full-Stokes imaging polarimetry using dielectric metasurfaces, ACS Photonics 5 (8) (2018) 3132–3140, https://doi.org/10.1021/acsphotonics.8b00362.
[36] I. Karakasoglu, M. Xiao, S. Fan, Polarization control with dielectric helix metasurfaces and arrays, Optics Express 26 (17) (2018) 21664, https://doi.org/10.1364/oe.26.021664.
[37] F.R. Gómez, J.R. Mejía-Salazar, P. Albella, All-dielectric chiral metasurfaces based on crossed-bowtie nanoantennas, ACS Omega 4 (25) (2019) 21041–21047, https://doi.org/10.1021/acsomega.9b02381.
[38] Q. Fan, M. Liu, C. Zhang, W. Zhu, Y. Wang, P. Lin, F. Yan, L. Chen, H. Lezec, Y. Lu, A. Agrawal, T. Xu, Independent amplitude control of arbitrary orthogonal states of polarization via dielectric metasurfaces, Physical Review Letters 125 (26) (2020) 267402, https://doi.org/10.1103/physrevlett.125.267402.
[39] B. Semnani, J. Flannery, R. Al Maruf, M. Bajcsy, Spin-preserving chiral photonic crystal mirror, Light: Science & Applications 9 (1) (2020) 23, https://doi.org/10.1038/s41377-020-0256-5.
[40] A.S. Rana, I. Kim, M.A. Ansari, M.S. Anwar, M. Saleem, T. Tauqeer, A. Danner, M. Zubair, M.Q. Mehmood, J. Rho, Planar achiral metasurfaces-induced anomalous chiroptical effect of optical spin isolation, ACS Applied Materials

& Interfaces 12 (43) (2020) 48899–48909, https://doi.org/10.1021/acsami.0c10006.

[41] Q. Song, A. Baroni, R. Sawant, P. Ni, V. Brandli, S. Chenot, S. Vézian, B. Damilano, P. de Mierry, S. Khadir, P. Ferrand, P. Genevet, Ptychography retrieval of fully polarized holograms from geometric-phase metasurfaces, Nature Communications 11 (1) (2020) 2651, https://doi.org/10.1038/s41467-020-16437-9.

[42] K. Tanaka, D. Arslan, S. Fasold, M. Steinert, J. Sautter, M. Falkner, T. Pertsch, M. Decker, I. Staude, Chiral bilayer all-dielectric metasurfaces, ACS Nano 14 (11) (2020) 15926–15935, https://doi.org/10.1021/acsnano.0c07295.

[43] S.A. Dyakov, N.A. Gippius, I.M. Fradkin, S.G. Tikhodeev, Vertical routing of spinning-dipole radiation from a chiral metasurface, Physical Review Applied 14 (2) (2020) 024090, https://doi.org/10.1103/physrevapplied.14.024090.

[44] M.V. Gorkunov, A.A. Antonov, Y.S. Kivshar, Metasurfaces with maximum chirality empowered by bound states in the continuum, Physical Review Letters 125 (9) (2020) 093903, https://doi.org/10.1103/physrevlett.125.093903.

[45] M.V. Gorkunov, A.A. Antonov, V.R. Tuz, A.S. Kupriianov, Y.S. Kivshar, Bound states in the continuum underpin near-lossless maximum chirality in dielectric metasurfaces, Advanced Optical Materials (2021) 2100797, https://doi.org/10.1002/adom.202100797.

[46] Z. Yue, C. Zheng, J. Li, J. Li, J. Liu, G. Wang, M. Chen, H. Xu, Q. Tan, H. Zhang, Y. Zhang, Y. Zhang, J. Yao, A dual band spin-selective transmission metasurface and its wavefront manipulation, Nanoscale 13 (24) (2021) 10898–10905, https://doi.org/10.1039/d1nr02624k.

[47] H.S. Khaliq, I. Kim, A. Zahid, J. Kim, T. Lee, T. Badloe, Y. Kim, M. Zubair, K. Riaz, M.Q. Mehmood, J. Rho, Giant chiro-optical responses in multipolar-resonances-based single-layer dielectric metasurfaces, Photonics Research 9 (9) (2021) 1667, https://doi.org/10.1364/prj.424477.

[48] T. Shi, Z.-L. Deng, G. Geng, X. Zeng, Y. Zeng, G. Hu, A. Overvig, J. Li, C.-W. Qiu, A. Alù, Y.S. Kivshar, X. Li, Planar chiral metasurfaces with maximal and tunable chiroptical response driven by bound states in the continuum, Nature Communications 13 (1) (2022) 4111, https://doi.org/10.1038/s41467-022-31877-1.

[49] J. Li, J. Li, C. Zheng, Z. Yue, S. Wang, M. Li, H. Zhao, Y. Zhang, J. Yao, Active controllable spin-selective terahertz asymmetric transmission based on all-silicon metasurfaces, Applied Physics Letters 118 (22) (2021) 221110, https://doi.org/10.1063/5.0053236.

[50] S. Wang, Z.-L. Deng, Y. Wang, Q. Zhou, X. Wang, Y. Cao, B.-O. Guan, S. Xiao, X. Li, Arbitrary polarization conversion dichroism metasurfaces for all-in-one full Poincaré sphere polarizers, Light: Science & Applications 10 (1) (2021) 24, https://doi.org/10.1038/s41377-021-00468-y.

[51] G. Long, G. Adamo, J. Tian, M. Klein, H.N.S. Krishnamoorthy, E. Feltri, H. Wang, C. Soci, Perovskite metasurfaces with large superstructural chirality, Nature Communications 13 (1) (2022) 1551, https://doi.org/10.1038/s41467-022-29253-0.

[52] K. Voronin, A.S. Taradin, M.V. Gorkunov, D.G. Baranov, Single-handedness chiral optical cavities, ACS Photonics 9 (8) (2022) 2652–2659, https://doi.org/10.1021/acsphotonics.2c00134.

[53] X. Zhang, Y. Liu, J. Han, Y. Kivshar, Q. Song, Chiral emission from resonant metasurfaces, Science 377 (6611) (2022) 1215–1218, https://doi.org/10.1126/science.abq7870.

[54] K. Koshelev, Y. Tang, Z. Hu, I.I. Kravchenko, G. Li, Y. Kivshar, Resonant chiral effects in nonlinear dielectric metasurfaces, ACS Photonics 10 (1) (2023) 298–306, https://doi.org/10.1021/acsphotonics.2c01926.

[55] C. Menzel, C. Rockstuhl, F. Lederer, Advanced Jones calculus for the classification of periodic metamaterials, Physical Review A 82 (5) (2010) 053811, https://doi.org/10.1103/physreva.82.053811.

[56] M.V. Gorkunov, V.E. Dmitrienko, A.A. Ezhov, V.V. Artemov, O.Y. Rogov, Implications of the causality principle for ultra chiral metamaterials, Scientific Reports 5 (1) (2015) 9273, https://doi.org/10.1038/srep09273.

[57] I. Fernandez-Corbaton, M. Fruhnert, C. Rockstuhl, Objects of maximum electromagnetic chirality, Physical Review X 6 (3) (2016) 031013, https://doi.org/10.1103/physrevx.6.031013.

[58] W. Chen, Q. Yang, Y. Chen, W. Liu, Extremize optical chiralities through polarization singularities, Physical Review Letters 126 (25) (2021) 253901, https://doi.org/10.1103/physrevlett.126.253901.

[59] X. Garcia-Santiago, S. Burger, C. Rockstuhl, I. Fernandez-Corbaton, Measuring the electromagnetic chirality of 2D arrays under normal illumination, Optics Letters 42 (20) (2017) 4075, https://doi.org/10.1364/ol.42.004075.

[60] L. Kühner, F.J. Wendisch, A.A. Antonov, J. Bürger, L. Hüttenhofer, L. de S. Menezes, S.A. Maier, M.V. Gorkunov, Y. Kivshar, A. Tittl, Unlocking the out-of-plane dimension for photonic bound states in the continuum to achieve maximum optical chirality, arXiv:2210.05339, 2022.

[61] E. Plum, N.I. Zheludev, Chiral mirrors, Applied Physics Letters 106 (22) (2015) 221901, https://doi.org/10.1063/1.4921969.

[62] C. Hermann, Tensoren und Kristallsymmetrie, Zeitschrift für Kristallographie - Crystalline Materials 89 (1–6) (1934) 32–48, https://doi.org/10.1524/zkri.1934.89.1.32.

[63] S. Fan, W. Suh, J.D. Joannopoulos, Temporal coupled-mode theory for the Fano resonance in optical resonators, Journal of the Optical Society of America A 20 (3) (2003) 569, https://doi.org/10.1364/josaa.20.000569.

[64] W. Suh, Z. Wang, S. Fan, Temporal coupled-mode theory and the presence of non-orthogonal modes in lossless multimode cavities, IEEE Journal of Quantum Electronics 40 (10) (2004) 1511–1518, https://doi.org/10.1109/jqe.2004.834773.

[65] K. Koshelev, S. Lepeshov, M. Liu, A. Bogdanov, Y. Kivshar, Asymmetric metasurfaces with high-Q resonances governed by bound states in the continuum, Physical Review Letters 121 (19) (2018) 193903, https://doi.org/10.1103/physrevlett.121.193903.

[66] C.W. Hsu, B.G. DeLacy, S.G. Johnson, J.D. Joannopoulos, M. Soljačić, Theoretical criteria for scattering dark states in nanostructured particles, Nano Letters 14 (5) (2014) 2783–2788, https://doi.org/10.1021/nl500340n.

[67] P.T. Kristensen, S. Hughes, Modes and mode volumes of leaky optical cavities and plasmonic nanoresonators, ACS Photonics 1 (1) (2013) 2–10, https://doi.org/10.1021/ph400114e.

[68] B. Hopkins, A.N. Poddubny, A.E. Miroshnichenko, Y.S. Kivshar, Circular dichroism induced by Fano resonances in planar chiral oligomers, Laser & Photonics Reviews 10 (1) (2015) 137–146, https://doi.org/10.1002/lpor.201500222.

[69] F. Alpeggiani, N. Parappurath, E. Verhagen, L. Kuipers, Quasinormal-mode expansion of the scattering matrix, Physical Review X 7 (2) (2017) 021035, https://doi.org/10.1103/physrevx.7.021035.

[70] P.T. Leung, S.Y. Liu, K. Young, Completeness and orthogonality of quasinormal modes in leaky optical cavities, Physical Review A 49 (4) (1994) 3057–3067, https://doi.org/10.1103/physreva.49.3057.

[71] H.A. Haus, Waves and Fields in Optoelectronics, Prentice-Hall, Englewood Cliffs, NJ, 1984.

[72] C.W. Hsu, B. Zhen, A.D. Stone, J.D. Joannopoulos, M. Soljačić, Bound states in the continuum, Nature Reviews Materials 1 (9) (2016) 16048, https://doi.org/10.1038/natrevmats.2016.48.

[73] V.A. Fedotov, M. Rose, S.L. Prosvirnin, N. Papasimakis, N.I. Zheludev, Sharp trapped-mode resonances in planar metamaterials with a broken structural symmetry, Physical Review Letters 99 (14) (2007) 147401, https://doi.org/10.1103/physrevlett.99.147401.

[74] P. Banzer, P. Woźniak, U. Mick, I.D. Leon, R.W. Boyd, Chiral optical response of planar and symmetric nanotrimers enabled by heteromaterial selection, Nature Communications 7 (1) (2016) 13117, https://doi.org/10.1038/ncomms13117.

[75] K. Ullah, B. Garcia-Camara, M. Habib, X. Liu, A. Krasnok, S. Lepeshov, J. Hao, J. Liu, N.P. Yadav, Chiral all-dielectric trimer nanoantenna, Journal of Quantitative Spectroscopy & Radiative Transfer 208 (2018) 71–77, https://doi.org/10.1016/j.jqsrt.2018.01.015.

[76] L. Lin, S. Lepeshov, A. Krasnok, T. Jiang, X. Peng, B.A. Korgel, A. Alù, Y. Zheng, All-optical reconfigurable chiral meta-molecules, Materials Today 25 (2019) 10–20, https://doi.org/10.1016/j.mattod.2019.02.015.

[77] R. Zheng, R. Pan, C. Sun, S. Du, A. Jin, C. Li, G. Geng, C. Gu, J. Li, Bidirectional origami inspiring versatile 3D metasurface, Advanced Materials Technologies 7 (8) (2022) 2200373, https://doi.org/10.1002/admt.202200373.

[78] A. Passaseo, M. Esposito, M. Cuscunà, V. Tasco, Materials and 3D designs of helix nanostructures for chirality at optical frequencies, Advanced Optical Materials 5 (16) (2017) 1601079, https://doi.org/10.1002/adom.201601079.

[79] J.C.W. Lee, C.T. Chan, Polarization gaps in spiral photonic crystals, Optics Express 13 (20) (2005) 8083, https://doi.org/10.1364/opex.13.008083.

[80] T.-H. Kao, L.-Y.C. Chien, Y.-C. Hung, Dual circular polarization gaps in helix photonic metamaterials, Optics Express 23 (19) (2015) 24416, https://doi.org/10.1364/oe.23.024416.

[81] M. Thiel, M. Decker, M. Deubel, M. Wegener, S. Linden, G. von Freymann, Polarization stop bands in chiral polymeric three-dimensional photonic crystals, Advanced Materials 19 (2) (2007) 207–210, https://doi.org/10.1002/adma.200601497.

[82] M. Esposito, M. Manoccio, A. Leo, M. Cuscunà, Y. Sun, E. Ageev, D. Zuev, A. Benedetti, I. Tarantini, A. Passaseo, V. Tasco, 3D chiral MetaCrystals, Advanced Functional Materials 32 (12) (2021) 2109258, https://doi.org/10.1002/adfm.202109258.

[83] M. Hentschel, M. Schäferling, X. Duan, H. Giessen, N. Liu, Chiral plasmonics, Science Advances 3 (5) (2017) e1602735, https://doi.org/10.1126/sciadv.1602735.

[84] R. Pan, Z. Li, Z. Liu, W. Zhu, L. Zhu, Y. Li, S. Chen, C. Gu, J. Li, Rapid bending origami in micro/nanoscale toward a versatile 3D metasurface, Laser & Photonics Reviews 14 (1) (2019) 1900179, https://doi.org/10.1002/lpor.201900179.

[85] H.H. Li, Refractive index of silicon and germanium and its wavelength and temperature derivatives, Journal of Physical and Chemical Reference Data 9 (3) (1980) 561–658, https://doi.org/10.1063/1.555624.

[86] D.G. Baranov, C. Schäfer, M.V. Gorkunov, Toward Molecular Chiral Polaritons, ACS Photonics (2023) acsphotonics.2c02011, https://doi.org/10.1021/acsphotonics.2c02011.
[87] C. Huang, C. Zhang, S. Xiao, Y. Wang, Y. Fan, Y. Liu, N. Zhang, G. Qu, H. Ji, J. Han, L. Ge, Y. Kivshar, Q. Song, Ultrafast control of vortex microlasers, Science 367 (6481) (2020) 1018–1021, https://doi.org/10.1126/science.aba4597.
[88] Y. Fan, P. Tonkaev, Y. Wang, Q. Song, J. Han, S.V. Makarov, Y. Kivshar, S. Xiao, Enhanced multiphoton processes in perovskite metasurfaces, Nano Letters 21 (17) (2021) 7191–7197, https://doi.org/10.1021/acs.nanolett.1c02074.
[89] K. Koshelev, S. Kruk, E. Melik-Gaykazyan, J.-H. Choi, A. Bogdanov, H.-G. Park, Y. Kivshar, Subwavelength dielectric resonators for nonlinear nanophotonics, Science 367 (6475) (2020) 288–292, https://doi.org/10.1126/science.aaz3985.

10

Transparent phase dielectric metasurfaces

Willie J. Padilla[a] **and Kebin Fan**[b]

[a] *Department of Electrical and Computer Engineering, Duke University, Durham, NC, United States.* [b] *School of Electronic Science and Engineering, Nanjing University, Nanjing, Jiangsu, China*

10.1 Introduction

Transparent phase dielectric metasurfaces represent a cutting-edge innovation in the field of optics, with their potential to transform the landscape of optical materials and devices being immense. These versatile structures consist of subwavelength dielectric elements, which enable fine-tuned manipulation of the phase, amplitude, and polarization of light. This remarkable control over light-matter interactions opens up a wealth of possibilities for applications in various domains, from telecommunications to defense systems. In recent years, a diverse range of transparent phase dielectric metasurfaces have been developed, with each type possessing distinct properties and potential use cases. As interest in these novel structures continues to grow, so does the need for a comprehensive understanding of their underlying principles, recent breakthroughs, and potential applications. This chapter aims to provide readers with an in-depth look at these metasurfaces, offering a detailed examination of their fundamental concepts and exploring their potential to revolutionize the field of optics.

The chapter commences with an introduction to simple harmonic oscillator and coupled oscillator models, which play a crucial role in understanding the principles that govern the design of transparent phase Fano dielectric metasurfaces. In later chapters, we also introduce the surface equivalence principle, temporal coupled mode theory, and multipole decomposition models, which shed light on the behavior of the subwavelength dielectric elements that constitute the metasurfaces, allowing researchers to pinpoint the specific resonant modes that can be excited to manipulate light in a variety of ways. By establishing a solid theo-

All-Dielectric Nanophotonics. https://doi.org/10.1016/B978-0-32-395195-1.00015-6
Copyright © 2024 Elsevier Ltd. All rights reserved.

retical foundation, readers will be able to better grasp the complex interactions at play in these metasurfaces and the design principles that enable their unique capabilities. Additionally, these models provide valuable insights into the fundamental properties of light-matter interactions and enable researchers to make informed decisions when selecting materials and designing metasurface architectures. With this foundation in place, we can delve deeper into the design principles of different metasurface types and gain a better appreciation of their unique characteristics and functionalities.

We cover several types of transparent phase dielectric metasurfaces, including Fano metasurfaces, Huygens metasurfaces, transverse Kerker metasurfaces, hybrid anapole metasurfaces, and Pancharatnam–Berry phase metasurfaces. Each metasurface type operates based on distinct principles and possesses unique features, making them suitable for a wide array of applications. We provide an in-depth discussion of the fundamental physics governing each metasurface, highlighting their individual strengths and limitations. Furthermore, recent advancements in the design and fabrication of these metasurfaces are explored, showcasing the remarkable progress that has been made in recent years. Potential applications for each metasurface type are presented, emphasizing their use in diverse domains such as imaging, sensing, and communication technologies. This comprehensive analysis will enable readers to appreciate the breadth of possibilities offered by these innovative structures.

In summary, this chapter endeavors to equip readers with a thorough understanding of the state-of-the-art in transparent phase dielectric metasurfaces. Our goal is to inspire continued research in this exhilarating field, ultimately contributing to the development of novel optical materials and devices that boast unprecedented capabilities. As a potentially revolutionary force in the realm of optical technology, transparent phase dielectric metasurfaces present a compelling avenue for researchers to investigate and develop groundbreaking applications that can significantly impact numerous industries. By providing a detailed overview of these metasurfaces, their underlying principles, and their many potential applications, we hope to spark further interest and innovation in this rapidly evolving field, paving the way for new discoveries and advancements that will reshape the future of optics.

10.1.1 Harmonic oscillator models

The classical theory of the response of bound and free charges to electromagnetic waves in solids is primarily due to Hendrik

Lorentz and Paul Drude, respectively. The electromagnetic properties of an insulator are well described by the Lorentz model, and the Drude model is equally applicable to conductors. The Lorentz model is that of a driven damped harmonic oscillator, where electrons are bound to their respective cores by harmonic forces and are subjected to external applied harmonic fields. On the other hand, the basic assumption of the Drude model is that valence electrons are free to move about like a gas of electrons. A further assumption of the Drude model is that the ion cores are immobile and provide a scattering mechanism for electrons so as to bring them into thermal equilibrium. The kinetic theory of gases is then used in the Drude model to describe the free electron gas.

Although the models of both Lorentz and Drude are phenomenological – as originally derived – the Drude model may be derived semi-classically from the Boltzmann transport equation with approximating the collision integral with a single collision frequency [1], or from the Kubo formula by assuming exponential decay of the current-current correlation function (relaxation time approximation) [2]. Both the Drude and Lorentz models may be derived from a quantum mechanical approach [3–5]. Thus the quantum mechanical equivalent models are viewed as generalizations of their classical counterparts [4]. Indeed since quantum theory is first principles, it is viewed as the fundamental theory which describes the response of atoms, molecules, liquids, and solids to electromagnetic fields. Notably, the polarizabilities, and therefore the permittivity and permeability, derived from quantum theory is the same form shown by Lorentz in a classical approach [4,5]. The Lorentz model therefore includes direct interband transitions, with no change in k-vector, and the Drude model includes intraband transitions as well. Therefore, the phenomenological Drude and Lorentz models are more fundamental than they initially appear, and accurately describe the properties of natural [6] and artificial materials [7,8], although in some cases the models are extended to describe more complex materials [9,10].

A Drude–Lorentz oscillator for the relative permittivity ϵ_r is written as:

$$\epsilon_r(\omega) = \epsilon_\infty + \sum_{i=1}^{N} \frac{\omega_{p,i}^2}{\omega_{0,i}^2 - \omega^2 - i\gamma_i\omega}, \tag{10.1}$$

where the sum is over N oscillators, $\omega_p = \sqrt{ne^2/\epsilon_0 m}$ is the plasma frequency, ω_0 is the center frequency, γ is the damping frequency, and ϵ_∞ are contributions to the relative permittivity that occur at higher frequencies. The Drude portion of the response is obtained

by setting $\omega_0 = 0$ for one oscillator with an appropriate oscillator strength ω_p, while the Lorentz terms are given by $\omega_0 \neq 0$.

The classical Drude–Lorentz form, shown in Eq. (10.1), is derived from a driven damped harmonic oscillator model of an electron (mass m and charge e), bound to a nucleus. A similar approach may be used to derive the general form of a Drude–Lorentz–Fano oscillator by considering two coupled driven damped harmonic oscillators:

$$\ddot{\mathbf{r}}_1 + \gamma_1 \dot{\mathbf{r}}_1 + \omega_1^2 \mathbf{r}_1 + \nu_{12} \mathbf{r}_2 = \mathbf{F}/m_1, \tag{10.2}$$

$$\ddot{\mathbf{r}}_2 + \gamma_2 \dot{\mathbf{r}}_2 + \omega_2^2 \mathbf{r}_2 + \nu_{12} \mathbf{r}_2 = \mathbf{F}/m_2, \tag{10.3}$$

where ω_i and γ_i are the center frequency, and damping frequency of the ith oscillator ($i = 1, 2$), $\mathbf{F}$ is the driving force, and ν_{12} is the coupling strength. The correspondence with the Fano model here is that Eq. (10.2) represents a resonance with coupling (ν_{12}) to a continuum, which is represented by Eq. (10.3). If the position vectors $\mathbf{r}_i$ and driving force $\mathbf{F}$ are taken to vary in time as $e^{-i\omega t}$, then the solutions to Eqs. (10.2) and (10.3) are:

$$\mathbf{r}_1 = \frac{\mathbf{F}/m_1 - \nu_{12}\mathbf{r}_2}{\omega_1^2 - \omega^2 - i\gamma_1\omega}, \tag{10.4}$$

$$\mathbf{r}_2 = \frac{\mathbf{F}/m_2 - \nu_{12}\mathbf{r}_1}{\omega_2^2 - \omega^2 - i\gamma_2\omega}, \tag{10.5}$$

which we can write as:

$$\mathbf{r}_1 = \mathbf{F}\frac{\Gamma_2/m_1 - \nu_{12}/m_2}{\Gamma_1\Gamma_2 - \nu_{12}^2}, \tag{10.6}$$

$$\mathbf{r}_2 = \mathbf{F}\frac{\Gamma_1/m_2 - \nu_{12}/m_1}{\Gamma_1\Gamma_2 - \nu_{12}^2}, \tag{10.7}$$

where $\Gamma_1 \equiv \omega_1^2 - \omega^2 - i\gamma_1\omega$ and $\Gamma_2 \equiv \omega_2^2 - \omega^2 - i\gamma_2\omega$. The polarization is:

$$\mathbf{P} = \epsilon_0 \chi_e \mathbf{E} = \epsilon_0(\epsilon_r - 1)\mathbf{E} = -ne\mathbf{r}, \tag{10.8}$$

where χ_e is the electric susceptibility, n is the number density, and $\mathbf{r} = \mathbf{r}_1 + \mathbf{r}_2$. Thus, substituting the position vectors from Eqs. (10.6) and (10.7) into Eq. (10.8), and considering a driving force of the form $\mathbf{F} = -e\mathbf{E}$, we find a form for a Drude–Lorentz–Fano oscillator as:

$$\epsilon_r(\omega) = \epsilon_\infty + \frac{\Gamma_2\omega_{p,1}^2 - \nu_{12}\omega_{p,2}^2}{\Gamma_1\Gamma_2 - \nu_{12}^2} + \frac{\Gamma_1\omega_{p,2}^2 - \nu_{12}\omega_{p,1}^2}{\Gamma_1\Gamma_2 - \nu_{12}^2}, \tag{10.9}$$

where $\omega_{p,i}$ is the plasma frequency of the ith oscillator ($i = 1, 2$), and we have made the substitution $1 \rightarrow \epsilon_\infty$ to match Eq. (10.1) and for a more general model. Notice that if the coupling between the two oscillators is zero ($\nu_{12} = 0$), then Eq. (10.9) reduces to the standard Drude–Lorentz oscillator Eq. (10.1), with $N = 2$.

10.2 Fano metasurfaces

In some dielectric and metallic metamaterials, the resonant lineshape may take on an asymmetric character, which is commonly referred to as a Fano resonance. Fano resonances are general and arise due to the interference between a resonance (discrete state) and a background continuum [11], and experiments in 1965 showed resulting transparency windows in the autoionizing spectrum of helium [12]. However, the Fano resonance is a general phenomenon and thus can be found in numerous electromagnetic systems as well [13]. For example, although the original lineshape was proposed to describe the photo-absorption cross-section, the frequency (energy) dependence of the Fano resonance exhibits a universal form given as:

$$\sigma = \frac{(\Omega + q)^2}{\Omega^2 + 1}, \tag{10.10}$$

where:

$$\Omega = \frac{2\hbar}{\gamma}(\omega - \omega_0), \tag{10.11}$$

is the reduced energy, and ω_0 and γ are the center frequency and damping frequency (linewidth), respectively, of the discrete state. It is evident that Eq. (10.10) realizes only two extrema, with a minima and maxima occurring at:

$$\omega_{min} = \omega_0 - \gamma\frac{q}{2\hbar}, \tag{10.12}$$

$$\omega_{max} = \omega_0 + \gamma\frac{1}{2\hbar q}. \tag{10.13}$$

The parameter q is related to the inverse of the strength of the interaction between the discrete state and the continuum, and is termed the *asymmetry parameter*, which can vary from $-\infty \leq q \leq \infty$, see Fig. 10.1. The particular form of the asymmetry corresponds to the energy range that the resonance (discrete state) is coupled. For example, a line shape that dips on the low-frequency (low-energy) side of the resonant frequency ω_0 indicates the discrete state interacts with a continuum at higher energies, where the sign of q is positive, in this case – Fig. 10.1 (a). For $1/q = 0$,

a symmetric line shape is recovered – see, for example, Fig. 10.1 (b) – where the lineshapes are increasingly more symmetric for decreasing values of $1/q$.

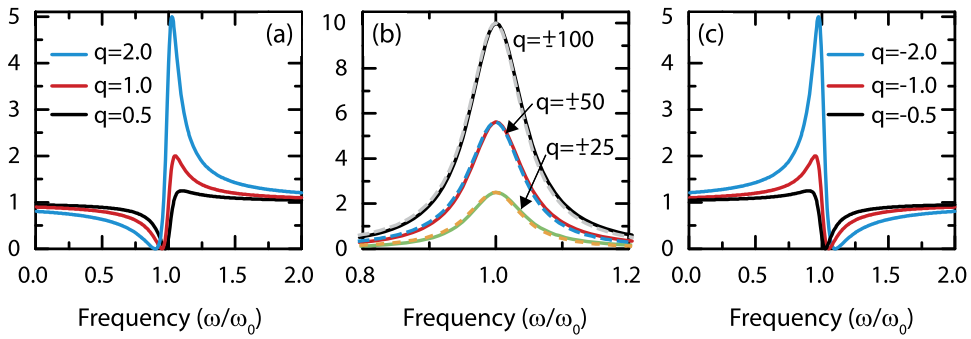

Figure 10.1. Plots of the normalized frequency dependence of the Fano asymmetry parameter q for (a) positive small values, (b) large positive and negative values, and (c) small negative values. In (b), the solid curves correspond to positive q values, and the dashed curves to negative q. The vertical scale in (b) should be scaled $\times 10^3$.

In the literature, Fano resonances in metamaterials and metasurfaces have also been associated with electromagnetic-induced transparency (EIT) [14–17]. Electromagnetically induced transparency is a coherent quantum phenomenon and has been observed in three-level atomic systems [18]. Here, the response of an atomic system to coherent light at a given "coupling" energy $\hbar\omega_c$ modifies the system permitting transmission of coherent light at a second "probe" energy $\hbar\omega_{probe}$ [19,20]. There are three possible arrangements of atomic levels which permit EIT, and are termed *Ladder*, *Lambda*, and *Vee*. However, they have in common that both ω_c and ω_{probe} are dipole allowed states, whereas $|\omega_{probe} \pm \omega_c|$ is dipole forbidden.

Care should be given when describing resonances as "Fano", since many materials, optical, or scattering parameter lineshapes naturally possess an asymmetric form as a function of frequency or wavelength. For example, the reflection coefficient $r(\omega)$, transmission coefficient $t(\omega)$, reflectivity $R(\omega)$, and transmissivity $T(\omega)$ are all frequency-dependent scattering functions, which are bounded, and thus may appear asymmetric. For example, $R(\omega)$ and $T(\omega)$ are constrained to lie between 0 and 1, and thus when there are multiple resonances with similar resonance frequencies, the lineshape may take on an asymmetric form.

As mentioned, the Fano resonance consists of a discrete resonant state coupled to a continuum. In the literature, a Fano model was derived where $\mathbf{F}_2 = 0$, and assuming $\gamma_2 = 0$ in Eq. (10.9), where the approximation $\nu_{12}/(\omega_2^2 - \omega_1^2) << 1$ was used [21]. Following

reference [21], we may rewrite Eq. (10.9) (with the above assumptions) by defining two parameters $q = (\omega_2^2 - \omega_1^2)/(\gamma_1\omega_2)$ and a reduced energy $\Omega = q\left[(\omega_2^2 - \omega_1^2)(\omega^2 - \omega_2^2) - \nu_{12}^2\right]/\nu_{12}^2$,

$$\epsilon_r(\omega) = 1 + \frac{\Omega + q}{\Omega + i}\frac{\omega_{p,1}^2}{\omega_1^2 - \omega_2^2} \tag{10.14}$$

We therefore find that $|\epsilon_r(\omega)|^2$ is of the same form as the Fano equation shown in Eq. (10.10).

10.3 Huygens metasurfaces

Huygens' principle was proposed over three centuries ago and treats every point touched by a wave as a source itself of re-radiating spherical waves (in the forward direction only), where the sum of the secondary waves determines the new wavefront. In the 19th century, Fresnel showed that Huygens' principle, when combined with the principle of interference, can explain wave propagation as the interference of waves emanating from secondary sources on the wavefront, and therefore not only explained rectilinear propagation, but also diffraction. An approximation of both approaches is that these secondary sources have different phases but possess unitary transmission [22]. A more rigorous formulation of Huygens' principle was introduced by Schelkunoff in 1936 and is termed the surface equivalence theorem [23]. This theorem demonstrates that radiating fields outside an imaginary closed surface can be obtained by placing surface electric and magnetic-current density over the closed surface, as long as the boundary conditions are met. Consequently, radiating fields can be determined by the surface sources alone. In both the microwave and optical regimes, several examples have been created and demonstrated the capability to mimic artificial surface sources, including phased array antennas and diffractive gratings. However, the large size of these diffractive structures can result in strong sidelobe radiation, reducing the efficiency of Huygens' sources for beam forming and steering, among other applications.

In recent years, metasurfaces have emerged as a promising option to create artificial surface sources. These surfaces are made up of two-dimensional subwavelength meta-atoms that can be modeled as effective electric and magnetic dipoles on a planar surface. Due to the subwavelength spacing of the dipoles, the surface can be homogenized as a Schelkunoff surface with spatially varying electric and magnetic current sources. Through modification of the geometry, material properties, and spatial arrangement of the meta-atoms, metasurfaces enable the manipulation of sub-

wavelength scatters to reshape the electromagnetic wavefront. For example, when the electric and magnetic dipoles are orthogonal and possess in-phase and matched amplitude response, as shown in Fig. 10.2 (a), metasurfaces can exhibit unidirectional forward radiation with significantly suppressed backscattering, effectively achieving a transparent phase. These metasurfaces are commonly referred to as Huygens' metasurfaces (HMSs), which satisfy the first Kerker condition [24,25]. Through spatially engineering the Huygens' meta-atoms, HMSs have demonstrated intriguing phenomena for wavefront control, including anomalous refraction [26,27], focusing [28], holograms [29], and active electromagnetic cloaking [30,31].

We first begin with a simple analytical description of Huygens' metasurfaces. The metasurface depicted in Fig. 10.2 (a) can support both electric and magnetic response, and therefore a linear x-polarized incident wave (as shown) will induce electric and magnetic polarization with effective dipole moments p_x and m_y, given as [32]:

$$\begin{aligned} \frac{1}{\varepsilon_0} p_x^{\pm} &= \hat{\alpha}_{ee}^{xx} E_i^x \pm \hat{\alpha}_{em}^{xy} \eta_0 H_i^y, \\ \eta_0 m_y^{\pm} &= \pm \hat{\alpha}_{me}^{yx} E_i^x + \hat{\alpha}_{mm}^{yy} \eta_0 H_i^y, \end{aligned} \tag{10.15}$$

where ϵ_0 is the vacuum permittivity, η_0 is the wave impedance of free space, $\pm$ indicates if the wave propagates in the $+z$ or $-z$ direction, respectively, $\hat{\alpha}_{ee}^{xx}$, $\hat{\alpha}_{mm}^{yy}$, $\hat{\alpha}_{em}^{xy}$ and $\hat{\alpha}_{me}^{yx}$ are effective (collective) electric, magnetic, magneto-electric and electro-magnetic polarizability components, which include the contributions from the electric and magnetic interactions [33]. The latter two terms denote the bianisotropy, which indicates that electric and magnetic responses can be excited by incident magnetic and electric fields, respectively. The relationship between the collective polarizabilities and the individual polarizabilities are given in the literature [32] and [34]. For linear metasurfaces, which observe time-reversal symmetry, the bianisotropic polarizabilities obey the Onsager-Casimir conditions with $\hat{\alpha}_{em}^{xy} = -(\hat{\alpha}_{me}^{yx})^T$, where T denotes the transpose operation [35]. For an arrayed metasurface with a square lattice size of a, the corresponding dipole density is $\rho = 1/a^2$. Under normal incidence and in the dipole limit approximation, which assumes that the response of high-order multipoles contributes negligibly, the reflection and transmission coefficients are [36–38]:

$$r^{\pm} = \frac{ik\rho}{2}(\hat{\alpha}_{ee} \mp 2\hat{\alpha}_{em} - \hat{\alpha}_{mm}), \tag{10.16}$$

$$t = 1 + \frac{ik\rho}{2}(\hat{\alpha}_{ee} + \hat{\alpha}_{mm}). \tag{10.17}$$

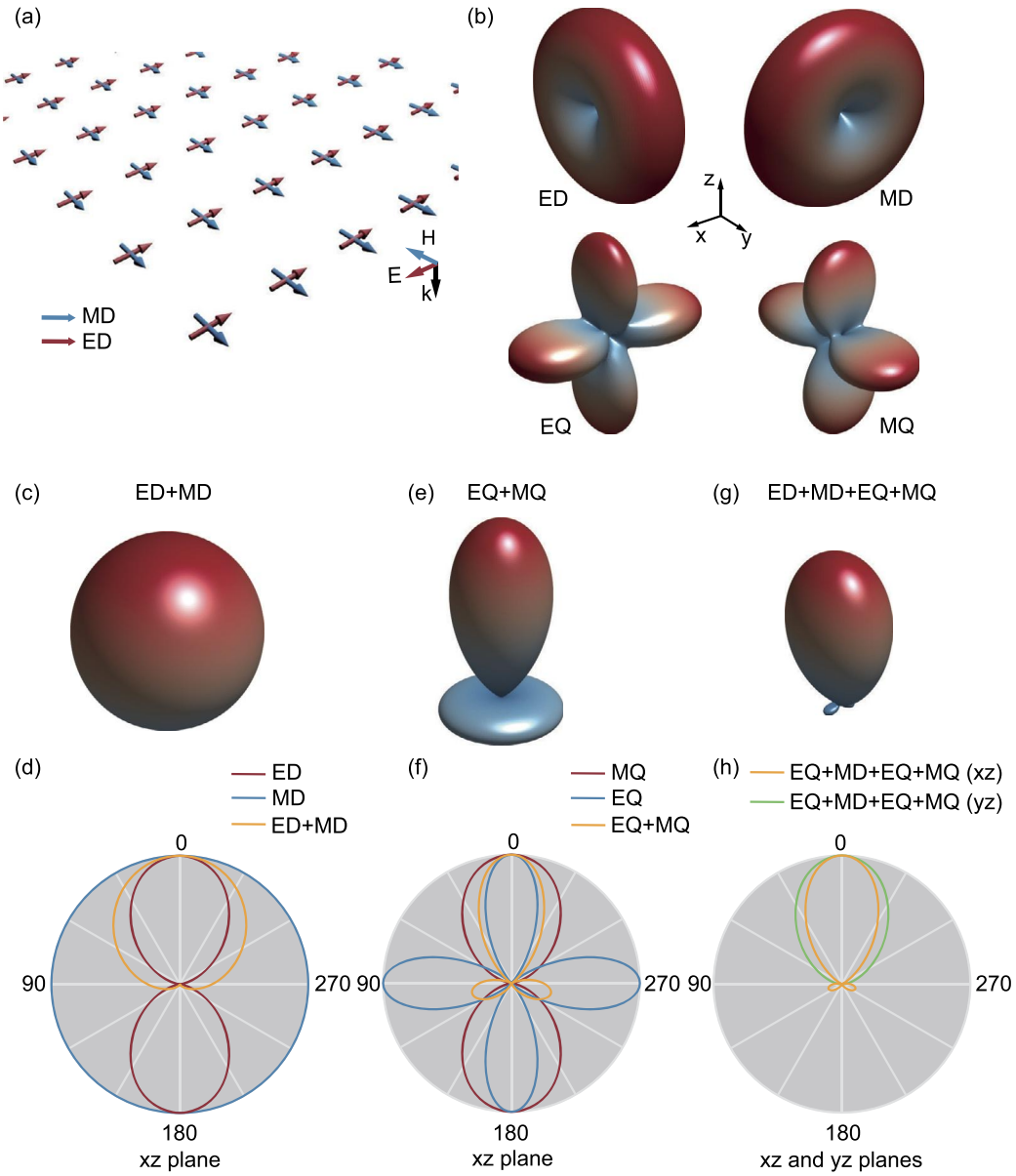

Figure 10.2. (a) Illustration of an equivalent Huygens' metasurfaces with excited arrayed electric and magnetic dipoles. (b) The scattering patterns of an electric dipole (ED), magnetic dipole (MD), electric quadrupole (EQ), and magnetic quadrupole (MQ). (c) The scattering pattern with suppressed backward scattering realized by the combination of electric and magnetic dipoles, and (d) shows the separate scattering patterns for ED (red), MD (blue) and ED+MD (yellow). (e) The scattering pattern with suppressed backward scattering realized by the combination of ED+MQ, and (f) show each scattering pattern for MQ (red), EQ (blue), and EQ+MQ (yellow). (g) The scattering pattern with suppressed backward scattering realized through combination of ED+MD+EQ+MQ, and (h) shows the xz (yellow) and yz (green) cross sections.

In the following, we drop superscripts on the polarizabilities in order to simplify the equations. From of Eqs. (10.16), (10.17) it can be observed that the reflection is dependent on the bianisotropic coefficient $\hat{\alpha}_{em}$, while the transmission is independent of bianisotropy, as required by the reciprocity theorem. Clearly, when $\hat{\alpha}_{em} = 0$, there is zero reflection full transparency from both sides implies that no electromagnetic coupling exists in the system. However, one-way transparency is possible for chiral and nonreciprocal metasurfaces [33]. It has been demonstrated that bianisotropic Huygens' metasurfaces can be used for polarization conversion and asymmetric absorption [32,39,40]. If inversion symmetry exists in the meta-atoms with respect to the wave propagation direction, the bianisotropic coefficients can be set to zero and the reflection from both sides is equal. Under these conditions, the normal reflection and transmission coefficients read:

$$r = \frac{ik\rho}{2}(\hat{\alpha}_{ee} - \hat{\alpha}_{mm}), \tag{10.18}$$

$$t = 1 + \frac{ik\rho}{2}(\hat{\alpha}_{ee} + \hat{\alpha}_{mm}). \tag{10.19}$$

The top row of Fig. 10.2 (b) shows the far-field scattering cross-section of electric and magnetic dipoles arranged as depicted in Fig. 10.2 (a). Here, the ED and MD are matched (equal magnitude response) and in phase, so backward scattering in the normal direction is totally eliminated. The transmission may reach unity with $T = |t|^2 = 1$ under the condition of $|\hat{\alpha}_{ee}|^2 = |\hat{\alpha}_{mm}|^2 = \frac{2}{k\rho}\mathrm{Im}\{\hat{\alpha}_{ee}\}$. As shown in Fig. 10.2 (c), and as the yellow curve in Fig. 10.2 (d), where the scattering cross-section from matched electric and magnetic dipoles is significantly suppressed in the backward direction, leaving a prominent forward scattering. We note that such a relation does not violate the optical theorem, which is based on the energy conservation with the condition of $\frac{k^3}{6\pi}\alpha^{\dagger}\alpha = \frac{1}{2i}(\alpha^{\dagger} - \alpha)$. The optical theorem requires an integral of the total power over the space in all directions, but the Eqs. (10.18) and (10.19) are only valid for normally propagating waves. Fig. 10.2 (c) demonstrates that the matched condition with $\hat{\alpha}_{ee} = \hat{\alpha}_{mm}$ achieves zero backward scattering for $\theta = \pi$. However, upon closer inspection of Fig. 10.2 (d), it is evident that there is still some backward transverse scattering (yellow curve). As the imaginary part of α_{ee} approaches zero, both polarizabilities also approach zero, resulting in nearly zero radiative loss. This condition leads to the Huygens' metasurface approaching a bound state in the continuum (BIC) with an infinite quality factor. Recently, an extreme Huygens' metasurface was experimentally demonstrated using four elliptical cylinders arranged in a zigzag structure with mirror symmetry

in both the x and y planes [41]. By tuning the rotation angle of the cylinders, the electric quasi-BIC and the magnetic quasi-BIC gradually merge together, resulting in unity transmission at resonance. Additionally, by introducing fractional loss into the material, a perfect absorber with an extremely narrow bandwidth can be achieved [42,43].

It is important to note that Huygens' metasurfaces are not limited to dipole-only responses. High-order multipoles have been proposed to modify both forward and backward scattering, enabling the realization of Huygens' metasurfaces with zero backward scattering [44,45]. Fig. 10.2 (e) illustrates that the electric and magnetic quadrupoles can be used to further suppress backward scattering with better angular directivity, and Fig. 10.2 (f) shows the scattering for MQ (red) EQ (blue) and EQ+MQ (yellow curve). We find, however, that the transversal scattering in the backward direction (yellow curve of Fig. 10.2 (f)) is slightly stronger than that achieved with dipole-only responses. Backward suppression can also be achieved by using multipoles with different orders, as shown in Figs. 10.2 (g) and (h) through the combination of dipoles and quadrupoles, achieving much better suppression of backward scattering. In general, backward suppression is possible using more complex combinations of high-order multipoles with opposite parity [46]. In Section 10.4, we will demonstrate that incorporating high-order multipoles can even completely suppress both forward and backward scattering [47].

Unity transmission with Huygens' metasurfaces can also be explained using temporal-coupled mode theory, which involves placing a resonator in a two-port system that supports both symmetric and antisymmetric modes (i.e., even and odd modes, respectively). In this scenario, the scattering matrix can be expressed as:

$$\mathbf{S} = \left\{ \mathbf{I} - \frac{\gamma_1}{-i(\omega-\omega_{01})+\gamma_1+\delta_1}\begin{bmatrix}1 & 1\\ 1 & 1\end{bmatrix} - \frac{\gamma_2}{-i(\omega-\omega_{02})+\gamma_2+\delta_2}\begin{bmatrix}1 & -1\\ -1 & 1\end{bmatrix} \right\} \begin{bmatrix}\tilde{r}_b & \tilde{t}_b\\ \tilde{t}_b & \tilde{r}_b\end{bmatrix}, \tag{10.20}$$

where $\tilde{r}_b$ and $\tilde{t}_b$ represent the direct reflection and transmission between the two ports without the resonator included. Additionally, $\omega_{0,i}$ $(i = 1, 2)$ is the resonant frequency of mode i, γ_i is the radiative loss rate of mode i, and δ_i is the material loss rate of mode i. Mode 1 and 2 correspond to the even and odd modes, respectively, and the even and odd modes can be used to explain the unity transmission achieved by Huygens' metasurfaces. The transmission and reflection coefficients for propagation in the normal

direction are:

$$r = -\frac{\gamma_1}{-i(\omega-\omega_{01})+\gamma_1+\delta_1} + \frac{\gamma_2}{-i(\omega-\omega_{02})+\gamma_2+\delta_2},$$
$$t = 1 - \frac{\gamma_1}{-i(\omega-\omega_{01})+\gamma_1+\delta_1} - \frac{\gamma_2}{-i(\omega-\omega_{02})+\gamma_2+\delta_2}. \tag{10.21}$$

Upon comparing Eqs. (10.21) to Eq. (10.18) and Eq. (10.19), we observe that the Lorentzian response of the even mode (mode 1) describes the behavior of electric dipoles (EDs), while the Lorentzian response of the odd mode (mode 2) contributes to magnetic dipoles (MDs). For simplicity, we assume negligible material loss, allowing us to set the material loss rate to zero. When the two modes are spectrally separated, for instance, $(\omega_{02}-\omega_{01})/\omega_{01} = 0.15$ as shown in Fig. 10.3 (a), transmission values for frequencies between ω_{01} and ω_{02} are strictly less than 1, while the reflection can be as high as 1. As a result, the phase (blue curve in Fig. 10.3 (b)) exhibits a maximum (and abrupt) phase change of π at the resonant frequencies, as indicated by the dashed gray lines. However, as the two modes become degenerate (i.e., $\omega_{01} = \omega_{02}$), the backward scattering from the even mode and the odd mode destructively interfere, leading to zero reflection at the resonant frequency – see red curve in Fig. 10.3(a). Meanwhile, the incident field cancels out the scattering from one of the two dipoles, leaving the other dipole radiating with unity transmission, as depicted by the solid red curves in Fig. 10.3(a). Due to the two overlapping in-phase resonances in the forward direction, there is a total 2π phase change around the resonance, as shown in Fig. 10.3(b). Complete phase coverage allows for precise wavefront control, such as generating vortex beams, creating hologram images, and beam steering [48–51]. Furthermore, in addition to modifying the geometry of the meta-atoms, the transmitted phase can be adjusted by altering the lattice size. For example, for a dielectric Huygens' metasurface composed of silicon nanodisks with a diameter of 534 nm and a height of 243 nm, the phase at a wavelength of 1477 nm can vary from 0 to 270° as the periodicity decreases from 975 nm to 695 nm, while the transmittance remains close to unity [48].

The initial demonstration of Huygens' metasurfaces was achieved in the microwave region using stacked structures consisting of metallic wires and loops, operating as effective EDs and MDs, respectively [52–54]. However, in the infrared and visible ranges, the plasmonic oscillation is accompanied by the significant metallic loss which inhibits the scattering efficiency [55]. Further, the stacking of multilayer nanostructures requires challenging fabricational techniques, thereby imposing a significant

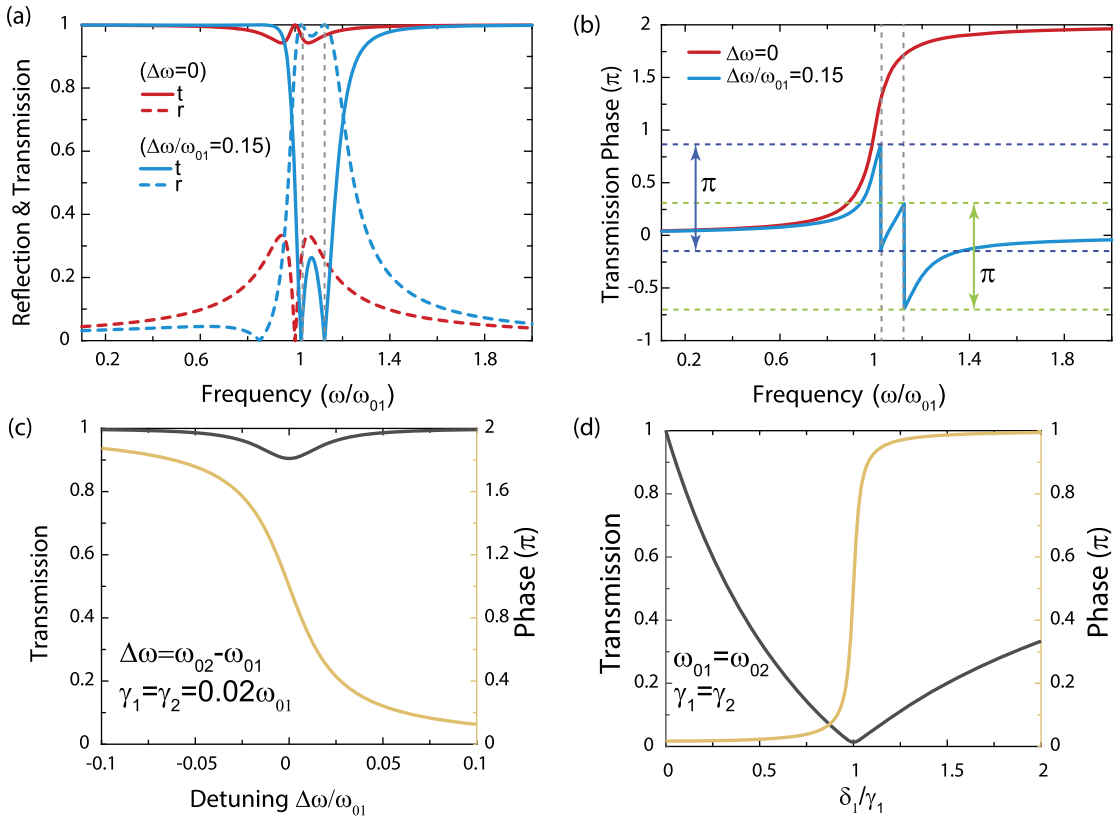

Figure 10.3. Temporal coupled mode theory of an all-dielectric Huygens' metasurface consisting of arrayed silicon nano-disks. (a) Transmission coefficient (solid red and blue curves) and reflection coefficient (dashed red and blue curves) for degenerate even and odd modes (red curves) with $\delta\omega = \omega_{02} - \omega_{01} = 0$ and spectrally separated modes (blue curves) with $\delta\omega/\omega_{01} = 0.15$. For both cases shown, we use $\gamma_2/\gamma_1 = 2$. (b) The frequency dependent transmitted phase for the two cases shown in (a). (c) The transmission amplitude (black curve) and phase (yellow curve) at ω_{01} as a function of the detuning of resonant frequencies of the two modes of a low-loss Huygens' metasurfaces ($\Delta\omega = \omega_{02} - \omega_{01}$). (d) The transmission amplitude (black curve) and phase (yellow curve) change near the resonant frequency vs a change in the ratio of the material loss rate (δ_1) to radiative loss rate (γ_1) for degenerate modes ($\omega_{01} = \omega_{02}$). The radiative loss rates are assumed to be the same for both modes.

barrier to obtain high-performance devices. Dielectrics with limited material loss enable a promising route to achieve engineered scattering with high efficiency. Studies have shown that dielectric resonators, such as dielectric spheres, cylinders, and cubes, can support electric and magnetic resonances [56–58]. The first all-dielectric Huygens' metasurface was experimentally demonstrated in the near-IR range [59]. As shown in Fig. 10.4 (a), the arrayed silicon nano-disks were patterned from a silicon-on-insulator wafer. To mediate the extra Fabry-Pérot resonance due

to the thick substrate, the silicon handle-wafer was removed and the entire array was embedded in a spin-on glass, which has a similar refractive index as the silicon-oxide layer from the wafer. The measured transmittance at the resonance shown in Fig. 10.4 (b) is greater than 55%, which deviates slightly from simulations due to the fabrication tolerance. By dividing the gradient metasurfaces into four quadrants, as shown in Fig. 10.4 (c), and incrementing the phase by $\pi/2$ in the counterclockwise direction between subsequent quadrants, a vortex beam with a phase singularity can be clearly observed [48]. Fig. 10.4 (d) shows the reconstructed phase of the object beam with a gradient phase change in the azimuthal direction. In addition, gradient Huygens' metasurfaces can be used as beam-steering devices. By etching arrayed cylinders with nine different radii into amorphous silicon, a linear phase gradient can be created, as shown in Fig. 10.4 (e). Fig. 10.4 (f) shows the measured beam diffraction at a wavelength of 1340 nm with a maximum efficiency of 63.6%.

Figs. 10.3 (a) and (b) show that the scattering amplitude and phase are highly sensitive to the separation of the two modes. Even a small deviation from the degeneracy of the two modes can induce a significant modulation of the electromagnetic response. Fig. 10.3 (c) demonstrates that for a low-loss Huygens' metasurface, the transmission amplitude and phase at frequencies ω_0 vary as a function of the detuning of the two modes ($\Delta\omega = \omega_{02} - \omega_{01}$). By shifting the resonant frequency by $\pm 10\%$, the transmission amplitude remains above 90%, but the phase changes by nearly 2π. Furthermore, the additional material loss can also lead to a significant change in the transmission amplitude [61]. For a Huygens' metasurface with degenerate modes and similar radiative loss rates, modifying the material loss could result in a 2π phase change, as illustrated in Fig. 10.3 (d). However, there is a tradeoff between amplitude and phase: the amplitude is relatively small, as the phase increases rapidly. It is worth noting that, when the material loss rate equals the radiative loss rate, the transmission can be completely suppressed. According to Eq. (10.21), under such conditions, namely a critically coupled state, both the transmission and reflection at the resonant frequency $\omega_{01} = \omega_{02}$ become zero, resulting in a perfect absorption state [62,63]. Unlike conventional one-port metallic perfect absorbers with a metallic ground plane, such an all-dielectric absorber exhibits perfect absorption from both sides, indicating a fully zero rank of the scattering matrix S for a two-port system. When only one of the modes achieves a critical coupling state, the metasurface can perform as a coherent perfect absorber, operating at the mode with coherent incidences from both sides [64].

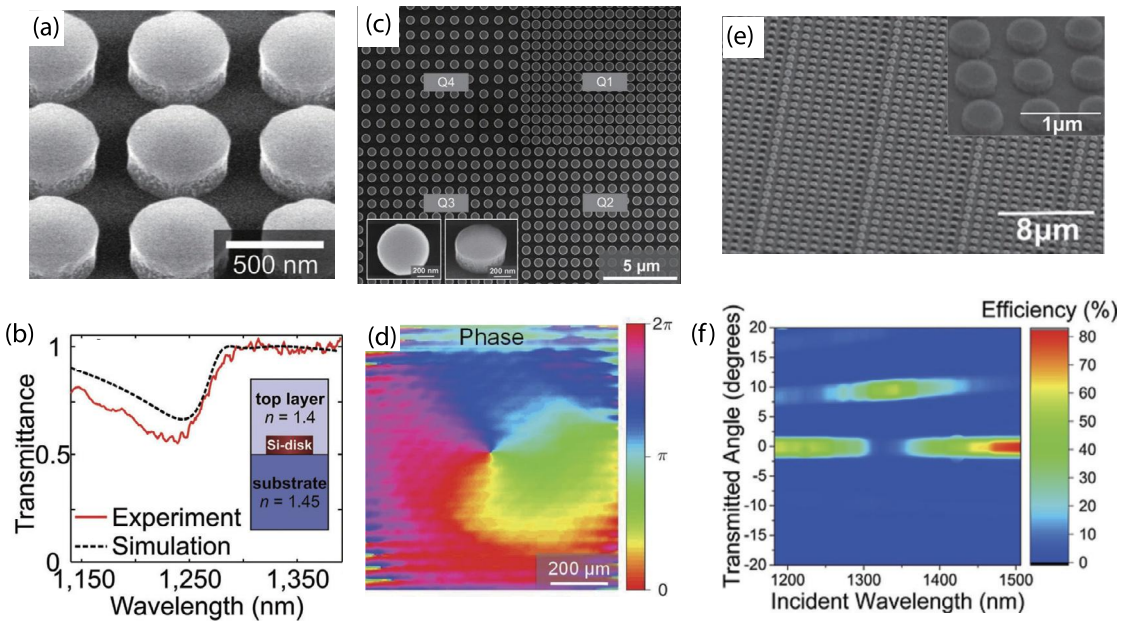

Figure 10.4. (a) Oblique-view of a fabricated sample consisting of silicon disks on an SOI substrate. The disk radius is 242 nm, the height is 220 nm, and the periodicity is 666 nm. (b) Experimentally measured (red-solid line) and simulated (black-dashed line) transmittance spectra with silicon disks embedded in the spin-on glass after the handle silicon wafer was removed. (c) SEM image of a fabricated vortex-beam generator with silicon nanodisk diameter of 590 nm and height of 243 nm. The phase in each quadrant is tuned by the periodicity from 695 nm for the first quadrant to 974 nm for the fourth quadrant. (d) Reconstructed phase from measured results with the gradual phase change in the azimuthal direction and a phase singularity at the center. (e) SEM image of a fabricated beam-steering metasurface consisting of 9 different silicon Huygens' meta-atoms in a supercell. (f) Experimentally measured transmission angle and efficiency as a function of the incident wavelength. (a) and (b) Reprinted with permission from ref. [59] ©2015 Wiley. (c) and (d) Reprinted with permission from ref. [48] ©2015 ACS (e) and (f) Reprinted with permission from ref. [60] ©2018 ACS.

Huygens' metasurfaces are structures that are highly sensitive to their geometry and material loss, making them attractive for use as active devices to manipulate electromagnetic waves. Initial prototypes of dynamic Huygens' metasurfaces were developed in the microwave region, using active varactors to control transmission phase and amplitude [68]. In all-dielectric metasurfaces, photodoping on semiconductors can be utilized to generate free carriers, which can easily modify the dielectric property of meta-atoms. However, as the excessively generated free carriers in the semiconductors could significantly increase the material loss tangent, the degeneracy of the Huygens' metasurface is lifted because the material dissipation rate of the odd eigenmode rises much faster than that of the even mode, and the critically coupled state

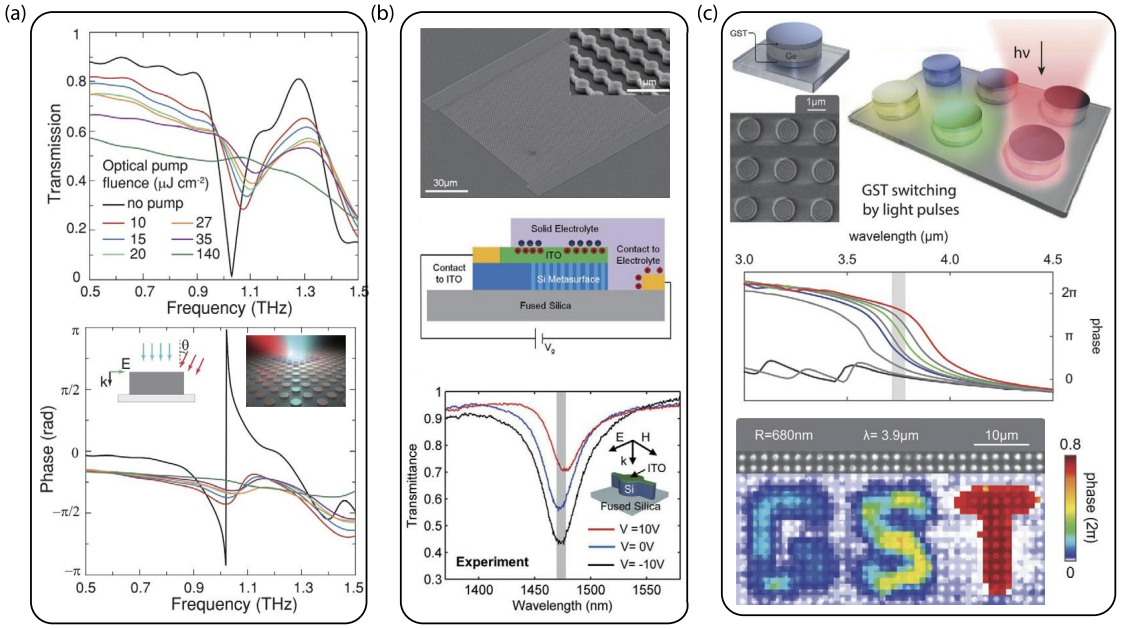

Figure 10.5. Examples of dynamic Huygens' metasurfaces. (a) Experimentally measured transmission amplitude (top panel) and phase (bottom panel) for different values of the optical fluence. The black curve shows the transmission coefficient without photoexcitation on the silicon metasurface. The left inset in the bottom panel shows optical-pump (red) and terahertz-probe beams incident onto the cylinders. The right inset illustrates the tunable all-dielectric Huygens' metasurface pumped by an ultrafast 800 nm beam (red), and the terahertz beam is shown in light-blue color. (b) Electrically tunable Huygens' metasurface operating in the near-infrared range. Top: SEM image of the fabricated metasurface with silicon connections in between. Middle: Illustration of the working principle. The control of the ITO permittivity is attributed to the formed electric bilayer at the solid electrolyte/ITO interface. Bottom: Measured transmittance spectra with different applied bias voltage. (c) Top: Illustration of a multi-layer Huygens' meta-atom with germanium sandwiched between the phase-change material of GST, SEM image of the fabricated metasurface, and illustration of the programmable Huygens' metasurface spatially controlled by the illumination of ultrafast laser pulses. Middle: Simulated transmission phase for different crystallization states of GST. Bottom: Encoded phase imaging with letters: "G", "S", and "T". The image is overlaid on an optical image of the metasurface. (a) Reprinted with permission from ref. [65] ©2018 Wiley. (b) Reprinted with permission from ref. [66] ©2018 Optica (c) Reprinted with permission from ref. [67] ©2020 Wiley.

is destroyed. As shown in Fig. 10.5a, with only 10 μJ cm^{-2} fluence of an 800-nm ultrafast pulse incident on a terahertz dielectric perfect absorber, the modulation depth of transmission intensity reaches as high as 99.93%, while the transmitted phase changes $\pi/2$ rad [65]. The gradual increase of carriers can also induce a dynamic transition from the under-damped state ($\delta_i < \gamma_i$) to the over-damped state ($\delta_i > \gamma_i$) [69]. A spatially modulated beam on the Huygens' metasurface could further realize a programmable metasurface for phase-encoded imaging. An optically tunable in-

frared Huygens' metasurface based on the phase-change material (PCM) of $Ge_3Sb_2Te_6$ (GST) was demonstrated (see, Fig. 10.5 (c)), in which optical pumping directly on the GST can activate a phase transition of the GST from the amorphous state to the crystalline state. The result is that both the electric and magnetic resonances in the dielectric resonators exhibit a pronounced spectral shift with increased pumping power, leading to their degeneracy and a phase change of nearly 2π as shown in the middle panel of Fig. 10.5 (c). With a spatially controlled pump beam incident on the sample, a phase-encoded image operating at 3.9 μm can be constructed. By changing the dimension of resonators around the degenerated state, dynamic meta-lens can also be achieved [70].

In addition to optical tuning, dynamic all-dielectric Huygens' metasurfaces can also be achieved through electrical biasing. However, traditional electrical tuning with metallic wires and electrodes can result in inherent losses. To overcome this, solid electrolytes, liquid crystals, or heavily doped semiconductors can be utilized to modify the carrier density of semiconductors without introducing these losses [66,71,72]. By applying a bias voltage between a solid electrolyte and a conductive indium tin oxide (ITO) thin film, as illustrated in Fig. 10.5 (b), an electric bilayer can be created, which increases the carrier density at the interface, leading to a shift in the plasma frequency of ITO and the corresponding permittivity [66]. Experimental results have demonstrated that increasing the voltage from −10 V to 10 V can enhance the transmission by about 70%.

It has been demonstrated that Huygens' metasurface-based dielectric transparency possesses great potential for controlling and tailoring electromagnetic wave fronts with high efficiencies, such as beam forming, steering, hologram, and imaging. Recently, a highly transparent Huygens' metasurface has been developed as a compact 3D near-eye display for augmented and virtual reality (AR/VR) applications [73]. By tuning the diameter of the silicon cylinders from 150 nm to 300 nm, the metasurface exhibits a full 2π phase change at a wavelength of 680 nm while maintaining high transmission. This display, fabricated using deep-ultraviolet immersion photolithography, has an exit pupil of 10 mm × 8.6 mm with over 108 active pixels and a continuous depth ranging from 0.5 to 2 m. Further tunable metasurfaces will undoubtedly open up the potential for real-time AR/VR displays. In addition to the optical, electric, and phase-changing strategies discussed in this section, nonlinear and time-modulated Huygens' metasurfaces could also provide new routes to obtain additional functionalities, such as optical limiting, parametric amplification, magnetless non-reciprocity, and spectral camouflage [74–76].

10.4 Transverse Kerker metasurfaces

The interaction of light with dielectric particles of finite size can induce oscillating electric displacement currents. These coherently oscillating currents act as sources that radiate electromagnetic waves into free space. Given that the size of the scatterers is only a fraction of the operating wavelength, the characteristics of the radiation are well described by Mie scattering. They can be further described using multipole decomposition, which considers the scattering fields and patterns as the result of the interference of multipoles, including dipoles, quadrupoles, octupoles, etc. In Section 10.3, we showed that manipulating the interference between electric dipoles (EDs) and magnetic dipoles (MDs) with electric and magnetic polarizabilities satisfying $\alpha_{ee} = \alpha_{mm}$ can lead to asymmetric scattering with zero backward scattering (ZBS) and total forward scattering, also known as the first Kerker condition [24]. This effect enables the creation of Huygens' metasurfaces with very high transmission efficiency and 2π full phase change. The condition for zero forward scattering (ZFS) with $\alpha_{ee} = -\alpha_{mm}$ is similarly named as the second Kerker condition. However, as dictated by energy conservation and the optical theorem, the total extinction cross-section is proportional to the forward scattering. Zero forward scattering would mean zeros of absorption cross-section and scattering cross-section, which is impossible for a passive visible scatter [77,78]. Therefore, ZFS cannot be exactly zero, but nearly zero forward scattering (NZFS) can still be supported by the combination of EDs and MDs. In addition to demonstrating Huygens' sources or metasurfaces [59,79], structures with directional scattering have also been experimentally realized for antireflective coatings [80], Brewster effect [81], and other applications.

Although Huygens' metasurfaces have achieved unity transmission and invisibility, there is still a π phase difference between incoming and outgoing waves. For perfect invisibility, both forward and backward scattering must be suppressed, and scattering should be directed transversely. To meet these requirements, more generalized Kerker conditions that take into account quadrupoles and higher-order multipoles must be implemented [47]. To understand the design process and inherent mechanism of transverse Kerker metasurfaces, we begin with the Mie theory for a single spherical particle scattering in a homogeneous environment. For more detailed analysis, please refer to [47]. For a spherical scattering, the angular distribution of the differential scattering cross-

section can be presented as:

$$\frac{d\sigma_{sca}(\theta)}{d\Omega} = \frac{1}{k^2}\left\{\cos^2\varphi|S_{\parallel}(\theta)|^2 + \sin^2\varphi|S_{\perp}(\theta)|^2\right\}, \tag{10.22}$$

where θ andφ are the polar and azimuthal scattering angles, respectively, k is the wavevector in the surrounding environment, $S_{\parallel}(\theta)$ and $S_{\perp}(\theta)$ are the polarized scattering field parallel and perpendicular to the scattering plane in the far-field zone, respectively. They are given as:

$$S_{\parallel}(\theta) = \sum_{n=0}^{\infty}\frac{2n+1}{n(n+1)}\left[a_n\frac{dP_n^1(\cos\theta)}{d\theta} + b_n\frac{p_n^1(\cos\theta)}{\sin\theta}\right], \tag{10.23a}$$

$$S_{\perp}(\theta) = \sum_{n=0}^{\infty}\frac{2n+1}{n(n+1)}\left[b_n\frac{dP_n^1(\cos\theta)}{d\theta} + a_n\frac{p_n^1(\cos\theta)}{\sin\theta}\right], \tag{10.23b}$$

where n is the order of the multipoles (e.g., $n=1$ for dipole, $n=2$ for quadrupole, etc.); $p_n^1(\cos\theta)$ is the associated Legendre polynomials of order 1; $a_n(b_n)$ are the complex Mie coefficients, corresponding to electric (magnetic) multipoles.

To achieve transverse scattering with zero scattering in the forward ($\theta=0$) and backward ($\theta=\pi$) directions, rigorous expressions for any combination of multipoles can be derived as [46,77]:

$$\theta = 0: \sum_{n=0}^{\infty}(-1)^{(n+1)}(2n+1)a_n = \sum_{n=0}^{\infty}(-1)^{(n+1)}(2n+1)b_n, \tag{10.24}$$

$$\theta = \pi: \sum_{n=0}^{\infty}(2n+1)a_n = -\sum_{n=0}^{\infty}(2n+1)b_n. \tag{10.25}$$

To achieve ZFS and NZBS using only dipoles, the scattering coefficients must satisfy $a_1 = b_1$ and $a_1 = -b_1$. However, this condition requires the phase difference to be simultaneously 0 and $\pm\pi$, which is impossible for any scattering system [77]. When both dipoles and quadrupoles are considered, from Eqs. (10.24) and (10.25) the condition to suppress the scattering in both directions simultaneously can be obtained as:

$$a_1 = -\frac{5}{3}b_2, \qquad \text{and} \qquad b_1 = -\frac{5}{3}a_2, \tag{10.26}$$

which indicates a π phase difference between the electric (magnetic) dipole and the magnetic (electric) quadrupole, and a magnitude ratio between them of 5/3. By substituting Eq. (10.26) into

Eq. (10.22), we can obtain the angular distribution of the differential scattering cross section as:

$$\frac{d\sigma_{sca}(\theta)}{d\Omega} \sim \cos^2\varphi \sin^4\theta |a_2|^2 + \sin^2\varphi \sin^4\theta |b_2|^2. \tag{10.27}$$

If the condition in Eq. (10.26) is satisfied, it would result in suppression of both forward and backward scattering, leaving only transverse scattering. The transverse scattering pattern in the x-y plane depends on the magnitude ratio of scattering coefficients between the electric quadrupoles (EQs) and the magnetic quadrupoles (MQs), i.e., a_2/b_2. Figs. 10.6 (a)-(c) and (d)-(f) display the radiation patterns with the magnitude ratio of $a_2/b_2 = 1$ and 2, respectively. In both cases, the forward and backward scattering is minimized. When $a_2/b_2 = 1$, the scattering in the transversal directions is isotropic as the scattering contributions from dipoles and quadrupoles are the same. However, when $a_2/b_2 = 2$, the transverse scattering in the y-direction is much smaller than that in the x-direction due to the unequal scattering from the dipoles and the quadrupoles. As mentioned earlier, exact FS violates the optical theorem. The forward scattering can only be approximately zero with $d\sigma(\theta)/d\Omega \simeq 0$. To achieve generalized Kerker condition with nearly zero forward scattering and zero backward scattering, a trilayer nanosphere consisting of CdTe/Si/TiO2 was proposed as shown in Fig. 10.7a [82]. Its radiation pattern (Fig. 10.7b) is very similar to that shown in Fig. 10.6d, but its backward scattering is suppressed to near zero. Fig. 10.7c and d show the scattering pattern of a nanosphere composite at $\varphi = 0$ and $\varphi = \pi/2$ in the x-z plane and y-z plane, respectively. Due to the suppressed longitudinal scattering, the field is mainly scattered in the transversal direction. It is clear that only NZFS and ZBS are achieved in such a structure. In addition to the combination of four multipoles, transverse scattering can also be obtained with EQ and MD only, when $a_1 = b_2 = 0$, or the combination of EDs and MQs [83,84].

For particles with arbitrary geometry, the Cartesian multipole decomposition method is utilized for scattering analysis. The scattered electric field can be considered as a superposition of fields from multipoles:

$$\begin{aligned}\mathbf{E}_{sca}(\mathbf{n}) \cong \frac{k^2 e^{i\mathbf{k}\cdot\mathbf{s}}}{4\pi s\varepsilon_0}\Big\{&[\mathbf{n}\times(\mathbf{p}\times\mathbf{n})] + \frac{1}{c}[\mathbf{m}\times\mathbf{n}] \\ &+ \frac{ik}{6}[\mathbf{n}\times(\mathbf{n}\times\hat{Q}\mathbf{n})] + \frac{ik}{2c}[\mathbf{n}\times\hat{M}\mathbf{n}]\Big\},\end{aligned} \tag{10.28}$$

where $\mathbf{n}$ is the unit vector along the radius vector $\mathbf{s}$, $\mathbf{k}$ is the wavevector, c is the speed of light, $\mathbf{p}$ and $\mathbf{m}$ are the total ED (in-

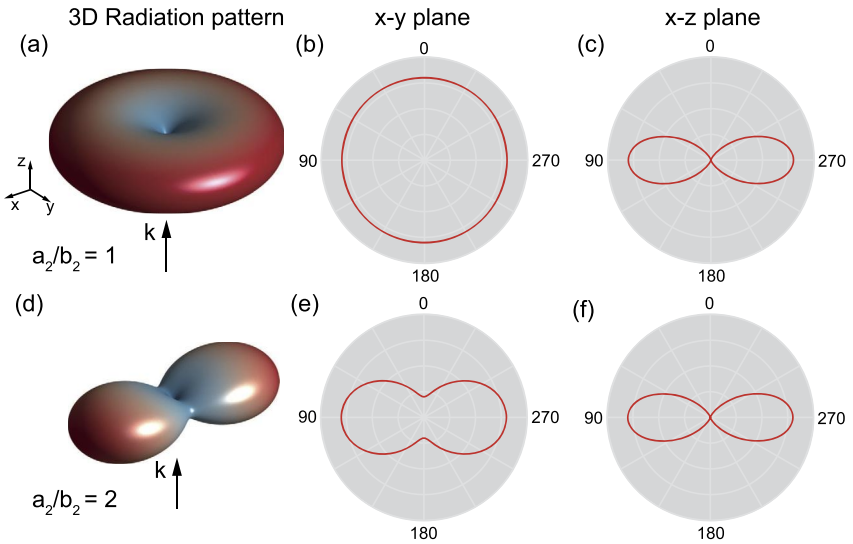

Figure 10.6. Transversal scattering with different ratios of quadrupole coefficients a_2/b_2. (a) shows the 3D scattering pattern for $a_2/b_2 = 1$ and (b) and (c) show the $x-y$ and $x-z$ plane cross sections, respectively. For a quadrupole ratio of $a_2/b_2 = 2$ (d) shows a 3D scattering pattern, and cross sections of the $x-y$ and $x-z$ planes are shown in (e) and (f), respectively.

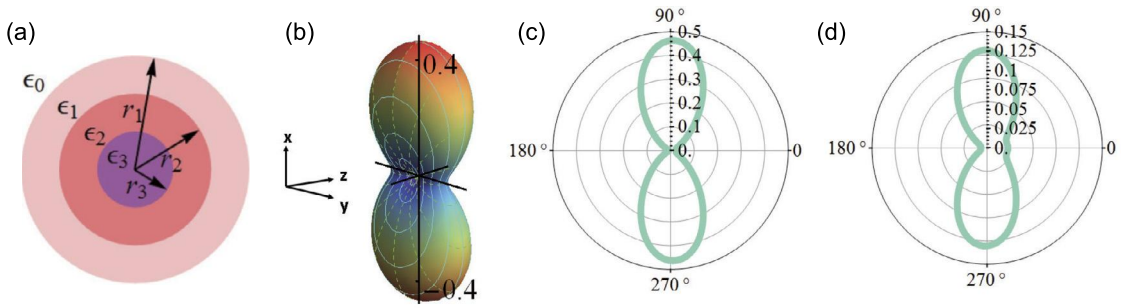

Figure 10.7. (a) A trilayer nanosphere consisting of CdTe/Si/TiO2 with a radii of $r_1 = 100$ nm, $r_2 = 87.7$ nm, and $r_3 = 26.3$ nm, respectively. (b) The 3D radiation pattern of the nanosphere at the operational wavelength of 500 nm. (c) and (d) show 2D radiation patterns for $x-z$ plane with $\varphi = 0$, and $y-z$ plane with $\varphi = \pi/2$, respectively. (b) Reprinted with permission from ref. [82] ©2018 Optica.

cluding toroidal) and MD moments, $\hat{Q}$ ($\hat{M}$) is the EQs (MQs). For a dielectric resonator with an arbitrary size, the exact Cartesian multipole expressions for the induced multipole moments can be obtained as [85]:

$$p_\alpha = -\frac{1}{i\omega}\Big\{\int d^3\mathbf{s} J_\alpha^\omega j_0(ks) + \frac{k^2}{2}\int d^3\mathbf{s}\big[3(\mathbf{s}\cdot\mathbf{J}_\omega)s_\alpha - s^2 J_\alpha^\omega\big]\frac{j_2(ks)}{(ks)^2}\Big\},$$

$$
\begin{aligned}
m_\alpha &= \frac{3}{2}\int d^3\mathbf{s}(\mathbf{s}\times\mathbf{J}_\omega)_\alpha \frac{j_1(ks)}{ks},\\
Q_{\alpha\beta} &= -\frac{3}{i\omega}\Big\{\int d^3\mathbf{s}\big[3(s_\beta J_\alpha + s_\alpha J_\beta) - 2(\mathbf{s}\cdot\mathbf{J}_\omega)\delta_{\alpha\beta}\big]\frac{j_1(ks)}{ks},\\
&\quad + 2k^2\int d^3\mathbf{s}\big[5s_\alpha s_\beta(\mathbf{s}\cdot\mathbf{J}_\omega) - s^2(s_\beta J_\alpha + s_\alpha J_\beta)\\
&\quad - r^2(\mathbf{s}\cdot\mathbf{J}_\omega)\delta_{\alpha\beta}\big]\frac{j_3(ks)}{(ks)^3}\Big\},\\
M_{\alpha\beta} &= 5\int d^3\mathbf{s}\Big\{s_\alpha(\mathbf{s}\times\mathbf{J}_\omega)_\beta + s_\beta(\mathbf{s}\times\mathbf{J}_\omega)_\alpha\Big\}\frac{j_2(ks)}{ks},
\end{aligned}
\tag{10.29}
$$

where $\alpha, \beta = x, y, z$, $j_i(x), i = 0, 1, 2, 3$ are the spherical Bessel functions, $\mathbf{J}_\omega(\mathbf{s}) = i\omega\varepsilon_0(\varepsilon_r - 1)\mathbf{E}_\omega(\mathbf{s})$ is the induced electric current density by the local electric field of $\mathbf{E}_\omega(\mathbf{s})$ in an object with the relative permittivity of ε_r. The second term in the brackets of electric dipole moment is contributed from the toroidal dipole, which will be discussed further in Section 10.5. We note that the first term of p_α also contributes to the toroidal dipole moment.

Assuming the dielectric scatters have rotational and inversion symmetry, and the incident field is polarized in the x-direction, $\mathbf{E}_{\text{inc}} = E_{0,x}e^{ik_0 s}$, the induced polarization current $\mathbf{J}_p = (J_x, 0, 0)^T$, leading to non-zero multipoles being $p_x, m_y, Q_{zx} = Q_{xz}$, and $M_{yz} = M_{zy}$. The scattered field in the forward direction ($\mathbf{s} = (0, 0, 1)$ and $\theta = 0$) and backward direction ($\mathbf{s} = (0, 0, -1)$ and $\theta = \pi$) can be described as:

$$
E(\mathbf{s})^{+,0}_{sca,x} \simeq \frac{k^2}{4\pi\epsilon_0}\frac{e^{iks}}{s}\Big[p_x + \frac{1}{c}m_y + \frac{k}{6i}Q_{zx} + \frac{k}{2ic}M_{zy}\Big], \tag{10.30}
$$

$$
E(\mathbf{s})^{-,\pi}_{sca,x} \simeq \frac{k^2}{4\pi\epsilon_0}\frac{e^{iks}}{s}\Big[p_x - \frac{1}{c}m_y - \frac{k}{6i}Q_{zx} + \frac{k}{2ic}M_{zy}\Big]. \tag{10.31}
$$

Applying the transversal scattering condition to Eqs. (10.30) and (10.31), one possible solution of the multipole moment relations for a transverse Kerker metasurface can be given as [47,86]:

$$
p_x = \frac{m_y}{c}, \qquad \frac{Q_{zx}}{3} = \frac{M_{yz}}{c}, \qquad \text{and} \qquad p_x = -\frac{k}{2ic}M_{yz}. \tag{10.32}
$$

The first term in Eq. (10.32) corresponds to the Kerker condition for dipoles, while the second term represents the generalized Kerker condition with the contribution from quadrupoles only. The last term indicates the phase difference between the dipoles and quadrupoles. Fig. 10.8 (a) illustrates the calculated amplitude ratios among the dipoles and quadrupoles for a single silicon nanocubic particle with a height of 250 nm [47,86]. At

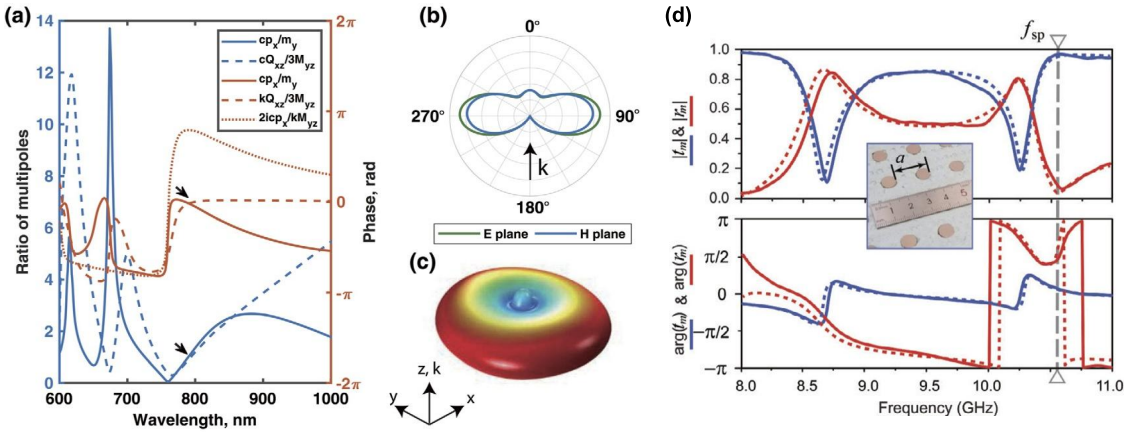

Figure 10.8. (a) Simulated amplitudes (blue lines) and phases (red lines) of the multipole ratios from Eq. (10.32). A silicon nanocube with an edge length of 250 nm was used for the modeling. The arrows indicate the transverse scattering at the wavelength of 780 nm. (b), (c) Two- and three-dimensional scattering patterns at the wavelength of 780 nm. The 3D radiation pattern of the nanosphere at the operational wavelength of 500 nm. (d) Simulated (dashed lines) and measured (solid lines) transmission and reflection coefficients of an all-dielectric metasurface consisting of arrayed disks. The inset shows the arranged metasurface array, where the lattice spacing is 20 mm, height of the disk is 5 mm, and the diameter is 8 mm. The dielectric constant of the disk is $\epsilon = 23 + i0.0138$. (a)-(c) Reprinted with permission from ref. [47] ©2019 American Physical Society (d) Reprinted with permission from ref. [86] ©2019 American Physical Society.

the wavelength of 788 nm, both the dipole and quadrupole ratios are close to unity, with corresponding phase differences near zero, as indicated by the black arrows. The phase difference between the electric dipole and the magnetic quadrupole is about 0.75π, slightly smaller than the predicted value of π. The discrepancies are mainly attributed to the not perfectly suppressed forward scattering, resulting from the optical theorem. Figs. 10.8 (b) and (c) display the corresponding scattering patterns with scattered waves predominantly propagating perpendicular to the incident wavevector. In the forward direction, there are still some forward scattered waves, while the backward scattering in the normal direction is suppressed. The experimental demonstration of transverse scattering was achieved in the microwave range using arranged ceramic disks, as shown in the inset of Fig. 10.8 (d) [86]. At the resonant frequency around $f_{sp} = 10.5$ GHz, the transmission is nearly unity, and the corresponding phase is approximately zero, indicating transparency with both amplitude and phase unperturbed compared to the incidence.

The optical theorem dictates that the forward scattering cannot be completely eliminated, but it is possible to further suppress it by considering the scattering parity. Symmetric scattering,

which is characterized by an even parity, is indicated by simultaneously zero forward and backward scattering. Hence, the scattering from magnetic dipoles (MDs) and electric quadrupoles (EQs), which have odd parity, should be significantly reduced compared to that from electric dipoles (EDs) and magnetic quadrupoles (MQs). The conditions for achieving transverse scattering can be derived from Eqs. (10.30) and (10.31) as follows:

$$|\frac{m_y}{c}| \approx 0, \qquad |\frac{kQ_{zx}}{6}| \approx 0, \qquad p_x = -\frac{k}{2ic} M_{yz}. \tag{10.33}$$

With negligible scattering from MDs and EQs, transverse scattering is mainly determined by the destructive interference between EDs and MQs. This method for achieving transparency was numerically validated in an ultrathin metasurface with a silicon nanoplate thickness of only 50 nm, which is approximately 1/21 of the operational wavelength. Due to the ultrathin cross-section, transparency was observed at oblique incidences up to 60° for a TM plane wave [83].

In summary, combining dipoles with high-order multipoles has opened up a new avenue for controlling far-field radiation. Theoretical analysis has shown that achieving transverse scattering is not limited to structures with inversion symmetry. In addition to regular shapes like cylinders and cubes, it is also possible to achieve transverse scattering for particles with significant bianisotropy, such as conical and pyramidal particles, although the scattering from these asymmetric particles depends on the incidence direction [87]. It should also be noted that transversal scattering is achievable under other types of waves, such as incidence from a point source [88]. By placing a radiating dipole-type source close to a dielectric antenna, the far-field radiation can be deflected perpendicular to the dipole moment. By modifying the geometry of the cylindrical antenna, the transverse Kerker effect can be achieved for magnetic dipoles, electric dipoles, and even chiral dipole emitters. Furthermore, transverse scattering phenomena generally do not involve any absorption in the structure. However, when a dielectric metasurface that supports the transverse Kerker effect is placed on a conductive ground plane at a specific distance, a perfect absorption effect due to the Fabry-Pérot resonances can be observed [86].

10.5 Hybrid anapole metasurfaces

In addition to electric and magnetic multipoles, toroidal multipoles induced by poloidal currents on the surface of a torus have been introduced as a new class of multipoles to describe electromagnetic scattering. A static toroidal dipole moment generated from a constant poloidal surface current, known as a static anapole, can produce a static magnetic field fully confined within a coil without any field leaking out. Zel'dovich first introduced this static anapole in 1957 to explain parity violation in nuclear physics [89]. However, a dynamic toroidal dipole generated from time-varying poloidal surface currents can radiate into surrounding space with a field pattern replicated from an electric dipole. Due to the same radiation patterns and parity symmetry, they are indistinguishable in the far field. Therefore, they cannot be separated from the spherical multipole expansion, which is based on field expansion. However, the Cartesian multipole expansion, which is calculated from induced current sources inside the scatterers, can identify the contributions between electric dipoles $\mathbf{p}_{car}$ and toroidal dipoles $\mathbf{T}_{car}$. In Eq. (10.29), p_α represents the total electric dipole moment contributed by the Cartesian electric dipole and toroidal dipole. As the radiation of the Cartesian electric dipole is out-of-phase with the toroidal dipole, i.e., destructive interference between the two dipoles, the total electric dipole radiation can be totally annihilated, as shown in Fig. 10.9 (a). This state is similar to the static toroidal dipole, also called anapole. Recent review articles cover detailed theoretical analyzes of anapoles [90]. In this section, we also present some up-to-date progress on anapoles.

To separate the Cartesian electric, magnetic and toroidal multipoles, within the subwavelength approximation, the Cartesian electric and magnetic multipoles can be written as [92]:

$$\begin{aligned}
\mathbf{p}_{car} &= -\frac{1}{i\omega}\int d^3\mathbf{s}\,\mathbf{J},\\
\mathbf{m}_{car} &= \frac{1}{2}\int d^3\mathbf{s}\,(\mathbf{s}\times\mathbf{J}),\\
Q^{\alpha\beta}_{car} &= -\frac{1}{i\omega}\int d^3\mathbf{s}\left[3(s_\beta J_\alpha + s_\alpha J_\beta) - 2(\mathbf{s}\cdot\mathbf{J})\delta_{\alpha\beta}\right],\\
M^{\alpha\beta}_{car} &= \int d^3\mathbf{s}\left\{s_\alpha(\mathbf{s}\times\mathbf{J})_\beta + s_\beta(\mathbf{s}\times\mathbf{J})_\alpha\right\},
\end{aligned} \tag{10.34}$$

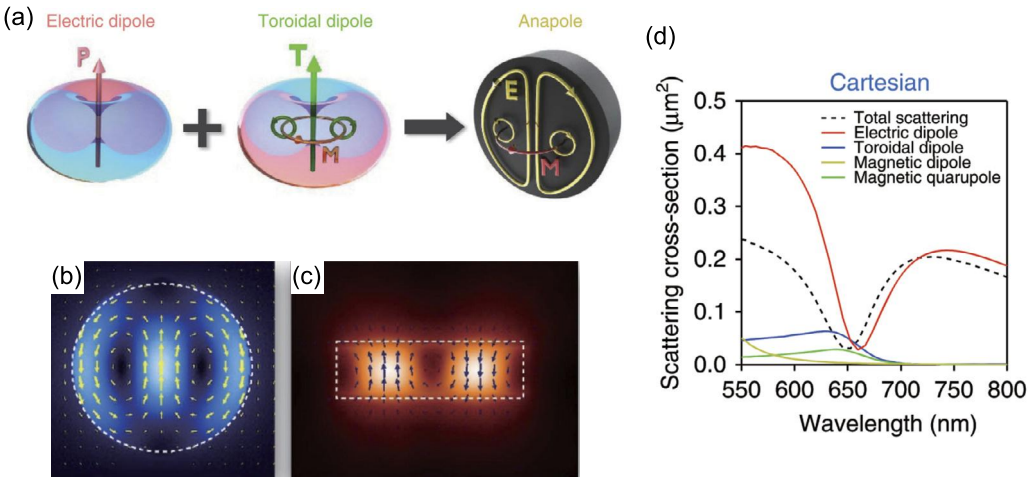

Figure 10.9. (a) Illustration of an anapole supported by a dielectric cylinder. The anapole is caused by the destructive interference of an electric dipole P and a toroidal dipole T. (b) and (c) show the simulated electric and magnetic scattered near-field distribution, respectively, at a wavelength of 650 nm. (d) The Cartesian multipole decompositions of the scattering spectra for a silicon disk with a diameter of 310 nm. Scattered fields from the two leading dipoles: ED and TD are out of phase and cancel each other in the far field. As a result, an anapole state is obtained at a wavelength of around 650 nm. Reprinted with permission from ref. [91] ©2015 Springer Nature.

and the corresponding toroidal multipoles are:

$$\begin{aligned}
\mathbf{T}^{p} &= \frac{1}{10c}\int d^3\mathbf{s}\left[3(\mathbf{s}\cdot\mathbf{J}(\omega))\mathbf{s} - 2s^2\mathbf{J}(\omega)\right],\\
\mathbf{T}^{m} &= \frac{ik}{20}\int d^3\mathbf{s}\left[s^2(\mathbf{s}\times\mathbf{J})\right],\\
\mathbf{T}^{Q}_{\alpha\beta} &= \frac{1}{14c}\int d^3\mathbf{s}\left[4s_\alpha s_\beta(\mathbf{s}\cdot\mathbf{J}) - 5s^2(s_\alpha J_\beta + s_\beta J_\alpha)\right],\\
\mathbf{T}^{M}_{\alpha\beta} &= \frac{ik}{14}\int d^3\mathbf{s}\, s^2\left[s_\alpha(\mathbf{s}\times\mathbf{J})_\alpha + s_\beta\mathbf{s}\times\mathbf{J})_\alpha\right],
\end{aligned} \tag{10.35}$$

where $\mathbf{T}^{p(m)}$ is the moment for the electric (magnetic) toroidal dipole; $\mathbf{T}^{Q(M)}_{\alpha\beta}$ is the electric (magnetic) toroidal quadrupole. Here, we have applied the subwavelength approximation to p_α in Eq. (10.29) with $j_0(ks) \approx 1-(ks)^2/6$ and $j_2(ks) \approx (ks)^2/15$. The total electric dipole moment is:

$$\mathbf{p}_{total} = \mathbf{p}_{Car} + ik\mathbf{T}_{car.} \tag{10.36}$$

Therefore, the radiated electric field in the far field from these two types of dipoles is given as:

$$\mathbf{E}_{sca} \sim \frac{k_0^2}{4\pi\varepsilon_0}\mathbf{n} \times \mathbf{p}_{total} \times \mathbf{n} \tag{10.37}$$

When the Cartesian electric dipole oscillates out of phase with the toroidal dipole such that $\mathbf{p}Car = -ik\mathbf{T}_{Car}$, the scattered field becomes zero, i.e., $E_{sca} = 0$. As a result, the anapole mode is often associated with invisibility because the scattering from other multipoles is negligible. Moreover, since radiation is absent, the radiative loss can be suppressed. This implies that a high Q-factor mode could be achievable for a low-loss or lossless oscillating system. Previous studies have shown that the scatterings of magnetic dipoles (MD), electric quadrupoles (EQ), and magnetic quadrupoles (MQ) are very small, leading to a transmission that is nearly unity at the high-Q anapole mode, which is known as anapole-induced transparency [92–94].

The key to obtaining an anapole is to enhance the response of toroidal dipoles while suppressing the response from magnetic dipoles and quadrupoles. The microwave range has seen pioneering work investigating the anapole state on a single scatter using 4-fold and 8-fold symmetric dumbbell-shaped apertures [93]. These apertures induce strong toroidal dipole responses through excited poloidal currents flowing around the circular aperture edge. By altering the meta-atoms' geometry, the induced electric and toroidal dipoles can be balanced, leading to the observation of two sharp peaks with high Q-factors in the transmission spectra for each of these two structures.

Although extremely high Q-factor anapole modes have been demonstrated on metallic metasurfaces in the microwave range, the inherent metallic loss impedes scaling to higher frequency ranges [95,96]. To overcome the drawback of metallic loss, high-index dielectric materials such as silicon, GaAs, phase-change materials, and ceramics have been considered as alternatives with great potential for use in the optical and infrared ranges. The anapole mode on a single dielectric scatter was first observed on a silicon disk with a diameter of 310 nm and a height of 50 nm [91]. As shown in Fig. 10.9 (b) and (c), opposite circular displacement currents are excited in the disk at the anapole wavelength, inducing a circular magnetic moment distribution perpendicular to the disk surface. Such a circulating magnetic moment leads to a strong toroidal dipole moment parallel to the disk surface, as illustrated in Fig. 10.9 (a). The destructive interference of the toroidal dipole and the electric dipole in the far field results in significant suppression of the total scattering. Fig. 10.9 (d) shows that

the scattering is mainly contributed by the electric and toroidal dipoles. When the scattering spectra of these two types of dipoles cross each other, the total scattering reaches a minimal value at the wavelength of 650 nm, indicating destructive interference of the two dipoles in the far field. This suppressed scattering was further verified by a near-field scanning optical microscope (NSOM) experiment. The anapole mode was visually observed near the wavelength of 640 nm with a hotspot in the middle of the disk, matching the simulation results. In addition to a single scatter, a meta-molecular cluster comprising four dielectric cylinders can also support a strong toroidal dipole response [97]. By placing a matching electric dipole antenna in the center of the cluster, the measured results with strongly suppressed scattering clearly identify the anapole mode [98]. A similar complementary design with four holes in a silicon membrane was proposed later in the visible range [99].

As stated in the previous section, dictated by the optical theorem and energy conservation, the forward scattering cannot be perfectly diminished. While the fundamental anapole has shown significant suppression of forward scattering, it is also possible to further reduce the forward scattering by obtaining higher-order anapole states, and even hybrid anapoles, which simultaneously achieve destructive interference for the major multipoles and their toroidal counterparts as $p_{l,car}^{(e,m)} + ikT_{l,car}^{(e,m)} = 0$, where $p_{car}^{(e,m)}$ denotes the l_{th} order of electric (e) or magnetic (m) multipole moments, and the corresponding electric and magnetic toroidal moments with $T_{l,car}^{e}$ and $T_{l,car}^{m}$. By breaking the scatter's spherical symmetry, hybrid anapoles are possible by tuning the two parameters of a cylinder [100]. A direct identification of anapoles with different orders can be implemented using a near-field detection method to monitor the normal component of the electric field. It is found that high-order anapole states possess stronger energy concentration and narrower bandwidth of the resonances [101]. Because of the significant reduction of the forward scattering, the transmission can be close to 1. Surprisingly, the hybrid anapoles are found to be robust against the change of inter-particle separation, disorder, and substrate [92]. For silicon resonators with a diameter of 260 nm, height of 370 nm, and lattice size of 560 nm, the scattering contributions from the dipoles and quadrupoles are remarkably suppressed around 750 nm due to the destructive interferences of the dipoles and quadrupoles with their corresponding toroidal multipoles, respectively. At such a hybrid anapole state, the numerical simulation also shows that the unity transmission can be obtained if the material loss is ignored.

Not only can anapole states suppress the total scattered field, but they can also lead to significant enhancement in the near field [91,101]. The field enhancement in the anapole state has initiated many potential applications, such as enhanced nonlinear processes for Raman emission and harmonic generation [102–105]. The excitation of the anapole state can efficiently suppress the elastic scattering in silicon, which minimizes the light-matter interaction. However, the field enhancement at the anapole state can significantly promote the emission at Stokes and anti-Stokes wavelengths, leading to enhanced Raman signals with a factor of 80 for the Stokes emission compared to an unstructured Si film [104]. Through designing single germanium nanodisks with the anapole state at 1650 nm, the enhanced field can remarkably increase the generation of the third harmonic by 4 orders of magnitude compared to that on an unstructured germanium film [102]. Even higher enhancement of harmonics generation was observed on germanium nanodisks with high-order anapole states [103]. In addition to Raman emission and high harmonic generation, the field enhancement in anapoles can also be used for other nonlinear applications, such as nanolasing [105,106]. Patterning of a freestanding InGaAsP membrane into arrayed split-nanodisk resonators permits the cancellation of the scattering due to the balanced electric dipole and toroidal dipole moments at 1474.5 nm, and enables a high quality factor Q over 200 from the experimental demonstration. Applying a pump pulse with a fluence over 10 $\mu J/cm^3$ at a wavelength of 980 nm, a sharp lasing with a peak at 1503 nm was observed [105].

The sensitivity of the scattering to the surrounding environment in anapole states also makes them promising for refractive index sensing. However, the strong field confinement within dielectric anapoles is often hindered by the lack of interaction between the enhanced field and the chemicals. Recently, a plasmonic metasurface with an anapole mode around 1340 nm was shown to achieve a high figure of merit of 330 nm/RIU [107]. This metasurface, consisting of a 30-nm dumbbell-perforated gold film patterned over an array of vertical split-ring resonators, achieves a large electric field enhancement factor of 15.2 in the gaps of the dumbbell-perforated film. When oil with a refractive index ranging from 1.3 to 1.39 is deposited on the metasurface, the resonant wavelength shifts by 33 nm from 1435.5 nm due to the increased sensitivity of the field to the change in refractive index in the surrounding environment. In addition to static anapoles, the hybridization of metasurfaces with active materials, such as phase change materials $Ge_2Se_2Te_5$ [108] and semiconductors [109], en-

ables dynamic control of anapole states, which is of great interest for applications in sensing, lasing, and optical switches.

10.6 Pancharatnam–Berry phase metasurfaces

Pancharatnam–Berry Phase (PBP) metasurfaces have emerged as a powerful tool for manipulating the phase of light. Unlike conventional optical devices, which rely on the interaction between light and bulk material properties, PBP metasurfaces operate by manipulating the phase of light at a subwavelength scale, making them much thinner and more compact than traditional approaches. The concept of geometric phase was first introduced by Indian physicist, R. Pancharatnam [110], and Berry further developed this concept through consideration of the adiabatic phase in slowly varying quantum systems [111,112]. The underlying physics of PBP metasurfaces lies in the geometric phase, which is an additional phase acquired by light when its polarization undergoes an evolution, which may be described as a path on the Poincaré sphere [113,114]. For example, a polarization which traces out a closed path on the Poincaré sphere should return to its original state. However, even for closed paths, a Pancharatnam–Berry phase Φ_{pb} arises, which is given by half of the solid angle Ω subtended by the polarization, i.e. $\Phi_{pb} = \Omega/2$ [115].

In PBP metasurfaces, this geometric phase can be controlled by the orientation of subwavelength structures on a surface [118]. When light passes through the PBP metasurface, it acquires a phase shift that depends on the orientation of the unit-cells [119]. Through manipulation of the symmetry and orientation of these features, PBP metasurfaces can control the polarization, phase, and amplitude of light. The design of PBP metasurfaces typically involves optimizing their geometry to achieve the desired phase profile, which can be achieved through various computational methods such as finite element simulations or rigorous coupled wave analyzes.

PBP metasurfaces have numerous applications in fields such as imaging, sensing, and holography [120,121]. One promising application of PBP metasurfaces is in optical communication [122], where researchers demonstrated the use of a PBP metasurface to achieve quasi-perfect vortices [123]. The metasurface consisted of an array of subwavelength elliptical resonators that were designed to induce a spatially dependent transmission phase shift, allowing light to pass through the material with minimal loss. This technology has the potential to significantly improve the

efficiency of optical communication systems. PBP metasurfaces have also been used to achieve nearly any desired optical phase element. Researchers demonstrated continuous metal gratings, which achieve phase that is not due to optical path differences, but rather occurs due to the geometric phase [115]. The continuous nature of the grating further enables continuity of the resulting field and eliminating diffraction due to discontinuities. Since the elements are polarization sensitive, they are suitable for applications such as optical switching, optical interconnects, and beam splitting. The authors presented both a theoretical and experimental study showing a Pancharatnam–Berry phase-based diffraction grating operating at a wavelength of 10.6 μm [115]. PBP metasurfaces also have potential in the field of nonlinear optics. In one study, researchers used a PBP metasurface to produce diffraction orders of both second-harmonic and fourwave-mixing radiation [124]. The metasurface consisted of an array of nanorods that were designed to induce a phase shift in the second harmonic wave, allowing for efficient second harmonic generation. This technology has potential applications in fields such as spectroscopy, imaging, and quantum optics.

Prior theoretical work indicated that the cross-polarization transmission efficiency with a single metasurface layer is bounded by an upper limit of 25% [125]. Another limitation may arise when using metasurfaces, since they are typically fashioned with resonant elements the bandwidth is usually small and therefore limited. To address the above limitations, a different study focused on the development of a fully controllable Pancharatnam–Berry metasurface array using metallic split-ring resonators (SRRs), which achieved high cross-polarized transmission of left circularly polarized (LCP) and right circularly polarized (RCP) radiation with broad bandwidth operation [116]. The authors demonstrated a polarizing beam splitter using an array of split ring resonators where each split ring resonators were formed into a 1×6 super-cell where each SRR was rotated in plane – see inset to Fig. 10.10 (b). Here, each rotated SRR was used to achieve a specific transmitted phase of RCP or LCP with nearly constant transmitted amplitude. Simulations indicate that for normally incident linear polarized (LP) radiation, that two beams would emerge at $-45°$ (LCP) and $+45°$ (RCP) on the other side of the metasurface. Further, for LCP (RCP) input a RCP (LCP) beam would be transmitted.

Experiments were carried out in an anechoic chamber in the frequency range of 8-12 GHz using two circular polarized horns and a vector network analyzer – see Fig. 10.10 (a). In a series of experiments, the authors used a normally incident input a beam of a particular polarization (LCP, RCP, or LP) to the metasurface po-

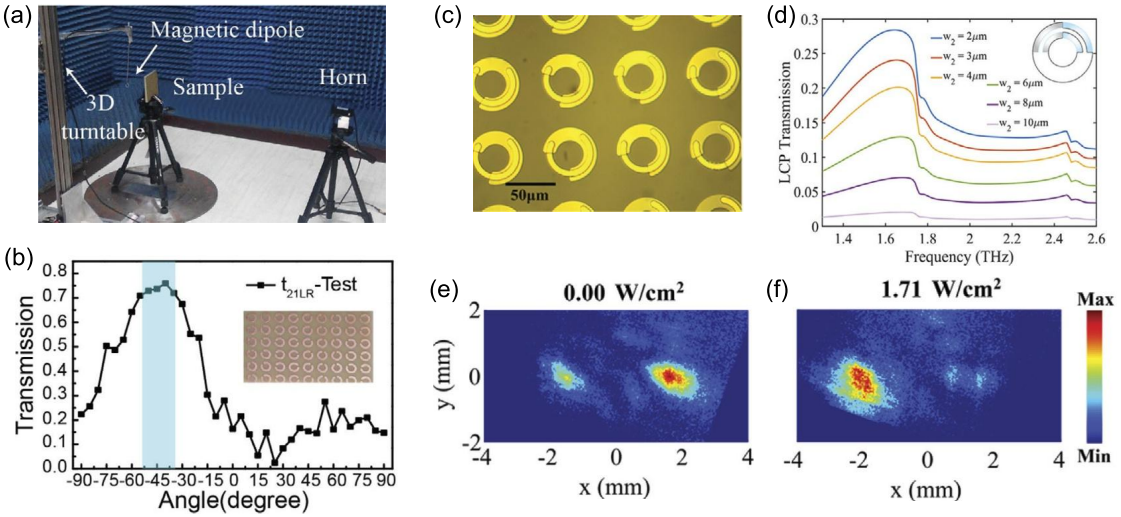

Figure 10.10. (a) Measurement setup of the 3D near-field scanning system in an anechoic chamber. (b) Experimentally measured amplitude transmission with varying the detecting angles. (c) Microscopic image of the fabricated metalens sample. (d) Simulated results of the cross-polarization efficiency with different widths of the ring. (e)-(f) Experimentally measured the electric field distributions varying with the optical pumping power. (a)-(b) Reprinted with permission from ref. [116] ©2016 Springer Nature. (c)-(f) Reprinted with permission from ref. [117] ©2022 Optica Publishing Group.

larizing beam splitter, and performed 3D near-field scanning to measure both the input and output fields. For the specific case of a normally incident RCP wave to the metasurface polarizing beam splitter, the authors measured an output LCP beam at an angle of $-43°$ with a maximum amplitude transmission of 80%, as shown in Fig. 10.10 (b). The researchers efficiently manipulated polarization coupling in multilayer metasurfaces to achieve a high conversion coefficient of circularly polarized waves within a broad bandwidth. They also demonstrate the ability to fully control the Pancharatnam-Berry phase, which enables the realization of a polarized beam splitter with abnormal transmission and high conversion efficiency. This technology has potential applications in the field of optical switching, and optical interconnects.

A different study explored the option of achieving a dynamic Pancharatnam-Berry phase with metasurfaces using photodoping as an external control mechanism. The metasurfaces were fashioned from SRRs and consisted of gold and silicon resonant elements supported by a sapphire substrate, and the two SRRs were aligned uniaxially. A key tuning parameter was the angle that each formed with the array axis and also with each other, (see Fig. 10.10 (c)), while the other geometrical parameters were

also carefully selected for high transmission in the THz range. In Fig. 10.10 (c), the larger SRR is formed from silicon, while the smaller SRR is made from gold. The width of the gold SRR is denoted by w_2, and this geometrical parameter was used to control the transmission of LCP light. In Fig. 10.10 (d), the simulated cross-polarization efficiency as a function of frequency is shown across the THz frequency range for various values of w_2, as indicated by the inset legend.

The metasurface was fabricated using a silicon-on-sapphire wafer, and the authors used an optical pump to dynamically modify the conductivity of silicon, which permitted control of the focusing properties of the metasurface for circularly polarized light. The fabricated metasurface is shown in Fig. 10.10 (c) and experiments were conducting with both THz radiation and the optical pump incident from the sapphire side. The THz radiation was normally incident, while the optical pump was at an angle of 25° with respect to the surface normal. The wavelength of the optical pump was chosen to 532 nm and was provide by a CW laser. The THz radiation was continuous and linearly polarized at a frequency of 2.52 THz, which was generated by a far infrared (FIR) laser based on CO_2 pumping of low pressure of methanol molecules. In Fig. 10.10 (e) and (f) an image of the THz electric field is shown for no optical pumping (e), and for a pump power of 1.71 W/m^2. In initially with zero pump power, the metasurface lens focuses at the point $x = 2$ mm. However, as the pump power is increased, the silicon SRR increases in conductivity, thereby adding an additional phase to the transmitted THz radiation, causing the focus point of the field to shift to $x = -2$ mm. The study has the capability to add dynamical control to the aforementioned potential application of Pancharatnam–Berry phase metasurfaces.

In conclusion, PBP metasurfaces are a powerful tool for manipulating the phase of light at a subwavelength scale. They have a wide range of applications in fields such as optical communication, sensing, super-resolution imaging, holography, beam shaping and steering, nonlinear optics, and color display technology. The unique properties of PBP metasurfaces make them a subject of intense research, and there are many exciting developments on the horizon.

Acknowledgments

WJP acknowledges support from the US Department of Energy (DESC0014372). KBF acknowledges support from the National Natural Science Foundation of China (62275118) and the Fundamental Research Funds for the Central Universities.

CRediT authorship contribution statement

Willie J. Padilla: Conceptualization of this study, Methodology, Software.

References

[1] S.G. Louie, M.L. Cohen, Conceptual Foundations of Materials: Volume 2. Contemporary Concepts of Condensed Matter Science, 2nd edition, Elsevier Science, London, England, Sept. 2006.

[2] M. Dressel, G. Gruner, Electrodynamics of Solids, Cambridge University Press, Cambridge, England, Jan. 2002.

[3] H. Kitamura, Derivation of the Drude conductivity from quantum kinetic equations, European Journal of Physics 36 (6) (Nov. 2015) 065010.

[4] F.F. Wooten, Optical Properties of Solids, Academic Press, ISBN 0127634509, 1972.

[5] A. Zangwill, Modern electrodynamics, Cambridge University Press, ISBN 9780521896979, 2013.

[6] D.N. Basov, R.D. Averitt, D. van der Marel, M. Dressel, K. Haule, Electrodynamics of correlated electron materials, Reviews of Modern Physics 83 (2) (June 2011) 471–541, https://doi.org/10.1103/revmodphys.83.471.

[7] Y. Peng, T. Paudel, W.-C. Chen, W.J. Padilla, Z.F. Ren, K. Kempa, Percolation and polaritonic effects in periodic planar nanostructures evolving from holes to islands, Applied Physics Letters 97 (4) (July 2010) 041901, https://doi.org/10.1063/1.3462935.

[8] W.-C. Chen, N.I. Landy, K. Kempa, W.J. Padilla, A subwavelength extraordinary-optical-transmission channel in Babinet metamaterials, Advanced Optical Materials 1 (3) (Feb. 2013) 221–226, https://doi.org/10.1002/adom.201200016.

[9] W. Götze, P. Wölfle, Homogeneous dynamical conductivity of simple metals, Physical Review B 6 (4) (Aug. 1972) 1226–1238, https://doi.org/10.1103/physrevb.6.1226.

[10] S. Shulga, O. Dolgov, E. Maksimov, Electronic states and optical spectra of HTSC with electron-phonon coupling, Physica C: Superconductivity 178 (4–6) (Aug. 1991) 266–274, https://doi.org/10.1016/0921-4534(91)90073-8.

[11] U. Fano, Sullo spettro di assorbimento dei gas nobili presso il limite dello spettro d'arco, Nuovo Cimento 12 (1935) 154–161.

[12] R.P. Madden, K. Codling, Two-electron excitation states in helium, The Astrophysical Journal 141 (Feb. 1965) 364, https://doi.org/10.1086/148132.

[13] A.E. Miroshnichenko, S. Flach, Y.S. Kivshar, Fano resonances in nanoscale structures, Reviews of Modern Physics 82 (3) (Aug. 2010) 2257–2298, https://doi.org/10.1103/revmodphys.82.2257.

[14] S. Zhang, D.A. Genov, Y. Wang, M. Liu, X. Zhang, Plasmon-induced transparency in metamaterials, Physical Review Letters 101 (4) (July 2008), https://doi.org/10.1103/physrevlett.101.047401.

[15] N. Papasimakis, V.A. Fedotov, N.I. Zheludev, S.L. Prosvirnin, Metamaterial analog of electromagnetically induced transparency, Physical Review Letters 101 (25) (Dec. 2008), https://doi.org/10.1103/physrevlett.101.253903.

[16] P. Tassin, L. Zhang, T. Koschny, E.N. Economou, C.M. Soukoulis, Low-loss metamaterials based on classical electromagnetically induced

transparency, Physical Review Letters 102 (5) (Feb. 2009), https://doi.org/10.1103/physrevlett.102.053901.
[17] B. Peng, Ş.K. Özdemir, W. Chen, F. Nori, L. Yang, What is and what is not electromagnetically induced transparency in whispering-gallery microcavities, Nature Communications 5 (1) (Oct. 2014), https://doi.org/10.1038/ncomms6082.
[18] K.-J. Boller, A. Imamoğlu, S.E. Harris, Observation of electromagnetically induced transparency, Physical Review Letters 66 (20) (May 1991) 2593–2596, https://doi.org/10.1103/physrevlett.66.2593.
[19] C. Liu, Z. Dutton, C.H. Behroozi, L.V. Hau, Observation of coherent optical information storage in an atomic medium using halted light pulses, Nature 409 (6819) (Jan. 2001) 490–493, https://doi.org/10.1038/35054017.
[20] M. Fleischhauer, A. Imamoglu, J.P. Marangos, Electromagnetically induced transparency: optics in coherent media, Reviews of Modern Physics 77 (2) (July 2005) 633–673, https://doi.org/10.1103/revmodphys.77.633.
[21] M. Iizawa, S. Kosugi, F. Koike, Y. Azuma, The quantum and classical Fano parameter q, Physica Scripta 96 (5) (Feb. 2021) 055401, https://doi.org/10.1088/1402-4896/abe580.
[22] C. Huygens, Treatise on Light, BiblioLife, Charleston, SC, May 2008.
[23] S.A. Schelkunoff, Some equivalence theorems of electromagnetics and their application to radiation problems, The Bell System Technical Journal 15 (1) (Jan. 1936) 92–112, https://doi.org/10.1002/j.1538-7305.1936.tb00720.x.
[24] M. Kerker, D.-S. Wang, C.L. Giles, Electromagnetic scattering by magnetic spheres, Journal of the Optical Society of America 73 (6) (June 1983) 765, https://doi.org/10.1364/josa.73.000765.
[25] R. Alaee, R. Filter, D. Lehr, F. Lederer, C. Rockstuhl, A generalized Kerker condition for highly directive nanoantennas, Optics Letters 40 (11) (June 2015) 2645, https://doi.org/10.1364/ol.40.002645.
[26] F. Monticone, N.M. Estakhri, A. Alù, Full control of nanoscale optical transmission with a composite metascreen, Physical Review Letters 110 (20) (May 2013), https://doi.org/10.1103/physrevlett.110.203903.
[27] C. Liu, L. Chen, T. Wu, Y. Liu, J. Li, Y. Wang, Z. Yu, H. Ye, L. Yu, All-dielectric three-element transmissive Huygens' metasurface performing anomalous refraction, Photonics Research 7 (12) (Dec. 2019) 1501, https://doi.org/10.1364/prj.7.001501.
[28] Q. Yang, S. Kruk, Y. Xu, Q. Wang, Y.K. Srivastava, K. Koshelev, I. Kravchenko, R. Singh, J. Han, Y. Kivshar, I. Shadrivov, Mie-resonant membrane Huygens' metasurfaces, Advanced Functional Materials 30 (4) (Nov. 2019) 1906851, https://doi.org/10.1002/adfm.201906851.
[29] W. Zhao, H. Jiang, B. Liu, J. Song, Y. Jiang, C. Tang, J. Li, Dielectric Huygens' metasurface for high-efficiency hologram operating in transmission mode, Scientific Reports 6 (1) (July 2016), https://doi.org/10.1038/srep30613.
[30] M. Selvanayagam, G.V. Eleftheriades, Experimental demonstration of active electromagnetic cloaking, Physical Review X 3 (4) (Nov. 2013), https://doi.org/10.1103/physrevx.3.041011.
[31] P. Ang, G. Xu, G.V. Eleftheriades, Invisibility cloaking with passive and active Huygens's metasurfaces, Applied Physics Letters 118 (7) (Feb. 2021) 071903, https://doi.org/10.1063/5.0041996.
[32] M. Yazdi, M. Albooyeh, R. Alaee, V. Asadchy, N. Komjani, C. Rockstuhl, C.R. Simovski, S. Tretyakov, A bianisotropic metasurface with resonant asymmetric absorption, IEEE Transactions on Antennas and Propagation 63 (7) (July 2015) 3004–3015, https://doi.org/10.1109/tap.2015.2423855.
[33] Y. Ra'di, V.S. Asadchy, S.A. Tretyakov, One-way transparent sheets, Physical Review B 89 (7) (Feb. 2014), https://doi.org/10.1103/physrevb.89.075109.

[34] S. Tretyakov, Analytical Modeling in Applied Electromagnetics, Artech House Electromagnetic Analysis Series, Artech House, Norwood, MA, May 2003.

[35] R. Marques, F. Martin, M. Sorolla, Metamaterials with Negative Parameters, Wiley Series in Microwave and Optical Engineering, Wiley-Interscience, New York, Jan. 2008.

[36] R. Alaee, M. Albooyeh, M. Yazdi, N. Komjani, C. Simovski, F. Lederer, C. Rockstuhl, Magnetoelectric coupling in nonidentical plasmonic nanoparticles: theory and applications, Physical Review B 91 (Mar 2015) 115119, https://doi.org/10.1103/PhysRevB.91.115119, https://link.aps.org/doi/10.1103/PhysRevB.91.115119.

[37] R. Alaee, M. Albooyeh, A. Rahimzadegan, M.S. Mirmoosa, Y.S. Kivshar, C. Rockstuhl, All-dielectric reciprocal bianisotropic nanoparticles, Physical Review B 92 (Dec 2015) 245130, https://doi.org/10.1103/PhysRevB.92.245130, https://link.aps.org/doi/10.1103/PhysRevB.92.245130.

[38] K. Fan, I.V. Shadrivov, A.E. Miroshnichenko, W.J. Padilla, Infrared all-dielectric Kerker metasurfaces, Optics Express 29 (7) (Mar. 2021) 10518, https://doi.org/10.1364/oe.421187.

[39] C. Pfeiffer, C. Zhang, V. Ray, L.J. Guo, A. Grbic, High performance bianisotropic metasurfaces: asymmetric transmission of light, Physical Review Letters 113 (2) (July 2014), https://doi.org/10.1103/physrevlett.113.023902.

[40] V. Asadchy, I. Faniayeu, Y. Ra'di, S. Khakhomov, I. Semchenko, S. Tretyakov, Broadband reflectionless metasheets: frequency-selective transmission and perfect absorption, Physical Review X 5 (3) (July 2015), https://doi.org/10.1103/physrevx.5.031005.

[41] M. Liu, D.-Y. Choi, Extreme Huygens' metasurfaces based on quasi-bound states in the continuum, Nano Letters 18 (12) (Nov. 2018) 8062–8069, https://doi.org/10.1021/acs.nanolett.8b04774.

[42] J. Tian, Q. Li, P.A. Belov, R.K. Sinha, W. Qian, M. Qiu, High-q all-dielectric metasurface: super and suppressed optical absorption, ACS Photonics 7 (6) (Apr. 2020) 1436–1443, https://doi.org/10.1021/acsphotonics.0c00003.

[43] R. Masoudian Saadabad, L. Huang, A.E. Miroshnichenko, Polarization-independent perfect absorber enabled by quasibound states in the continuum, Physical Review B 104 (Dec 2021) 235405, https://doi.org/10.1103/PhysRevB.104.235405, https://link.aps.org/doi/10.1103/PhysRevB.104.235405.

[44] R. Dezert, P. Richetti, A. Baron, Isotropic Huygens dipoles and multipoles with colloidal particles, Physical Review B 96 (18) (Nov. 2017), https://doi.org/10.1103/physrevb.96.180201.

[45] A. Rahimzadegan, D. Arslan, D. Dams, A. Groner, X. Garcia-Santiago, R. Alaee, I. Fernandez-Corbaton, T. Pertsch, I. Staude, C. Rockstuhl, Beyond dipolar Huygens' metasurfaces for full-phase coverage and unity transmittance, Nanophotonics 9 (1) (Nov. 2019) 75–82, https://doi.org/10.1515/nanoph-2019-0239.

[46] R. Dezert, Theoretical study of isotropic Huygens particles for metasurfaces, Theses, Université de Bordeaux, Dec. 2019, https://tel.archives-ouvertes.fr/tel-02869591.

[47] H.K. Shamkhi, K.V. Baryshnikova, A. Sayanskiy, P. Kapitanova, P.D. Terekhov, P. Belov, A. Karabchevsky, A.B. Evlyukhin, Y. Kivshar, A.S. Shalin, Transverse scattering and generalized Kerker effects in all-dielectric Mie-resonant metaoptics, Physical Review Letters 122 (19) (May 2019), https://doi.org/10.1103/physrevlett.122.193905.

[48] K.E. Chong, I. Staude, A. James, J. Dominguez, S. Liu, S. Campione, G.S. Subramania, T.S. Luk, M. Decker, D.N. Neshev, I. Brener, Y.S. Kivshar, Polarization-independent silicon metadevices for efficient optical wavefront control, Nano Letters 15 (8) (July 2015) 5369–5374, https://doi.org/10.1021/acs.nanolett.5b01752.

[49] K.E. Chong, L. Wang, I. Staude, A.R. James, J. Dominguez, S. Liu, G.S. Subramania, M. Decker, D.N. Neshev, I. Brener, Y.S. Kivshar, Efficient polarization-insensitive complex wavefront control using Huygens' metasurfaces based on dielectric resonant meta-atoms, ACS Photonics 3 (4) (Mar. 2016) 514–519, https://doi.org/10.1021/acsphotonics.5b00678.

[50] Tianhua Feng, Alexander A. Potapov, Zixian Liang, Yi Xu, Huygens metasurfaces based on congener dipole excitations, Physical Review Applied 13 (2) (2020) 021002.

[51] T.-A. Chen, Y.-C. Chou, T.-Y. Huang, Y.-J. Lu, Y.-P. Kuang, T.-J. Yen, TiO_2 nanodisk arrays as all-dielectric Huygens' metasurfaces for engineering the wavefront of near-UV light, ACS Applied Nano Materials 5 (1) (Dec. 2021) 925–930, https://doi.org/10.1021/acsanm.1c03585.

[52] C. Pfeiffer, A. Grbic, Metamaterial Huygens' surfaces: tailoring wave fronts with reflectionless sheets, Physical Review Letters 110 (19) (May 2013), https://doi.org/10.1103/physrevlett.110.197401.

[53] J.P.S. Wong, M. Selvanayagam, G.V. Eleftheriades, Polarization considerations for scalar Huygens metasurfaces and characterization for 2-D refraction, IEEE Transactions on Microwave Theory and Techniques 63 (3) (Mar. 2015) 913–924, https://doi.org/10.1109/tmtt.2015.2392931.

[54] A. Epstein, J.P.S. Wong, G.V. Eleftheriades, Cavity-excited Huygens' metasurface antennas for near-unity aperture illumination efficiency from arbitrarily large apertures, Nature Communications 7 (1) (Jan. 2016), https://doi.org/10.1038/ncomms10360.

[55] C. Pfeiffer, N.K. Emani, A.M. Shaltout, A. Boltasseva, V.M. Shalaev, A. Grbic, Efficient light bending with isotropic metamaterial Huygens' surfaces, Nano Letters 14 (5) (Apr. 2014) 2491–2497, https://doi.org/10.1021/nl5001746.

[56] J. van de Groep, A. Polman, Designing dielectric resonators on substrates: combining magnetic and electric resonances, Optics Express 21 (22) (Oct. 2013) 26285, https://doi.org/10.1364/oe.21.026285.

[57] Y. Yang, A.E. Miroshnichenko, S.V. Kostinski, M. Odit, P. Kapitanova, M. Qiu, Y.S. Kivshar, Multimode directionality in all-dielectric metasurfaces, Physical Review B 95 (16) (Apr. 2017), https://doi.org/10.1103/physrevb.95.165426.

[58] Michael A. Cole, David A. Powell, Ilya V. Shadrivov, Strong terahertz absorption in all-dielectric Huygens' metasurfaces, Nanotechnology 27 (42) (2016) 424003.

[59] M. Decker, I. Staude, M. Falkner, J. Dominguez, D.N. Neshev, I. Brener, T. Pertsch, Y.S. Kivshar, High-efficiency dielectric Huygens' surfaces, Advanced Optical Materials 3 (6) (Feb. 2015) 813–820, https://doi.org/10.1002/adom.201400584.

[60] A.J. Ollanik, J.A. Smith, M.J. Belue, M.D. Escarra, High-efficiency all-dielectric Huygens metasurfaces from the ultraviolet to the infrared, ACS Photonics 5 (4) (Feb. 2018) 1351–1358, https://doi.org/10.1021/acsphotonics.7b01368.

[61] A. Cardin, K. Fan, W. Padilla, Role of loss in all-dielectric metasurfaces, Optics Express 26 (13) (June 2018) 17669, https://doi.org/10.1364/oe.26.017669.

[62] X. Liu, K. Fan, I.V. Shadrivov, W.J. Padilla, Experimental realization of a terahertz all-dielectric metasurface absorber, Optics Express 25 (1) (Jan. 2017) 191, https://doi.org/10.1364/oe.25.000191.
[63] X. Ming, X. Liu, L. Sun, W.J. Padilla, Degenerate critical coupling in all-dielectric metasurface absorbers, Optics Express 25 (20) (Sept. 2017) 24658, https://doi.org/10.1364/oe.25.024658.
[64] J.Y. Suen, K. Fan, W.J. Padilla, A zero-rank, maximum nullity perfect electromagnetic wave absorber, Advanced Optical Materials 7 (8) (Jan. 2019) 1801632, https://doi.org/10.1002/adom.201801632.
[65] K. Fan, J. Zhang, X. Liu, G.-F. Zhang, R.D. Averitt, W.J. Padilla, Phototunable dielectric Huygens' metasurfaces, Advanced Materials 30 (22) (Apr. 2018) 1800278, https://doi.org/10.1002/adma.201800278.
[66] A. Howes, W. Wang, I. Kravchenko, J. Valentine, Dynamic transmission control based on all-dielectric Huygens metasurfaces, Optica 5 (7) (June 2018) 787, https://doi.org/10.1364/optica.5.000787.
[67] A. Leitis, A. Heßler, S. Wahl, M. Wuttig, T. Taubner, A. Tittl, H. Altug, All-dielectric programmable Huygens' metasurfaces, Advanced Functional Materials 30 (19) (Mar. 2020) 1910259, https://doi.org/10.1002/adfm.201910259.
[68] K. Chen, Y. Feng, F. Monticone, J. Zhao, B. Zhu, T. Jiang, L. Zhang, Y. Kim, X. Ding, S. Zhang, A. Alù, C.-W. Qiu, A reconfigurable active Huygens' metalens, Advanced Materials 29 (17) (Feb. 2017) 1606422, https://doi.org/10.1002/adma.201606422.
[69] L. Cong, R. Singh, Spatiotemporal dielectric metasurfaces for unidirectional propagation and reconfigurable steering of terahertz beams, Advanced Materials 32 (28) (May 2020) 2001418, https://doi.org/10.1002/adma.202001418.
[70] L. Zhang, J. Ding, H. Zheng, S. An, H. Lin, B. Zheng, Q. Du, G. Yin, J. Michon, Y. Zhang, Z. Fang, M.Y. Shalaginov, L. Deng, T. Gu, H. Zhang, J. Hu, Ultra-thin high-efficiency mid-infrared transmissive Huygens meta-optics, Nature Communications 9 (1) (Apr. 2018), https://doi.org/10.1038/s41467-018-03831-7.
[71] S.-Q. Li, X. Xu, R.M. Veetil, V. Valuckas, R. Paniagua-Domínguez, A.I. Kuznetsov, Phase-only transmissive spatial light modulator based on tunable dielectric metasurface, Science 364 (6445) (June 2019) 1087–1090, https://doi.org/10.1126/science.aaw6747.
[72] M.M. Salary, H. Mosallaei, Tunable all-dielectric metasurfaces for phase-only modulation of transmitted light based on quasi-bound states in the continuum, ACS Photonics 7 (7) (June 2020) 1813–1829, https://doi.org/10.1021/acsphotonics.0c00554.
[73] W. Song, X. Liang, S. Li, D. Li, R. Paniagua-Domínguez, K.H. Lai, Q. Lin, Y. Zheng, A.I. Kuznetsov, Large-scale Huygens' metasurfaces for holographic 3D near-eye displays, Laser & Photonics Reviews 15 (9) (Aug. 2021) 2000538, https://doi.org/10.1002/lpor.202000538.
[74] A. Howes, Z. Zhu, D. Curie, J.R. Avila, V.D. Wheeler, R.F. Haglund, J.G. Valentine, Optical limiting based on Huygens' metasurfaces, Nano Letters 20 (6) (May 2020) 4638–4644, https://doi.org/10.1021/acs.nanolett.0c01574.
[75] M. Liu, A.B. Kozyrev, I.V. Shadrivov, Time-varying metasurfaces for broadband spectral camouflage, Physical Review Applied 12 (5) (Nov. 2019), https://doi.org/10.1103/physrevapplied.12.054052.
[76] E. Galiffi, R. Tirole, S. Yin, H. Li, S. Vezzoli, P.A. Huidobro, M.G. Silveirinha, R. Sapienza, A. Alù, J.B. Pendry, Photonics of time-varying media, Advanced Photonics 4 (01) (Feb. 2022), https://doi.org/10.1117/1.ap.4.1.014002.

[77] J.Y. Lee, A.E. Miroshnichenko, R.-K. Lee, Reexamination of Kerker's conditions by means of the phase diagram, Physical Review A 96 (4) (Oct. 2017), https://doi.org/10.1103/physreva.96.043846.

[78] J. Olmos-Trigo, D.R. Abujetas, C. Sanz-Fernández, J.A. Sánchez-Gil, J.J. Sáenz, Optimal backward light scattering by dipolar particles, Physical Review Research 2 (1) (Feb. 2020), https://doi.org/10.1103/physrevresearch.2.013225.

[79] M.F. Picardi, A.V. Zayats, F.J. Rodríguez-Fortuño, Janus and Huygens dipoles: near-field directionality beyond spin-momentum locking, Physical Review Letters 120 (11) (Mar. 2018), https://doi.org/10.1103/physrevlett.120.117402.

[80] P. Spinelli, M. Verschuuren, A. Polman, Broadband omnidirectional antireflection coating based on subwavelength surface Mie resonators, Nature Communications 3 (1) (Jan. 2012), https://doi.org/10.1038/ncomms1691.

[81] R. Paniagua-Domínguez, Y.F. Yu, A.E. Miroshnichenko, L.A. Krivitsky, Y.H. Fu, V. Valuckas, L. Gonzaga, Y.T. Toh, A.Y.S. Kay, B. Luk'yanchuk, A.I. Kuznetsov, Generalized Brewster effect in dielectric metasurfaces, Nature Communications 7 (1) (Jan. 2016), https://doi.org/10.1038/ncomms10362.

[82] J.Y. Lee, A.E. Miroshnichenko, R.-K. Lee, Simultaneously nearly zero forward and nearly zero backward scattering objects, Optics Express 26 (23) (Nov. 2018) 30393, https://doi.org/10.1364/oe.26.030393.

[83] X. Zhang, A.L. Bradley, Wide-angle invisible dielectric metasurface driven by transverse Kerker scattering, Physical Review B 103 (May 2021) 195419, https://doi.org/10.1103/PhysRevB.103.195419, https://link.aps.org/doi/10.1103/PhysRevB.103.195419.

[84] M.M. Bukharin, V.Y. Pecherkin, A.K. Ospanova, V.B. Il'in, L.M. Vasilyak, A.A. Basharin, B. Luk'yanchuk, Transverse Kerker effect in all-dielectric spheroidal particles, Scientific Reports 12 (1) (May 2022), https://doi.org/10.1038/s41598-022-11733-4.

[85] R. Alaee, C. Rockstuhl, I. Fernandez-Corbaton, An electromagnetic multipole expansion beyond the long-wavelength approximation, Optics Communications 407 (Jan. 2018) 17–21, https://doi.org/10.1016/j.optcom.2017.08.064.

[86] H.K. Shamkhi, A. Sayanskiy, A.C. Valero, A.S. Kupriianov, P. Kapitanova, Y.S. Kivshar, A.S. Shalin, V.R. Tuz, Transparency and perfect absorption of all-dielectric resonant metasurfaces governed by the transverse Kerker effect, Physical Review Materials 3 (8) (Aug. 2019), https://doi.org/10.1103/physrevmaterials.3.085201.

[87] P.D. Terekhov, K.V. Baryshnikova, Y.A. Artemyev, A. Karabchevsky, A.S. Shalin, A.B. Evlyukhin, Multipolar response of nonspherical silicon nanoparticles in the visible and near-infrared spectral ranges, Physical Review B 96 (3) (July 2017), https://doi.org/10.1103/physrevb.96.035443.

[88] F. Qin, Z. Zhang, K. Zheng, Y. Xu, S. Fu, Y. Wang, Y. Qin, Transverse Kerker effect for dipole sources, Physical Review Letters 128 (19) (May 2022), https://doi.org/10.1103/physrevlett.128.193901.

[89] I.B. Zel'dovich, Electromagnetic interaction with parity violation, Soviet Physics, JETP 6 (1958) 6, https://www.osti.gov/biblio/4309791.

[90] Y. Yang, S.I. Bozhevolnyi, Nonradiating anapole states in nanophotonics: from fundamentals to applications, Nanotechnology 30 (20) (Mar. 2019) 204001, https://doi.org/10.1088/1361-6528/ab02b0.

[91] A.E. Miroshnichenko, A.B. Evlyukhin, Y.F. Yu, R.M. Bakker, A. Chipouline, A.I. Kuznetsov, B. Luk'yanchuk, B.N. Chichkov, Y.S. Kivshar, Nonradiating

anapole modes in dielectric nanoparticles, Nature Communications 6 (1) (Aug. 2015), https://doi.org/10.1038/ncomms9069.

[92] A.V. Kuznetsov, A.C. Valero, M. Tarkhov, V. Bobrovs, D. Redka, A.S. Shalin, Transparent hybrid anapole metasurfaces with negligible electromagnetic coupling for phase engineering, Nanophotonics 10 (17) (Oct. 2021) 4385–4398, https://doi.org/10.1515/nanoph-2021-0377.

[93] V.A. Fedotov, A.V. Rogacheva, V. Savinov, D.P. Tsai, N.I. Zheludev, Resonant transparency and non-trivial non-radiating excitations in toroidal metamaterials, Scientific Reports 3 (1) (Oct. 2013), https://doi.org/10.1038/srep02967.

[94] A.A. Basharin, V. Chuguevsky, N. Volsky, M. Kafesaki, E.N. Economou, Extremely high q-factor metamaterials due to anapole excitation, Physical Review B 95 (3) (Jan. 2017), https://doi.org/10.1103/physrevb.95.035104.

[95] X. Cui, Y. Lai, R. Ai, H. Wang, L. Shao, H. Chen, W. Zhang, J. Wang, Anapole states and toroidal resonances realized in simple gold nanoplate-on-mirror structures, Advanced Optical Materials 8 (23) (Oct. 2020) 2001173, https://doi.org/10.1002/adom.202001173.

[96] X. Zhao, C. Chen, K. Kaj, I. Hammock, Y. Huang, R.D. Averitt, X. Zhang, Terahertz investigation of bound states in the continuum of metallic metasurfaces, Optica 7 (11) (Nov. 2020) 1548, https://doi.org/10.1364/optica.404754.

[97] A.A. Basharin, M. Kafesaki, E.N. Economou, C.M. Soukoulis, V.A. Fedotov, V. Savinov, N.I. Zheludev, Dielectric metamaterials with toroidal dipolar response, Physical Review X 5 (1) (Mar. 2015), https://doi.org/10.1103/physrevx.5.011036.

[98] N.A. Nemkov, I.V. Stenishchev, A.A. Basharin, Nontrivial nonradiating all-dielectric anapole, Scientific Reports 7 (1) (Apr. 2017), https://doi.org/10.1038/s41598-017-01127-2.

[99] A.K. Ospanova, I.V. Stenishchev, A.A. Basharin, Anapole mode sustaining silicon metamaterials in visible spectral range, Laser & Photonics Reviews 12 (7) (May 2018) 1800005, https://doi.org/10.1002/lpor.201800005.

[100] A.C. Valero, E.A. Gurvitz, F.A. Benimetskiy, D.A. Pidgayko, A. Samusev, A.B. Evlyukhin, V. Bobrovs, D. Redka, M.I. Tribelsky, M. Rahmani, K.Z. Kamali, A.A. Pavlov, A.E. Miroshnichenko, A.S. Shalin, Theory, observation, and ultrafast response of the hybrid anapole regime in light scattering, Laser & Photonics Reviews 15 (10) (Aug. 2021) 2100114, https://doi.org/10.1002/lpor.202100114.

[101] V.A. Zenin, A.B. Evlyukhin, S.M. Novikov, Y. Yang, R. Malureanu, A.V. Lavrinenko, B.N. Chichkov, S.I. Bozhevolnyi, Direct amplitude-phase near-field observation of higher-order anapole states, Nano Letters 17 (11) (Oct. 2017) 7152–7159, https://doi.org/10.1021/acs.nanolett.7b04200.

[102] G. Grinblat, Y. Li, M.P. Nielsen, R.F. Oulton, S.A. Maier, Enhanced third harmonic generation in single germanium nanodisks excited at the anapole mode, Nano Letters 16 (7) (June 2016) 4635–4640, https://doi.org/10.1021/acs.nanolett.6b01958.

[103] G. Grinblat, Y. Li, M.P. Nielsen, R.F. Oulton, S.A. Maier, Efficient third harmonic generation and nonlinear subwavelength imaging at a higher-order anapole mode in a single germanium nanodisk, ACS Nano 11 (1) (Dec. 2016) 953–960, https://doi.org/10.1021/acsnano.6b07568.

[104] D.G. Baranov, R. Verre, P. Karpinski, M. Käll, Anapole-enhanced intrinsic Raman scattering from silicon nanodisks, ACS Photonics 5 (7) (June 2018) 2730–2736, https://doi.org/10.1021/acsphotonics.8b00480.

[105] A. Tripathi, H.-R. Kim, P. Tonkaev, S.-J. Lee, S.V. Makarov, S.S. Kruk, M.V. Rybin, H.-G. Park, Y. Kivshar, Lasing action from anapole metasurfaces, Nano Letters 21 (15) (2021) 6563–6568.
[106] J.S.T. Gongora, A.E. Miroshnichenko, Y.S. Kivshar, A. Fratalocchi, Anapole nanolasers for mode-locking and ultrafast pulse generation, Nature Communications 8 (1) (May 2017), https://doi.org/10.1038/ncomms15535.
[107] J. Yao, J.-Y. Ou, V. Savinov, M.K. Chen, H.Y. Kuo, N.I. Zheludev, D.P. Tsai, Plasmonic anapole metamaterial for refractive index sensing, PhotoniX 3 (1) (Oct. 2022), https://doi.org/10.1186/s43074-022-00069-x.
[108] J. Tian, H. Luo, Y. Yang, F. Ding, Y. Qu, D. Zhao, M. Qiu, S.I. Bozhevolnyi, Active control of anapole states by structuring the phase-change alloy Ge2Sb2Te5, Nature Communications 10 (1) (Jan. 2019), https://doi.org/10.1038/s41467-018-08057-1.
[109] W. Wang, Y.K. Srivastava, M. Gupta, Z. Wang, R. Singh, Photoswitchable anapole metasurfaces, Advanced Optical Materials 10 (4) (Dec. 2021) 2102284, https://doi.org/10.1002/adom.202102284.
[110] S. Pancharatnam, Generalized theory of interference, and its applications, Proceedings of the Indian Academy of Sciences - Section A 44 (5) (Nov. 1956) 247–262, https://doi.org/10.1007/bf03046050.
[111] M. Berry, Quantal phase factors accompanying adiabatic changes, Proceedings of the Royal Society of London. Series A, Mathematical and Physical Sciences 392 (1802) (Mar. 1984) 45–57, https://doi.org/10.1098/rspa.1984.0023.
[112] M. Berry, The adiabatic phase and Pancharatnam's phase for polarized light, Journal of Modern Optics 34 (11) (Nov. 1987) 1401–1407, https://doi.org/10.1080/09500348714551321.
[113] S.A.H. Gangaraj, M.G. Silveirinha, G.W. Hanson, Berry phase, Berry connection, and Chern number for a continuum bianisotropic material from a classical electromagnetics perspective, IEEE Journal on Multiscale and Multiphysics Computational Techniques 2 (2017) 3–17, https://doi.org/10.1109/jmmct.2017.2654962.
[114] A. Hannonen, H. Partanen, A. Leinonen, J. Heikkinen, T.K. Hakala, A.T. Friberg, T. Setälä, Measurement of the Pancharatnam–Berry phase in two-beam interference, Optica 7 (10) (Oct. 2020) 1435, https://doi.org/10.1364/optica.401993.
[115] Z. Bomzon, G. Biener, V. Kleiner, E. Hasman, Space-variant Pancharatnam–Berry phase optical elements with computer-generated subwavelength gratings, Optics Letters 27 (13) (July 2002) 1141, https://doi.org/10.1364/ol.27.001141.
[116] C. Liu, Y. Bai, Q. Zhao, Y. Yang, H. Chen, J. Zhou, L. Qiao, Fully controllable Pancharatnam-Berry metasurface array with high conversion efficiency and broad bandwidth, Scientific Reports 6 (1) (Oct. 2016), https://doi.org/10.1038/srep34819.
[117] H. He, G. Dai, H. Cheng, Y. Wang, X. Jia, M. Yin, Q. Huang, Y. Lu, Arbitrary active control of the Pancharatnam-Berry phase in a terahertz metasurface, Optics Express 30 (7) (Mar. 2022) 11444, https://doi.org/10.1364/oe.450117.
[118] C.P. Jisha, S. Nolte, A. Alberucci, Geometric phase in optics: from wavefront manipulation to waveguiding, Laser & Photonics Reviews 15 (10) (Aug. 2021) 2100003, https://doi.org/10.1002/lpor.202100003.
[119] Z. Gao, S. Golla, R. Sawant, V. Osipov, G. Briere, S. Vezian, B. Damilano, P. Genevet, K.E. Dorfman, Revealing topological phase in Pancharatnam–Berry metasurfaces using mesoscopic electrodynamics, Nanophotonics 9 (16) (Sept. 2020) 4711–4718, https://doi.org/10.1515/nanoph-2020-0365.

[120] H.-T. Chen, A.J. Taylor, N. Yu, A review of metasurfaces: physics and applications, Reports on Progress in Physics 79 (7) (June 2016) 076401, https://doi.org/10.1088/0034-4885/79/7/076401.
[121] W. Zhuo, S. Sun, Q. He, L. Zhou, A review of high-efficiency Pancharatnam–Berry metasurfaces, Terahertz Science and Technology 13 (3) (Sept. 2020) 73–89, https://doi.org/10.1051/tst/2020133073.
[122] Y. Liu, Y. Ke, J. Zhou, Y. Liu, H. Luo, S. Wen, D. Fan, Generation of perfect vortex and vector beams based on Pancharatnam-Berry phase elements, Scientific Reports 7 (1) (Mar. 2017), https://doi.org/10.1038/srep44096.
[123] Z. Xiang, Z. Shen, Y. Shen, Quasi-perfect vortices generated by Pancharatnam-Berry phase metasurfaces for optical spanners and OAM communication, Scientific Reports 12 (1) (Jan. 2022), https://doi.org/10.1038/s41598-022-05017-0.
[124] S.D. Gennaro, Y. Li, S.A. Maier, R.F. Oulton, Nonlinear Pancharatnam-Berry phase metasurfaces beyond the dipole approximation, ACS Photonics 6 (9) (Aug. 2019) 2335–2341, https://doi.org/10.1021/acsphotonics.9b00877.
[125] X. Ding, F. Monticone, K. Zhang, L. Zhang, D. Gao, S.N. Burokur, A. de Lustrac, Q. Wu, C.-W. Qiu, A. Alù, Ultrathin pancharatnam-berry metasurface with maximal cross-polarization efficiency, Advanced Materials 27 (7) (Dec. 2014) 1195–1200, https://doi.org/10.1002/adma.201405047.

11

Nonlinear phenomena empowered by resonant dielectric nanostructures

Rocio Camacho Morales[a], **Khosro Zangeneh Kamali**[a], **Lei Xu**[b], **Andrey Miroshnichenko**[c], **Mohsen Rahmani**[b], **and Dragomir Neshev**[a]

[a]*ARC Centre of Excellence for Transformative Meta Optical Systems (TMOS), Research School of Physics, Australian National University, Canberra, ACT, Australia.* [b]*Advanced Optics & Photonics Laboratory, Nottingham Trent University, Nottingham, United Kingdom.* [c]*School of Engineering and Information Technology, University of New South Wales, Canberra, ACT, Australia*

11.1 Introduction

Photonic nanostructures have attracted much attention because they can strongly confine light and re-emit or scatter it with the desired phase, polarization, or color. Subwavelength arrays of such nanostructures with spatially tailored scattering are called metasurfaces and play an important role in light manipulation, emission, and detection. Both photonic nanostructures and metasurfaces have gained much attention in the past decade and have proven their strong applicability in many applications, including 3D imaging, light detection and ranging (LiDAR) technologies, image processing, and biosensing. We are currently experiencing a large industrial interest in these technologies, with more functionalities and applications emerging continuously.

The materials library used for the fabrication of such nanostructures is also expanding. Nanostructure photonics and metaoptics began with nanostructures fabricated from plasmon metals [1]. Currently, however, the field is largely dominated by high-index dielectric nanostructures that offer a larger design degree of freedom and lower losses [2]. Several different materials have been explored, including silicon, germanium, amorphous glasses, III–V semiconductors, TiO_2, and other metal oxides. The shapes of the nanostructures have also evolved from the simple shapes

All-Dielectric Nanophotonics. https://doi.org/10.1016/B978-0-32-395195-1.00016-8
Copyright © 2024 Elsevier Ltd. All rights reserved.

of spheres [3] and cylinders [4] to free-form designs [5] and 3D structures [6]. The common feature of all these designs is that their functionality is always driven by the resonances excited in the nanostructures. Most commonly studied are the Mie-type resonances that are a property of the individual nanoresonators and form an electric and magnetic family of solutions [7]. However, extended lattice mode resonances can also be excited in periodic metasurfaces, and their radiation to free space can be carefully controlled through the concept of bound states in the continuum (BIC) [8].

This resonant nature of the dielectric nanostructures and metasurface implies strong field concentration inside the dielectric nanostructures or in their surrounding environment. A consequence of these strongly enhanced near-fields is enhancing all kinds of nonlinear effects at modest input powers. The field enhancement inside these nanocavities is proportional to the resonances' quality factor (Q-factor). This is the ratio between the stored energy inside the resonator and the energy radiated or dissipated inside. As an example, for Mie-resonant dielectric nanostructures, the practically achievable Q-factors are of the order of 10 to 50, implying tens of times enhancement of the near field, while the corresponding intensity is enhanced hundreds of times. As the nonlinear effects are proportional to the nonlinear power of the field, they can be enhanced thousands of times. The enhancement could be even stronger in the case of BIC resonances, where the Q-factor can experimentally reach values from 100 to 10,000 corresponding to an enhancement of hundred of times in the near-field. We note, however, that this increase in the near-field is accompanied by a reduction of the spectral bandwidth.

For example, in the sum-frequency generation (SFG) process, which is a three-wave mixing process, see Fig. 11.1, the metasurface (small dielectric cylinders) is designed to be resonant at all three participating wavelengths. The nonlinear enhancement, in this case, is proportional to the product of all three Q-factors, $\textit{Enhancement} \sim \mathrm{Q}(\omega_1)\ \mathrm{Q}(\omega_2)\ \mathrm{Q}(\omega_3)$, which for the modest enhancement, results in 100,000 times enhancement of the SFG process. At such enhancement rates, a thin metasurface of just a few hundreds of nanometers can act as a 1 mm thick nonlinear crystal, being simultaneously cheaper and potentially flexible.

In the more general case, the enhancement of the near-fields can boost the nonlinear polarization inside the high-index dielectric material. The general expression of the nonlinear polarization in the non-perturbative regime is given by:

$$P = \varepsilon_0(\chi^{(1)}E + \chi^{(2)}E^2 + \chi^{(3)}E^3 + \cdots),$$

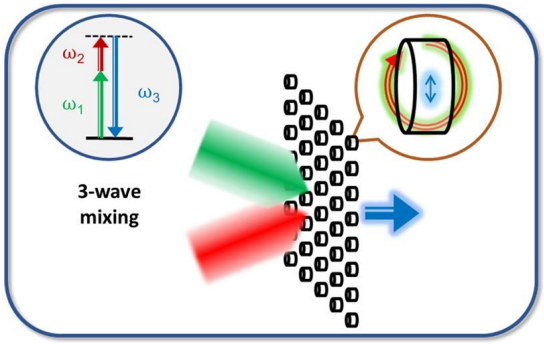

Figure 11.1. Nonlinear processes are strongly enhanced in the presence of a resonant environment due to the excitation of resonances at all of the participating wavelengths. In the example of three-wave mixing, the resonances at the three participating waves (ω_1, ω_2, and ω_3, green, red, and blue colors) enhance the frequency conversion by a factor proportional to the product of the three Q-factors.

where E is the local electric field, $\chi^{(1)}$ is the linear optical susceptibility related to the material linear refractive index, $\chi^{(1)} = n^2 - 1$. $\chi^{(2)}$ is the second-order nonlinear susceptibility, which is a third-rank tensor, and $\chi^{(3)}$ is the cubic nonlinear susceptibility. The series can be further expanded to higher-order nonlinear terms.

The large range of nonlinear phenomena has driven multiple studies on nonlinear phenomena in dielectric nanostructures and metasurfaces. For example, in Ref. [9] Liu et al. excited a GaAs metasurface with two beams at different wavelengths, see Fig. 11.2a. They observed the simultaneous generation of seven nonlinear processes, demonstrating the power of resonant enhancement in the dielectric metasurface. The observed nonlinear processes correspond to the contributions from the different nonlinear susceptibilities. The cubic-type nonlinear effects, or $\chi^{(3)}$ effects, see Fig. 11.2b, include third harmonic generation (THG), four-wave mixing (FWM), and self-phase modulation (SPM). In the case of two different input beams, one can also observe cross-phase modulation (CPM). SPM and CPM are exemplified by the effect of nonlinear change of the refractive index, which can occur in an ultra-fast time frame on the order of the duration of the excitation pulse.

However, the lowest and strongest order is the second-order nonlinear term, or $\chi^{(2)}$ term, Fig. 11.2c. This term only exists in materials that lack a crystalline center of symmetry, such as in III–V semiconductors. From this nonlinear term, one can observe the effects of up- or down-conversion. The up-conversion processes include SFG and second harmonic generation (SHG). The down-conversion processes include difference-frequency gen-

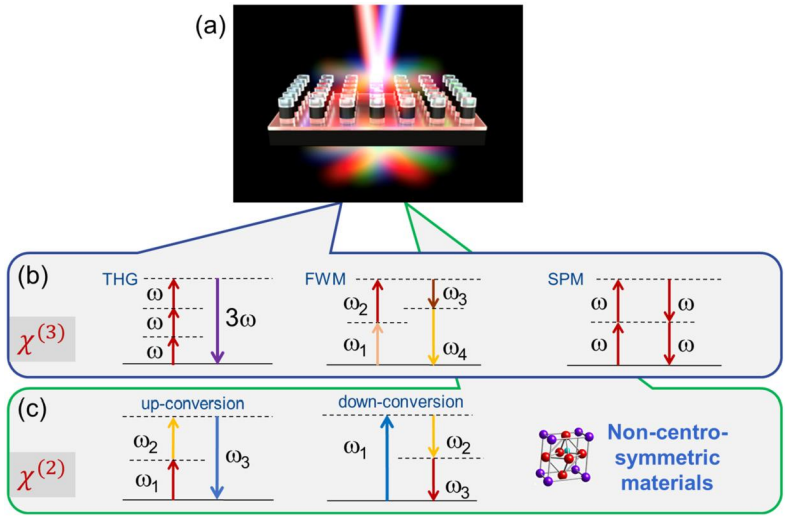

Figure 11.2. Nonlinear meta-optics empower the nonlinear optical phenomena through resonances inside the dielectric nanostructures. (a) Illustration of nonlinear dielectric metasurfaces generating seven nonlinear processes by mixing two laser beams [9]. (b) Energy diagrams of the most studied cubic nonlinear processes in dielectric nanostructures and metasurfaces. These include third harmonic generation (THG), four-wave mixing (FWM), and self-phase modulation (SPM) or cross-phase modulation, often exemplified by the effect of nonlinear change of the refractive index. (c) Energy diagrams of the most commonly studied quadratic nonlinear processes. These include up-conversion, exemplified by second harmonic generation (SHG) and sum-frequency generation (SFG), as well as nonlinear down-conversion, exemplified by difference-frequency generation (DFG) and spontaneous parametric down-conversion (SPDC). These processes are only possible in materials with a non-centrosymmetric crystalline structure.

eration (DFG) and spontaneous parametric down-conversion (SPDC). Importantly, such processes can allow for important applications of nonlinear dielectric nanostructures, which include bio-sensing [10] and nonlinear imaging [11].

This chapter discusses these fundamental nonlinear processes and their generation in dielectric nanostructures and metasurfaces, complementing the several existing reviews in the field [12,13]. First, we start with the third-order nonlinear processes, covered in Section 11.2. We review the fundamental physics and applications of such processes and review the current state of the art. In Section 11.3, we describe the nonlinear effects arising from second-order nonlinearity and review the recent achievements in the field. In Sections 11.2 and 11.3, the efficiencies reported correspond to $\eta = P_{NL}/P_{FB}$, where P_{NL} is the average power of the nonlinear emission (NL), and P_{FB} is the average

power of the fundamental beam (FB). A more useful definition, which is power independent, is the normalized efficiency defined as $\eta_{norm} = P_{NL}/P_{FB}^2$ (W^{-1}) in the case of SHG and $\eta_{norm} = P_{NL}/P_{FB}^3$ (W^{-2}) in the case of THG. However, normalized efficiencies have been reported only by few recent works thus they have has not been included here. Finally, Section 11.4 provides the general conclusions and outlook on future development. Overall, this chapter demonstrates the unique properties of nonlinear dielectric nanostructures and metasurfaces to enhance and shape nonlinear emission. Namely, (i) the possibility of generating any complex output polarization from any input polarization; and (ii) the possibility of controlling the directionality of emission, either forward/backward or distributing the energy into different diffraction orders. These properties are not readily available in bulk crystals and offer unique opportunities for new applications of nonlinear optics not possible before.

11.2 Third-order nonlinear effects in dielectric nanostructures

In recent years, many materials, such as oxides, nitrides, and even 2D materials, have been proposed as promising platforms for realizing third-order nonlinear metasurfaces with strong nonlinear susceptibility $\chi^{(3)}$ at material interfaces. Among all materials, group IV materials, such as silicon (Si) and germanium (Ge), have remained ideal candidates thanks to their large nonlinearity, high refractive index, low ohmic losses, and CMOS compatibility. In the past decade, Si/Ge nanostructures have been used to exhibit strong Mie-type resonances of both electric and magnetic natures in "all-dielectric nanophotonics". Such a unique capability has enabled complete control of the phase, amplitude, and polarization of light beams. Since such nanostructures facilitate strong light-matter interaction on a subwavelength scale, allowing abrupt changes in beam parameters, they are ideal alternatives to conventional optical elements, which rely on long propagation distances. These advantages, together with the large third-order nonlinearity of Si/Ge materials, have made them the primary focus for exploring nonlinear processes in recent years. It has been shown that by employing the characteristics of various resonances and matching them with the frequencies involved in the nonlinear interaction, one can significantly enhance the nonlinear interactions and subsequently use them for real-world applications, which are discussed in the following sections.

11.2.1 Cubic nonlinear interactions and enhancement strategies

The third-order nonlinear tensor describes processes where four photons simultaneously interact via a nonlinear medium. It can be categorized into different mixing processes based on the frequencies involved. When using three different frequencies as the input ($\omega_1, \omega_2, \omega_3$), a nondegenerate FWM process takes place, and four different frequencies can be generated at $\omega_1 + \omega_2 + \omega_3$, $\omega_1 + \omega_2 - \omega_3$, $\omega_1 + \omega_3 - \omega_2$, and $\omega_2 + \omega_3 - \omega_1$. When the input consists of two beams with different frequencies (ω_1, ω_2), a degenerate FWM takes place, and four different new frequencies can be generated via $\omega_{\mathrm{FWM}} = 2\omega_{1,2} \pm \omega_{2,1}$. One special and widely explored case of cubic nonlinear effects is THG, where the three input photons, all with the same frequency ω_1, are combined to create a fourth one with frequency $\omega_{\mathrm{THG}} = 3\omega_1$. With the development of nanotechnology and nanofabrication, various strategies based on dielectric nanostructures have been put into practice to enhance and shape the $\chi^{(3)}$ nonlinear optical emissions.

Dielectric nanostructures can support various optically-induced electric and magnetic resonances [2]. These resonances can be spatially and spectrally tuned by designing the nanostructures with special shapes and by controlling the size and other geometric parameters. The electromagnetic near-fields can be enhanced significantly by exciting these resonances, providing a powerful platform for enhancing the nonlinear light-matter interactions. With the development of the meta-optics field in recent years, optically resonant dielectric nanostructures have formed new building blocks to explore the $\chi^{(3)}$ nonlinear light-matter interactions at the nanoscale.

One of the first widely explored resonances supported by dielectric nanostructures is the magnetic dipole (MD) resonance, which is characterized by the circular displacement currents excited inside the nanostructures [14]. Benefiting from the large mode volume and strong electric field penetrating inside the nanostructures, MD resonance can substantially enhance the third-harmonic emissions [15,16]. For example, the field confinement in the vicinity of MD resonance at 1.24 μm of a Si nanodisk leads to two orders of magnitude enhancement of the THG intensity as compared to unpatterned bulk Si film. This experiments is illustrated in Fig. 11.3a, where Fig. 11.3a.ii gives the photographic image of the sample irradiated with the invisible beam at a wavelength of 1.26 μm [15]. When considering the degenerate FWM process case where the input consists of two incident beams with different frequencies, adjusting the aspect ratio of the nanodisk (the radius of the disk divided by the thickness of the disk) can

spectrally control the position of two different resonances to make them overlap simultaneously with the frequencies of the incident beams [17]. Taking the silicon Mie resonators as an example, Colom et al. have shown that by designing silicon Mie resonators to exhibit two resonances of strong internal electric field intensity around the frequency range of the pumps, the FWM signal can be enhanced by more than 2 orders of magnitude compared to the FWM signal generated by the unpatterned silicon film [18], as illustrated in Fig. 11.3b.

Another important feature of dielectric nanostructures is the multipolar interference effects, that is, they can support multiple resonances at the same spectral position, and the interferences between different types of electromagnetic multipoles open new possibilities for nanoscale light manipulation. One especially interesting case is when the interference between two different resonances cancels their far-field radiation and realizes a nonradiating anapole configuration. For example, by overlapping the Cartesian electric dipole and the toroidal dipole moments, an electric anapole state can be formed in a dielectric nanodisk [19]. Similarly, a magnetic anapole state can be formed by overlapping the Cartesian magnetic dipole and mean radius distribution component of the magnetic dipole [20,21]. Such anapole states can suppress the scattering contributions in the far-field domain from the two interfering resonances and maintain a strong near-field distribution inside the nanostructures. In 2016, the anapole state was employed to enhance the $\chi^{(3)}$ nonlinear generation in Ge nanodisks, where the THG conversion efficiency reached 0.0001%, which is four orders of magnitude THG enhancement compared to unstructured Ge film [22]. By combining with plasmonic material to form hybrid nanostructures, the near-field enhancement in the anapole state can be further improved through the spatial overlap of enhanced or resonantly excited Cartesian electric and toroidal dipole modes. For example, when placing the Si nanodisk surrounded by a gold ring, a THG conversion efficiency that reaches 0.007% has been experimentally obtained [23]. Another approach proposed by Xu et al. is to employ a metallic mirror under the dielectric nanoresonators (Fig. 11.3c). Such a configuration demonstrates a giant enhancement on the near-fields at the anapole state and can significantly boost the THG conversion efficiency reaching 0.01% [24]. Moreover, resonant interference effects can also be obtained by placing several nanoresonators together to form dimers, trimers, or other oligomers [25,26]. Hybridizing individual resonances from each nanoresonator can significantly enhance the electromagnetic fields and shape the nonlinear radiation patterns. For example, using three silicon nan-

odisks to form a trimer, the THG spectra can be reshaped by controlling the distances between the nanodisks in the trimer [26], as illustrated in Fig. 11.3d.

Another strategy to enhance the nonlinear emission is to engineer the pump beam. For example, by employing structured beam configurations, one can excite special resonances that are not accessible under linearly polarized beam illumination [27–29]. Using a structured beam that shares the same or similar multipolar contents as the resonances supported by the structure, the harmonic emission can be dramatically enhanced, as well as the nonlinear radiations can be shaped by selectively generating different types of nonlinear multipoles [28,29] (Fig. 11.3e,f).

Besides individual nanostructures, where the supported resonances generally possess low-Q factors and broadband responses, metasurfaces consisting of a periodic arrangement of nanoresonators have been designed to support different types of high-Q resonances for enhancing $\chi^{(3)}$ nonlinear processes [30–34]. Furthermore, by combining silicon with the phase change material $Ge_2Sb_2Te_5$ (GST), forming a hybrid dielectric metasurface that supports strong Fano resonance, dynamic control of the enhanced THG emission was demonstrated by tuning over the multiple phase states of GST [35,36].

In recent years, the rapidly growing field of topological photonics has sparked interest in employing topological states for nonlinear light-matter interactions in dielectrics. Topological dielectric metasurfaces can support backscattering-immune photonic topological edge states with enhanced fields. In 2019, Smirnova et al. employed nonlinear topological Si metasurfaces to realize topology-driven localization of the enhanced THG fields and enable the independent, high-contrast imaging of THG from either bulk modes or spin-momentum-locked edge states [37]. This concept is illustrated in Fig. 11.3g, showing a THG image generated from geometry-independent edge states with a silicon metasurface.

Bound states in the continuum (BIC) based on dielectric nanostructures provide another promising route for enhancing and shaping nonlinear emissions. Employing the symmetry-protected BICs supported by dielectric metasurface can significantly enhance the THG emission [38–43]. As one example shown in Fig. 11.3(h), by engineering the symmetry properties of the metasurface, consisting of Si blocks arranged in a square lattice, a quasi-BIC with a Q-factor up to 18511 can be excited under normal pump illumination, and subsequently, such an ultrasharp resonance can boost the THG conversion efficiency exceptionally (Fig. 11.3h.ii).

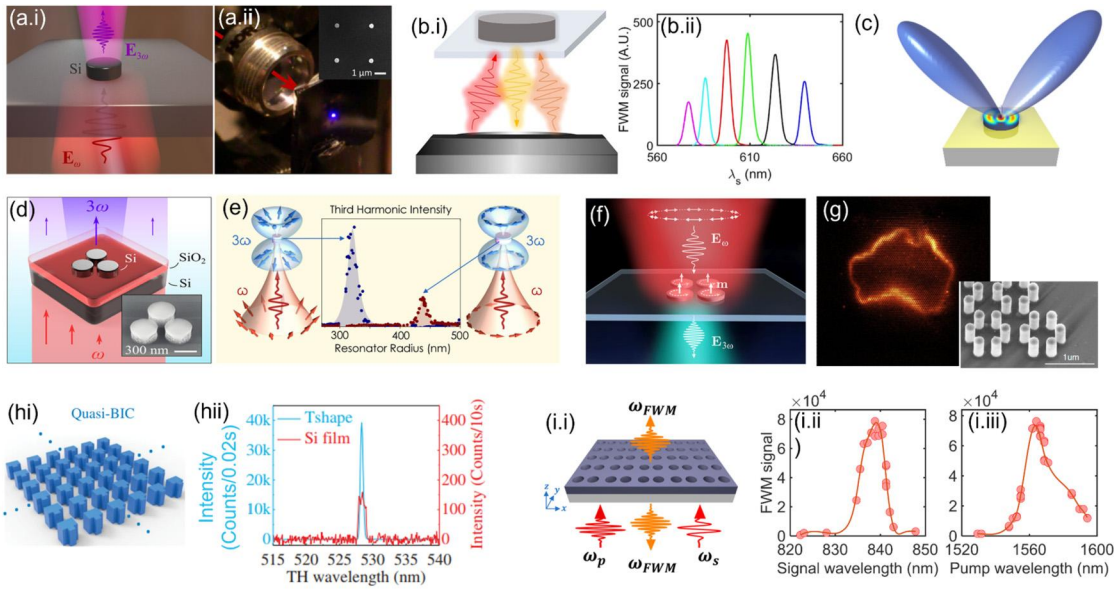

Figure 11.3. (a) THG process and enhancement from a Si nanodisk driven by MD resonance [15]. (b) Enhanced FWM with a doubly resonant Si nanoresonator [18]. (c) THG radiation from a mirror-enhanced anapole resonator made by silicon nanodisk on a Gold mirror surface [24]. (d) THG process with a Si nanodisk trimer [26]. (e) Illustration of the selective THG from Si nanodisks with structured light pump [28]. (f) THG emission from a Si oligomer excited by an azimuthally-polarized pump [29]. (g) TH imaging and enhancement based on the geometry-independent edge state with a topological metasurface [37]. (h) Enhanced THG emission from a Si metasurface driven by a high-Q quasi-bound state in the continuum [38]. (i) FWM enhancement from a multi-resonant Si dimer-hole membrane metasurface [44].

In the case of FWM, the pump beam involves more than one frequency. Designing a metasurface to support multiple resonances with a large mode overlap area at the frequencies involved can significantly enhance the interactions between the pump beams and facilitate the nonlinear wave mixing process. By taking advantage of the symmetry properties of the metasurface as well as the multipolar resonant feature of dielectric nanostructures, Xu et al. designed a multi-resonant membrane metasurface consisting of dimer holes on a Si slab to support a strong toroidal dipole quasi-BIC and a strong resonant response near the two wavelengths of the input beams at 1560 nm and 840 nm [44]. The generated visible light radiation based on the degenerate FWM process has shown a remarkable enhancement when pumped near the two resonances, as shown in Fig. 11.3hi.

The modeling of nonlinear interactions is usually performed using COMSOL multiphysics, where a perturbative approach in the frequency domain is used via two steps: first the linear re-

sponse and electric field distribution is simulated, under pump excitation, at the fundamental wavelength; then the induced nonlinear polarization is used as a source to simulate the light response and generated field at the harmonic wavelength. This approach is effective when the intensity of the nonlinear emission is low as compared to the pump intensity. However, when the conversion efficiency is sufficiently high, the electric field amplitudes of the nanostructures at the fundamental and harmonic wavelengths can become comparable. In such case, a coupled model is employed to account for the depletion of both, nonlinear generation and pump [47]. Alternatively, the nonlinear interactions can be simulated in the time domain using finite-difference time-domain (FDTD) methods [48].

In general, the nonlinear interactions, e.g. THG and FWM, and the enhancement strategies discussed above require careful modeling and simulations to realize metasurfaces with the desired properties. Today, designing metasurfaces with such capabilities is usually achieved via continuous tuning of one or two parameters via brute-force simulations [24]. This slow approach results in a random success on the output parameters of the desired resonances. However, deep learning approaches based on artificial neural networks (ANNs) have recently emerged as promising alternatives to designing metasurfaces that exhibit the desired optical properties. Consequently, employing a deep learning algorithm for the nanophotonic inverse design leads to design flexibility that can exceed the one obtained using conventional methods. The inverse-design approach exploits a training process that enables fast prediction of complex optical properties of nanostructures with intricate architectures.

Fig. 11.4 demonstrates the potential of this approach for designing metasurfaces with third-order nonlinearity. However, for the inverse design via a deep-learning approach, the following issue can arise: an identical far-field electromagnetic response can correspond to different designs. Therefore, the non-uniqueness of the response-to-design mapping induces conflicting examples within the training set. Subsequently, it can prevent convergence. To avoid this issue, Xu et al. proposed an adapted model to the tandem network (TN) approach, consisting of an inverse-design network connected to a forward model network (see Fig. 11.4a) [45]. First, the forward model network is trained in advance, and then the whole network is trained with fixed weights in the pre-trained forward model network. Being trained in this way, the inverse-design network is not constrained to produce a pre-specified design. Instead, it is free to infer any design that results in the desired forward behavior.

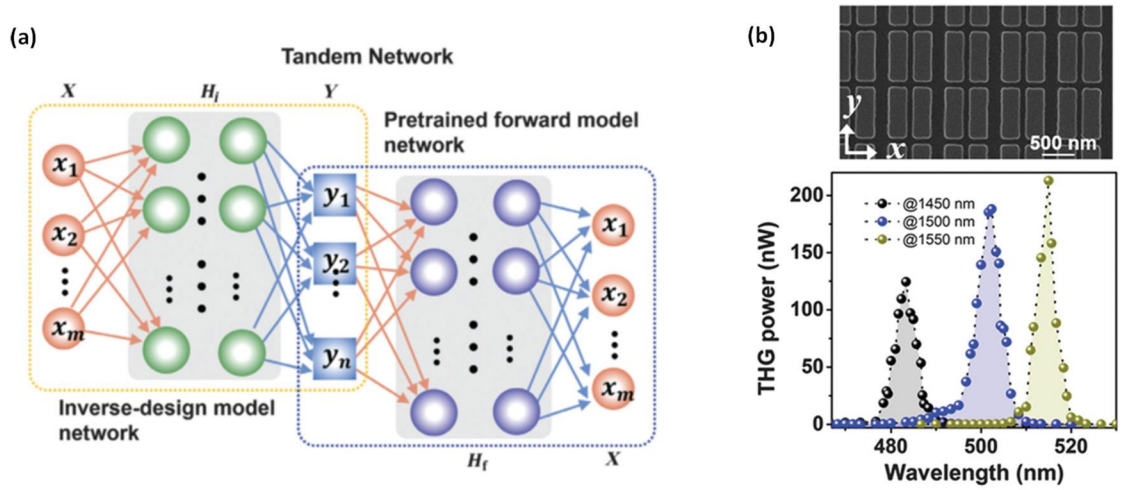

Figure 11.4. (a) The TN model's architecture consists of an inverse-design network connected to a pre-trained forward model network. X represents the input and output, which is the transmission spectra data in our case, and Y represents the output in the middle layer, which is the structural parameters here [45]. (b) SEM image of the fabricated sample with design and experimentally measured THG spectra of the samples [45].

Fig. 11.4b demonstrates an example of the double nano bars designed via this approach and subsequently examined. The SEM image of the fabricated metasurface is shown on the top panel of Fig. 11.4b. In this example, the final goal was to design metasurfaces generating TH light at 483, 500, and 517 nm; in other words, metasurfaces with resonances at the fundamental wavelengths of 1450, 1500, and 1550 nm, respectively. The employed machine learning approach enabled the authors to realize the exact dimensions, including length, width, and separation of the bars for such purpose. As shown in Fig. 11.4b bottom panel, the enhancement of the THG at the desired wavelengths was achieved.

11.2.2 Applications

Many applications of linear metasurfaces, where the frequency of the input laser does not change, have already been commercialized. However, the demand for optical imaging, high-density optical storage, materials characteristics, etc., have recently driven intensive research attention into the nonlinear metasurfaces where the operating frequency changes. Fig. 11.5 demonstrates a few recent applications of third-order nonlinear metasurfaces. Fig. 11.5a demonstrates the dynamical switching of images generated by an ultrathin silicon nonlinear metasurface [39]. The left panel shows an experimental high-quality leaky mode formed by par-

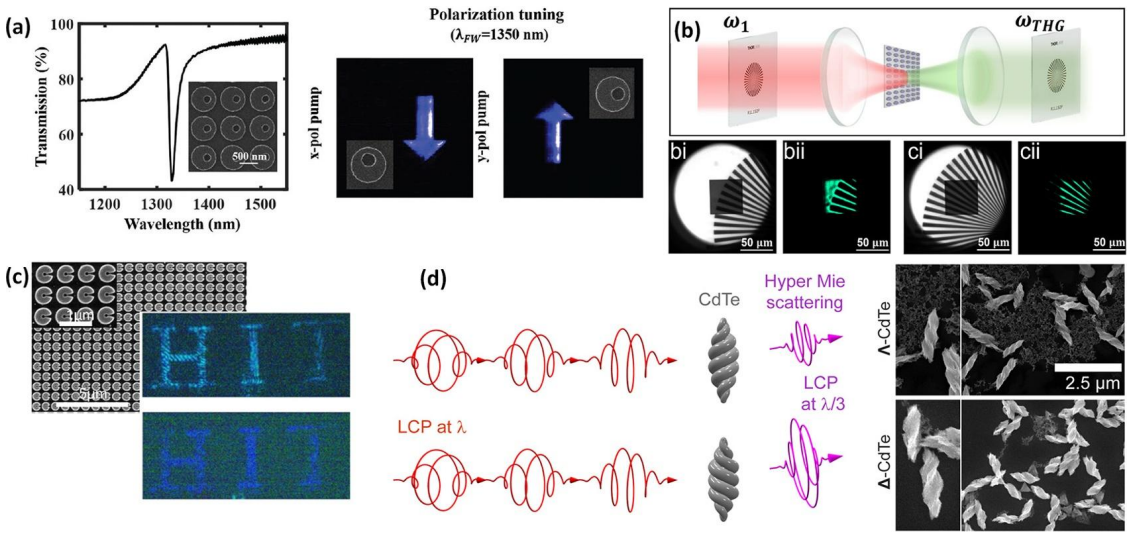

Figure 11.5. (a) Left: Experimentally measured linear transmission spectrum of disk-hole design. Middle and right: Nonlinear image tuning through the designed metasurfaces by polarization tuning [39]. (b) The schematic of THG imaging based on Si membrane metasurfaces: bi and ci are the images of the target and the metasurfaces under white light source illumination. bii and cii are transformed visible images (at 504 nm) of the target via membrane metasurfaces under NIR light illumination (at 1512 nm) [49]. (c) Left: SEM image of the C-shaped Si metasurface. The inset shows the enlarged top-view SEM image. Right: Experimentally obtained holographic images at 483 nm (top) and 417 nm (bottom) [50]. (d) Schematic diagram of third-harmonic Mie scattering (THMS) optical activity. Following illumination with LCP light at wavelength λ, the intensity of THMS light (at $\lambda/3$) depends on the handedness of the CdTe nano-helices, accompanied by Scanning electron micrographs of the left- and right-handed CdTe nano-helices, indicated as Λ-CdTe and Δ-CdTe, respectively [51].

tially breaking a BIC through a disk-hole metasurface. As can be seen in the middle and right panels, the sharp spectral features and asymmetry of the unit cell enable tailoring the nonlinear emissions over spectral or polarization responses.

Fig. 11.5b shows the potential of THG imaging for arbitrary objects. The near-infrared signal with frequency ω_1 ($\lambda_1 = 1512$ nm) passes through the target, then is being up-converted into the visible spectrum via the metasurface, forming the target image on the CCD camera [49]. Here the greenish color has been used to indicate the nonlinear radiation frequency ω_{THG} ($\lambda_{THG} = 504$ nm). Schlickriede et al. have also demonstrated the potential of imaging applications through third-order nonlinear metalens [46]. They illuminated an object, specifically an L-shape aperture, by infrared light and recorded their generated images at the visible third-harmonic wavelengths. Meanwhile, Gao et al. [50] have shown nonlinear holographic metasurfaces via THG (see Fig. 11.5c). After introducing phase changes from 0 to 2π, blue THG holograms

have been experimentally demonstrated in Si metasurface for the very first time. Fig. 11.5d shows how THG can be used to realize the chirality of materials. Fig. 11.5d-left illustrates how THG conversion efficiency depends on the chirality of the cadmium telluride (CdTe) helix and the handedness of the incident circularly polarized light. CdTe nano-helices were synthesized via a method used by Ohnoutek et al. [51] to produce helicoids with a geometry approaching that of twisted ribbons (right panels of Fig. 11.5d). The nonlinear ellipticity can be as high as 3° and it changes sign for Λ- and Δ-CdTe nanohelices.

11.2.3 Time-variant metasurfaces by ultrafast index modulation

The wave propagation in a time-variant medium was first studied by Morgenthaler in 1958; however, it received deserved attention only a few decades later [52]. Few works considering stimuli in different realms, ranging from magnetic to optomechanical systems, have experimentally demonstrated time-variant systems [53–57]. These systems exhibit slow modulation due to the nature of their stimuli. Ideally, an effective time-variant medium exhibits modulation in a similar temporal scale as the optical frequency in the electromagnetic field of interest. Structures with sub-wavelength dimensions, such as metasurfaces, are ideal candidates for a time-variant medium, as the time-varying effect strongly affects their scattering properties [58].

Generally, time-variant modulation has been studied in two different media: Epsilon-near zero (ENZ) and dielectric materials. Materials that exhibit an electric permittivity close to zero at their plasma frequency are known as ENZ materials. The ENZ materials show unity order index change (Δn) by inducing a static electric field or intense optical pumping [59,60]. However, due to their smaller than unity refractive index, ENZ materials rarely support light confinement, and therefore it is difficult to exploit their time-variant properties. On the other hand, optical dielectric materials that support two-photon absorption and exhibit the Kerr effect are fertile ground to exploit ultrafast and time-varying effects.

The variation of the material's permittivity in time can be originated from dynamics involved in the photoexcitation of the material and recombination of the electron-hole pairs. In this process, the absorption efficiency, induced free charge carrier's lifetime, and carrier concentration determine the duration and degree of this tuning mechanism. Fig. 11.6a illustrates the observation of the time-variant effect by the pump-probe experiment. As shown

in the left panel, the free carrier generation dynamics and the properties of the refractive index during carrier generation can be summarized in single or multi-photon absorption, generation of free carriers, and the thermo-optical effect by the heat generated in the electron-hole recombination process. The material's third-order susceptibility ($\chi^{(3)}$) is associated with the two-photon absorption (TPA), nonlinear index of refraction (Kerr effect), and THG. Light absorption and photoexcitation is the fastest process, usually occurring in times shorter than 100 fs. In this time window, the electromagnetic wave is still present in the medium, leading to a coherent flow of the electron gas. The energy of the excited charges does not reach Maxwell–Boltzmann distribution, but is underway to thermalization by the decay of the incident electromagnetic field and carrier-carrier scattering. Then, the energy of the charge reaches the Boltzmann equilibrium and starts to lose some energy due to electron-phonon scattering over the lifetime of electron-hole pairs. In the end, the free carriers and generated electron-hole pairs lose their energy, recombine, and release their energy in the system as heat. The thermo-optical effect governs the changes in the modulation of scattering properties of the metasurface. As shown in Fig. 11.6b-c, each of these individual processes has a different effect on the material's refractive index and happens at different time scales. By introducing a time delay between the pump and probe illumination, one can study the collective effect of the pump on the material [61,63].

The generalized temporal dynamics of the pulse interaction by a pump-probe experiment are illustrated in Fig. 11.6d-i [62]. If the delay between the probe (green) and pump (red) signals is large enough that the excited modes (blue) by the probe have decayed by the time of interaction, the TPA and free carrier (FC) generation does not interfere with the optical modes, and the resonance features retain their designed form (Fig. 11.6d and e). Suppose the photoexcitation occurs by the pump for a short while (<carrier lifetime) before the probe excites the optical modes in the system. In that case, the refractive index changes, resulting from the existence of the free carriers, leading to a resonance blue shift and reduction in the Q-factor of the resonators (Fig. 11.6f and g). If the photoexcitation initiated by the pump occurs after the excitation of optical modes by the probe signal, the abrupt refractive index change perturbed the optical resonances in the metasurface, resulting in the alternation of its phase and amplitude. In this case, the modulated light interferes with the non-coupled probe pulse input, emerging as interference fringes (Fig. 11.6h and i).

The temporal scale between the cavity mode lifetime and the induced ultrafast effects plays a crucial role in the modulation

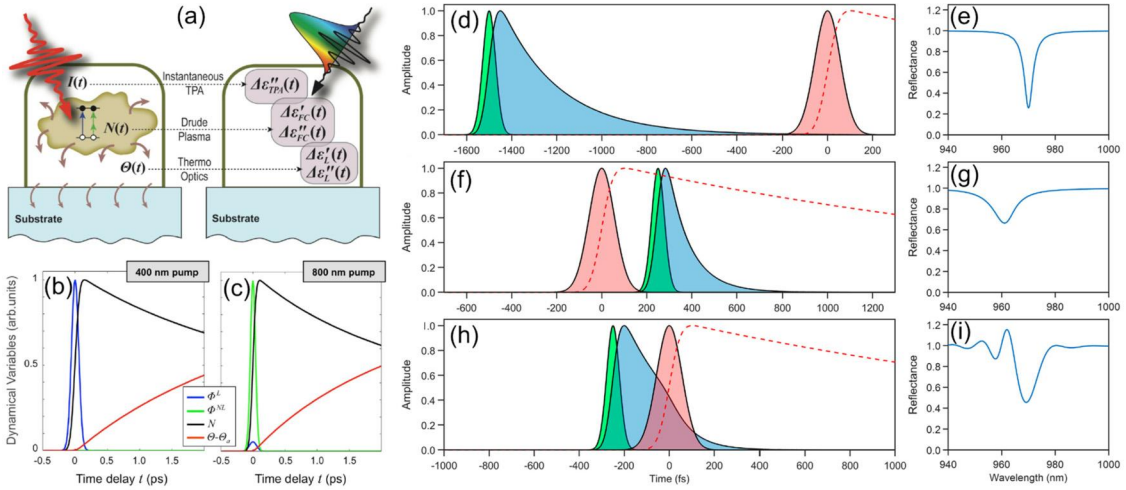

Figure 11.6. a) Illustration of the ultrafast nonlinear optical process in the pump-probe experiment. The monochromatic pump beam interaction with the resonators results in the absorption and generation of free charge carriers, which transforms into heat generation upon subsequential electron-hole pairs recombination process. These effects can be investigated under broadband probe illumination. The pump wavelength can be larger or smaller than the material's band gap resulting in b) nonlinear and c) linear absorption. d-i) Effect of free carrier generation by a pump on the optical modes excited by a probe signal at different temporal conditions. Reprinted from [62,63].

dynamics. If the optically induced ultrafast effects take a much longer time than the lifetime of the cavity mode, the variation of refractive index in the resonators is observed by the shift in the resonance wavelength of the system. The time-varying effect - which is an ultrafast process - can exhibit frequency conversion. This process occurs when the cavity mode lifetime and the variation in refractive index caused by the ultrafast pump pulse occur on a similar temporal scale. In this configuration, the shift in the cavity mode, along with an instantaneous change in the phase of the confined light, leads to a shift in the optical frequency of the cavity mode. Therefore, high Q-factor optical resonators that exhibit ultrafast optical effects, such as the Kerr effect, are good candidates for frequency conversion applications.

11.2.3.1 Ultrafast response of indirect band gap semiconductors

In indirect semiconductors, as the valence band maximum and conduction band minimum are located at different momentum, electron-hole pair generation and recombination require the assistance of intermediate processes to match their momenta. As a result, indirect semiconductors do not support efficient electron-hole pair generation and recombination. Therefore, indirect semi-

conductor metasurfaces have longer free-carrier recombination times and require higher illumination intensities. However, in a particular setting where the material is transparent to the illumination wavelength and at low fluence, indirect materials support the sole observation of the ultrafast optical Kerr effect. This results in an ultrafast response that only depends on the spontaneous Kerr effect (below 30 fs in GaP), without other dynamics such as excitation or relaxation processes playing a role [64].

A preliminary study on the effect of photoexcitation on the scattering of Mie resonators has been done by Makarov et al. [65]. This work studies the electron-hole generation in amorphous silicon nanoparticles by using 100 fs laser pulses at 790 nm central wavelength with a repetition rate of 80 MHz. The fluence is limited to 100 mJ/cm^2 to avoid potential damage to the sample. This work shows that the scattering cross-section and directionality of the particles could be altered significantly by increasing the pump's fluence and electron-hole concentration (Fig. 11.7a and b). Shcherbakov et al. first realized the time-variant behavior of the dielectric metasurfaces by performing z-scan (Fig. 11.7c) and I-scan measurements in various metasurfaces [66]. This work investigates the self-modulating response of an amorphous silicon (a-Si) metasurface in a pump-probe experiment by performing I-scan measurements at different illumination intensities. At low fluence, the metasurface normalized transmittance reduces linearly, which indicates the presence of two-photon absorption (TPA) in the a-Si disks. Once the fluence exceeds a limit, the thermo-optical effect dominates the TPA effect, and the transmittance curve loses its linear nature. Increasing the fluence further results in permanent damage to the metasurface due to the heat. In the same year, Yuanmu et al. performed the pump-probe experiment on an amorphous silicon metasurface exhibiting Fano-resonance. By surveying the time delay, the authors noticed a sharp drop in the transmission intensity of the pump (1 kHz repetition rate) that is attributed to the TPA and Kerr effect, exhibiting 490 fs switching time, which is longer compared to the 65 fs observed in simple nanodisk metasurfaces (Fig. 11.7d). This longer switching period is likely due to higher Q-factor resonances of the structures [30]. After the thermalization of electrons, the variation in the amorphous silicon refractive index due to the existence of the FC gradually diminishes until all the electron-hole pairs recombine. This effect is shown as the lower transmission intensity after the pumping and in Fig. 11.7d for pump-probe delay > 490 fs. Pumping the metasurface with a high repetition rate of 80 MHz and an intensity up to 2 GW/cm^2, resulted in continuous generation and recombination of electron-hole pairs, which

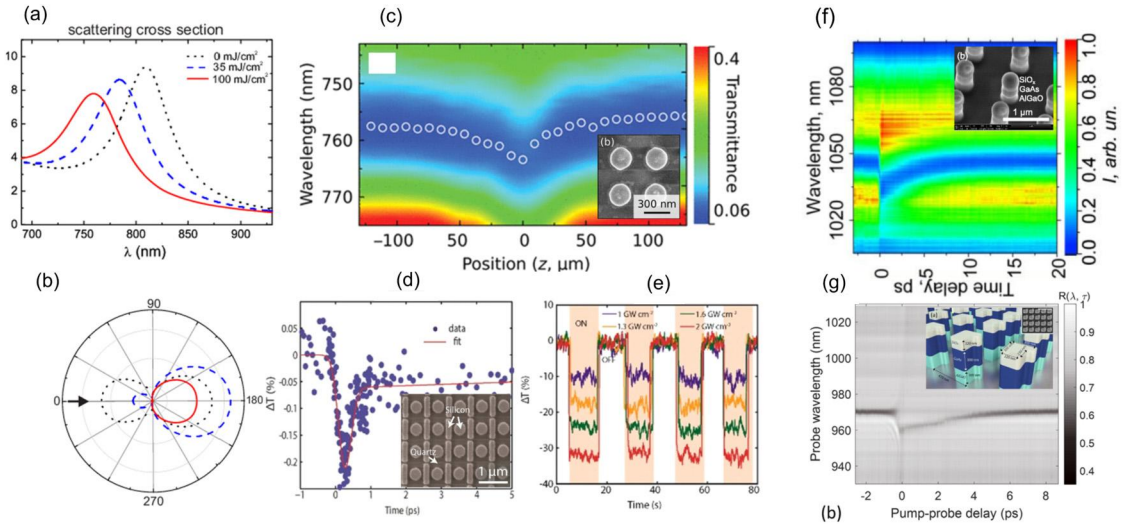

Figure 11.7. Examples of ultrafast tuning in metasurfaces. a) The simulated scattering cross section of spherical particles before and after photoexcitation by a pump signal at different fluence rates, and b) its emission directionality [65]. c) The resonant shift of an a-Si metasurface measured in the z-scan experiment. The pump-probe experiment on an a-Si sample with small delays shows the effect of TPA as a large drop in the transmission intensity and free carrier generation as a small lower transmission after excitation. d) Ultrafast response of the metasurface obtained at a low repetition rate to avoid the thermo-optical effect. e) Due to the high repetition rate (500 MHz) and pump intensity, the thermo-optical effect has a prominent role in reducing the transmission intensity of a-Si silicon [30]. The comparison between two similarly made metasurfaces, one is symmetrical (f), and one is asymmetrical (g). The asymmetrical metasurfaces exhibit a much higher quality factor resonance and therefore require much lower fluence for TPA (89 and 270 μJ/cm^2) [62,68]. Reprinted from [30,62,65,66,68].

heats the structures constantly over time. Under this condition and at longer operation periods, the change in the refractive index, via the thermo-optical effect, contributes to the resonance shift in the metasurface and a transmission modulation of 36% (see Fig. 11.7e).

11.2.3.2 Ultrafast response of direct band gap semiconductors

Direct semiconductors have the same momentum for the maximum valence and minimum conduction bands, leading to efficient electron-hole pair generation and recombination. As a result, direct band gap materials at absorptive wavelengths support a much faster modulation process caused by free carrier plasma due to both the electron-hole pair generation and recombination process. However, due to the higher efficiency of multi-photon absorption in direct semiconductor materials, observing solely the Kerr effect is challenging.

GaAs, which features a direct band gap, has been used as the absorbing material in ultrafast and time-variant metasurfaces. A metasurface made of this material has achieved reflectance modulation of 0.35 and even larger linear absorption at fluences of less than 400 μJ/cm^2, with a relaxation constant < 2 ps [67,68]. This performance largely overcomes the performance of the indirect bandgap silicon metasurface, which has shown a small modulation of 0.2 at a fluence >1 mJ/cm^2, and carrier relaxation times of ∼30 ps [66] (Fig. 11.7f). As shown in Fig. 11.7g, the metasurface, exhibiting high Q-factor resonance, allows the effect to be observed at lower fluence and the resonance width to be reduced upon illumination [62,69].

11.3 Quadratic nonlinear effects in dielectric nanostructures

Quadratic nonlinear effects are governed by the second-order nonlinear tensor $\chi^{(2)}$. This section discusses several second-order nonlinear processes that we classify into two categories. The first category is SHG, a degenerate nonlinear process where two photons of the same frequency ω illuminate a nanostructure to obtain an output of a single photon of frequency 2ω. The second category corresponds to non-degenerate three-wave mixing processes, where photons of different frequencies interact inside the material to be up- or down-converted in frequency. In the case of SFG, two incident photons with frequencies ω_1 and ω_2 interact inside a nanostructure to obtain a single up-converted photon with frequency $\omega_{SFG} = \omega_1 + \omega_2$. In the inverse case of SPDC, a single photon of frequency ω_{SPDC} illuminates the nanostructure to be down-converted, obtaining at the output two photons with lower frequencies ω_1 and ω_2, where $\omega_{SPDC} = \omega_1 + \omega_2$.

11.3.1 Second harmonic generation

11.3.1.1 Dielectric nanoantennas

The studies of SHG in single dielectric nanoantennas were initiated with nanoantennas made of GaAs and AlGaAs alloys. GaAs is a semiconductor material with a non-centrosymmetric crystalline structure and a high value of its nonlinear susceptibility (100 pm/V). In 2015, Luca et al. investigated the SHG in AlGaAs nanoantennas by calculating the scattering efficiency and multipolar decomposition of a single nanoantenna, as shown in Fig. 11.8a [70]. In these calculations, the nanoantenna suspended in the air was illuminated by an x-polarized plane wave, which

excites several resonant peaks around the near-infrared (IR) spectral range. The strongest resonance, observed at the fundamental wavelength $\lambda_{FW} = 1640$ nm, was mainly induced by an MD resonance whose field distribution across the x-z plane is shown in the inset of Fig. 11.8a. The scattering efficiency was also studied for nanoantennas of different radii suspended on a substrate with $n = 1.6$, which is equivalent to the refractive index of aluminum oxide (AlOx). The authors found that the scattering efficiency did not change significantly compared to the case of $n = 1$ (air).

Next, the SHG efficiency of the nanoantenna was calculated and plotted as a function of λ_{FW} (see Fig. 11.8b). A maximum SHG efficiency was observed at $\lambda_{FW} = 1675$ nm, which is 35 nm red-shifted from the MD resonant peak. The red shift was explained by the overlap between the resonant modes generated at the fundamental and second-harmonic wavelength λ_{SHG}. The nonlinear nanoantennas proposed by Luca et al. were soon experimentally investigated, reporting a conversion efficiency of 1.1×10^{-5} using a fundamental beam with an intensity of $I = 1.6$ GW/cm^2 [71]. The AlGaAs nanoantennas, fabricated on an AlOx substrate, observed the excitation of an MD resonance when illuminated by a fundamental beam at $\lambda_{FW} = 1554$ nm. Another work reported the strong dependence between the second-harmonic polarization of AlGaAs nanoantennas and the modes at the second-harmonic wavelength [72]. However, most works were limited to backward SHG due to the non-transparent substrates used in the fabrication process. Camacho et al. solved this limitation by using a novel fabrication procedure, where AlGaAs nanoantennas were partially embedded in a transparent layer and bonded to a glass substrate [73]. By using this fabrication technique, both the forward and backward SHG emission from AlGaAs nanoantennas could be investigated, as schematically shown in Fig. 11.8c. The forward and backward SHG efficiencies were measured as a function of the diameter of the nanoantennas, as shown in Fig. 11.8d. A maximum total SHG efficiency of 8.5×10^{-5} was found for a nanoantenna with a diameter d = 490 nm. The polarization state and radiation pattern of the most efficient nanoantenna are shown in the inset of Fig. 11.8d. The observed far-field doughnut radiation pattern and the polarization state of the SHG alluded to the generation of a radially polarized vector beam. The observed doughnut far-field nonlinear emission with zero normal SHG was insensitive to the geometry of the nanoantennas and hence was attributed to the symmetry of the AlGaAs nonlinear tensor.

The characteristic doughnut far-field second-harmonic emission of AlGaAs nanoantennas [74,75] posed a serious challenge for practical applications. The use of high numerical aperture (NA)

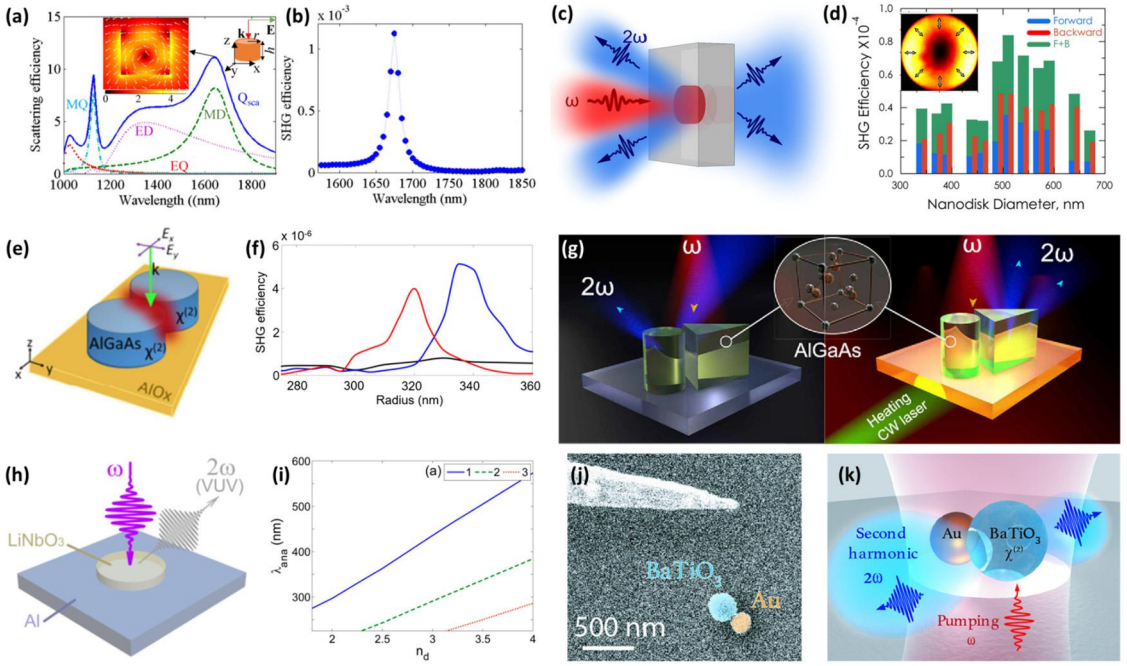

Figure 11.8. a,b) Studies of AlGaAs nanoantenna ($r = 225$ nm and $h = 400$ nm) suspended in the air. a) Scattering efficiency, decomposed in magnetic dipole (MD), electric dipole (ED), magnetic quadrupole (MQ), and electric quadrupole (EQ) contributions as a function of wavelength. Inset: schematics of the nanoantenna in the x-z plane with the incident field and the cross-section of normalized |(E)| [70]. b) SHG efficiency as a function of the fundamental wavelength [70]. c) Schematic of single AlGaAs nanoantenna emitting forward and backward SHG [73]. d) Experimentally measured SHG efficiency from single nanoantennas of different diameters at $\lambda_{FW} = 1556$ nm. Blue indicates forward radiation, red indicates backward radiation, and green indicates the sum of forward and backward [73]. e) Pictorial view of the proposed AlGaAs nanodimer structure [81]. f) Numerical calculations of the SHG for x-polarized (blue line) and y-polarized (red line) fundamental beams as a function of the nanoantennas radius with respect to the SHG of the single (black line) nanoantenna [81]. g) Schematic of the SHG tunability concept. CW heating of a nanodimer structure steers the SHG far-field emission pattern. The nanodimer consists of a triangular prism and a cylinder of AlGaAs located on a glass substrate [85]. h) Schematic of $LiNbO_3$ nanoantenna on aluminum (Al) substrate, emitting SHG in the vacuum ultraviolet (VUV) spectral range [88]. i) Resonance wavelengths of several order anapole modes as a function of the refractive index n_d of the dielectric nanoantenna supported by an Al substrate. The blue solid line indicates the first-order anapole mode, the green dashed line is the second-order anapole mode, and the red dotted line is the third-order anapole mode [88]. j,k) Scanning electron microscopy (left) and schematic (right) images of heterodimer used to investigate SHG. The heterodimer consists of gold and barium titanate ($BaTiO_3$) spherical nanoantennas [92].

objectives was required to collect the SHG emitted at very broad angles, and even then, only a portion of the nonlinear emission was collected. Different approaches were proposed to solve this challenge, including using a tilted incident beam to excite the nanoantennas [76]. However, this approach proved to be diffi-

cult to implement experimentally. Sautter et al. suggested a more practical approach using dielectric nanoantennas grown with a different crystalline orientation to break the symmetry of the system [77]. By using the (111) crystalline orientation, as opposed to the commonly employed (100) crystalline orientation, nonzero normal SHG was demonstrated in (111)-GaAs nanoantennas, together with polarization-independent SHG conversion efficiency. Major control in the directionality of the SHG was demonstrated when using (110)-GaAs nanoantennas, including unidirectional SHG and all-optical switch between forward and backward SHG [78]. Other schemes have been investigated to achieve non-zero normal SHG, including using two adjacent nanoantennas [79] and semi-cylindrical nanoantennas [80].

While the use of Mie resonances and, in particular, the MD resonance proved to enhance the efficiency of SHG, the excitation of resonances with higher-Q factor such as the anapole states is desirable to enable higher conversion efficiencies and major control over the SHG properties. To excite anapole-like states, Rocco et al. utilized a pair of AlGaAs nanoantennas, also known as nanodimers (see Fig. 11.8e) [81]. The AlGaAs nanodimers showed improved SHG efficiency compared to single isolated nanodisks, as shown in Fig. 11.8f. The excitation of anapole-like states in single AlGaAs nanoantennas was later demonstrated using azimuthally- and radially-polarized vector beams, also known as cylindrical vector beams (CVBs) [82]. The anapole-like states excited by the incident CVBs demonstrated the enhancement of not only SHG but also THG in single AlGaAs nanoantennas. The use of CVBs to illuminate AlGaAs nanoantennas was later investigated to excite higher Q-factor resonances known as BIC [75]. In particular, using an azimuthally-polarized vector beam demonstrated an improvement in SHG efficiency by several orders of magnitude compared to radially- or linearly-polarized incidence, confirming the high selectivity of the BIC resonances. Novel designs to improve the efficiency and control of SHG in AlGaAs nanoantennas continue to be investigated, including double-resonant nanoantennas [83,84]. However, a more interesting avenue recently investigated is the tunability of SHG [85]. Pashina et al. suggested an AlGaAs nanodimer structure consisting of cylindrical and triangular nanoantennas, as depicted in the left Fig. 11.8g. A near-IR pulsed laser was used for SHG, while a CW visible laser simultaneously heated the nanodimer, as depicted in the right of Fig. 11.8g. In their design, the resonances of the individual nanoantennas were detuned from each other to compensate for the thermal drift of the resonances induced by the CW laser. Reconfigured emission

patterns were theoretically demonstrated without significant loss of the SHG.

Although GaAs and its alloys have been the preferred platform for studying SHG in dielectric nanoantennas, their applications in the visible regime are hindered by the absorption of the III–V semiconductor material in this spectral range. Gallium phosphide (GaP) has been identified as an attractive alternative for the study of second-order nonlinear processes [86,87], having a non-centrosymmetric crystalline structure, a high refractive index ($n = 3.3$), and a higher band gap than GaAs and their alloys. Another attractive material for generating nonlinear emission in the visible and even the ultraviolet spectral range is the ferroelectric material lithium niobite ($LiNbO_3$). Although $LiNbO_3$ has a lower refractive index ($n \sim 2.5$) than Ge, Si, and GaAs, the excitation of Mie resonant modes can be achieved by providing a high index contrast between the nanoantennas and the substrate [88]. With this idea in mind, Kim and Rim demonstrated vacuum ultraviolet (VUV) SHG from $LiNbO_3$ nanoantennas on an aluminum substrate, as shown in the schematic of Fig. 11.8h. The SHG was enhanced when illuminating the nanoantennas with a fundamental beam at $\lambda_{FW} = 351$ nm via the excitation of an anapole state. Further calculations demonstrated first-order anapole modes could be excited in dielectric nanoantennas with a refractive index n_d as low as 1.8 (see blue curve in Fig. 11.8i) when using a near-zero-index material substrate such as aluminum. The $LiNbO_3$ nanoantennas achieved a theoretical SHG efficiency on the order of 10^{-4}, the highest efficiency reported for nonlinear nanostructures at the time. Later, $LiNbO_3$ cube nanoantennas were experimentally investigated to enhance SHG by exciting Mie resonances [89]. Compared to bulk $LiNbO_3$, an enhancement of 10^7 was demonstrated in the SHG obtained in the cube nanoantennas at a wavelength $\lambda_{SHG} = 360$ nm. Similarly, the enhancement of SHG was investigated in $LiNbO_3$ spherical nanoantennas excited by Mie resonances [90]. The spherical nanoantennas, deposited via laser ablation on a SiO_2 substrate, reported an efficiency of 4.45×10^{-8} under the illumination of a fundamental beam at $\lambda_{FW} = 750$ nm with a peak intensity $I = 2$ GW/cm^2. The proposed excitation of anapole states in $LiNbO_3$ nanoantennas was experimentally demonstrated via a near-zero index hyperbolic metamaterial substrate [91]. A maximum SHG efficiency of 10^{-4} was achieved using a fundamental beam with an intensity of $I = 11$ GW/cm^2 and $\lambda_{FW} = 565$ nm.

Finally, the use of hybrid dielectric-plasmonic has also been explored to enhance SHG. Renaut et al. investigated a heterodimer constructed by positioning gold and barium titanate ($BaTiO_3$)

nanoantennas next to each other as shown in the SEM image (Fig. 11.8j) [92]. The electromagnetic coupling of the heterodimer was investigated through nonlinear second-harmonic spectroscopy, as schematically shown in Fig. 11.8k. In the heterodimer, the formation of hybridized modes was observed, led by the overlap of plasmonic and Mie resonant modes, with an SHG enhancement of 2 orders of magnitude in the visible spectral range. Other hybrid nanostructures investigated for SHG enhancement include gold-$LiNbO_3$ nanoantennas [93], potassium titanyl phosphate (KTP)-gold nanostructures [94], and GaP/gold nanostructures [95].

11.3.1.2 Dielectric metasurfaces

Parallel to the developments in dielectric nanoantennas, dielectric metasurfaces have also been employed in studying parametric second-order nonlinear emissions. Mie-resonant metasurfaces were first investigated to enhance the SHG through GaAs [96–98], ZnO [99], and $LiNbO_3$ [100–102] metasurfaces. Lochner et al. first performed studies on the polarization-dependence of SHG by employing AlGaAs/GaAs metasurfaces (see Fig. 11.9a) [103]. Using Fourier imaging, the authors demonstrated that the SHG is predominantly emitted into the first diffraction orders of the metasurfaces (see Fig. 11.9b). Most importantly, they identified the experimental conditions for which the polarization dependence of the SHG efficiency is fundamentally different with respect to a bulk GaAs wafer structure. Gili et al. further investigated the SHG polarization control by engineering the fundamental beam's polarization state and the orientation of the nanoantennas conforming to the AlGaAs metasurfaces [104]. The polarization state of the SHG was also investigated in $LiNbO_3$ metasurfaces, where the SHG diffraction orders reported preferential emission in the direction along the polarization of the fundamental beam [105]. To increase the efficiency of the SHG, Fano resonances were proposed in GaAs [106] and $LiNbO_3$ [107] metasurfaces.

The excitation of BIC resonances in non-centrosymmetric materials was first demonstrated by Anthur et al. using GaP metasurfaces [108]. The unit cell of the GaP metasurfaces consisted of elliptical nanodimers with a relative tilting angle between them (see the gray background in Fig. 11.9c). The tilting angle breaks the symmetry of the metasurface, thus opening a leaky channel in the normal direction and forming a quasi-BIC resonance, demonstrated by the high enhancement of the incident field (see inset in Fig. 11.9d). Then, the metasurface was illuminated by a CW fundamental beam generating SHG (Figs. 11.9c and d) with a conversion efficiency of 10^{-7}, using a fundamental beam with an intensity of

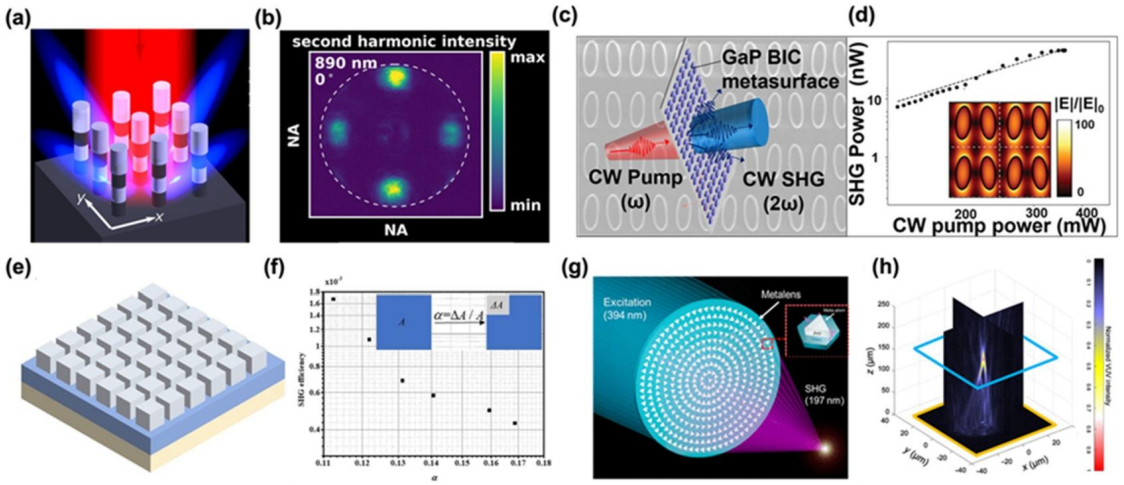

Figure 11.9. a) Schematic illustrating the excitation and emission of SHG by a GaAs metasurface [103]. b) Typical Fourier space second-harmonic intensity distribution measured by a CCD camera, showing the zeroth diffraction order in the center and the first orders in the x- and y-directions. The large dashed white circle indicates the numerical aperture (NA) of the collecting objective [103]. c) Schematic of a GaP metasurface comprising a square lattice of dimers formed by two elliptical cylinders with a relative tilting by an angle θ between their major axes [108]. d) SHG power as a function of input CW pump power. Inset: Amplitude of the electric near-field distribution at the quasi-BIC resonance in the xy-plane passing through the center of the particles [108]. e) 3D schematic of the designed etchless $LiNbO_3$ metasurface [110]. f) Maximum SHG efficiency as a function of the asymmetry parameter α of the L-shaped nanopillars. Inset: definition of the asymmetry parameter α [110]. g) Idealized schematic of ZnO metasurface. Inset: unit cell of the metasurface arranged in a hexagonal lattice [120]. h) Focusing profile of ZnO metasurface showing the focusing spot (blue cross-section) with $z = 142$ μm [120].

$I = 1$ kW/cm^2. Later work demonstrated the excitation of BIC resonances in GaP metasurfaces, yielding a strong enhancement of the SHG [109]. In this work, the GaP layer was directly grown on a sapphire substrate, tackling the problem of wafer bonding.

Due to the very low absorption of $LiNBO_3$ in the visible to the near-IR spectral range, $LiNbO_3$ metasurfaces have been identified as another attractive platform to enhance the SHG. In 2020, Yang et al. investigated $LiNbO_3$ metasurfaces consisting of a low refractive index polymer on top of a $LiNbO_3$ film (Fig. 11.9e) [110]. In the symmetry-protected BIC metasurface, the light was localized in the $LiNbO_3$ film, where the second-order nonlinearity of the material was exploited. By introducing an asymmetry α into the system (see inset of Fig. 11.9f), the symmetry-protected BICs were degraded to quasi-BICs resonances with high Q-factors. The SHG of the high Q-factor $LiNbO_3$ metasurfaces was investigated, predicting an SHG efficiency of 10^{-3} when using a fundamental beam with an intensity $I = 30$ MW/cm^2. Further designs were explored

to excite quasi-BICs in $LiNBO_3$ metasurfaces, including tilted elliptical nanodimers [111], nanoantenna cones [112], and nanodisk arrays [113].

Another platform that has gained interest in the generation of second harmonic signals is the coupling of resonant metasurfaces to 2D materials. In this configurations, the second-order nonlinearity is provided by the 2D material such as gallium selenide [114] and transition metal dichalcogenides layers [115,116], while the metasurface provides the resonant field enhancement required to increase the SHG efficiency.

The potential applications of metasurfaces [9], together with the search for tunable [117,118] and time-variant [119] metasurfaces, have become one the main drivers in the research field of nonlinear metasurfaces. For example, Tseng et al. recently demonstrated nonlinear metalenses through ZnO metasurfaces [120]. In their work, the metasurface was illuminated by a circularly polarized (CP) fundamental beam at 394 nm, generating an SHG at 197 nm and simultaneously focusing on the generated VUV light (Fig. 11.9g). Under CP excitation, the unit cell of the metasurfaces are required to have C_3 rotational symmetry, which was achieved by designing triangularly shaped nanoantennas (inset of Fig. 11.9g). At the focal plane, a spot of 1.7 mm diameter was obtained with a 21-fold power density enhancement as compared to the wavefront at the metalens surface (Fig. 11.9h).

11.3.2 Non-degenerate three-wave mixing

The case when the incident waves are degenerated by frequency or polarization offers rich opportunities for tailoring the nonlinear emission in both polarization, efficiency, or spatial distribution. For example, by varying the polarization of the two input beams, it is possible to engineer the polarization of the generated SFG photons in the entire Poincare sphere. This idea was demonstrated by Weissflog et al., who studied the polarization emitted from a Mie-resonant (110) GaAs nano-cylinder [121]. They showed that by varying the angle of polarization between the signal and the idler (see Fig. 11.10a), the generated output polarization fully circles the Poincare sphere, generating linear or elliptically polarized SFG. These ideas can be fully generalized to design metasurfaces of complex geometries that can generate any output desired polarization.

Another important use of the SFG process was to demonstrate the generation of frequencies of 3ω by mixing ω and 2ω in a nonlinear nanoresonator, see Fig. 11.10b. This mixing process was significantly more efficient than generating 3ω through the process

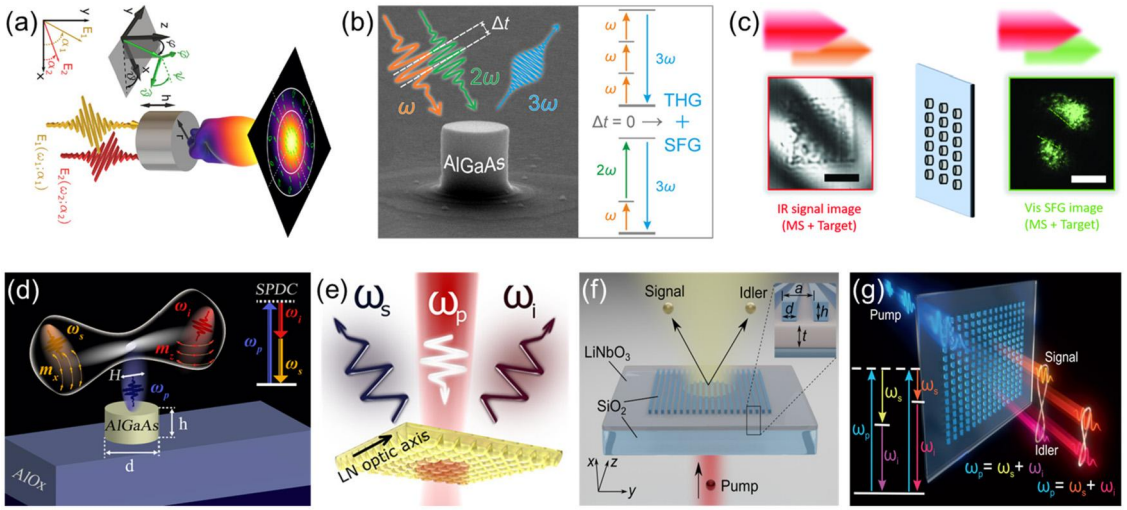

Figure 11.10. (a-c) Non-degenerate up-conversion processes. (a) Engineering of the output SFG polarization by controlling the incident polarization of the input beam [121]. (b) Generation of enhanced THG by mixing the fundamental and second harmonic waves from a nonlinear quadratic process [122]. (c) Application of the SFG process in infrared imaging through nonlinear up-conversion in an ultra-thin metasurface [11]. (d-g) Nonlinear down-conversion process for generation of bi-photon states. (d) SPDC generation from a nanoscale dielectric Mie-resonator [123]. (e) SPDC from a Lithium Niobate Mie-resonant metasurface [124]. (f) High-rate SPDC from a lithium niobate high-Q metasurface [125]. (g) High-Q GaAs metasurfaces for generating complex quantum states [126].

of THG. Finally, the SFG process is linearly proportional to the signal beam intensity. It, therefore, allows for the up-conversion of images, including infrared images of low intensity, by mixing them with a plane wave but high intensity pump beam. Such infrared image conversion opens new applications for infrared imaging and night vision technology. This idea was pioneered by Camacho-Morales et al., who demonstrated the conversion of images at 1550 nm to visible in a GaAs metasurface, see Fig. 11.10c.

The reversed process of SFG is the down-conversion process, Fig. 11.2c-middle. A very important example of such a down-conversion process is the generation of bi-photon pairs in the process of SPDC. In this process, the bi-photons are emitted in different directions and at different frequencies. The exact relationship between angle and frequency is governed by the radiation pattern of the nanoresonator or the dispersion relations of the metasurface. The first generation of SPDC photons from a Mie-resonant AlGaAs nano-cylinder was performed by Marino et al. [123], see Fig. 11.10d. This pioneering experiment demonstrated SPDC from the smallest volume of material, though the generation rate was only 35 Hz, requiring 24 hours of integration time. The pump fre-

quency was also close to the band gap of the semiconductor, resulting in a large background emission. The low generation rate can be circumvented by using an array of nanoresonators in the form of a dielectric metasurface. This concept was realized by Santiago-Cruz et al. [124], see Fig. 11.10e using an x-cut lithium niobate metasurface. They demonstrated over 100 times SPDC enhancement in the Mie-resonant compared to the plane film.

To increase the rate of the SPDC emission, Zhang et al. utilized a high-Q lithium niobate metasurface based on guided wave resonance grating operating at the quasi-BIC condition [125], see Fig. 11.10f. The photon-pair rate was strongly enhanced by 450 times, as compared to unpatterned films because of high-Q resonances of this metasurface. The high rate and good coincidence to the accidental ratio of these measurements allowed for estimating the entanglement of the emitted bi-photons. By estimating the Cauchy-Schwarz inequality, it was found that the emitted photons are non-classical with a strong degree of entanglement. In a similar approach, using quasi-BIC modes in GaAs metasurface, Santiago-Cruz et al. [126] demonstrated a boost of the emission of nondegenerate entangled photons within multiple narrow resonance bands and over a wide spectral range. A single resonance or several resonances in the same sample, pumped at multiple wavelengths, could generate multifrequency quantum states, including cluster states. These features reveal metasurfaces as versatile sources of complex states for quantum state sources.

11.4 Conclusions and outlook

In summary, this chapter describes the fundamental physics of nonlinear processes in dielectric nanostructures and metasurfaces. It highlights the important advantages coming from the resonant properties of such nanostructures. In addition to a versatile light manipulation in the linear regime, they pave the way to access and enhance the nonlinear properties in the subwavelength regime, allowing the design of the thinnest structures with the strongest nonlinear response. It can be achieved by tuning the geometrical and/or material properties of the nanostructures. The ability to control resonant modes excitations of both electric and magnetic origin offers unprecedented opportunities for nonlinear wavefront shaping.

In the chapter, we review the recent advances in the field and highlight the important applications. These include the cubic nonlinear phenomena of THG and FWM, which can be dramatically enhanced in resonant nanostructures. In addition, we review

the phenomena of ultra-fast index modulation of such nanostructures, leading to new phenomena of space-time modulated metasurfaces. We further discuss the effects arising from the quadratic nonlinear response of the material and include important effects, including SHG and SFG. These effects open new opportunities for novel light sources and infrared imaging.

Outlook

Importantly, the associated near-field enhancement might lead to strong light-matter interaction in the subwavelength structures, leading to a number of new effects, such as Rabi splitting, high-harmonic generation, ultra-short pulses, etc. Importantly, resonant magnetic modes might lead to a new direction in nonlinear optics, exploring magnetic-type nonlinearities, which are not studied well so far. Despite the clear advantages, there are still some open challenges, such as improving the conversion efficiencies of various nonlinear processes. In addition to resonant modes excitation, there is a possibility to separately control the fundamental and second- or third-harmonic scattering efficiency, allowing to trap the near-field excitations in the nanostructures at various frequencies. In addition to enhanced quantum effects, it might lead to improved sensing and catalytic effects.

Here, we covered the most recent progress and advances in the field of nonlinear dielectric nanostructures and highlighted the important applications, such as frequency conversion, light sources, optical sensing, nonlinear holograms and imaging, entangled photons generation, and catalytic effects. We believe that this emerging field will grow significantly in the near future and will offer even more exciting applications in biomedical imaging, optical communications, and quantum computing.

References

[1] S.A. Maier, Plasmonics: Fundamentals and Applications, Springer US, 2007.

[2] A.I. Kuznetsov, A.E. Miroshnichenko, M.L. Brongersma, Y.S. Kivshar, B. Luk'yanchuk, Optically resonant dielectric nanostructures, Science 354 (2016) 846.

[3] A.B. Evlyukhin, S.M. Novikov, U. Zywietz, R.L. Eriksen, C. Reinhardt, S.I. Bozhevolnyi, B.N. Chichkov, Demonstration of magnetic dipole resonances of dielectric nanospheres in the visible region, Nano Letters 12 (2012) 3749–3755.

[4] I. Staude, A.E. Miroshnichenko, M. Decker, N.T. Fofang, S. Liu, E. Gonzales, J. Dominguez, T.S. Luk, D.N. Neshev, I. Brener, Y. Kivshar, Tailoring directional scattering through magnetic and electric resonances in subwavelength silicon nanodisks, ACS Nano 7 (2013) 7824–7832.

[5] T. Phan, D. Sell, E.W. Wang, S. Doshay, K. Edee, J. Yang, J.A. Fan, High-efficiency, large-area, topology-optimized metasurfaces, Light: Science & Applications 8 (2019) 48.

[6] C. Gigli, G. Marino, A. Artioli, D. Rocco, C. De Angelis, J. Claudon, J.-M. Gérard, G. Leo, Tensorial phase control in nonlinear meta-optics, Optica 8 (2021) 269–276.

[7] G. Mie, Beiträge zur Optik trüber Medien, speziell kolloidaler Metallösungen, Annalen der Physik 330 (1908) 377–445.

[8] C.W. Hsu, B. Zhen, A.D. Stone, J.D. Joannopoulos, M. Soljačić, Bound states in the continuum, Nature Reviews Materials 1 (2016) 16048.

[9] S. Liu, P.P. Vabishchevich, A. Vaskin, J.L. Reno, G.A. Keeler, M.B. Sinclair, I. Staude, I. Brener, An all-dielectric metasurface as a broadband optical frequency mixer, Nature Communications 9 (2018) 2507.

[10] A. Krasnok, M. Tymchenko, A. Alù, Nonlinear metasurfaces: a paradigm shift in nonlinear optics, Materials Today 21 (2018) 8–21.

[11] R. Camacho-Morales, D. Rocco, L. Xu, V.F. Gili, N. Dimitrov, L. Stoyanov, Z. Ma, A. Komar, M. Lysevych, F. Karouta, Infrared upconversion imaging in nonlinear metasurfaces, Advanced Photonics 3 (2021) 036002.

[12] T. Pertsch, Y. Kivshar, Nonlinear optics with resonant metasurfaces, MRS Bulletin 45 (2020) 210–220.

[13] G. Grinblat, Nonlinear dielectric nanoantennas and metasurfaces: frequency conversion and wavefront control, ACS Photonics 8 (2021) 3406–3432.

[14] A.I. Kuznetsov, A.E. Miroshnichenko, Y.H. Fu, J. Zhang, B. Luk'yanchuk, Magnetic light, Scientific Reports 2 (2012) 492.

[15] M.R. Shcherbakov, D.N. Neshev, B. Hopkins, A.S. Shorokhov, I. Staude, E.V. Melik-Gaykazyan, M. Decker, A.A. Ezhov, A.E. Miroshnichenko, I. Brener, A.A. Fedyanin, Y.S. Kivshar, Enhanced third-harmonic generation in silicon nanoparticles driven by magnetic response, Nano Letters 14 (2014) 6488–6492.

[16] D.A. Smirnova, A.B. Khanikaev, L.A. Smirnov, Y.S. Kivshar, Multipolar third-harmonic generation driven by optically induced magnetic resonances, ACS Photonics 3 (2016) 1468–1476.

[17] G. Grinblat, Y. Li, M.P. Nielsen, R.F. Oulton, S.A. Maier, Degenerate four-wave mixing in a multiresonant germanium nanodisk, ACS Photonics 4 (2017) 2144–2149.

[18] R. Colom, L. Xu, L. Marini, F. Bedu, I. Ozerov, T. Begou, J. Lumeau, A.E. Miroshnishenko, D. Neshev, B.T. Kuhlmey, Enhanced four-wave mixing in doubly resonant Si nanoresonators, ACS Photonics 6 (2019) 1295–1301.

[19] A.E. Miroshnichenko, A.B. Evlyukhin, Y.F. Yu, R.M. Bakker, A. Chipouline, A.I. Kuznetsov, B. Luk'yanchuk, B.N. Chichkov, Y.S. Kivshar, Nonradiating anapole modes in dielectric nanoparticles, Nature Communications 6 (2015) 8069.

[20] A.G. Lamprianidis, A.E. Miroshnichenko, Excitation of nonradiating magnetic anapole states with azimuthally polarized vector beams, Beilstein Journal of Nanotechnology 9 (2018) 1478–1490.

[21] E. Zanganeh, A. Evlyukhin, A. Miroshnichenko, M. Song, E. Nenasheva, P. Kapitanova, Anapole meta-atoms: nonradiating electric and magnetic sources, Physical Review Letters 127 (2021) 096804.

[22] G. Grinblat, Y. Li, M.P. Nielsen, R.F. Oulton, S.A. Maier, Enhanced third harmonic generation in single germanium nanodisks excited at the anapole mode, Nano Letters 16 (2016) 4635–4640.

[23] T. Shibanuma, G. Grinblat, P. Albella, S.A. Maier, Efficient third harmonic generation from metal–dielectric hybrid nanoantennas, Nano Letters 17 (2017) 2647–2651.
[24] L. Xu, M. Rahmani, K. Zangeneh Kamali, A. Lamprianidis, L. Ghirardini, J. Sautter, R. Camacho-Morales, H. Chen, M. Parry, I. Staude, G. Zhang, D. Neshev, A.E. Miroshnichenko, Boosting third-harmonic generation by a mirror-enhanced anapole resonator, Light: Science & Applications 7 (2018) 44.
[25] L. Wang, S. Kruk, L. Xu, M. Rahmani, D. Smirnova, A. Solntsev, I. Kravchenko, D. Neshev, Y. Kivshar, Shaping the third-harmonic radiation from silicon nanodimers, Nanoscale 9 (2017) 2201–2206.
[26] M.R. Shcherbakov, A.S. Shorokhov, D.N. Neshev, B. Hopkins, I. Staude, E.V. Melik-Gaykazyan, A.A. Ezhov, A.E. Miroshnichenko, I. Brener, A.A. Fedyanin, Y.S. Kivshar, Nonlinear interference and tailorable third-harmonic generation from dielectric oligomers, ACS Photonics 2 (2015) 578–582.
[27] T. Das, P.P. Iyer, R.A. DeCrescent, J.A. Schuller, Beam engineering for selective and enhanced coupling to multipolar resonances, Physical Review B 92 (2015) 241110.
[28] E.V. Melik-Gaykazyan, S.S. Kruk, R. Camacho-Morales, L. Xu, M. Rahmani, K. Zangeneh Kamali, A. Lamprianidis, A.E. Miroshnichenko, A.A. Fedyanin, D.N. Neshev, Y.S. Kivshar, Selective third-harmonic generation by structured light in Mie-resonant nanoparticles, ACS Photonics 5 (2018) 728–733.
[29] M.K. Kroychuk, A.S. Shorokhov, D.F. Yagudin, D.A. Shilkin, D.A. Smirnova, I. Volkovskaya, M.R. Shcherbakov, G. Shvets, A.A. Fedyanin, Enhanced nonlinear light generation in oligomers of silicon nanoparticles under vector beam illumination, Nano Letters 20 (2020) 3471–3477.
[30] Y. Yang, W. Wang, A. Boulesbaa, I.I. Kravchenko, D.P. Briggs, A. Puretzky, D. Geohegan, J. Valentine, Nonlinear Fano-resonant dielectric metasurfaces, Nano Letters 15 (2015) 7388–7393.
[31] A.S. Shorokhov, E.V. Melik-Gaykazyan, D.A. Smirnova, B. Hopkins, K.E. Chong, D.-Y. Choi, M.R. Shcherbakov, A.E. Miroshnichenko, D.N. Neshev, A.A. Fedyanin, Y.S. Kivshar, Multifold enhancement of third-harmonic generation in dielectric nanoparticles driven by magnetic Fano resonances, Nano Letters 16 (2016) 4857–4861.
[32] S. Chen, M. Rahmani, K.F. Li, A. Miroshnichenko, T. Zentgraf, G. Li, D. Neshev, S. Zhang, Third harmonic generation enhanced by multipolar interference in complementary silicon metasurfaces, ACS Photonics 5 (2018) 1671–1675.
[33] M. Semmlinger, M. Zhang, M.L. Tseng, T.-T. Huang, J. Yang, D.P. Tsai, P. Nordlander, N.J. Halas, Generating third harmonic vacuum ultraviolet light with a TiO2 metasurface, Nano Letters 19 (2019) 8972–8978.
[34] A. Tognazzi, K.I. Okhlopkov, A. Zilli, D. Rocco, L. Fagiani, E. Mafakheri, M. Bollani, M. Finazzi, M. Celebrano, M.R. Shcherbakov, A.A. Fedyanin, C. De Angelis, Third-harmonic light polarization control in magnetically resonant silicon metasurfaces, Optics Express 29 (2021) 11605–11612.
[35] O.A.M. Abdelraouf, A.P. Anthur, Z. Dong, H. Liu, Q. Wang, L. Krivitsky, X. Renshaw Wang, Q.J. Wang, H. Liu, Multistate tuning of third harmonic generation in Fano-resonant hybrid dielectric metasurfaces, Advanced Functional Materials 31 (2021) 2104627.
[36] M. Zhu, S. Abdollahramezani, T. Fan, A. Adibi, Dynamically tunable third-harmonic generation with all-dielectric metasurfaces incorporating phase-change chalcogenides, Optics Letters 46 (2021) 5296–5299.

[37] D. Smirnova, S. Kruk, D. Leykam, E. Melik-Gaykazyan, D.-Y. Choi, Y. Kivshar, Third-harmonic generation in photonic topological metasurfaces, Physical Review Letters 123 (2019) 103901.

[38] Z. Liu, Y. Xu, Y. Lin, J. Xiang, T. Feng, Q. Cao, J. Li, S. Lan, J. Liu, High-Q quasibound states in the continuum for nonlinear metasurfaces, Physical Review Letters 123 (2019) 253901.

[39] L. Xu, K. Zangeneh Kamali, L. Huang, M. Rahmani, A. Smirnov, R. Camacho-Morales, Y. Ma, G. Zhang, M. Woolley, D. Neshev, A.E. Miroshnichenko, Dynamic nonlinear image tuning through magnetic dipole quasi-BIC ultrathin resonators, Advanced Science 6 (2019) 1802119.

[40] K. Koshelev, Y. Tang, K. Li, D.-Y. Choi, G. Li, Y. Kivshar, Nonlinear metasurfaces governed by bound states in the continuum, ACS Photonics 6 (2019) 1639–1644.

[41] K.I. Okhlopkov, A. Zilli, A. Tognazzi, D. Rocco, L. Fagiani, E. Mafakheri, M. Bollani, M. Finazzi, M. Celebrano, M.R. Shcherbakov, C. De Angelis, A.A. Fedyanin, Tailoring third-harmonic diffraction efficiency by hybrid modes in high-Q metasurfaces, Nano Letters 21 (2021) 10438–10445.

[42] M. Gandolfi, A. Tognazzi, D. Rocco, C. De Angelis, L. Carletti, Near-unity third-harmonic circular dichroism driven by a quasibound state in the continuum in asymmetric silicon metasurfaces, Physical Review A 104 (2021) 023524.

[43] G. Yang, S.U. Dev, M.S. Allen, J.W. Allen, H. Harutyunyan, Optical bound states in the continuum enabled by magnetic resonances coupled to a mirror, Nano Letters 22 (2022) 2001–2008.

[44] L. Xu, D.A. Smirnova, R. Camacho-Morales, R.A. Aoni, K.Z. Kamali, M. Cai, C. Ying, Z. Zheng, A.E. Miroshnichenko, D.N. Neshev, M. Rahmani, Enhanced four-wave mixing from multi-resonant silicon dimer-hole membrane metasurfaces, New Journal of Physics 24 (2022) 035002.

[45] L. Xu, M. Rahmani, Y. Ma, D.A. Smirnova, K.Z. Kamali, F. Deng, Y.K. Chiang, L. Huang, H. Zhang, S. Gould, D.N. Neshev, A.E. Miroshnichenko, Enhanced light-matter interactions in dielectric nanostructures via machine-learning approach, Advanced Photonics 2 (2020) 026003.

[46] C. Schlickriede, S.S. Kruk, L. Wang, B. Sain, Y. Kivshar, T. Zentgraf, Nonlinear imaging with all-dielectric metasurfaces, Nano Letters 20 (2020) 4370–4376.

[47] I. Volkovskaya, L. Xu, L. Huang, A.I. Smirnov, A.E. Miroshnichenko, D. Smirnova, Multipolar second-harmonic generation from high-Q quasi-BIC states in subwavelength resonators, Nanophotonics 9 (2020) 3953–3963.

[48] A. Bourgeade, E. Freysz, Computational modeling of second-harmonic generation by solution of full-wave vector Maxwell equations, Journal of the Optical Society of America B 17 (2000) 226–234.

[49] Z. Zheng, L. Xu, L. Huang, D. Smirnova, K. Zangeneh Kamali, A. Yousefi, F. Deng, R. Camacho-Morales, C. Ying, A. Miroshnichenko, D.N. Neshev, M. Rahmani, Third-harmonic generation and imaging with resonant Si membrane metasurface, Opto-Electronic Advances 6 (2023) 220174 (pp. 1–10).

[50] Y. Gao, Y. Fan, Y. Wang, W. Yang, Q. Song, S. Xiao, Nonlinear holographic all-dielectric metasurfaces, Nano Letters 18 (2018) 8054–8061.

[51] L. Ohnoutek, J.-Y. Kim, J. Lu, B.J. Olohan, D.M. Răsădean, G. Dan Pantoş, N.A. Kotov, V.K. Valev, Third-harmonic Mie scattering from semiconductor nanohelices, Nature Photonics 16 (2022) 126–133.

[52] F.R. Morgenthaler, Velocity modulation of electromagnetic waves, IRE Transactions on Microwave Theory and Techniques 6 (1958) 167–172.

[53] V. Bacot, G. Durey, A. Eddi, M. Fink, E. Fort, Phase-conjugate mirror for water waves driven by the Faraday instability, Proceedings of the National Academy of Sciences 116 (2019) 8809–8814.

[54] K. Schultheiss, N. Sato, P. Matthies, L. Körber, K. Wagner, T. Hula, O. Gladii, J.E. Pearson, A. Hoffmann, M. Helm, J. Fassbender, H. Schultheiss, Time refraction of spin waves, Physical Review Letters 126 (2021) 137201.

[55] E.A. Kittlaus, N.T. Otterstrom, P. Kharel, S. Gertler, P.T. Rakich, Non-reciprocal interband Brillouin modulation, Nature Photonics 12 (2018) 613–619.

[56] N. Kinsey, C. DeVault, A. Boltasseva, V.M. Shalaev, Near-zero-index materials for photonics, Nature Reviews Materials 4 (2019) 742–760.

[57] H. Lira, Z. Yu, S. Fan, M. Lipson, Electrically driven nonreciprocity induced by interband photonic transition on a silicon chip, Physical Review Letters 109 (2012) 033901.

[58] E. Galiffi, R. Tirole, S. Yin, H. Li, S. Vezzoli, P. Huidobro, M. Silveirinha, R. Sapienza, A. Alù, J. Pendry, Photonics of time-varying media, Advanced Photonics 4 (2022) 014002.

[59] E. Feigenbaum, K. Diest, H.A Atwater, Unity-order index change in transparent conducting oxides at visible frequencies, Nano Letters 10 (2010) 2111–2116.

[60] K.-H Kim, Unity-order nonlinear optical index change in epsilon-near-zero composite materials of gain media and metal nanoparticles, Annalen der Physik 530 (2018) 1700259.

[61] C. De Angelis, G. Leo, D.N. Neshev, Nonlinear Meta-Optics, CRC Press, 2020.

[62] N. Karl, P.P. Vabishchevich, M.R. Shcherbakov, S. Liu, M.B. Sinclair, G. Shvets, I. Brener, Frequency conversion in a time-variant dielectric metasurface, Nano Letters 20 (2020) 7052–7058.

[63] G. Della Valle, B. Hopkins, L. Ganzer, T. Stoll, M. Rahmani, S. Longhi, Y.S. Kivshar, C. De Angelis, D.N. Neshev, G. Cerullo, Nonlinear anisotropic dielectric metasurfaces for ultrafast nanophotonics, ACS Photonics 4 (2017) 2129–2136.

[64] G. Grinblat, M.P. Nielsen, P. Dichtl, Y. Li, R.P. Oulton, S.A. Maier, Ultrafast sub–30-fs all-optical switching based on gallium phosphide, Science Advances 5 (2019) eaaw3262.

[65] S. Makarov, S. Kudryashov, I. Mukhin, A. Mozharov, V. Milichko, A. Krasnok, P. Belov, Tuning of magnetic optical response in a dielectric nanoparticle by ultrafast photoexcitation of dense electron–hole plasma, Nano Letters 15 (2015) 6187–6192.

[66] M.R. Shcherbakov, P.P. Vabishchevich, A.S. Shorokhov, K.E. Chong, D.-Y. Choi, I. Staude, A.E. Miroshnichenko, D.N. Neshev, A.A. Fedyanin, Y.S. Kivshar, Ultrafast all-optical switching with magnetic resonances in nonlinear dielectric nanostructures, Nano Letters 15 (2015) 6985–6990.

[67] M.R. Shcherbakov, S. Liu, V.V. Zubyuk, A. Vaskin, P.P. Vabishchevich, G. Keeler, T. Pertsch, T.V. Dolgova, I. Staude, I. Brener, A.A. Fedyanin, Ultrafast all-optical tuning of direct-gap semiconductor metasurfaces, Nature Communications 8 (2017) 17.

[68] P.P. Vabishchevich, A. Vaskin, N. Karl, J.L. Reno, M.B. Sinclair, I. Staude, I. Brener, Ultrafast all-optical diffraction switching using semiconductor metasurfaces, Applied Physics Letters 118 (2021) 211105.

[69] N. Karl, P.P. Vabishchevich, S. Liu, M.B. Sinclair, G.A. Keeler, G.M. Peake, I. Brener, All-optical tuning of symmetry protected quasi bound states in the continuum, Applied Physics Letters 115 (2019) 141103.

[70] L. Carletti, A. Locatelli, O. Stepanenko, G. Leo, C. De Angelis, Enhanced second-harmonic generation from magnetic resonance in AlGaAs nanoantennas, Optics Express 23 (2015) 26544–26550.
[71] V.F. Gili, L. Carletti, A. Locatelli, D. Rocco, M. Finazzi, L. Ghirardini, I. Favero, C. Gomez, A. Lemaître, M. Celebrano, C. De Angelis, G. Leo, Monolithic AlGaAs second-harmonic nanoantennas, Optics Express 24 (2016) 15965–15971.
[72] L. Ghirardini, L. Carletti, V. Gili, G. Pellegrini, L. Duò, M. Finazzi, D. Rocco, A. Locatelli, C. De Angelis, I. Favero, M. Ravaro, G. Leo, A. Lemaître, M. Celebrano, Polarization properties of second-harmonic generation in AlGaAs optical nanoantennas, Optics Letters 42 (2017) 559–562.
[73] R. Camacho-Morales, M. Rahmani, S. Kruk, L. Wang, L. Xu, D.A. Smirnova, A.S. Solntsev, A. Miroshnichenko, H.H. Tan, F. Karouta, S. Naureen, K. Vora, L. Carletti, C. De Angelis, C. Jagadish, Y.S. Kivshar, D.N. Neshev, Nonlinear generation of vector beams from AlGaAs nanoantennas, Nano Letters 16 (2016) 7191–7197.
[74] S.S. Kruk, R. Camacho-Morales, L. Xu, M. Rahmani, D.A. Smirnova, L. Wang, H.H. Tan, C. Jagadish, D.N. Neshev, Y.S. Kivshar, Nonlinear optical magnetism revealed by second-harmonic generation in nanoantennas, Nano Letters 17 (2017) 3914–3918.
[75] K. Koshelev, S. Kruk, E. Melik-Gaykazyan, J.-H. Choi, A. Bogdanov, H.-G. Park, Y. Kivshar, Subwavelength dielectric resonators for nonlinear nanophotonics, Science 367 (2020) 288–292.
[76] L. Carletti, A. Locatelli, D. Neshev, C. De Angelis, Shaping the radiation pattern of second-harmonic generation from AlGaAs dielectric nanoantennas, ACS Photonics 3 (2016) 1500–1507.
[77] J.D. Sautter, L. Xu, A.E. Miroshnichenko, M. Lysevych, I. Volkovskaya, D.A. Smirnova, R. Camacho-Morales, K. Zangeneh Kamali, F. Karouta, K. Vora, H.H. Tan, M. Kauranen, I. Staude, C. Jagadish, D.N. Neshev, M. Rahmani, Tailoring second-harmonic emission from (111)-GaAs nanoantennas, Nano Letters 19 (2019) 3905–3911.
[78] L. Xu, G. Saerens, M. Timofeeva, D.A. Smirnova, I. Volkovskaya, M. Lysevych, R. Camacho-Morales, M. Cai, K. Zangeneh Kamali, L. Huang, Forward and backward switching of nonlinear unidirectional emission from GaAs nanoantennas, ACS Nano 14 (2019) 1379–1389.
[79] L. Xu, M. Rahmani, D. Smirnova, K. Zangeneh Kamali, G. Zhang, D. Neshev, A.E. Miroshnichenko, Highly-efficient longitudinal second-harmonic generation from doubly-resonant AlGaAs nanoantennas, in: Photonics, Multidisciplinary Digital Publishing Institute, 2018, p. 29.
[80] D. Rocco, C. Gigli, L. Carletti, G. Marino, M.A. Vincenti, G. Leo, C.D. Angelis, Vertical second harmonic generation in asymmetric dielectric nanoantennas, IEEE Photonics Journal 12 (2020) 1–7.
[81] D. Rocco, V.F. Gili, L. Ghirardini, L. Carletti, I. Favero, A. Locatelli, G. Marino, D.N. Neshev, M. Celebrano, M. Finazzi, G. Leo, C. De Angelis, Tuning the second-harmonic generation in AlGaAs nanodimers via non-radiative state optimization, Photonics Research 6 (2018) B6–B12.
[82] R. Camacho-Morales, G. Bautista, X. Zang, L. Xu, L. Turquet, A. Miroshnichenko, H.H. Tan, A. Lamprianidis, M. Rahmani, C. Jagadish, Resonant harmonic generation in AlGaAs nanoantennas probed by cylindrical vector beams, Nanoscale 11 (2019) 1745–1753.
[83] D. de Ceglia, L. Carletti, M.A. Vincenti, C. De Angelis, M. Scalora, Second-harmonic generation in Mie-resonant GaAs nanowires, Applied Sciences 9 (2019) 3381.

[84] H. Jiang, Y. Cai, Z. Han, Strong second-harmonic generation in dielectric optical nanoantennas resulting from the hybridization of magnetic dipoles and lattice resonances, Journal of the Optical Society of America B 37 (2020) 3146–3151.
[85] O. Pashina, K. Frizyuk, G. Zograf, M. Petrov, Thermo-optical reshaping of second-harmonic emission from dimer all-dielectric nanoresonators, Optics Letters 47 (2022) 1992–1995.
[86] J. Cambiasso, G. Grinblat, Y. Li, A. Rakovich, E. Cortés, S.A. Maier, Bridging the gap between dielectric nanophotonics and the visible regime with effectively lossless gallium phosphide antennas, Nano Letters 17 (2017) 1219–1225.
[87] B. Tilmann, G. Grinblat, R. Berté, M. Özcan, V.F. Kunzelmann, B. Nickel, I.D. Sharp, E. Cortés, S.A. Maier, Y. Li, Nanostructured amorphous gallium phosphide on silica for nonlinear and ultrafast nanophotonics, Nanoscale Horizons 5 (2020) 1500–1508.
[88] K.-H. Kim, W.-S. Rim, Anapole resonances facilitated by high-index contrast between substrate and dielectric nanodisk enhance vacuum ultraviolet generation, ACS Photonics 5 (2018) 4769–4775.
[89] F. Timpu, J. Sendra, C. Renaut, L. Lang, M. Timofeeva, M.T. Buscaglia, V. Buscaglia, R. Grange, Lithium niobate nanocubes as linear and nonlinear ultraviolet Mie resonators, ACS Photonics 6 (2019) 545–552.
[90] J. Wang, Z. Liu, J. Xiang, B. Chen, Y. Wei, W. Liu, Y. Xu, S. Lan, J. Liu, Ultraviolet second harmonic generation from Mie-resonant lithium niobate nanospheres, Nanophotonics 10 (2021) 4273–4278.
[91] Y. Li, Z. Huang, Z. Sui, H. Chen, X. Zhang, W. Huang, H. Guan, W. Qiu, J. Dong, W. Zhu, J. Yu, H. Lu, Z. Chen, Optical anapole mode in nanostructured lithium niobate for enhancing second harmonic generation, Nanophotonics 9 (2020) 3575–3585.
[92] C. Renaut, L. Lang, K. Frizyuk, M. Timofeeva, F.E. Komissarenko, I.S. Mukhin, D. Smirnova, F. Timpu, M. Petrov, Y. Kivshar, R. Grange, Reshaping the second-order polar response of hybrid metal–dielectric nanodimers, Nano Letters 19 (2019) 877–884.
[93] M. Hentschel, B. Metzger, B. Knabe, K. Buse, H. Giessen, Linear and nonlinear optical properties of hybrid metallic–dielectric plasmonic nanoantennas, Beilstein Journal of Nanotechnology 7 (2016) 111–120.
[94] N. Chauvet, M. Ethis de Corny, M. Jeannin, G. Laurent, S. Huant, T. Gacoin, G. Dantelle, G. Nogues, G. Bachelier, Hybrid KTP–plasmonic nanostructures for enhanced nonlinear optics at the nanoscale, ACS Photonics 7 (2020) 665–672.
[95] D. Pidgayko, I. Deriy, V. Fedorov, A. Mozharov, I. Mukhin, Y. Zadiranov, M. Petrov, A. Samusev, A. Bogdanov, Second harmonic generation in hybrid GaP/Au nanocylinders, Journal of Physics. Conference Series 2015 (2021) 012172.
[96] S. Liu, M.B. Sinclair, S. Saravi, G.A. Keeler, Y. Yang, J. Reno, G.M. Peake, F. Setzpfandt, I. Staude, T. Pertsch, I. Brener, Resonantly enhanced second-harmonic generation using III–V semiconductor all-dielectric metasurfaces, Nano Letters 16 (2016) 5426–5432.
[97] G. Marino, D. Rocco, C. Gigli, G. Beaudoin, K. Pantzas, S. Suffit, P. Filloux, I. Sagnes, G. Leo, C.D. Angelis, Harmonic generation with multi-layer dielectric metasurfaces, Nanophotonics (2021).
[98] G. Marino, C. Gigli, D. Rocco, A. Lemaître, I. Favero, C. De Angelis, G. Leo, Zero-order second harmonic generation from AlGaAs-on-insulator metasurfaces, ACS Photonics 6 (2019) 1226–1231.

[99] M. Semmlinger, M.L. Tseng, J. Yang, M. Zhang, C. Zhang, W.-Y. Tsai, D.P. Tsai, P. Nordlander, N.J. Halas, Vacuum ultraviolet light-generating metasurface, Nano Letters 18 (2018) 5738–5743.
[100] L. Carletti, C. Li, J. Sautter, I. Staude, C. De Angelis, T. Li, D.N. Neshev, Second harmonic generation in monolithic lithium niobate metasurfaces, Optics Express 27 (2019) 33391–33398.
[101] A. Fedotova, M. Younesi, J. Sautter, A. Vaskin, F.J.F. Löchner, M. Steinert, R. Geiss, T. Pertsch, I. Staude, F. Setzpfandt, Second-harmonic generation in resonant nonlinear metasurfaces based on lithium niobate, Nano Letters 20 (2020) 8608–8614.
[102] J. Ma, F. Xie, W. Chen, J. Chen, W. Wu, W. Liu, Y. Chen, W. Cai, M. Ren, J. Xu, Nonlinear lithium niobate metasurfaces for second harmonic generation, Laser & Photonics Reviews 15 (2021) 2000521.
[103] F.J.F. Löchner, A.N. Fedotova, S. Liu, G.A. Keeler, G.M. Peake, S. Saravi, M.R. Shcherbakov, S. Burger, A.A. Fedyanin, I. Brener, T. Pertsch, F. Setzpfandt, I. Staude, Polarization-dependent second harmonic diffraction from resonant GaAs metasurfaces, ACS Photonics 5 (2018) 1786–1793.
[104] C. Gigli, G. Marino, S. Suffit, G. Patriarche, G. Beaudoin, K. Pantzas, I. Sagnes, I. Favero, G. Leo, Polarization- and diffraction-controlled second-harmonic generation from semiconductor metasurfaces, Journal of the Optical Society of America B 36 (2019) E55–E64.
[105] L. Carletti, A. Zilli, F. Moia, A. Toma, M. Finazzi, C. De Angelis, D.N. Neshev, M. Celebrano, Steering and encoding the polarization of the second harmonic in the visible with a monolithic LiNbO3 metasurface, ACS Photonics 8 (2021) 731–737.
[106] P.P. Vabishchevich, S. Liu, M.B. Sinclair, G.A. Keeler, G.M. Peake, I. Brener, Enhanced second-harmonic generation using broken symmetry III–V semiconductor Fano metasurfaces, ACS Photonics 5 (2018) 1685–1690.
[107] Z. Huang, H. Lu, H. Xiong, Y. Li, H. Chen, W. Qiu, H. Guan, J. Dong, W. Zhu, J. Yu, Y. Luo, J. Zhang, Z. Chen, Fano resonance on nanostructured lithium niobate for highly efficient and tunable second harmonic generation, Nanomaterials 9 (2019) 69.
[108] A.P. Anthur, H. Zhang, R. Paniagua-Dominguez, D.A. Kalashnikov, S.T. Ha, T.W.W. Maß, A.I. Kuznetsov, L. Krivitsky, Continuous wave second harmonic generation enabled by quasi-bound-states in the continuum on gallium phosphide metasurfaces, Nano Letters 20 (2020) 8745–8751.
[109] D. Khmelevskaia, D.I. Markina, V.V. Fedorov, G.A. Ermolaev, A.V. Arsenin, V.S. Volkov, A.S. Goltaev, Y.M. Zadiranov, I.A. Tzibizov, A.P. Pushkarev, A.K. Samusev, A.A. Shcherbakov, P.A. Belov, I.S. Mukhin, S.V. Makarov, Directly grown crystalline gallium phosphide on sapphire for nonlinear all-dielectric nanophotonics, Applied Physics Letters 118 (2021) 201101.
[110] Q. Yang, Y. Liu, X. Gan, C. Fang, G. Han, Y. Hao, Nonlinear bound states in the continuum of etchless lithium niobate metasurfaces, IEEE Photonics Journal 12 (2020) 1–9.
[111] L. Kang, H. Bao, D.H. Werner, Efficient second-harmonic generation in high Q-factor asymmetric lithium niobate metasurfaces, Optics Letters 46 (2021) 633–636.
[112] X. Zhang, L. He, X. Gan, X. Huang, Y. Du, Z. Zhai, Z. Li, Y. Zheng, X. Chen, Y. Cai, X. Ao, Quasi-bound states in the continuum enhanced second-harmonic generation in thin-film lithium niobate, Laser & Photonics Reviews 16 (2022) 2200031.
[113] K.-H. Kim, I.-P. Kim, Efficient near UV-vacuum UV sources based on second-harmonic generation enhanced by high-Q quasi-BICs in

all-dielectric metasurfaces of low-index materials, Photonics and Nanostructures - Fundamentals and Applications 51 (2022) 101053.
[114] Qingchen Yuan, et al., Second harmonic and sum-frequency generations from a silicon metasurface integrated with a two-dimensional material, ACS Photonics 6 (9) (2019) 2252–2259, https://doi.org/10.1021/acsphotonics.9b00553.
[115] Nils Bernhardt, et al., Quasi-BIC resonant enhancement of second-harmonic generation in WS2 monolayers, Nano Letters 20 (7) (2020) 5309–5314, https://doi.org/10.1021/acs.nanolett.0c01603, PMID: 32530635.
[116] Franz J.F. Löchner, et al., Hybrid dielectric metasurfaces for enhancing second-harmonic generation in chemical vapor deposition grown MoS2 monolayers, ACS Photonics 8 (1) (2021) 218–227, https://doi.org/10.1021/acsphotonics.0c01375.
[117] D. Rocco, M. Gandolfi, A. Tognazzi, O. Pashina, G. Zograf, K. Frizyuk, C. Gigli, G. Leo, S. Makarov, M. Petrov, C. De Angelis, Opto-thermally controlled beam steering in nonlinear all-dielectric metastructures, Optics Express 29 (2021) 37128–37139.
[118] M. Celebrano, D. Rocco, M. Gandolfi, A. Zilli, F. Rusconi, A. Tognazzi, A. Mazzanti, L. Ghirardini, E.A.A. Pogna, L. Carletti, C. Baratto, G. Marino, C. Gigli, P. Biagioni, L. Duò, G. Cerullo, G. Leo, G. Della Valle, M. Finazzi, C. De Angelis, Optical tuning of dielectric nanoantennas for thermo-optically reconfigurable nonlinear metasurfaces, Optics Letters 46 (2021) 2453–2456.
[119] M.R. Shcherbakov, P. Shafirin, G. Shvets, Overcoming the efficiency-bandwidth tradeoff for optical harmonics generation using nonlinear time-variant resonators, Physical Review A 100 (2019) 063847.
[120] M.L. Tseng, M. Semmlinger, M. Zhang, C. Arndt, T.-T. Huang, J. Yang, H.Y. Kuo, V.-C. Su, M.K. Chen, C.H. Chu, B. Cerjan, D.P. Tsai, P. Nordlander, N.J. Halas, Vacuum ultraviolet nonlinear metalens, Science Advances 8 (2022) eabn5644.
[121] M.A. Weissflog, M. Cai, M. Parry, M. Rahmani, L. Xu, D. Arslan, A. Fedotova, G. Marino, M. Lysevych, H.H. Tan, C. Jagadish, A. Miroshnichenko, G. Leo, A.A. Sukhorukov, F. Setzpfandt, T. Pertsch, I. Staude, D.N. Neshev, Far-field polarization engineering from nonlinear nanoresonators, Laser & Photonics Reviews 16 (2022) 2200183.
[122] A. Zilli, D. Rocco, M. Finazzi, A. Di Francescantonio, L. Duò, C. Gigli, G. Marino, G. Leo, C. De Angelis, M. Celebrano, Frequency tripling via sum-frequency generation at the nanoscale, ACS Photonics 8 (2021) 1175–1182.
[123] G. Marino, A.S. Solntsev, L. Xu, V.F. Gili, L. Carletti, A.N. Poddubny, M. Rahmani, D.A. Smirnova, H. Chen, A. Lemaître, G. Zhang, A.V. Zayats, C. De Angelis, G. Leo, A.A. Sukhorukov, D.N. Neshev, Spontaneous photon-pair generation from a dielectric nanoantenna, Optica 6 (2019) 1416–1422.
[124] T. Santiago-Cruz, A. Fedotova, V. Sultanov, M.A. Weissflog, D. Arslan, M. Younesi, T. Pertsch, I. Staude, F. Setzpfandt, M. Chekhova, Photon pairs from resonant metasurfaces, Nano Letters 21 (2021) 4423–4429.
[125] J. Zhang, J. Ma, M. Parry, M. Cai, R. Camacho-Morales, L. Xu, D.N. Neshev, A.A. Sukhorukov, Spatially entangled photon pairs from lithium niobate nonlocal metasurfaces, Science Advances 8 (2022) eabq4240.
[126] T. Santiago-Cruz, S.D. Gennaro, O. Mitrofanov, S. Addamane, J. Reno, I. Brener, M.V. Chekhova, Resonant metasurfaces for generating complex quantum states, Science 377 (2022) 991–995.

12

Active nanophotonics

Angela Barreda Gomez[a,b,c], **Ayesheh Bashiri**[a,b], **Jeeyoon Jeong**[d], **Isabelle Staude**[a,b], **and Igal Brener**[e,f,g]

[a]*Institute of Solid State Physics, Friedrich Schiller University Jena, Jena, Germany.* [b]*Institute of Applied Physics, Abbe Center of Photonics, Friedrich Schiller University Jena, Jena, Germany.* [c]*Group of Displays and Photonics Applications, Carlos III University of Madrid, Madrid, Spain.* [d]*Department of Physics and Institute of Quantum Convergence Technology, Kangwon National University, Gangwon, Republic of Korea.* [e]*Center for Integrated Nanotechnologies, Sandia National Laboratories, Albuquerque, NM, United States.* [f]*Sandia National Laboratories, Albuquerque, NM, United States*

12.1 Theoretical concepts

12.1.1 Purcell factor enhancement

Enhancing light-matter interactions is of great relevance for a wide range of applications, including sensing, surface enhanced spectroscopy, solar energy harvesting, or quantum effects such as nonlinear frequency generation or spontaneous and stimulated emission. Over the last years, several configurations have been proposed to enhance the emission of quantum emitters. In particular, with the development of nanotechnology, the possibility of using optical antennas to increase the emission rate of different emitters has been demonstrated, see [1] and references therein.

It was established by E. M. Purcell in the 1940s that the spontaneous emission of an emitter can be increased by engineering the photonic environment where the emitter is located [2]. The Purcell factor measures the local density of optical states (LDOS) at resonance. LDOS can be expressed in terms of the Green's function tensor $\overleftrightarrow{\mathbf{G}}$ [3].

Considering a two-level quantum emitter located at position $\mathbf{r}_0$, and weakly coupled to an antenna, its decay rate, according to Fermi's Golden Rule is given by:

$$\Gamma = \frac{\pi\omega}{3\hbar\epsilon_0}|\langle g|\hat{\mathbf{p}}|e\rangle|^2 \boldsymbol{\rho}_{\mathbf{p}}(\mathbf{r}_0, \omega), \tag{12.1}$$

[g]National Technology & Engineering Solutions of Sandia, LLC, under Contract No. DE-NA0003525 with the U.S Department of Energy.

All-Dielectric Nanophotonics. https://doi.org/10.1016/B978-0-32-395195-1.00017-X
Copyright © 2024 Elsevier Ltd. All rights reserved.

where $\langle g|\hat{\mathbf{p}}|e\rangle$ is the transition dipole moment between the excited state $|e\rangle$ and the ground state $|g\rangle$ of the emitter. ω corresponds to the transition frequency, $\hbar$ is the reduced Planck's constant, ϵ_0 is the vacuum dielectric permittivity, and $\boldsymbol{\rho}_{\mathbf{p}}$ represents the partial LDOS, which is expressed as:

$$\boldsymbol{\rho}_{\mathbf{p}}(\mathbf{r}_0,\omega)=\frac{6\omega}{\pi c^2}[\mathbf{n}_p\cdot \mathrm{Im}\{\overleftrightarrow{\mathbf{G}}(\mathbf{r}_0,\mathbf{r}_0,\omega)\}\cdot\mathbf{n}_p], \tag{12.2}$$

where $\mathbf{n}_p$ is a unit vector along the direction of the dipole $\mathbf{p}$.

The Green's function can be related to the electric field $\mathbf{E}$ at the observation point $\mathbf{r}$ generated by a dipole $\mathbf{p}$ located at $\mathbf{r}_0$ as follows:

$$\mathbf{E}(\mathbf{r})=\frac{1}{\epsilon_0}\frac{\omega^2}{c^2}\overleftrightarrow{\mathbf{G}}(\mathbf{r}_0,\mathbf{r}_0,\omega)\mathbf{p}. \tag{12.3}$$

To obtain the total LDOS, it is necessary to average the partial LDOS over all the possible orientations of the dipole:

$$\boldsymbol{\rho}(\mathbf{r}_0,\omega)=\langle\boldsymbol{\rho}_{\mathbf{p}}(\mathbf{r}_0,\omega)\rangle=\frac{2\omega}{\pi c^2}\mathrm{Im}\{\mathrm{Tr}[\overleftrightarrow{\mathbf{G}}(\mathbf{r}_0,\mathbf{r}_0,\omega)]\}, \tag{12.4}$$

where Tr denotes the trace of a matrix.

By inspection of the previous equations, it can be inferred that the LDOS takes into account the changes in the medium where the emitter is located by means of the Green's function of the system $\overleftrightarrow{\mathbf{G}}$. This suggests that, by changing the LDOS, it is possible to increase or decrease the spontaneous emission rate of the emitter [4].

In free space (i.e., in the absence of an antenna), the partial LDOS (Eq. (12.5)) and the emitter decay rate (Eq. (12.6)) can be expressed as:

$$\boldsymbol{\rho}_{\mathbf{p}}=\frac{\omega^2}{\pi^2c^3}, \tag{12.5}$$

$$\Gamma_0=\frac{\omega^2|\langle g|\hat{\mathbf{p}}|e\rangle|^2}{3\pi\epsilon_0\hbar c^3}. \tag{12.6}$$

So far, a quantum mechanical description has been used for a two-level system. However, it is possible to relate this theory to its classical counterpart. In fact, the two-level system can be replaced by a dipole [3].

The power dissipated by a classical dipole is given by:

$$P=\frac{\omega}{2}\mathrm{Im}\{\mathbf{p}^*\cdot\mathbf{E}(\mathbf{r}_0)\}. \tag{12.7}$$

Taking into account Eq. (12.3), the power dissipated by the dipole is related to the Green's function through the following ex-

pression:

$$P = \frac{\pi\omega^2}{12\epsilon_0}|\mathbf{p}|^2\boldsymbol{\rho}_{\mathbf{p}}(\mathbf{r}_0,\omega). \tag{12.8}$$

The ratio between the emission rate of the dipole in presence and absence of the antenna is known as the Purcell factor:

$$\frac{P}{P^0} = \boldsymbol{\rho}_{\mathbf{p}}(\mathbf{r}_0,\omega)\frac{\pi^2c^3}{\omega^2}, \tag{12.9}$$

with P^0 given by:

$$P^0 = \frac{|\mathbf{p}|^2\omega^4}{12\pi\epsilon_0 c^3}, \tag{12.10}$$

where c is the speed of light in vacuum.

The power in Eq. (12.8) accounts both radiative and non-radiative channels, the latter mainly being dissipated into heat. In the far-field, only the radiated power can be measured. In addition, the non-radiative power can be detrimental to many different applications [5]. For these reasons, to enhance the emission of a quantum emitter that can be collected in the far-field, not only it is necessary to increase the Purcell factor, but the ratio between the radiative and non-radiative power must also be considered. This ratio is known as the radiation efficiency:

$$\epsilon_{\text{rad}} = \frac{P_{\text{rad}}}{P} = \frac{P_{\text{rad}}}{P_{\text{rad}} + P_{\text{nr}}}. \tag{12.11}$$

The efficiency of the emitter in the absence of the antenna is known as the intrinsic quantum yield. It is a property of the emitter and is given by:

$$\eta_i = \frac{P^0_{\text{rad}}}{P^0_{\text{rad}} + P^0_{\text{nr}}}. \tag{12.12}$$

Considering the intrinsic quantum yield, the radiation efficiency is given by:

$$\epsilon_{\text{rad}} = \frac{\frac{P_{\text{rad}}}{P^0_{\text{rad}}}}{\frac{P_{\text{rad}}}{P^0_{\text{rad}}} + \frac{P_{\text{antenna nr}}}{P^0_{\text{rad}}} + \frac{[1-\eta_i]}{\eta_i}}. \tag{12.13}$$

The antenna gives rise to an enhancement of LDOS at the emission wavelength, thus decreasing the radiative lifetime. While for inefficient emitters this may produce a relevant enhancement of quantum yield and of the radiative power density, for efficient emitters ($\eta_i = 1$), in the weak excitation regime, the antenna cannot further enhance the quantum yield and may even decrease

it by introducing some losses. Nevertheless, a high Purcell factor is still desired to accelerate the emission process. Moreover, for resonant pumping, the antenna can produce an excitation enhancement, generating an increase in the radiated power density [6].

To enhance the emission of the quantum emitter, both a large Purcell factor F_P and a large radiation efficiency ϵ_{rad} are required. For the case of emission through a single channel, it was demonstrated that the Purcell factor can be expressed as [4]:

$$F_P = \frac{3}{4\pi^2}\lambda^3 \frac{Q}{\tilde{V}}, \tag{12.14}$$

where Q corresponds to the quality factor, which measures the lifetime of a photon in the cavity in units of optical cycles, λ is the wavelength, and $\tilde{V}$ is the effective mode volume, which can be expressed in the low-loss approximation as [4]:

$$\tilde{V} = \frac{\int \epsilon(\mathbf{r})|\mathbf{E}(\mathbf{r})|^2 d\tilde{V}}{\max(\epsilon(\mathbf{r})|\mathbf{E}(\mathbf{r})|^2)}. \tag{12.15}$$

For the case of lossy/open systems, Eq. (12.15) is not valid. In fact, it was demonstrated that, for plasmonic nanocavities, the mode volume takes complex values [7,8]. In these cases, to evaluate $\tilde{V}$ the electromagnetic field must be expressed by a superposition of quasi-normal modes (QNMs) [9].

In order to attain large values of the Purcell factor or, equivalently, of the LDOS, it is required that the photonics systems are able to strongly concentrate the light both spatially and spectrally. This suggests that photonic systems with high Q-factor and small $\tilde{V}$ are necessary. To fulfill this objective, different configurations, including all-dielectric oligomers, all-dielectric nanoholes, cuboid arrays, and metasurfaces of broken symmetry dielectric resonators among others, have been proposed [10–14].

12.1.2 Photoluminescence emission enhancement

Photoluminescence (PL) emission of quantum emitters can be modified by coupling them to resonant optical nanostructures such as metasurfaces. Fluorescence is a particular form of PL process in which quantum emitters, such as molecules, quantum dots, etc., can be excited by absorbing a photon at a certain wavelength and later decay by spontaneously emitting a photon at usually a longer wavelength, or by non-radiative decay mechanisms, such as conversion of energy to phonons [15].

The fluorescence count rate of a single emitter such as a point electric dipole $\mathbf{p}_{\text{em}}$ located at the position $\mathbf{r}_{\text{em}}$ from a nanostructure can be defined by four factors as [16]:

$$I(\mathbf{r}_{\text{em}}, \mathbf{p}_{\text{em}}, \omega_{\text{exc}}, \omega_{\text{em}}) \propto \Gamma_{\text{exc}}(\mathbf{r}_{\text{em}}, \mathbf{p}_{\text{em}}, \omega_{\text{exc}}) \cdot \eta_{\text{QY}}(\mathbf{r}_{\text{em}}, \mathbf{p}_{\text{em}}, \omega_{\text{em}}) \cdot \eta_{\text{ext}}(\mathbf{r}_{em}, \mathbf{p}_{\text{em}}, \omega_{em}) \cdot \eta_{\text{coll}}(\mathbf{r}_{\text{em}}, \mathbf{p}_{\text{em}}, \omega_{\text{em}}). \tag{12.16}$$

The first term refers to the excitation rate, which can be enhanced by the nanostructure due to its capability to confine the excitation field. The excitation rate enhancement for $\mathbf{p}_{\text{em}}$ placed at $\mathbf{r}_{\text{em}}$ is:

$$\Gamma_{\text{exc}}(\mathbf{r}_{\text{em}}, \mathbf{p}_{\text{em}}, \omega_{\text{exc}}) / \Gamma^0_{\text{exc}} = |\mathbf{E}(\mathbf{r}_{\text{em}}, \mathbf{p}_{\text{em}}, \omega_{\text{exc}})|^2 / |\mathbf{E}_0|^2, \tag{12.17}$$

where Γ^0_{exc} is the excitation rate of the emitter in free space, $|\mathbf{E}_0|$ and ω_{exc} are the amplitude and frequency of the excitation field, respectively, and $\mathbf{E}(\mathbf{r}_{\text{em}}, \mathbf{p}_{\text{em}}, \omega_{\text{exc}})$ is the local electric field strength at the position $\mathbf{r}_{\text{em}}$. Therefore, a nanostructure with the proper geometry provides local field enhancement of the excitation pump intensity. This assumption only stands for the weak excitation regime, where the PL signal is proportional to the excitation pump power.

The intrinsic quantum yield of the emitter as a function of decay rates can be expressed as:

$$\eta^0_{\text{QY}} = \Gamma^0_{\text{rad}} / (\Gamma^0_{\text{rad}} + \Gamma^0_{\text{i}}). \tag{12.18}$$

Γ^0_{rad} is the radiative decay rate of the emitter where a photon at the Stokes shifted frequency ω_{em} will be emitted during the decay process, and Γ^0_{i} is the decay rate corresponding to the intra-molecular dissipation without the emission of a photon. After coupling to the nanostructure, based on Fermi's golden rule (Eq. (12.1)), the decay rate of the emitter (Γ), which includes both radiative Γ_{rad} and non-radiative Γ_{nr} decay rates, is modified. The quantum yield in the presence of the nanostructure η_{QY}, the second factor in Eq. (12.16), can be expressed as:

$$\eta_{\text{QY}} = \Gamma_{\text{rad}} / (\Gamma_{\text{rad}} + \Gamma_{\text{nr}} + \Gamma^0_{\text{i}}). \tag{12.19}$$

The third factor in Eq. (12.16) is the extraction efficiency. It takes into account the fraction of the emitted photons that can escape the nanostructure and couple to free space [17]. $\eta_{\text{ext}}(\mathbf{r}_{\text{em}}, \mathbf{p}_{\text{em}}, \omega_{\text{em}})$ can be defined as the ratio of the power radiated by the emitter to free space $P^{\text{out}}_{\text{rad}}$ to the total power radiated

by the emitter:

$$\eta_{\text{ext}}(\mathbf{r}_{\text{em}}, \mathbf{p}_{\text{em}}, \omega_{\text{em}}) = P_{\text{rad}}^{\text{out}}/P_{\text{rad}}, \tag{12.20}$$

where $P_{\text{rad}}^{\text{out}}$ can be calculated as:

$$P_{\text{rad}}^{\text{out}} = \iint \mathbf{S}(\mathbf{r}, \omega_{\text{em}}) \cdot d\mathbf{A}, \tag{12.21}$$

which indicates the integration over the flux of the Poynting vector $\mathbf{S}(\mathbf{r}, \omega_{\text{em}})$ through a spherical surface surrounding the nanostructure. P_{rad} is the sum of $P_{\text{rad}}^{\text{out}}$ and other dark electromagnetic modes, such as guided modes, which can be trapped in the nanostructure via total internal reflection and cannot be extracted.

Another significant impact of a properly designed nanostructure on the emission properties of nearby emitters is to efficiently tailor their emission directionality. The measured PL signal from the emitters depends on the collection optics used in the experiment. The last factor in Eq. (12.16) refers to collection efficiency, which is the ratio of power collected by collection optics (CO) and the total power radiated in free space $P_{\text{rad}}^{\text{out}}$:

$$\eta_{\text{coll}} = \frac{1}{P_{\text{rad}}^{\text{out}}} \iint_{\text{CO}} P(\theta, \phi) \sin\theta d\phi d\theta, \tag{12.22}$$

where $P(\theta, \phi)$ (power per steradian) is the angular power density radiated in free space along the direction of the polar angle θ and azimuthal angle ϕ. $P(\theta, \phi)$ can be calculated as:

$$P(\theta, \phi) = \lim_{r/\lambda \to \infty} r^2 \frac{\mathbf{r}}{r} \cdot \mathbf{S}(\mathbf{r}, \omega_{em}), \tag{12.23}$$

where $\mathbf{S}(\mathbf{r}, \omega_{em})$ is the time-averaged Poynting vector indicating the directional flux, $\mathbf{r} = (r\sin\theta\cos\phi, r\sin\theta\sin\phi, r\cos\theta)$ and $\lambda = 2\pi c/\omega_{\text{em}}$.

In a typical experiment including an emissive layer coupled to a nanostructure and in a weak coupling regime, the PL signal from one individual emitter adds incoherently to the overall PL of the system since the ensemble of the arbitrarily oriented emitters is distributed over the whole emissive layer. Therefore, the behavior of an individual emitter is independent of others and strongly dependent on its own position and orientation.

12.1.3 Strong coupling regime of emitters and optical modes in nanostructures

We may also consider the coupling of a quantum emitter with resonant modes of nanostructures in the view of cavity quantum

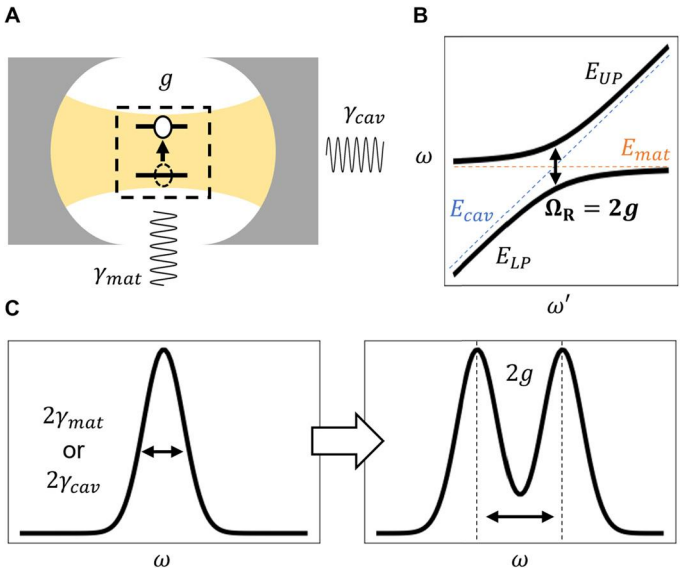

Figure 12.1. Schematic description of strong coupling phenomena. (A) A two-level system coupled to a cavity. The cavity-material coupling rate g should be larger than both cavity and material losses γ_{cav} and γ_{mat} to achieve strong coupling. (B) Dispersion curve of a strongly coupled system, showing the characteristic anti-crossing behavior. One generally obtains spectra of the cavity-material system (ω), while tuning the cavity resonances (ω') via angle of incidence, change in geometric parameters, etc., to obtain the dispersion curve. (C) Spectra of individual cavity or material (left) and that of strongly coupled system (right). Unlike in Fano-type resonances, strongly coupled systems show comparable or larger polariton bandwidths than those of the individual resonances.

electrodynamics, such that the transition dipole of the emitter undergoes incoherent field damping, incoherent interaction with the continuum of vacuum modes, and/or coherent interaction with the cavity field. The aforementioned Purcell effect is essentially an enhancement of the second interaction, which means that interaction of the emitter is dominantly incoherent and mostly affected by losses and field damping. Therefore, this regime is often referred to as a weak coupling regime, since the absence of the third interaction implies that coupling between the emitter and the resonant nanostructure is not strong enough (see Fig. 12.1A) [18].

In the strong coupling regime, the coherent interaction between the emitter and the cavity field becomes the dominant mechanism. This can be achieved when energy exchange rate between an optical cavity mode and a material excitation exceeds losses in the system. In this regime, vacuum Rabi oscillation, an oscillatory exchange of energy quanta between matter and light,

takes place at a rate determined by the coupling strength g, creating half/matter-half/light quasiparticles, called polaritons, which now become new eigenstates of the system. Using the rotating wave approximation (RWA), we can express the system as two coupled oscillators with a Hamiltonian:

$$\begin{pmatrix} E_{mat} + i\gamma_{mat} & g \\ g & E_{cav} + i\gamma_{cav} \end{pmatrix} \begin{pmatrix} \alpha \\ \beta \end{pmatrix} = E \begin{pmatrix} \alpha \\ \beta \end{pmatrix}, \tag{12.24}$$

which in turn leads to eigenvalues of:

$$E_{LP,UP} = \frac{1}{2}\{E_{mat} + E_{cav} + i(\gamma_{mat} + \gamma_{cav}) \pm \sqrt{4g^2 + [E_{mat} - E_{cav} + i(\gamma_{cav} - \gamma_{mat})]^2}\}. \tag{12.25}$$

Here, $E_{LP,UP}$ is the eigenenergy of lower or upper polariton (LP or UP), E_{mat} (E_{cav}) is the resonant energy of the material (cavity), and γ_{mat} (γ_{cav}) is the decay rate of the material transition (cavity photon). The eigenvectors are expressed in α, β which denote material and cavity fractions for each polariton state. Note that g should be larger than $|\gamma_{cav} + \gamma_{mat}|/2$ for the strong coupling to be observed, that is, for the splitting between the new eigenenergies to be larger than the linewidth of each eigenenergy. In a nearly ideal case of $g \gg \gamma_{cav} \simeq \gamma_{mat}$, separation of LP and UP energies minimizes to $E_{UP} - E_{LP} \simeq 2g$ when cavity and material resonances overlap ($E_{mat} = E_{cav}$). This is called Rabi splitting and may be determined from the separation between the two anti-crossing dispersion curves of the polaritonic states (see Fig. 12.1B,C).

Reaching the strong coupling regime reduces to a problem of minimizing the cavity loss γ_{cav} and/or increasing the cavity-material coupling g. Here, the strong coupling figure of merit can be expressed as $g/\gamma_{cav} \sim \sqrt{N}\mu_e \times Q/\sqrt{\tilde{V}}$, where N and μ_e are number and strength of transition dipoles, Q is the quality factor of the resonator, and $\tilde{V}$ is the mode volume [19]. Strong coupling in metallic structures utilize small $\tilde{V}$ from plasmonic nanoconfinement of electromagnetic field. In dielectric structures, $\tilde{V}$ is generally limited to $\sim \lambda/2n^3$ where n is refractive index of the dielectric; therefore, a general strategy is to increase the Q of the resonance [20–22]. Another viable approach is to increase the oscillator strength $\sqrt{N}\mu_e$, which corresponds to a collective excitation or strong excitons as in J-aggregates [23–26] and intersubband transitions [27–30]. Transition metal dichalcogenides (TMDC) are also an emerging material platform for strong light-matter coupling, as will be discussed below. Also, recent studies suggest that if the whole cavity is made of an active material, g may reach an ultimate

value regardless of $\tilde{V}$ and strong coupling may be achieved in dielectric structures without need for either high Q or ultrasmall $\tilde{V}$ [31].

12.2 Configurations for enhancing the emission of quantum emitters

Traditionally, optical cavities have been introduced to enhance the emission of quantum emitters. Cavities made of dielectric materials enable very large Q-factor values. Over the last years, Si cavities operating in the telecom spectral range have demonstrated Q-factors larger than 10^4 using lithography-defined 1D or 2D photonic crystals [32,33]. However, the mode volume is $\tilde{V} \approx 1$, expressed in units of wavelength cubed in the medium of interest. An additional limitation of optical cavities is their narrow linewidth [1]. An alternative to optical cavities is metallic nanoparticles (NPs). When the incident radiation illuminates a metallic NP, its free electrons start oscillating at the same frequency as the incident radiation, generating localized surface plasmons (LSPs). At resonance, strong electromagnetic energy concentrations are observed in the surroundings of the NP. By using isolated plasmonic NPs, or aggregates thereof, subwavelength confinement of the electromagnetic radiation is observed; for example, photoluminescent enhancement of quantum emitters has been experimentally explored by using isolated and dimers of metallic NPs [34,35].

To achieve an extremely small $\tilde{V}$, some novel configurations have been proposed, consisting of metallic NPs separated from metallic substrates by gaps as small as 1 nm. These tiny gaps can be achieved through a thin organic or semiconductor spacer layer. In these geometries, known as nanoparticle-on-a-mirror (NPoM) configurations, the localized surface plasmons in the isolated metallic NPs couple to image charges induced in the metallic film, thus giving rise to a coupled plasmonic mode. This mode is tightly localized within the gap between the NP and the film, confining optical fields to sub-1-nm^3 picocavities [36–39].

In addition to enhancing the emission, it is also desirable for the antenna to be able to control the direction of the scattered radiation, improving the collection efficiency of the light. However, accomplishing this with metallic nanostructures is by no means straightforward. For particles that are small compared to the wavelength of the incident radiation, the quasi-static approximation holds and the scattering pattern of the particle exhibits a doughnut-like shape, typical for the radiation pattern of elec-

tric or magnetic dipoles. Larger particles are required to attain directional properties due to the excitation of higher-multipolar orders. To enhance the directionality effects, plasmonic nanoantenna arrays, such as Yagi-Uda, were used [40]. One of the largest limitations of the latter is their low Q-values ($Q \approx 3 - 10$) due to the large Ohmic losses [1], which lead to low quantum yield values. Hybrid nanostructures like bulls-eye shaped metal-dielectric nano-antennas, which contain a single nanocrystal QD at their center, have been experimentally demonstrated to be efficient single-photon sources due to emission enhancement into a very low numerical aperture [41]. Another possibility to enhance the radiation of a quantum emitter and control its directionality is to use high refractive index (HRI) dielectric NPs, as we will explain in this chapter.

12.2.1 High refractive index dielectric nanostructures

All-dielectric resonant nanostructures [42–44] offer vast opportunities for manipulation of light-matter interaction in the sub-wavelength range. Strong electromagnetic field localization in such structures, can effectively boost the light emission process as well as other effects of light-matter interaction. High radiation efficiency, low absorption losses, and the potential of directional far-field coupling are some of the advantages, which make dielectric nanostructures an adequate replacement for their plasmonic counterparts.

High refractive index (HRI) dielectric nanostructures can support multipolar Mie-type resonances. Mie theory [45] was originally formulated as the solution of the scattering problem in a spherical-shaped particle and later generalized for non-spherical particles with a size comparable to the wavelength. The resonant properties of the nanostructure can be controlled by both size and shape of the NPs.

Magnetic dipole (MD) modes, with similar polarizabilities to the electric dipole (ED) modes, can arise in a dielectric NP if its geometrical dimension is comparable to the wavelength inside the NP, i.e. $\lambda/n \approx 2a$. a and n are the radius and refractive index of the corresponding NP, respectively, and λ is the wavelength in free space. Excitation of MD modes in dielectric NPs stems from the coupling of the incident light to the modes corresponding to circular displacement current inside the NP. Due to the sub-wavelength size of the NP, a high refractive index material is required. Furthermore, for larger NP sizes in comparison to the excitation wavelength, higher-order Mie-modes, such as elec-

tric quadrupole (EQ), magnetic quadrupole (MQ), etc., can also be supported.

Besides Mie modes of a single NP, other physical mechanisms arising from the energy exchange in the NP arrangements, can contribute to the field enhancement by HRI dielectric resonant nanostructures. For instance, in a proper arrangement of NPs, Fano resonances can be excited, which originate from interference between different individual localized and collective modes. As it was demonstrated in [10], silicon (Si) oligomers (Fig. 12.2A) exhibit strong Fano resonances resulting from the interference of the resonant excitation of the central NP and off-resonance outer NPs. Other geometries supporting Fano resonances, such as an asymmetric dielectric wire pair [46], Si nanoholes cuboid arrays [11], and a dielectric metasurface composed of broken symmetry cubic resonators [12], were also investigated (see Fig. 12.2B,C,D, respectively).

The electromagnetic near-field of photonic nanostructures can enhance the decay rate of both ED and MD transitions of quantum emitters through the Purcell effect, introduced in Section 12.1.1. As we described, a large Purcell factor requires a photonic system with high Q-factor resonance characteristics as well as small mode volume $\tilde{V}$. The latter can be realized in a configuration including two NPs next to each other forming a gap, which can be considered as an electromagnetic field hot-spot. In this case, by placing the electric or magnetic dipolar emitters in the gap, their spontaneous emission rates and their quantum efficiencies can be modified. This has been theoretically studied in [47] and experimentally demonstrated in [48] by means of single dimer-like Si nanoantennas.

Among the different mechanisms leading to high Q-factor resonances, one of the most promising corresponds to the excitation of bound states in the continuum (BICs) [13,49]. BICs emerged originally as a quantum mechanical concept, but later were explained as a result of vanishing coupling between the eigenmodes of the nanostructures and the free space electromagnetic radiation. BICs can be categorized as either symmetry-protected BICs, corresponding to the modes whose in-plane mirror symmetry is mismatched with the symmetry of the incident waves, and consequently, the coupling is prohibited, or accidental BICs, where the coupling to radiative waves vanishes accidentally via tuning the parameters of the system continuously. A true BIC is characterized by an infinite value of the Q factor and vanishing resonance width, and only exists in ideal lossless infinite structures [13]. However, high Q quasi-BICs with a finite value of Q factor and resonance linewidth, have been realized experimentally in

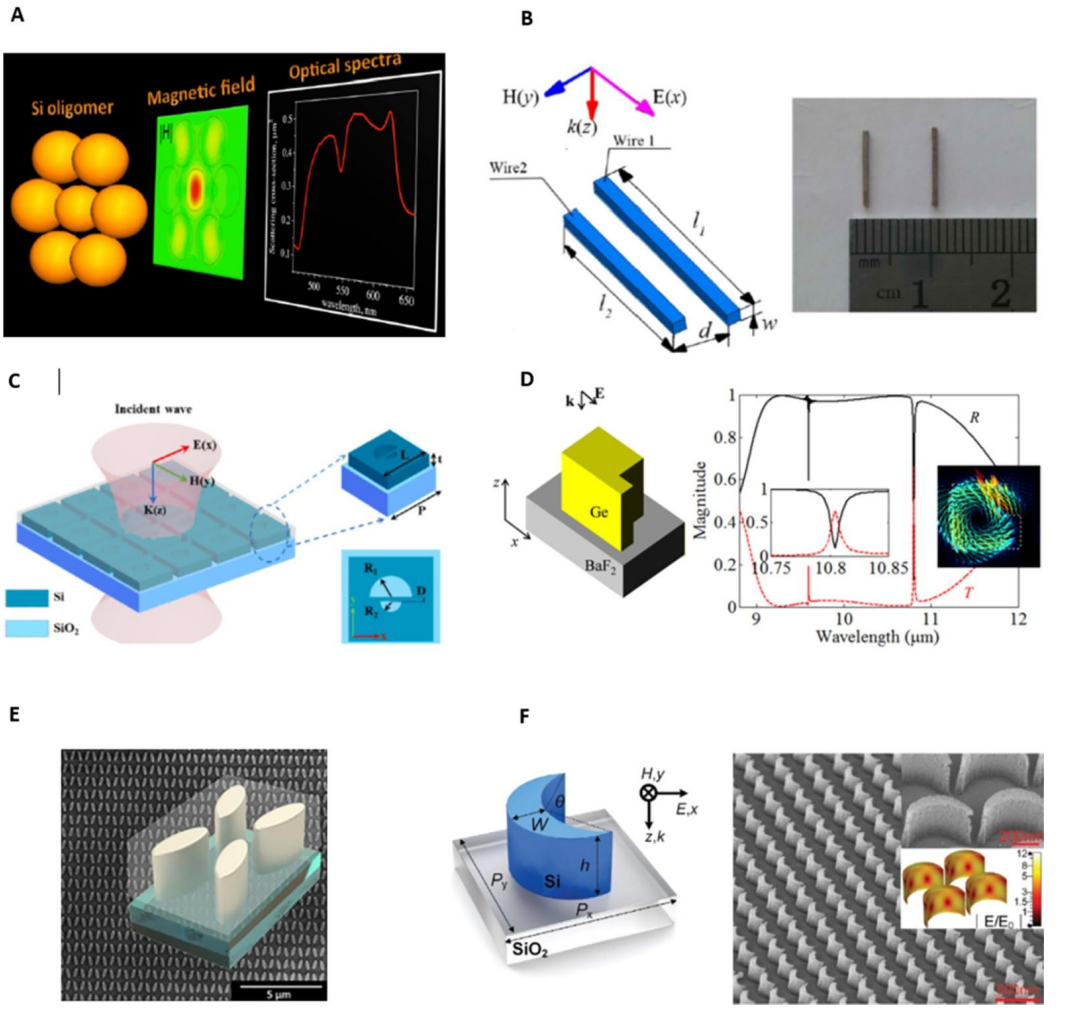

Figure 12.2. Various HRI dielectric nanostructures supporting Fano (A-D) and BIC (E,F) resonances. (A) Scheme of a Si heptamer structure (left), magnetic near-field distribution in the heptamer structure, which is concentrated inside the central particle (middle), and scattering cross-section of the heptamer (right). Reproduced with permission [10]. Copyright 2012, American Chemical Society. (B) Schematic view (left) and photograph (right) of an asymmetric dielectric wire pair. Reproduced with permission [46]. Copyright 2014, American Institute of Physics. (C) Scheme of a metasurface composed of Si cuboids etched with two semicircular holes, on SiO_2 substrate. Reproduced with permission [11]. Copyright 2021, Elsevier. (D) Schematic of one unit cell of the broken symmetry metasurface supporting Fano resonances (left), and numerically calculated reflection (R, solid black) and transmission (T, dashed red) spectra of the Fano metasurface showing high Q-factor resonances (right). The inset on the right shows the electric field in the x-y resonator mid-plane presenting a circular pattern. Reproduced with permission [12]. Copyright 2016, American Chemical Society. (E) Scanning electron micrograph (SEM) of a zigzag array of Si elliptical cylinders. The inset shows the scheme of one unit-cell covered with a PMMA layer. Reproduced with permission [50]. Copyright 2018, American Chemical Society. (F) Sketch of the unit-cell of a Si metasurface composed of crescent meta-atoms on a fused silica (SiO_2) substrate (left), SEM image of the fabricated sample with an inset representing the near-field distribution of the meta-atoms (right) [51]. Copyright 2021, John Wiley and Sons.

optical structures such as photonic crystals, optical cavities, metamaterials, and metasurfaces. In principle, through slightly breaking the in-plane symmetry of the nanostructure, a weak coupling between the bright and dark modes can occur, which leads to the emergence of sharp high Q-factor resonances, since the radiation loss is suppressed and energy is stored inside the nanostructure [14]. Various geometries supporting quasi-BIC have been investigated (see Fig. 12.2E,F) such as an array of tilted elliptical cylinders [50] and a metasurface composed of crescent meta-atoms [51]. All such structures can be implemented as highly efficient platforms for PL emission enhancement of quantum emitters coupled to them.

In addition to spontaneous emission enhancement of the quantum emitters, all-dielectric nanostructures can offer robust control over the directionality of the emission of the nearby emitters due to the presence of both electric and magnetic Mie-type modes, and the constructive and destructive interference of these modes along different directions of the far-field radiation propagation [52]. Furthermore, the presence of higher-order multipolar modes adds new possibilities for directional scattering. In fact, far-field emission patterns of Mie modes become narrower for higher multipolar orders, observing directional scattering into a reduced solid angle [53,54]. The ability to control the emission directionality allows to optimize the HRI dielectric nanostructures for particular collection optics to enhance the collection efficiency and consequently the signal brightness, as described in Eq. (12.22).

12.2.1.1 Light emitting all-dielectric nanostructures

In a semiconductor quantum dot (QD), spontaneous emission originates from the electronic interband transition of the material. The emission wavelength can be engineered over a broad spectral range from UV to VIS and near-infrared (NIR). Strong PL emission enhancement of QDs can be achieved by incorporating them into Mie-resonant nanostructures. Yuan et al. [55] demonstrated three-orders of magnitude PL enhancement for a structure consisting of a periodic lattice of asymmetric air holes in a silicon-on-insulator (SOI) slab embedded with four layers of self-assembled Ge QDs. A Q-factor of 10^{11} was reported. Spectral and directional control of spontaneous emission from InAs QDs embedded into GaAs metasurfaces was investigated in reference [56]. Liu et al. [14] observed a brightness enhancement of up to two orders of magnitude in the self-assembled InAs QDs embedded in a broken-symmetry GaAs metasurface supporting high Q-factor Fano resonances. They also showed that the directionality of the emission pattern can be engineered for a particular emission wavelength defined by the meta-

surface design (see Fig. 12.3A-C). An active toroidal metasurface composed of Si split nanodisk arrays with embedded Ge QDs was introduced in [57]. Over two orders of magnitude PL enhancement was reported compared to the unstructured area, resulting from near- and far-field characteristics of the toroidal modes.

Atomically thin transition metal dichalcogenides (TMDCs) are another fascinating class of emissive materials with attractive optoelectronic properties, such as direct bandgap in VIS and NIR spectral range that results in near-unity quantum yield for their PL emission [42,58]. In addition, due to their two-dimensional (2D) nature, excitons with high binding energy can be excited, which can strongly interact with light thanks to their direct bandgap. In [59], an actively tunable and atomically thin zone plate lens, which is carved directly out of monolayer tungsten disulfide (WS_2), with strong excitonic resonance in visible spectral range was demonstrated. In this case, the design of the structure relies on properly engineering and modifying the materials' resonance.

Optical all-dielectric metasurfaces are convenient platforms for tailoring the PL emission and directionality of 2D mono or multilayered semiconductors, including TMDCs, since they share the same planar nature. Integration of monolayers of molybdenum disulfide (MoS_2) with Mie-resonant metasurfaces was experimentally investigated by Bucher et al. [60], and spectral and directional reshaping of the emission, as well as strong PL enhancement, were observed. Muhammad et al. [61] exploited a quasi-BIC in a symmetry-broken MoS_2 based Mie nanoresonator, and significant directional emission was reported. In [62], a single-layer of tungsten diselenide (WSe_2) coupled to a titanium dioxide (TiO_2) dielectric metasurface supporting toroidal resonances was presented, and a robust exciton emission enhancement by more than order of magnitude, as well as selective enhancement of Purcell effect, were reported (see Fig. 12.3D,E).

In the last decades, halide perovskites have emerged as one of the most promising materials in realizing light-emitting devices [42,58]. Similar to TMDCs, the compositions of halide perovskite offer excitonic states at room temperature with large binding energy and PL emission with high quantum yield. Makarov et al. [63] presented metasurfaces based on nanoimprinted perovskite films optimized by alloying the organic cation part of perovskites. They observed up to 70-fold enhancement in both linear and nonlinear regimes employing unique optical properties of both Mie-resonant metasurfaces and halide perovskites (see Fig. 12.3F).

The study of light-matter interaction has been mainly focused on the electric dipolar nature of light, since the interaction of the electric field with ED transitions of the quantum emitters is typ-

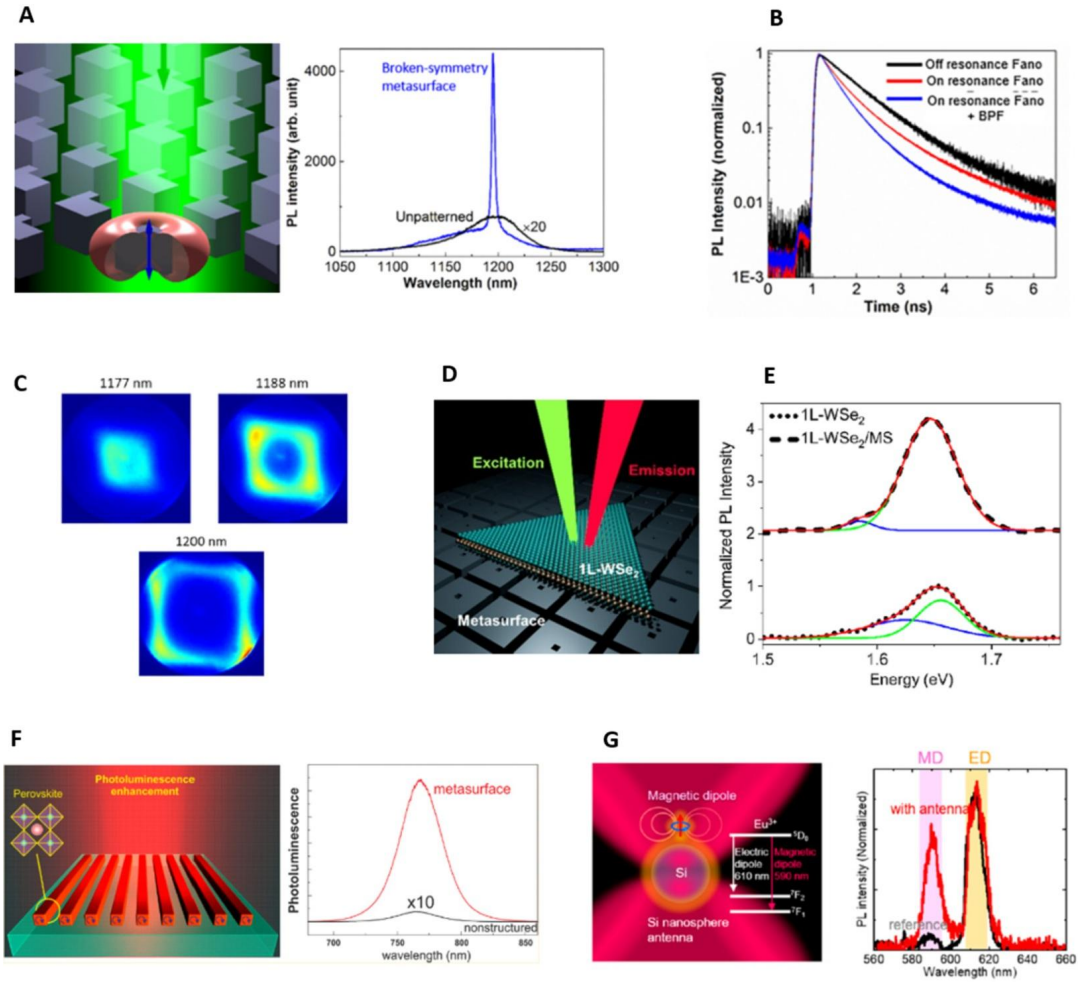

Figure 12.3. (A) Scheme of a symmetry-broken semiconductor metasurface (left), measured room-temperature PL spectra for the symmetry-broken metasurface embedded with InAs QDs (right, blue) and for an unstructured QD layer as reference (right, black). (B) Measured time-resolved PL spectra for the sample represented in (A). Blue, red, and black curves show the measurements for the full spectral range, in presence of a bandpass filter, and for the unstructured area, respectively. (C) Measured back-focal plane images of emission from the sample represented in (A) for different wavelengths. (A-C) reproduced with permission [14]. Copyright 2018, American Chemical Society. (D) Scheme of 1L-WS_2 integrated with a TiO_2 cuboid metasurface. (E) Measured PL spectra for the sample represented in (D) on bare 1L-WS_2 (bottom) and the 1L-WS_2 on the metasurface (top). Red solid lines are fitted PL spectra using two Gaussian functions (blue and green solid lines). The blue and green peaks belong to trion and neutral exciton emission, respectively. (D,E) reproduced with permission [62]. Copyright 2021, American Chemical Society. (F) Scheme of a halide perovskite metasurface (left), measured PL spectra (right) for the metasurface (red), and an unstructured perovskite film (black). Reproduced with permission [63]. Copyright 2017, American Chemical Society. (G) Scheme of MD emission of Eu^{3+} coupled to a Si nanosphere (left). Measured PL spectra of Eu^{3+} (right) in the presence (red) and absence (black) of the Si nanosphere. Reproduced with permission [68]. Copyright 2021, American Chemical Society.

ically up to 4 orders of magnitude stronger than the interaction of the magnetic field with MD transitions. However, trivalent lanthanide ions such as Eu^{3+} and Er^{3+} offer a robust MD-dominated transition as a consequence of selection rule forbidden ED transition [64,65]. Thus, due to a strong optical magnetic response, all-dielectric nanostructures are an exquisite candidate for tailoring the fluorescence emission properties of MD transition in trivalent lanthanide ions. This uncovers new prospects in nanophotonics and optoelectronics, exploiting the magnetic nature of light.

Sanz-Paz et al. [66] demonstrated selective enhancement of magnetic emission from colloidal NPs doped with Eu^{3+} via a Si nanoantenna attached to a tip of a scanning probe microscope. Vaskin et al. [67] investigated Si metasurfaces coated with a layer of Eu^{3+} doped polymer, and reported a value of 1.12 for the intensity ratio of the MD to ED transition of Eu^{3+} emitters. In a recent work by Sugimuto et al. [68] large magnetic Purcell enhancement was reported in a composite system including Eu^{3+} emitters integrated with a Si nanosphere (see Fig. 12.3G). In this work, up to 7-fold enhanced branching ratio between the MD and ED transitions was presented.

12.2.1.2 All-dielectric polaritonic nanostructures

The first experimental observation of strong coupling regime was made by Haroche and co-workers in 1983, where sodium atoms coupled to a high-Q microwave cavity exhibited Rabi oscillation in Rydberg states [20]. In 1992, Weisbuch et al. reported the first observation of exciton-polariton in a quantum well optical microcavity and brought the strong coupling phenomena from atomic physics to solid-state physics [21]. Here, the authors placed the quantum well layer in a distributed Bragg reflector (DBR)-based cavity and observed mode splitting in the reflection spectrum. Due to its high Q and lack of need for complex lithographic procedures, the DBR-based microcavity has become the most popular geometry for studying strong coupling in an all-dielectric environment. The first observation of strong coupling in 2D-TMDC in all-dielectric environment was also made in this configuration, where chemical vapor deposition-grown monolayer-MoS_2 was embedded in a DBR-based cavity [22].

Attempts to utilize dielectric nanostructures for strong coupling have been made only recently. In 2018, Tserkezis et al. theoretically analyzed strong coupling of excitons and Mie resonances in an isolated core-shell NP, where excitonic material comprised the shell [69]. Lepeshov et al. also theoretically discussed the possibility of strong coupling in a single Si NP, covered with a monolayer WS_2 [70]. In both studies, strong coupling was observed

when excitonic resonance of the shell material spectrally overlapped with magnetic dipole resonance of the NP, which was attributed to the stronger electric field overlap compared to the case of electric dipole resonance. While these studies opened the possibility of strongly coupling Mie metasurfaces with low-dimensional materials such as 2D-TMDC, limited light-matter coupling arising from small volume of the active material has hampered experimental observation of such systems.

Instead, researchers have turned to an alternate method of building dielectric metasurfaces with active material itself. This enables an ultimate overlap of the electromagnetic mode and the excitonic system and dramatically boosts g. In 2019, Verre et al. focused on the fact that TMDCs have large in-plane permittivity (16) and experimentally observed Mie resonances in nanodisks made of multilayer WS_2 [71]. When one of the dark modes spectrally overlaps with the exciton resonance of WS_2, characteristic Rabi splitting of 190 meV could be observed. This value is much larger than that observed in a 2D-TMDC strongly coupled to a DBR-based microcavity (40 meV) and is attributed to a better mode-material overlap and larger number of transition dipoles (see Fig. 12.4A).

III–V semiconductors are also good building blocks for polaritonic dielectric metasurfaces as they have high refractive indices, low losses below bandgap, and advantage of seamless integration with epitaxial quantum dots or quantum wells. Sarma et al. have fabricated metasurfaces with InGaAs/InAlAs multi-quantum wells (MQW) to couple Mie resonances with intersubband transitions (IST) of the MQW [28]. The authors observe strong coupling of IST to both in-plane magnetic dipole and out-of-plane electric dipole resonances, as IST of the MQW have their transition dipole moment aligned perpendicular to the surface normal. The Rabi splitting is much more pronounced for magnetic dipole resonance than for electric dipole resonance due to a larger field enhancement (see Fig. 12.4B).

Organic-inorganic hybrid perovskites are also an attractive option due to their large exciton binding energy and their ease of fabrication via solution-based processes. Especially, two-dimensional (2D) perovskites can form self-assembled multi-quantum well structures, leading to strong oscillator strengths of excitons suitable for strong coupling. In two independent studies by Kim et al. and Dang et al., rectangular arrays of 2D perovskite disks support a leaky BIC mode that strongly couples to the exciton resonance and exhibit Rabi splitting of 200 meV [72,73]. Photoluminescence pattern in the Fourier plane reveals topological signatures such as polarization vortices. Also, when the unit cell pattern

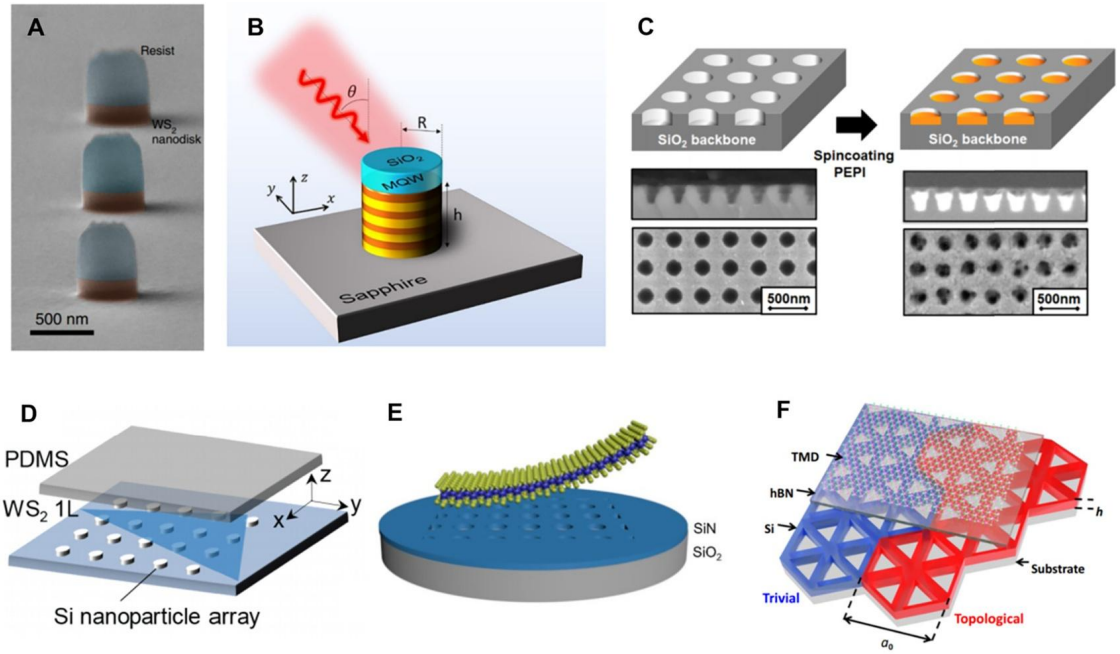

Figure 12.4. Various all-dielectric polaritonic metasurfaces. (A) Nanodisks made of multilayer TMDC flakes, exhibiting strong coupling at their anapole resonances. Reprinted with permission from Springer Nature: Springer Nature, Nature Nanotechnology, Copyright (2019). [71] (B) Mie resonators made with quantum wells, coupling intersubband transitions with an out-of-plane magnetic dipole mode. Reproduced with permission. Copyright 2021, American Chemical Society. [28] (C) Nanodisk array of two-dimensional perovskites, fabricated by spincoating the perovskites onto a SiO_2 backbone. Reproduced with permission. Copyright 2020, American Chemical Society. [72] (D-F) Polaritonic metasurfaces with 1L-TMDC strongly coupled to (D) lattice-Mie resonances of Si NP array, [74] (E) leaky modes of SiN hole array, [75] and (F) edge modes of a topological metasurface [76]. Reproduced with permission from: American Chemical Society, Copyright 2020 (74), American Chemical Society, Copyright 2020 (75), Springer Nature: Springer Nature, Nature Communications, Copyright (2021) (76).

is changed to a symmetry-broken triangle, polaritonic circular-polarized eigenstates are formed and an intense PL emission with very high degree of circular polarization (0.835) is obtained (see Fig. 12.4C).

Another possibility that is actively being explored is a dielectric metasurface integrated with 2D-TMDC placed on top. While there are many different configurations that have led to enhancement of photoluminescence, modulation of exciton dynamics and annihilation, etc., only a few among them have successfully observed the formation of polaritonic branches. So far, only guided modes or leaky modes were successfully able to strongly couple to the excitons in 2D-TMDC. Wang et al. designed Si NP arrays that exhibit Mie-surface lattice resonances (Mie-SLR) and coupled it

with a 2D-TMDC (see Fig. 12.4D) [74]. While ordinary Mie resonances incorporate electromagnetic field enhancement within the resonator, Mie-SLR show inter-resonator field enhancement, exhibiting collective nature of the resonance. Among different types of Mie-SLR, only the one with dominant in-plane electric field enhancement exhibits strong coupling (with a Rabi splitting of 32 meV). Chen et al. also observed strong coupling in 2D-TMDC integrated onto an array of holes in SiN film supporting guided mode resonance (see Fig. 12.4E) [75]. As well as a Rabi splitting of 18 meV, the polaritonic metasurface shows strongly modified far-field emission pattern, which the authors attribute to the diffraction effect of the metasurface. Li et al. demonstrated that excitons in 2D-TMDC can also strongly couple to edge states in a topological photonic metasurface (see Fig. 12.4F) [76]. Photonic edge states transform to polaritonic edge states in $MoSe_2$-metasurface heterostructure and exhibit Rabi splitting of 27.3 meV. The hybrid metasurface also retains the one-way spin-polarized character of the topological edge state, which manifests as asymmetric differential real-space images of the domain wall upon excitation with laser pulses of the opposite helicity.

As of 2022, the study of polaritons in dielectric metasurfaces is still in its infancy, and there are only limited number of reported cases of polaritonic metasurfaces in practical applications. One of the few cases is nonlinear polaritonic metasurfaces. Since metasurfaces are a good testbed for nonlinear optical processes due to alleviation of phase matching requirements, strong coupling and nonlinear metasurfaces can become good partners. For instance, a record-high second harmonic conversion efficiency for nonlinear dielectric metasurfaces is achieved when intersubband transition of multiple quantum wells is strongly coupled to the Mie resonance. Sarma et al. reported second-harmonic power conversion of 0.5 mW/W^2 with an efficiency of 0.015% [77]. This is more than threefold enhancement compared to the previously reported maximum efficiency, where quasi-BIC modes with ultra-high Q-factors were utilized. More impressively, this conversion efficiency is achieved with pump intensity of 11 kW/cm^2, which is three orders of magnitude lower than in the previous studies. It should also be noted that intensity and direction of the nonlinear emission from intersubband transitions can be dynamically controlled by a bias voltage, which incorporates quantum-confined Stark effect [78].

Among many other possible future applications, polariton lasers combined with dielectric metasurfaces are expected to be especially useful in many optoelectronic devices. As exciton-polaritons are bosonic quasiparticles, they also show Bose-Ein-

stein condensate (BEC)-like transition behavior [79]. Unlike a conventional BEC, however, the polariton condensate is dynamic, that is, not in thermal equilibrium with the cavity, and the transition is accompanied by emission of coherent light, which is referred to as *polariton lasing*. Such polariton lasing is "spontaneous" and occurs at orders of magnitude lower exciton densities compared to classical lasing, as it does not require population inversion. For instance, in a quantum well microcavity, threshold exciton density for polariton lasing was reported to be 3×10^9 cm^{-2}, being 2 orders of magnitude smaller than the density required for population inversion at 15 meV above the bandgap [79]. As well-designed dielectric metasurfaces can tilt, focus, or beam spontaneous emission, a similar approach applied to polaritonic dielectric metasurfaces may enable ultralow-threshold compact lasers with great controllability in emission direction.

Also, a new regime can be reached when the coupling strength g becomes comparable to the resonant energy of the material or the cavity, E_{mat} or E_{cav} ($\eta = g/E_{mat} > 0.1$) [80]. This regime is called ultrastrong coupling, and as the definition does not include the loss of the system, it is fundamentally different from a strong coupling with a larger g. This difference is due to non-negligible contribution of counter-rotating terms in the quantum Rabi Hamiltonian. Such inclusion of the new Hamiltonian terms enables deterministic nonlinear optics, where, for instance, perfect conversion efficiency can be reached with a very small number of photons. Various quantum phenomena, such as Purcell effect and electromagnetically induced transparency, may also change drastically and enable new applications. Also, as coherent exchange of energy between light and matter may be considered analogous to quantum gates, ultrastrong-coupled systems can be especially useful for quantum information processing applications. As of 2022, ultrastrong coupling is realized in a very limited set of material systems and mostly with metallic structures such as NPoM, split ring resonators and mirror-based cavities [81–84]. When combined with the versatility that dielectric metasurfaces can provide, ultrastrong coupling can become a central building block for advanced optoelectronic and quantum-optical devices.

12.2.2 Hybrid metal-dielectric nanostructures

As previously introduced, both metallic and dielectric nanostructures have advantages and disadvantages as far as the enhancement of radiation of quantum emitters is concerned. Such comparative analysis should take into account not only the emission enhancement, but also the quantum yield and the extraction

efficiency (i.e., the light that can be collected by the objective of a microscope with a certain numerical aperture). Hybrid metal-dielectric configurations can combine the best of both metallic and dielectric structures. They can incorporate both the strong enhancement of the electromagnetic radiation in the surroundings of the metallic structures (small $\tilde{V}$) and the directionality properties and low-losses (high Q-factor) of HRI dielectric structures. It has been demonstrated that the strong confinement of electromagnetic radiation in small volumes can enhance the spontaneous emission of a quantum emitter, and the HRI dielectric structure can redirect the emitted light into the desired direction without introducing notable ohmic losses. Different hybrid configurations have been proposed, including metal-dielectric nanoantennas, HRI dielectric NPs on metallic substrates, and hybrid photonic-plasmonic cavities.

In the case of hybrid metal-dielectric nanoantennas, in [85] a Au nanorod dimer was used to increase the decay rate of an emitter. The metallic dimer was separated from a Si cylinder by means of a thin dielectric (SiO_2) spacer. The Si NP was responsible for the directionality effects of the emitted radiation. Furthermore, a high radiation efficiency was reported ($> 70\%$) in a broadband spectral range. In [86], a similar effect was demonstrated through a Au nanosphere located on a Si truncated cone. For this geometry, ultrahigh Purcell factors were observed ($\approx 10^{3.5}$) and unidirectional emission patterns were also attained.

Hybrid metal-dielectric dimers were also proposed with the same aim. A 40% fluorescence excitation rate higher than that of the pure dielectric dimer, and a 30% quantum yield higher than that of the metallic dimer were achieved for a dimer composed by two nanospheres, one dielectric ($\epsilon = 25$) and the other one made of Ag [87]. As a consequence of the larger size of the dielectric NP with respect to the metallic one, most of the radiation was scattered toward the dielectric NP.

Some more complex geometries have been also explored. A hybrid mushroom-shaped nanoantenna was devised to attain high excitation rates, quantum yields, and fluorescent enhancements (average fluorescent enhancement of 10). The metallic stripe was designed to resonate at the excitation wavelength, while the dielectric cap resonated at the emission wavelength of the emitter. The dielectric cap was able to provide high radiative decay rates (≈ 90) and quantum yields (≈ 0.8). Furthermore, about 70% of the radiation was scattered toward the cap [88]. Fluorescent enhancement was also shown for a hybrid nanoantenna consisting of an inner metal nanodisk and an outer dielectric ring. With this nanostructure, a fluorescent enhancement factor of 80 was

achieved. It corresponds to 10 times more than observed for the pure metallic or dielectric structure. Moreover, 70% of the radiation was emitted upwards [89].

Other configurations combine dimers of metallic NPs with dielectric Yagi-Uda-like antennas to get strong emission enhancement (thanks to the dimer) and directionality effects (caused by the dielectric antenna). In [90], a quantum emitter was located in the gap of a Au bowtie antenna, as represented in Fig. 12.5A. The enhanced emission was coupled to a dielectric antenna consisting of three Si nanorods. With this geometry, a Purcell factor of 1800 was reported. In addition, unidirectional in-plane directivity was experimentally demonstrated. Fig. 12.5B shows the experimental and numerical back focal plane images of the described hybrid configuration. Asymmetric emission lobes were observed, being the radiation mainly scattered at $\theta_{max} = 45.5°$ and $\phi_{max} = 90°$ with a full width at half maximum (FWHM) of $\Delta\theta_{max} = 4.6 \pm 0.4°$ and $\Delta\phi_{max} = 27.3 \pm 2.1°$. Taking into account the numerical aperture of the lens in the experiment, it is not possible to collect the light from emission angles larger than 67.3°. These numbers led to a directivity of (≈ 49.2). In [91], a Au cylinder dimer surrounded by Si cylinders was proposed as an efficient structure to enhance the emission of single quantum emitters located in the gap of the Au dimer and to redirect the incident radiation into the forward direction. Purcell factors larger than 3300 were numerically obtained with high radiation efficiencies (> 0.7). Furthermore, values of 5.6 were reported for the directivity.

Hybrid NPoM configurations play an important role in the design of photonic structures for the development of efficient quantum emitters. In particular, HRI dielectric NPs separated from metallic substrates by thin dielectric layers (see Fig. 12.5C) have been proposed to enhance the luminescence of emitters located in the dielectric gap. Due to the strong electromagnetic energy concentration in the dielectric layer (Fig. 12.5D), a photoluminescence enhancement factor of 786 was experimentally demonstrated for a monolayer of colloidal QDs, which conforms the nanogap between a Si NP and a Au substrate. In Fig. 12.5E, it is represented the PL spectra of the QD monolayer on a Au film with (red curve) or without (black curve) Si NP [92]. In [93], the change in the decay rate of a self-assembled CdSe/ZnS QD monolayer (thickness 10 nm), placed on a thin Al_2O_3 layer, which acts as a gap between a Si NP and a Au substrate, was 42-fold compared to the QDs on glass. With respect to the photoluminescence enhancement, for the hybrid configuration, it is 17-fold compared to QDs on glass, 37-fold compared to QDs on a Au film with a 5 nm Al_2O_3 spacer layer, and 188-fold compared to QDs on a bare Au

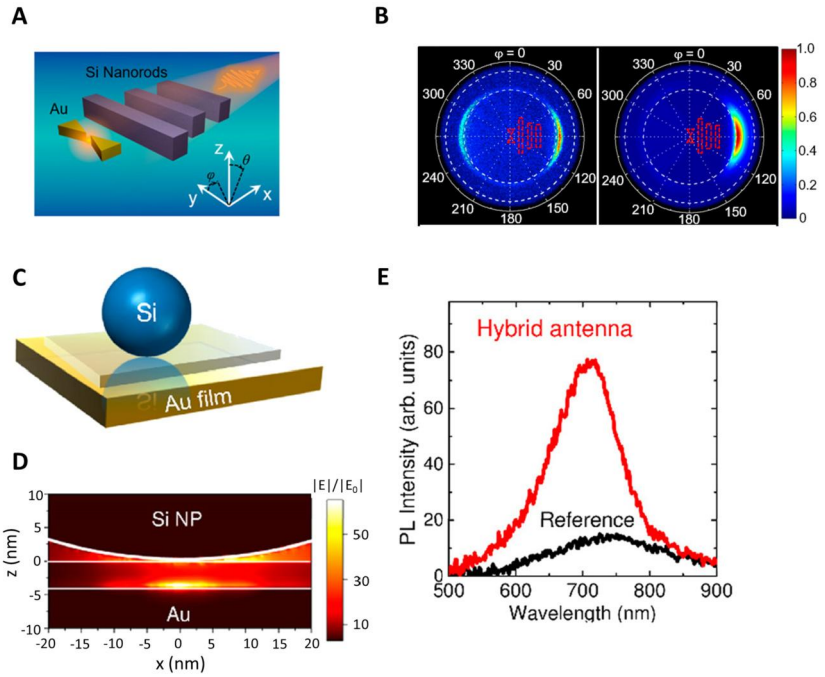

Figure 12.5. (A) Scheme of the hybrid metal-dielectric Yagi-Uda antenna constituted by a Au bowtie antenna and three Si nanorods. (B) Experimental (left) and numerical (right) back focal plane images of the hybrid antennas in (A). Reproduced with permission [90]. Copyright 2018, American Chemical Society. (C) Scheme of a hybrid NPoM configuration. A Si NP is separated of a Au substrate by means of a thin dielectric layer. (D) Electric field enhancement for the configuration in (A) at $\lambda = 650$ nm. (E) PL spectra of the QD monolayer on a Au substrate without the Si NP (black curve) or with the Si NP (red curve). Reproduced with permission [92]. Copyright 2018, American Chemical Society.

film. Furthermore, high quantum efficiencies were attained (more than 80%).

The combination of optical cavities with metallic nanoantennas can provide larger emission enhancements than those achieved with the bare constituents. The hybrid modes due to the coupling between the dielectric cavity and the metallic nanoantenna present large Q-factor values, which come from the cavity, as well as small $\tilde{V}$, due to the metallic nanoantenna, giving rise to extraordinarily high Purcell factors. In addition, both the Q-factor and the $\tilde{V}$ values can be tuned through the hybridization of the plasmonic and photonic modes, thus allowing to achieve the desired Purcell factor value for the required application. In [94], it was demonstrated that in order to observe improved results for the hybrid system compared to the bare cavity or antenna, the cavity resonance must be red-detuned with respect to the antenna resonance.

To understand the electromagnetic behavior of these hybrid systems, Doeleman et al. developed an analytical model based on coupled harmonic oscillators [94]. Both the antenna and cavity are described as coupled harmonic oscillators driven by a dipole source corresponding to the emitter. The application of the model is restricted to weak coupling between the antenna and the cavity. Within this model, the LDOS is expressed as:

$$\boldsymbol{\rho}(\mathbf{r}_0, \omega) = 1 + \frac{6\pi\epsilon_0 c^3}{\omega^3 n}\mathrm{Im}\Big[\alpha_{\mathrm{H}} G_{\mathrm{bg}}^2 + 2G_{\mathrm{bg}}\alpha_{\mathrm{H}}\chi + \chi_{\mathrm{H}}\Big], \tag{12.26}$$

where n is the refractive index of the surrounding medium, c is the speed of light in vacuum, ω corresponds to the optical frequency, ϵ_0 is the vacuum electric permittivity and $\mathbf{r}_0$ is the dipole position.

As can be observed from Eq. (12.26), LDOS is determined by the interference of three different terms. Each of these incorporates the response functions of the antenna and the cavity, given by the multiple scattering interactions between them. $\alpha_{\mathrm{H}} = \alpha/(1-\alpha\chi)$ corresponds to the antenna polarizability, which is perturbed by the presence of the antenna itself, and $\chi_{\mathrm{H}} = \chi/(1-\alpha\chi)$ represents the cavity response function that is modified by the presence of the antenna. These hybrid quantities depend on the bare antenna polarizability α and the bare cavity response function χ. G_{bg} is the Green's function in the surrounding background medium.

Some examples of hybrid photonic-plasmonic cavities are metallic NPs or dimers coupled to dielectric photonic crystals. In [94], the emission enhancement was reported for a whispering-gallery mode cavity coupled to a Au antenna. A scheme of the configuration is depicted in Fig. 12.6A. As it can be observed from Fig. 12.6B, both the antenna and the cavity contribute to the total emission enhancement in the hybrid system. Moreover, from the comparison of the yellow curve (only cavity) with the green one (hybrid system), it is observed how the scattering is enhanced for the hybrid system. The experimental demonstration of such a design was given in [95]. An Al antenna and a silicon nitride (SiN) microdisk conformed the hybrid system. The emitter (QD) was located in the plasmonic hot-spot. The lifetime of the a single QD was decreased by a factor of ≈ 6 compared to obtained for a QD on a glass substrate.

Larger electromagnetic field enhancements and smaller $\tilde{V}$ can be attained by means of dimers, specifically bowtie antennas. With a Au bowtie antenna coupled to a silicon nitride (SiN) photonic crystal, Purcell factors as high as $10^3 - 10^6$ were reported for gaps sizes between the two NPs of the antenna ranging from 25 nm to 1 nm [96]. It was also evidenced that Q-factor and $\tilde{V}$ can take

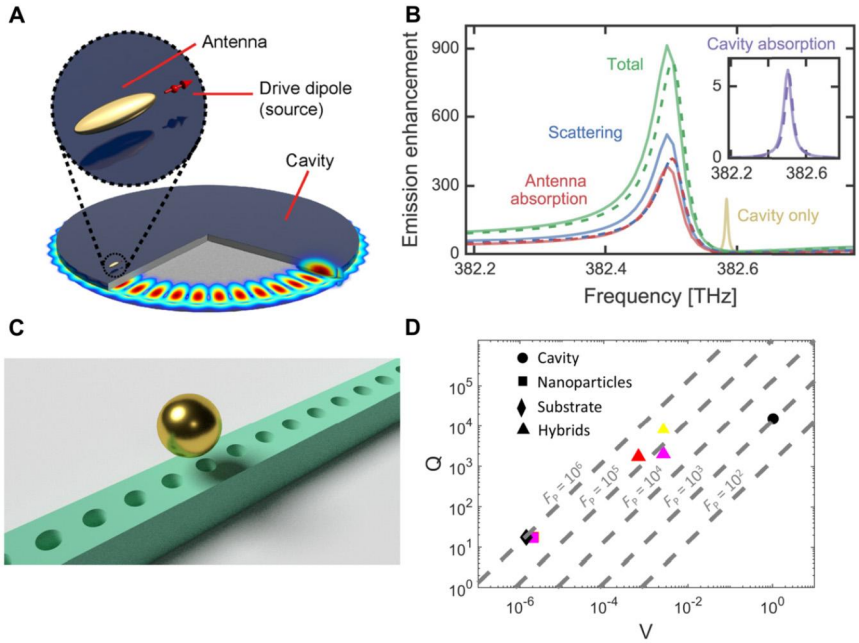

Figure 12.6. (A) Scheme of a hybrid photonic-plasmonic cavity consisting of a disk supporting a whispering gallery mode and a Au ellipsoid. The system is driven by a dipolar source. (B) Total emission enhancement for the hybrid system described in (A) (green). The enhancement due to the scattering into free space and due to the antenna absorption are represented in blue and red lines, respectively. The enhancement due to the cavity absorption is shown as an inset (purple). The enhancement due to the bare cavity is shown in yellow. Solid and dashed lines corresponds to numerical and analytical (oscillator model) results, respectively. Reproduced with permission [94]. Copyright 2016, American Chemical Society. (C) NPoM configuration coupled to a dielectric cavity. A Au NP is located on the top of a (Gallium Phosphide) GaP photonic crystal cavity. (D) Q-factor and $\tilde{V}$ for the bare cavity (circle), bare antennas (cubes), a Au spherical NP ($R = 40$ nm) on a nonstructured GaP substrate, i.e., a Au NP on the GaP photonic crystal without the nanoholes (diamond, called Substrate in the legend), and hybrid system (triangles). The colors correspond to the different geometries considered for the metallic NPs: sphere, yellow; ellipsoid, red; and cube, magenta. Diagonal dashed lines are lines of constant Purcell factor. Reproduced with permission [99]. Copyright 2022, Optica Publishing Group.

intermediate values with respect to the bare cavity (highest Q-factor and highest $\tilde{V}$) and the bare nanoantenna (lowest Q-factor and lowest $\tilde{V}$). A similar structure was proposed in [97]. The optical cavity corresponded to a L3 photonic crystal and the antenna is a Au bowtie. In this work, the ratio $Q/\tilde{V}$ was 25-fold that of a bare L3 photonic crystal and 60-fold the corresponding to a plasmonic bowtie antenna. Strong coupling between light and a single emitter was claimed for such a configuration.

As previously established, apart from emission enhancement, directional properties are also necessary for efficient collection of

the emitted light. A Au nanorod dimer coupled to photonic crystal nanobeam cavity provided an enhancement of the spontaneous emission of 5060 for a single emitter and a collection efficiency of 67% into the dielectric waveguide [98].

Recently, the possibility of combining a NPoM plasmonic cavity and a dielectric nanobeam photonic crystal cavity has been proposed as an alternative to the hybrid structures composed of a bowtie antenna and a dielectric photonic crystal [99]. In the latter configuration, the gap between the NPs of the antenna is lithographically defined, limiting its values experimentally to ≈ 10 nm [100]. However, by means of the NPoM configuration, vertical gaps as small as 1 nm are feasible with the current technology [101].

In [99], it was numerically demonstrated that a system involving a NPoM plasmonic cavity and a dielectric nanobeam photonic crystal cavity (see Fig. 12.6C), operating at transverse-magnetic polarization, can provide Purcell factors larger than 10^5, as it is observed for the diagram in Fig. 12.6D. These Purcell factor values are one order of magnitude larger than those expected for hybrid structures made of plasmonic bowtie antennas and photonic crystals, when gaps of ≈ 10 nm are considered. The described configuration works in the visible spectral region. For that reason, the material chosen for the dielectric cavity was GaP to avoid the losses of other HRI dielectric materials like Si at those wavelengths. Following the same idea of combining NPoM plasmonic cavities with dielectric photonic crystals, a hybrid configuration consisting of a Si photonic crystal cavity with a slot at its center, in which a Au NP is introduced, has been proposed [102]. This structure achieves Purcell factors of $\approx 10^7 - 10^8$. One of the most important differences of this geometry with respect to the one previously described is that it operates in the NIR spectral region, which is of great interest for optical communications. Moreover, Si can be used for the fabrication of the photonic crystal, as its absorption is negligible at wavelengths ≈ 1550 nm. This represents an important advantage as Si photonics have become a mainstream technology for photonic integrated circuits.

12.3 Outlook

The enhancement of light-matter interactions is crucial for many different applications in classical and quantum optics. The increase of the spontaneous emission of a quantum emitter can be achieved by engineering its environment. Over the last decades, different configurations have been proposed to increase the Purcell factor or, equivalently, the LDOS. With the development of

nanotechnology, the possibility of using photonic nanostructures to boost the Purcell factor has been vastly investigated. In particular, metallic NPs have been proposed as an alternative to traditional optical cavities, which are characterized by high Q-factors but also high $\tilde{V}$. On the contrary, the strong electromagnetic energy confinement in the surroundings of metallic nanostructures provides small $\tilde{V}$. Novel designs of NPoM configurations seem promising for pushing $\tilde{V}$ to even smaller values, reaching confinements below 1 nm^3 by means of subwavelength cavities (picocavities). However, the ohmic losses of metallic materials prevent the observation of high Q-factors.

High refractive index dielectric materials present some important advantages with respect to their metallic counterparts. On the one hand, they show low-losses in certain spectral regions, such as visible or near-infrared. On the other hand, in spite of being non-magnetic materials, electric and magnetic resonances can be excited. Furthermore, the coherent interference effects between electric and magnetic modes confer HRI dielectric nanostructures directional properties. Hence, through these nanostructures, high Q-factors, quantum yield values and collection efficiencies can be attained. Nevertheless, HRI dielectric nanostructures also present some disadvantages relative to the metallic ones, namely the larger $\tilde{V}$ and the smaller electromagnetic energy enhancements.

Over the past years, hybrid photonic systems combining metallic and dielectric structures have been explored, as they can merge the best of both worlds: high Q-factors and directional properties of HRI dielectric nanostructures, and small $\tilde{V}$ and strong electromagnetic energy enhancement of metallic nanostructures. Hybrid photonic-plasmonic cavities can enhance the Purcell factor to values of $\approx 10^7$. In addition, by means of the hybridization of the plasmonic and photonic modes, both the Q-factor and the $\tilde{V}$ values can be tuned, obtaining the required Purcell enhancement for a particular application.

Despite the considerable progress in the nanophotonic enhancement of the emission of QDs, 2D materials, perovskites, lanthanide ions, and other quantum emitters, several advances still need to be made to develop quantum emitters that are bright and fast single-photon sources. With the development of quantum information and computation, sources that emit single or entangled photons on demand are of utmost importance. In particular, high quantum yield and fast radiative decay are required. For these reasons, we are convinced that this field will continue to be of interest to the scientific community.

References

[1] A.F. Koenderink, Single-photon nanoantennas, ACS Photonics 4 (4) (2017) 710–722.
[2] E.M. Purcell, Spontaneous Emission Probabilities at Radio Frequencies, Springer US, Boston, MA, 1995, pp. 839–839.
[3] P. Bharadwaj, B. Deutsch, L. Novotny, Optical antennas, Adv. Opt. Photonics 1 (3) (2009) 438–483.
[4] S.I. Lepeshov, A.E. Krasnok, P.A. Belov, A.E. Miroshnichenko, Hybrid nanophotonics, Phys. Usp. 61 (11) (2018) 1035–1050.
[5] K. Wang, E. Schonbrun, P. Steinvurzel, K.B. Crozier, Trapping and rotating nanoparticles using a plasmonic nano-tweezer with an integrated heat sink, Nat. Commun. 2 (2011) 469.
[6] C. Weisbuch, Review—on the search for efficient solid state light emitters: past, present, future, ECS J. Solid State Sci. Technol. 9 (1) (2020) 016022.
[7] A.F. Koenderink, On the use of Purcell factors for plasmon antennas, Opt. Lett. 35 (24) (2010) 4208–4210.
[8] S.A. Maier, Effective mode volume of nanoscale plasmon cavities, Opt. Quantum Electron. 38 (2006) 257–267.
[9] C. Sauvan, J.P. Hugonin, I.S. Maksymov, P. Lalanne, Theory of the spontaneous optical emission of nanosize photonic and plasmon resonators, Phys. Rev. Lett. 110 (2013) 237401.
[10] A.E. Miroshnichenko, Y.S. Kivshar, Fano resonances in all-dielectric oligomers, Nano Lett. 12 (12) (2012) 6459–6463.
[11] S. Yu, H. Li, Y. Wang, Z. Gao, T. Zhao, J. Yu, Multiple Fano resonance excitation of all-dielectric nanoholes cuboid arrays in near infrared region, Results Phys. 28 (2021) 104569.
[12] S. Campione, S. Liu, L.I. Basilio, L.K. Warne, W.L. Langston, T.S. Luk, J.R. Wendt, J.L. Reno, G.A. Keeler, I. Brener, M.B. Sinclair, Broken symmetry dielectric resonators for high quality factor Fano metasurfaces, ACS Photonics 3 (12) (2016) 2362–2367.
[13] K. Koshelev, A. Bogdanov, Y. Kivshar, Engineering with bound states in the continuum, Opt. Photonics News 31 (1) (2020) 38.
[14] S. Liu, A. Vaskin, S. Addamane, B. Leung, M.-C. Tsai, Y. Yang, P.P. Vabishchevich, G.A. Keeler, G. Wang, X. He, Y. Kim, N.F. Hartmann, H. Htoon, S.K. Doorn, M. Zilk, T. Pertsch, G. Balakrishnan, M.B. Sinclair, I. Staude, I. Brener, Light-emitting metasurfaces: simultaneous control of spontaneous emission and far-field radiation, Nano Lett. 18 (11) (2018) 6906–6914.
[15] L. Novotny, B. Hecht, Principles of Nano-Optics, Cambridge University Press, 2006.
[16] A. Vaskin, R. Kolkowski, A.F. Koenderink, I. Staude, Light-emitting metasurfaces, Nanophotonics 8 (7) (2019) 1151–1198.
[17] G. Lozano, S.R.K. Rodriguez, M.A. Verschuuren, J. Gómez Rivas, Metallic nanostructures for efficient LED lighting, Light: Sci. Appl. 5 (6) (2016) e16080.
[18] Serge Haroche, Daniel Kleppner, Cavity quantum electrodynamics, Phys. Today 42 (1) (1989) 24–30, https://doi.org/10.1063/1.881201.
[19] Denis G. Baranov, Martin Wersäll, Jorge Cuadra, Tomasz J. Antosiewicz, Timur Shegai, Novel nanostructures and materials for strong light–matter interactions, ACS Photonics 5 (1) (jan 2018) 24–42.
[20] P. Goy, J.M. Raimond, M. Gross, S. Haroche, Observation of cavity-enhanced single-atom spontaneous emission, Phys. Rev. Lett. 50 (24) (jun 1983) 1903–1906.

[21] C. Weisbuch, M. Nishioka, A. Ishikawa, Y. Arakawa, Observation of the coupled exciton-photon mode splitting in a semiconductor quantum microcavity, Phys. Rev. Lett. 69 (23) (dec 1992) 3314–3317.
[22] Xiaoze Liu, Tal Galfsky, Zheng Sun, Fengnian Xia, Erh-chen Lin, Yi-Hsien Lee, Stéphane Kéna-Cohen, Vinod M. Menon, Strong light–matter coupling in two-dimensional atomic crystals, Nat. Photonics 9 (1) (2015) 30–34.
[23] Tal Ellenbogen, Paul Steinvurzel, Kenneth B. Crozier, Strong coupling between excitons in J-aggregates and waveguide modes in thin polymer films, Appl. Phys. Lett. 98 (26) (jun 2011) 261103.
[24] Gülis Zengin, Göran Johansson, Peter Johansson, Tomasz J. Antosiewicz, Mikael Käll, Timur Shegai, Approaching the strong coupling limit in single plasmonic nanorods interacting with J-aggregates, Sci. Rep. 3 (1) (2013) 3074.
[25] Nche T. Fofang, Nathaniel K. Grady, Zhiyuan Fan, Alexander O. Govorov, Naomi J. Halas, Plexciton dynamics: exciton–plasmon coupling in a J-aggregate–Au nanoshell complex provides a mechanism for nonlinearity, Nano Lett. 11 (4) (apr 2011) 1556–1560.
[26] Nche T. Fofang, Tae-Ho Park, Oara Neumann, Nikolay A. Mirin, Peter Nordlander, Naomi J. Halas, Plexcitonic nanoparticles: plasmon–exciton coupling in nanoshell–J-aggregate complexes, Nano Lett. 8 (10) (oct 2008) 3481–3487.
[27] Jongwon Lee, Seungyong Jung, Pai-Yen Chen, Feng Lu, Frederic Demmerle, Gerhard Boehm, Markus-Christian Amann, Andrea Alù, Mikhail A. Belkin, Ultrafast electrically tunable polaritonic metasurfaces, Adv. Opt. Mater. 2 (11) (nov 2014) 1057–1063.
[28] Raktim Sarma, Nishant Nookala, Kevin James Reilly, Sheng Liu, Domenico de Ceglia, Luca Carletti, Michael D. Goldflam, Salvatore Campione, Keshab Sapkota, Huck Green, George T. Wang, John Klem, Michael B. Sinclair, Mikhail A. Belkin, Igal Brener, Strong coupling in all-dielectric intersubband polaritonic metasurfaces, Nano Lett. 21 (1) (jan 2021) 367–374.
[29] Y. Todorov, A.M. Andrews, I. Sagnes, R. Colombelli, P. Klang, G. Strasser, C. Sirtori, Strong light-matter coupling in subwavelength metal-dielectric microcavities at terahertz frequencies, Phys. Rev. Lett. 102 (18) (may 2009) 186402.
[30] Y. Todorov, A.M. Andrews, R. Colombelli, S. De Liberato, C. Ciuti, P. Klang, G. Strasser, C. Sirtori, Ultrastrong light-matter coupling regime with polariton dots, Phys. Rev. Lett. 105 (19) (nov 2010) 196402.
[31] Adriana Canales, Denis G. Baranov, Tomasz J. Antosiewicz, Timur Shegai, Abundance of cavity-free polaritonic states in resonant materials and nanostructures, J. Chem. Phys. 154 (2) (jan 2021) 24701.
[32] P.B. Deotare, M.W. McCutcheon, I.W. Frank, M. Khan, M. Lončar, High quality factor photonic crystal nanobeam cavities, Appl. Phys. Lett. 94 (12) (2009) 121106.
[33] Y. Akahane, T. Asano, B.-S. Song, S. Noda, High-q photonic nanocavity in a two-dimensional photonic crystal, Nature 425 (2003) 944–947.
[34] A. Samanta, R. Gangopadhyay, C.K. Ghosh, M. Ray, Enhanced photoluminescence from gold nanoparticle decorated polyaniline nanowire bundles, RSC Adv. 7 (2017) 27473–27479.
[35] D. Sivun, C. Vidal, B. Munkhbat, N. Arnold, T.A. Klar, C. Hrelescu, Anticorrelation of photoluminescence from gold nanoparticle dimers with hot-spot intensity, Nano Lett. 16 (11) (2016) 7203–7209.
[36] F. Benz, R. Chikkaraddy, A. Salmon, H. Ohadi, B. de Nijs, J. Mertens, C. Carnegie, R.W. Bowman, J.J. Baumberg, SERS of individual nanoparticles on

a mirror: size does matter, but so does shape, J. Phys. Chem. Lett. 7 (12) (2016) 2264–2269.
[37] J.J. Baumberg, J. Aizpurua, M.H. Mikkelsen, D.R. Smith, Extreme nanophotonics from ultrathin metallic gaps, Nat. Mater. 18 (2019) 668–678.
[38] Daniela F. Cruz, Cassio M. Fontes, Daria Semeniak, Jiani Huang, Angus Hucknall, Ashutosh Chilkoti, Maiken H. Mikkelsen, Ultrabright fluorescence readout of an inkjet-printed immunoassay using plasmonic nanogap cavities, Nano Lett. 20 (6) (2020) 4330–4336.
[39] Hiroyuki Kishida, Maiken H. Mikkelsen, Ultrafast lifetime and bright emission from graphene quantum dots using plasmonic nanogap cavities, Nano Lett. 22 (3) (2022) 904–910.
[40] T. Coenen, F.B. Arango, A.F. Koenderink, A. Polman, Directional emission from a single plasmonic scatterer, Nat. Commun. 5 (2014) 3250.
[41] Nitzan Livneh, Moshe G. Harats, Daniel Istrati, Hagai S. Eisenberg, Ronen Rapaport, Highly directional room-temperature single photon device, Nano Lett. 16 (4) (2016) 2527–2532.
[42] I. Staude, T. Pertsch, Y.S. Kivshar, All-dielectric resonant meta-optics lightens up, ACS Photonics 6 (4) (2019) 802–814.
[43] A.I. Kuznetsov, A.E. Miroshnichenko, M.L. Brongersma, Y.S. Kivshar, B. Luk'yanchuk, Optically resonant dielectric nanostructures, Science 354 (6314) (2016).
[44] I. Staude, J. Schilling, Metamaterial-inspired silicon nanophotonics, Nat. Photonics 11 (5) (2017) 274–284.
[45] Gustav Mie, Beiträge zur Optik trüber Medien, speziell kolloidaler Metallösungen, Ann. Phys. 330 (3) (1908) 377–445.
[46] F. Zhang, X. Huang, Q. Zhao, L. Chen, Y. Wang, Q. Li, X. He, C. Li, K. Chen, Fano resonance of an asymmetric dielectric wire pair, Appl. Phys. Lett. 105 (17) (2014) 172901.
[47] P. Albella, M.A. Poyli, M.K. Schmidt, S.A. Maier, F. Moreno, J.J. Sáenz, J. Aizpurua, Low-loss electric and magnetic field-enhanced spectroscopy with subwavelength silicon dimers, J. Phys. Chem. C 117 (26) (2013) 13573–13584.
[48] M. Caldarola, P. Albella, E. Cortés, M. Rahmani, T. Roschuk, G. Grinblat, R.F. Oulton, A.V. Bragas, S.A. Maier, Non-plasmonic nanoantennas for surface enhanced spectroscopies with ultra-low heat conversion, Nat. Commun. 6 (1) (2015).
[49] S. Li, C. Zhou, T. Liu, S. Xiao, Symmetry-protected bound states in the continuum supported by all-dielectric metasurfaces, Phys. Rev. A 100 (6) (2019).
[50] Mingkai Liu, Duk-Yong Choi, Extreme Huygens' metasurfaces based on quasi-bound states in the continuum, Nano Lett. 18 (12) (November 2018) 8062–8069.
[51] Juan Wang, Julius Kühne, Theodosios Karamanos, Carsten Rockstuhl, Stefan A. Maier, Andreas Tittl, All-dielectric crescent metasurface sensor driven by bound states in the continuum, Adv. Funct. Mater. 31 (46) (August 2021) 2104652.
[52] R. Gómez-Medina, Electric and magnetic dipolar response of germanium nanospheres: interference effects, scattering anisotropy, and optical forces, J. Nanophotonics 5 (1) (2011) 053512.
[53] M. Decker, I. Staude, Resonant dielectric nanostructures: a low-loss platform for functional nanophotonics, J. Opt. 18 (10) (2016) 103001.
[54] A. Vaskin, J. Bohn, K.E. Chong, T. Bucher, M. Zilk, D.Y. Choi, D.N. Neshev, Y.S. Kivshar, T. Pertsch, I. Staude, Directional and spectral shaping of light

emission with Mie-resonant silicon nanoantenna arrays, ACS Photonics 5 (4) (2018) 1359–1364.
[55] S. Yuan, X. Qiu, C. Cui, L. Zhu, Y. Wang, Y. Li, J. Song, Q. Huang, J. Xia, Strong photoluminescence enhancement in all-dielectric Fano metasurface with high quality factor, ACS Nano 11 (11) (2017) 10704–10711.
[56] A. Vaskin, S. Liu, S. Addamane, P.P. Vabishchevich, Y. Yang, G. Balarishnan, M.B. Sinclair, T. Pertsch, I. Brener, I. Staude, Manipulation of quantum dot emission with semiconductor metasurfaces exhibiting magnetic quadrupole resonances, Opt. Express 29 (4) (2021) 5567.
[57] C. Cui, S. Yuan, X. Qiu, L. Zhu, Y. Wang, Y. Li, J. Song, Q. Huang, C. Zeng, J. Xia, Light emission driven by magnetic and electric toroidal dipole resonances in a silicon metasurface, Nanoscale 11 (30) (2019) 14446–14454.
[58] P. Tonkaev, I.S. Sinev, M.V. Rybin, S.V. Makarov, Y. Kivshar, Multifunctional and transformative metaphotonics with emerging materials, Chem. Rev. 122 (19) (2022) 15414–15449.
[59] J. van de Groep, J.-H. Song, U. Celano, Q. Li, P.G. Kik, M.L. Brongersma, Exciton resonance tuning of an atomically thin lens, Nat. Photonics 14 (7) (2020) 426–430.
[60] T. Bucher, A. Vaskin, R. Mupparapu, F.J.F. Löchner, A. George, K.E. Chong, S. Fasold, C. Neumann, D.-Y. Choi, F. Eilenberger, F. Setzpfandt, Y.S. Kivshar, T. Pertsch, A. Turchanin, I. Staude, Tailoring photoluminescence from MoS_2 monolayers by Mie-resonant metasurfaces, ACS Photonics 6 (4) (2019) 1002–1009.
[61] N. Muhammad, Y. Chen, C.-W. Qiu, G.P. Wang, Optical bound states in continuum in MoS_2-based metasurface for directional light emission, Nano Lett. 21 (2) (2021) 967–972.
[62] L. Yuan, J. Jeong, K.W.C. Kwock, E.S. Yanev, M. Grandel, D.A. Rhodes, T.S. Luk, P.J. Schuck, D. Yarotski, J.C. Hone, I. Brener, R.P. Prasankumar, Manipulation of exciton dynamics in single-layer WSe_2 using a toroidal dielectric metasurface, Nano Lett. 21 (23) (2021) 9930–9938.
[63] S.V. Makarov, V. Milichko, E.V. Ushakova, M. Omelyanovich, A. Cerdan Pasaran, R. Haroldson, B. Balachandran, H. Wang, W. Hu, Y.S. Kivshar, A.A. Zakhidov, Multifold emission enhancement in nanoimprinted hybrid perovskite metasurfaces, ACS Photonics 4 (4) (2017) 728–735.
[64] T.H. Taminiau, S. Karaveli, N.F. van Hulst, R. Zia, Quantifying the magnetic nature of light emission, Nat. Commun. 3 (1) (2012).
[65] R. Hussain, S.S. Kruk, C.E. Bonner, M.A. Noginov, I. Staude, Y.S. Kivshar, N. Noginova, D.N. Neshev, Enhancing Eu^{3+} magnetic dipole emission by resonant plasmonic nanostructures, Opt. Lett. 40 (8) (2015) 1659.
[66] M. Sanz-Paz, C. Ernandes, J.U. Esparza, G.W. Burr, N.F. van Hulst, A. Maitre, L. Aigouy, T. Gacoin, N. Bonod, M.F. Garcia-Parajo, S. Bidault, M. Mivelle, Enhancing magnetic light emission with all-dielectric optical nanoantennas, Nano Lett. 18 (6) (2018) 3481–3487.
[67] A. Vaskin, S. Mashhadi, M. Steinert, K.E. Chong, D. Keene, S. Nanz, A. Abass, E. Rusak, D.-Y. Choi, I. Fernandez-Corbaton, T. Pertsch, C. Rockstuhl, M.A. Noginov, Y.S. Kivshar, D.N. Neshev, N. Noginova, I. Staude, Manipulation of magnetic dipole emission from Eu^{3+} with Mie-resonant dielectric metasurfaces, Nano Lett. 19 (2) (2019) 1015–1022.
[68] H. Sugimoto, M. Fujii, Magnetic Purcell enhancement by magnetic quadrupole resonance of dielectric nanosphere antenna, ACS Photonics 8 (6) (2021) 1794–1800.
[69] C. Tserkezis, P.A.D. Gonçalves, C. Wolff, F. Todisco, K. Busch, N.A. Mortensen, Mie excitons: understanding strong coupling in dielectric nanoparticles, Phys. Rev. B 98 (15) (oct 2018) 155439.

[70] S. Lepeshov, A. Krasnok, O. Kotov, A. Alu, Strong coupling in Si nanoparticle core - 2D WS_2 shell structure, J. Phys. Conf. Ser. 1092 (2018) 12077.
[71] Ruggero Verre, Denis G. Baranov, Battulga Munkhbat, Jorge Cuadra, Mikael Käll, Timur Shegai, Transition metal dichalcogenide nanodisks as high-index dielectric Mie nanoresonators, Nat. Nanotechnol. 14 (July 2019) 679–684.
[72] Nguyen Ha My Dang, Dario Gerace, Emmanuel Drouard, Gaëlle Trippé-Allard, Ferdinand Lédée, Radoslaw Mazurczyk, Emmanuelle Deleporte, Christian Seassal, Hai Son Nguyen, Tailoring dispersion of room-temperature exciton-polaritons with perovskite-based subwavelength metasurfaces, Nano Lett. 20 (3) (mar 2020) 2113–2119.
[73] Seongheon Kim, Byung Hoon Woo, Soo-Chan An, Yeonsoo Lim, In Cheol Seo, Dai-Sik Kim, SeokJae Yoo, Q-Han Park, Young Chul Jun, Topological control of 2D perovskite emission in the strong coupling regime, Nano Lett. 21 (23) (dec 2021) 10076–10085.
[74] Shaojun Wang, T.V. Raziman, Shunsuke Murai, Gabriel W. Castellanos, Ping Bai, Anton Matthijs Berghuis, Rasmus H. Godiksen, Alberto G. Curto, Jaime Gómez Rivas, Collective Mie exciton-polaritons in an atomically thin semiconductor, J. Phys. Chem. C 124 (35) (sep 2020) 19196–19203.
[75] Yueyang Chen, Shengnan Miao, Tianmeng Wang, Ding Zhong, Abhi Saxena, Colin Chow, James Whitehead, Dario Gerace, Xiaodong Xu, Su-Fei Shi, Arka Majumdar, Metasurface integrated monolayer exciton polariton, Nano Lett. 20 (7) (jul 2020) 5292–5300.
[76] Mengyao Li, Ivan Sinev, Fedor Benimetskiy, Tatyana Ivanova, Ekaterina Khestanova, Svetlana Kiriushechkina, Anton Vakulenko, Sriram Guddala, Maurice Skolnick, Vinod M. Menon, Dmitry Krizhanovskii, Andrea Alù, Anton Samusev, Alexander B. Khanikaev, Experimental observation of topological Z2 exciton-polaritons in transition metal dichalcogenide monolayers, Nat. Commun. 12 (1) (2021) 4425.
[77] Raktim Sarma, Jiaming Xu, Domenico de Ceglia, Luca Carletti, Salvatore Campione, John Klem, Michael B. Sinclair, Mikhail A. Belkin, Igal Brener, An all-dielectric polaritonic metasurface with a giant nonlinear optical response, Nano Lett. 22 (3) (feb 2022) 896–903.
[78] Jaeyeon Yu, Seongjin Park, Inyong Hwang, Daeik Kim, Frederic Demmerle, Gerhard Boehm, Markus-Christian Amann, Mikhail A. Belkin, Jongwon Lee, Electrically tunable nonlinear polaritonic metasurface, Nat. Photonics 16 (1) (2022) 72–78.
[79] Deng Hui, Weihs Gregor, Snoke David, Bloch Jacqueline, Yamamoto Yoshihisa, Polariton lasing vs. photon lasing in a semiconductor microcavity, Proc. Natl. Acad. Sci. 100 (26) (dec 2003) 15318–15323.
[80] Anton Frisk Kockum, Adam Miranowicz, Simone De Liberato, Salvatore Savasta, Franco Nori, Ultrastrong coupling between light and matter, Nat. Rev. Phys. 1 (1) (2019) 19–40.
[81] Mathieu Jeannin, Giacomo Mariotti Nesurini, Stéphan Suffit, Djamal Gacemi, Angela Vasanelli, Lianhe Li, Alexander Giles Davies, Edmund Linfield, Carlo Sirtori, Yanko Todorov, Ultrastrong light-matter coupling in deeply subwavelength THz LC resonators, ACS Photonics 6 (5) (2019) 1207–1215.
[82] G. Günter, A.A. Anappara, J. Hees, A. Sell, G. Biasiol, L. Sorba, S. De Liberato, C. Ciuti, A. Tredicucci, A. Leitenstorfer, R. Huber, Sub-cycle switch-on of ultrastrong light–matter interaction, Nature 458 (7235) (2009) 178–181.
[83] G. Scalari, C. Maissen, D. Turčinková, D. Hagenmüller, S. De Liberato, C. Ciuti, C. Reichl, D. Schuh, W. Wegscheider, M. Beck, J. Faist, Ultrastrong

coupling of the cyclotron transition of a 2D electron gas to a THz metamaterial, Science 335 (6074) (2012) 1323–1326.
[84] Salvatore Gambino, Marco Mazzeo, Armando Genco, Omar Di Stefano, Salvatore Savasta, Salvatore Patanè, Dario Ballarini, Federica Mangione, Giovanni Lerario, Daniele Sanvitto, Giuseppe Gigli, Exploring light–matter interaction phenomena under ultrastrong coupling regime, ACS Photonics 1 (10) (oct 2014) 1042–1048.
[85] E. Rusak, I. Staude, M. Decker, J. Sautter, A.E. Miroshnichenko, D.A. Powell, D.N. Neshev, Y.S. Kivshar, Hybrid nanoantennas for directional emission enhancement, Appl. Phys. Lett. 105 (22) (2014) 221109.
[86] Y. Sun, V. Yaroshenko, A. Chebykin, E. Ageev, S. Makarov, D. Zuev, Metal-dielectric nanoantenna for radiation control of a single-photon emitter, Opt. Mater. Express 10 (1) (2020) 29–35.
[87] S. Sun, M. Li, Q. Du, C.E. Png, P. Bai, Metal–dielectric hybrid dimer nanoantenna: coupling between surface plasmons and dielectric resonances for fluorescence enhancement, J. Phys. Chem. C 121 (23) (2017) 12871–12884.
[88] S. Sun, R. Li, M. Li, Q. Du, C.E. Png, P. Bai, Hybrid mushroom nanoantenna for fluorescence enhancement by matching the Stokes shift of the emitter, J. Phys. Chem. C 122 (26) (2018) 14771–14780.
[89] S. Sun, T. Zhang, Q. Liu, L. Ma, Q. Du, H. Duan, Enhanced directional fluorescence emission of randomly oriented emitters via a metal-dielectric hybrid nanoantenna, J. Phys. Chem. C 123 (34) (2019) 21150–21160.
[90] J. Ho, Y.H. Fu, Z. Dong, R. Paniagua-Dominguez, E.H.H. Koay, Y.F. Yu, V. Valuckas, A.I. Kuznetsov, J.K.W. Yang, Highly directive hybrid metal-dielectric Yagi-Uda nanoantennas, ACS Nano 12 (8) (2018) 8616–8624.
[91] A. Barreda, S. Hell, M.A. Weissflog, A. Minovich, T. Pertsch, I. Staude, Metal, dielectric and hybrid nanoantennas for enhancing the emission of single quantum dots: a comparative study, J. Quant. Spectrosc. Radiat. Transf. 276 (2021) 107900.
[92] H. Sugimoto, M. Fujii, Broadband dielectric–metal hybrid nanoantenna: silicon nanoparticle on a mirror, ACS Photonics 5 (5) (2018) 1986–1993.
[93] G. Yang, Y. Niu, H. Wei, B. Bai, H.-B. Sun, Greatly amplified spontaneous emission of colloidal quantum dots mediated by a dielectric-plasmonic hybrid nanoantenna, Nanophotonics 8 (12) (2019) 2313–2319.
[94] H.M. Doeleman, E. Verhagen, A.F. Koenderink, Antenna-cavity hybrids: matching polar opposites for purcell enhancements at any linewidth, ACS Photonics 3 (10) (2016) 1943–1951.
[95] H.M. Doeleman, C.D. Dieleman, C. Mennes, B. Ehrler, A.F. Koenderink, Observation of cooperative Purcell enhancements in antenna–cavity hybrids, ACS Nano 14 (9) (2020) 12027–12036.
[96] I.M. Palstra, H.M. Doeleman, A.F. Koenderink, Hybrid cavity-antenna systems for quantum optics outside the cryostat?, Nanophotonics 8 (9) (2019) 1513–1531.
[97] H. Zhang, Y.-C. Liu, C. Wang, N. Zhang, C. Lu, Hybrid photonic-plasmonic nano-cavity with ultra-high Q/V, Opt. Lett. 45 (17) (2020) 4794–4797.
[98] G. Zhu, Q. Liao, Highly efficient collection for photon emission enhanced by the hybrid photonic-plasmonic cavity, Opt. Express 26 (24) (2018) 31391–31401.
[99] A.I. Barreda, M. Zapata-Herrera, I.M. Palstra, L. Mercadé, J. Aizpurua, A. Femius Koenderink, A. Martínez, Hybrid photonic-plasmonic cavities based on the nanoparticle-on-a-mirror configuration, Photon. Res. 9 (12) (2021) 2398–2419.

[100] N.A. Hatab, C.-H. Hsueh, A.L. Gaddis, S.T. Retterer, J.-H. Li, G. Eres, Z. Zhang, B. Gu, Free-standing optical gold bowtie nanoantenna with variable gap size for enhanced Raman spectroscopy, Nano Lett. 10 (12) (2010) 4952–4955.
[101] C. Carnegie, J. Griffiths, B. de Nijs, C. Readman, R. Chikkaraddy, W.M. Deacon, Y. Zhang, I. Szabó, E. Rosta, J. Aizpurua, J.J. Baumberg, Room-temperature optical picocavities below 1 nm^3 accessing single-atom geometries, J. Phys. Chem. Lett. 9 (24) (2018) 7146–7151.
[102] Angela Barreda, Laura Mercadé, Mario Zapata-Herrera, Javier Aizpurua, Alejandro Martínez, Hybrid photonic-plasmonic cavity design for very large Purcell factors at telecommunication wavelengths, Phys. Rev. Appl. 18 (2022) 044066.

13

Summary, future perspectives, and new directions

Due to their multiple advantages, all-dielectric metasurfaces (ADM) have emerged as a viable technique in modern optical technologies. Optical metasurfaces provide miniaturization of optical components, enabling smart features that are difficult to achieve with conventional optics and quick real-time reconfigurability of optical functions. They also provide an opportunity to investigate various spectral ranges that are not accessible with standard glass optics and CMOS cameras, particularly in the infrared spectrum. Over the past five years, the development of all-dielectric metasurfaces has resulted in an exponential growth of ideas in the research field. Machine vision is an important use of this technology, with capabilities that exceed human eyesight and enable machine autonomy. The use of metasurfaces in augmented reality (AR) and virtual reality (VR) technologies, and machine-human interfaces is becoming increasingly essential. The use of metasurfaces in space applications is also interesting, although it requires thorough space testing to ensure compatibility.

One of the major issues in this sector is the tunability of the metasurface's optical response, which includes amplitude and phase of transmission, polarization, and dispersion, among other things. The capacity to modify the transmitted phase can transform a single metasurface into a tunable focal length lens, a beam shaper, or a hologram. The tunability of metasurfaces can be enabled by three generic tuning principles: changing the resonator material, the surrounding environment, and the shape. The application limitations will most likely define the appropriate mechanism for each application. Other major hurdles in this field include full control of angular and spectral dispersion and the requirement for tools to fully construct large-area optical systems. Inverse design activities such as end-to-end designs and large-scale meta-optics have been developed to solve these issues. A prominent area of interest is the coupling of optical metasurfaces to other material degrees of freedom, such as atomic, ex-

All-Dielectric Nanophotonics. https://doi.org/10.1016/B978-0-32-395195-1.00018-1
Copyright © 2024 Elsevier Ltd. All rights reserved.

citonic, phononic, and polaritonic excitations. In the strong coupling regime, optical and material properties hybridize, resulting in new physical phenomena that can only be revealed in the future. One example of a novel phenomenon is the alteration of chemical reactions.

All-dielectric metasurfaces can exhibit a strong nonlinear response due to their light-matter interaction properties. By using an all-dielectric metasurface, for example, it is possible to enhance the Kerr effect, allowing it to achieve a much stronger nonlinear response compared to bulk materials. The electrostriction effect is another important nonlinear mechanism in all-dielectric metasurfaces. It arises from the deformation of a material in response to an applied electric field. By engineering the geometry of the metasurface, it is possible to enhance the electrostriction effect, which can be used to create efficient modulators and sensors. Alternatively, piezoelectricity occurs when a substance develops an electric field in response to mechanical stress. Piezoelectricity can be observed in all-dielectric metasurfaces due to their subwavelength geometry. This effect has the potential to be utilized in the development of efficient mechanical sensors and energy harvesters.

Realizing nonlinear effects and light-matter interactions in all-dielectric metasurfaces can be difficult. A strong nonlinear response, for example, necessitates a high optical field intensity, which is difficult to generate with standard laser sources. Furthermore, designing and fabricating all-dielectric metasurfaces with the required subwavelength features and precise geometry can be difficult and may necessitate the use of advanced fabrication techniques such as electron beam lithography or focused ion beam milling. Nonetheless, recent advancements in fabrication techniques and material design have enabled us to overcome these obstacles and fully realize the potential of all-dielectric metasurfaces for nonlinear optics and optoelectronics.

ADMs research is a rapidly expanding topic with considerable application possibilities. Recent advancements in ADMs have shown promise in terms of producing high-efficiency, low-loss, and tunable metasurfaces. The discovery of innovative materials and designs and the development of scalable fabrication procedures are important research fields. Despite substantial advances in ADMs research, a number of obstacles and opportunities remain. One of the most difficult issues is establishing scalable and low-cost production procedures for large-area metasurfaces with great uniformity and reproducibility. Another difficulty is creating metasurfaces that can operate across a wide range of wavelengths, angles of incidence, and polarization states.

To enable large-scale and low-cost ADM manufacture, there is an urgent and ongoing search for innovative technologies and materials to tackle these challenges.

Simultaneously, a new class of materials with promising properties for all-dielectric metasurfaces is being explored, such as transition metal dichalcogenides (TMDCs), a 2D material family. One of the primary benefits of TMDCs is their strong light-matter interaction due to their high oscillator strength and the existence of excitons. When firmly linked to resonant dielectric structures, these excitons can generate hybrid light-matter states with enhanced absorption, emission, and nonlinear optical effects. Furthermore, by adjusting the size, shape, and orientation of the TMDC flakes, TMDC-based metasurfaces provide flexibility in tuning optical properties such as absorption, polarization, and light directionality. Another significant advancement in TMDC-based metasurfaces is the ability to construct chiral and nonreciprocal optical responses. They are able to selectively transmit or reflect circularly polarized light by stacking TMDC flakes with opposing handedness or breaking the system's symmetry, paving the way for possible applications in chiral sensing, polarization imaging, and optoelectronic devices. Furthermore, recent advances in TMDC-based metasurfaces have focused on achieving ultra-high Q-factors and bound-states-in-the-continuum (BICs), which can improve sensor sensitivity and selectivity as well as the performance of optical resonators. This has been accomplished by employing innovative designs, such as hybrid photonic-plasmonic resonators, and sophisticated production techniques, such as atomic layer deposition and focused ion beam milling. Metasurfaces based on TMDC offer enormous promise for optics, sensing, and nanophotonics use. They are promising candidates for next-generation all-dielectric metasurfaces because of their strong light-matter interaction, polarization control, chiral and nonreciprocal effects, and ultra-high Q-factors and BICs. However, more research is required to overcome the challenges of large-scale fabrication and integration with other materials and devices, and to optimize their optical properties for specific applications.

Tunable metasurfaces present a significant challenge in the field of optical metasurfaces. The ability to tune the optical response of metasurfaces is critical for many applications, such as programmable meta-optical elements, which can perform arbitrary operations depending on an external stimulus. Tunable metasurfaces can also enable reconfigurable optics and provide flexibility in optical system design.

Controlling amplitude and phase modulation, polarization, and dispersion simultaneously is a major challenge for tunable

metasurfaces. To achieve this, a unified strategy and appropriate mechanism that meets the constraints of various applications must be developed. Most investigations on tunable metasurfaces have only shown amplitude modulation to date. On the other hand, the ability to change the transmitted phase can turn a single metasurface into a lens with a variable focal length, a beam shaper, or a hologram. Similarly, the ability to tune polarization allows for polarization-sensitive imaging or optical field polarization management. To do this, two optical modes of the metasurface must be managed at the same time, which mandates the use of two control parameters.

Tuning metasurfaces is based on three general principles: changing the resonator material, changing the surrounding environment, and modifying the shape. Different physical mechanisms, such as the incorporation of phase-change materials, thermo-optic effects, electro-optic effects, carrier injection, liquid crystals, and mechanical actuation, can all contribute to these tuning principles. GST ($Ge_2Sb_2Te_5$) and other phase-change materials are showing promise for phase modulation in metasurfaces. These materials can transition from an amorphous to a crystalline phase, which causes significant changes in their optical characteristics. Tuning can take advantage of thermo-optic phenomena, which modify the refractive index of materials with temperature. Tuning can also be accomplished by using electro-optic phenomena, which affect the refractive index of materials in the presence of an electric field. Carrier injection can be used to modify the electrical characteristics of materials to change their refractive index. Another possibility is liquid crystals, which may be aligned in a given direction by applying an electric or magnetic field, resulting in polarization control of the transmitted light. Finally, mechanical actuation can change the metasurface's optical properties by tuning its geometry.

Despite the promise of these mechanisms, no cohesive strategy exists so far, and most publications have merely presented amplitude modulation. Furthermore, achieving full continuous 2π phase modulation or full polarization control remains challenging. For example, attaining 2π phase modulation necessitates tuning the resonator geometry, material properties, and surrounding environment, all of which are complex and interrelated. Furthermore, some tuning mechanisms, such as thermo-optic effects, can be slow and consume much power. As a result, an appropriate mechanism for a certain application must be designed by considering its constraints, such as response time, power consumption, and compatibility with other optical components.

Regardless of current limitations, the maturation and development of all-dielectric metasurfaces have opened up a multitude of new prospects in modern optical technology. Among the challenges addressed in this subject are the tunability of the metasurface's optical response, full control of angular and spectral dispersion, and the need for tools to design large-area optical systems. Another exciting study area is the relationship between optical metasurfaces and other material degrees of freedom.

This page intentionally left blank

Index

M

Q

R

S

T

This page intentionally left blank

ALL-DIELECTRIC NANOPHOTONICS

NANOPHOTONICS SERIES

EDITED BY

ALEXANDER S. SHALIN, ADRIÀ CANÓS VALERO, AND ANDREY MIROSHNICHENKO

All-Dielectric Nanophotonics aims to review the underlying principles, advances, and future directions of research in the field. Chapters are written by leading scientists in all-dielectric nanophotonics and provide a comprehensive theoretical background to all the core concepts.

In particular, this book reviews the progress in all-dielectric metasurfaces and nanoantennas, new types of excitations, such as magnetic and toroidal modes, and associated anapole states. Ultrahigh-Q resonant modes such as bound states in the continuum are covered, and the promise of replacing conventional bulky optical elements with nanometer-scale structures with enhanced functionality is discussed.

All-Dielectric Nanophotonics is suitable for new entrants to the field as an overview of this research area. Experienced researchers and professionals in the field may also find this book suitable as a reference.

Key Features

- Provides an overview of the fundamental principles, theories, and calculation techniques underpinning all-dielectric nanophotonics research
- Reviews the current progress in the field, such as all-dielectric metasurfaces and nanoantennas, new types of excitations, and associated anapole states
- Discusses emerging applications such as active nanophotonics with in-depth analysis

About the Editors

Dr. Alexander S. Shalin is a Principal Researcher in Moscow Institute of Physics and Technology and an Associate Professor at Riga Technical University. He has contributed extensively to the development of all-dielectric nanophotonics, including but not limited to the introduction of higher-order toroidal moments and hybrid anapole states, studies on the optomechanical interactions of dielectric nanoparticles, the first proposal of the unusual transverse Kerker effect and new principles of superscattering.

Dr. Adrià Canós Valero received his MSc in Materials Science and Engineering from the EEIGM, France. After a period at the European Organization for Nuclear Research (CERN) in Switzerland, where his research focused on the study of superconducting materials, he proceeded to pursue his passion for theoretical electromagnetism at the Institute of Physics, University of Graz, Austria. His research is centered around the study of nonradiating sources and non-Hermitian effects arising in all-dielectric nanophotonic platforms.

Dr. Andrey Miroshnichenko is currently a professor at UNSW Canberra in the School of Engineering & Information Technology, Australia. During his career, he has made several fundamental contributions to the development of photonic crystals and played a crucial role in introducing the Fano resonance concept to nanophotonics.

ISBN 978-0-323-95195-1

9 780323 951951

ELSEVIER

elsevier.com/books-and-journals